15 YEARS OF THE FEDERATION OF AFRICAN SOCIETIES OF CHEMISTRY (FASC)

EDITED BY: Neil Coville, James Darkwa, Marian Asantewah Nkansah, Adebola Omowunmi Oyedeji and Mama El Rhazi

PUBLISHED IN: Frontiers in Chemistry

frontiers Research Topics

ISSN 1664-8714
ISBN 978-2-83250-604-2
DOI 10.3389/978-2-83250-604-2

About Frontiers

Frontiers is more than just an open-access publisher of scholarly articles: it is a pioneering approach to the world of academia, radically improving the way scholarly research is managed. The grand vision of Frontiers is a world where all people have an equal opportunity to seek, share and generate knowledge. Frontiers provides immediate and permanent online open access to all its publications, but this alone is not enough to realize our grand goals.

Frontiers Journal Series

The Frontiers Journal Series is a multi-tier and interdisciplinary set of open-access, online journals, promising a paradigm shift from the current review, selection and dissemination processes in academic publishing. All Frontiers journals are driven by researchers for researchers; therefore, they constitute a service to the scholarly community. At the same time, the Frontiers Journal Series operates on a revolutionary invention, the tiered publishing system, initially addressing specific communities of scholars, and gradually climbing up to broader public understanding, thus serving the interests of the lay society, too.

Dedication to Quality

Each Frontiers article is a landmark of the highest quality, thanks to genuinely collaborative interactions between authors and review editors, who include some of the world's best academicians. Research must be certified by peers before entering a stream of knowledge that may eventually reach the public - and shape society; therefore, Frontiers only applies the most rigorous and unbiased reviews.
Frontiers revolutionizes research publishing by freely delivering the most outstanding research, evaluated with no bias from both the academic and social point of view. By applying the most advanced information technologies, Frontiers is catapulting scholarly publishing into a new generation.

What are Frontiers Research Topics?

Frontiers Research Topics are very popular trademarks of the Frontiers Journals Series: they are collections of at least ten articles, all centered on a particular subject. With their unique mix of varied contributions from Original Research to Review Articles, Frontiers Research Topics unify the most influential researchers, the latest key findings and historical advances in a hot research area! Find out more on how to host your own Frontiers Research Topic or contribute to one as an author by contacting the Frontiers Editorial Office: frontiersin.org/about/contact

15 YEARS OF THE FEDERATION OF AFRICAN SOCIETIES OF CHEMISTRY (FASC)

Topic Editors:
Neil Coville, University of the Witwatersrand, South Africa
James Darkwa, Botswana Institute for Technology Research and Innovation (BITRI), Botswana
Marian Asantewah Nkansah, Kwame Nkrumah University of Science and Technology, Ghana
Adebola Omowunmi Oyedeji, Walter Sisulu University, South Africa
Mama El Rhazi, Faculty of Sciences and Technologies of Mohammedia, Morocco

Citation: Coville, N., Darkwa, J., Nkansah, M. A., Oyedeji, A. O., El Rhazi, M., eds. (2022). 15 Years of the Federation of African Societies of Chemistry (FASC). Lausanne: Frontiers Media SA. doi: 10.3389/978-2-83250-604-2

Table of Contents

frontiers | Frontiers in Chemistry

TYPE Editorial
PUBLISHED 12 October 2022
DOI 10.3389/fchem.2022.1046430

OPEN ACCESS

EDITED AND REVIEWED BY
Valeria Conte,
University of Rome Tor Vergata, Italy

*CORRESPONDENCE
James Darkwa,
jdarkwa@gmail.com
Neil J. Coville,
neil.coville@wits.ac.za

SPECIALTY SECTION
This article was submitted to Green and Sustainable Chemistry, a section of the Frontiers in Chemistry

RECEIVED 16 September 2022
ACCEPTED 27 September 2022
PUBLISHED 12 October 2022

CITATION
Darkwa J, Coville NJ, Nkansah MA, Oyedeji AO and El Rhazi M (2022), Editorial: 15 years of the Federation of African Societies of Chemistry (FASC). *Front. Chem.* 10:1046430. doi: 10.3389/fchem.2022.1046430

Editorial: 15 years of the Federation of African Societies of Chemistry (FASC)

James Darkwa[1,2]*, Neil J. Coville[3]*, Marian A. Nkansah[4], Adebola O. Oyedeji[5] and Mama El Rhazi[6]

[1]Natural Resources and Materials Department, Botswana Institute for Technology Research and Innovation, Gaborone, Botswana, [2]Department of Chemical Sciences, University of Johannesburg, Johannesburg, South Africa, [3]Materials Science Institute, School of Chemistry, University of the Witwatersrand, Johannesburg, South Africa, [4]Department of Chemistry, Kwame Nkrumah University of Science and Technology, Kumasi, Ghana, [5]Department of Chemical and Physical Sciences, Walter Sisulu University, Mthatha, South Africa, [6]Faculty of Science and Technology of Mohammedia, University Hassan II Casablanca, Casablanca, Morocco

KEYWORDS

15th anniversary, FASC, green chemistry, chemical research in Africa, international collaboration

Editorial on the Research Topic
15 years of the Federation of African Societies of Chemistry (FASC)

This Research Topic of Frontiers in Chemistry is produced to celebrate the 15th anniversary of the Federation of African Societies of Chemistry (FASC). Established on the 23rd of February 2006, FASC was set up to promote the advancement of chemical sciences and the practice of chemistry that could be instrumental to the fulfillment of the development aspiration and objective of the people in Africa. In order to achieve the above aim, FASC set up the following objectives:

- To promote and maintain effective communication throughout the community of chemists and chemical scientists in Africa.
- To promote collaborative activity among member societies and among the individual members of these societies.
- To maintain and promote high professional, educational and ethical standards.
- To disseminate chemical knowledge.
- To act in an advisory, consultative and representative capacity in relation to African institutions and regional initiatives.
- To promote cooperation with other international organizations and similar regional and international networks.

FASC has championed Green Chemistry as one area of chemistry that could lift the continent into sustainable development. Although FASC conferences have always set aside 1 day during for presentations on either Green Chemistry or Green Chemistry related research, for this Research Topic we broadened the areas for

article submission in order to accommodate as many manuscript submissions as possible. In doing so, we obtained submissions from our community that would reflect contemporary research taking place on the continent. As will also be observed from the list of 61 authors, many African chemists have partnered with chemical scientists from Europe, Asia and North America, some of whom have supported FASC activities over the years. In all we received 19 manuscripts for consideration to be published in this Research Topic. Of these, 12 articles were accepted for publication. The published articles provide a spectrum of some areas of research activities on the continent.

Of the submissions, there are four reviews or perspective articles and eight articles that report data that have not been published before. The articles cover topics such as solar energy, liquid fuels, greener ways to make known materials, water treatment, and a computational approach to making materials from biomass.

The article by Muchuweni et al. provides insight into recent advances on how carbon nanotubes can be used in organic solar cell applications where efficiencies were improved from 0.68% to above 14%. Three more articles report the use of carbon nanotubes or carbon spheres, as supports for catalysts in catalytic reactions. The article by Salhi et al. uses functionalized multi-walled carbon nanotubes as an electrode for the electrochemical sensing of nitrite. The outcome of this study could be used to produce a low-cost, but highly sensitive rapid detection method for nitrite in water, a problem that is prevalent in rural water supplies in developing countries that rely on underground water, possibly contaminated by sewage. In another article, by El Attar et al., a catalyst made by supporting $Cu(OH)_2$-CuO/polypyrrole on multiwalled-carbon nanotubes was shown to efficiently oxidize ethanol in an alkaline medium using electrocatalysis. The third article that uses platinum nanocatalysts supported on a hollow carbon sphere support, by Mashindi et al., revealed the material to be a highly durable and efficient catalyst in oxygen reduction reactions, results that have potential impact on the durability of hydrogen fuel cells.

Another impactful article is that by Mensah et al. The authors explored a DFT approach to understanding how the base-catalyzed cleavage of β-O-4 ether linkages can lead to selective depolymerization of lignin to produce phenolic compounds that are currently produced from fossil fuels. This should encourage synthetic chemists on the continent to use the insights provided in this article to further investigate the large-scale production of phenols from biomass.

Two of the remaining seven articles cover the synthesis of filter materials from local starting materials The perspectives on the development of filter media for "*point of use*' water filters by Chigome et al. provides a case study for how arsenates can be removed from arsenic polluted waters to make such waters potable. This article is a clear demonstration that some of the pollution problems that we have on the continent can be solved using available local resources. Similarly, Nkansah et al. have used the scales of tilapia, a fish that is abundant in the tropical parts of Africa, to fabricate efficient low-cost filters to remove fluoride from water, especially useful for East African communities where high fluoride concentrations in water is a problem.

Three articles in this Research Topic cover the topic of environmental pollution. For example, Labidi and Megriche have used locally available natural fluorapatite to demonstrate that their addition of this natural fluorapatite to Portland Cement manufacturing plants in Tunisia decreased CO_2 emissions. In another article, by Amakali et al., the use of zinc sulfide nanostructured materials was shown to photo-catalytically degrade Rhodamine dye, a dye that finds its way into water bodies from textile factories. A third article by Obuseng et al. described the use of moringa oleifera seed pods for the removal of toxic metals from wastewater to produce potable water for irrigation and industrial use. The article also discussed the more significant issue of using plant biomass as an "economic commodity," and how non-edible plants can provide nutrients and metals that are beneficial for plant growth.

Two articles are on more classical catalytic chemistry. Sonali Anantha et al. have provided a review of how heterogeneous catalysts have been used in what they term "multicomponent synthesis of dihydropyridines under green conditions" which summarises work form their research and other laboratories. The article by Dembaremba et al. provides a "perspective on strategies for improving ultra-deep desulfurization of liquid fuels through hydrotreatment." Both these reviews succeed in providing an update to readers on developments in the two focus areas.

It was hoped that the articles will be of interest to the readership of Frontiers in Chemistry. Indeed, early impact matrices show that as of the 7 September 2022, there were already 18,066 views and 2,315 downloads of articles in this Research Topic. This is an excellent sign that readers have interest in the subject matter covered in the articles.

The Editorial Group of this Research Topic would like to take this opportunity to thank Frontiers in Chemistry and its staff, especially those who worked closely with the Editorial Group on this issue (Jos Kellie (October 2020-January 2021; Lucy Chappel (February 2021-October 2021 and Shannon Lee (November 2021-present), in giving FASC the opportunity to tell its story during this 15th Anniversary of the organization.

Author contributions

All authors listed have made a substantial, direct, and intellectual contribution to the work and approved it for publication.

Conflict of interest

JD was employed by Botswana Institute for Technology Research and Innovation.

The remaining authors declare that the research was conducted in the absence of any commercial or financial relationships that could be construed as a potential conflict of interest.

Publisher's note

frontiers in Chemistry

REVIEW
published: 22 December 2021
doi: 10.3389/fchem.2021.800236

Recent Progresses in the Multicomponent Synthesis of Dihydropyridines by Applying Sustainable Catalysts Under Green Conditions

Immandhi Sai Sonali Anantha[1], *Nagaraju Kerru*[2,3], *Suresh Maddila*[1,3] *and Sreekantha B. Jonnalagadda*[3]*

[1]Department of Chemistry, GITAM Institute of Sciences, GITAM University, Visakhapatnam, India, [2]Department of Chemistry, GITAM School of Science, GITAM University, Bengaluru, India, [3]School of Chemistry and Physics, University of KwaZulu-Natal, Westville Campus, Chiltern Hills, Durban, South Africa

The synthesis of dihydropyridines, valuable molecules with diverse therapeutic properties, using eco-friendly heterogeneous catalysts as a green alternative received significant consideration. By selecting appropriate precursors, these compounds can be readily modified to induce the desired properties in the target product. This review focused on synthesising diverse dihydropyridine derivatives in single-pot reactions using magnetic, silica, and zirconium-based heterogeneous catalytic systems. The monograph describes preparation techniques for various catalyst materials in detail. It covers facile and benign magnetic, silica, zirconium-based, and ionic liquid catalysts, exhibiting significant efficacy and consistently facilitating excellent yields in short reaction times and in a cost-effective way. Most of the designated protocols employ Hantzsch reactions involving substituted aldehydes, active methylene compounds, and ammonium acetate. These reactions presumably follow Knoevenagel condensation followed by Michael addition and intra-molecular cyclisation. The multicomponent one-pot protocols using green catalysts and solvents have admirably increased the product selectivity and yields while minimising the reaction time. These sustainable catalyst materials retain their viability for several cycles reducing the expenditure are eco-friendly.

Keywords: green synthesis, 1,4-dihydropyridines, heterogeneous catalyst, multi-component reactions, one-pot synthesis

OPEN ACCESS

Edited by:
James Darkwa, Botswana Institute for Technology Research and Innovation (BITRI), Botswana

Reviewed by:
Bubun Banerjee, Akal University, India
Tamer S. Saleh, National Research Centre (Egypt), Egypt

***Correspondence:**
Sreekantha B. Jonnalagadda
jonnalagaddas@ukzn.ac.za

Specialty section:
This article was submitted to Inorganic Chemistry, a section of the journal Frontiers in Chemistry

Received: *22 October 2021*
Accepted: *19 November 2021*
Published: *22 December 2021*

Citation:
Sonali Anantha IS, Kerru N, Maddila S and Jonnalagadda SB (2021) Recent Progresses in the Multicomponent Synthesis of Dihydropyridines by Applying Sustainable Catalysts Under Green Conditions. Front. Chem. 9:800236. doi: 10.3389/fchem.2021.800236

INTRODUCTION

Synthesis of small heterocyclic organic molecules has advanced a long way with numerous applications in the academic and pharmaceutical industry, which are also valuable synthons for preparing elaborate bioactive molecules (Rotstein et al., 2014). The strategy of sustainable green methodologies for novel functionalised heterocyclic scaffolds is receiving substantial attention (Védrine, 2017; Kerru et al., 2019a; Bhaskaruni et al., 2020; Kerru et al., 2021a). Over the past two decades, heterogeneous catalysts have gained significant importance in synthetic organic chemistry due to their tunable acid–base properties, flexible textural characteristics, recyclability, excellent thermal stability, easy accessibility, and nontoxicity (Hutchings, 2009; José Climent et al.,

2012; Maddila et al., 2020c; Devi et al., 2020; Ganta et al., 2021). Various materials have been explored as heterogeneous catalysts for synthesising small value-added heterocycles with improved atom efficiency and selectivity (Kerru et al., 2020a; Kerru et al., 2020b; Kerru et al., 2020c; Kerru et al., 2020i; Kerru et al., 2021b). These studies have provided insight for developing novel materials and understanding the reactivity and reaction mechanisms allowing the synthetic chemists to apply their innovations in scheming structures of organic synthesis reactions and utilise these molecules of potential activity (Rao et al., 2021a; Kerru et al., 2021c; Muralidhar et al., 2021; Suryanarayana et al., 2021).

The importance of sustainable heterogeneous catalysts and fiscal benefits is renascent through effective fusion procedures, which are deemed crucial in advanced organic chemistry (Kerru et al., 2020d; Kerru et al., 2020e; Kerru et al., 2020f). Recently, multicomponent reactions (MCRs) have been accepted as a significantly powerful tool in medicinal chemistry and thereby drug development programs (Slobbe et al., 2012; Maddila et al., 2020a). MCRs allow the building of multiple bonds and functionalised scaffolds in a one-pot manner, thus boosting efficiency and minimising the generation of by-products and purification techniques, meeting the green chemistry criteria (Maddila et al., 2020b; Maddila et al., 2020c; Devi et al., 2020). Using green principles has been gaining prominence in sustainable/combinatorial chemistry due to the global urge to enhance green credentials on production (Cioc et al., 2014; Shahid et al., 2017; Mokhtar et al., 2021). Sustainable methodologies by the MCR approach driven by green chemistry and green solvents, replacing the volatile and toxic solvents, are crucial in organic synthesis (Sheldon, 2005; Gu, 2012; Ferrazzano et al., 2019). Increasing environmental awareness drives designing of viable green protocols to gain prominence in organic synthesis (Kerru et al., 2019b; Maddila et al., 2019; Kerru et al., 2020g; Kerru et al., 2020h; Kerru et al., 2020j).

Nitrogen-based heterocyclic skeletons have prominence in synthetic organic chemistry because of their valuable biological applications (Kerru et al., 2019c; Kerru et al., 2020k; Kerru et al., 2020l; Rao et al., 2021b; Kumar et al., 2021). Among the several nitrogen heterocycles, dihydropyridines have received enormous attention due to their wide range of therapeutic properties. Such properties include calcium channel blocking, anti-mycobacterial, antioxidant, anti-dyslipidemic, Alzheimer's disease, and antidiabetic activities (Kumar et al., 2010; Sirisha et al., 2011; Niaz et al., 2015; Schaller et al., 2018; Malek et al., 2019). Because of the growing reputation of dihydropyridines in the pharmaceutical field, numerous MCRs have been designed to synthesise 1,4-dihydropyridine scaffolds by utilising various heterogeneous catalysts (da Costa Cabrera et al., 2019; Rajesh et al., 2013; Mahinpour et al., 2018; Heydari et al., 2016; Bhaskaruni et al., 2017; Balaboina et al., 2019). Thus, the new MCRs with green protocols have drawn considerable interest, mainly in organic synthesis, drug development, and material science areas with green approaches using effective recyclable heterogeneous catalysts, sustainable procedures with remarkable atom, and carbon efficiency as added benefits. The review summarises the advances in constructing various dihydropyridine frameworks through the MCR approach by utilising diverse, robust heterogeneous catalysts.

SYNTHESIS OF DIHYDROPYRIDINES

The 1,4-dihydropyridine is a significant six-membered nitrogen-based heterocyclic molecule, a valuable moiety in medicinal chemistry. In 1881, Arthur R, Hantzsch first reported the dihydropyridine molecule through a one-pot reaction of two moles of ethyl acetoacetate with carbonyl compound and nitrogen source (ammonia or ammonium acetate) (**Scheme 1**) (Hantzsch, 1881). The process proceeded through the formation of enamine (**I**) and chalcone (**II**) intermediates and further underwent cyclisation to generate a 1,4-dihydropyridine product (**Scheme 2**) (Katrinsky et al., 1986). Currently, many dihydropyridine drugs are available in the market (felodipine, nimodipine, amlodipine, nifedipine, and nicardipine) (**Figure 1**). These scaffolds found importance in biological applications, particularly in calcium channel antagonists and treatment of hypertension (Janjua and Mayer, 2003; Triggle, 2003; Edraki et al., 2009). Therefore, the varied bioactive applications of dihydropyridine analogues have considerable attention for synthesising. The current review emphasises the various synthetic approaches for 1,4-dihydropyridine analogues using different metal-based heterogeneous catalyst materials.

Magnetic Nanocatalysts

Lately, catalytic compounds in synthetic processes have been a topic of concern due to their nature and adverse effects on the environment, drawing attention to eco-friendly alternatives. The emerging challenge was to modify the naturally available compounds for multiple uses without compromising their vitality. The construction of magnetic nanoparticles with promising catalytic activity offers many advantages compared to traditional inorganic catalysts. A huge surface area-to-volume ratio and a high atomic accommodation capacity are advantageous for these particles. These catalysts can be easily separated from the final product using external magnetic fields owing to their magnetic efficiency. Magnetic nanocatalysts have gained paramount importance in organic and industrial reactions because of their interactions with various reagents and environmentally amiable properties, such as anchoring various functional groups or organic moieties onto the hydroxyl projections of their surface area. Integrating transitional metals or other plant-extracted enzymes with Fe_3O_4 nanoparticles has evolved as a good strategy. The magnetic nanoparticles coalesce with exchangeable electron ligands such as phosphorous or nitrogen offering the electron-donating sites to encourage affiliation to metal cations to form stable and streamlined catalyst structures. The fabrication of iron-based catalysts has enticed many scientists due to their easy accessibility, high performance, easy separation, and cost-effectiveness. The magnetic nanoparticles were prepared using Fe^{+3} and Fe^{+2} oxides in the ratio of 2:1 co-precipitated in an alkaline environment. The prepared nanoparticles elucidated using

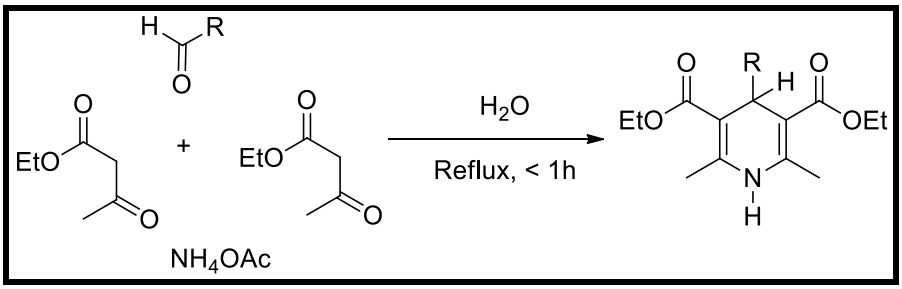

SCHEME 1 | Hantzsch dihydropyridine synthesis.

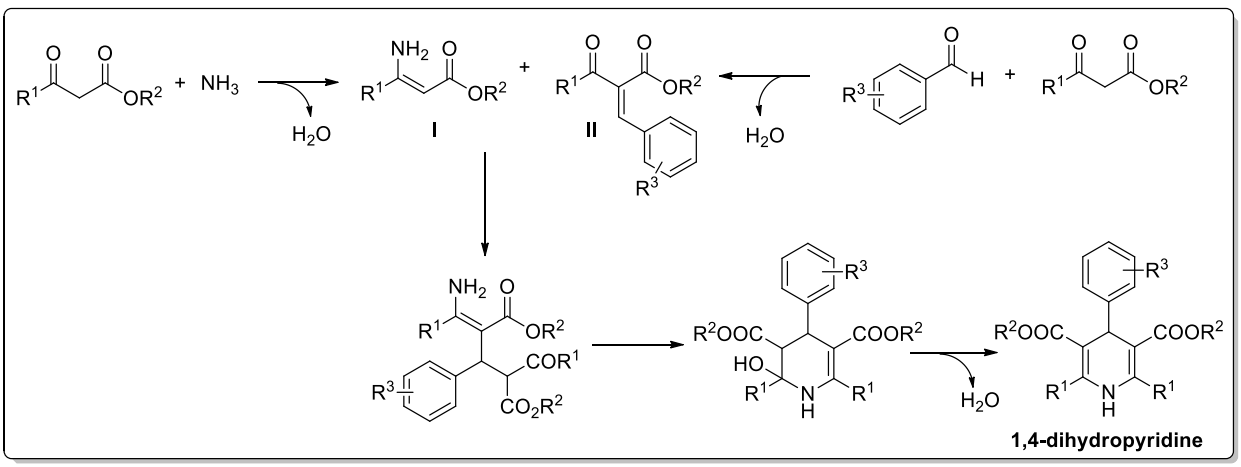

SCHEME 2 | Synthetic route of dihydropyridine formation.

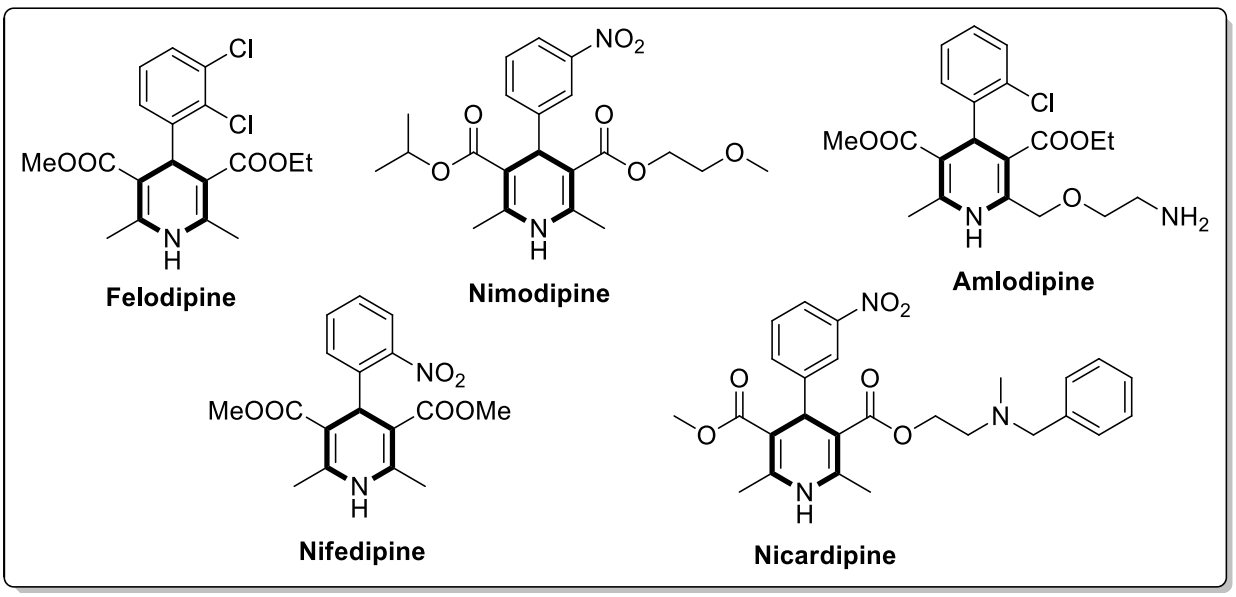

FIGURE 1 | Commercially used 1,4-dihydropyridine drugs.

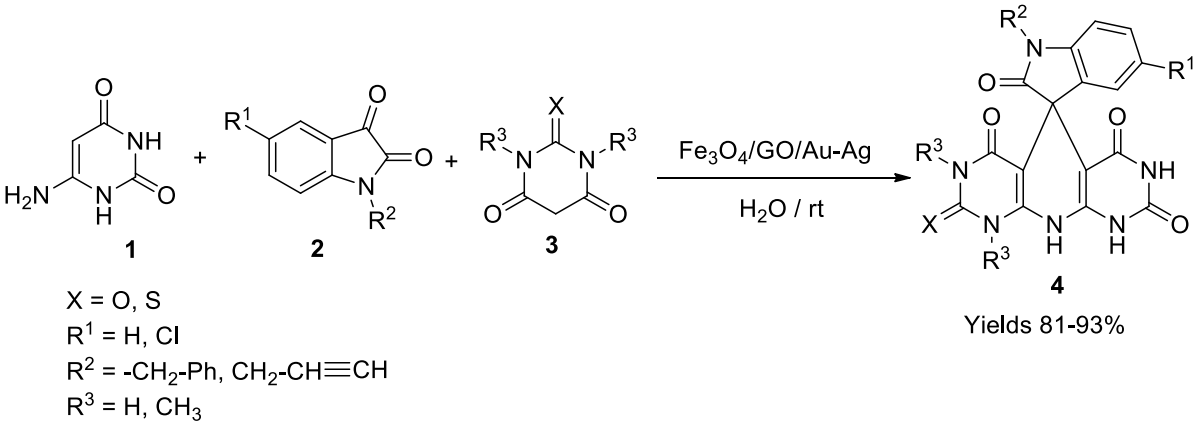

SCHEME 3 | Synthesis of spirooxindole-dihydropyridines by the Fe_3O_4/GO/Au-Ag catalyst.

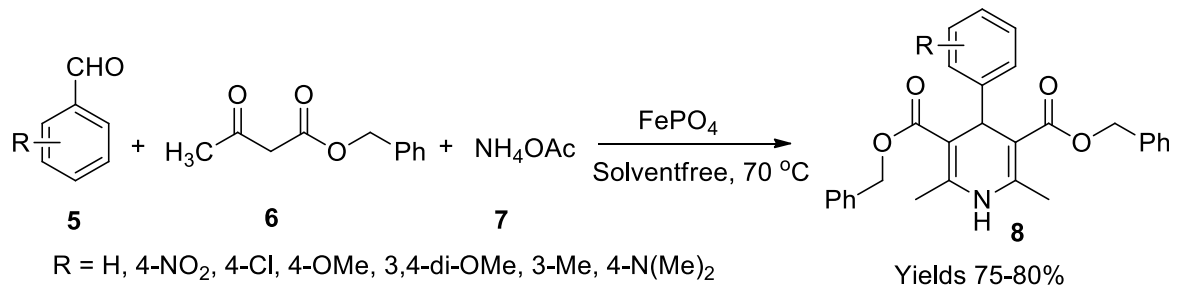

SCHEME 4 | Synthesis of dihydropyridines by the $FePO_4$ catalyst.

various analytical techniques such as FT-IR, SEM, and TEM analysis possess a spherical shape with a diameter of 10–15 nm. Their magnetic saturation was observed through value stream mapping (VSM) data. Catalyst accommodation capacity and microwave array capacity are the two fundamental factors for the optimisation of the catalyst.

Kavyani *et al.* (Kavyani and Baharfar, 2020) synthesised the (Fe_3O_4/GO/Au–Ag) nano-catalyst with Au–Ag particles clipped on Fe_3O_4 and graphene oxide. The nanocatalyst's activity was utilised to synthesise dihydropyridine-spiro oxindole analogues (**4**). The condensation reaction was carried out between uracil-6-amine (**1**), substituted isatin derivatives (**2**), and various barbituric acids (**3**) underwater at room temperature. The nanocatalyst was significantly thermally stable up to 600°C, and the average particle size was about 15 nm. The use of 20 mg of the nanocatalyst gave superior results with high yields (81%–93%) for <5 h of reaction time (**Scheme 3**). The catalyst was stable up to five successive runs without loss of its catalytic activity. Broad functional group tolerance, excellent yields, green solvent medium, and recyclability are the merits of this protocol.

Behbahani and coworkers (Farahnaz and Banafsheh, 2019) practised the Hantzsch reaction to synthesise 1,4-dihydropyridines (**8**) utilising iron(III) phosphate aiming for a solvent-free synthetic method (**Scheme 4**). They employed different types of aldehydes (**5**) with benzyl acetoacetate (**6**) and ammonium acetate (**7**) under the influence of a catalyst (Fe_3PO_4). The reaction proceeds by activating the carbonyl group of the aldehyde advocated by Fe_3PO_4, which acts as a Lewis acid, at a minimal catalytic usage of 10mol% to obtain an appropriate amount of yield. The reaction initially included benzaldehyde, benzyl acetoacetate, and ammonium acetate at an optimal temperature of 70°C. The aldehydes with +I substitution groups like $-NO_2$, $-OCH_3$, $-CH=CH_2$ were observed to serve a better yield of 80% within a reaction time of 50 min using a minimal amount of 5 mol% of the catalyst.

Allahresani *et al.* (Allahresani et al., 2020) synthesised a nanocatalyst with magnetic properties by adhering Co(II) onto $CoFe_2O_4$@SiO_2 nanoparticles and characterised using various spectroscopic techniques. Catalyst synthesis is a combination of multiple components. The first step involved the preparation of $CoFe_2O_4$ nanoparticles by dissolving Fe $(NO_3)_3.9H_2O$ and Co $(NO_3)_2.6H_2O$ in a molar ratio of 2:1 in 100 ml of water and sonication. A volume of 20 ml of 1 M NaOH solution was added to the resulting solution and subjected to sonication once again. The resulting black precipitate was gathered using an external magnetic field and dried in the oven. The second step consisted of the addition of

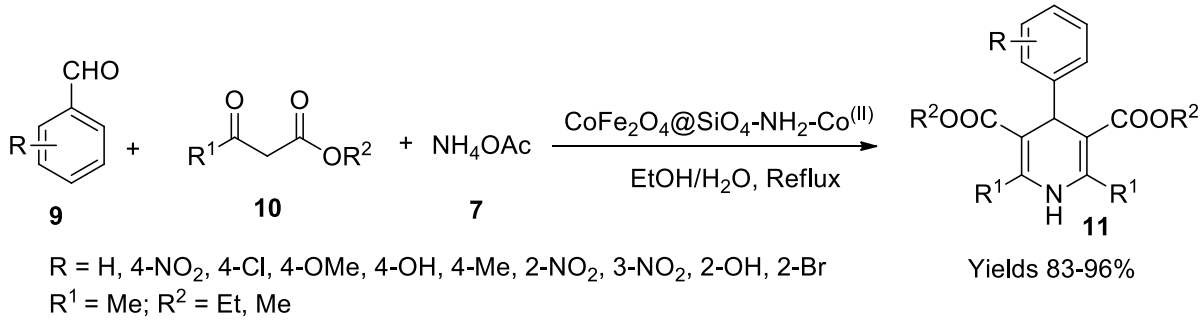

SCHEME 5 | Synthesis of dihydropyridines by the $CoFe_2O_4@SiO_4$-NH_2-$Co^{(II)}$ catalyst.

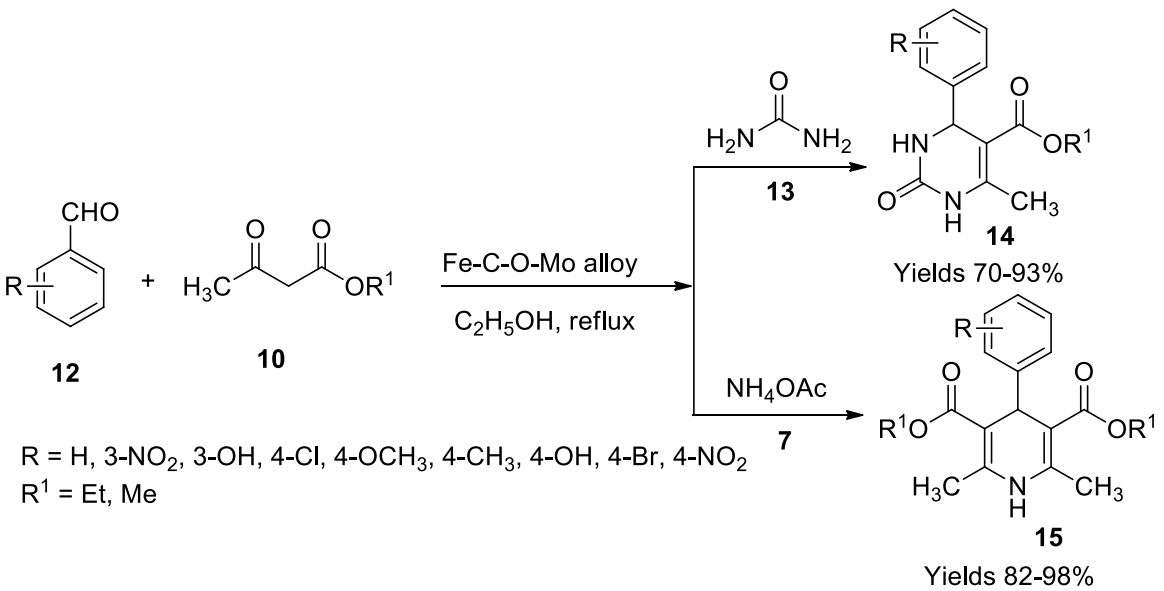

SCHEME 6 | Synthesis of dihydropyrimidinone and dihydropyridines by Fe–C–O–Mo catalyst.

tetraethylorthosilicate to obtain $CoFe_2O_4@SiO_2$. In the third step, NH_2-Pr was synthesised by reacting triethanolamine, triethylenetetramine, and 3-chloropropyltriethoxysilane in ethyl alcohol. Upon adding Co $(NO_3)_2.6H_2O$ to the above-obtained product, NH_2-Pr-Co(II) formed was dispersed in dry toluene to which a solution of $CoFe_2Co_4@SiO_2$ in dry toluene was added dropwise, resulting in the precipitate of desired catalyst $CoFe_2O_4@SiO_2$-NH_2-Co(II). The XRD values of the synthesised catalyst explored its polycrystalline structure with an average particle size of 20–90 nm, as suggested by TEM analysis. The VSM values indicate that the magnetic properties of the catalyst depended on the surface arrangement of the catalytic particles, which were stable up to 560°C as per thermogravimetric analysis (TGA) analysis. The catalyst (180 mg) facilitated a 96% yield in 2 h, in aqueous ethanol (1:1). Several dihydropyridine derivatives (**11**) have been synthesised in a single-pot mild reaction, including aldehydes (**9**), ethyl acetoacetate (**10**), and ammonium acetate (**7**), aiding $CoFe_2O_4@SiO_4$-NH_2-Co(II) as a catalyst owing to its active metallic nucleus, sustainability, and high-yielding capacity (**Scheme 5**). The reaction was observed to follow the Knoevenagel condensation method and Michael addition to obtain various pyridine derivatives.

Wua and coworkers (Wu et al., 2020) developed a magnetic nanocatalytic alloy mediated by a wasted screw adopting the top-down method. The catalyst is an alloy combination of iron and molybdenum bridged by carbon and oxygen. The catalyst was prepared by suspending the screws in a solution containing dimethyl sulphoxide and sodium hypochlorite, which was further decomposed by adding 60% nitric acid. The formation of red fuming gas indicates the decomposition initiation due to the expulsion of nitrous acid. The complete dissolution of the screw and the appearance of a brown colour solution marked the completion of the reaction. The required catalyst (Fe–C–O–Mo alloy) was obtained by centrifugation, and the brown-coloured powder was filtered and stored. The performance of the catalyst was examined to prepare dihydropyridines (**15**) using

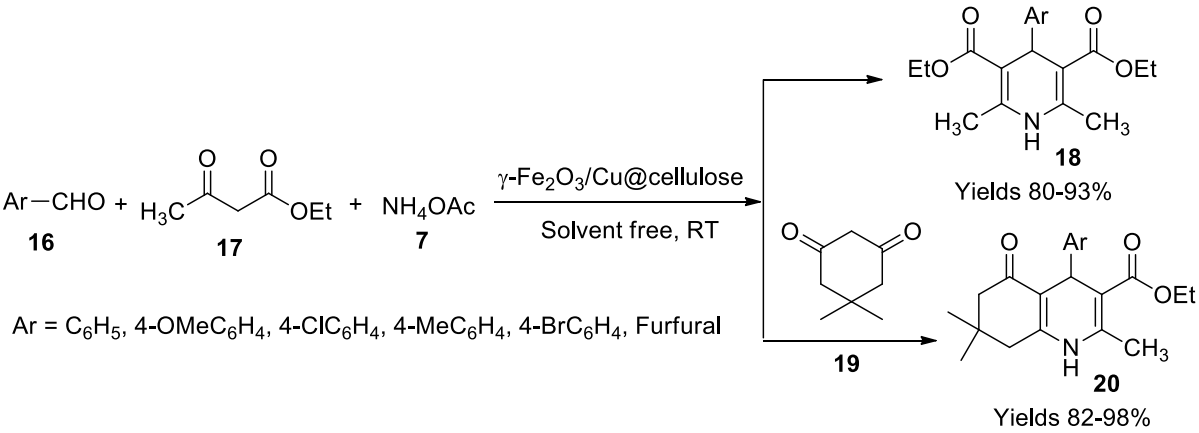

SCHEME 7 | Synthesis of dihydropyridine and hydroquinolines by the Fe_2O_3/Cu@cellulose catalyst.

benzaldehyde (**12**), ethyl acetate (**10**), and ammonium acetate (**7**) as reagents. Dihydropyrimidinone (**14**) compounds were also reported using urea (**13**) instead of ammonium acetate (**7**) (**Scheme 6**). The catalyst with stability up to 1,000°C showed worthy competence of 96% yield within a reaction time of 2.5 h with minimal use of 0.1 g of catalyst in the ethyl alcohol medium. Molybdenum acts as a Lewis acid that reacts with the carbonyl group and the beta diketones. Their nucleophilic attack on the reactants yields the desired result.

Maleki and his team (Maleki et al., 2019a) have tailored a magnetic bio nanocomposite using copper nanoparticles embedded in a cellulose matrix (γ-Fe_2O_3/Cu@cellulose), which showed magnificent catalytic efficiency during the Hantzsch reaction. High yields of 1,4 dihydropyridine (**19**) and polyhydroquinoline (**20**) were observed upon employing γ-Fe_2O_3/Cu@cellulose for their preparation. They prepared a homogenous solution of cellulose in an aqueous mixture of sodium hydroxide and urea bearing a ratio of 81:7:21, whose temperature was dropped to −12°C using an ice bath incorporated with salt. An aqueous solution of iron chloride with Fe^{+3} and Fe^{+2} in the ratio of 1:2 was added to the above solution while continuously stirring for 6 h, resulting in γ-Fe_2O_3-implanted cellulose assisted by co-precipitation. The $CuSO_4.4H_2O$ solution was added to the above mixture; owing to the oxidative nature of the γ-Fe_2O_3 nanoparticles, Cu^{+2} is protected from reduction. The mixture was stirred continuously for 2 h before washing and collecting the product. From TEM analysis, the obtained catalyst's particle size was 25–30 nm, and the EXD data confirmed the presence of C, O, Cu, and Fe. It showed engaging activity with a high yield of around 92%–95% within a short reaction time of 15–20 min in a solvent-free environment (**Scheme 7**).

Bodaghifard *et al.* (Bodaghifard, 2020) fabricated an organic bolstered magnetic nanocatalyst which was promising in preparing dihydropyridines. The catalyst was manufactured by preparing Fe_3O_4 nanoparticles by co-precipitation of Fe^{+2} and Fe^{+3} in a 1:2 ratio under basic pH. The gathered nanoparticles were laminated with silicon using the Stomper method. The obtained Fe_3O_4@SiO_2 nanoparticles were treated with 3-chloropropyltrimethoxysilane resulting in Fe_3O_4@SiO_2-PrCl. 4-Aminoquinaldine adheres to the gathered nanoparticles to bequeath the desired catalyst. The obtained catalyst was subjected to various spectroscopic assays to elucidate its morphology which described spherical nanoparticles with 25–35 nm in diameter, as suggested by SEM. The crystallite size was 20.1 nm as per XRD data. The VSM data advocated the magnetisation of the catalyst to be around 42 emu/g. The efficacy of the material was assessed *via* the synthesis of 1,4-dihydropyridines (**23**) and polyhydroquinoline (**24**) derivatives (**Scheme 8**). The synthesis process involved benzaldehyde (**21**), ethyl acetoacetate (**17**), malononitrile (**22**), and ammonium acetate (**7**) in equal quantities. The reaction is presumed to follow Knoevenagel condensation to form arylidene malononitrile. The intermediate further participates in Michael addition. The catalyst increased the yield to 96% and dropped the reaction time to 30 min in an aqueous medium. The catalyst material was isolated by applying an external magnetic field.

Khazaei *et al.* (Khazaei et al., 2018) worked on high-density ionic liquid that adhered onto magnetic nanoparticle Fe_3O_4 and its eminence in the production of hexahydroquinolines. The nanoparticle was initially fabricated using Fe^{+2} and Fe^{+3} in the ratio 1:2 dispersed in water and adding 28% (wt%) of ammonia solution to obtain a black precipitate of Fe_3O_4 nanoparticles after continuously stirring the solution at 80°C for 2 h under the influence of the N_2 environment. A percentage of 28% (wt%) of tetramethyl orthosilicate was added to a solution of Fe_3O_4 nanoparticles suspended in ethanol:water (80:20 wt%) mixture to gather Fe_3O_4@SiO_2 nanoparticles. The above-formed nanoparticles were taken in toluene and refluxed with (3-chloropropyl)triethoxysilane to obtain Fe_3O_4@SiO_2@Si-$(CH_2)_3$Cl nanoparticles, which were further added to a solution of melamine and K_2CO_3, dissolved in 70 ml of DMSO to affix melamine to the above formed NPs. A methanolic solution of picoline aldehyde was added to the NPs, followed by 30 ml of dichloromethane to the pre-dried NPs under $MgSO_4$. A 24-mmol chlorosulphonic solution in 20 ml of dichloromethane was further added dropwise to form Fe_3O_4@SiO_2@Si-$(CH_2)_3$@melamine-picolineimine@SO_3H nanoparticles. Different spectral data obtained from FT-IR and

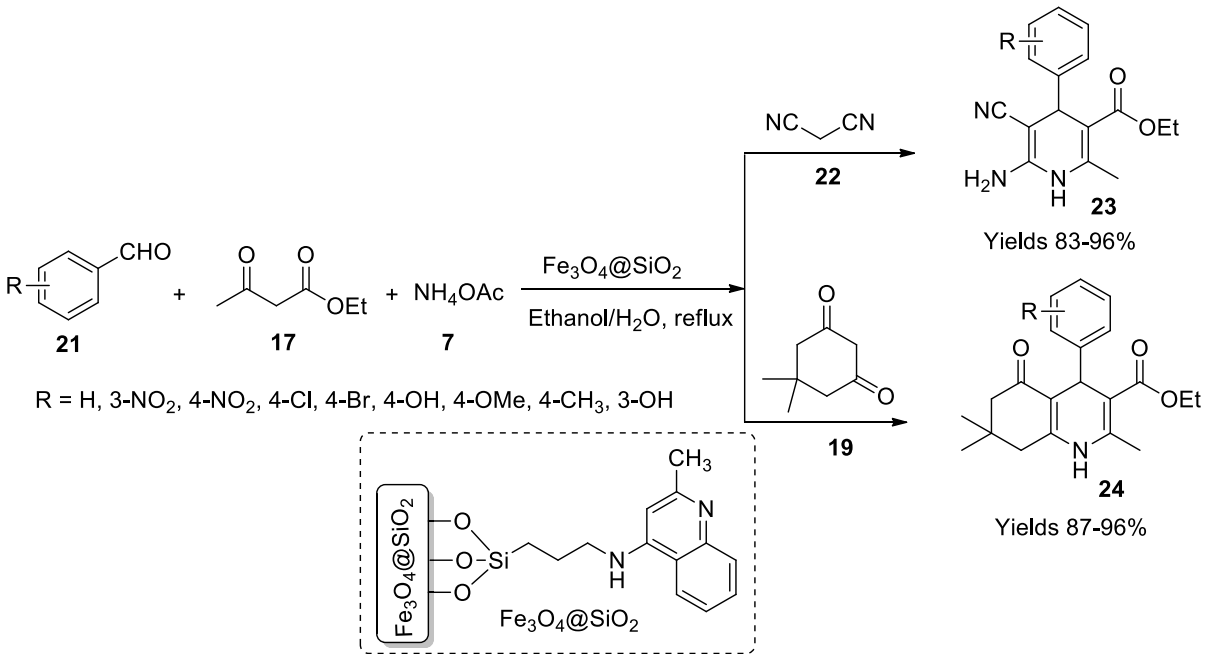

SCHEME 8 | Synthesis of dihydropyridine and hydroquinolines by the Fe_3O_4@SiO_2 catalyst.

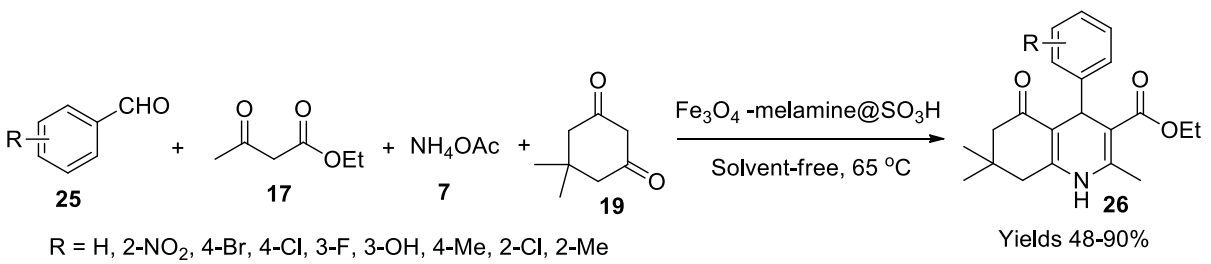

SCHEME 9 | Synthesis of hydroquinolines by the Fe_3O_4-melamine@SO_3H catalyst.

XRD suggest that the crystallite size of the catalyst is 14.98 nm whereas SEM analysis advocates for the high interaction of the HSO_3 group on the surface along with TEM data which proves the lamination of the core–shell. The EDS analysis helped elucidate the nanoparticles' morphology with dominant levels of Fe, Si, O, N, S, and Cl. The VSM analysis evaluated its magnetic nature, and the material was stable at 600°C as suggested by TGA data. A series of polyhydroquinolines (**26**) were reported using aryl aldehydes (**25**), β-keto esters (**17**), dimedones (**19**), and ammonium acetate (**7**) in equal proportions confirming the catalytic potential of the magnetic nanoparticles (**Scheme 9**). The obtained products were characterised using FT-IR, ^{1}H, and ^{13}C NMR while being evaluated by TLC. The highest yields were observed when the aryl aldehyde had an electron-donating group of +I category. With p-anisaldehyde, a 90% yield was registered under solvent-free abode with 40 mg of the catalyst at 65°C. The catalyst sustained its viability for four cycles.

Fekri *et al.* (Fekri et al., 2020) have fabricated a Copper/Schiff–base complex immobilised on KIT-6-NH_2 nanoparticles, which can be used as a catalyst to prepare dihydropyridine derivatives. Several steps were followed to tailor the desired catalyst complex. Initially, Fe_3O_4 nanoparticles were synthesised using a mixture of Fe^{+2} and Fe^{+3} salts in the ratio of 1:2 treated with ammonia solution to obtain a black precipitate of nanoparticles. The nanoparticles were laminated with a layer of silica and further overlapped with Kit-6 silica to impart a mesoporous nature to the product. The post-synthetic grafting method was used for the amine functionalisation of the magnetic nanoparticles, where 3-aminopropyl triethoxysilane was silylated using surface silanol. The Schiff's base was adhered onto the amino functionalised magnetic nanoparticles (MNPs) using 1-(2-hydroxy-5-(4-nitrophenyl)-diazenyl)-phenyl)-ethenone. The final catalytic conclusion involves the induction of copper to the MNPs using $CuCl_2$ to achieve a Copper/Schiff–base complex immobilised on KIT-6-NH_2 magnetic nanoparticles. The

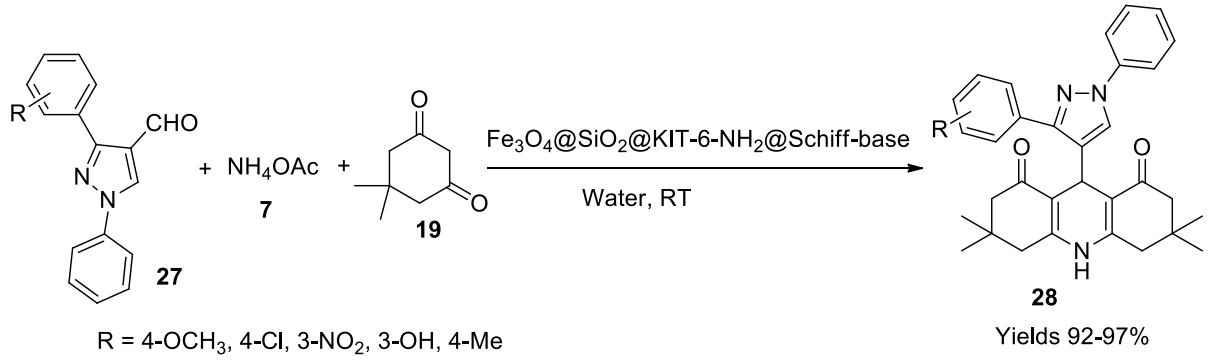

SCHEME 10 | Synthesis of hydroquinolines by the Fe_3O_4-SiO_2 Schiff–base catalyst.

gathered compound was morphologically elucidated using various methods such as BET analysis, representing its particle size of 51.43°m^2/g. The VSM is used to assess its magnetic nature. TEM images explored the spherical shape of the particles with a diameter of 33–40 nm along with aggregation and stacking of particles. XRD showed a highly crystalline cubic spinel structure, and the elemental analysis energy-dispersive X-ray analysis (EDX) revealed that the catalyst contains Fe, O, N, C, Cu, and Si. TGA analysis suggested stability up to 520°C. The catalytic activity of MNPs was tested on Hantszch's single-pot reaction method to synthesise polyhydroquinolines (**28**) using aryl aldehyde (**27**), cyclic ketone (**19**), and ammonium acetate (**7**) in the presence of the above-prepared catalyst (**Scheme 10**). The reaction was assumed to follow Knoevenagel condensation followed by Michael addition and intramolecular addition. The reaction conclusion was determined using TCL, where the products were characterised using FT-IR, ^{1}H, and ^{13}C NMR methods. The catalyst proved to enhance the reaction with high yields around 92%–97% within 15 min of reaction time. The catalyst was separated magnetically and used without any resentment for seven consecutive cycles.

Maleki and his colleagues (Maleki et al., 2019b) fabricated a heterogeneous magnetic nanocatalyst bolstered with sulphonyl skeleton to prepare pyrans and polyhydroquinolines. Initially, 1 g of diethylenetriamine in 5 ml of dried methane and 10 g methyl acrylate in 25 ml of dried methanol were stirred continuously till the solvent was evaporated entirely to obtain pioneer dendrimer. The dendrimer terminals with 5-OCH_3 groups were modified to 5-NH_2 by dissolving it in a solution of 20 ml methanol and 40 ml of ethylenediamine. The modified dendrite generation was isolated from unreacted reagent and methanol using vacuum. The acquired dendrite was further modified by adding 30 ml of methyl acrylate to 6.74 g of the modified pioneer dendrite. The stirring was continued for 7 days in an inert environment to gain a thick yellow liquid consisting of 10 branched dendrimers with -OCH_3, which was further modified using 60 ml of ethylenediamine, and the procedure was repeated to gather a pale-yellow oily material. The prepared dendritic material was magnetised by dispersing it in a 1:2 ratio Fe^{+2} and Fe^{+3} solution and subjecting it to sonication. It was later functionalised by adding 2.3 ml of 1,4-butane sultone dropwise followed by sonication. The final Fe_3O_4@D-NH-$(CH_2)_4$-SO_3H nanoparticles were isolated using an external magnetic field. The prepared catalyst was evaluated using SEM and TEM imaging, representing the uniform distribution of nanoparticles with spherical structure. The catalyst was stable up to 700°C owing to the dendrimers of D-NH-$(CH_2)_4$-SO_3H side chains. The prepared catalyst was used in the production of tetrahydrobenzo pyrans (**31**), 2-amino-3-cyano-4H-pyrans (**32**), and polyhydroquinolines (**33**). The former pyrans were prepared by refluxing a reaction mixture of aldehydes (**29**), malononitrile (**22**), and 1,3-cyclohexanedione (**19**) or ethyl acetoacetate (**17**) in 5 ml of ethanol in the presence of the above-prepared catalyst. The polyhydroquinolines were produced by refluxing a reaction mixture containing aldehydes (**29**), 1,3-cyclohexanedione (**19**), ethyl acetoacetate (**17**), and ammonium acetate (**7**) in the presence of the same catalyst. The reaction was assumed to proceed through Knoevenagel condensation to produce 2-benzylidenemelanonitrile. The intermediate endures Michael with enolised dimedone to generate enamine intermediate. The enamine undergoes cyclisation and tautomerism to give the product a high yield (96%) within 20 min using 0.05 g of the catalyst (**Scheme 11**). The gathered products were subjected to FT-IR, ^{1}H, and ^{13}C NMR spectroscopy.

Zeynizadeh *et al.* (Zeynizadeh et al., 2019) fabricated a catalyst for the synthesis of 1,4-dihydropyridines by adhering sulphonic acid onto silica-layered $NiFe_2O_4$, which could be isolated magnetically and reused multiple times. Initially, the magnetic nanoparticle base was produced by grinding a reaction mixture containing nickel acetate, ferric nitrate, sodium hydroxide, and sodium chloride taken in the ratio of 1:2:8:2. The ground mixture was washed with DM water and dried at 80°C for 2 h and further calcinated at 700°C–900°C for 2 h. The prepared nanocatalyst was functionalised with a silica solution. A volume of 1.5 g of the prepared nanoparticles along with 200 ml of *i*-PrOH and 20 ml of DM water was irradiated with ultrasound and added to a solution containing 5.36 g of PEG-400 in 20 ml DM water, 10 ml of 28% aqueous ammonia, and 2 ml of tetraethyl orthosilicate (TEOS) and stirred continuously for a day and a half to obtain $NiFe_2O_4$@SiO_2 nanoparticles. A volume of 2 g of the prepared nanoparticles was suspended in 15 ml of chloroform to which 0.5 g of sulphonyl chloride was added dropwise and stirred while maintaining a

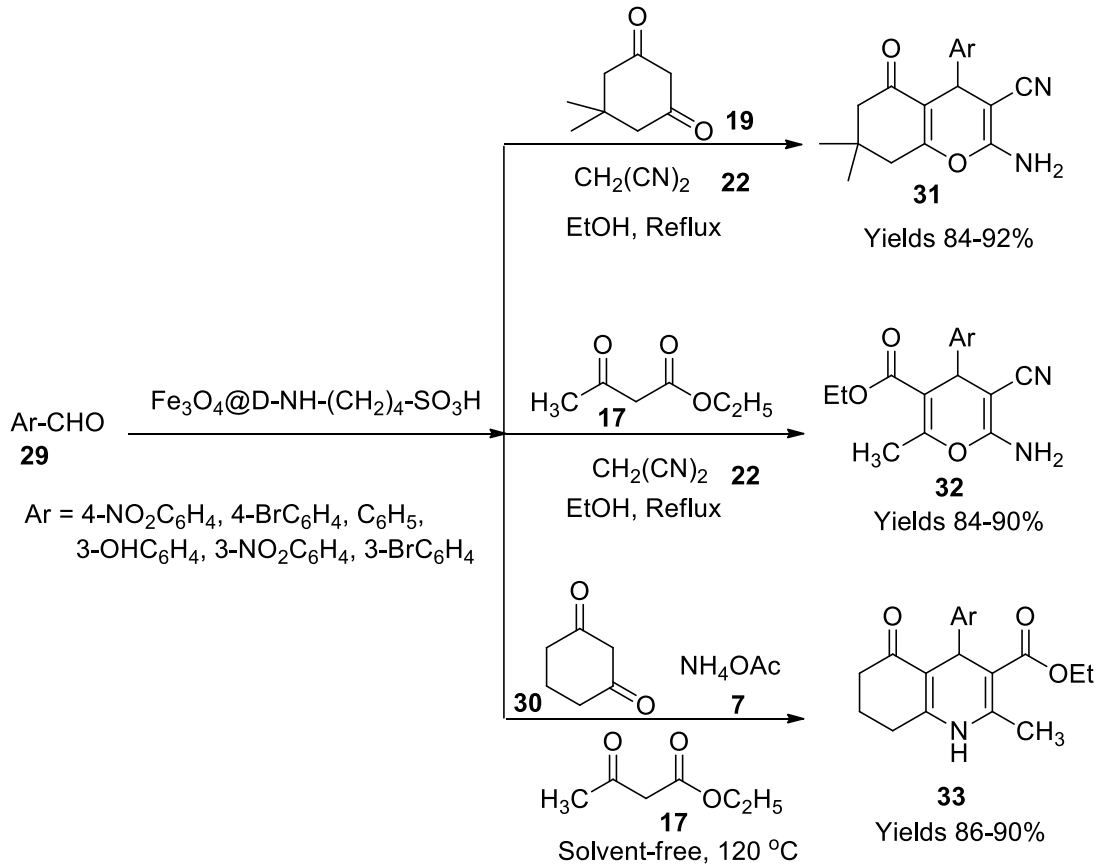

SCHEME 11 | Synthesis of hydroquinolines by the Fe_3O_4 catalyst.

temperature range ≥5°C. The resulting mixture was filtered and dried at room temperature to obtain a black precipitate of $NiFe_2O_4@SiO_2@SO_3H$ nanoparticles. The gathered catalytic nanoparticles were elucidated using various techniques such as XRD analysis which describes its rhombic crystalline structure. The SEM analysis showed a 60–90-nm nanosize, and the material was stable up to 600°C. The gathered catalyst was subjected to trial to determine its efficiency for the preparation of 1,4-dihydropyridines (**37** and **38**) by employing a single-pot Hantzsch reaction mixture consisting of aromatic aldehyde (**34**), ethyl acetoacetate (**17**), or 4-hydroxycoumarin (**36**) and 28% aqueous ammonia 28% (**35**) in 2 ml of DM water (**Scheme 12**). The completion of the reaction was determined using TLC using n-hexane and ethyl acetate as eluent. The resulting product was isolated using the solvent extraction method and dried over Na_2SO_4 under reduced pressure. The prepared 1,4-dihydropyridine derivatives were characterised using FT-IR, ^1H, and ^{13}C NMR spectroscopy. The products were with a high yield of 95% within a reaction time of 20 min with the catalyst sustainability for seven consecutive cycles. Besides the synthesis of dihydropyridines, Cu–adenine–boehmite was also used in the Suzuki coupling reaction and oxidation of sulphides.

Bhaskaruni *et al.* (Bhaskaruni et al., 2019) have constructed a green route to prepare 1,4-dihydropyridines under the catalytic influence of Fe_2O_3/ZrO_2. The catalyst was prepared by wet impregnating 2 g of zirconium oxide with equal amounts of ferric nitrate in 50 ml of water while continuously stirring at room temperature for 7 h. The obtained slurry was filtered and vacuum dried at 120°C for 5 h followed by calcinating it at 450°C for 4 h. The prepared material was elucidated using various techniques, which described its polycrystalline structure as having a 10.23-nm diameter. The nanoparticles were irregular oval-shaped with a particle size of 8.5 nm as represented by TEM and SEM analysis. The surface area of the catalyst was 84.34 cm^2/g with a mesoporous cavity size of 8.9 nm and a volume of 0.25 cm^3/g, through BET data. The catalytic activity of Fe_2O_3/ZrO_2 was assessed in preparing hydroquinolines (**41**). A single-pot system consisting of equimolar amounts of aromatic aldehyde (**39**), 1,3-cyclohexadiene (**30**), acetoacetanilide (**40**), and ammonium acetate (**7**) was subjected to stirring for 20 min at room temperature (**Scheme 13**). The catalyst was isolated from the products through filtration. The product was extracted using ethyl acetate and recrystallised from ethanol. The reaction is presumed to follow Knoevenagel condensation and Michael addition to form an enamine which further undergoes tautomerism. An excellent 98% yield was gained with minimal use of the catalyst within 20 min. The gathered product was confirmed using various spectroscopic techniques.

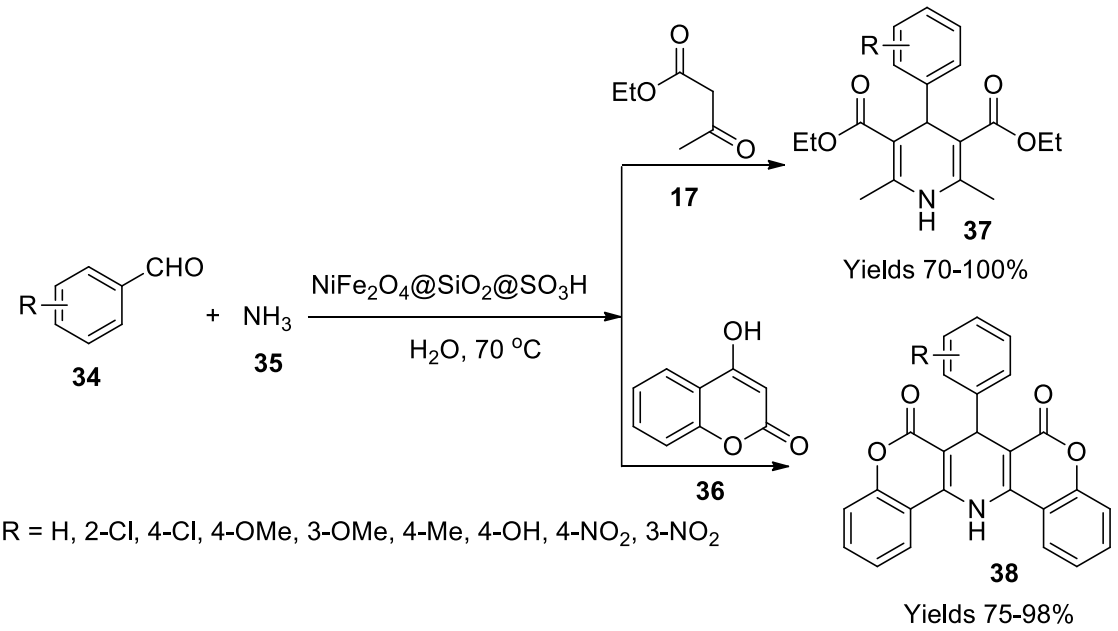

SCHEME 12 | Synthesis of dihydropyridines by the $NiFe_2O_4$-SiO_2@SO_3H catalyst.

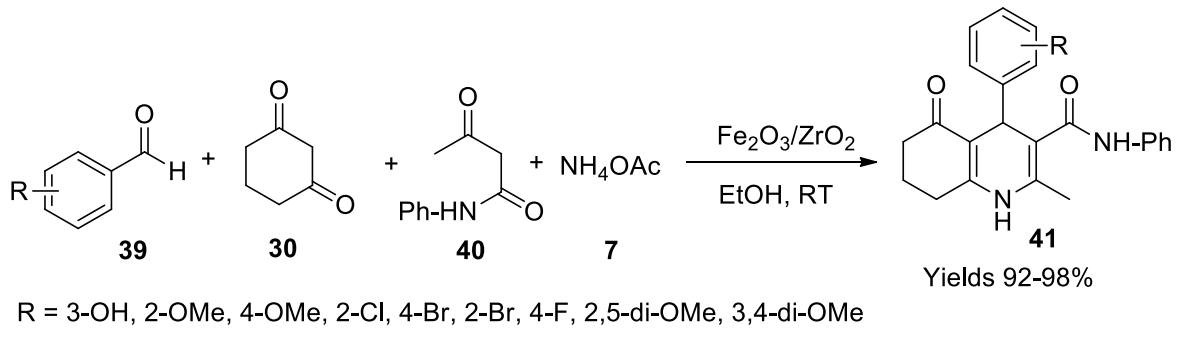

SCHEME 13 | Synthesis of hydroquinolines by the Fe_2O_3/ZrO_2 catalyst.

Sadeghzadeh reported a magnetic KCC1 catalyst stabilised by bis(4-pyridylamino)triazine, a green catalyst with good chemo selectivity (Sadeghzadeh, 2016). The production of Fe_3O_4 nanoparticles was achieved by dissolving Fe^{+2} and Fe^{+3} in 200 ml of water with a ratio of 1:3 and adding 2 ml of concentrated ammonium solution along with 0.2 g of tetraethyl orthosilicate and continuously stirring for a day. The nanoparticles of Fe_3O_4/SiO_2 were gathered by filtering the obtained black precipitate and air drying it at 60°C after washing. A volume of 0.25 g of the gathered nanoparticles was dispersed in 30 ml of urea solution containing 0.3 g of urea and subjected to sonication for an hour. To 0.5 g of acetylpyridine bromide dissolved in a mixture of 0.75 ml of n-pentanol and 30 ml of cyclohexane, 1.25 g of tetraethyl orthosilicate was slowly added under continuous stirring at 120°C for 5 h. The desired microspheres were isolated using an external magnetic field and washed in acetone and oven-dried at 40°C overnight followed by calcination at 550°C for 5 h. A volume of 1 g of the gathered nanoparticles along with 20 mmol of sodium hydride was dispersed in 20 ml of tetrahydrofuran (THF) and subjected to ultrasonication which was added with 22 mmol of 3-aminopropyltriethoxysilane while continuously stirring for 6 h at 60°C the resulting Fe_3O_4/SiO_2/KCC-1/aminopropyl MNPs, which were washed and vacuum dried for another 2 h at 60°C. A volume of 1 g of the gathered product was added to a solution of 1 ml of N-ethyldiisopropylamine and 10 ml of dry THF while maintaining the temperature below 5°C and adding 1 g of triazine trichloride while continuously stirring for a whole day. Fe_3O_4/KCC-1/TCl_2 nanoparticles were gathered and washed with hot toluene to isolate pure products. A volume of 1 g of the currently gathered nanoparticles along with 1 g of pyridine was dissolved in a solution of 1.3 ml of N-ethyl diisopropylamine and 10 ml of dry toluene while continuously stirring for 16 h at 80°C. Fe_3O_4/KCC-1/BPAT

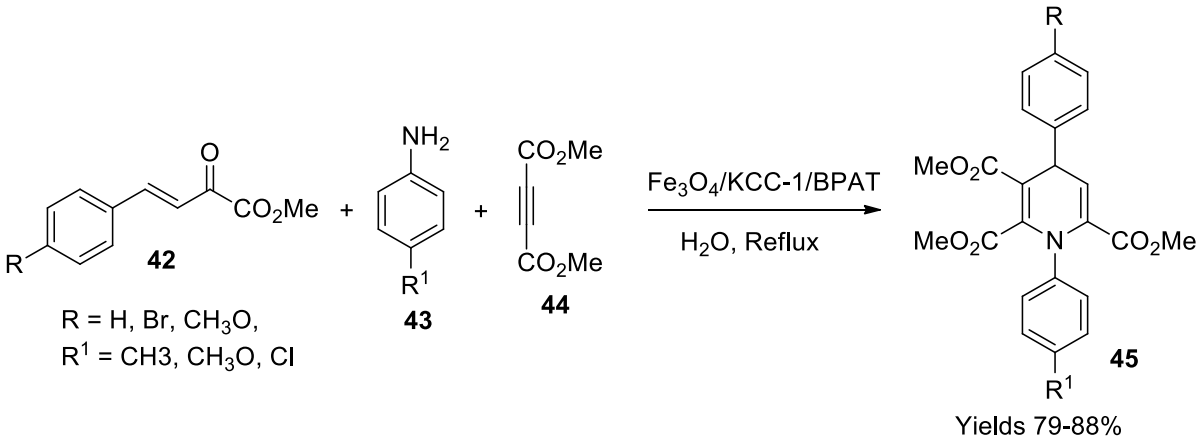

SCHEME 14 | Synthesis of dihydropyridines by the Fe_3O_4/KCC-1 catalyst.

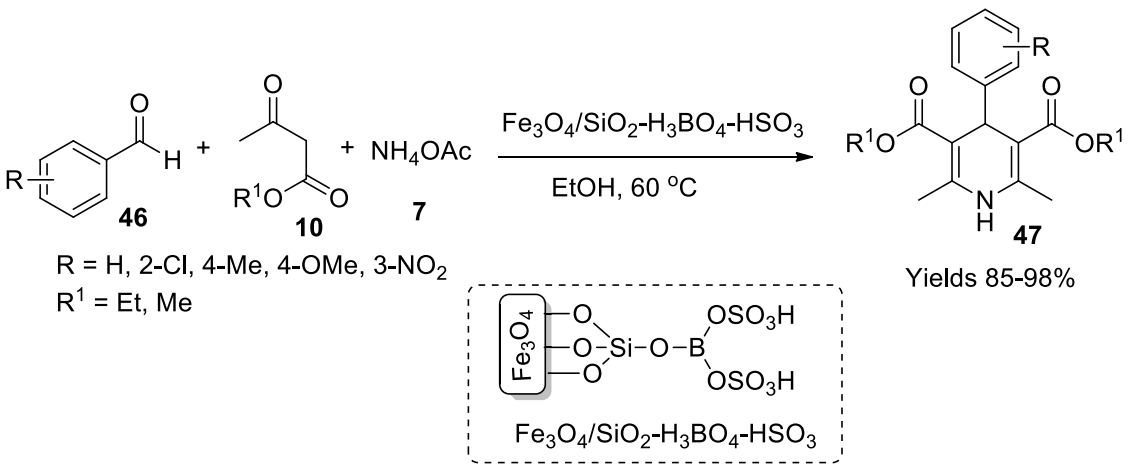

SCHEME 15 | Synthesis of dihydropyridines by the Fe_3O_4/SiO_2 catalyst.

nanoparticles were separated from the reaction solution by an external magnet, washed with ethanol, and dried at 50°C. Represented by SEM and TEM data, the stoked nanoparticles had 20–30-nm particle size. The magnetic saturation was 55.1 and 42.4 emu/g following VSM data, and the material was stable up to 700°C. The catalytic efficiency of the prepared nanocomposite was assessed by a single-pot synthesis of 1,4-dihydropyridines (**45**). The equimolar mixture of primary amine (**43**), dimethyl acetylene dicarboxylate (**44**), and methyl (arylmethylide) pyruvate (**42**) was refluxed for 4 h in the presence of Fe_3O_4/KCC-1/BPAT (**Scheme 14**). The solvent was removed by dropping its pressure to obtain an oily residue, treated with methanol, and recrystallised to isolate pure product. The reaction proceeds through Knoevenagel condensation along with Michael addition. Various spectroscopic methods characterised the isolated 1,4-dihydropyridine derivative. A good yield of around 85% with 8 mg of the catalyst within a reaction time of 2 h was reported.

Azizi and his colleagues (Heydari et al., 2016) have fabricated sulphated boric acid-functionalised magnetic nanoparticles and utilised them as a catalyst to synthesise esters from the Hantzsch reaction method. The magnetic nanoparticles were synthesised by refluxing a reaction mixture of Fe^{+2} and Fe^{+3} with a molar ratio of 1:2 and further treated with chlorosulphonic acid. The functionalised nanoparticles were reacted with boric acid, adhered to silica to obtain Fe_3O_4/SiO_2-H_3BO_4-HSO_3 nanoparticles, and filtered and washed with ethanol to isolate pure material. XRD analysis suggests a perovskite crystalline structure and stability up to 350°C as represented by TGA data with a boric acid concentration of 1.2 mmol/g. The catalytic efficiency was assessed in the Hantzsch ester formation reaction to synthesise 1.4-dihydropyridine derivatives (**47**). The single-pot reaction involved equimolar amounts of aldehyde (**46**) and ammonium acetate (**7**) and a double equimolar quantity of β-keto esters (**10**) (**Scheme 15**). The reaction proceeds through Knoevenagel condensation followed

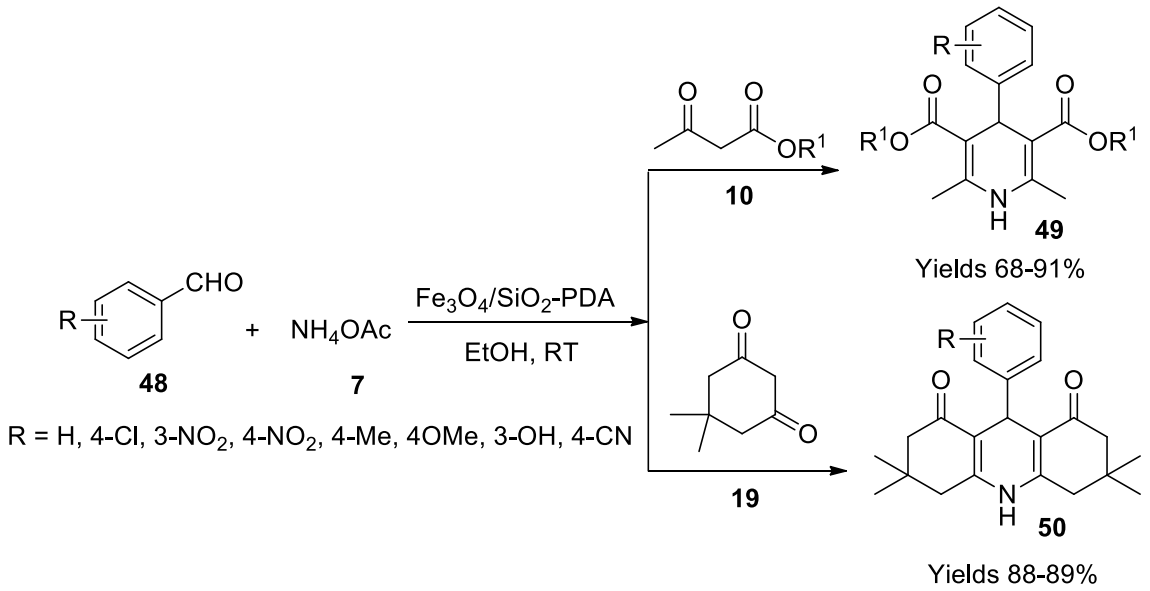

SCHEME 16 | Synthesis of dihydropyridine and hydroquinolines by the Fe_3O_4/SiO_2-PDA catalyst.

by Michael addition. The obtained precipitate was filtered and dried to gather the desired derivatives and characterised using various spectroscopic methods. The catalyst was isolated from the reaction mixture by an external magnetic field and reused for four to five reaction cycles without losing its efficiency.

Taheri-Ledari *et al.* (Taheri-Ledari et al., 2019) have investigated a comparative synthetic method for preparing pyrimidine-2,4-diamine-functionalised magnetic nanoparticles *via* refluxing, ultrasonication, and microwave methods to prepare 1,4-dihydropyridines. The Fe_3O_4 nanoparticles initially prepared were laminated with silica in the presence of PEG-300 and aqueous ammonia using TEOS as a silica source. The nanoparticles were manipulated with TMVS to adhere to vinyl terminals and were sonicated after adding 50 ppm melamine solution and then transferred into an ultrasound bath 50 KHz at 50°C. The obtained nanoparticles were separated using an external magnetic field, washed with ethanol, and then dried at 60°C. The gathered nanocomposites were characterised by FT-IR, ^{1}H NMR, ^{13}C NMR, mass, XRD, TGA, SEM, and AFM analyses. The analyses advocate enhanced texture conservation surface functionalisation along with reduced aggregation of the nanoparticles. High yielding capacity with 89% product formation dihydropyridines (**49**) and hydroquinolines (**50**) was observed within a short reaction time of 10 min (**Scheme 16**).

Silica-Based Catalysts

Silica has been used as a bolster for other adhesive elements to construct an efficient catalytic structure. Owing to its colossal surface area of 800 m^2/g, it can accommodate many reagent particles on its surface, exposing them to interact with one another to obtain the desired product. It is a readily available material that can be restructured with acidic functional groups such as phenolic or carboxylic groups or other cationic moieties. The silica-based nanostructures were fabricated to serve as efficient, recyclable material with intransigent sustainability. Usually, silica is doped with different d-block elements to enhance catalytic efficiency by offering amplification of reagent interaction. Various methods such as co-precipitation, sol–gel, micro-emulsion, laser pyrolysis, thermal decomposition, hydrothermal process, sonication, and microwave irradiation have been utilised (Neamani et al., 2020).

Neamani and his colleagues (Neamani et al., 2020) developed basic hollow mesoporous N-doped silica rods with magnetic properties. The material synthesis consisted of several steps where a mixture of multilayered carbon nanotubes was dissolved in methylene chloride and then subjected to sonication. A mix of acetic acid and $KMnO_4$ was added and agitated at 80°C to ensure hydroxylation of multiwalled carbon nanotubes. An Fe^{+3} and Fe^{+2} solution in 1.75 ratios was then added, and the product was washed with ammonia. The magnetised nanotubes were then doped with silica using a TEOS and DEA solution mixture while using CTAB as a structural directing agent. The vast surface area of around 10.4 and 493.8 m^3/g was established through BET analysis. Spiro oxindole-1,4-dihydropyridine derivatives (**53**) were synthesised in the presence of the prepared material as a catalyst. A good 80% yield was observed with minimal use of N-1.2% weight of m-SiO_2 in the presence of ethyl alcohol. The sequential mechanism of Knoevenagel condensation followed by Michael addition and cyclisation was observed. +I substituents in the reactant heterocyclic compound aided better yield as high as 92% within 6 h (**Scheme 17**). Also, the catalyst showed a good deal of consistency after several consequent usages.

Sharma and Gupta have composed a silica-based sulphonic acid catalyst that was laminated with ionic liquid (Sharma and Gupta, 2015). The silica activated with 50% HCl (HCl: H_2O 1:1)

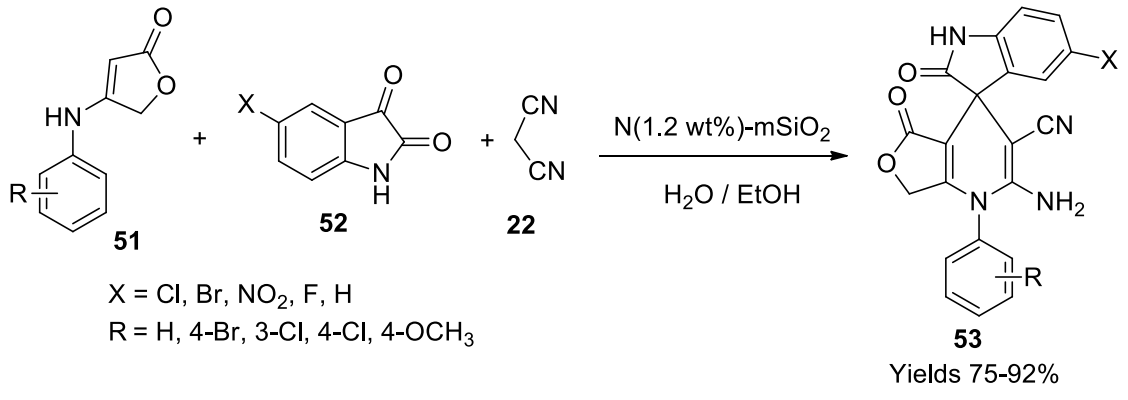

SCHEME 17 | Synthesis of spiro oxindole-1,4-dihydropyridines by the N-doped silica catalyst.

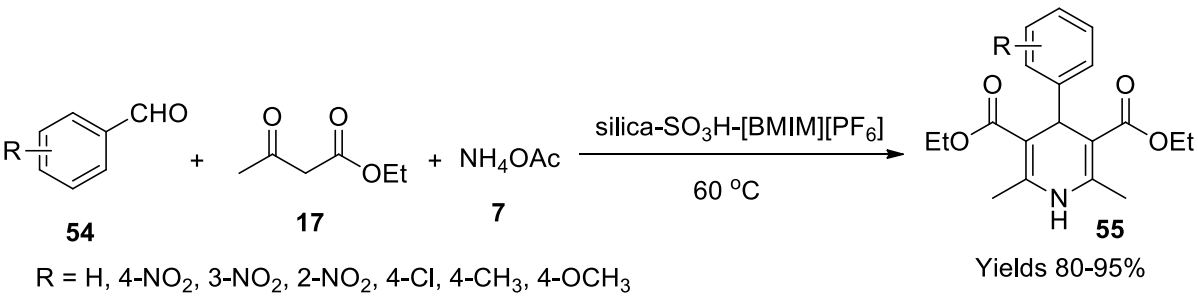

SCHEME 18 | Synthesis of dihydropyridines by the silica-SO_3H-[BMIM][PF_6] catalyst.

was treated with 3-mercaptopropyl (trimethoxyl) silica and toluene and refluxed for 24 h. The resulting 3-mercaptopropyl silica is then filtered and treated with 30% H_2O_2 solution and concentrated H_2SO_4 while constantly stirring for 20 h. The obtained material by filtration was dried and characterised. The catalyst was a porous powder with an amorphous structure of the particles as deemed by SEM and TEM imaging. The material retained its form up to 360°C. A [BMIM][PF_6]-laminated (20%) silica-based sulphonic acid catalyst was found to be most efficient among other derivatives. The material showed excellent catalytic activity in synthesising 1,4-dihydropyridines (**55**), offering high yields of 95% within a reaction time of 15 min (**Scheme 18**). The catalyst showed similar activity even after several cycles.

Choghamarani and his team (Ghorbani-Choghamarani et al., 2019) have fabricated a green heterogeneous catalyst by adhering cobalt onto the surface of SBA-15, which showed exceptional ability in oxidising sulphides and the manufacture of polyhydroquinolines. The mesoporous SBA-15 was prepared by the sol–gel method and functionalised by refluxing it with 1.5 ml of 3-chloropropyltrimethoxysilane in 20 ml of dry toluene medium. The resulting CPTMS (SBA-15-Cl) was functionalised by refluxing it with 2-amino-2-methyl-1,3-propanediol and triethylamine dispersed in dry toluene. The final product was adhered to with cobalt by using 0.73 g of $Co(NO_3)_2.6H_2O$ as the cobalt source and refluxing it for 16 h, which was later washed with ethanol to obtain the pure product free from by-products. The homogenous dispersion of the Co metal onto the surface of the modified SBA-15 gave a mesoporous cavity with a volume of 0.534 cm^3/g and a surface area of 238.47 m^2/g, which was represented by X-ray mapping and BET analysis, respectively. The prepared catalyst was used to synthesise polyhydroquinolines using the Hantzsch reaction mixture and oxidation of sulphides. The polyhydroquinolines (**57**) were prepared by using a reaction mixture of dimedone (**19**), aldehyde (**56**), ammonium acetate (**7**), and ethyl acetoacetate (**17**) using 1 mmol each aided with 8 g of SBA-15@AMPD-Co nanocatalyst (**Scheme 19**). The prepared yellow solid was filtered and washed with ethanol to gather polyhydroquinolines in the range of 86%–97% within 35 min. Apart from the above method, sulphides were oxidised using SBA-15@AMPD-Co in the presence of H_2O_2 in a solvent-free environment. TLC determined the reaction completion, and the gathered products were confirmed using FT-IR, ^1H, and ^{13}C NMR spectroscopic data.

Zirconium-Based Catalysts

Zirconium oxide or zirconia is a ceramic oxide material used as a catalyst by incorporating it in various polymeric structures, making it a biocompatible catalyst. Due to its high thermal

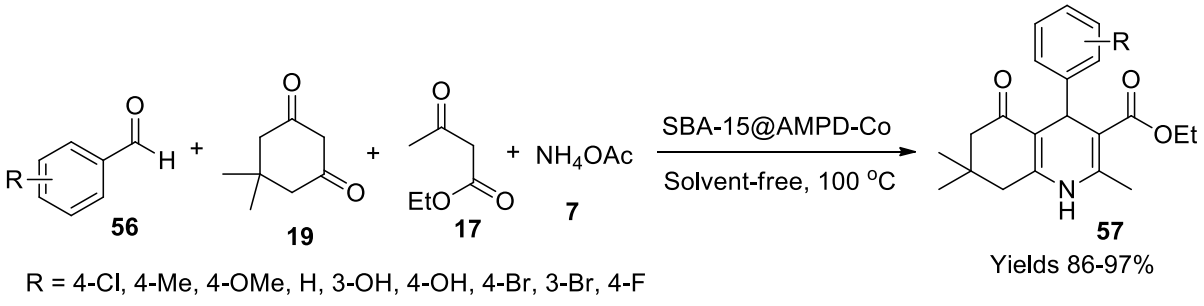

SCHEME 19 | Synthesis of hydroquinolines by the SBA-15@AMPD-Co catalyst.

capacity and thermal insulation properties, zirconia can be used at high temperatures where other similar materials fail. According to the literature and structural survey, zirconia acts as a Lewis acid and base and thus as a bifunctional catalyst. The optimisation of zirconia is still a work in progress because of its exiguous charge transfer and pH sensitivity. Zirconia is also used with other transitional metals such as silver, palladium, and iron or other metallic oxides such as ceria, titania, silica, and vanadia. Zirconia is used as a catalyst in many organic transformations and shift reactions such as epoxidation, isomerisation, and alkylations. Synthetic methods such as co-precipitation, which is used as a wet process, and the sol–gel method and hydrothermal processes aid in preparing solid zirconia particles. Its physical characteristics have been studied intensively to analyse its surface area, nanoparticle structure, and size using various analytical spectroscopic techniques such as FT-IR, SEM, and TEM analysis.

Majhi and his team (Majhi et al., 2019) worked on fabricating a microporous heterogeneous catalyst Al-pillared α-ZrP adhered with sulphamic acid to be employed during the preparation of 1,4-dihydropyridines. The tailoring protocol involves a set of subsequent steps initiated with the preparation of α-zirconium phosphate (ZP) by dissolving 10 g of $ZrOCl_2.8H_2O$ in 100 ml of phosphoric acid in a round-bottomed flask equipped with a reflux condenser and refluxed for 24 h. The solid formed as a result is isolated *via* centrifugation and collected by decanting the supernatant. The gathered solid was washed with hot DM water to get rid of any unwanted reagents like AgCl. The accumulated product was dried in a hot air oven to obtain α-ZrP compound.

Further, 2 g of the earlier prepared compound was dissolved in 200 ml of 0.1 M n-propyl amine solution while continuously stirring for 24 h to form an opaque white colloidal solution subjected to *in-situ* polymerisation to obtain alumina pillared α-ZrP (AZP). Alternatively, 250 ml of 0.2 M $AlCl_3$ solution was added to the colloidal solution with continuous stirring to which 1.2 M NaOH solution was introduced in a molar ratio of 1:2 with Al. The solid obtained is centrifuged to collect it and washed with hot DM water to eliminate unwanted Cl^- molecules and dried at 100°C. The gathered product was ground to powder and subjected to calcination for 2 h at 300°C to achieve AZP. Furthermore, 1 g of AZP was dissolved in a 20-ml solution of SA in water to gain a mesoporous surface. The aqueous solution was continuously stirred for 6 h at 90°C to attain a solid and further dried at 120°C to achieve a SAxAZP composite. The catalyst was subjected to various elucidation techniques, including XRD, which exposed its crystalline structure with an H3-type surface area of 118 m^2/g and a pore volume of 0.19 cm^3/g with a particle size of 25–50 nm as represented by SEM analysis. TGA analysis showed that the catalyst was stable up to 600°C. Its catalytic activity was evaluated using the Hantzsch reaction to prepare 1,4-dihydropyridines (**59**), exercising single-pot synthesis with a reaction mixture of aryl aldehyde (**58**), acetoacetic esters (**17**), and ammonium acetate (**7**) in the presence of the above-obtained catalyst (**Scheme 20**). The reaction proceeded through Knoevenagel condensation and Michael addition with enhanced Bronsted acid sites. The yield obtained ranged from 75% to 90% depending on the aryl aldehyde used in ethyl alcohol. The products gained were characterised using FT-IR, ^1H, and ^{13}C NMR methods.

Kusampally *et al.* (Kusampally et al., 2020) studied diverse reaction conditions to synthesise 1.4-dihydropyridines (**62** and **63**) using zeolite-anchored Zr-ZSM-5 as an illustrious catalyst. To tailor the material, ammonium ZSM-5 was initially calcinated using a muffled furnace set to 500°C under aerobic conditions subjected to a heating ramp rate of 5°C per minute for 4 h to acquire H-ZSM-5. A solution of zirconium nitrate in water was added dropwise into H-ZSM-5 while constantly stirring the solution to incorporate zirconium nitrate into H-ZSM-5. The generated catalyst was dried at 120°C for 12 h, and the dry product was recalcinated in a muffled furnace at 500°C. The gathered catalyst was subjected to XRD, SEM/EDS, and BET SA-PSD spectroscopic techniques, exploring its crystalline structure. The high surface area of 341 m^2/g allows the zeolite catalyst to interact with the reagents increasing the active sites. The classic Hantzsch reaction was examined using the Zr-ZSM-5 Zeolite catalyst in a single-pot reaction. The process involved benzaldehyde (**60**), ethyl acetoacetate (**17**), and ammonium hydroxide (**61**) in obtaining 1,4-dihydropyridines (**Scheme 21**). The use of catalyst gained a high yield of the product, around 96%, with minimal use of 30 mg within 25–35 min. With the microwave-assisted protocol, the reaction mixture and catalyst were placed in a preheated microwave oven at a temperature of 300°C. The enamine formed as an intermediate participated in Michael addition to give the target compound. The catalyst retained its viability even after five consequent cycles.

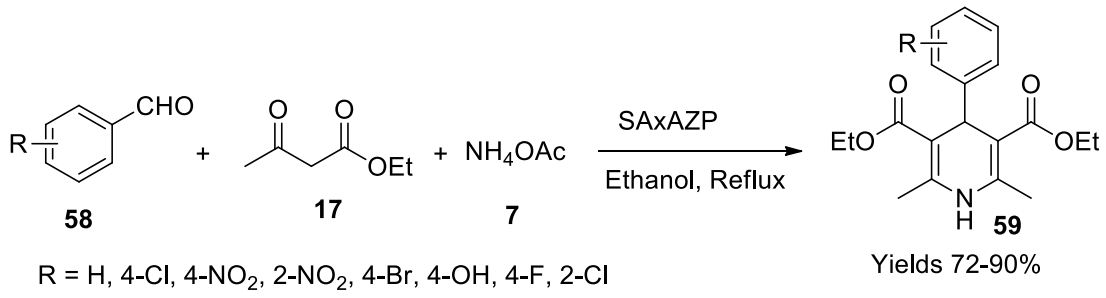

SCHEME 20 | Synthesis of dihydropyridines by the zirconium phosphate catalyst.

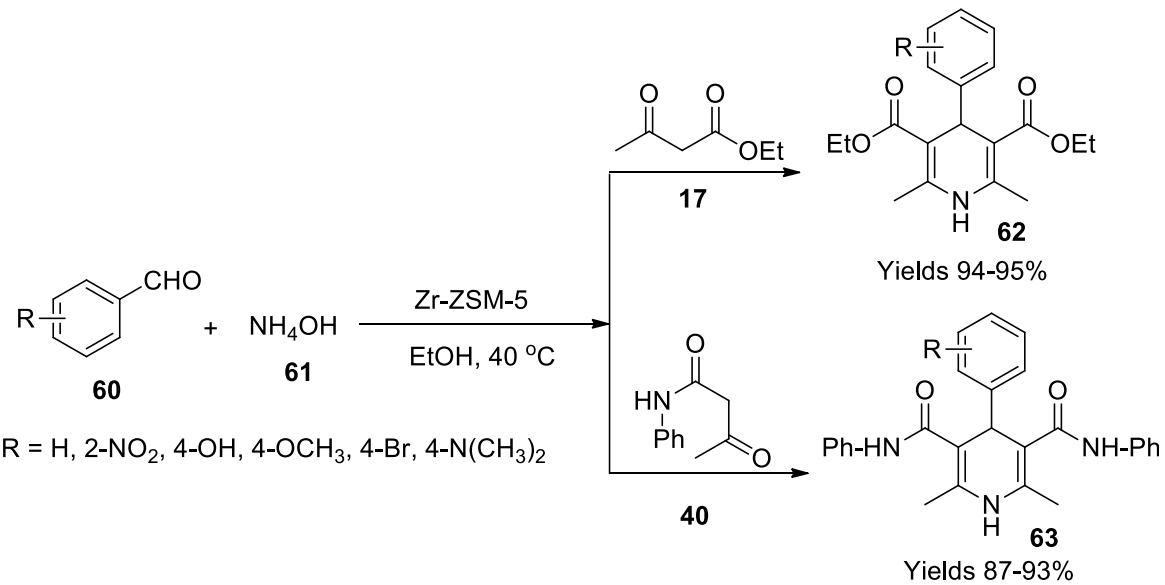

SCHEME 21 | Synthesis of dihydropyridines by th eZr-ZSM-5 catalyst.

Apart from its sustainability, the catalyst's efficiency to reduce the reminiscent reagent brands it an eco-catalyst.

Amoozadeh and his colleagues (Amoozadeh et al., 2016) have fabricated a solid heterogeneous catalyst, the sulphonic acid immobilised on nano zirconia. Initially, nano-ZrO_2 particles were produced *via* chemical precipitation of a 100-ml solution of $ZrOCl_2.8H_2O$, whose pH was adjusted to 10 by adding 2 M NaOH solution. The precipitate was filtered and dried at 120°C, which was later calcinated over a temperature range of 500–1,200°C. Later 0.5 ml of chlorosulphonic acid was introduced into nano-ZrO_2 dispersed in dry dichloromethane. The obtained reaction mixture was transferred into a suction flask facilitated with a constant-pressure dropping funnel and a gas inlet tube, allowing the conduction of HCl gas to be adsorbed onto the solvent, i.e., water, while continuously stirring the solution. A light cream colour powder was isolated after 30 min, which was washed with ethanol and dried at 100°C. It was found stable up to 150°C. FE-SEM data established the spherical shape of 30–40 nm in diameter. Its crystalline structure through XRD analysis showed a growth rate of 554. In a single-pot preparation of polyhydroquinoline derivatives in a solvent-free environment, the catalyst exhibited good performance. A reaction mixture consisting of 1,3-cyclic diketone (**65**), different aromatic aldehydes (**64**), ammonium acetate (**7**), and malononitrile (**22**) was used to produce polyhydroquinoline derivatives (**66**) (**Scheme 22**). The obtained products were filtered and washed with hot ethanol to eliminate any unreacted reagents and dried at optimum temperatures. The gathered hydroxyquinoline derivatives were structurally elucidated using FT-IR, ^1H, and ^{13}C NMR spectroscopic analysis; high yields of products ranging from 87% to 95% were obtained advocating its catalytic potential. Optimal conditions for the preparation were determined through the central composite deposit.

Bhaskaruni *et al.* (Bhaskaruni et al., 2017) have constructed a heterogeneous catalyst, RuO_2/ZrO_2, for the preparation of dihydropyridine derivatives (**69**), adopting a single-pot synthetic method using a reaction mixture

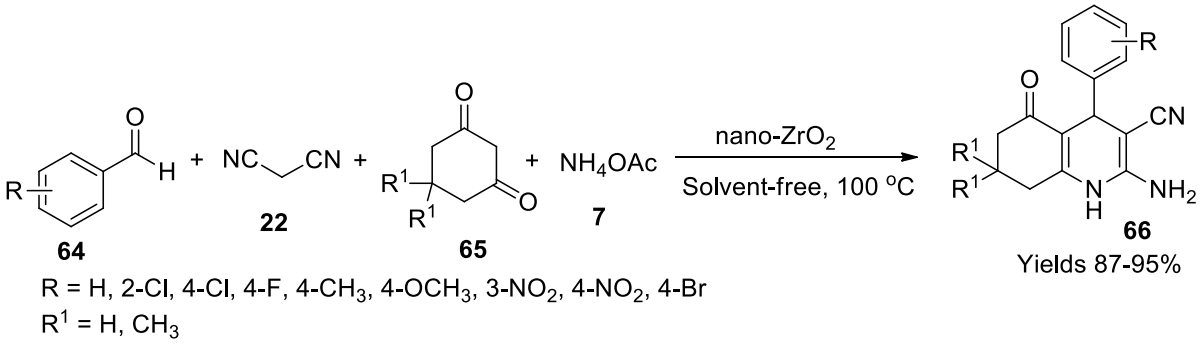

SCHEME 22 | Synthesis of hydroquinolines by the nano-ZrO_2 catalyst.

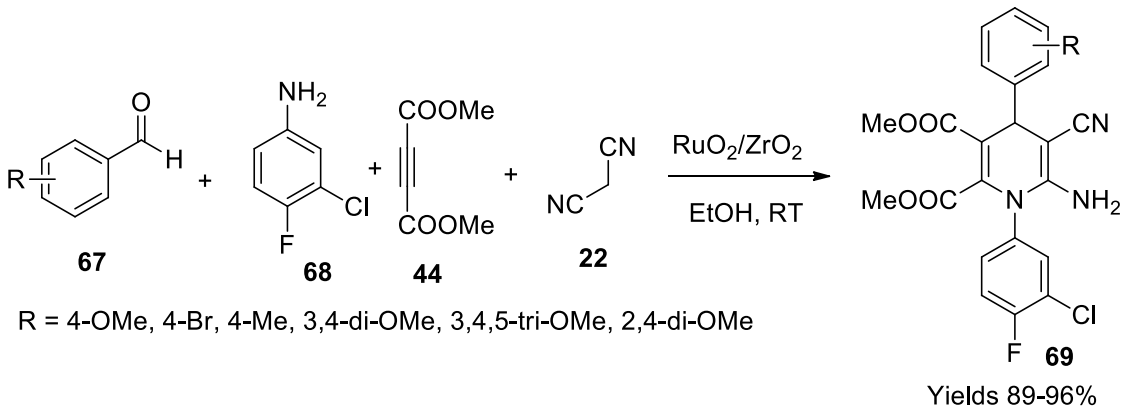

SCHEME 23 | Synthesis of dihydropyridines by the RuO_2/ZrO_2 catalyst.

consisting of equimolar amounts of aldehyde (**67**), malononitrile (**22**), diethyl acetylene dicarboxylate (**44**), and 3-chloro 4-fluoroaniline (**68**) under the influence of RuO_2/ZrO_2 in 10 ml of ethyl alcohol medium. The reaction mixture was continuously stirred, and the produced derivatives were filtered and washed with ethanol (**Scheme 23**). The gathered derivatives were spectroscopically analysed using FTIR, ^1H, and ^{13}C NMR techniques. The catalyst was prepared through the wet impregnation technique by dissolving equal amounts of ZrO_2 and $RuCl_3.xH_2O$ in 100 ml of water while continuously stirring at room temperature for 8 h. The slurry obtained from filtration was oven-dried for 5 h at 110°C–120°C followed by calcination at 450°C for another 5 h to gain the Ru_2O/ZrO_2 whose structure was explored using various analytical techniques such as XRD analysis describing its polycrystalline structure with a diameter of 6.3 nm while the particle size of the nanoparticles was 11 nm with irregular shapes with a uniform dispersion of RuO_2 onto the zirconium surface as assessed through TEM and SEM data. The BET analysis of the catalyst exposed its mesoporous surface area of 41.99 m^2/g with a pore volume of 0.134 cm^3/g and a pore size of 12.7 nm. It was observed to retain its catalytic viability for seven consecutive cycles without losing its efficiency.

Bhaskaruni *et al.* (Bhaskaruni et al., 2018) have constructed a contemporary reaction method under the catalytic influence of V_2O_5/ZrO_2 adopting a single-pot cyclic condensation of a reaction mixture consisting of equimolar amounts of benzaldehyde (**70**), 5,5-dimethyl-1,3-cyclohexanedione (**19**), acetoacetanilide (**40**), and ammonium acetate (**7**) in the presence of V_2O_5/ZrO_2 nanoparticles using 5 ml of ethanol as solvent (**Scheme 24**). The reaction mixture is continuously stirred for 15 min, and then the desired hydroxyquinoline products (**71**) were isolated through solvent extraction using ethyl acetate followed by evaporation. The reaction proceeded through Knoevenagel condensation along with Michael addition and cyclisation. The gathered product was recrystallised from ethanol to gain a pure product which was subjected to various spectroscopic analyses for characterisation. The catalyst was prepared by wet impregnation method by dissolving equal amounts of V_2O_5 and ZrO_2 in 100–150 ml of DM water while continuously stirring at room temperature for 8 h. The slurry obtained from filtration was oven-dried for 5 h at 120°C–150°C followed by calcination at 450°C for another 5 h to gain V_2O_5/ZrO_2. Its structure explored using various

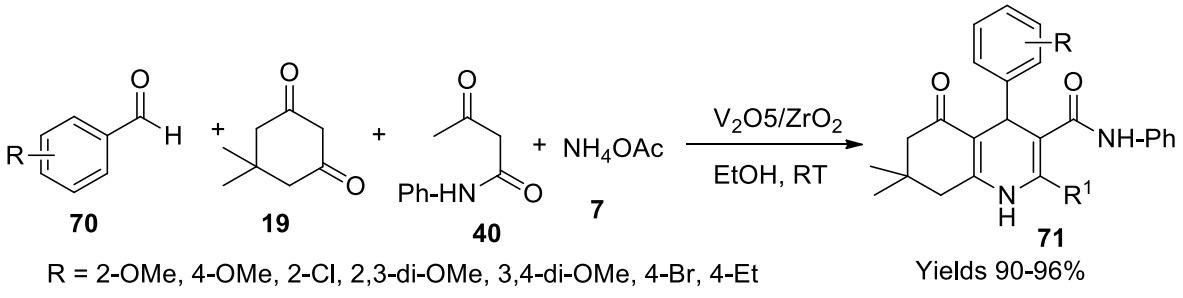

SCHEME 24 | Synthesis of hydroquinolines by the V_2O_5/ZrO_2 catalyst.

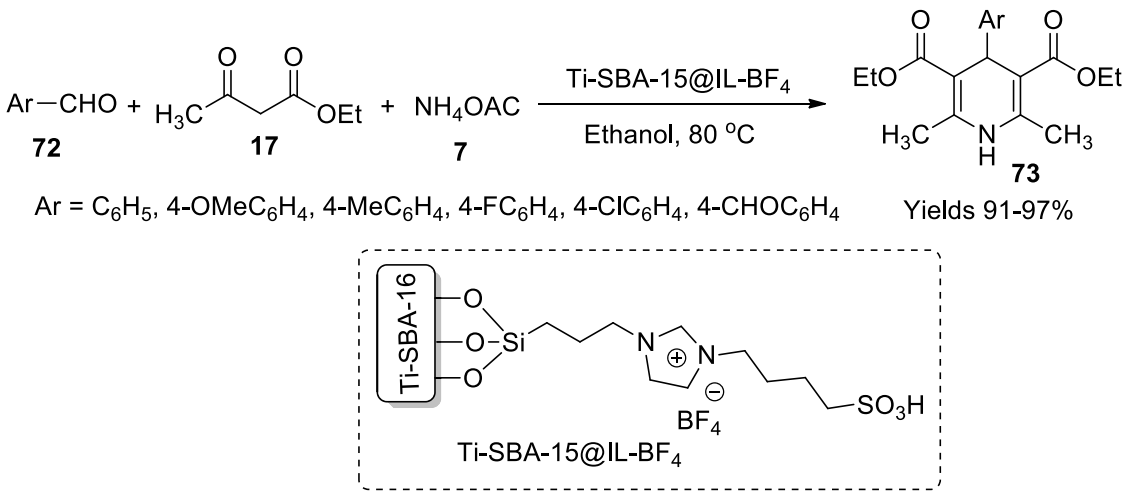

SCHEME 25 | Synthesis of dihydropyridines by the Ti-SBA-15@IL-BF_4 catalyst.

analytical techniques such as XRD analysis confirms its polycrystalline structure with a 7.6 nm diameter. The SEM imaging and TEM imaging display massive irregular structures due to the aggregation of zirconium and vanadium moieties. The surface area of the catalyst was 89.2219 m^2/g with a mesoporous pore volume of 0.327 cm^3/g and a pore size of 10.32 nm. The catalytic use gained high yields around 90%–96% with a short reaction time of ≤20 min while retaining its catalytic efficiency for five to six consecutive cycles. The exciting feature of this method is the easy access to pure products without chromatographic separation.

Ionic Liquid-Based Catalysts

Ionic liquids are a brilliant alternative for the vintage volatile solvents, made of ionic components such as anions or cations with covalent crystalline structures. The only difference between molten salts and ionic liquids is the melting point which is presumed to be <100°C for ionic liquids, making them stable and efficient solvents. The low-volatility, low-melting-point, and low-vapour pressure impart heterogeneous characteristics to these ionic liquids aiding their hassle-free separation. The ionic components of the liquids account for their intense polarity, which validates their physical and chemical properties. Because of high solubility and eminent anti-corrosion activity, ionic liquids are used as anti-corrosion agents for metals and alloys and as a significant solvent catalyst in various industrial and laboratory preparations. Followed by the ammonium-hinged ionic liquid invention, researchers designed different ionic liquids incorporating imidazolium, pyridinium, phosphonium, and tetra-ammonium components.

In contrast to their ionic nature, ionic liquids are poor conductors of electricity and can dissolve polar and non-polar materials. Ionic liquids are differentiated depending on the functional groups of the side chains, which act as electron-exchangeable sites, where the electron-donating groups impart basic nature. In contrast, electron-withdrawing nature imparts an acidic nature to the liquids.

Tan and his colleagues (Tan et al., 2019) have formulated a technique for incorporating titanium into a mesoporous material to catalyse Hantzsch reaction mediated by an ionic liquid (**Scheme 25**). The tailored catalyst Ti-SBA-15@IL-BF_4 was used to form 1,4-dihydropyridine derivatives (**73**) which showed high yielding capacity and sustained its catalytic ability even after running for five consequent cycles. The catalytic activity is aided by the mesoporosity of the material and the acidic nature of the

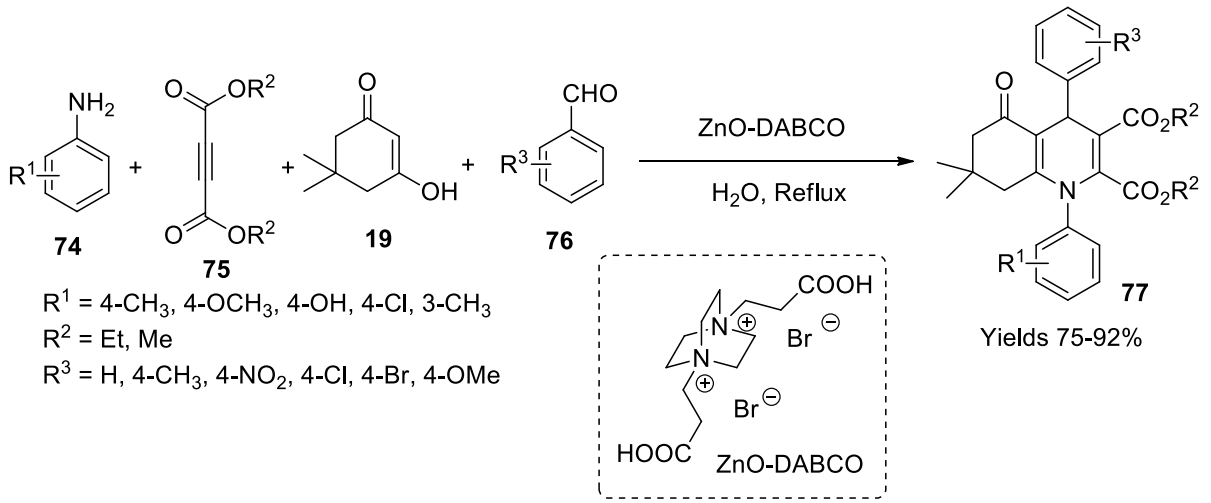

SCHEME 26 | Synthesis of hydroquinolines by the ZnO-DABCO catalyst.

ionic liquid with a product yield that gained excellent yields around 93% within a short reaction time.

Mondal and her colleagues (Mondal et al., 2019) fabricated quasi-heterogeneous DABCO-based ZnO nanoparticles mediated by the acidic ionic liquid using the solvothermal technique. DABCO is a 3-amine with a localised electron lone pair of nitrogen in a cage-like structure. The DABCO is di-substituted with the carboxylic group when reacted with 3-bromopropionic acid. The combined size of the catalyst particle was 200–400 nm, whereas the size of the ZnO NP was 5–6 nm offering a greater surface area-to-volume ratio. The magnificence of this catalyst lies in the fact that it carries acidic moiety imparted by the ionic liquid apart from the basic nature inherited by the amorphous zinc oxide; hence, it possesses both acidic and basic nature in a single structure. They analysed the catalytic performance of synthesising hydroxyquinoline derivatives (**77**), namely, N-aryl poly-hydro quinoline-based drugs, which resulted in excellent yields as high as 91% within a minimum reaction time of 2 h using water as a solvent (**Scheme 26**).

Agarwal and Kasana synthesised ferromagnetic nanocomposite, [Fesipmim]Cl, by the sol–gel method, and used it as a catalyst for generating dihydropyridines (**79**) *via* the Hantzsch reaction (Agrwal and Kasana, 2020). To prepare the desired nanocomposite, initially, a 1:2 ratio of Fe^{+2} and Fe^{+3} was dispersed in 200 ml of water, while vigorously stirring 25 ml of ammonium solution (30%) which was added and further subjected to mechanical stirring for 24 h to obtain black nanoparticles, which were washed and dried at 80°C. The gathered nanoparticles were laminated with silica employing the sol–gel method. A volume of 1.2 ml of tetraethyl orthosilicate is introduced into a nanoparticle-dispersed solution of ethanol, water, and ammonia while constantly stirring for 12 h. The obtained ferrite@SiO_2 nanoparticles were washed and dried. The dried nanoparticles were gathered and dispersed in water. Simultaneously, ionic liquid, [Sipmim]Cl, was also prepared by refluxing 4.8 ml of 0.06 mol 1-methylimidazole and 14.5 ml of 0.07 mol (3-chloropropyl) triethoxysilane. Later, 2 g of ferrite@SiO_2 NPs and 25 ml of dry toluene were mixed in a beaker, and 1 g of [Sipmim]Cl was introduced dropwise into it. The obtained nanoparticles were washed and dried at 60°C for 2 h. The size catalyst nanoparticle was 7–11 nm from TEM analysis, and the catalyst's magnetisation was assessed to be 13 emu/g from VSM data. Its catalytic efficiency was investigated on the three-component Hantzsch reaction involving benzaldehyde (**78**), ethyl acetoacetate (**10**), and ammonium acetate (**7**) (**Scheme 27**). A good 95% yield of dihydropyridines within a solvent-free abode with a minimum catalyst (100 mg) and a short reaction time was observed. The ferrite@SiO_2 NPs sustained their vitality for seven consequent cycles.

Baghery and Zolfigol have reported the ability of 3,6-dioxaoctamethylenediamminium trifluoromethanesulfonate, a convenient ionic liquid, as a catalyst for synthesising 1,4-dihydropyridines (**83**) (BagheryZolfigol and Zolfigol, 2017). To prepare the ionic liquid, 6 mmol of trifluoromethanesulfonic acid was dropwise added to 3 mmol of 3,6-dioxaoctamethylenediamine at 5°C under stirring. Stirring continued for 25 min at room temperature. The acquired yellow-coloured product was washed with diethyl ether to decant the ruminants and vacuum dried at 50°C for 1 h. FT-IR, ^{1}H, ^{13}C and ^{19}F NMR, MS, TG, difference thermo gravimetric (DTG), and difference thermo analysis (DTA) data were used to characterise the material. The single-pot four-component reaction involved substituted aldehyde (**80**), malononitrile (**22**), acetylene dicarboxylates (**82**), and anilines (**81**) in equal 1-mmol quantities in solvent-free abode at 50°C. 3,6-Dioxaoctamethylenediamminium trifluoromethanesulfonate showed remarkable activity. The reaction was assumed to follow Knoevenagel condensation along with Michael addition and intramolecular cyclisation. The yield of 1,4-dihydropyridines was high, around 93%–96%, with minimal use of a catalyst (2–5%) within 30 min (**Scheme 28**). The product was

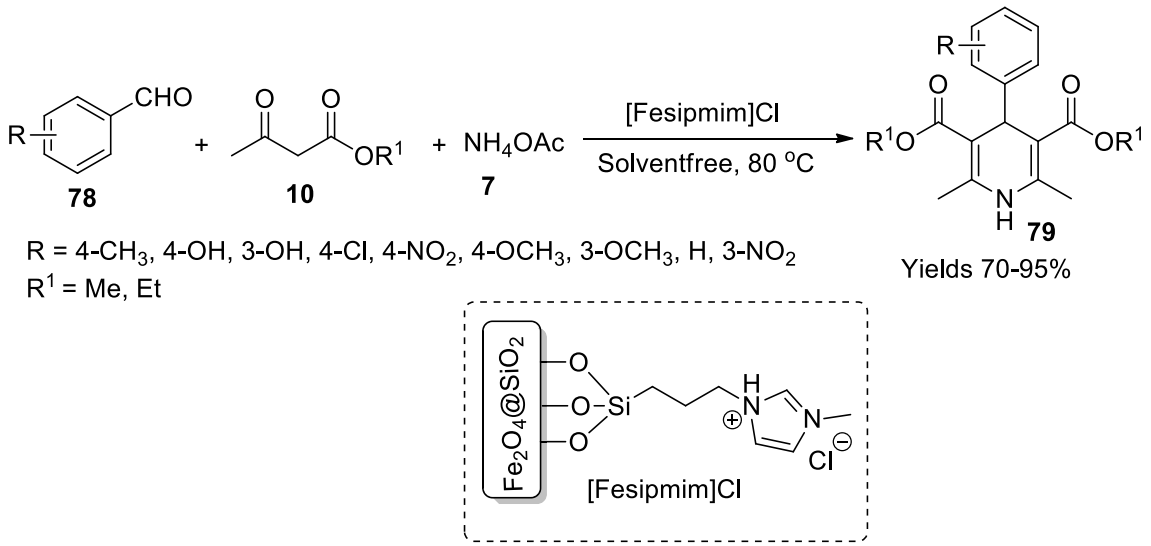

SCHEME 27 | Synthesis of dihydropyridines by the [Fesipmim]Cl catalyst.

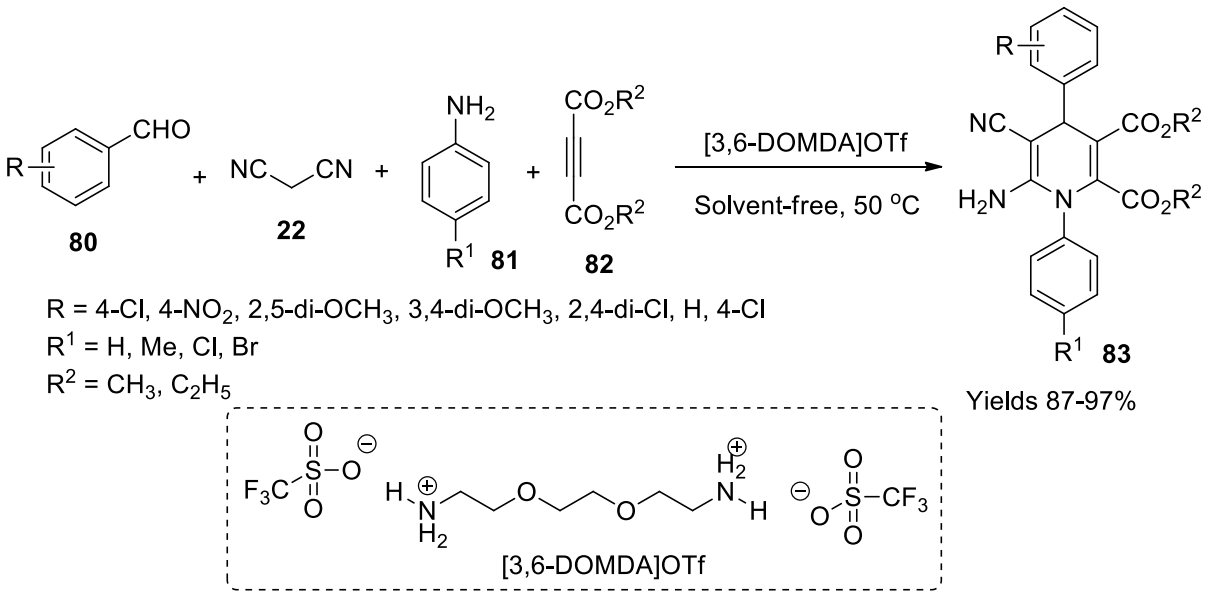

SCHEME 28 | Synthesis of dihydropyridines by the [3,6-DOMDA]OTf catalyst.

confirmed by using FT-IR, ^{1}H, and ^{13}C NMR. The catalyst sustained its activity even after six consecutive cycles.

Moheiseni *et al.* (Moheiseni et al., 2021) designed a dicationic liquid bolstered with β-cyclodextrin/imidazolium, which was adhered to a silicon gel. The composite was used as a facile catalyst in the condensation of the Hantzsch reaction. The preparation of the catalyst involved several steps. Initially, mono-Ts-βCD was prepared using a solution of β-cyclodextrin taken in NaOH dissolved in 10 ml of distilled water. The temperature of the mixture was dropped to 0°C–5°C while adding THF and continuously stirred. While maintaining the same temperature range, a solution of TsCl in THF was added dropwise while stirring. The reaction mixture was neutralised using 2 N HCl and later poured into ice to obtain a white-coloured precipitate filtered and washed with acetone. Simultaneously, a reaction mixture of imidazole and NaOH was added to 10 ml of DMSO and stirred at 60°C while adding 1,4-dibromobutane. The mixture was allowed to drop its temperature and poured into water to obtain 1,4-bis(imidazol-1-yl)-butane as a white solid. [βCD/Im](OTs)$_2$ was prepared by

SCHEME 29 | Synthesis of hydroquinolines by silica supported ionic liquid catalyst.

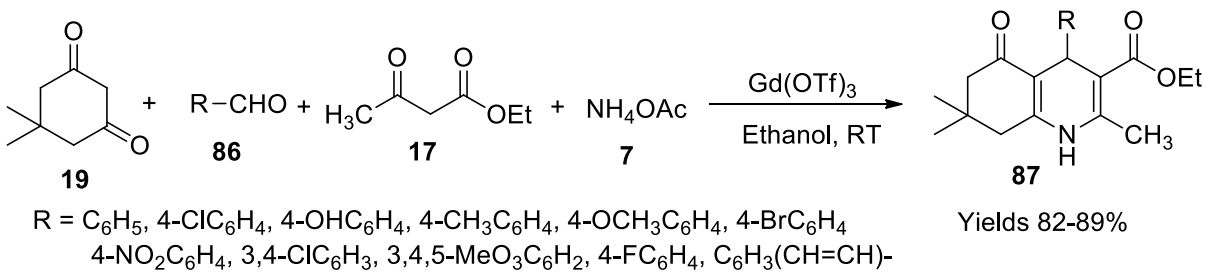

SCHEME 30 | Synthesis of hydroquinolines by the $Gd(OTf)_3$ catalyst.

mixing solutions of mono-Ts-βCD and 2.5 ml of dimethylformamide (DMF) into a mixture of 1,4-bis(imidazol-1-yl)-butane and 2.5 ml of DMF while maintaining the temperature between 40°C and 60°C. The white precipitate obtained was filtered and washed with CCl_4. To adhere the prepared ionic product onto silica gel, to the solution containing $[\beta CD/Im](OTs)_2$ in 30 ml of DMF and NaOH, 3-chloro propyl trimethoxysilane was added slowly under continuous stirring and temperature maintained at 90°C in an N_2 environment after 30 min. The product was filtered and added to a solution containing tetraethoxysilane and 1-butanol in 0.7 ml of water. The mixture was neutralised using 2 M HCl. The hydrogel was stirred continuously for 3 h at 80°C to obtain a final white precipitate filtered and washed with lukewarm water and acetone. The gathered catalyst was characterised by FTIR, SEM, and NMR using TMS as a standard. The authors established the catalytic efficiency of the di-ionic liquid on a single-pot Hantzsch condensation reaction between aromatic aldehyde (**84**), a β-dicarbonyl compound (**19**), and ammonium acetate (**7**) at a temperature of 90°C to obtain the product, hydroquinolines (**85**). The product was filtered and recrystallised in ethyl alcohol (**Scheme 29**). The catalyst showed high efficiency with 0.02 g of the catalyst offering a high 90% yield at 90°C in 20 min, which is relatively high compared with Tripodo's technique which gives 35%.

Miscellaneous Catalysts

Mansoor *et al.* (Sheik Mansoor et al., 2017) observed the advantageous characteristics of gadolinium(III) trifluoromethanesulphonate $\{Gd(OTf)_3\}$ to synthesise polyhydroquinolines (**87**) at room temperature. It showed significant potential to perform ideally in both polar and nonpolar solvents, making it a desirable catalyst. $Gd(OTf)_3$ acted efficiently as a mild Lewis acid catalyst for the four-component coupling reaction between benzaldehyde (**86**), an active methyl group (ethyl acetoacetate) (**17**), 5,5-dimethyl-1,3-cyclohexanedione (dimedone) (**19**), and ammonium acetate (**7**) (**Scheme 30**). After confirming the completion of the reaction through TLC, the obtained product was recrystallised for purification. A good yield (82%–89%) of the target product was achieved at a minimal catalytic use as small as 1 mol%. Good retention of the catalytic activity was observed at 5 mol% using ethanol as solvent. Other solvents like acetone generated undesirable by-products due to rapid reactivity accompanied by the usage of a catalyst. The catalyst was retrieved comfortably from the filtrate, aiding its slightly higher potential to be soluble in water than organic solvents. The filtrate was subjected to evaporation under reduced pressure to gather the catalyst for further usage.

Balaboina and his colleagues (Balaboina et al., 2019) have prepared spiro oxindole-hydroquinolines (**90**), which paves a contemporary pathway for the drugs against cancer cells employing a single-pot method aside from Ag(I) and organo-*N*-heterocyclic carbenes used as a catalyst. This new catalyst was a progeny from labile Ag(I)-NHC in ethanol; therefore, it accommodates acidic Ag(I) alongside a basic NHC. A 3%–5% metal to organic–complex ratio was maintained for a smooth reaction. A single-pot four-component reaction between isatin

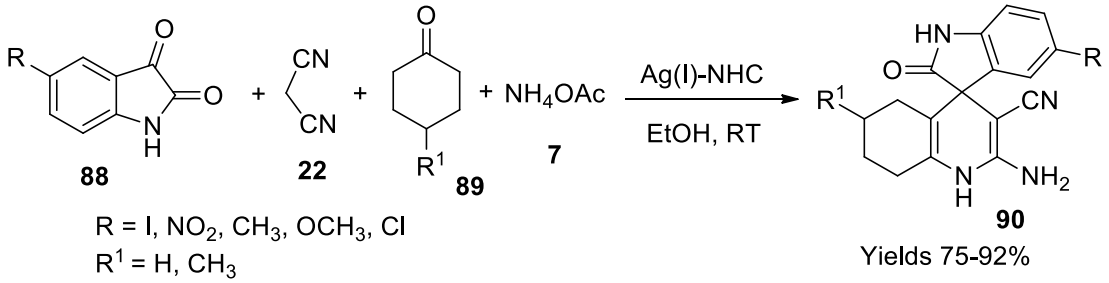

SCHEME 31 | Synthesis of spiro oxindole-hydroquinolines by the Ag-NHC catalyst.

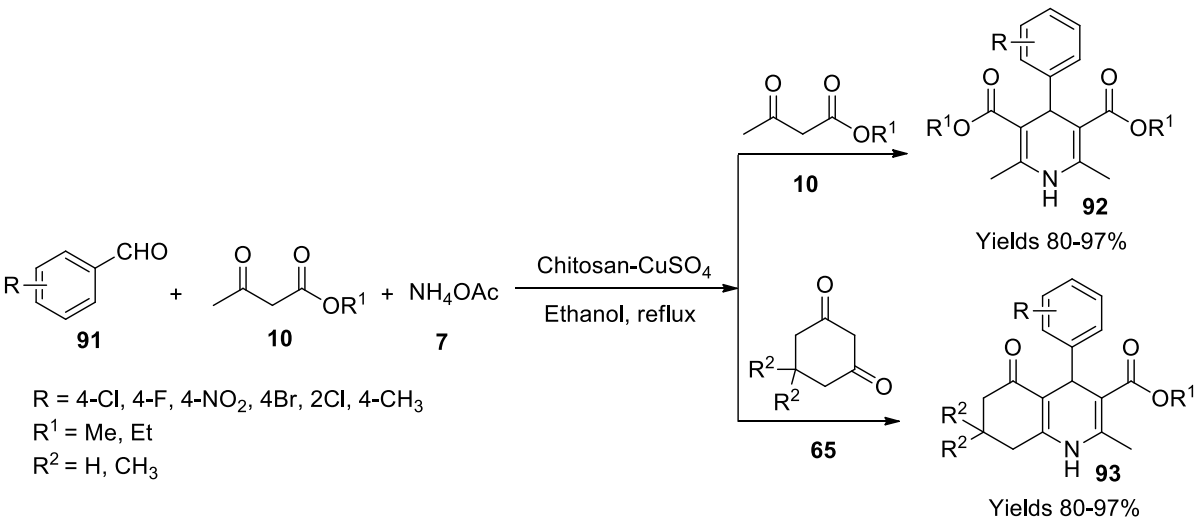

SCHEME 32 | Synthesis of dihydropyridine and hydroquinolines by the chitosan-$CuSO_4$ catalyst.

(**88**), malononitrile (**22**), cyclo ketones (**89**), and ammonium acetate (**7**) was utilised (**Scheme 31**). The formation of spiro oxindole was established by TLC, EA, ESI-Mass, ^{1}H, and ^{13}C-NMR spectroscopic techniques apart from the MP value and XRD data. It was assumed to follow Knoevenagel condensation along with Michael addition yielding a high amount of product around 91% within 10 min. The prepared drugs were studied for their combating capacity toward two types of cancer cells, namely, MCF-7 and HepG2, which showed appreciable cytotoxicity.

Dekamin and his team (Dekamin et al., 2016) have explored a chitosan macromolecular-based $CuSO_4$ catalyst to synthesise Hantzsch products. A volume of 5 g of chitosan in 100 ml of water was dispersed, to which 1 g of $CuSO_4$ was added under continuous stirring. The desired catalyst was isolated upon centrifuging the resultant mixture after 2 h. The catalyst was characterised using FT-IR, ICP-AES, FESEM, and EDX. 1,4-Dihydropyridines (**92**) and phenyl hydroxyquinoline derivatives (**93**) were synthesized by refluxing a mixture of aldehydes (**91**), β-dicarbonyls (**10**), and ammonium acetate (**7**) in an ethanolic medium; the catalyst facilitated high 97% yields with minimal loading of 0.02 g within a reaction time of 15 min (**Scheme 32**). The reaction pathway was assumed to follow Knoevenagel condensation along with Michael addition and tautomerism. The hygroscopic nature of chitosan assisted in the adsorption of water molecules allowing better interaction which promotes activation of carbonyl compounds.

Pasunooti and his colleagues (Pasunooti et al., 2010) have explored a single-pot multicomponent synthetic method for hydroquinolines (**95**) using a copper catalyst under microwave irradiation. Cupric (II) trifluoromethanesulphonate [$Cu(OTf)_2$] was perceived to be a promising catalyst to obtain a high yield around 90% with a minimal amount of catalytic molar percentage, i.e., 2% at 100°C within 15 min of reaction time (**Scheme 33**). They optimised the Hantzsch reaction conditions, using benzaldehyde (**94**), ethyl acetoacetate (**17**), dimedone (**65**), and ammonium acetate (**7**) along with ethyl alcohol and $Cu(OTf)_2$. The components were irradiated under microwave to achieve 1,4-dihydropyridines.

Bitaraf *et al.* (Bitaraf et al., 2016) appraised the significance of tungsten trioxide-bolstered sulphonic acid nano (n-WSA) composites in the preparation of 1,4-dihydropyridines (**98**). This nanocatalyst was prepared using powdered nano-WO_3, and dichloromethane took in a suction flash connected to a

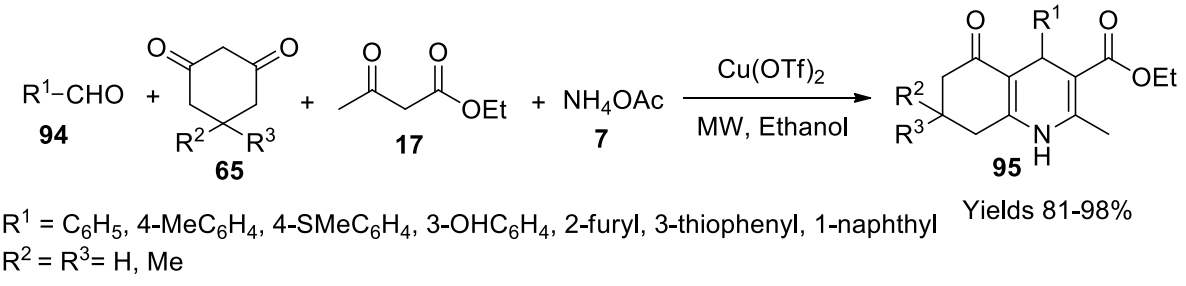

SCHEME 33 | Synthesis of hydroquinolines by the $Cu(OTf)_2$ catalyst.

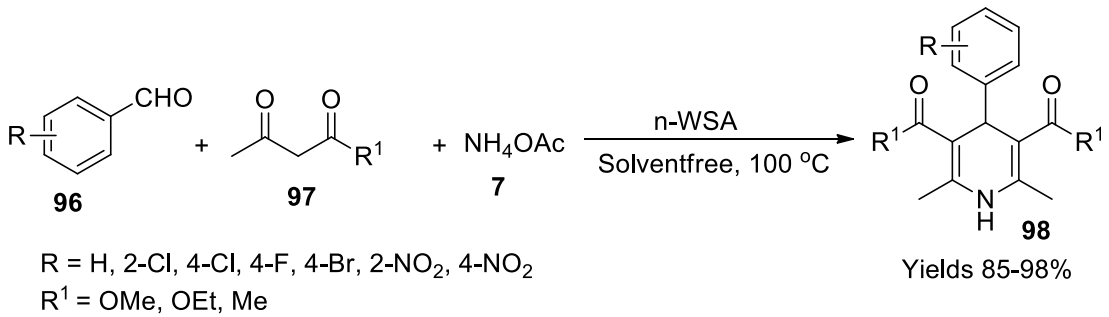

SCHEME 34 | Synthesis of dihydropyridines by the nano-WO_3 catalyst.

pressure dropping funnel and a gas inlet tube facilitating the conduction of HCl gas over the water adsorbent. Chlorosulphonic acid was introduced into it dropwise, which resulted in the evolution of HCl gas. After the HCl gas ceased, the reaction mixture was stirred continuously for 30 min. The unreacted dichloromethane was removed under reduced pressure to obtain a dark green powder, washed with ethanol, and dried for 6 h at 120°C. The FE-SEM images suggest that the particle size of the nanocatalyst is around 60–70 nm. A single-pot three-component reaction involving aromatic aldehydes (**96**), β-dicarbonyls (**97**), and ammonium acetate (**7**) in a solvent-free abode in the presence of n-WSA was considered (**Scheme 34**). The method was presumed to follow Knoevenagel condensation along with Michael addition. The catalyst showed promising performance with an excellent yielding capacity of 98% within 15 min of reaction time. The reaction parameters were optimised under a central metal composite design.

Momeni and his colleagues (Momeni et al., 2020) developed a routine to synthesise 1,4-dihydropyridines (**100**) and polyhydro quinolines (**101**), employing $H_5BW_{12}O_{40}$ as a novel catalyst. They implemented a single-pot Hantzsch reaction mechanism using substituted aldehydes (**99**), acetoacetic esters (**17**), and ammonium acetate (**7**) refluxed using borotungstic acid ($H_5BW_{12}O_{40}$) as a catalyst. The negative charge of the catalyst aids in its activity as a Bronsted acid. The resultants were assessed using TLC in combination with n-hexane and ethyl acetate in the ratio 7:3. The reminiscent was washed using ethyl acetate, and the products were dried using Na_2SO_4. The electron-withdrawing group, such as NO_2 at aldehyde, was observed to gain the highest yield of 98% within 45 min (**Scheme 35**). The reaction was presumed to follow Knoevenagel condensation along with Michael addition. The gathered products were characterised using FT-IR, ^1H, and ^{13}C NMR spectral data.

Mirjalilil *et al.* (Mirjalili et al., 2018) used a Lewis acid catalyst, $TiCl_2$/nano-γ-Al_2O_3, to prepare hydroxyquinoline derivatives. A volume of 60 ml of 1 M NaOH solution was initially added into a beaker containing 66 g of $Al_2(SO_4)_3.18H_2O$ and stirred vigorously to obtain a white precipitate of $Al(OH)_3$, which was washed with distilled water and dried. A volume of 20 g of $Al(OH)_3$ was dissolved in 100 ml of 1 M NaOH, and 3% (v/v%) polyethylene glycol was added. The pH of the mixture was adjusted to eight and subjected to vigorous stirring to obtain a solid separated by centrifugation. The solid was collected and washed using distilled water and calcinated at 800°C for 3 h to get nano-γ-Al_2O_3. To 1 g of nano-γ-Al_2O_3 dissolved in 10 ml of dichloromethane, 0.5 ml of $TiCl_2$ was added dropwise. The resulting solution was vigorously stirred till precipitation. The residue separated by filtration was washed using $CHCl_3$ and dried at room temperature. The SEM revealed its amorphous shape with 50 nm of particle size and a surface area of 75.6 m^2/g through BET analysis. The material was found stable up to 400°C. The catalyst's capacity was assessed in the preparation of hydroquinolines (**103**) in a single-pot reaction method using 1 mmol of aryl aldehyde (**102**), 2 mmol of 1,3-dicarbonyl ester (**17**), and 1.5 mmol of ammonium acetate (**7**) in the presence of

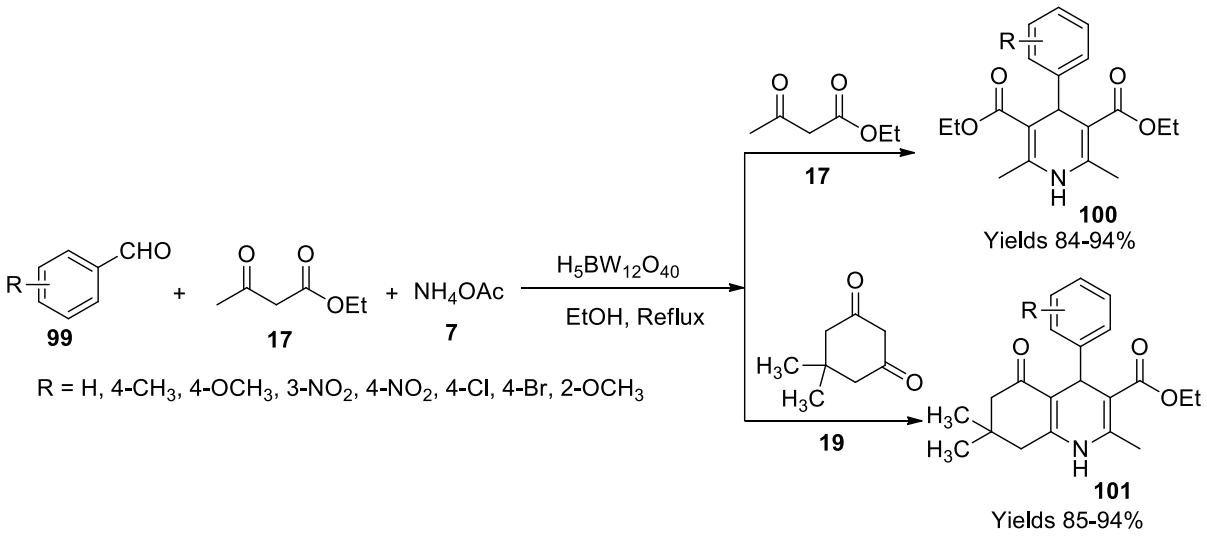

SCHEME 35 | Synthesis of dihydropyridine and hydroquinolines by the $H_5BW_{12}O_{40}$ catalyst.

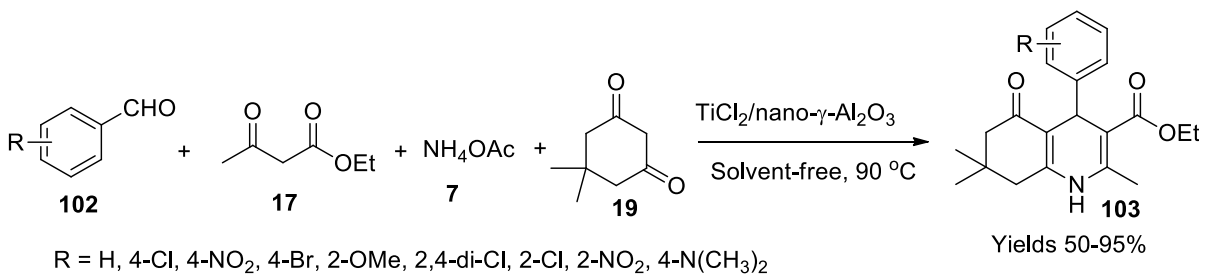

SCHEME 36 | Synthesis of hydroquinolines by the $TiCl_2$-Al_2O_3 catalyst.

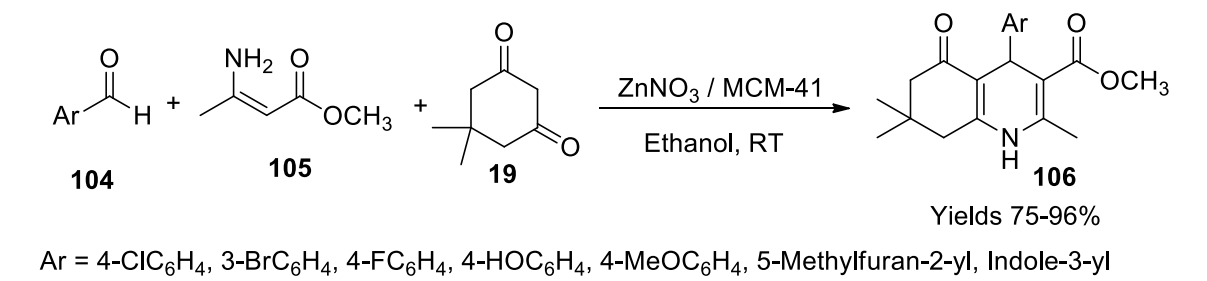

SCHEME 37 | Synthesis of hydroquinolines by the Zn-MCM-41 catalyst.

0.05 ml of $TiCl_2$/Nano-γ-Al_2O_3 in a solvent-free abode (**Scheme 36**). The product obtained was filtered and appraised using FT-IR, ^1H, and ^{13}C NMR spectroscopic methods. Aldehyde substituted with the +I group gained a higher yield of around 95% within 26 min.

Oskuie and his colleagues (Oskuie et al., 2020) worked on the catalytic preparation of the Hantzsch reaction to produce polyhydroquinolines (**106**) catalysed by Zn/MCM-41. The impregnation method was used to induce $ZnNO_3$ onto MCM-41. The vintage Hantzsch reaction mixture consisting of aryl aldehyde (**104**), dimedone (**19**), and methyl-3-aminocrotonate (**105**) was employed in the presence of the prepared catalyst in a solvent-free environment. The reaction proceeded by activating the carbonyl groups through Zn^{+2} for Knoevenagel condensation, and the enamine intermediate participates in Michael addition. The acquired product was filtered and dried. High yields were

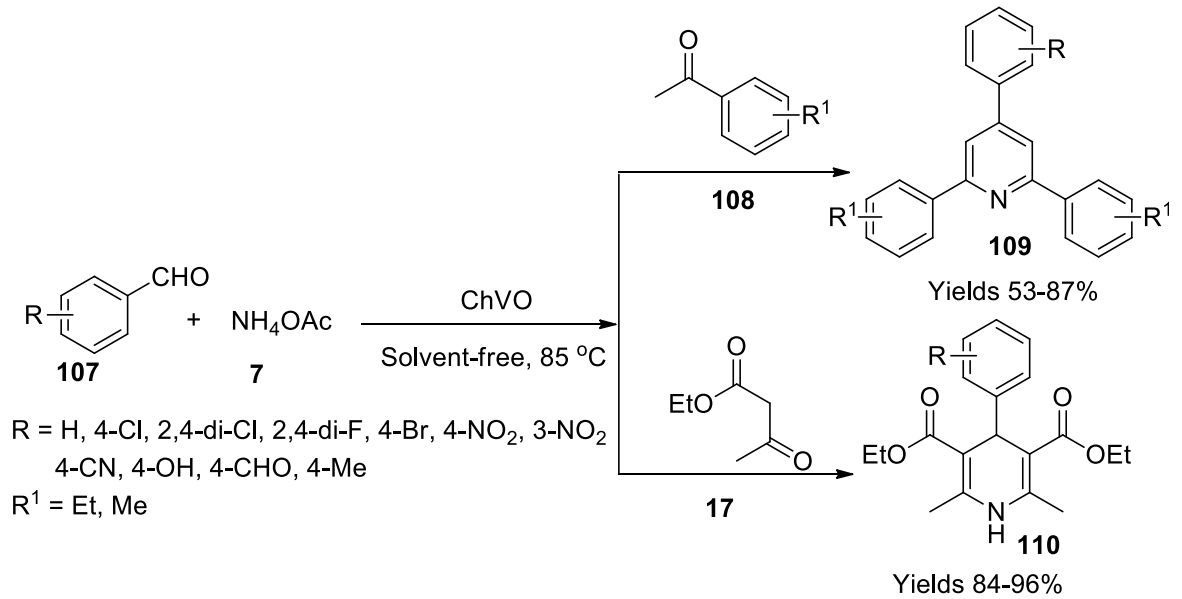

SCHEME 38 | Synthesis of dihydropyridine and triaryl pyridines by the chitosan vanadium catalyst.

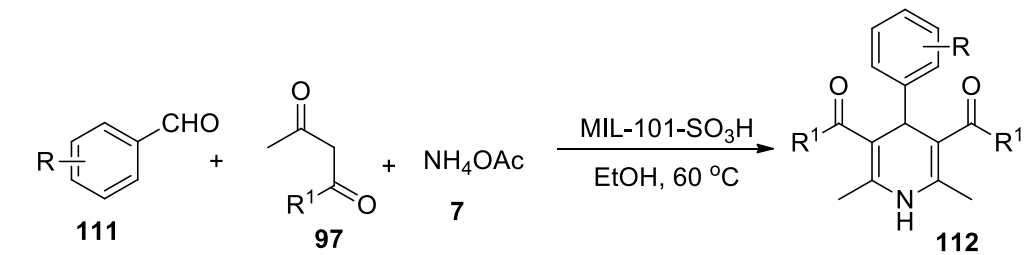

SCHEME 39 | Synthesis of dihydropyridines by the MIL-101-SO_3H catalyst.

achieved by using 3- and 4-fluorobenzaldehyde, salicylaldehyde, and 4-hydroxybenzaldehyde in combination with methyl 3-aminocrotonate and 5-methyl furfural, while the lowest yield was attained with 3-indole-carboxaldehyde (**Scheme 37**). The highest 97% yield was observed within a reaction time of 2 h. The obtained product was explored using FT-IR, ^{1}H, and ^{13}C NMR spectroscopic analysis. Cytotoxicity of the prepared polyhydroquinolines was assessed against MCF 7, SK BR-3, and HT 29 cancer cell lines employing cell cytotoxicity assay by MTT to determine their IC_{50} values 2.5 mg/cm^3 and 180 mm^3 RPMI value.

Safaiee and his coworkers (Safaiee et al., 2018) have constructed a vanadium oxo catalyst bolstered on chitosan and effectively used to synthesise series of 1,4-dihydropyridines (**110**) and 2,4,6-triarylpyridines (**109**) adopting anomeric-based oxidation. Chitosan was refluxed with vanadium pentoxide in water to form a black precipitate after 24 h, which was filtered and washed with hot DM water followed by drying it at 80°C. By FT-IR, XRD, SEM, EDX, ICP-MS, and TGA analyses, the material was characterised. XRD amorphous structure SEM and wavelength-dispersive X-ray analysis (WDX) confirmed the presence of V, N, O, and C atoms. Tg and DTG stability of the catalyst was at 225°C. The reaction mixture of aldehyde (**107**), *β*-ketoester (**17**), and ammonium acetate (**7**) in the presence of 5 mg of ChVO catalyst in a solvent-free abode at 80°C gave 1,4-dihydropyridines in good yields (**Scheme 38**). The obtained product was filtered and dissolved in hot ethyl acetate to isolate the catalyst and refiltered to retrieve the heterogeneous catalyst. The product solution was evaporated, washed, and recrystallised from a solution mixture of ethanol and water taken in the ratio of 1:10. In the other reaction, a mixture containing aromatic aldehydes, acetophenone derivatives, and

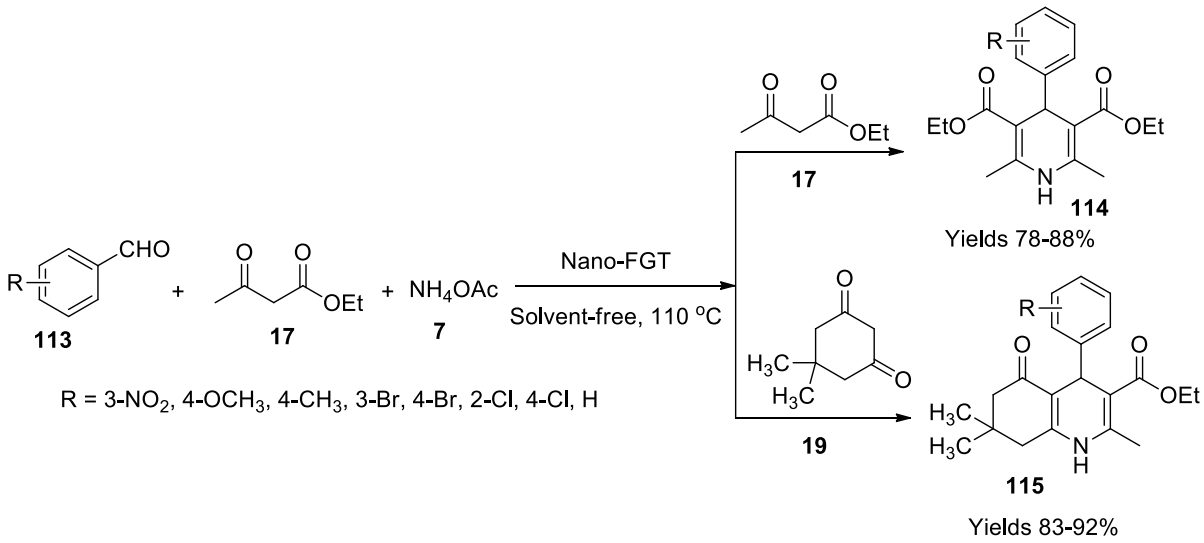

SCHEME 40 | Synthesis of dihydropyridines by the glutathione catalyst.

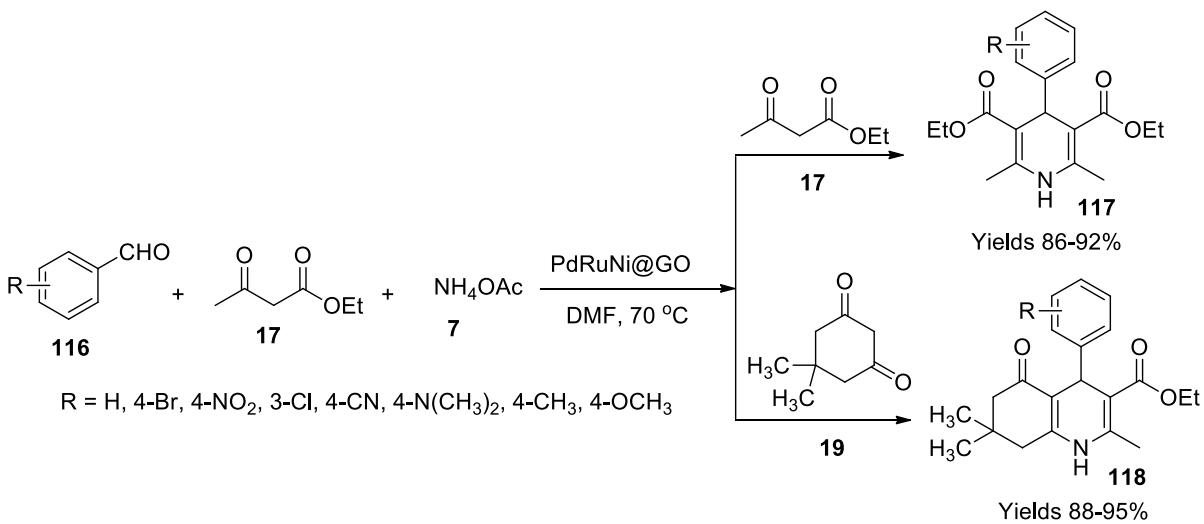

SCHEME 41 | Synthesis of dihydropyridine and hydroquinolines by the PdRuNi@GO catalyst.

ammonium acetate were reacted in the presence of 5 g of the ChVO catalyst to obtain 2,4,6-triarylpyridines at a temperature of 130°C in a hot oil bath. Hot ethanol was added to the reaction solution to dissolve the product formed and isolate the heterogeneous catalyst. The reaction solution was evaporated and recrystallised to gather 2,4,6-triarylpyridines. As per TG and DTA analyses, the catalyst material is stable up to 225°C. The amorphous structure of the catalyst was represented by SEM images, whereas the WDX images gave a note about the elements present in the catalyst. The TLC method concluded the reactions with a medium containing n-hexane and ethyl acetate in the ratios 3:7 and 4:15. The obtained derivatives of 1,4-dihydropyridines and 2,4,6-triarylpyridines were examined using FT-IR, ^{1}H, and ^{13}C NMR analyses. The use of the ChVO catalyst greatly enhanced the yield (89%) while reducing the reaction time to 45 min. The retrieved catalyst retained its viability and catalytic potential for several consequent cycles.

Devarajan and Suresh (Devarajan and Suresh, 2019) studied the performance of a solid heterogeneous Bronsted acid catalyst, MIL-101-SO_3H metal-organic framework, in the synthesis of 1,4-dihydropyridines (**56**) using Hantzsch reaction. Initially, a reaction mixture of monosodium 2-sulfoterephthalic acid and CrO_3 was dissolved in a solution of 0.53 ml of HCl and 20 ml of water and autoclaved at 180°C for 168 h. It was allowed to drop to room temperature and filtered. The product was washed with

400 ml of DM water and 100 ml of methanol. The green powder was dissolved in DMF, heated at 120°C for 24 h, and again added to a solution of aqueous methanol at the same temperature to achieve microcrystalline powder. The collected green powder was dissolved in a solution containing 0.08 M of HCl. The obtained product was treated with aqueous methanol for three consecutive cycles. Finally, the green powder was washed with water and vacuum dried at 120°C. It showed a crystalline structure with 1,497 m^2/g of surface area, as XRD represented and BET values. The MIL-101-SO_3H aggregation was explored by SEM analysis. EDAX showed that the catalyst contains 13.47 wt% of chromium and 3.47% of sulphur which has stability up to 500°C. The catalytic potential was assessed by administering 20% (wt%) of MIL-101-SO_3H MOF in Hantzsch single pot reaction, including aldehyde (**111**), 1,3-dicarbonyl compound (**97**), and ammonium acetate (**7**) to produce 1,4-dihydropyridines (**Scheme 39**). After the reaction completion, the catalyst was isolated by centrifugation and washed with ethanol repeatedly. The retrieved catalyst was heated with DMF at 100°C for 1 h. After removal of DMF by filtration, the material was dried at 120°C for 3 h. The catalyst gained a high 99% yield on sonication, and in addition to the excellent yield, the catalyst retained its viability and potential for several consecutive cycles.

Maleki *et al.* (Maleki et al., 2019c) have produced 1,4-dihydropyridines (**114**) and hydroquinolines (**115**) using a single-pot system under the influence of magnetic nanoparticles infused with glutathione. The desired catalyst was prepared by adding ferric oxide to water and methyl alcohol solution and subjecting it to sonication. A volume of 0.4 g of glutathione was added, and the mixture was further sonicated for 2 h. The magnetic material was separated using an external magnetic field, and the resulting solution was filtered by washing it with water and methyl alcohol and oven-dried at 50°C–60°C. The adhesion of glutathione onto the magnetic particles was confirmed by various analytical methods such as FT-IR, XRD, TGA, TEM, VSM, EDX, and elemental analysis. The EXD images show the presence of Fe, O, N, and S. The catalytic activity and viability of the material were established using the Hantzsch reaction to synthesise 1,4-dihydropyridines (**Scheme 40**). The reaction mixture in a solvent-free environment consisted of benzaldehyde (**113**), ethyl acetoacetate (**17**), ammonium acetate (**7**), and dimedone (**19**). A Knoevenagel condensation followed by Michael addition generates the dihydropyridine derivative. The method offers a 90% yield within 35 min with minimal use of 0.02 g of the prepared catalyst.

Demirci and the team (Demirci et al., 2016) investigated mono-dispersed PdRuni@GO prepared by the double solvent reduction method as a catalyst in Hantzsch reaction to prepare dihydropyridine (**117**) and hydroxyquinoline (**118**) derivatives in a single-pot system. A lysed mixture of 0.25 mmol of Pd, Ni, and Ru in dehydrated tetrahydrofuran in 0.25 mmol of octane thiol was subjected to ultrasonication till the solution turned black-brown, suggesting the formation of Pd–Ni–Ru nanoparticles which was vacuum dried. The gathered nanoparticles were combined with graphene oxide in an equal molar ratio and subjected to sonication to gain Pd-Ni-Ru@GO nanoparticles. The XRD values of the gathered nanoparticles describe their perovskite crystalline structure with 3.64 nm of diameter with a surface area of 136.2 cm^2/g as represented by BET images. The catalytic performance of the prepared nanoparticles was assessed in preparing 1,4-dihydropyridines. The reaction mixture involved an equimolar amount of ammonium acetate (**7**), ethyl acetoacetate (**17**), and 1 mmol of aldehyde (**116**) suspended in 2 ml of DMF, plus 6 mg of Pd-Ni-Ru@GO nanoparticles as a catalyst, under 70°C for 45 min (**Scheme 41**). After the completion of the reaction, the mixture was centrifuged and poured into 20 ml of ice-cold water to form a vacuum filtered, washed, and dried precipitate. With substituted aldehydes, high yields of 93%–98% were obtained within a reaction time of 45 min. The gathered product was subjected to various spectroscopic analyses to elucidate the derivatives. The catalyst was gathered and reused for five consecutive cycles without losing its vitality when subjected to trial under ICP-OES analyses.

CONCLUSION

The review highlighted the eminence of mainly the heterogeneous catalyst materials in preparing different novel dihydropyridine derivatives. The monograph described preparation techniques for various catalyst materials in detail. It covered facile and benign magnetic, silicon- and zirconium-bolstered, and ionic liquid-based heterogeneous catalysts, which can coherently facilitate excellent yields in short reaction times in a cost-effective and eco-friendly way. The target products are valuable molecules proficient in curing long-term disorders and drug delivery to the target tissue. The catalyst materials and protocols considered in this review are easy to handle, nontoxic, and easily prepared. High-temperature and pressure resistance ranges make them ideal and sustainable catalysts for preparing heterocyclic compounds, dihydropyridine in particular. These innovative pathways tailored for the synthesis of dihydropyridine derivatives have paved fresh approaches for further research.

AUTHOR CONTRIBUTIONS

All authors are equal contribution authors.

REFERENCES

Agrwal, A., and Kasana, V. (2020). [Fesipmim]Cl as Highly Efficient and Reusable Catalyst for Solventless Synthesis of Dihydropyridine Derivatives Through Hantzsch Reaction. *J. Chem. Sci.* 132, 67. doi:10.1007/s12039-020-01770-9

Allahresani, A., Mohammadpour Sangani, M., and Nasseri, M. A. (2020). CoFe 2 O 4 @SiO 2 -NH 2 -Co II NPs Catalyzed Hantzsch Reaction as an Efficient, Reusable Catalyst for the Facile, Green, One-pot Synthesis of Novel Functionalized 1,4-dihydropyridine Derivatives. *Appl. Organomet. Chem.* 34, e5759. doi:10.1002/aoc.5759

Amoozadeh, A., Rahmani, S., Bitaraf, M., Abadi, F. B., and Tabrizian, E. (2016). Nano-zirconia as an Excellent Nano Support for Immobilization of Sulfonic Acid: A New, Efficient and Highly Recyclable Heterogeneous Solid Acid Nanocatalyst for Multicomponent Reactions. *New J. Chem.* 40, 770–780. doi:10.1039/C5NJ02430G

BagheryZolfigol, S. M. A., and Zolfigol, M. A. (2017). 3,6-Dioxaoctamethylenediamminium Trifluoromethanesulfonate [3,6-DOMDA] OTf as a Novel Ionic Liquid Catalyst for the Synthesis of Functionalized 1,4-dihydropyridines. *J. Mol. Liquids* 232, 174–181. doi:10.1016/j.molliq.2017.02.073

Balaboina, R., Thirukovela, N. S., Kankala, S., Balasubramanian, S., Bathula, S. R., Vadde, R., et al. (2019). Synergistic Catalysis of Ag(I) and Organo- N -heterocyclic Carbenes: One-Pot Synthesis of New Anticancer Spirooxindole-1,4-dihydropyridines. *ChemistrySelect* 4, 2562–2567. doi:10.1002/slct.201803507

Bhaskaruni, S. V. H. S., Maddila, S., van Zyl, W. E., and Jonnalagadda, S. B. (2017). RuO2/ZrO2 as an Efficient Reusable Catalyst for the Facile, Green, One-Pot Synthesis of Novel Functionalized Halopyridine Derivatives. *Catal. Commun.* 100, 24–28. doi:10.1016/j.catcom.2017.06.023

Bhaskaruni, S. V. H. S., Maddila, S., van Zyl, W. E., and Jonnalagadda, S. B. (2018). V 2 O 5 /ZrO 2 as an Efficient Reusable Catalyst for the Facile, Green, One-Pot Synthesis of Novel Functionalized 1,4-dihydropyridine Derivatives. *Catal. Today* 309, 276–281. doi:10.1016/j.cattod.2017.05.038

Bhaskaruni, S. V. H. S., Maddila, S., van Zyl, W. E., and Jonnalagadda, S. B. (2019). A Green Protocol for the Synthesis of New 1,4-dihydropyridine Derivatives Using Fe2O3/ZrO2 as a Reusable Catalyst. *Res. Chem. Intermed.* 45, 4555–4572. doi:10.1007/s11164-019-03849-6

Bhaskaruni, S. V. H. S., Maddila, S., Gangu, K. K., and Jonnalagadda, S. B. (2020). A Review on Multi-Component Green Synthesis of N-Containing Heterocycles Using Mixed Oxides as Heterogeneous Catalysts. *Arabian J. Chem.* 13, 1142–1178. doi:10.1016/j.arabjc.2017.09.016

Bitaraf, M., Amoozadeh, A., and Otokesh, S. (2016). A Simple and Efficient One-Pot Synthesis of 1,4-dihydropyridines Using Nano-WO3- Supported Sulfonic Acid as an Heterogeneous Catalyst Under Solvent-free Conditions. *Jnl Chin. Chem. Soc* 63, 336–344. doi:10.1002/jccs.201500453

Bodaghifard, M. A. (2020). Organic Base Grafted on Magnetic Nanoparticles as a Recoverable Catalyst for the Green Synthesis of Hydropyridine Rings. *J. Iran. Chem. Soc.* 17, 483–492. doi:10.1007/s13738-019-01788-y

Cioc, R. C., Ruijter, E., and Orru, R. V. A. (2014). Multicomponent Reactions: Advanced Tools for Sustainable Organic Synthesis. *Green. Chem.* 16, 2958–2975. doi:10.1039/C4GC00013G

da Costa Cabrera, D., Santa-Helena, E., Leal, H. P., de Moura, R. R., Nery, L. E. M., Gonçalves, C. A. N., et al. (2019). Synthesis and Antioxidant Activity of New Lipophilic Dihydropyridines. *Bioorg. Chem.* 84, 1–16. doi:10.1016/j.bioorg.2018.11.009

Dekamin, M. G., Kazemi, E., Karimi, Z., Mohammadalipoor, M., and Naimi-Jamal, M. R. (2016). Chitosan: An Efficient Biomacromolecule Support for Synergic Catalyzing of Hantzsch Esters by CuSO 4. *Int. J. Biol. Macromolecules* 93, 767–774. doi:10.1016/j.ijbiomac.2016.09.012

Demirci, T., Çelik, B., Yıldız, Y., Eriş, S., Arslan, M., Sen, F., et al. (2016). One-pot Synthesis of Hantzsch Dihydropyridines Using a Highly Efficient and Stable PdRuNi@GO Catalyst. *RSC Adv.* 6, 76948–76956. doi:10.1039/C6RA13142E

Devarajan, N., and Suresh, P. (2019). MIL-101-SO3H Metal-Organic Framework as a Brønsted Acid Catalyst in Hantzsch Reaction: An Efficient and Sustainable Methodology for One-Pot Synthesis of 1,4-dihydropyridine. *New J. Chem.* 43, 6806–6814. doi:10.1039/C9NJ00990F

Devi, L., Nagaraju, K., Maddila, S., and Jonnalagadda, S. B. (2020). A Green, Efficient Protocol for the Catalyst-free Synthesis of Tetrahydro-1h-Pyrazolo-[3,4-B]-Quinolin-5(4h)-Ones Supported by Ultrasonicirradiation. *Chem. Data Collections* 30, 100566. doi:10.1016/j.cdc.2020.100566

Edraki, N., Mehdipour, A. R., Khoshneviszadeh, M., and Miri, R. (2009). Dihydropyridines: Evaluation of Their Current and Future Pharmacological Applications. *Drug Discov. Today* 14, 1058–1066. doi:10.1016/j.drudis.2009.08.004

Farahnaz, K. B., and Banafsheh, Y. (2019). Iron(III) Phosphate Catalyzed Synthesis of 1,4-dihydropyridines. *Arab. J. Chem.* 12, 1353–1357. doi:10.1016/j.arabjc.2014.11.027

Fekri, L. Z., Pour, K. H., and Zeinali, S. (2020). Synthesis, Characterization and Application of Copper/Schiff-Base Complex Immobilized on KIT-6-NH2 Magnetic Nanoparticles for the Synthesis of Dihydropyridines. *J. Organomet. Chem.* 915, 121232. doi:10.1016/j.jorganchem.2020.121232

Ferrazzano, L., Corbisiero, D., Martelli, G., Tolomelli, A., Viola, A., Ricci, A., et al. (2019). Green Solvent Mixtures for Solid-phase Peptide Synthesis: A Dimethylformamide-free Highly Efficient Synthesis of Pharmaceutical-Grade Peptides. *ACS Sust. Chem. Eng.* 7, 12867–12877. doi:10.1021/acssuschemeng.9b01766

Ganta, R. K., Kerru, N., Maddila, S., and Jonnalagadda, S. B. (2021). Advances in Pyranopyrazole Scaffolds' Syntheses Using Sustainable Catalysts-A Review. *Molecules* 26, 3270. doi:10.3390/molecules26113270

Ghorbani-Choghamarani, A., Mohammadi, M., Tamoradi, T., and Ghadermazi, M. (2019). Covalent Immobilization of Co Complex on the Surface of SBA-15: Green, Novel and Efficient Catalyst for the Oxidation of Sulfides and Synthesis of Polyhydroquinoline Derivatives in Green Condition. *Polyhedron* 158, 25–35. doi:10.1016/j.poly.2018.10.054

Gu, Y. (2012). Multicomponent Reactions in Unconventional Solvents: State of the Art. *Green. Chem.* 14, 2091–2128. doi:10.1039/C2GC35635J

Hantzsch, A. (1881). Condensationsprodukte aus Aldehydammoniak und ketonartigen Verbindungen. *Ber. Dtsch. Chem. Ges.* 14, 1637–1638. doi:10.1002/cber.18810140214

Heydari, A., Azizi, K., Azarnia, J., Karimi, M., and Yazdani, E. (2016). Novel Magnetically Separable Sulfated Boric Acid Functionalized Nanoparticles for Hantzsch Ester Synthesis. *Synlett* 27, 1810–1813. doi:10.1055/s-0035-1561441

Hutchings, G. J. (2009). Heterogeneous Catalysts-Discovery and Design. *J. Mater. Chem.* 19, 1222–1235. doi:10.1039/B812300B

Janjua, N., and Mayer, S. A. (2003). Cerebral Vasospasm After Subarachnoid Hemorrhage. *Curr. Opin. Crit. Care* 9, 113–119. doi:10.1097/00075198-200304000-00006

José Climent, M., Corma, A., and Iborra, S. (2012). Homogeneous and Heterogeneous Catalysts for Multicomponent Reactions. *RSC Adv.* 2, 16–58. doi:10.1039/C1RA00807B

Katrinsky, A. R., Ostercamp, D. L., and Yousaf, T. I. (1986). The Mechanism of the Hantzsch Pyridine Synthesis: A Study by 15N and 13C NMR Spectroscopy. *Tetrahedron* 42, 5729–5738. doi:10.1016/S0040-4020(01)88178-3

Kavyani, S., and Baharfar, R. (2020). Design and Characterization of Fe 3 O 4 /GO/Au-Ag Nanocomposite as an Efficient Catalyst for the Green Synthesis of Spirooxindole-dihydropyridines. *Appl. Organometal. Chem.* 34, e5560. doi:10.1002/aoc.5560

Kerru, N., Bhaskaruni, S. V. H. S., Gummidi, L., Maddila, S. N., Maddila, S., and Jonnalagadda, S. B. (2019). Recent Advances in Heterogeneous Catalysts for the Synthesis of Imidazole Derivatives. *Synth. Commun.* 49, 2437–2459. doi:10.1080/00397911.2019.1639755

Kerru, N., Bhaskaruni, S. V. H. S., Gummidi, L., Maddila, S. N., Rana, S., Singh, P., et al. (2019). Synthesis of Novel Pyrazole-based Triazolidin-3-one Derivatives by Using ZnO/ZrO 2 as a Reusable Catalyst Under Green Conditions. *Appl. Organometal. Chem.* 33, e4722. doi:10.1002/aoc.4722

Kerru, N., Maddila, S. N., Maddila, S., Sobhanapuram, S., and Jonnalagadda, S. B. (2019). Synthesis and Antimicrobial Activity of Novel Thienopyrimidine Linked Rhodanine Derivatives. *Can. J. Chem.* 97, 94–99. doi:10.1139/cjc-2018-0220

Kerru, N., Lalitha Gummidi, M., Kumar Gangu, K., Maddila, S., and Jonnalagadda, S. B. (2020). Synthesis of Novel Furo[3,2-c]coumarin Derivatives Through Multicomponent [4+1] Cycloaddition Reaction Using ZnO/FAp as a Sustainable Catalyst. *ChemistrySelect* 5, 4104–4110. doi:10.1002/slct.202000796

Kerru, N., Gummidi, L., Bhaskaruni, S. V. H. S., Maddila, S. N., and Jonnalagadda, S. B. (2020). Green Synthesis and Characterization of Novel 1,2,4,5-tetrasubstituted Imidazole Derivatives with Eco-Friendly Red Brick Clay as Efficacious Catalyst. *Mol. Divers.* 24, 889–901. doi:10.1007/s11030-019-10000-5

Kerru, N., Gummidi, L., Maddila, S., and Jonnalagadda, S. B. (2020). Gadolinium Oxide Loaded Zirconia and Multi-Component Synthesis of Novel Dihydro-Pyrazolo[3,4-D]pyridines Under Green Conditions. *Sust. Chem. Pharm.* 18, 100316. doi:10.1016/j.scp.2020.100316

Kerru, N., Gummidi, L., Bhaskaruni, S. V. H. S., Maddila, S. N., and Jonnalagadda, S. B. (2020). Ultrasound-assisted Synthesis and Antibacterial Activity of Novel 1,3,4-Thiadiazole-1h-Pyrazol-4-Yl-Thiazolidin-4-One Derivatives. *Monatsh. Chem.* 151, 981–990. doi:10.1007/s00706-020-02625-2

Kerru, N., Gummidi, L., Maddila, S. N., Bhaskaruni, S. V. H. S., and Jonnalagadda, S. B. (2020). Bi 2 O 3 /FAp, a Sustainable Catalyst for Synthesis of Dihydro-[1,2,4]triazolo[1,5-a]pyrimidine Derivatives Through Green Strategy. *Appl. Organometal. Chem.* 34, e5590. doi:10.1002/aoc.5590

Kerru, N., Gummidi, L., Maddila, S., and Jonnalagadda, S. B. (2020). Polyethylene Glycol (PEG-400) Mediated One-pot Green Synthesis of 4,7-Dihydro-2 H -pyrazolo[3,4- B

]pyridines Under Catalyst-free Conditions. *ChemistrySelect* 5, 12407–12410. doi:10.1002/slct.202002538

Kerru, N., Bhaskaruni, S. V. H. S., Gummidi, L., Maddila, S. N., Singh, P., and Jonnalagadda, S. B. (2020). Efficient Synthesis of Novel Pyrazole-Linked 1,2,4-Triazolidine-3-Thiones Using Bismuth on Zirconium Oxide as a Recyclable Catalyst in Aqueous Medium. *Mol. Divers.* 24, 345–354. doi:10.1007/s11030-019-09957-0

Kerru, N., Gummidi, L., Bhaskaruni, S. V. H. S., Maddila, S. N., and Jonnalagadda, S. B. (2020). One-pot Green Synthesis of Novel 5,10-Dihydro-1h-Pyrazolo[1,2-B]phthalazine Derivatives with Eco-Friendly Biodegradable Eggshell Powder as Efficacious Catalyst. *Res. Chem. Intermed.* 46, 3067–3083. doi:10.1007/s11164-020-04135-6

Kerru, N., Gummidi, L., Maddila, S. N., Gangu, K. K., and Jonnalagadda, S. B. (2020i). Four-component Rapid Protocol with Nickel Oxide Loaded on Fluorapatite as a Sustainable Catalyst for the Synthesis of Novel Imidazole Analogs. *Inorg. Chem. Commun.* 116, 107935. doi:10.1016/j.inoche.2020.107935

Kerru, N., Gummidi, L., Maddila, S., Gangu, K. K., and Jonnalagadda, S. B. (2020j). A Review on Recent Advances in Nitrogen-Containing Molecules and Their Biological Applications. *Molecules* 25, 1909. doi:10.3390/molecules25081909

Kerru, N., Maddila, S., and Jonnalagadda, S. B. (2020k). Design of Carbon-Carbon and Carbon-Heteroatom Bond Formation Reactions Under Green Conditions. *Coc* 23, 3154–3190. doi:10.2174/1385272823666191202105820

Kerru, N., Gummidi, L., Maddila, S. N., Bhaskaruni, S. V. H. S., Maddila, S., and Jonnalagadda, S. B. (2020l). Green Synthesis and Characterisation of Novel [1,3,4]thiadiazolo/benzo[4,5]thiazolo[3,2-A]pyrimidines via Multicomponent Reaction Using Vanadium Oxide Loaded on Fluorapatite as a Robust and Sustainable Catalyst. *RSC Adv.* 10, 19803–19810. doi:10.1039/D0RA02298E

Kerru, N., Gummidi, L., Maddila, S., and Jonnalagadda, S. B. (2021). A Review of Recent Advances in the Green Synthesis of Azole- and Pyran-Based Fused Heterocycles Using MCRs and Sustainable Catalysts. *Coc* 25, 4–39. doi:10.2174/1385272824999201020204620

Kerru, N., Gummidi, L., Maddila, S., and Jonnalagadda, S. B. (2021). Efficient Synthesis of Novel Functionalized Dihydro-pyrazolo[3,4-D]pyridines via the Three-Component Reaction Using MgO/HAp as a Sustainable Catalyst. *Inorg. Chem. Commun.* 123, 108321. doi:10.1016/j.inoche.2020.108321

Kerru, N., Maddila, S., and Jonnalagadda, S. B. (2021). A Facile and Catalyst-free Microwave-Promoted Multicomponent Reaction for the Synthesis of Functionalised 1,4-Dihydropyridines with Superb Selectivity and Yields. *Front. Chem.* 9, 638832. doi:10.3389/fchem.2021.638832

Khazaei, A., Sarmasti, N., and Yousefi Seyf, J. (2018). Anchoring High Density Sulfonic Acid Based Ionic Liquid on the Magnetic Nano-Magnetite (Fe3O4), Application to the Synthesis of Hexahydroquinoline Derivatives. *J. Mol. Liquids* 262, 484–494. doi:10.1016/j.molliq.2018.04.125

Kumar, A., Maurya, R. A., Sharma, S., Kumar, M., and Bhatia, G. (2010). Synthesis and Biological Evaluation of N-Aryl-1,4-Dihydropyridines as Novel Antidyslipidemic and Antioxidant Agents. *Eur. J. Med. Chem.* 45, 501–509. doi:10.1016/j.ejmech.2009.10.036

Kumar, T. S., Robert, A. R., Ganja, H., Muralidhar, P., Nagaraju, K., and Maddila, S. (2021). Purification Free, Chemoselective N-Acylation of Non-nucleophilic Nitrogen Heterocycles Using Oxyma and Benzotriazole Activations. *Chem. Data Collections* 32, 100654. doi:10.1016/j.cdc.2021.100654

Kusampally, U., Dhachapally, N., Kola, R., and Kamatala, C. R. (2020). Zeolite Anchored Zr-ZSM-5 as an Eco-Friendly, Green, and Reusable Catalyst in Hantzsch Synthesis of Dihydropyridine Derivatives. *Mater. Chem. Phys.* 242, 122497. doi:10.1016/j.matchemphys.2019.122497

Maddila, S., Nagaraju, K., Chinnam, S., and Jonnalagadda, S. B. (2019). Microwave-Assisted Multicomponent Reaction: A Green and Catalyst-Free Method for the Synthesis of Poly-Functionalized 1,4-Dihydropyridines. *ChemistrySelect* 4, 9451–9454. doi:10.1002/slct.201902779

Maddila, S., Nagaraju, K., and Jonnalagadda, S. B. (2020). Synthesis and Antimicrobial Evaluation of Novel Pyrano[2,3-*D*]-Pyrimidine Bearing 1,2,3-triazoles. *Chem. Data Collections* 28, 100486. doi:10.1016/j.cdc.2020.100486

Maddila, S. N., Maddila, S., Kerru, N., Bhaskaruni, S. V. H. S., and Jonnalagadda, S. B. (2020). Facile One-pot Synthesis of Arylsulfonyl-4H-pyrans Catalyzed by Ru Loaded Fluorapatite. *ChemistrySelect* 5, 1786–1791. doi:10.1002/slct.201901867

Maddila, S. N., Maddila, S., Bhaskaruni, S. V. H. S., Kerru, N., and Jonnalagadda, S. B. (2020). MnO2 on Hydroxyapatite: A green Heterogeneous Catalyst and Synthesis of Pyran-Carboxamide Derivatives. *Inorg. Chem. Commun.* 112, 107706. doi:10.1016/j.inoche.2019.107706

Mahinpour, R., Moradi, L., Zahraei, Z., and Pahlevanzadeh, N. (2018). New Synthetic Method for the Synthesis of 1,4-dihydropyridine Using Aminated Multiwalled Carbon Nanotubes as High Efficient Catalyst and Investigation of Their Antimicrobial Properties. *J. Saudi Chem. Soc.* 22, 876–885. doi:10.1016/j.jscs.2017.11.001

Majhi, D., Bhoi, Y. P., Das, K., Pradhan, S., and Mishra, B. G. (2019). Sulfamic Acid Well Dispersed in the Micropores of Al-Pillared α-ZrP as Efficient Heterogeneous Catalyst for Synthesis of Structurally Diverse 1,4-dihydropyridines Under Mild Conditions. *J. Porous Mater.* 26, 1391–1405. doi:10.1007/s10934-019-00741-x

Malek, R., Maj, M., Wnorowski, A., Jóźwiak, K., Martin, H., Iriepa, I., et al. (2019). Multi-target 1,4-dihydropyridines Showing Calcium Channel Blockade and Antioxidant Capacity for Alzheimer's Disease Therapy. *Bioorg. Chem.* 91, 103205. doi:10.1016/j.bioorg.2019.103205

Maleki, A., Eskandarpour, V., Rahimi, J., and Hamidi, N. (2019). Cellulose Matrix Embedded Copper Decorated Magnetic Bionanocomposite as a Green Catalyst in the Synthesis of Dihydropyridines and Polyhydroquinolines. *Carbohydr. Polym.* 208, 251–260. doi:10.1016/j.carbpol.2018.12.069

Maleki, B., Reiser, O., Esmaeilnezhad, E., and Choi, H. J. (2019). SO3H-dendrimer Functionalized Magnetic Nanoparticles (Fe3O4@D NH (CH2)4SO3H): Synthesis, Characterization and its Application as a Novel and Heterogeneous Catalyst for the One-Pot Synthesis of Polyfunctionalized Pyrans and Polyhydroquinolines. *Polyhedron* 162, 129–141. doi:10.1016/j.poly.2019.01.055

Maleki, B., Atharifar, H., Reiser, O., and Sabbaghzadeh, R. (2019). Glutathione-coated Magnetic Nanoparticles for One-Pot Synthesis of 1,4-dihydropyridine Derivatives. *Polycyclic Aromatic Comp.* 41, 721–734. doi:10.1080/10406638.2019.1614639

Mirjalili, B. B. F., Bamoniri, A., and Salmanpoor, L. S. (2018). $TiCl_2$/Nano-γ-Al_2O_3 as a Novel lewis Acid Catalyst for Promotion of One-Pot Synthesis of 1,4-dihydropyridines. *J. Nanostruct* 8, 276–287. doi:10.22052/JNS.2018.03.007

Moheiseni, F., Reza Kiasat, A., and Badri, R. (2021). Synthesis, Characterization and Application of β-Cyclodextrin/Imidazolium Based Dicationic Ionic Liquid Supported on Silica Gel as a Novel Catalyst in Hantzsch Condensation Reaction. *Polycyclic Aromatic Comp.* 41, 1–13. doi:10.1080/10406638.2019.1650784

Mokhtar, M., Saleh, T. S., Narasimharao, K., and Al-Mutairi, E. (Forthcoming 2021). New Green Perspective to Dihydropyridines Synthesis Utilizing Modified Heteropoly Acid Catalysts. *Catal. Today*. doi:10.1016/j.cattod.2021.07.006

Momeni, T., Heravi, M. M., Hosseinnejad, T., Mirzaei, M., and Zadsirjan, V. (2020). H5BW12O40-Catalyzed Syntheses of 1,4-dihydropyridines and Polyhydroquinolines via Hantzsch Reaction: Joint Experimental and Computational Studies. *J. Mol. Struct.* 1199, 127011. doi:10.1016/j.molstruc.2019.127011

Mondal, P., Chatterjee, S., Sarkar, P., Bhaumik, A., and Mukhopadhyay, C. (2019). Preparation of DABCO-Based Acidic-Ionic-Liquid-Supported ZnO Nanoparticles and Their Application for Ecofriendly Synthesis of N -Aryl Polyhydroquinoline Derivatives. *ChemistrySelect* 4, 11701–11710. doi:10.1002/slct.201902427

Muralidhar, P., Kumar, B. S., Nagaraju, K., and Maddila, S. (2021). A Novel Method for the Synthesis of 3-aminoindoles Using Iodine and Cs2CO3 as Catalyst. *Chem. Data Collections* 33, 100731. doi:10.1016/j.cdc.2021.100731

Neamani, S., Moradi, L., and Sun, M. (2020). Synthesis of Magnetic Hollow Mesoporous N-Doped Silica Rods as a Basic Catalyst for the Preparation of Some Spirooxindole-1,4-Dihydropyridine Derivatives. *Appl. Surf. Sci.* 504, 144466. doi:10.1016/j.apsusc.2019.144466

Niaz, H., Kashtoh, H., Khan, J. A. J., Khan, A., Wahab, A.-t., Alam, M. T., et al. (2015). Synthesis of Diethyl 4-Substituted-2,6-Dimethyl-1,4-Dihydropyridine-3,5-Dicarboxylates as a New Series of Inhibitors Against Yeast α-glucosidase. *Eur. J. Med. Chem.* 95, 199–209. doi:10.1016/j.ejmech.2015.03.018

Oskuie, E. F., Azizi, S., Ghasemi, Z., Pirouzmand, M., Kojanag, B. N., and Soleymani, J. (2020). Zn/MCM-41-catalyzed Unsymmetrical Hantzsch Reaction and the Evaluation of Optical Properties and Anti-cancer Activities of the Polyhydroquinoline Products. *Monatsh. Chem.* 151, 243–249. doi:10.1007/s00706-020-02549-x

Pasunooti, K. K., Nixon Jensen, C., Chai, H., Leow, M. L., Zhang, D.-W., and Liu, X.-W. (2010). Microwave-assisted Copper(II)-catalyzed One-Pot Four-Component Synthesis of Multifunctionalized Dihydropyridines. *J. Comb. Chem.* 12, 577–581. doi:10.1021/cc100060s

Rajesh, U. C., Manohar, S., and Rawat, D. S. (2013). Hydromagnesite as an Efficient Recyclable Heterogeneous Solid Base Catalyst for the Synthesis of Flavanones, Flavonols and 1,4-dihydropyridines in Water. *Adv. Synth. Catal.* 355, 3170–3178. doi:10.1002/adsc.201300555

Rao, B. S., Reddy, K. V. N. S., Nagaraju, K., and Maddila, S. (2021). An Efficient Synthesis of Drug-like Small Molecules Library Based on 2-(substituted Benzylthio)-4,6-Dichloropyrimidin-5-Amines. *Chem. Data Collections* 33, 100704. doi:10.1016/j.cdc.2021.100704

Rao, D. J., Nagaraju, K., and Maddila, S. (2021). Microwave Irradiated Mild, Rapid, One-Pot and Multi-Component Synthesis of Isoxazole-5(4h)-Ones. *Chem. Data Collections* 32, 100669. doi:10.1016/j.cdc.2021.100669

Rotstein, B. H., Zaretsky, S., Rai, V., and Yudin, A. K. (2014). Small Heterocycles in Multicomponent Reactions. *Chem. Rev.* 114, 8323–8359. doi:10.1021/cr400615v

Sadeghzadeh, S. M. (2016). Bis(4-pyridylamino)triazine-stabilized Magnetite KCC-1: A Chemoselective, Efficient, Green and Reusable Nanocatalyst for the Synthesis of N-Substituted 1,4-dihydropyridines. *RSC Adv.* 6, 99586–99594. doi:10.1039/C6RA20488K

Safaiee, M., Ebrahimghasri, B., Zolfigol, M. A., Baghery, S., Khoshnood, A., and Alonso, D. A. (2018). Synthesis and Application of Chitosan Supported Vanadium Oxo in the Synthesis of 1,4-dihydropyridines and 2,4,6-triarylpyridines via Anomeric Based Oxidation. *New J. Chem.* 42, 12539–12548. doi:10.1039/C8NJ02062K

Schaller, D., Gündüz, M. G., Zhang, F. X., Zamponi, G. W., and Wolber, G. (2018). Binding Mechanism Investigations Guiding the Synthesis of Novel Condensed 1,4-dihydropyridine Derivatives with L-/T-type Calcium Channel Blocking Activity. *Eur. J. Med. Chem.* 155, 1–12. doi:10.1016/j.ejmech.2018.05.032

Shahid, A., Ahmed, N., Saleh, T., Al-Thabaiti, S., Basahel, S., Schwieger, W., et al. (2017). Solvent-free Biginelli Reactions Catalyzed by Hierarchical Zeolite Utilizing a Ball Mill Technique: A green Sustainable Process. *Catalysts* 7, 84. doi:10.3390/catal7030084

Sharma, P., and Gupta, M. (2015). Silica Functionalized Sulphonic Acid Coated with Ionic Liquid: An Efficient and Recyclable Heterogeneous Catalyst for the One-Pot Synthesis of 1,4-dihydropyridines Under Solvent-free Conditions. *Green. Chem.* 17, 1100–1106. doi:10.1039/C4GC00923A

Sheik Mansoor, S., Aswin, K., Logaiya, K., and Sudhan, S. P. N. (2017). An Efficient One-Pot Multi Component Synthesis of Polyhydroquinoline Derivatives Through Hantzsch Reaction Catalysed by Gadolinium Triflate. *Arabian J. Chem.* 10, S546–S553. doi:10.1016/j.arabjc.2012.10.017

Sheldon, R. A. (2005). Green Solvents for Sustainable Organic Synthesis: State of the Art. *Green. Chem.* 7, 267–278. doi:10.1039/B418069K

Sirisha, K., Bikshapathi, D., Achaiah, G., and Reddy, V. M. (2011). Synthesis, Antibacterial and Antimycobacterial Activities of Some New 4-Aryl/heteroaryl-2,6-Dimethyl-3,5-Bis-N-(aryl)-Carbamoyl-1,4-Dihydropyridines. *Eur. J. Med. Chem.* 46, 1564–1571. doi:10.1016/j.ejmech.2011.02.003

Slobbe, P., Ruijter, E., and Orru, R. V. A. (2012). Recent Applications of Multicomponent Reactions in Medicinal Chemistry. *Med. Chem. Commun.* 3, 1189–1218. doi:10.1039/C2MD20089A

Suryanarayana, K., Robert, A. R., Kerru, N., Pooventhiran, T., Thomas, R., Maddila, S., et al. (2021). Design, Synthesis, Anticancer Activity and Molecular Docking Analysis of Novel Dinitrophenylpyrazole Bearing 1,2,3-triazoles. *J. Mol. Struct.* 1243, 130865. doi:10.1016/j.molstruc.2021.130865

Taheri-Ledari, R., Rahimi, J., and Maleki, A. (2019). Synergistic Catalytic Effect Between Ultrasound Waves and Pyrimidine-2,4-Diamine-Functionalized Magnetic Nanoparticles: Applied for Synthesis of 1,4-dihydropyridine Pharmaceutical Derivatives. *Ultrason. Sonochem.* 59, 104737. doi:10.1016/j.ultsonch.2019.104737

Tan, J., Liu, X., Yao, N., Hu, Y. L., and Li, X. H. (2019). Novel and Effective Strategy of Multifunctional Titanium Incorporated Mesoporous Material Supported Ionic Liquid Mediated Reusable Hantzsch Reaction. *ChemistrySelect* 4, 2475–2479. doi:10.1002/slct.201803739

Triggle, D. J. (2003). 1,4-dihydropyridine Calcium Channel Ligands: Selectivity of Action. The Roles of Pharmacokinetics, State-dependent Interactions, Channel Isoforms, and Other Factors. *Drug Dev. Res.* 58, 5–17. doi:10.1002/ddr.10124

Védrine, J. (2017). Heterogeneous Catalysis on Metal Oxides. *Catalysts* 7, 341. doi:10.3390/catal7110341

Wu, P., Feng, L., Liang, Y., Zhang, X., Mahmoudi, B., and Kazemnejadi, M. (2020). Magnetic Fe-C-O-Mo alloy Nano-Rods Prepared from Chemical Decomposition of a Screw (A Top-Down Approach): An Efficient and Cheap Catalyst for the Preparation of Dihydropyridine and Dihydropyrimidone Derivatives. *Appl. Catal. A: Gen.* 590, 117301. doi:10.1016/j.apcata.2019.117301

Zeynizadeh, B., Rahmani, S., and Eghbali, E. (2019). Anchored Sulfonic Acid on Silica-layered NiFe2O4: A Magnetically Reusable Nanocatalyst for Hantzsch Synthesis of 1,4-dihydropyridines. *Polyhedron* 168, 57–66. doi:10.1016/j.poly.2019.04.035

Conflict of Interest: The authors declare that the research was conducted in the absence of any commercial or financial relationships that could be construed as a potential conflict of interest.

Publisher's Note: All claims expressed in this article are solely those of the authors and do not necessarily represent those of their affiliated organizations, or those of the publisher, the editors, and the reviewers. Any product that may be evaluated in this article, or claim that may be made by its manufacturer, is not guaranteed or endorsed by the publisher.

frontiers in Chemistry

REVIEW
published: 06 January 2022
doi: 10.3389/fchem.2021.733552

Recent Applications of Carbon Nanotubes in Organic Solar Cells

Edigar Muchuweni[†], *Edwin T. Mombeshora, Bice S. Martincigh and Vincent O. Nyamori* *

School of Chemistry and Physics, University of KwaZulu-Natal, Durban, South Africa

In recent years, carbon-based materials, particularly carbon nanotubes (CNTs), have gained intensive research attention in the fabrication of organic solar cells (OSCs) due to their outstanding physicochemical properties, low-cost, environmental friendliness and the natural abundance of carbon. In this regard, the low sheet resistance and high optical transmittance of CNTs enables their application as alternative anodes to the widely used indium tin oxide (ITO), which is toxic, expensive and scarce. Also, the synergy between the large specific surface area and high electrical conductivity of CNTs provides both large donor-acceptor interfaces and conductive interpenetrating networks for exciton dissociation and charge carrier transport. Furthermore, the facile tunability of the energy levels of CNTs provides proper energy level alignment between the active layer and electrodes for effective extraction and transportation of charge carriers. In addition, the hydrophobic nature and high thermal conductivity of CNTs enables them to form protective layers that improve the moisture and thermal stability of OSCs, thereby prolonging the devices' lifetime. Recently, the introduction of CNTs into OSCs produced a substantial increase in efficiency from ~0.68 to above 14.00%. Thus, further optimization of the optoelectronic properties of CNTs can conceivably help OSCs to compete with silicon solar cells that have been commercialized. Therefore, this study presents the recent breakthroughs in efficiency and stability of OSCs, achieved mainly over 2018–2021 by incorporating CNTs into electrodes, active layers and charge transport layers. The challenges, advantages and recommendations for the fabrication of low-cost, highly efficient and sustainable next-generation OSCs are also discussed, to open up avenues for commercialization.

Keywords: carbon nanotubes, organic solar cells, photoactive layer, hole transport layer, electron transport layer

OPEN ACCESS

Edited by:
Neil Coville,
University of the Witwatersrand, South Africa

Reviewed by:
Aniruddha Pramod Kulkarni,
Commonwealth Scientific and Industrial Research Organisation (CSIRO), Australia
Zivayi Chiguvare,
University of Namibia, Namibia

***Correspondence:**
Vincent O. Nyamori
nyamori@ukzn.ac.za

[†]*On leave from Department of Engineering and Physics, Bindura University of Science Education, Bindura, Zimbabwe*

Specialty section:
This article was submitted to Electrochemistry, a section of the journal Frontiers in Chemistry

Received: *01 July 2021*
Accepted: *13 December 2021*
Published: *06 January 2022*

Citation:
Muchuweni E, Mombeshora ET, Martincigh BS and Nyamori VO (2022) Recent Applications of Carbon Nanotubes in Organic Solar Cells. Front. Chem. 9:733552. doi: 10.3389/fchem.2021.733552

INTRODUCTION

Recently, there has been a dramatic increase in the global demand for renewable and green energy sources due to the exhaustion and environmental issues associated with conventional energy sources, such as fossil fuels and nuclear energy (Rego de Vasconcelos and Lavoie, 2019; Ashok et al., 2020; Lin et al., 2020; Subhan et al., 2020; Tiwari et al., 2020). In this regard, solar energy, a low-cost, renewable, naturally abundant and clean energy source, has attracted enormous research effort as a promising alternative to traditional energy sources (Subramanyam et al., 2019; Zhong et al., 2020; Rabaia et al., 2021). Among the new-generation photovoltaic devices that convert solar energy into electricity, organic solar cells (OSCs) are being widely investigated owing to their low production cost, facile fabrication procedure, abundance of raw materials, easy scalability, lightweight, excellent flexibility and

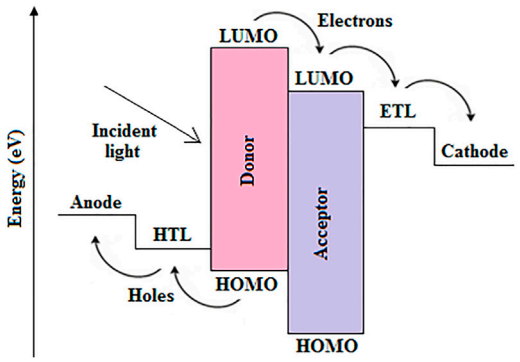

FIGURE 1 | Schematic energy level diagram of a typical BHJ-OSC.

environmentally friendly nature (Gusain et al., 2019; Lee, 2019; Li et al., 2020a; Shah et al., 2020; Shoyiga et al., 2020; Liu et al., 2021).

A typical OSC is composed of the electrodes (cathode and anode), charge transport layers (electron transport layer (ETL) and hole transport layer (HTL)), and the photoactive layer, assembled in the conventional or inverted configurations, as presented elsewhere (Muchuweni et al., 2020a). In an OSC, photons from incident solar radiation are transmitted through the substrate, bottom electrode and charge transport layer, so that they reach the photoactive layer, where they are absorbed by the donor material, in which excitons, i.e., strongly bound electron-hole pairs, are generated (Jeon et al., 2017; Ramasamy et al., 2019; Wang et al., 2020; Kang et al., 2021) and localized owing to the large exciton binding energy in the polymer matrix (Hatton et al., 2008). The photogenerated excitons subsequently diffuse within their limited diffusion distance to the interface between materials with dissimilar electron affinities and ionization potentials, i.e., between the donor-acceptor interface, where they are absolutely separated into free charge carriers after overcoming the binding energies (Tessema Mola et al., 2018). However, since the exciton diffusion length in OSCs is small, a bulk heterojunction (BHJ) should exist within the short diffusion distance so that excitons can always reach the donor-acceptor interface for charge separation to occur, and a continuous interpenetrating channel should exist for transporting charge carriers to the electrodes (Jeon Y.-J. et al., 2018; Ramasamy et al., 2019). Actually, the charge carriers are separated into electrons and holes in the acceptor's lowest unoccupied molecular orbital (LUMO) and donor's highest occupied molecular orbital (HOMO) levels, respectively, as illustrated in **Figure 1**. Hence, for the efficient transportation of electrons from the LUMO via the ETL to the cathode, the LUMO level of the acceptor should match well with the ETL's work function (Huang et al., 2019). Similarly, for the efficient transportation of holes through the HTL to the anode, the donor HOMO level should be well-matched with the HTL's work function (Huang et al., 2019). Thus, free electrons are transported to the cathode via the ETL, whereas holes are transported in the opposite direction to the anode via the HTL under internal electric fields, which lead to photocurrent generation (Amollo et al., 2018). Finally, the electrodes allow the flow of the photogenerated current to and from the external circuit so that the cell can power a given load.

Despite having a lower projected cost of < $0.07/Wp relative to < $0.35/Wp for commercially available silicon solar cells (Riede et al., 2021), the power conversion efficiency (PCE) of state-of-the-art OSCs (18–25%) (Cho et al., 2020; PV-Magazine, 2020; Salim et al., 2020) is still lower than that of commercially available silicon-based solar cells (above 26%) (Andreani et al., 2018). In addition, when compared with silicon solar cells, OSCs suffer from poor long-term environmental stability, which limits their commercialization (Chen, 2019; Burlingame et al., 2020; Duan and Uddin, 2020; Wang et al., 2021). Hence, this has prompted significant research interest in developing highly efficient and sustainable devices through approaches, such as incorporating novel materials into the different components of OSCs, to overcome the limitations of the commonly used traditional materials.

In this respect, carbon-based materials, such as graphitic carbon nitride, carbon quantum dots, carbon nanotubes (CNTs) and graphene (Jeon et al., 2018b; Nguyen et al., 2019; Ouyang, 2019; Hu et al., 2020; Pan et al., 2020; Qin et al., 2020; Subramanyam et al., 2020; Shin et al., 2021; Vercelli, 2021), have attracted considerable research attention due to their unique physicochemical properties, low-cost, natural abundance of carbon, non-toxicity and compatibility with large-scale solution synthesis (Delacou et al., 2017). Among these, CNTs are more appealing owing to their large specific surface area, tunable band gap, high optical transmittance in the visible region, competitive electrical conductivity, high charge carrier mobility, excellent flexibility and superior mechanical, thermal and chemical stability (Khan et al., 2018; Oseni et al., 2018).

CNTs, one of the stiffest and strongest materials ever discovered, consist of a cylindrical nanostructure of hexagonally oriented carbon atoms as shown in **Figure 2**, and can be classified as either semiconducting or metallic depending on their length, diameter and arrangement of hexagonal rings (Alturaif et al., 2014). Also, how graphene layers are wrapped to form a nanotubular morphology, i.e., the chirality of the tubes, significantly determines the electrical properties of the CNTs (Alturaif et al., 2014). CNTs that consist of a single round roll of graphene with a typical diameter of around 0.4–10 nm are referred to as single-walled CNTs (SWCNTs), whereas those consisting of two or more rolled layers of graphene sheets with a typical diameter of 1.4–100 nm are called double-walled CNTs (DWCNTs) and multiwalled CNTs (MWCNTs), respectively (Hatton et al., 2008; Agbolaghi, 2019b; Nguyen et al., 2019). Currently, SWCNTs have been relatively more studied than MWCNTs owing to the novel properties of SWCNTs, such as their band gap energy that can be tuned from 0 to ~2 eV, thereby varying their electrical conductivity. In addition, the diameter of SWCNTs falls within the preferred range of up to 20 nm for OSC applications since the thickness of the organic layer in OSCs is typically up to 200 nm (Hatton et al., 2008). Hence, SWCNTs exhibit unusual properties of either semiconducting or metallic materials, whereas MWCNTs are zero band gap materials with metallic properties (Obaidullah et al., 2018; Ouyang, 2019).

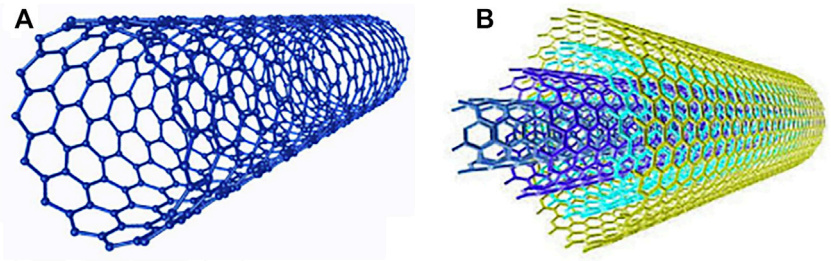

FIGURE 2 | The structure of **(A)** SWCNTs and **(B)** MWCNTs. Adapted with permission (Ouyang, 2019). Copyright 2019, Nano Materials Science.

CNTs have been prepared by means of several techniques, such as chemical vapour deposition (CVD), laser ablation and arc discharge (Jeon et al., 2018c; Khan et al., 2021; Shen, 2021). Among these, CVD is more appealing owing to its potential for large-scale synthesis. Also, CNTs can be deposited onto various components of OSCs by using different techniques, such as spray coating, dip coating, spin coating, sputtering and CVD (Khan et al., 2018). However, the insolubility in organic solvents, entanglement and poor alignment of CNTs, in addition to the presence of metal impurities, are the main limitations for the incorporation of CNTs into various layers of OSCs. These limitations cause unfavourable short-circuits, surface charge carrier trapping and reduction in charge carrier mobility, thereby increasing leakage current and recombination pathways (Oseni et al., 2018). Although sonication has been employed to disperse CNTs, it often causes them to break and alter their properties; hence, covalent and non-covalent functionalization have been developed in an attempt to improve the dispersibility of CNTs (Tasis et al., 2006; Hadi et al., 2020; Khan et al., 2021). Among these functionalization techniques, covalent functionalization involves the use of chemical reactions to introduce various functional groups onto the surfaces of CNTs (Nan et al., 2016). Nonetheless, the harsh chemical reactions impair the π-bonds of CNTs and degrade the CNTs' intrinsic electrical, mechanical and thermal properties (Nan et al., 2016).

On the other hand, non-covalent functionalization involves the adsorption of dispersants onto the surface of CNTs through non-covalent interactions, such as interactions between the π-electronic systems of CNTs and dispersants, which break the van der Waals forces between the individual CNTs, without any disruptions to the CNTs' π-electron conjugated structure (Keru et al., 2014). This, in turn, improves the interaction of CNTs with other constituent materials that make up the different components of OSCs, thereby increasing charge carrier mobility (An et al., 2017; Hadi et al., 2020). This also addresses the challenge of leakage current due to short-circuits that usually originate from the bundling of poorly dispersed CNTs. In addition, magnetic or electric fields may be applied, or the CNTs may be grown along a single direction to improve their alignment (Khan et al., 2021), thereby minimizing undesirable short-circuits that usually emanate from poorly aligned CNTs, and facilitating the efficient transportation of charge carriers, which subsequently leads to a substantial improvement in device performance.

However, the PCE of CNT-based OSCs is still relatively lower than that of OSCs based on traditional materials; hence, the optoelectronic properties of CNTs need further optimization for them to produce devices that can compete with those based on their traditional counterparts. Also, recent applications of carbonaceous nanostructures, especially CNTs, to improve the efficiency and sustainability of BHJ-OSCs for possible commercialization are yet to be satisfactorily reported. Therefore, this review focuses on the recent applications of CNTs, mainly over 2018–2021, in the electrodes, active layers and charge transport layers of OSCs, to improve not only the PCE, but also to enhance the long-term operational stability, thereby paving the way for the commercial application of OSCs. In addition, the merits, limitations and outlook for the future fabrication of high performance and sustainable OSCs are discussed.

TRANSPARENT CONDUCTING ELECTRODE

The most widely used transparent conducting electrode is indium tin oxide (ITO) due to its high optical transparency and electrical conductivity (Zhang Y. et al., 2020; Du et al., 2021), which facilitate the entrance of more light into the cell, and the efficient collection and transportation of photogenerated charge carriers to the external circuit. However, indium is an expensive and toxic rare earth metal, which limits the sustainability of ITO (Muchuweni et al., 2016a; Muchuweni et al., 2016b; Muchuweni et al., 2017a; Muchuweni et al., 2017b). Also, ITO is brittle; hence, not compatible with flexible substrates, and has instability issues in acidic and basic environments, which lead to device degradation (Jeon et al., 2015; Patil et al., 2021). In addition, good quality ITO is usually prepared using complicated, expensive and high-temperature vacuum-based processes (Lu et al., 2017; Muchuweni et al., 2020b).

Therefore, considerable effort has been exerted on developing alternative transparent conducting electrodes by using novel materials, such as metal grids (Mo et al., 2016; Jeong et al., 2018), silver nanowires (AgNWs) (Sun et al., 2019; Arulkumar et al., 2021), CNTs (Yu et al., 2016; Jeon et al.,

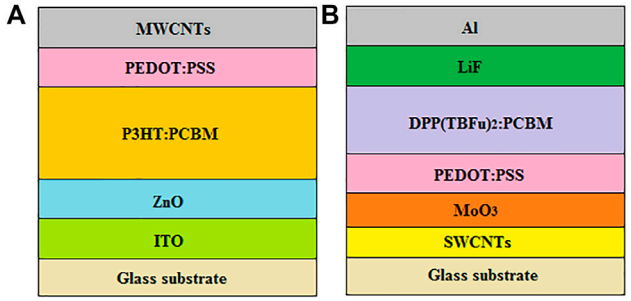

FIGURE 3 | Schematic diagram of **(A)** an inverted OSC based on a MWCNT anode and **(B)** a conventional OSC based on a SWCNT anode.

2017) and graphene (Jeon et al., 2017; Keyvani-Someh et al., 2017), owing to their competitive optoelectronic properties. Among these, CNTs are more appealing due to their low-cost, easy availability of raw materials, low-temperature solution processability, large specific area, flexibility, stability, and capability of offering a good balance between high optical transmittance in the visible region and low sheet resistance (Lu et al., 2017; Matsuo, 2021; Shen, 2021). In addition, the work function of CNTs is comparable to that of ITO, which reduces the energy barrier; hence, facilitating the efficient collection of photogenerated charge carriers at the electrode.

Although CNTs have been recently employed to replace or modify the commonly used ITO anode in conventional OSCs, relatively few or no detailed studies have reported their application as the cathode, mainly due to the relatively higher work function of CNTs, as compared with the low work function of the widely used ETLs, which increases the potential barrier, thereby limiting the collection of electrons at the cathode. Thus, for the cathode to efficiently collect and transport electrons, its work function should be relatively lower than that of the ETL (Muchuweni et al., 2020a); hence, making the high work function of CNTs not suitable for cathode applications. Therefore, this section only reviews the recent application of CNTs in the anode of BHJ-OSCs.

Anode

As mentioned earlier, CNTs have recently gained tremendous research attention as promising alternatives to the commonly used ITO bottom electrodes, i.e., anodes in conventional OSCs. Nevertheless, CNT-based electrodes still exhibit relatively higher sheet resistances of ~100 Ω sq^{-1} at a transparency of 85% in the visible region when compared with the required sheet resistance of ~10 Ω sq^{-1} at 85% transparency (Yang and Lee, 2020), thereby giving rise to devices with relatively low efficiency. Hence, as a future research direction, a substantial reduction in the sheet resistance of CNTs, while maintaining high optical transparency, is required.

On the other hand, the most commonly used anode materials in inverted OSCs, i.e., top electrodes, are the high work function metals, such as Ag or Au (Ali et al., 2018). However, these metal electrodes are opaque and reflective. Moreover, they are usually deposited under high vacuum and temperature conditions using thermal evaporation, which is complicated and expensive, thereby limiting the facile fabrication of low-cost and sustainable devices (Zhang et al., 2018; Kumar et al., 2020). In addition, Ag has stability issues, and Au is expensive (Lee et al., 2018). Therefore, there has been significant research interest in developing alternative materials with comparable performance, of which CNTs are more attractive due to their low-cost, facile fabrication procedures, competitive optoelectronic properties and excellent stability.

In this respect, MWCNTs have been employed as anodes in inverted OSCs based on an ITO cathode, zinc oxide (ZnO) ETL, poly (3,4-ethylenedioxythiophene):poly (styrenesulfonate) (PEDOT:PSS) HTL and poly (3-hexylthiophene) [6,6]-phenyl-C_{61}-butyric acid methyl ester (P3HT:PC_{61}BM) active layer (Ali et al., 2018), as illustrated in **Figure 3A**. The high optical transmittance of MWCNTs (85% for a single sheet) permitted the passage of more light to the active layer, which significantly improved photon harvesting; hence, promoting the generation of excitons. In addition, the low sheet resistance of MWCNTs (149 Ω sq^{-1}) facilitated the efficient collection and transportation of holes from the HTL to the anode, thereby increasing the J_{sc}. This resulted in devices with an optimum PCE of 1.46%, which was comparable to 2.25% for the Ag anode-based reference cell. Interestingly, the MWCNT-based devices managed to retain above 80% of their original PCE after storage for 10 days under environmental conditions, and also managed to maintain their initial PCE, above 90%, after 100 bending cycles, demonstrating their superior long-term environmental stability and excellent flexibility. Recently, a relatively high PCE of 7% has been obtained after introducing Ag nanoparticles (NPs) into MWCNT-based anodes of inverted OSCs (Zhang et al., 2021), demonstrating the significance of nanocomposites towards enhancing the efficiency of devices. In similar studies, but with conventional OSCs based on MWCNTs (Mugadza et al., 2017) and DWCNTs (Zhang et al., 2018), as anodes, more stable devices with optimum PCEs of 0.68 and 1.71%, respectively, were fabricated. This demonstrates the ample potential of CNTs as low-cost alternative electrodes for the future fabrication of highly efficient, stable and flexible devices.

SWCNTs have also been employed as anodes in conventional OSCs with the SWCNTs/molybdenum trioxide (MoO_3)/PEDOT:PSS/3,6-bis [5-(benzofuran-2-yl)thiophen-2-yl]-2,5-bis(2-ethylhexyl)pyrrolo [3,4-c]pyrrole-1,4-dione ($DPP(TBFu)_2$):PCBM/lithium fluoride (LiF)/aluminium (Al) configuration, as illustrated in **Figure 3B**, which exhibited a best PCE of 1.9% (Delacou et al., 2017). However, this PCE was lower than 4.4% for the control devices based on ITO anodes, which was attributed to the lower J_{sc} of 3.16 mA cm^{-2} for the SWCNT-based devices, when compared with 9.38 mA cm^{-2} for the ITO reference devices. This was probably due to the relatively lower electrical conductivity of SWCNTs than that of ITO, emanating from the relatively higher series resistance of SWCNTs (40 Ω cm^2) than 22 Ω cm^2 for ITO. In addition, the SWCNT-based devices had a relatively lower shunt resistance of 2.2×10^4 Ω cm^2, in comparison with 1.7×10^6 Ω cm^2 for the ITO control devices, which indicated the presence of significant charge carrier recombination, resulting in a lower FF; and, hence, giving rise to poor device performance.

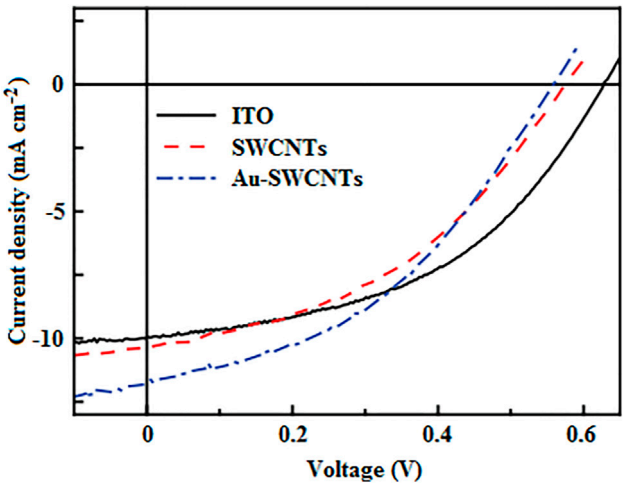

FIGURE 4 | J-V characteristics of conventional OSCs employing ITO, SWCNTs, and Au-SWCNTs as anodes. Adapted with permission (Fan et al., 2017). Copyright 2017, Chinese Physical Society and Institute of Physics.

A further improvement was made by doping SWCNTs with Au, which reduced the sheet resistance from 182 Ω sq^{-1} at a transmittance of 85% for the pristine SWCNTs to 60 Ω sq^{-1} at 82% transmittance (Fan et al., 2017). The resulting Au-SWCNTs were employed as anodes in conventional OSCs, which displayed the best PCE of 2.74%. This outperformed the pristine SWCNT-based device with a PCE of 2.52% and was comparable to 2.93% for the ITO reference device. The relatively poor performance of pristine SWCNT-based devices was attributed to their slightly low V_{oc}, emanating from short-circuits due to protruding SWCNTs. Also, the relatively low optical transmittance of the as-prepared SWCNTs usually obstructs the passage of more light to the active layer, resulting in low photon absorption and poor exciton generation, which impair device performance. In addition, the relatively high sheet resistance of pristine SWCNTs often leads to high series resistance, which restricts the efficient flow of holes to the anode, thereby giving rise to a low J_{sc}, as shown in **Figure 4**, and hence results in low device efficiency.

In a similar study, SWCNTs were doped with tetrafluoroethylene-based fluoropolymer-copolymer sulfonic acid (TFES), trifluoromethanesulfonic acid (TFMS) and nitric acid (HNO_3), and employed as anodes in conventional OSCs, which exhibited PCEs of 8.0, 8.3, and 8.5%, respectively (Jeon et al., 2018a). This outperformed the pristine SWCNT-based device with a PCE of 4.4%, and was comparable to the ITO reference device with a PCE of 9.1%. The relatively low efficiency of the as-prepared SWCNT-based devices was attributed to their relatively high series resistance (60 Ω cm^2) and low shunt resistance (320 Ω cm^2), resulting in low J_{sc} and FF, due to poor hole transport and high charge carrier recombination. In addition, the devices based on pristine SWCNTs, TFES-SWCNTs, TFMS-SWCNTs and HNO_3-SWCNTs, respectively, managed to retain above 70, 87, 63, and 41% of their initial PCE after storage for 60 days in a dark and N_2 environment, demonstrating their excellent long-term stability. Therefore, as a future research direction, the chemical doping of CNT-based electrodes can be employed to yield highly efficient and sustainable devices.

Recently, nanocomposites of SWCNTs and AgNWs with a low sheet resistance of 50 Ω sq^{-1} and a high average optical transmittance of 94% in the visible region have also been used as anodes in conventional OSCs, which exhibited a maximum PCE of 2.21% (Yang and Lee, 2020). This outperformed the pristine AgNW-based devices with a PCE of 1.43%, mainly due to the relatively high sheet resistance of the pristine AgNWs of 154 Ω sq^{-1}, giving rise to low electrical conductivity, and hence poor hole transport. Also, the root mean square surface roughness (R_{rms}) of 13.5 nm for the smooth SWCNT/AgNW composite electrode, which was relatively lower than 23.8 nm for the rough pristine AgNWs, resulted in a relatively high shunt resistance, thereby suppressing charge carrier recombination and leakage current when compared with pristine AgNWs that had a low shunt resistance; and hence, were prone to significant charge carrier recombination and leakage current, which subsequently reduce the device's efficiency.

Table 1 summarizes the photovoltaic parameters of OSCs based on CNT anodes discussed in this work. Interestingly, the best PCE of 8.5% was obtained when HNO_3-SWCNTs were used as the anode (Jeon et al., 2018a). Therefore, the chemical doping of CNTs is one of the best techniques that can be employed in future research to produce a substantial improvement in the optoelectronic properties and stability of the anode, thereby opening up avenues for the future realization of low-cost, flexible, highly efficient and sustainable carbon-based devices.

ACTIVE LAYER

The active layer of BHJ-OSCs is composed of an intimate blend of electron donor and acceptor materials, which does not only absorb light, generate excitons and provide multiple sites with large donor-acceptor interfacial area for effective dissociation of charge carriers, but also removes the requirement for long exciton diffusion lengths, and provides percolation pathways for efficient charge carrier transport (Oseni and Mola, 2017; Hou et al., 2018; Rafique et al., 2018; Gusain et al., 2019; Wu et al., 2019; Chen et al., 2020; Song et al., 2020; Xu et al., 2021). However, the photoactive layer often has issues, such as low optical absorption in the visible range, the need for more energy to dissociate the strongly bound photogenerated excitons, the presence of defects and charge carrier traps, short lifetime of charge carriers owing to recombination, discontinuous pathways for charge carrier transport, poor charge carrier mobility due to the hopping transport mechanism, and long-term instability due to degradation of the active layer materials (Paul et al., 2017; Subramanyam et al., 2020). Hence, traditional active layer materials need to be replaced or modified; to broaden the absorption spectrum for effective photon absorption and exciton generation; to increase the donor-acceptor interfacial area for significant exciton dissociation; to provide additional conductive networks for efficient charge carrier transport; and to

TABLE 1 | Photovoltaic parameters of OSCs employing CNT-based anodes.

Anode	V_{oc} (V)	J_{sc} (mA cm^{-2})	FF	PCE (%)	References
MWCNTs	0.57	7.53	0.34	1.46	Ali et al. (2018)
AgNPs/MWCNTs	0.76	15.23	0.60	7.00	Zhang et al. (2021)
MWCNTs	0.17	15.62	0.26	0.68	Mugadza et al. (2017)
DWCNTs	0.50	10.90	0.32	1.71	Zhang et al. (2018)
SWCNTs	0.80	3.20	0.40	1.90	Delacou et al. (2017)
SWCNTs	0.58	10.40	0.42	2.52	Fan et al. (2017)
Au-SWCNTs	0.56	11.70	0.42	2.74	Fan et al. (2017)
SWCNTs	0.80	12.00	0.46	4.40	Jeon et al. (2018a)
TFES-SWCNTs	0.80	14.30	0.70	8.00	Jeon et al. (2018a)
TFMS-SWCNTs	0.81	14.10	0.73	8.30	Jeon et al. (2018a)
HNO_3-SWCNTs	0.81	14.20	0.74	8.50	Jeon et al. (2018a)
SWCNTs/AgNWs	0.61	7.60	0.48	2.21	Yang and Lee (2020)

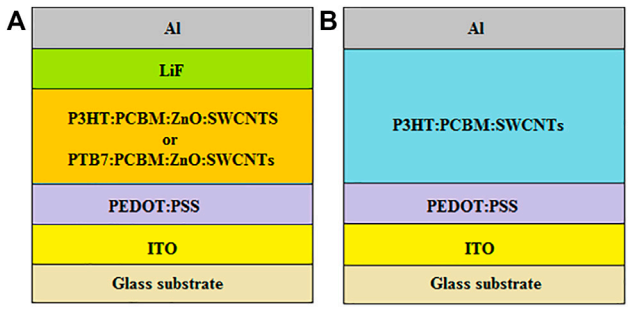

FIGURE 5 | Schematic diagram of conventional BHJ-OSCs with **(A)** ZnO:SWCNTs and **(B)** SWCNTs in the active layers.

prevent air and moisture penetration for improving long-term stability.

The most commonly used donor and acceptor materials are the p-type semiconducting polymer, P3HT, and fullerene, PCBM, respectively (Lim et al., 2018; Rathore et al., 2018; Dlamini et al., 2020; Gao et al., 2020; Milanovich et al., 2020; Ghosekar and Patil, 2021). This is due to the merits of P3HT, such as outstanding solubility in organic solvents, high absorption in the visible region, enhanced crystallinity, excellent charge carrier mobility and high stability (Khanh et al., 2020). In addition, PCBM has an excellent electron accepting capability and forms suitable nanoscale morphological networks with P3HT (Sivakumar et al., 2020). However, PCBM suffers from drawbacks, such as high-cost, low electrical conductivity, low charge carrier mobility, limited energy level engineering, weak optical absorption in the visible region, inferior mechanical flexibility, poor air and thermal stability, and complicated synthesis procedures (Amollo et al., 2017; Aïssa et al., 2019; Liang et al., 2019; Sivakumar et al., 2020; Zhao et al., 2020). Therefore, to address the aforementioned limitations, recent studies have focussed on replacing or modifying PCBM with carbon-based materials, particularly CNTs, owing to their excellent electron-accepting capability, large specific surface area, broad absorption spectrum, low reflectance, high charger carrier mobility, facile tunability of band gap, superior stability, and low-cost (Bhatia and Kumar, 2017; Fraga Domínguez et al., 2017). Furthermore, the band offset of CNTs and the donor polymer, and high built-in electric field at the polymer-CNT interface, have the potential to enhance the dissociation of excitons at the donor-acceptor interface, thereby facilitating the efficient transfer of electrons from the polymer to the CNTs (Fraga Domínguez et al., 2017; Agbolaghi, 2019b).

Being motivated by this, ZnO:SWCNTs have been incorporated into the polythieno [3,4-b]thiophene-co-benzodithiophene (PTB7):PCBM and P3HT:PCBM active layer blends of conventional BHJ-OSCs (Oseni et al., 2018), as illustrated in **Figure 5A**. Increasing the ZnO:SWCNT concentration to 6 wt% improved the generation of excitons and enhanced the interpenetrating networks for both hole and electron transport, which increased the J_{sc} and FF, resulting in relatively higher PCEs of 4.66 and 3.10% for the devices based on PTB7:PCBM:ZnO:SWCNTs and P3HT:PCBM:ZnO:SWCNTs, respectively, when compared with 2.76 and 1.92% for the pristine PTB7:PCBM and P3HT:PCBM devices, respectively. However, the introduction of excessive concentrations of ZnO:SWCNTs into the active layer led to a decrease in the J_{sc} and FF, probably due to the high series resistance and low shunt resistance, originating from the agglomeration and bundling of nanotubes, which produces charge carrier traps that prevent the smooth flow of charge carriers, resulting in high charge carrier recombination, as well as causing high leakage current due to short-circuits, thereby impairing device performance.

SWCNTs have also been incorporated into the P3HT:PCBM active layer blend of BHJ-OSCs (Kadem et al., 2018; Aïssa et al., 2019) as illustrated in **Figure 5B**. This resulted in devices with optimum PCEs of 2.20 and 3.54%, which outperformed their pristine P3HT:PCBM-based counterparts that had PCEs of 1.52 and 1.17%, respectively. This was attributed to the synergy between the electron-accepting nature of the fullerene and the rapid transportation of electrons through the additional percolation pathways created by the SWCNTs, which promoted the effective separation and transportation of charge carriers, thereby increasing the photogenerated current. In addition, the low R_{rms} of the SWCNT-based active layers of less than 5 nm, demonstrated that the hybrid active layer films were smooth and homogeneous; hence, prone to fewer short-circuits and few charge carrier traps, resulting in low leakage

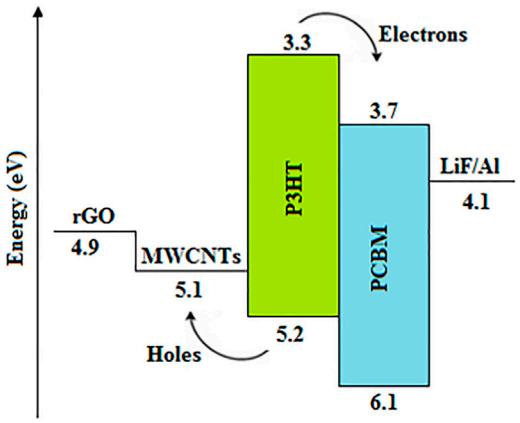

FIGURE 6 | Schematic energy level diagram of the P3HT:PCBM: MWCNT active layer-based OSC.

current and less recombination, which improves electron transport and subsequently increases the devices' PCE. A further increase in PCE from 2.20 to 2.32% was observed after incorporating acid-treated SWCNTs into the P3HT:PCBM blend (Kadem et al., 2018), which was ascribed to the increase in electrical conductivity from 130 mS cm^{-1} for the P3HT:PCBM blend with non-treated SWCNTs to 230 mS cm^{-1} for the P3HT: PCBM blend with acid-treated SWCNTs.

A further improvement was made by introducing MWCNTs: rGO into the P3HT:PCBM active layer blend of BHJ-OSCs, which resulted in more stable devices with a relatively higher PCE of 4.13% when compared with 2.91% for the pristine P3HT:PCBM devices (Mahakul et al., 2019). This was ascribed to the introduction of MWCNTs:rGO as additives to P3HT:PCBM, which not only increased the optical absorbance and donor-acceptor interfacial area for effective photon harvesting, exciton generation and exciton dissociation, but also provided smooth conductive pathways for the efficient transportation of photogenerated charge carriers and acted as protective layers against air and moisture penetration; hence, improving device performance and stability.

MWCNTs have also been integrated with the P3HT:PCBM active layer blend of OSCs (Khanh et al., 2020; Subramanyam et al., 2020; Khan et al., 2021), which significantly enhanced the optical absorption and created large donor-acceptor interfaces for improving the generation and dissociation of excitons. Also, the relatively higher work function of the MWCNTs of ~5.1 eV provided proper energy level alignment for the fast extraction and transportation of holes from the polymer blend to the MWCNTs, in addition to the faster electron transport by PCBM as illustrated in **Figure 6**, which played a substantial role in suppressing charge carrier recombination, thereby increasing the FF and J_{sc}, resulting in devices with relatively higher PCEs of 2.35 (Khanh et al., 2020), 1.88 (Khan et al., 2021), and 4.86% (Subramanyam et al., 2020), when compared with the pristine P3HT:PCBM-based devices. Nevertheless, extremely high concentrations of MWCNTs reduced the J_{sc} and FF, which in turn impaired the device performance due to the agglomeration of MWCNTs as their quantity increased, giving rise to leakage current through short-circuits. Furthermore, the agglomeration of CNTs often reduces the surface area available for the formation of heterojunctions, thereby reducing exciton generation; hence, significantly reducing the photogenerated current, and subsequently giving rise to devices with low PCE (Mahakul et al., 2019).

Recently, MWCNTs grafted with poly (3-dodecylthiophene) (MWCNTs-*graft*-PDDT) were crystallized with P3HT (Agbolaghi, 2019b; Hadi et al., 2020) and poly[bis(triiso-propylsilylethynyl) benzodithiophene-bis(decyltetradecylthien) naphthobisthiadiazole] (PBDT-TIPS-DTNT-DT) (Agbolaghi, 2019a), and the resulting nanohybrids were integrated with P3HT:$PC_{71}BM$ (Agbolaghi, 2019b; Hadi et al., 2020) and PBDT-TIPS-DTNT-DT:$PC_{71}BM$ (Agbolaghi, 2019a) active layer blends of BHJ-OSCs. Interestingly, the surface modification of MWCNTs helped to increase their dispersion in organic solvents, which enhanced the interaction between the P3HT and MWCNT phases. This, in turn, reduced the agglomeration of MWCNTs, and hence reduced short-circuits, surface charge trapping and recombination, resulting in devices with relatively higher PCEs of 5.40 (Agbolaghi, 2019b) and 4.18% (Hadi et al., 2020), respectively, when compared with 2.13 and 1.14% for the corresponding unmodified MWCNT-based devices. Also, the larger specific surface area and larger crystallite sizes of MWCNTs-*graft*-PDDT/P3HT with fewer grain boundaries and better crystallinity, respectively, increased the donor-acceptor interfacial area and formed conductive pathways, which increased the exciton dissociation rate and charge carrier mobility, resulting in high J_{sc}, thereby improving the device performance. However, the grafting of MWCNTs to PDDT weakened the assembling and crystallization of the PBDT-TIPS-DTNT-DT chains onto the MWCNTs, which reduced the PCE from 4.07 to 3.69% for the unmodified MWCNT- and the grafted MWCNT-based devices, respectively (Agbolaghi, 2019a).

Table 2 summarizes the photovoltaic parameters of OSCs with CNT-based active layers. From the reviewed reports, the highest PCE of 5.40% was observed in P3HT:PCBM:MWCNTs-*graft*-PDDT/P3HT active layer-based devices (Agbolaghi, 2019b). This demonstrates the excellent potential of CNTs as future additives of choice to the P3HT:PCBM active layer blend, rather than as substitutes to PCBM, capable of increasing not only the donor-acceptor interfacial area for the effective dissociation and extraction of excitons, but also providing smooth conductive pathways for the efficient transportation of photogenerated charge carriers, and as protective layers against air and moisture penetration; hence, improving device performance and stability.

CHARGE TRANSPORT LAYER

The extraction and transportation of charge carriers from the active layer to the electrodes of OSCs have been significantly improved by introducing charge transport layers that reduce the energy barrier and prevent the direct contact between the active

TABLE 2 | Photovoltaic parameters of OSCs employing CNT-based active layers.

Active layer	V_{oc} (V)	J_{sc} (mA cm^{-2})	FF	PCE (%)	References
P3HT:PCBM:ZnO:SWCNTs	0.57	11.22	0.49	3.10	Oseni et al. (2018)
PTB7:PCBM:ZnO:SWCNTs	0.75	14.40	0.43	4.66	Oseni et al. (2018)
P3HT:PCBM:SWCNTs	0.55	7.34	0.55	2.20	Kadem et al. (2018)
P3HT:PCBM:acid-treated SWCNTs	0.54	8.00	0.54	2.32	Kadem et al. (2018)
P3HT:PCBM:SWCNTs	0.66	9.95	0.54	3.54	Aïssa et al. (2019)
P3HT:PCBM:MWCNTs:rGO	0.65	11.01	0.50	4.13	Mahakul et al. (2019)
P3HT:PCBM:MWCNTs	0.87	5.05	0.54	2.35	Khanh et al. (2020)
P3HT:PCBM:MWCNTs	0.49	8.64	0.44	1.88	Khan et al. (2021)
P3HT:PCBM:MWCNTs	0.67	11.81	0.62	4.86	Subramanyam et al. (2020)
P3HT:PCBM:MWCNTs	0.61	8.18	0.42	2.13	Agbolaghi (2019b)
P3HT:PCBM:MWCNTs-*graft*-P3HT	0.61	11.99	0.56	4.11	Agbolaghi (2019b)
P3HT:PCBM:MWCNTs-*graft*-PDDT/P3HT	0.63	13.11	0.65	5.40	Agbolaghi (2019b)
P3HT:PCBM:MWCNTs-*graft*-PDDT/P3HT	0.62	11.25	0.60	4.18	Hadi et al. (2020)
P3HT:MWCNTs-*graft*-PDDT/P3HT	0.63	9.69	0.52	3.17	Hadi et al. (2020)
P3HT:PCBM:MWCNTs/P3HT	0.65	8.78	0.48	2.74	Hadi et al. (2020)
P3HT:MWCNTs/P3HT	0.64	4.56	0.39	1.14	Hadi et al. (2020)
PBDT-TIPS-DTNT-DT:PCBM:MWCNTs/PBDT-TIPS-DTNT-DT	0.69	10.17	0.58	4.07	Agbolaghi, (2019a)
PBDT-TIPS-DTNT-DT:PCBM:MWCNTs-*graft*-PDDT/PBDT-TIPS-DTNT-DT	0.68	9.51	0.57	3.69	Agbolaghi, (2019a)

layer and electrodes for the effective extraction and transportation of charge carriers and suppression of recombination (Amollo et al., 2018; Ramasamy et al., 2019; Tian et al., 2021). From this viewpoint, HTLs and ETLs extract and transport holes and electrons from the photoactive layer to the anode and cathode, respectively, while selectively blocking electrons (for HTLs) and holes (for ETLs), thereby suppressing charge carrier recombination. In addition, the charge transport layers are usually transparent to allow the incoming photons to reach the active layer for exciton generation. Also, the charge transport layers improve the stability of devices by forming protective layers that seal the active layer materials from the diffusion of moisture and air (Rafique et al., 2018; Amusan et al., 2019; Liu et al., 2019). Therefore, the charge transport layers play a substantial role in determining the overall efficiency and stability of OSCs.

Hole Transport Layer

HTLs are high work function p-type materials that are responsible for reducing the potential barrier and providing an Ohmic contact at the active layer-anode interface, which improves the extraction and transportation of holes from the active layer to the anode, while selectively blocking electron transport, thereby suppressing charge carrier recombination (Amollo et al., 2018; Jeon Y.-J. et al., 2018). Several HTL materials, including the p-type semiconducting polymer PEDOT:PSS; inorganic metal oxides, e.g., nickel oxide (NiO), MoO_3, and vanadium pentoxide (V_2O_5); and carbon-based materials, e.g., CNTs and graphene, have been recently employed in OSCs (Mbuyise et al., 2017; Singh et al., 2017; Hilal and Han, 2019; Mohammad et al., 2019; Rafique et al., 2019; Li J. et al., 2020). Among these, PEDOT:PSS is the most commonly used HTL due to its high optical transmittance in the visible region, which permits more light to pass to the active layer for effective exciton generation, and its suitable work function, which aligns the energy levels between the active layer and anode for efficient hole extraction (Dang et al., 2018; Zhang W. et al., 2020). In addition, PEDOT:PSS is compatible with low-cost solution processing and has a smooth surface morphology, which moderates the surface roughness of the anode; hence, reducing the likelihood of undesirable effects, such as charge carrier traps and short-circuits, and thereby suppressing charge carrier recombination and leakage current (Ricciardulli et al., 2017; Sorkhishams et al., 2019). Nonetheless, the hygroscopic nature of PEDOT:PSS enables the unfavourable penetration of water into the active layer, and the acidity of PEDOT:PSS causes etching of the ITO anode, which subsequently leads to low device efficiency and poor long-term stability (Subramanyam et al., 2019). Furthermore, PEDOT:PSS has poor hole selectivity, i.e., weak electron blocking capabilities, and the insulating nature of PSS chains causes PEDOT:PSS to have a relatively low electrical conductivity (Dang et al., 2018; Pali et al., 2018; Hayat et al., 2019).

Although inorganic metal oxides have been proposed as potential alternatives to PEDOT:PSS due to their excellent hole collection property, suitable work function, electron-blocking capability and superior stability, their use has been limited by their requirement for high-vacuum and high-temperature deposition equipment (Ricciardulli et al., 2017), which is expensive and complicated to use, incompatible with flexible substrates, and consumes more energy (Zhang et al., 2019; Xu et al., 2020). Hence, to overcome the aforementioned drawbacks, CNTs have been recently reported as one of the most promising alternative HTL materials, capable of modifying or replacing PEDOT:PSS, due to their ballistic charge transport capability, high electrical conductivity, high optical transmittance in the visible range, excellent stability, high flexibility, and solution processability (Subramanyam et al., 2020).

Inspired by this, ZnO-doped SWCNTs (ZnO:SWCNTs) have been incorporated into PEDOT:PSS and used as a composite HTL in BHJ-OSCs, resulting in devices with a relatively higher PCE of

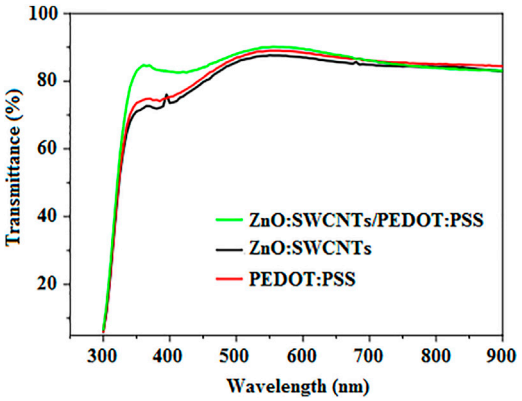

FIGURE 7 | The optical transmittance spectra of ZnO:SWCNTs/PEDOT:PSS, ZnO:SWCNTs and PEDOT:PSS films on ITO-coated glass substrates. Adapted with permission (Mbuyise et al., 2017). Copyright 2017, Elsevier.

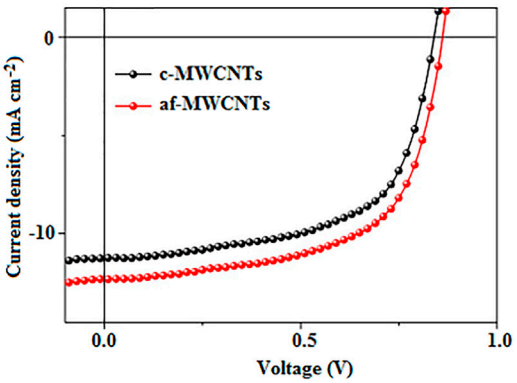

FIGURE 9 | J-V characteristics of OSCs based on af-MWCNTs and c-MWCNTs. Adapted with permission (Zhang et al., 2019). Copyright 2019, Elsevier.

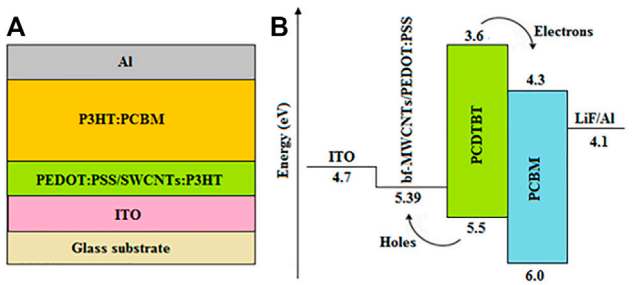

FIGURE 8 | (A) Schematic diagram of the PEDOT:PSS/SWCNTs:P3HT-based BHJ-OSC, and **(B)** energy level diagram of the bf-MWCNTs/PEDOT:PSS HTL-based OSC with the poly [N-9′-heptadecanyl-2,7-carbazole-alt-5,5-(4′,7′-di-2-thienyl-2′,1′,3′-benzothiadiazole)] (PCDTBT):PCBM active layer blend.

4.1% when compared with the pristine PEDOT:PSS reference device that had a PCE of 1.9% (Mbuyise et al., 2017). This was attributed to the high optical transmittance of the ZnO:SWCNTs/PEDOT:PSS HTL in the visible region, as shown in **Figure 7**, which allowed the passage of more light to the active layer, thereby facilitating significant photon harvesting, leading to effective exciton generation. In addition, the ZnO:SWCNTs reduced the potential barrier between the P3HT:PCBM active layer and the ITO anode, which enhanced the extraction and mobility of holes, and provided better interfacial contact, which lowered the series resistance and facilitated the efficient collection of holes at the ITO anode, resulting in an enhanced J_{sc}. Also, the devices with ZnO:SWCNTs loading of 2.5, 5.0, and 10.0 wt% managed to retain 84, 51, and 83% of their original PCE, respectively, after being stored at 100°C without encapsulation in a nitrogen atmosphere, demonstrating their excellent stability.

In another study, acid-treated SWCNTs have been integrated with P3HT and the resulting hybrids were incorporated into the PEDOT:PSS HTLs of BHJ-OSCs (Kadem et al., 2018), as illustrated in **Figure 8A**. The formation of SWCNTs:P3HT hybrids caused the conjugated polymer to twist around SWCNTs, resulting in nanoscale interconnected networks that facilitated the efficient transfer of holes between P3HT and SWCNTs, while selectively blocking the way for electron transport. This increased the shunt resistance and suppressed charge carrier recombination, resulting in a relatively higher electrical conductivity of 165 mS cm^{-1} for the acid-treated SWCNTs:P3HT hybrid when compared with 20 mS cm^{-1} for pristine P3HT. Consequently, devices with the PEDOT:PSS/acid-treated SWCNTs:P3HT HTL exhibited higher J_{sc}; hence, a higher PCE of 2.52%, which outperformed devices based on P3HT/PEDOT:PSS HTLs that had a PCE of 2.48%. A significant increase in hole transport efficiency and electrical conductivity has also been observed after incorporating unzipped SWCNTs (uSWCNTs) into PEDOT:PSS to form a composite HTL of BHJ-OSCs (Zhang W. et al., 2020). This, in turn, increased the J_{sc} and FF, resulting in devices with a higher PCE of 14.60% when compared with 5.93 and 13.72% for the pristine uSWCNTs and PEDOT:PSS devices, respectively. The relatively poor performance of devices with pristine uSWCNTs was mainly associated with the inhomogeneity and high surface roughness of uSWCNTs, resulting in poor hole transport and current leakage due to charge carrier traps and short-circuits.

Boronic acid-functionalized MWCNTs (bf-MWCNTs) have also been incorporated into PEDOT:PSS and used as a composite HTL in OSCs (Dang et al., 2018). This increased the work function from 5.02 eV for the pristine PEDOT:SS HTL to 5.39 eV for the bf-MWCNTs/PEDOT:PSS HTL as illustrated in **Figure 8B**, and hence reduced the energy barrier by providing good energy level matching with the HOMO level of the PCDTBT donor and work function of the ITO anode. This subsequently improved the extraction and transportation of holes from the active layer to the anode, which significantly increased the hole mobility and electrical conductivity. Furthermore, the bf-MWCNTs/PEDOT:PSS-based devices were less affected by leakage current challenges due to their high shunt resistance (621 Ω cm^2) and low series resistance (6.26 Ω cm^2), which suppressed charge carrier recombination and increased the

photogenerated current. This, in turn, increased the FF and J_{sc}, resulting in MWCNTs/PEDOT:PSS-based devices with an optimum PCE of 6.95%, which outperformed the pristine MWCNT and PEDOT:PSS-based devices that had PCEs of 6.33 and 5.42%, respectively.

Also, the suitable work function of amino-functionalized MWCNTs (af-MWCNTs) of 5.22 eV enabled them to be used as HTLs in BHJ-OSCs to provide proper energy level alignment between the donor HOMO level (5.5 eV) and the work function of ITO (4.7 eV) (Zhang et al., 2019), which enhanced hole extraction and transport. In addition, the af-MWCNT-based devices exhibited a relatively lower series resistance (5.95 $\Omega\,cm^2$) and a higher shunt resistance (606.04 $\Omega\,cm^2$), when compared with 7.58 and 373.89 $\Omega\,cm^2$, respectively, for the control device based on carboxylated MWCNTs (c-MWCNTs). This indicated the presence of a smaller leakage current and lower charge carrier recombination rate in the OSCs with af-MWCNT HTLs, which improved their electrical conductivity, and hence increased their J_{sc} as illustrated in **Figure 9**, resulting in an optimum PCE of 6.97%, which outperformed the c-MWCNTs control device that had a PCE of 5.74%.

MWCNTs have also been integrated with poly (3-thiophene ethanol) (P3ThEt)-*graft*-PANI, and the resulting nanocomposites were used as HTLs in OSCs, which exhibited a relatively higher PCE of 5.30% when compared with 2.94 and 2.18% for the devices based on pristine MWCNTs and PEDOT:PSS, respectively (Sorkhishams et al., 2019). This was ascribed to the high optical transmittance (85–89%) of the MWCNTs/P3ThEt-*graft*-PANI HTL, which allowed more light to reach the active layer for effective exciton generation. In addition, the interpenetrated conductive networks formed by the MWCNTs/P3ThEt-*graft*-PANI nanocomposite facilitated the efficient transportation of photogenerated holes from the active layer to the anode. Also, the low R_{rms} of the smooth MWCNTs/P3ThEt-*graft*-PANI films resulted in a low series resistance and a high shunt resistance, which increased the electrical conductivity, reduced the leakage current and suppressed the recombination of charge carriers, thereby increasing the J_{sc} and FF, and subsequently increasing the device's efficiency. Interestingly, the MWCNTs/P3ThEt-*graft*-PANI-based devices managed to retain above 75% of their initial PCE after storage for 30 days when compared with ~23 and 60% for the pristine PEDOT:PSS and MWCNT-based devices, demonstrating their superior long-term stability.

Recently, the introduction of CNTs into PEDOT:PSS led to the formation of highly conducting interpenetrating networks throughout the HTL composite, which enhanced the transportation of holes, resulting in OSCs with relatively higher PCEs of 2.82 (Subramanyam et al., 2019), 3.76 (Subramanyam et al., 2020), and 6.44% (Oyeshola et al., 2020), when compared with the pristine PEDOT:PSS control devices. In addition, the chemical inertness of CNTs prevented the penetration of moisture and oxygen to the active layer, which significantly reduced the rapid degradation of materials. This enhanced the long-term stability of the CNTs/PEDOT:PSS-based devices when compared with the pristine PEDOT:PSS devices, which displayed a rapid drop in efficiency under the same environmental conditions due to the hygroscopic and acidic nature of PEDOT:PSS.

The photovoltaic parameters of OSCs with CNT-based HTLs, discussed in this work, are summarized in **Table 3**. Among these, the best PCE of 14.60% was obtained in more stable devices with uSWCNTs/PEDOT:PSS HTLs (Zhang W. et al., 2020). Hence, as a future research direction, the integration of CNTs with the conventional PEDOT:PSS HTL is envisaged to result in devices with excellent performance and stability, which is a significant step towards commercialization.

Electron Transport Layer

ETLs are low work function n-type materials that reduce the energy barrier between the LUMO level of the electron acceptor and work function of the cathode; hence, they provide an Ohmic contact at the interface between the active layer and cathode (Amusan et al., 2019). This improves the extraction and transportation of electrons from the photoactive layer to the cathode, while selectively blocking hole transport, thereby suppressing electron and hole recombination (Soh et al., 2019).

An assortment of ETL materials, including low work function metals or related salts, e.g., Ca (Anagnostou et al., 2019; Ghosekar and Patil, 2019; Lian et al., 2019; Song et al., 2019; Yu et al., 2019) and LiF (Zhao and Alford, 2018; Lee et al., 2019; Zheng et al., 2019; Adedeji et al., 2020; Li et al., 2020b), and n-type semiconducting metal oxides, e.g., ZnO (Upama et al., 2017; Ahmad et al., 2019; Frankenstein et al., 2019; Zhang X. et al., 2020; Usmani et al., 2021) and TiO_2 (Lin et al., 2013; Sun et al., 2016; Alhashimi et al., 2018; Abdallaoui et al., 2020; Chaudhary et al., 2021), have been commonly used to fabricate OSCs. However, Ca and LiF are usually deposited by thermal evaporation in a high vacuum environment at high temperature, which is expensive, complicated and incompatible with flexible devices; hence, making them unfavourable. Although, ZnO and TiO_2 have merits, such as low-cost, solution processability, non-toxicity, facile availability and high optical transmittance in the visible region (Mutlu et al., 2019; Wei et al., 2019), their choice is limited by poor charge transport due to defects incurred during film growth, which increases charge carrier recombination (Mohamad Noh et al., 2018), thereby reducing the efficiency of devices. This challenge can be addressed by high-temperature annealing to improve the physicochemical properties of ZnO and TiO_2 films, but high-temperature annealing is not compatible with flexible devices (Wang et al., 2018). As a consequence, carbon-based materials, particularly CNTs, have recently attracted considerable research interest as potential alternatives for ETL applications owing to their low-cost, solution-processability, high optical transparency, good electrical conductivity, high flexibility and superior stability.

In this regard, CNT-Au nanocomposites have been incorporated into ZnO NPs and employed as hybrid ETLs in OSCs (Hu et al., 2016; Li et al., 2019), as illustrated in **Figure 10A**. The CNTs provided a suitable template for the *in situ* growth of ZnO NPs, resulting in uniform films with low defect density and good electrical conductivity, whereas the Au NPs, bound uniformly to the CNTs as illustrated in **Figure 10B**, inducing

TABLE 3 | Photovoltaic parameters of OSCs employing CNT-based HTLs.

HTL	V_{oc} (V)	J_{sc} (mA cm^{-2})	FF	PCE (%)	References
ZnO:SWCNTs/PEDOT:PSS	0.53	14.00	0.55	4.10	Mbuyise et al. (2017)
PEDOT:PSS/acid-treated SWCNTs:P3HT	0.55	8.48	0.54	2.52	Kadem et al. (2018)
PEDOT:PSS/SWCNTs:P3HT	0.53	8.70	0.55	2.52	Kadem et al. (2018)
uSWCNTs/PEDOT:PSS	0.85	23.39	0.73	14.60	Zhang W. et al. (2020)
uSWCNTs	0.51	21.50	0.54	5.93	Zhang W. et al. (2020)
MWCNTs	0.87	11.73	0.62	6.33	Dang et al. (2018)
bf-MWCNTs	0.88	12.51	0.63	6.95	Dang et al. (2018)
af-MWCNTs	0.87	12.65	0.64	6.97	Zhang et al. (2019)
c-MWCNTs	0.84	11.23	0.61	5.74	Zhang et al. (2019)
MWCNTs/P3ThEt-*graft*-PANI	0.68	12.85	0.61	5.30	Sorkhishams et al. (2019)
MWCNTs	0.63	9.42	0.50	2.94	Sorkhishams et al. (2019)
CNTs/PEDOT:PSS	0.65	9.86	0.44	2.82	Subramanyam et al. (2019)
CNTs/PEDOT:PSS	0.66	10.83	0.53	3.76	Subramanyam et al. (2020)
CNTs/PEDOT:PSS	0.72	11.02	0.72	6.44	Oyeshola et al. (2020)

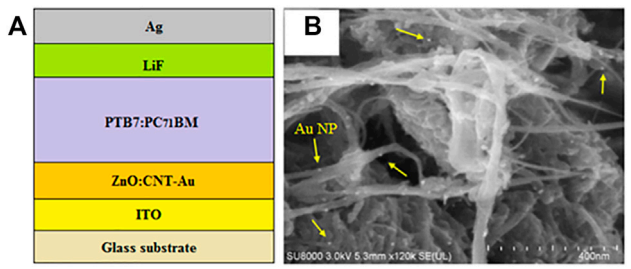

FIGURE 10 | (A) Schematic diagram of a conventional BHJ-OSC with a ZnO:CNTs-Au composite ETL and **(B)** SEM micrograph of the CNTs-Au film. Adapted with permission (Hu et al., 2016). Copyright 2016, Elsevier.

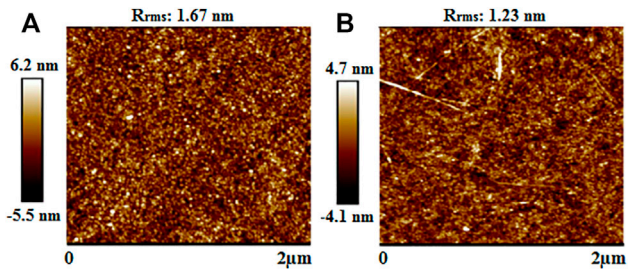

FIGURE 11 | AFM micrographs of **(A)** pristine ZnO NPs and **(B)** ASP-SWCNTs on ZnO NPs. Adapted with permission (Lee et al., 2020). Copyright 2020, American Chemical Society.

a surface plasmon effect, which enhanced the absorption of light in the active layer. This improved the generation of excitons, suppressed the recombination of charge carriers and facilitated the smooth transportation of electrons to the cathode. In addition, the incorporation of CNTs-Au into ZnO reduced the work function of the composite ETL, which provided better energy level alignment between the active layer and cathode for the effective extraction of electrons from the active layer

TABLE 4 | Photovoltaic parameters of OSCs employing CNT-based ETLs.

ETL	V_{oc} (V)	J_{sc} (mA cm^{-2})	FF	PCE (%)	References
ZnO:CNTs	0.72	16.37	0.64	7.60	Hu et al. (2016)
ZnO:CNTs-Au	0.72	16.81	0.65	7.90	Hu et al. (2016)
ZnO:CNTs-Au	0.80	18.37	0.72	10.49	Li et al. (2019)
ZnO:ASP-SWCNTs	0.80	17.72	0.66	9.45	Lee et al. (2020)
ZnO:ASP-SWCNTs	0.87	24.88	0.66	14.37	Lee et al. (2020)

and transportation to the cathode. This, in turn, increased exciton generation and electron mobility, as well as reducing charge carrier recombination, thereby increasing the J_{sc} and FF. Consequently, the ZnO:CNTs-Au-based devices displayed relatively higher PCEs of 7.90 (Hu et al., 2016) and 10.49% (Li et al., 2019), respectively, when compared with 7.00 and 8.41% for the corresponding pristine ZnO reference devices.

Recently, alcohol-soluble polyfluorene (ASP)-wrapped SWCNTs have been incorporated into ZnO NPs and employed as composite ETLs in OSCs (Lee et al., 2020). ASP facilitated the individual dispersion of SWCNTs in solution, which resulted in smooth films with low R_{rms} as shown in **Figure 11**, thereby addressing the issue of leakage current due to short-circuits, originating from the agglomeration and bundling of poorly dispersed SWCNTs in rough films. In addition, the ASP-SWCNTs played a significant role in increasing the internal quantum efficiency, balancing the mobility between holes and electrons, and reducing charge carrier recombination, which increased the J_{sc} and FF. This resulted in PCEs of 9.45 and 14.37% for the devices using the poly([2,6′-4,8-di(5-ethylhexylthienyl)benzo[1,2-b;3,3-b]dithiophene] (Subramanyam et al., 2020)) (PTB7-Th):$PC_{71}BM$ and poly[(2,6-(4,8-bis(5-(2-ethylhexyl-3-fluoro)thiophen-2-yl)-benzo [1,2-b:4,5-b']dithiophene))-alt-(5,5-(1′,3′-di-2-thienyl-5′,7′-bis(2-ethylhexyl)benzo [1′,2′-c:4′,5′-c']dithiophene-4,8-dione)]: (2,20-((2Z, 20Z)-((12,13-bis(2-ethylhexyl)-3,9-diundecyl-12,13-dihydro-[1,2,5]thiadiazolo [3,4-e]thieno

[2,"30':4′,50]thieno[20,30:4,5]pyrrolo[3,2-g]thieno[20,30:4,5]thieno[3,2-b]indole-2,10-diyl)bis(methanylylidene))bis(5,6-difluoro-3-oxo-2,3-dihydro-1H-indene-2,1-diylidene))dimalononitrile) (PM6:Y6) active layer blends, respectively, which outperformed the corresponding pristine ZnO devices that had PCEs of 7.97 and 13.73%.

The photovoltaic parameters of OSCs with CNT-based ETLs, discussed in this study, are summarized in **Table 4**. From these, the highest PCE of 14.37% was achieved by OSCs with the ZnO: ASP-SWCNTs ETL (Lee et al., 2020), demonstrating the suitability of CNT-based ETLs in the fabrication of highly efficient devices.

CONCLUSION AND OUTLOOK

This review has presented the recent trends in the application of CNTs in electrodes, active layers and charge transport layers of OSCs, in response to the increasing demand to develop alternative materials that can replace or modify the traditional materials, which are currently producing devices with relatively low PCE and poor long-term stability. Among the possible alternatives, carbon-based materials, especially CNTs, are more appealing due to their solution processability, non-toxicity, the natural abundance of carbon, low-cost, competitive optoelectronic properties and excellent stability. However, the efficiency of CNT-based OSCs is still relatively lower than that of the state-of-the-art OSCs fabricated with traditional materials due to drawbacks, such as the relatively low visible region optical transparency of CNT-based electrodes and charge transport layers, which limit the passage of incoming photons to the active layer, thereby reducing the exciton generation rate, and hence lowering the photogeneration of current. In addition, the sheet resistance of CNT-based electrodes is relatively higher than that of commonly used ITO electrodes. This limits the efficient collection and transfer of photogenerated current from the charge transport layers to the external circuit, thereby impairing device performance. Nonetheless, the tunable band gap of CNTs, in addition to selective charge carrier transportation and blocking capabilities of CNT-based charge transport layers, enable the provision of an Ohmic contact at the photoactive layer-electrode interface, thereby improving charge carrier extraction and mobility, which increases the efficiency of devices. Also, the hydrophobic nature of CNTs helps to prevent the diffusion of moisture and air into the photoactive layer, which protects the photoactive layer materials from degradation, thereby enhancing the stability of OSCs. Furthermore, the large specific surface area of CNTs provides a large interfacial area between the donor and acceptor, which enhances exciton dissociation, in addition to the highly conductive CNT interpenetrating network, which improves the transfer of electrons and holes to their respective electrodes before recombination, thereby improving device performance. Therefore, as a future research direction, optimization of the optoelectronic properties of CNTs via approaches, such as chemical doping and formation of nanocomposites, is envisaged to pave the way for the commercialization of CNT-based OSCs through the fabrication of highly efficient, sustainable and cost-effective devices.

AUTHOR CONTRIBUTIONS

EM and ETM were involved in the study and the design of the first draft of the review and provided revisions to the manuscript. BM and VN, through the university, provided the funding for this project. They also assisted in structuring/designing the manuscript, providing ideas, some literature background, and proofreading the article on progressive revisions and versions to the final manuscript draft. VN is the corresponding author.

ACKNOWLEDGMENTS

The authors are grateful to the College of Agriculture, Engineering and Science, University of KwaZulu-Natal (UKZN), for funding this work. Also, thanks to the UKZN Nanotechnology Platform, Eskom Tertiary Education Support Programme (TESP), National Research Foundation (NRF) of South Africa and Global Challenges Research Fund (GCRF) for supporting this work.

REFERENCES

Abdallaoui, M., Sengouga, N., Chala, A., Meftah, A. F., and Meftah, A. M. (2020). Comparative Study of Conventional and Inverted P3HT: PCBM Organic Solar Cell. *Opt. Mater.* 105, 109916–109925. doi:10.1016/j.optmat.2020.109916

Adedeji, M. A., Hamed, M. S. G., and Mola, G. T. (2020). Light Trapping Using Copper Decorated Nano-Composite in the Hole Transport Layer of Organic Solar Cell. *Solar Energy* 203, 83–90. doi:10.1016/j.solener.2020.04.005

Agbolaghi, S. (2019a). Pure and Complex Nanostructures Using Poly[bis(Triiso-Propylsilylethynyl) Benzodithiophene-bis(Decyltetradecyl-Thien) Naphthobisthiadiazole], Carbon Nanotubes and Reduced Graphene Oxide for High-performance Polymer Solar Cells. *Polym. Int.* 68, 1688–1697. doi:10.1002/pi.5872

Agbolaghi, S. (2019b). Saturation/Unsaturation of P3HT:PC71BM Photovoltaics with CNT Derivatives and Correlated Supramolecules. *Org. Electron.* 68, 271–279. doi:10.1016/j.orgel.2019.02.032

Ahmad, N., Zhang, X., Yang, S., Zhang, D., Wang, J., Zafar, S. u., et al. (2019). Polydopamine/ZnO Electron Transport Layers Enhance Charge Extraction in Inverted Non-Fullerene Organic Solar Cells. *J. Mater. Chem. C.* 7, 10795–10801. doi:10.1039/c9tc02781e

Aïssa, B., Ali, A., Bentouaf, A., Khan, W., Zakaria, Y., Mahmoud, K. A., et al. (2019). Influence of Single-Walled Carbon Nanotubes Induced Exciton Dissociation Improvement on Hybrid Organic Photovoltaic Devices. *J. Appl. Phys.* 126, 113101–113111. doi:10.1063/1.5105388

Al-hashimi, M. K., Kadem, B. Y., and Hassan, A. K. (2018). Rutile TiO_2 Films as Electron Transport Layer in Inverted Organic Solar Cell. *J. Mater. Sci. Mater. Electron.* 29, 7152–7160. doi:10.1007/s10854-018-8703-2

Ali, A., Kazici, M., Bozar, S., Keskin, B., Kaleli, M., Shah, S. M., et al. (2018). Laminated Carbon Nanotubes for the Facile Fabrication of Cost-Effective

Polymer Solar Cells. *ACS Appl. Energ. Mater.* 1, 1226–1232. doi:10.1021/acsaem.7b00345

Alturaif, H., ALOthman, Z., Shapter, J., and Wabaidur, S. (2014). Use of Carbon Nanotubes (CNTs) with Polymers in Solar Cells. *Molecules* 19, 17329–17344. doi:10.3390/molecules191117329

Amollo, T. A., Mola, G. T., Kirui, M. S. K., and Nyamori, V. O. (2017). Graphene for Thermoelectric Applications: Prospects and Challenges. *Crit. Rev. Solid State. Mater. Sci.* 43, 133–157. doi:10.1080/10408436.2017.1300871

Amollo, T. A., Mola, G. T., and Nyamori, V. O. (2018). High-Performance Organic Solar Cells Utilizing Graphene Oxide in the Active and Hole Transport Layers. *Solar Energy* 171, 83–91. doi:10.1016/j.solener.2018.06.068

Amusan, O., Louis, H., Zafar, S., Hamzat, A., and Peter, D. (2019). Different Interface Engineering in Organic Solar Cells: A Review. *Chem. Methodol.* 3, 425–441. doi:10.22034/chemm.2018.150142.1096

An, C. J., Lee, Y. C., Kang, Y. H., and Cho, S. Y. (2017). Improved Interaction between Semiconducting Polymer and Carbon Nanotubes in Thermoelectric Composites through Covalent Grafting. *Carbon* 124, 662–668. doi:10.1016/j.carbon.2017.09.022

Anagnostou, K., Stylianakis, M. M., Petridis, K., and Kymakis, E. (2019). Building an Organic Solar Cell: Fundamental Procedures for Device Fabrication. *Energies* 12, 2188–2210. doi:10.3390/en12112188

Andreani, L. C., Bozzola, A., Kowalczewski, P., Liscidini, M., and Redorici, L. (2018). Silicon Solar Cells: toward the Efficiency Limits. *Adv. Phys. X* 4, 1548305–2548327. doi:10.1080/23746149.2018.1548305

Arulkumar, S., Senthilkumar, T., Parthiban, S., Dharmalingam, G., Goswami, A., Alshehri, S. M., et al. (2021). AgNWs-a-TiOx: A Scalable Wire Bar Coated Core-Shell Nanocomposite as Transparent Thin Film Electrode for Flexible Electronics Applications. *J. Mater. Sci. Mater. Electron.* 32, 6454–6464. doi:10.1007/s10854-021-05362-2

Ashok, A., Regmi, G., Romero-Núñez, A., Solis-López, M., Velumani, S., and Castaneda, H. (2020). Comparative Studies of CdS Thin Films by Chemical Bath Deposition Techniques as a Buffer Layer for Solar Cell Applications. *J. Mater. Sci. Mater. Electron.* 31, 7499–7518. doi:10.1007/s10854-020-03024-3

Bhatia, R., and Kumar, L. (2017). Functionalized Carbon Nanotube Doping of P3HT:PCBM Photovoltaic Devices for Enhancing Short Circuit Current and Efficiency. *J. Saudi Chem. Soc.* 21, 366–376. doi:10.1016/j.jscs.2016.11.003

Burlingame, Q., Ball, M., and Loo, Y.-L. (2020). It's Time to Focus on Organic Solar Cell Stability. *Nat. Energ.* 5, 947–949. doi:10.1038/s41560-020-00732-2

Chaudhary, D. K., Dhawan, P. K., Patel, S. P., and Bhasker, H. P. (2021). Large Area Semitransparent Inverted Organic Solar Cells with Enhanced Operational Stability Using TiO_2 Electron Transport Layer for Building Integrated Photovoltaic Devices. *Mater. Lett.* 283, 128725–128728. doi:10.1016/j.matlet.2020.128725

Chen, J., Chen, Y., Feng, L.-W., Gu, C., Li, G., Su, N., et al. (2020). Hole (Donor) and Electron (Acceptor) Transporting Organic Semiconductors for Bulk-Heterojunction Solar Cells. *EnergyChem* 2, 100042–100105. doi:10.1016/j.enchem.2020.100042

Chen, L. X. (2019). Organic Solar Cells: Recent Progress and Challenges. *ACS Energ. Lett.* 4, 2537–2539. doi:10.1021/acsenergylett.9b02071

Cho, Y., Kumari, T., Jeong, S., Lee, S. M., Jeong, M., Lee, B., et al. (2020). Guest-Oriented Non-Fullerene Acceptors for Ternary Organic Solar Cells with over 16.0% and 22.7% Efficiencies under One-Sun and Indoor Light. *Nano Energy* 75, 104896–104906. doi:10.1016/j.nanoen.2020.104896

Dang, Y., Shen, S., Wang, Y., Qu, X., Huang, S., Dong, Q., et al. (2018). Hole Extraction Enhancement for Efficient Polymer Solar Cells with Boronic Acid Functionalized Carbon Nanotubes Doped Hole Transport Layers. *ACS Sustain. Chem. Eng.* 6, 5122–5131. doi:10.1021/acssuschemeng.7b04791

Delacou, C., Jeon, I., Seo, S., Nakagawa, T., Kauppinen, E. I., Maruyama, S., et al. (2017). Indium Tin Oxide-Free Small Molecule Organic Solar Cells Using Single-Walled Carbon Nanotube Electrodes. *ECS J. Solid State. Sci. Technol.* 6, M3181–M3184. doi:10.1149/2.0311706jss

Dlamini, M. W., Hamed, M. S. G., Mbuyise, X. G., and Mola, G. T. (2020). Improved Energy Harvesting Using Well-Aligned ZnS Nanoparticles in Bulk-Heterojunction Organic Solar Cell. *J. Mater. Sci. Mater. Electron.* 31, 9415–9422. doi:10.1007/s10854-020-03481-w

Du, J., Zhang, D., Wang, X., Jin, H., Zhang, W., Tong, B., et al. (2021). Extremely Efficient Flexible Organic Solar Cells with a Graphene Transparent Anode: Dependence on Number of Layers and Doping of Graphene. *Carbon* 171, 350–358. doi:10.1016/j.carbon.2020.08.038

Duan, L., and Uddin, A. (2020). Progress in Stability of Organic Solar Cells. *Adv. Sci.* 7, 1903259–1903297. doi:10.1002/advs.201903259

Fan, Q., Zhang, Q., Zhou, W., Yang, F., Zhang, N., Xiao, S., et al. (2017). Highly Conductive and Transparent Carbon Nanotube-Based Electrodes for Ultrathin and Stretchable Organic Solar Cells. *Chin. Phys. B.* 26, 028801–028807. doi:10.1088/1674-1056/26/2/028801

Fraga Domínguez, I., Distler, A., and Lüer, L. (2017). Stability of Organic Solar Cells: The Influence of Nanostructured Carbon Materials. *Adv. Energ. Mater.* 7, 1601320. doi:10.1002/aenm.201601320

Frankenstein, H., Leng, C. Z., Losego, M. D., and Frey, G. L. (2019). Atomic Layer Deposition of ZnO Electron Transporting Layers Directly onto the Active Layer of Organic Solar Cells. *Org. Electron.* 64, 37–46. doi:10.1016/j.orgel.2018.10.002

Gao, H., Meng, J., Sun, J., and Deng, J. (2020). Enhanced Performance of Polymer Solar Cells Based on P3HT:PCBM via Incorporating Au Nanoparticles Prepared by the Micellar Method. *J. Mater. Sci. Mater. Electron.* 31, 10760–10767. doi:10.1007/s10854-020-03626-x

Ghosekar, I. C., and Patil, G. C. (2021). Review on Performance Analysis of P3HT: PCBM-Based Bulk Heterojunction Organic Solar Cells. *Semicond. Sci. Technol.* 36, 045005. doi:10.1088/1361-6641/abe21b

Ghosekar, I. C., and Patil, G. C. (2019). Thermal Stability Analysis of Buffered Layer P3HT/P3HT:PCBM Organic Solar Cells. *IET Optoelectronics* 13, 240–246. doi:10.1049/iet-opt.2018.5173

Gusain, A., Faria, R. M., and Miranda, P. B. (2019). Polymer Solar Cells-Interfacial Processes Related to Performance Issues. *Front. Chem.* 7, 61–85. doi:10.3389/fchem.2019.00061

Hadi, A., Hekmatshoar, M. H., Abbasi, F., and Agbolaghi, S. (2020). Nanostructures of Chemically Modified Multi-Walled Carbon Nanotubes and Poly(3-hexylthiophene) to Improve Photophysic/Photovoltaic Features. *Carbon Lett.* 31, 107–115. doi:10.1007/s42823-020-00155-9

Hatton, R. A., Miller, A. J., and Silva, S. R. P. (2008). Carbon Nanotubes: A Multi-Functional Material for Organic Optoelectronics. *J. Mater. Chem.* 18, 1183–1192. doi:10.1039/b713527k

Hayat, M. B., Ali, D., Monyake, K. C., Alagha, L., and Ahmed, N. (2019). Solar Energy-A Look into Power Generation, Challenges, and a Solar-Powered Future. *Int. J. Energ. Res.* 43, 1049–1067. doi:10.1002/er.4252

Hilal, M., and Han, J. I. (2019). Enhancing the Photovoltaic Characteristics of Organic Solar Cells by Introducing Highly Conductive Graphene as a Conductive Platform for a PEDOT:PSS Anode Interfacial Layer. *J. Mater. Sci. Mater. Electron.* 30, 6187–6200. doi:10.1007/s10854-019-00921-0

Hou, J., Inganäs, O., Friend, R. H., and Gao, F. (2018). Organic Solar Cells Based on Non-Fullerene Acceptors. *Nat. Mater.* 17, 119–128. doi:10.1038/nmat5063

Hu, T., Li, L., Xiao, S., Yuan, K., Yang, H., Chen, L., et al. (2016). *In Situ* implanting Carbon Nanotube-Gold Nanoparticles into ZnO as Efficient Nanohybrid Cathode Buffer Layer for Polymer Solar Cells. *Org. Electron.* 38, 350–356. doi:10.1016/j.orgel.2016.09.015

Hu, Z., Wang, J., Ma, X., Gao, J., Xu, C., Yang, K., et al. (2020). A Critical Review on Semitransparent Organic Solar Cells. *Nano Energy* 78, 105376–105395. doi:10.1016/j.nanoen.2020.105376

Huang, X., Yu, H., Shi, S., and Huang, C. (2019). Improving the Performance of Inverted Polymer Solar Cells by the Efficiently Doping and Modification of Electron Transport Layer-ZnO. *Org. Electron.* 65, 311–320. doi:10.1016/j.orgel.2018.11.030

Jeon, I., Chiba, T., Delacou, C., Guo, Y., Kaskela, A., Reynaud, O., et al. (2015). Single-Walled Carbon Nanotube Film as Electrode in Indium-Free Planar Heterojunction Perovskite Solar Cells: Investigation of Electron-Blocking Layers and Dopants. *Nano Lett.* 15, 6665–6671. doi:10.1021/acs.nanolett.5b02490

Jeon, I., Delacou, C., Okada, H., Morse, G. E., Han, T.-H., Sato, Y., et al. (2018a). Polymeric Acid-Doped Transparent Carbon Nanotube Electrodes for Organic Solar Cells with the Longest Doping Durability. *J. Mater. Chem. A.* 6, 14553–14559. doi:10.1039/c8ta03383h

Jeon, I., Matsuo, Y., and Maruyama, S. (2018b). Single-Walled Carbon Nanotubes in Solar Cells. *Top. Curr. Chem. (Z)* 376, 4–31. doi:10.1007/s41061-017-0181-0

Jeon, I., Xiang, R., Shawky, A., Matsuo, Y., and Maruyama, S. (2018c). Single-Walled Carbon Nanotubes in Emerging Solar Cells: Synthesis and Electrode

Applications. *Adv. Energ. Mater.* 9, 1801312–1801338. doi:10.1002/aenm.201801312

Jeon, I., Yoon, J., Ahn, N., Atwa, M., Delacou, C., Anisimov, A., et al. (2017). Carbon Nanotubes Versus Graphene as Flexible Transparent Electrodes in Inverted Perovskite Solar Cells. *J. Phys. Chem. Lett.* 8, 5395–5401. doi:10.1021/acs.jpclett.7b02229

Jeon, Y.-J., Yun, J.-M., Kang, M., Lee, S., Jung, Y.-S., Hwang, K., et al. (2018). 2D/2D Vanadyl Phosphate (VP) on Reduced Graphene Oxide as a Hole Transporting Layer for Efficient Organic Solar Cells. *Org. Electron.* 59, 92–98. doi:10.1016/j.orgel.2018.03.021

Jeong, G., Jung, S., Choi, Y., Lee, J., Seo, J., Kim, D. S., et al. (2018). A Highly Robust and Stable Graphene-Encapsulated Cu-Grid Hybrid Transparent Electrode Demonstrating superior Performance in Organic Solar Cells. *J. Mater. Chem. A.* 6, 24805–24813. doi:10.1039/c8ta09868a

Kadem, B. Y., Kadhim, R. G., and Banimuslem, H. (2018). Efficient P3HT: SWCNTs Hybrids as Hole Transport Layer in P3HT:PCBM Organic Solar Cells. *J. Mater. Sci. Mater. Electron.* 29, 9418–9426. doi:10.1007/s10854-018-8974-7

Kang, Q., Zheng, Z., Zu, Y., Liao, Q., Bi, P., Zhang, S., et al. (2021). n-Doped Inorganic Molecular Clusters as a New Type of Hole Transport Material for Efficient Organic Solar Cells. *Joule* 5, 646–658. doi:10.1016/j.joule.2021.01.011

Keru, G., Ndungu, P. G., and Nyamori, V. O. (2014). A Review on Carbon Nanotube/Polymer Composites for Organic Solar Cells. *Int. J. Energ. Res.* 38, 1635–1653. doi:10.1002/er.3194

Keyvani-Someh, E., Hennighausen, Z., Lee, W., Igwe, R. C. K., Kramdi, M. E., Kar, S., et al. (2017). Organic Photovoltaics with Stacked Graphene Anodes. *ACS Appl. Energ. Mater.* 1, 17–21. doi:10.1021/acsaem.7b00020

Khan, D., Ali, Z., Asif, D., Kumar Panjwani, M., and Khan, I. (2021). Incorporation of Carbon Nanotubes in Photoactive Layer of Organic Solar Cells. *Ain Shams Eng. J.* 12, 897–900. doi:10.1016/j.asej.2020.06.002

Khan, D., Tan, Z. A., Khan, I., and Panjwani, M. K. (2018). A Review of the Challenges and Possibilities of Using Carbon Nanotubes in Organic Solar Cells. *Sci. Adv. Mater.* 10, 747–760. doi:10.1166/sam.2018.3260

Khanh, T. S. T., Nam, N. P. H., and Dinh, N. N. (2020). Facile Preparation, Characterization of Flexible Organic Solar Cells Using P3HT-MWCNTS Composite Photoactive Layer. *MSCE* 08, 1–10. doi:10.4236/msce.2020.810001

Kumar, S., Kim, H., Kim, D.-K., and Iyer, S. S. K. (2020). Spin and Doctor-Blade Coated PEDOT:PSS Back Electrodes in Inverted Organic Solar Cells. *Solar Energy* 204, 64–70. doi:10.1016/j.solener.2020.04.071

Lee, K.-T., Park, D., Baac, H., and Han, S. (2018). Graphene- and Carbon-Nanotube-Based Transparent Electrodes for Semitransparent Solar Cells. *Materials* 11, 1503–1522. doi:10.3390/ma11091503

Lee, M.-H. (2019). Performance and Matching Band Structure Analysis of Tandem Organic Solar Cells Using Machine Learning Approaches. *Energy Technol.* 8, 1900974. doi:10.1002/ente.201900974

Lee, S.-H., Ko, S.-J., Eom, S. H., Kim, H., Kim, D. W., Lee, C., et al. (2020). Composite Interlayer Consisting of Alcohol-Soluble Polyfluorene and Carbon Nanotubes for Efficient Polymer Solar Cells. *ACS Appl. Mater. Inter.* 12, 14244–14253. doi:10.1021/acsami.9b22933

Lee, S. L., Kim, H. S., Ha, J. W., Park, H. J., and Hwang, D. H. (2019). High Open-Circuit Voltage Organic Photovoltaics Fabricated Using an Alkylidene Fluorene Derivative as a Non-Fullerene Acceptor. *Bull. Korean Chem. Soc.* 41, 143–149. doi:10.1002/bkcs.11937

Li, C., Wang, G., Gao, Y., Wang, C., Wen, S., Li, H., et al. (2019). Highly Efficient Polymer Solar Cells Based on Low-Temperature Processed ZnO: Application of a Bifunctional Au@CNTs Nanocomposite. *J. Mater. Chem. C.* 7, 2676–2685. doi:10.1039/c8tc05653f

Li, J., Qin, J., Liu, X., Ren, M., Tong, J., Zheng, N., et al. (2020). Enhanced Organic Photovoltaic Performance through Promoting Crystallinity of Photoactive Layer and Conductivity of Hole-Transporting Layer by V_2O_5 Doped PEDOT:PSS Hole-Transporting Layers. *Solar Energy* 211, 1102–1109. doi:10.1016/j.solener.2020.10.036

Li, X., Du, X., Zhao, J., Lin, H., Zheng, C., and Tao, S. (2020a). Layer-by-Layer Solution Processing Method for Organic Solar Cells. *Sol. RRL* 5, 2000592–2000616. doi:10.1002/solr.202000592

Li, X., Xia, R., Yan, K., Yip, H.-L., Chen, H., and Li, C.-Z. (2020b). Multifunctional Semitransparent Organic Solar Cells with Excellent Infrared Photon Rejection. *Chin. Chem. Lett.* 31, 1608–1611. doi:10.1016/j.cclet.2019.08.046

Lian, H., Jun, N., Bolag, A., Hexig, A., Gerile, N., Tegus, O., et al. (2019). Optimization of PEDOT:PSS Hole Transport Layer toward the Organic Solar Cells with High Fill Factor. *Solid State Phenomena* 288, 113–118. doi:10.4028/www.scientific.net/ssp.288.113

Liang, Z., Tong, J., Li, H., Wang, Y., Wang, N., Li, J., et al. (2019). The Comprehensive Utilization of the Synergistic Effect of Fullerene and Non-Fullerene Acceptors to Achieve Highly Efficient Polymer Solar Cells. *J. Mater. Chem. A.* 7, 15841–15850. doi:10.1039/c9ta04286e

Lim, E. L., Yap, C. C., Hj Jumali, M. H., and Khairulaman, F. L. (2018). Solution-Dispersed Copper Iodide Anode Buffer Layer Gives P3HT:PCBM-Based Organic Solar Cells an Efficiency Boost. *J. Mater. Sci. Mater. Electron.* 30, 2726–2731. doi:10.1007/s10854-018-0548-1

Lin, Y., Zhang, S., Guan, L., and Tao, J. (2020). Prospect of Ni-Related Metal Oxides for High-Performance Supercapacitor Electrodes. *J. Mater. Sci.* 56, 1897–1918. doi:10.1007/s10853-020-05408-6

Lin, Z., Jiang, C., Zhu, C., and Zhang, J. (2013). Development of Inverted Organic Solar Cells with TiO_2 Interface Layer by Using Low-Temperature Atomic Layer Deposition. *ACS Appl. Mater. Inter.* 5, 713–718. doi:10.1021/am302252p

Liu, B., Wang, Y., Chen, P., Zhang, X., Sun, H., Tang, Y., et al. (2019). Boosting Efficiency and Stability of Organic Solar Cells Using Ultralow-Cost BiOCl Nanoplates as Hole Transporting Layers. *ACS Appl. Mater. Inter.* 11, 33505–33514. doi:10.1021/acsami.9b12583

Liu, D., Wang, T., Chang, Z., Zheng, N., Xie, Z., and Liu, Y. (2021). Fused or Unfused? Two-Dimensional Non-Fullerene Acceptors for Efficient Organic Solar Cells. *J. Mater. Chem. A.* 9, 2319–2324. doi:10.1039/d0ta10901k

Lu, S., Sun, Y., Ren, K., Liu, K., Wang, Z., and Qu, S. (2017). Recent Development in ITO-Free Flexible Polymer Solar Cells. *Polymers* 10, 5–34. doi:10.3390/polym10010005

Mahakul, P. C., Sa, K., Subramanyam, B. V. R. S., and Mahanandia, P. (2019). Mesoscopic Investigation of the Effect of MWCNT/rGO Network on the Performance of P3HT:PC60BM Solar Cells. *Mater. Chem. Phys.* 226, 113–117. doi:10.1016/j.matchemphys.2019.01.012

Matsuo, Y. (2021). Creation of Highly Efficient and Durable Organic and Perovskite Solar Cells Using Nanocarbon Materials. *Bull. Chem. Soc. Jpn.* 94, 1080–1089. doi:10.1246/bcsj.20200404

Mbuyise, X. G., Arbab, E. A. A., Kaviyarasu, K., Pellicane, G., Maaza, M., and Mola, G. T. (2017). Zinc Oxide Doped Single Wall Carbon Nanotubes in Hole Transport Buffer Layer. *J. Alloys Compd.* 706, 344–350. doi:10.1016/j.jallcom.2017.02.249

Milanovich, M., Sarkar, T., Popowski, Y., Low, J. Z., Campos, L. M., Kenig, S., et al. (2020). Enhancing P3HT/PCBM Blend Stability by Thermal Crosslinking Using Poly(3-hexylthiophene)-S,S-dioxide. *J. Mater. Chem. C.* 8, 7698–7707. doi:10.1039/d0tc00109k

Mo, L., Ran, J., Yang, L., Fang, Y., Zhai, Q., and Li, L. (2016). Flexible Transparent Conductive Films Combining Flexographic Printed Silver Grids with CNT Coating. *Nanotechnology* 27, 065202–065210. doi:10.1088/0957-4484/27/6/065202

Mohamad Noh, M. F., Teh, C. H., Daik, R., Lim, E. L., Yap, C. C., Ibrahim, M. A., et al. (2018). The Architecture of the Electron Transport Layer for a Perovskite Solar Cell. *J. Mater. Chem. C.* 6, 682–712. doi:10.1039/c7tc04649a

Mohammad, T., Bharti, V., Kumar, V., Mudgal, S., and Dutta, V. (2019). Spray Coated Europium Doped PEDOT:PSS Anode Buffer Layer for Organic Solar Cell: The Role of Electric Field during Deposition. *Org. Electron.* 66, 242–248. doi:10.1016/j.orgel.2018.12.034

Muchuweni, E., Martincigh, B. S., and Nyamori, V. O. (2020a). Organic Solar Cells: Current Perspectives on Graphene-Based Materials for Electrodes, Electron Acceptors and Interfacial Layers. *Int. J. Energ. Res.* 45, 6518–6549. doi:10.1002/er.6301

Muchuweni, E., Martincigh, B. S., and Nyamori, V. O. (2020b). Recent Advances in Graphene-Based Materials for Dye-Sensitized Solar Cell Fabrication. *RSC Adv.* 10, 44453–44469. doi:10.1039/d0ra08851j

Muchuweni, E., Sathiaraj, T. S., and Nyakotyo, H. (2016a). Effect of Gallium Doping on the Structural, Optical and Electrical Properties of Zinc Oxide Thin Films Prepared by Spray Pyrolysis. *Ceramics Int.* 42, 10066–10070. doi:10.1016/j.ceramint.2016.03.110

Muchuweni, E., Sathiaraj, T. S., and Nyakotyo, H. (2017a). Hydrothermal Synthesis of ZnO Nanowires on Rf Sputtered Ga and Al Co-Doped ZnO Thin Films for

Solar Cell Application. *J. Alloys Compd.* 721, 45–54. doi:10.1016/j.jallcom.2017.05.317

Muchuweni, E., Sathiaraj, T. S., and Nyakotyo, H. (2016b). Low Temperature Synthesis of Radio Frequency Magnetron Sputtered Gallium and Aluminium Co-Doped Zinc Oxide Thin Films for Transparent Electrode Fabrication. *Appl. Surf. Sci.* 390, 570–577. doi:10.1016/j.apsusc.2016.08.081

Muchuweni, E., Sathiaraj, T. S., and Nyakotyo, H. (2017b). Synthesis and Characterization of Zinc Oxide Thin Films for Optoelectronic Applications. *Heliyon* 3, e00285. doi:10.1016/j.heliyon.2017.e00285

Mugadza, K., Nyamori, V. O., Mola, G. T., Simoyi, R. H., and Ndungu, P. G. (2017). Low Temperature Synthesis of Multiwalled Carbon Nanotubes and Incorporation into an Organic Solar Cell. *J. Exp. Nanoscience* 12, 363–383. doi:10.1080/17458080.2017.1357842

Mutlu, A., Can, M., and Tozlu, C. (2019). Performance Improvement of Organic Solar Cell via Incorporation of Donor Type Self-Assembled Interfacial Monolayer. *Thin Solid Films* 685, 88–96. doi:10.1016/j.tsf.2019.05.064

Nan, X., Ma, J., Liu, J., Zhao, J., and Zhu, W. (2016). Effect of Surfactant Functionalization of Multi-Walled Carbon Nanotubes on Mechanical, Electrical and Thermal Properties of Epoxy Nanocomposites. *Fibers Polym.* 17, 1866–1874. doi:10.1007/s12221-016-6388-9

Nguyen, T. P., Nguyen, D. L. T., Nguyen, V. H., Le, T. H., Vo, D. N., Ly, Q. V., et al. (2019). Recent Progress in Carbon-Based Buffer Layers for Polymer Solar Cells. *Polymers* 11, 1858–1876. doi:10.3390/polym11111858

Obaidullah, M., Esat, V., and Sabah, C. (2018). Single- and Multi-Walled Carbon Nanotubes for Solar Cell Applications. *Int. J. Mod. Phys. B.* 32, 1830007–1830032. doi:10.1142/s0217979218300074

Oseni, S. O., Kaviyarasu, K., Maaza, M., Sharma, G., Pellicane, G., and Mola, G. T. (2018). ZnO:CNT Assisted Charge Transport in PTB7:PCBM Blend Organic Solar Cell. *J. Alloys Compd.* 748, 216–222. doi:10.1016/j.jallcom.2018.03.141

Oseni, S. O., and Mola, G. T. (2017). Properties of Functional Layers in Inverted Thin Film Organic Solar Cells. *Solar Energ. Mater. Solar Cell* 160, 241–256. doi:10.1016/j.solmat.2016.10.036

Ouyang, J. (2019). Applications of Carbon Nanotubes and Graphene for Third-Generation Solar Cells and Fuel Cells. *Nano Mater. Sci.* 1, 77–90. doi:10.1016/j.nanoms.2019.03.004

Oyeshola, H. O., Adisa, M. A., Adejumo, B. K., Babalola, K. K., Agboluaje, B. A., Adedokun, O., et al. (2020). Effect of Low Temperature Synthesis of Carbon Nanotube Nanocomposite on the Photovoltaic Performance of Anode Buffer Layer in Polymer Solar Cells. *IOP Conf. Ser. Mater. Sci. Eng.* 805, 012026. doi:10.1088/1757-899x/805/1/012026

Pali, L. S., Jindal, R., and Garg, A. (2018). Screen Printed PEDOT:PSS Films as Transparent Electrode and its Application in Organic Solar Cells on Opaque Substrates. *J. Mater. Sci. Mater. Electron.* 29, 11030–11038. doi:10.1007/s10854-018-9185-y

Pan, F., Bai, S., Wei, X., Li, Y., Tang, D., Chen, X., et al. (2020). 3D Surfactant-Dispersed Graphenes as Cathode Interfacial Materials for Organic Solar Cells. *Sci. China Mater.* 64, 277–287. doi:10.1007/s40843-020-1401-2

Patil, J. J., Chae, W. H., Trebach, A., Carter, K. J., Lee, E., Sannicolo, T., et al. (2021). Failing Forward: Stability of Transparent Electrodes Based on Metal Nanowire Networks. *Adv. Mater.* 33, 2004356. doi:10.1002/adma.202004356

Paul, S., Rajbongshi, B., Bora, B., Nair, R. G., and Samdarshi, S. K. (2017). Organic Photovoltaic Cells Using MWCNTs. *New Carbon Mater.* 32, 27–34. doi:10.1016/s1872-5805(17)60104-5

PV-Magazine (2020). An Organic Solar Cell with 25% Efficiency [Online]. Availbale at: https://www.pv-magazine.com/2020/03/24/an-organic-solar-cell-with-25-efficiency/ (Accessed September, 2020).

Qin, J., Lan, L., Chen, S., Huang, F., Shi, H., Chen, W., et al. (2020). Recent Progress in Flexible and Stretchable Organic Solar Cells. *Adv. Funct. Mater.* 30, 2002529–2002550. doi:10.1002/adfm.202002529

Rabaia, M. K. H., Abdelkareem, M. A., Sayed, E. T., Elsaid, K., Chae, K.-J., Wilberforce, T., et al. (2021). Environmental Impacts of Solar Energy Systems: A Review. *Sci. Total Environ.* 754, 141989–142007. doi:10.1016/j.scitotenv.2020.141989

Rafique, S., Abdullah, S. M., Sulaiman, K., and Iwamoto, M. (2018). Fundamentals of Bulk Heterojunction Organic Solar Cells: An Overview of Stability/Degradation Issues and Strategies for Improvement. *Renew. Sustain. Energ. Rev.* 84, 43–53. doi:10.1016/j.rser.2017.12.008

Rafique, S., Roslan, N. A., Abdullah, S. M., Li, L., Supangat, A., Jilani, A., et al. (2019). UV- Ozone Treated Graphene Oxide/PEDOT:PSS Bilayer as a Novel Hole Transport Layer in Highly Efficient and Stable Organic Solar Cells. *Org. Electron.* 66, 32–42. doi:10.1016/j.orgel.2018.12.005

Ramasamy, M. S., Ryu, K. Y., Lim, J. W., Bibi, A., Kwon, H., Lee, J.-E., et al. (2019). Solution-Processed PEDOT:PSS/MoS_2 Nanocomposites as Efficient Hole-Transporting Layers for Organic Solar Cells. *Nanomaterials* 9, 1328–1339. doi:10.3390/nano9091328

Rathore, P., Negi, C. M. S., Yadav, A., Verma, A. S., and Gupta, S. K. (2018). Influence of MWCNT Doping on Performance of Polymer Bulk Heterojunction Based Devices. *Optik* 160, 131–137. doi:10.1016/j.ijleo.2018.01.092

Rego de Vasconcelos, B., and Lavoie, J.-M. (2019). Recent Advances in Power-To-X Technology for the Production of Fuels and Chemicals. *Front. Chem.* 7, 392–415. doi:10.3389/fchem.2019.00392

Ricciardulli, A. G., Yang, S., Feng, X., and Blom, P. W. M. (2017). Solution-processable High-Quality Graphene for Organic Solar Cells. *ACS Appl. Mater. Inter.* 9, 25412–25417. doi:10.1021/acsami.7b09702

Riede, M., Spoltore, D., and Leo, K. (2021). Organic solar cells - Path to commercial success. *Adv. Energy Mater.* 11, 2002653–2002662. doi:10.1002/aenm.202002653

Salim, M. B., Nekovei, R., and Jeyakumar, R. (2020). Organic Tandem Solar Cells with 18.6% Efficiency. *Sol. Energ.* 198, 160–166. doi:10.1016/j.solener.2020.01.042

Shah, M. N., Shah, M. F., Ma, J., Shah, M. I., Yang, Y., and Pan, X. (2020). Synthesis of Small Molecule Dye Additive for Efficient and DIO-Free Ternary Organic Solar Cells. *J. Mater. Sci.* 56, 2528–2538. doi:10.1007/s10853-020-05390-z

Shen, J.-J. (2021). Recently-Explored Top Electrode Materials for Transparent Organic Solar Cells. *Synth. Met.* 271, 116582–116598. doi:10.1016/j.synthmet.2020.116582

Shin, D. H., Jang, C. W., Ko, J. S., and Choi, S.-H. (2021). Enhancement of Efficiency and Stability in Organic Solar Cells by Employing MoS_2 Transport Layer, Graphene Electrode, a Quantum Dots-Added Active Layer. *Appl. Surf. Sci.* 538, 148155–148160. doi:10.1016/j.apsusc.2020.148155

Shoyiga, H. O., Martincigh, B. S., and Nyamori, V. O. (2020). Hydrothermal Synthesis of Reduced Graphene Oxide-Anatase Titania Nanocomposites for Dual Application in Organic Solar Cells. *Int. J. Energ. Res.* 45, 7293–7314. doi:10.1002/er.6313

Singh, A., Gupta, S. K., and Garg, A. (2017). Inkjet Printing of NiO Films and Integration as Hole Transporting Layers in Polymer Solar Cells. *Sci. Rep.* 7, 1775–1786. doi:10.1038/s41598-017-01897-9

Sivakumar, G., Bernardo, D. R., Marchezi, P. E., and Nogueira, A. F. (2020). Synthesis and Characterization of Vinazene End Capped Dipyrrolo[2,3-B:2′,3′-E]pyrazine-2,6(1h,5h)-Dione Small Molecules as Non-Fullerene Acceptors for Bulk Heterojunction Organic Solar Cells. *Mater. Chem. Phys.* 240, 122176–122184. doi:10.1016/j.matchemphys.2019.122176

Soh, M. F., Noh, M. F. M., Mohamed, N. A., Safaei, J., Rosli, N. N., Lim, E. L., et al. (2019). Incorporation of G-C3N4/Ag Dopant in TiO_2 as Electron Transport Layer for Organic Solar Cells. *Mater. Lett.* 253, 117–120. doi:10.1016/j.matlet.2019.06.052

Song, J., Hu, Q., Zhang, M., Zhang, Q., Zhu, L., Ali, J., et al. (2020). Bimolecular Crystal Instability and Morphology of Bulk Heterojunction Blends in Organic and Perovskite Solar Cells. *J. Mater. Chem. C.* 8, 11695–11703. doi:10.1039/d0tc02030c

Song, X., Gasparini, N., Nahid, M. M., Paleti, S. H. K., Li, C., Li, W., et al. (2019). Efficient DPP Donor and Nonfullerene Acceptor Organic Solar Cells with High Photon-to-Current Ratio and Low Energetic Loss. *Adv. Funct. Mater.* 29, 1902441–1902448. doi:10.1002/adfm.201902441

Sorkhishams, N., Massoumi, B., Saraei, M., and Agbolaghi, S. (2019). Electrode Buffer Layers via Networks of Polythiophene/Polyaniline Bottlebrushes and Carbon Nanotubes in Organic Solar Cells. *J. Mater. Sci. Mater. Electron.* 30, 21117–21125. doi:10.1007/s10854-019-02482-8

Subhan, F. E., Khan, A. D., Khan, A. D., Ullah, N., Imran, M., and Noman, M. (2020). Optical Optimization of Double-Side-Textured Monolithic Perovskite-Silicon Tandem Solar Cells for Improved Light Management. *RSC Adv.* 10, 26631–26638. doi:10.1039/d0ra04634e

Subramanyam, B. V. R. S., Mahakul, P. C., Sa, K., Raiguru, J., Alam, I., Das, S., et al. (2019). Improved Stability and Performance of Organic Photovoltaic Cells by

Application of Carbon Nanostructures and PEDOT:PSS Composites as Additional Transparent Electrodes. *Solar Energy* 186, 146–155. doi:10.1016/j.solener.2019.04.097

Subramanyam, B. V. R. S., Mahakul, P. C., Sa, K., Raiguru, J., and Mahanandia, P. (2020). Investigation of Improvement in Stability and Power Conversion Efficiency of Organic Solar Cells Fabricated by Incorporating Carbon Nanostructures in Device Architecture. *J. Phys. Mater.* 3, 045004–045019. doi:10.1088/2515-7639/abbf44

Sun, J., Yu, S., Zheng, Q., Cheng, S., Wang, X., Zhou, H., et al. (2016). Improved Performance of Inverted Organic Solar Cells by Using La-Doped TiO_2 Film as Electron Transport Layer. *J. Mater. Sci. Mater. Electron.* 28, 2272–2278. doi:10.1007/s10854-016-5661-4

Sun, Y., Chang, M., Meng, L., Wan, X., Gao, H., Zhang, Y., et al. (2019). Flexible Organic Photovoltaics Based on Water-Processed Silver Nanowire Electrodes. *Nat. Electron.* 2, 513–520. doi:10.1038/s41928-019-0315-1

Tasis, D., Tagmatarchis, N., Bianco, A., and Prato, M. (2006). Chemistry of Carbon Nanotubes. *Chem. Rev.* 106, 1105–1136. doi:10.1021/cr050569o

Tessema Mola, G., Mbuyise, X. G., Oseni, S. O., Dlamini, W. M., Tonui, P., Arbab, E. A. A., et al. (2018). Nanocomposite for Solar Energy Application. *Nano Hybrids and Composites* 20, 90–107. doi:10.4028/www.scientific.net/nhc.20.90

Tian, L., Xue, Q., Hu, Z., and Huang, F. (2021). Recent Advances of Interface Engineering for Non-Fullerene Organic Solar Cells. *Org. Electron.* 93, 106141–106156. doi:10.1016/j.orgel.2021.106141

Tiwari, S., Purabgola, A., and Kandasubramanian, B. (2020). Functionalised Graphene as Flexible Electrodes for Polymer Photovoltaics. *J. Alloys Compd.* 825, 153954–153969. doi:10.1016/j.jallcom.2020.153954

Upama, M. B., Elumalai, N. K., Mahmud, M. A., Wright, M., Wang, D., Xu, C., et al. (2017). Interfacial Engineering of Electron Transport Layer Using Caesium Iodide for Efficient and Stable Organic Solar Cells. *Appl. Surf. Sci.* 416, 834–844. doi:10.1016/j.apsusc.2017.04.164

Usmani, B., Ranjan, R., PrateekGupta, S., Gupta, R., Nalwa, K., et al. (2021). Inverted PTB7-Th:$PC_{71}BM$ Organic Solar Cells with 11.8% PCE via Incorporation of Gold Nanoparticles in ZnO Electron Transport Layer. *Sol. Energ.* 214, 220–230. doi:10.1016/j.solener.2020.11.071

Vercelli, B. (2021). The Role of Carbon Quantum Dots in Organic Photovoltaics: A Short Overview. *Coatings* 11, 232–265. doi:10.3390/coatings11020232

Wang, J., Xie, Z., and Yeow, J. T. W. (2020). Review-State-of-the-Art Organic Solar Cells Based on Carbon Nanotubes and Graphene. *ECS J. Solid State. Sci. Technol.* 9, 105004–105010. doi:10.1149/2162-8777/abc3cd

Wang, Y., Bao, X., Pang, B., Zhu, Q., Wang, J., Zhu, D., et al. (2018). Solution-Processed Functionalized Reduced Graphene Oxide-An Efficient Stable Electron Buffer Layer for High-Performance Solar Cells. *Carbon* 131, 31–37. doi:10.1016/j.carbon.2018.01.090

Wang, Y., Lee, J., Hou, X., Labanti, C., Yan, J., Mazzolini, E., et al. (2021). Recent Progress and Challenges toward Highly Stable Nonfullerene Acceptor-Based Organic Solar Cells. *Adv. Energ. Mater.* 11, 2003002. doi:10.1002/aenm.202003002

Wei, J., Zhang, C., Ji, G., Han, Y., Ismail, I., Li, H., et al. (2019). Roll-to-Roll Printed Stable and Thickness-Independent ZnO:PEI Composite Electron Transport Layer for Inverted Organic Solar Cells. *Solar Energy* 193, 102–110. doi:10.1016/j.solener.2019.09.037

Wu, W., Wu, H., Zhong, M., and Guo, S. (2019). Dual Role of Graphene Quantum Dots in Active Layer of Inverted Bulk Heterojunction Organic Photovoltaic Devices. *ACS Omega* 4, 16159–16165. doi:10.1021/acsomega.9b02348

Xu, H., Yuan, F., Zhou, D., Liao, X., Chen, L., and Chen, Y. (2020). Hole Transport Layers for Organic Solar Cells: Recent Progress and Prospects. *J. Mater. Chem. A.* 8, 11478–11492. doi:10.1039/d0ta03511d

Xu, X., Yu, L., and Peng, Q. (2021). Recent Advances in Wide Bandgap Polymer Donors and Their Applications in Organic Solar Cells. *Chin. J. Chem.* 39, 243–254. doi:10.1002/cjoc.202000451

Yang, M. K., and Lee, J.-K. (2020). CNT/AgNW Multilayer Electrodes on Flexible Organic Solar Cells. *Electron. Mater. Lett.* 16, 573–578. doi:10.1007/s13391-020-00248-7

Yu, L., Shearer, C., and Shapter, J. (2016). Recent Development of Carbon Nanotube Transparent Conductive Films. *Chem. Rev.* 116, 13413–13453. doi:10.1021/acs.chemrev.6b00179

Yu, Z., Feng, W., Lu, W., Li, B., Yao, H., Zeng, K., et al. (2019). MXenes with Tunable Work Functions and Their Application as Electron- and Hole-Transport Materials in Non-Fullerene Organic Solar Cells. *J. Mater. Chem. A.* 7, 11160–11169. doi:10.1039/c9ta01195a

Zhang, W., Bu, F., Shen, W., Qi, X., Yang, N., Chen, M., et al. (2020). Strongly Enhanced Efficiency of Polymer Solar Cells through Unzipped SWNT Hybridization in the Hole Transport Layer. *RSC Adv.* 10, 24847–24854. doi:10.1039/d0ra03461d

Zhang, X., Cui, M., Nian, L., Wang, P., Rong, Q., Shui, L., et al. (2020). Ionic Liquid-Modified ZnO-Based Electron Transport Layer for Inverted Organic Solar Cells. *J. Mater. Sci. Mater. Electron.* 31, 12678–12683. doi:10.1007/s10854-020-03818-5

Zhang, X., Sun, S., and Liu, X. (2019). Amino Functionalized Carbon Nanotubes as Hole Transport Layer for High Performance Polymer Solar Cells. *Inorg. Chem. Commun.* 103, 142–148. doi:10.1016/j.inoche.2019.03.008

Zhang, Y., He, X., Babu, D., Li, W., Gu, X., Shan, C., et al. (2021). Efficient Semi-Transparent Organic Solar Cells with High Color Rendering Index Enabled by Self-Assembled and Knitted AgNPs/MWCNTs Transparent Top Electrode via Solution Process. *Adv. Opt. Mater.* 9, 2002108. doi:10.1002/adom.202002108

Zhang, Y., Ng, S.-W., Lu, X., and Zheng, Z. (2020). Solution-Processed Transparent Electrodes for Emerging Thin-Film Solar Cells. *Chem. Rev.* 120, 2049–2122. doi:10.1021/acs.chemrev.9b00483

Zhang, Z., Lv, R., Jia, Y., Gan, X., Zhu, H., and Kang, F. (2018). All-Carbon Electrodes for Flexible Solar Cells. *Appl. Sci.* 8, 152–162. doi:10.3390/app8020152

Zhao, C., Wang, J., Jiao, J., Huang, L., and Tang, J. (2020). Recent Advances of Polymer Acceptors for High-Performance Organic Solar Cells. *J. Mater. Chem. C.* 8, 28–43. doi:10.1039/c9tc05567c

Zhao, Z., and Alford, T. L. (2018). The Effect of Hole Transfer Layers and Anodes on Indium-Free TiO_2/Ag/TiO_2 Electrode and ITO Electrode Based P3HT:PCBM Organic Solar Cells. *Solar Energ. Mater. Solar Cell* 176, 324–330. doi:10.1016/j.solmat.2017.10.017

Zheng, Y., Yu, J., Tang, J., Yang, F., Wang, C., Wei, B., et al. (2019). Series of Polar Alcohol-Additives Assisted Improvement in the PEDOT:PSS Film Property and Bulk-Heterojunction Organic Solar Cell Performance. *J. Phys. D: Appl. Phys.* 52, 255104–255113. doi:10.1088/1361-6463/ab04dc

Zhong, F., Yang, M., Ding, M., and Jia, C. (2020). Organic Electroactive Molecule-Based Electrolytes for Redox Flow Batteries: Status and Challenges of Molecular Design. *Front. Chem.* 8, 451–464. doi:10.3389/fchem.2020.00451

Conflict of Interest: The authors declare that the research was conducted in the absence of any commercial or financial relationships that could be construed as a potential conflict of interest.

Publisher's Note: All claims expressed in this article are solely those of the authors and do not necessarily represent those of their affiliated organizations, or those of the publisher, the editors and the reviewers. Any product that may be evaluated in this article, or claim that may be made by its manufacturer, is not guaranteed or endorsed by the publisher.

frontiers in Chemistry

ORIGINAL RESEARCH
published: 04 February 2022
doi: 10.3389/fchem.2021.805654

Designing New Material Based on Functionalized Multi-Walled Carbon Nanotubes and $Cu(OH)_2$–Cu_2O/Polypyrrole Catalyst for Ethanol Oxidation in Alkaline Medium

*Anas El Attar, Sanaa Chemchoub, Mamadou Diallo Kalan, Larbi Oularbi and Mama El Rhazi **

Laboratory of Materials, Membranes, and Environment, Faculty of Science and Technology, University Hassan II of Casablanca, Mohammedia, Morocco

OPEN ACCESS

Edited by:
James Darkwa, Botswana Institute for Technology Research and Innovation (BITRI), Botswana

Reviewed by:
Ali Ehsani, University of Qom, Iran
Lokesh Koodlur Sannegowda, Vijayanagara Sri Krishnadevaraya University, India

***Correspondence:**
Mama El Rhazi
mama.elrhazi@fstm.ac.ma

Specialty section:
This article was submitted to Physical Chemistry and Chemical Physics, a section of the journal Frontiers in Chemistry

Received: *30 October 2021*
Accepted: *28 December 2021*
Published: *04 February 2022*

Citation:
El Attar A, Chemchoub S, Diallo Kalan M, Oularbi L and El Rhazi M (2022) Designing New Material Based on Functionalized Multi-Walled Carbon Nanotubes and $Cu(OH)_2$–Cu_2O/Polypyrrole Catalyst for Ethanol Oxidation in Alkaline Medium. Front. Chem. 9:805654. doi: 10.3389/fchem.2021.805654

In this work, copper(II) hydroxide ($Cu(OH)_2$) and copper oxide (Cu_2O) nanostructures are deposited on functionalized multi-walled carbon nanotubes/polypyrrole to report an efficient electrocatalyst for ethanol oxidation in alkaline medium. In the first step, the deposition of functionalized multi-walled nanotubes of carbon (F-MWCNTs) on the electrode surface was carried out using drop casting mode followed by the electrodeposition of polypyrrole (PPy) and copper nanoparticles (Cu-Nps) using galvanostatic mode. Scanning electron microscopy (SEM) and X-ray diffraction (XRD) were performed in order to study the morphology and the structure of the elaborated catalysts. Electrochemical characterization conducted by cyclic voltammetry (CV) and electrochemical impedance spectroscopy (EIS) revealed that the introduction of functionalized multi-walled carbon nanotubes enhances the electric properties of the nanocomposites and offers a large active surface area. The prepared electrocatalyst was then tested in a solution of 0.1 M NaOH containing 0.2 M of ethanol showing high performance (7 mA cm^{-2} at 0.85 V vs Ag/AgCl) and good stability (over 1800 s) toward ethanol oxidation.

Keywords: functionalized multi-walled carbon nanotube, carbon paste electrode, copper hydroxide–copper oxide, polypyrrole, ethanol oxidation

INTRODUCTION

Developing a new and cost-effective source of energy is key to keeping up with the growing global demand for energy (El-Houari et al., 2020; Rahman and Velayutham, 2020; Ivanovski et al., 2021). In response to the rising energy demand, different strategies have been adopted. Among them, fuel cells have been considered a promising candidate. Indeed, direct ethanol fuel cells (DEFCs) appear to be a good alternative and offer several benefits compared to the other types of fuel cells (Guo et al., 2018). Their excellent volumetric energy density (8 kWh kg^{-1}) (Eisa et al., 2020), ease of transportation and storage (Fontes et al., 2019; Souza et al., 2020), low toxicity (Mondal et al., 2019), and large availability of ethanol have made them extensively studied as potential tools for portable mobile devices and in automobile fields (Silva et al., 2019; Xaba et al., 2019). However, two crucial issues hinder the practical uses of DEFCs: i) the sluggish kinetic of ethanol oxidation reaction (EOR) and the poisoning of catalyst surface caused by the formation of intermediate species during ethanol oxidation

(Cermenek et al., 2019; Choudhary and Pramanik, 2020a; Choudhary and Pramanik, 2020b) and ii) the exorbitant price of catalysts (Liang et al., 2021). The design of new materials with high performance and low cost still remains a serious challenge for researchers. In this context, electrocatalysts based on carbon nanomaterials/conductive polymers as a support for metal nanoparticles have been studied (Fard et al., 2017; Ghosh et al., 2017; Boulaghi et al., 2018; Mozafari and Parsa, 2020a), which were synthetized as an appropriate support for ethanol oxidation in acid medium based on polyaniline and carbon nanotube (PANI/CNT) for platinum (Pt) particles. It has been proved that the combination of PANI and CNT increases the active surface area of the catalyst and ensures a good dispersion of platinum nanoparticles onto the polymer (De et al., 2017). In the same way, a facile synthesis of polyaniline–multi-walled carbon nanotubes–tin oxide on the titanium (Ti) mesh substrate was reported to provide a support for the palladium (Pd) catalyst (Mozafari and Parsa, 2020a). The high performance and good stability of the catalyst were directly related to the presence of MWCNT and SnO_2 inside the polymer. Recently, the polypyrrole/MWCNT nanocomposite–modified glassy carbon electrode was also used as a support for PdCo porous nanostructures (PNSs) leading to a better catalytic activity and high tolerance to poisoning of the surface by the intermediate species (Fard et al., 2017). It seems that the presence of carbon nanomaterials as a support for conductive polymers offers a high active surface area, while the presence of an amino-group in the backbone of conducting polymers ensures a good deposition of metal particles and facilitates accessibility to electrocatalytic sites of ethanol (Chemchoub et al., 2020; El Attar et al., 2020). However, very few studies have been devoted to a non-noble metal combined with carbon nanostructures and polymers. In our previous study, we studied the effect of the activation of the surface of Cu_2O-NDs/PPy/CPE and Cu_2O/PPy/CPE electrocatalysts on the performance of EOR. It has been demonstrated that the regeneration of copper in acidic medium plays an important role in the morphology of the material (copper oxide) varying from the octahedral particles to the dendritic one. This change in the morphology leads to an increase of the performance of the catalyst in terms of stability and durability toward ethanol oxidation (El Attar et al., 2020; El Attar et al., 2021). In this study, our goal is to explore the effect of F-MWCNTs on deposition of copper hydroxide–copper oxide nanoparticles. To the best of our knowledge, no studies have been devoted to the effect of deposition of copper hydroxide–copper oxide nanodendrites on PPy/F-MWCNTs for ethanol oxidation. In this context, we report for the first time a facile synthesis of the $Cu(OH)_2$–Cu_2O/PPy/F-MWCNT–modified carbon paste electrode (CPE) for ethanol oxidation. Two steps are required for the elaboration of the catalyst: The first step consists of the deposition of functionalized multi-walled carbon nanotubes on the surface of carbon paste electrode followed by polymerization of pyrrole by galvanostatic mode. Copper hydroxide–copper oxide is then electrodeposited on PPy/F-MWCNTs in the second step using galvanostatic mode followed by polarization of the electrode in alkaline solution. After carefully examining the morphology and the electrochemical properties of the electrocatalyst, nanocomposites are then applied for ethanol oxidation. The results of experimental studies indicated that $Cu(OH)_2$–Cu_2O dispersed onto the PPy/F-MWCNT/CPE catalyst shows excellent catalytic activity, high electrical conductivity, and long stability toward ethanol oxidation.

MATERIALS AND METHODS

Chemicals

Pyrrole (99%) was obtained from ACROS Organics and was purified by distillation prior to usage. Lithium perchlorate ($LiClO_4$; purum p.a. 98%), potassium ferri/ferrocyanide ($K_3Fe(CN)_6/K_4Fe(CN)_6{\cdot}3H_2O$; ACS reagent ≥99%), MWCNTs with an outside diameter of 6–13 nm and a length of 2.5–20 μm, graphite powder with the particle size less than 20 μm, paraffin oil, graphite powder with the size of particles <20 μm, copper(II) chloride dihydrate ($CuCl_2{\cdot}2H_2O$), and sodium sulfate (Na_2SO_4) were obtained from SIGMA-ALDRICH. Nitric acid (HNO_3; 68%) was procured from AnalaR NORMAPUR and sulfuric acid (H_2SO_4; 98%) from Fluka. Potassium chloride (KCl), sodium hydroxide (NaOH) (98%), and ethanol (99.98%) were obtained from VWR PROLABO CHEMICALS.

Synthesis of $Cu(OH)_2$–Cu_2O Modified PPy/CPE and PPy/F-MWCNTs/CPE

Functionalization of the MWCNTs

An appropriate amount of MWCNTs was dispersed in a mixture of concentrated H_2SO_4 and HNO_3 at a volume ratio of 1:3 under ultrasonic agitation for few minutes and then refluxed at 80 °C under magnetic stirring for 4 h. The MWCNTs were then filtered on a Millipore polycarbonate membrane (Ø 0.22 μm) and washed with bi-distilled water until the filtrate reaches a neutral pH value. Finally, the functionalized MWCNTs were dried under vacuum at 50°C for 5 h.

F-MWCNTs Modified CPE

A suspension of F-MWCNTs with a concentration of 1 mg ml^{-1} was prepared by dispersing the functionalized MWCNT in bi-distilled water under ultrasonic vibration. Then, a volume of 10 μl of the dispersed F-MWCNTs was dropped on the CPE surface and dried at 40 °C for 20 min. The modified electrode was named "F-MWCNTs/CPE."

PPy Modified Bare CPE and F-MWCNTs/CPE

Electrochemical deposition of PPy on bare CPE and F-MWCNTs/CPE was performed in an aqueous solution containing 0.1 M pyrrole and 0.5 M $LiClO_4$ using galvanostatic mode at a current density of 0.2 mA cm^{-2} for 40 s (Oularbi et al., 2019). The modified electrodes were named "PPy/CPE" and "PPy/F-MWCNTs/CPE," respectively.

$Cu(OH)_2$–Cu_2O Modified PPy/CPE and PPy/F-MWCNTs/CPE

Electrochemical deposition of Cu on PPy/CPE and PPy/F-MWCNTs/CPE was performed in an aqueous solution

containing 0.1 M $CuCl_2$ and 0.1 M Na_2SO_4 using galvanostatic mode at a constant current of −225 μA for 60 s. The electrodes were then polarized in a solution of 0.1 M NaOH by applying five cyclic sweeps between −0.2 and 1 V in order to form copper oxide. The modified electrodes were named "$Cu(OH)_2$–Cu_2O/PPy/CPE" and "$Cu(OH)_2$–Cu_2O/PPy/F-MWCNTs/CPE," respectively.

Morphological, Structural, and Elemental Characterization

The morphological properties of the copper oxide catalysts were characterized using a scanning electron microscope (FEI FEG 450) coupled to an EDX spectrum (BRUKER XFlash 6/30). An IRAffinity-1S SHIMADZU Fourier transform infrared (FTIR) spectrophotometer was equipped with a Golden Gate single reflection attenuated total reflectance (ATR) accessory. FTIR spectra were recorded in the range of 500–4000 cm^{-1} at a resolution of 16 cm^{-1} and were used to determine the structural properties of the catalysts. A PANalytical X-ray diffractometer (XRD) X'PERT PRO MPD, with Cu Kα = 1.540598 Å and operating at 45 kV and 30 mA, was used on the prepared electrode to determine the crystalline phase of $Cu(OH)_2$–Cu_2O supported on PPy/F-MWCNTs/CPE.

Electrochemical Measurements

All electrochemical measurements including cyclic voltammetry (CV), chronoamperometry, and electrochemical impedance spectroscopy (EIS) were performed using PalmSens4 controlled with PSTrace software version 5.8. The assembly used comprises an electrochemical cell, which contains three electrodes: the modified carbon paste electrode (CPE) as a working electrode, Ag/AgCl as a reference electrode, and a platinum electrode as an auxiliary electrode.

RESULTS AND DISCUSSIONS

Physicochemical Characterization of F-MWCNTs

The presence of functional groups of MWCNTs was investigated by Fourier transform infrared (FTIR) spectrum before and after treatment with acid (**Supplementary Figure S1A**).

As can be seen, the functionalized MWCNTs show new peaks compared to the untreated one. The bands observed at 3453, 1747, and 1098 cm^{-1} correspond to carboxylic groups (-COOH) and are attributed, respectively, to the elongation vibration of hydroxyl (-OH), carbonyl (C=O), and epoxy (C-O) groups. The peaks at 2925 and 2865 cm^{-1} are attributed to the symmetrical and asymmetrical C-H band vibrations produced at the defect sites of the MWCNT surface during acid treatment. The peak at 1648 cm^{-1} is attributed to the elongation vibration of the C=C double band linked to the carbon nanotube structure (Choudhary and Pramanik, 2020a). The peak observed at 2366 cm^{-1} corresponds to the elongation vibration of the strongly hydrogenated -OH bond of the carboxylic groups (−COOH) as mentioned by Oularbi et al. during the preparation of nanocomposites consisting of bismuth particles, polypyrrole, and multi-walled carbon nanotubes (Oularbi et al., 2019). Our results are in good agreement with those of the previous works in the literature confirming that the treated MWCNTs have been successfully oxidized with new functional groups on their surface (De et al., 2017; Adewoye et al., 2021; Qazi et al., 2021).

The morphological structure of MWCNTs after functionalization was examined using scanning electron microscopy (SEM) characterization. **Supplementary Figure S1B** shows a porous and fibrous nanostructure without impurities which are removed after the acid treatment.

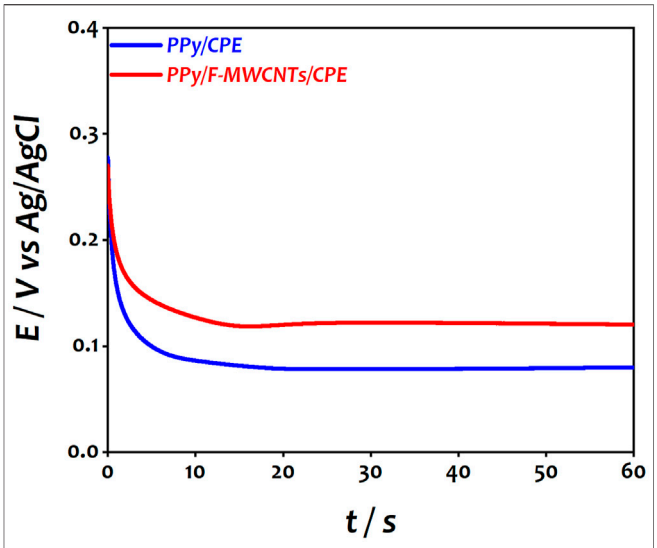

FIGURE 1 | Chronopotentiometric curve of PPy on CPE and F-MWCNTs/CPE during the electropolymerization process.

Electrodes Preparation and Characterization

After dispersion of F-MWCNTs on the electrode surface, the first step consists of the electropolymerization of the PPy film on CPE and F-MWCNTs/CPE using galvanostatic mode in 0.5 M $LiClO_4$ in the presence of 0.1 M pyrrole solution. **Figure 1** shows the chronopotentiometric curve recorded during the polymerization of polypyrrole on both electrodes.

As can be seen, the potential decreased gradually during the few first seconds and then reached a constant potential of 650 mV vs Ag/AgCl for CPE and 590 mV vs Ag/AgCl for F-MWCNTs/CPE, which corresponds to the growth of the polypyrrole film on different electrodes. The difference of the potential can be attributed to the presence of charge carriers on the F-MWCNT sheets, indicating an interaction between the F-MWCNT sheets and the PPy chain during electropolymerization of PPy. Moreover, the functional group of MWCNTs enhanced the charge transfer during polymerization leading to reduction of the deposition potential. This result is similar to the results reported in the literature during the polymerization of PPy on carbon nanofibers (CNFs) and carbon nanotubes (CNTs) (Oularbi et al., 2017; El

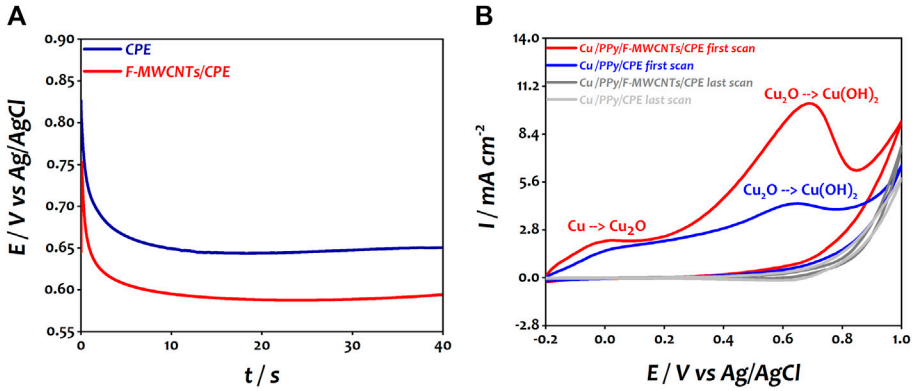

FIGURE 2 | (A) Chronopotentiometric curve of $CuCl_2$ on PPy/CPE and PPy/F-MWCNTs/CPE during the electrodeposition process. **(B)** Cyclic voltammetry of Cu/PPy/CPE and Cu/PPy/F-MWCNTs/CPE in 0.1 M NaOH at a scan rate of 50 mVs^{-1}.

Rhazi et al., 2018; Oularbi, 2018; Oularbi et al., 2019). After the polymerization of PPy on both surfaces, the electrochemical behavior of the modified electrodes was investigated in aqueous solution containing 0.5 M $LiClO_4$ using cyclic voltammetry (CV) showing a higher current and a well-defined redox behavior on PPy/F-MWCNTs/CPE with a decrease of the value of peak-to-peak separation (ΔE_p) of about 110 mV compared to that of PPy/CPE (**Supplementary Figure S2**). These results confirm the role of F-MWCNTs of promoting the electron transfer of the PPy film by providing a high active surface area and an easier electron transfer as reported by other authors (Rizi et al., 2021; Zeng et al., 2021).

In the second step, the copper nanoparticles were deposited on PPy/CPE and PPy/F-MWCNTs/CPE by applying a constant current of −225 μA for 60 s. As shown in **Figure 2A**, the deposition process of copper can be divided into two steps according to the potential variation characteristics. In the first step, the potential decreases rapidly on both electrodes which can possibly be due to the double layer charging and the initial nucleation of copper particles (Qiao and West, 2014; Yang et al., 2017). However, we can note that the initial potential for PPy/CPE is around 270 mV, while this value is around 274 mV on PPy/F-MWCNTs/CPE. Then, in the second stage, from 20 s onward, the potential remains practically stable at 80 and 120 mV for PPy/CPE and PPy/F-MWCNTs/CPE, respectively, indicating the deposition of Cu(0) on both electrodes. It should be noted that the nucleation sites of copper covered rapidly the surface of PPy/F-MWCNTs/CPE compared to PPy/CPE, indicating the high conductivity of the PPy/F-MWCNT composite. The increase of potential value at the end of electrodeposition of copper nanoparticles on PPy/F-MWCNTs/CPE confirms that the deposition of copper nanoparticles is easier on the electrode modified by F-MWCNTs owing to their good conductivity (Pérez-Fernández et al., 2017).

Right after that and in order to allow these particles to be oxidized into copper hydroxide and copper oxide, cyclic voltammetry was performed in 0.1 M NaOH solution under the potential range of −0.2 to 1 V vs Ag/AgCl at a scan rate of 50 mV s^{-1} for five cycles for both the electrodes. **Figure 2B** shows the first and five voltammograms obtained at Cu/PPy/CPE and Cu/PPy/F-MWCNTs/CPE.

The first voltammogram of polarization at both the electrodes shows two anodic peaks in agreement with our previous work (El Attar et al., 2020). The first anodic peak (30 mV vs Ag/AgCl at Cu/PPy/CPE and 0 mV vs Ag/AgCl at Cu/PPy/F-MWCNTs/CPE) is attributed to the oxidation of Cu(0) to Cu(I), which corresponds to Cu_2O form (**Eq. 1**) (Stępniowski et al., 2019). The second peak (650 mV vs Ag/AgCl at Cu/PPy/CPE and 690 mV vs Ag/AgCl at Cu/PPy/F-MWCNTs/CPE) corresponds to the oxidation of Cu_2O to $Cu(OH)_2$ as mentioned in the following equation (Moharam et al., 2016):

$$2Cu + 2OH^- \rightarrow Cu_2O + H_2O + 2e^- \quad (1)$$

$$Cu_2O + H_2O + 2\,OH^- \rightarrow 2Cu(OH)_2 + 2e^- \quad (2)$$

It should be noted that the anodic peaks at Cu/PPy/F-MWCNTs/CPE are well defined compared to those at Cu/PPy/CPE which can be attributed to the good deposition of copper particles on the modified electrode by the polymer and F-MWCNTs. However, for both electrodes, the current of the anodic peaks decreased progressively for the subsequent cycles, indicating the growth of a passive and stable film formed by copper hydroxide and copper oxide on the surface of the electrodes (Marathey et al., 2019; Stępniowski et al., 2019).

The X-ray diffraction (XRD) was used to characterize the crystalline phase of copper deposited on PPy/F-MWCNT/CPE support and is reported in **Figure 3A**. The spectrum presents well-defined peaks located at 26.57° (002 plane) and 44.42° (101 plane) attributed to the hexagonal structure of F-MWCNTs. The XRD pattern also revealed the presence of two crystalline phases of copper. The diffraction peaks at 16.8° (002 plane), 22.6° (021 plane), 50.7° (153 plane), 54.53° (103 plane), and 77.2° (311 plane) corresponded to the orthorhombic $Cu(OH)_2$ (JCPDS 01-072-0140) (Shahrokhian et al., 2019). The peaks at

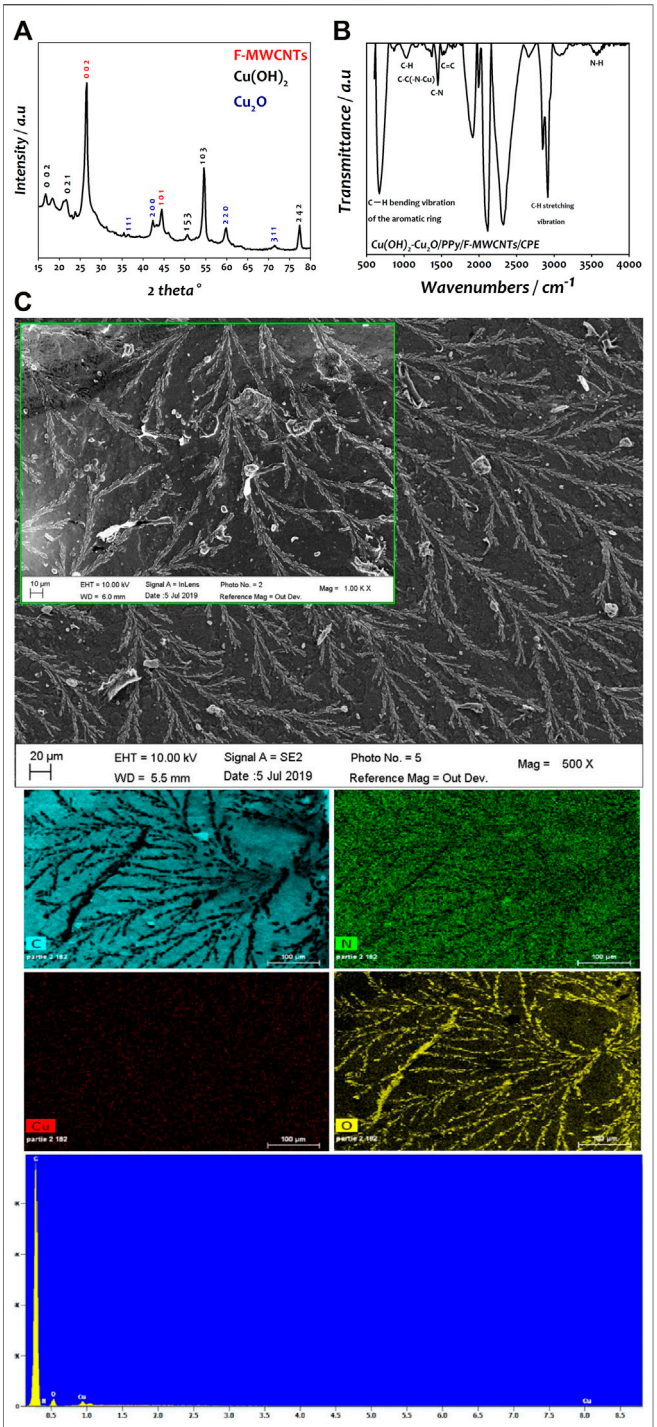

FIGURE 3 | (A) XRD analysis of $Cu(OH)_2$–Cu_2O/PPy/F-MWCNTs/CPE. **(B)** FTIR analysis of $Cu(OH)_2$–Cu_2O/PPy/F-MWCNTs/CPE. **(C)** SEM image of $Cu(OH)_2$–Cu_2O/PPy/F-MWCNTs/CPE and EDS and EDX elemental mapping of $Cu(OH)_2$–Cu_2O/PPy/F-MWCNTs/CPE.

36.4° (111 plane), 42.4° (200 plane), 59.8° (220 plane), and 71.4° (311 plane) were indexed to the cubic Cu_2O (JCPDS 01-077-0199) (Aguilar and Rosas, 2019). These results are similar to those obtained by Halim et al. (2021) when using polyphenylenediamine/carbon nanofiber (PpPD/CNF) as a support of Cu_2O–$Cu(OH)_2$ nanoparticles for methanol oxidation in alkaline medium (Halim et al., 2021).

The modified electrodes were investigated by FTIR spectroscopy (**Figure 3B**), which show different characteristic bands. The peaks at 666, 1018, and 2908 cm^{-1} corresponded to C-H vibration bands of the aromatic ring and C-H stretching vibration of PPy. The peaks observed at 1450 cm^{-1}, 3422 cm^{-1}, and 1504 cm^{-1} were attributed to C-N, N-H, and C=C, respectively, confirming the effective polymerization of the polypyrrole film on the electrode (Brachetti-Sibaja et al., 2021; Rizi et al., 2021). The peak at 1365 cm^{-1} was attributed to the C-C(-N-Cu) stretching vibration indicating the deposition of copper hydroxide/copper oxide on the surface of the PPy film (Guo et al., 2018; Peshoria and Narula, 2018). Based on the above analysis, we can conclude that $Cu(OH)_2$–Cu_2O/PPy/F-MWCNTs have been successfully synthesized on the modified electrode.

The morphological shape of the $Cu(OH)_2$–Cu_2O nanoparticles deposited on the surface of PPy/F-MWCNTs/CPE was characterized using scanning electron microscopy (SEM) (**Figure 3C**). As can be seen, $Cu(OH)_2$–Cu_2O was homogeneously deposited on PPy/F-MWCNTs with a three-dimensional nanodendritic structure constituted by multiple symmetrical branches attached to a pronounced central backbone. This kind of morphology is due to the presence of Cl^- ion present in copper solution as reported in the literature (Zhuo et al., 2017; El Attar et al., 2021; Halim et al., 2021).

The EDS and EDX mapping images of $Cu(OH)_2$–Cu_2O/PPy/F-MWCNTs/CPE (**Figure 3C**) show that the carbon element is well proportioned in the electrode surface, due to the presence of F-MWCNTs and the graphite flakes of the bare CPE. The nitrogen elements originating from PPy are well dispersed on the surface and certify the assembly of PPy thin film on the F-MWCNTs. Moreover, a homogeneous dispersion of copper element and the presence of oxygen confirm the formation of $Cu(OH)_2$–Cu_2O on the PPy/F-MWCNT/CPE surface, generating more active sites with more catalytic properties.

An electrochemical characterization was performed to evaluate the effect of introducing F-MWCNTs on the electrochemical properties of the modified $Cu(OH)_2$–Cu_2O/PPy/CPE. Therefore, the CVs of bare CPE, $Cu(OH)_2$–Cu_2O/PPy/CPE and $Cu(OH)_2$–Cu_2O/PPy/F-MWCNTs/CPE were recorded in 0.5 M KCl solution containing 10 mM of $[Fe(CN)_6]^{3/4-}$ as shown in **Figure 4A**.

As can be seen, the CV curves of the three electrodes show a pair of redox peaks corresponding to the reversible reaction of $[Fe(CN)_6]^{3/4-}$. The bare CPE has a small redox peak and a high peak-to-peak potential separation (ΔEp) of about 340 mV due to the relatively small surface area and low electron transfer (Salih et al., 2017a; Salih et al., 2017b; Salih et al., 2018; Oularbi et al., 2020). For the $Cu(OH)_2$–Cu_2O/PPy/CPE, the current densities of the anodic and cathodic peaks increased and the ΔEp value was reduced to 160 mV compared to those of the

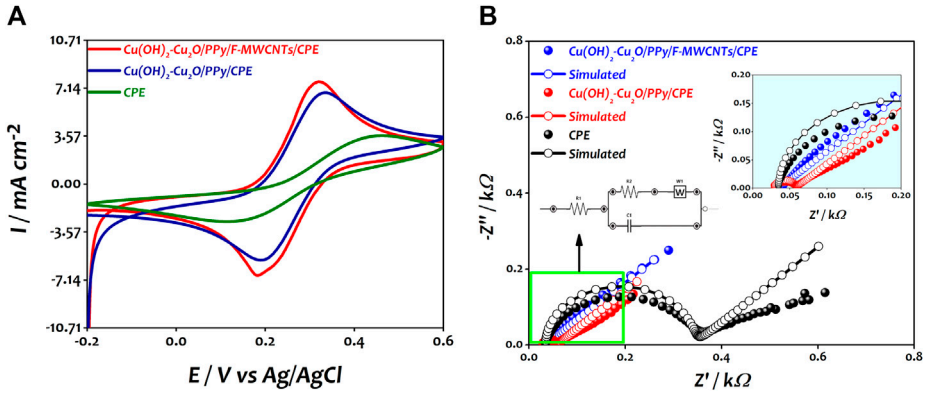

FIGURE 4 | (A) Typical cyclic voltammograms of CPE, Cu(OH)$_2$–Cu$_2$O/PPy/CPE, and Cu(OH)$_2$–Cu$_2$O/PPy/F-MWCNTs/CPE in 10 mM $[Fe(CN)_6]^{3/4-}$ in 0.5 M KCl at a scan rate of 100 mV s^{-1}. **(B)** Nyquist plots of CPE, Cu(OH)$_2$–Cu$_2$O/PPy/CPE, and Cu(OH)$_2$–Cu$_2$O/PPy/F-MWCNTs/CPE obtained in 10 mM $[Fe(CN)_6]^{3/4-}$ in 0.5 M KCl at 0.25 V.

bare CPE, indicating that the combination of the PPy film and copper oxide nanoparticles improved the conductivity of the electrode surface in agreement with our previous work (El Attar et al., 2020). In the case of Cu(OH)$_2$–Cu$_2$O/PPy/F-MWCNTs/CPE, the current density increased significantly by about 35.7% compared to that of bare CPE and 12.08% compared to that of Cu(OH)$_2$–Cu$_2$O/PPy/CPE and the ΔEp value was reduced to 120 mV. This result could be explained by the positive synergistic effect between F-MWCNTs and PPy leading to the enhancement of the surface area and

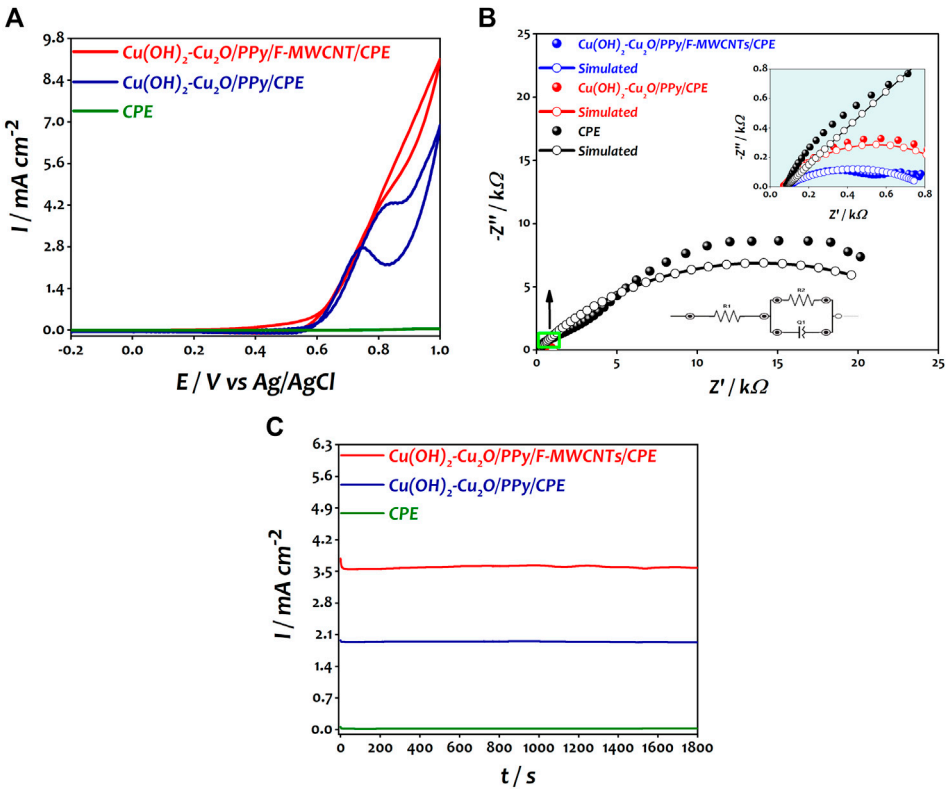

FIGURE 5 | (A) Catalytic response of CPE, Cu(OH)$_2$–Cu$_2$O/PPy/CPE, and Cu(OH)$_2$–Cu$_2$O/PPy/F-MWCNTs/CPE obtained in 0.2 M ethanol in 0.1 M NaOH. **(B)** Nyquist plots of CPE, Cu(OH)$_2$–Cu$_2$O/PPy/CPE, and Cu(OH)$_2$–Cu$_2$O/PPy/F-MWCNTs/CPE obtained in 0.2 M ethanol in 0.1 M NaOH at 0.6 V. **(C)** Chronoamperometric curves of CPE, Cu(OH)$_2$–Cu$_2$O/PPy/CPE, and Cu(OH)$_2$–Cu$_2$O/PPy/F-MWCNTs/CPE obtained in 0.2 M ethanol in 0.1 M NaOH at 0.7 V.

TABLE 1 | Characterization of anodic and cathodic peaks of modified electrodes.

Electrode	I_{pa} (mA cm^{-2})	I_{pc} (mA cm^{-2})	E_{pa} (mV)	E_{pc} (mV)	ΔE_p (mV)
Bare CPE	3.6	−2.8	460	120	340
$Cu(OH)_2$–Cu_2O/PPy/CPE	6.7	−5.62	340	180	160
$Cu(OH)_2$–Cu_2O/PPy/F-MWCNTs/CPE	7.62	−6.80	320	190	130

TABLE 2 | Impedance parameters obtained by fitting the impedance data.

Electrode	Rs (Ω)	R_{ct} (Ω)	C_f (μF)
Bare CPE	**34.60**	**307.1**	**0.36**
$Cu(OH)_2$–Cu_2O/PPy/CPE	**28.58**	**28.35**	**0.64**
$Cu(OH)_2$–Cu_2O/PPy/F-MWCNTs/CPE	**30.25**	**2.51**	**0.93**

TABLE 3 | Impedance components for various electrocatalysts by fitting the experimental impedance data based on the equivalent circuit at 0.6 V vs Ag/AgCl.

Electrocatalyst	Rs (Ω)	R_{ct} (Ω)	C (μF)
Bare CPE	85.21	28000	17.61
$Cu(OH)_2$–Cu_2O/PPy/CPE	70.33	948.4	44.34
$Cu(OH)_2$–Cu_2O/PPy/F-MWCNTs/CPE	76.64	728.2	96.87

improvement of the electronic transfer at the electrode surface as suggested by many authors (Fard et al., 2017; Kathiresan et al., 2021). The electrochemical parameters of the different electrodes recorded from the CV curves (**Figure 5A**) are reported in **Table 1**.

Since the enhancement of current is directly related to the electrochemically active surface area (EASA) of the electrode, we calculated it by using the Randles–Sevcik equation (**Eq. 3**), for different electrodes (Abbas et al., 2018):

$$\mathbf{i_{pa} = 2.69 \times 10^5 n^{3/2} AC D^{1/2} V^{1/2}}, \quad (3)$$

where i_{pa} is the anodic current (A), n is the number of electrons transferred (n = 1), A is the electroactive surface area (cm^2), C is the solution concentration (mol/cm^3), *V* is the potential scan rate ($V\ s^{-1}$), and D is the diffusion coefficient (cm^2/s). The calculated electroactive surface area was 0.086, 0.144, and 0.23 cm^2 for CPE, $Cu(OH)_2$–Cu_2O/PPy/CPE, and $Cu(OH)_2$–Cu_2O/PPy/F-MWCNTs/CPE, respectively. This indicates that the electroactive surface area of $Cu(OH)_2$–Cu_2O/PPy/F-MWCNTs/CPE is superior compared to the electroactive surface area of other tested electrodes.

In order to investigate the electrical interfacial properties of bare and modified electrodes, the electrochemical impedance spectroscopy (EIS) was conducted in the presence of $[Fe(CN)_6]^{3/4-}$ at a concentration of 10 mM containing 0.5 M KCl. **Figure 4B** shows the Nyquist plots of the bare CPE, $Cu(OH)_2$–Cu_2O/PPy/CPE, and $Cu(OH)_2$–Cu_2O/PPy/F-MWCNTs/CPE obtained in the frequency range from 100 KHz to 10 mHz. The EIS measurements were performed at a potential of 0.25 V vs Ag/AgCl for $[Fe(CN)_6]^{3-/4-}$ solution with an AC perturbation potential of 10 mV.

The charge transfer resistance (R_{ct}) and the capacity of the film (C_f) were determined by fitting impedance data using the Randles equivalent circuit. **Table 2** summarizes the results of the simulation. The Nyquist plot of the bare CPE displays a large semicircle in the higher frequency, which is characteristic of the highest charge transfer resistance (282.50 Ω) and the smallest capacity of the film. The straight line in low frequency is due to the diffusion limiting process. However, after the modification of the electrode by the PPy film and copper oxide nanoparticles, the diameter of the semicircle was significantly decreased, indicating an improvement of electron transfer at the modified electrode with a smallest R_{ct} value of 24.58 Ω and high C_f value of 0.64 μF compared to those at the CPE. Owing to their complementary properties, PPy and $Cu(OH)_2$–Cu_2O nanoparticles play an important role in the enhancement of conductivity of the surface. After the introduction of F-MWCNTs on $Cu(OH)_2$–Cu_2O/PPy/CPE, the charge transfer resistance continued to diminish reaching a value of 2.513 Ω. This result can be attributed to the good conductivity and the high surface area of F-MWCNTs as suggested by other authors (Fard et al., 2017). We can conclude that the electropolymerization of PPy on the F-MWCNT/CPE surface can generate a synergistic effect and present enhanced electrical properties. The incorporation of $Cu(OH)_2$–Cu_2O on PPy/F-MWCNTs offers a large number of active sites, and the high conductivity of $Cu(OH)_2$ might further accelerate the electron transfer, despite the low conductivity of Cu_2O (Pawar et al., 2017; Halim et al., 2021).

Electrocatalytic Oxidation of Ethanol Using Modified Electrocatalysts

The catalytic performances of the modified electrocatalysts toward the ethanol oxidation reaction were evaluated using cyclic voltammetry (CV), electrochemical impedance spectroscopy (EIS), and chronoamperometry (CA) in a solution containing 0.2 M of ethanol and 0.1 M NaOH. **Figure 5A** shows the cyclic voltammograms recorded at different electrodes.

As expected, no response was obtained at bare CPE; however, after the deposition of copper oxide nanoparticles on the PPy/CPE surface, a well-defined anodic peak of ethanol was observed at 0.8 V vs Ag/AgCl with a current density of 4.27 mA cm^{-2} corresponding to the oxidation of ethanol molecules. After the introduction of F-MWCNTs, the

TABLE 4 | Comparison of the performance of Cu(OH)$_2$–Cu$_2$O/PPy/F-MWCNTs/CPE with that of some other modified electrocatalysts for electrooxidation of ethanol and methanol.

Electrocatalyst	Preparation mode	Preparation time	Current density	Applied solution	Stability	Ref.
Pd/PANI-MWCNTs-SnO2/Ti	Chemical and electrochemical method	3 H	64.1 mA cm^{-2}	0.5 M KOH + 1 M ethanol	20 min	Mozafari and Parsa (2020a)
PdCo PNS/PPy@MWCNT	Chemical method	More 48 H	1.65 mA cm^{-2}	1 M KOH + 1 M ethanol	30 min	Fard et al. (2017)
Cu(OH)$_2$–Cu$_2$O/PpPD/CNF/CPE	Electrochemical method	30 min	42 mA cm^{-2}	0.1 M NaOH + 1 M methanol	6 H	Halim et al. (2021)
Ni/PPy/rGO	Chemical method	–	32.94 mA cm^{-2}	1 M KOH + 1 M methanol	10 min	Sarkar et al. (2019)
Cu(OH)$_2$–Cu$_2$O/PPy/F-MWCNTs/CPE	Electrochemical method	30 min	7 mA cm^{-2}	0.1 M NaOH + 0.2 M ethanol	30 min	This work

current density increased 1.6-fold and reached a value of 7 mA cm^{-2} compared to that at Cu(OH)$_2$–Cu$_2$O/PPy/CPE at a potential of 0.85 V vs Ag/AgCl. This increase can be attributed to the good synergistic effect between PPy/F-MWCNT support and Cu(OH)$_2$–Cu$_2$O nanoparticles. The modified electrode presented high adsorption capability of ethanol probably due to the high surface area offered by F-MWCNTs and to the presence of a large number of amine groups of the polymer which ensures a good dispersion of Cu(OH)$_2$–Cu$_2$O on the electrode surface. A similar behavior was reported by Halim et al. (2021) in the oxidation of methanol. Moreover, the nanodendritic morphology of Cu(OH)$_2$–Cu$_2$O ensures the existence of more catalytic sites, and easy migration of species by promoting the charge transfer, leading to the improvement of the catalytic response of ethanol oxidation as suggested by other authors (Parreira et al., 2017; Zhang et al., 2018; Farsadrooh et al., 2019).

In alkaline media, the Cu(OH)$_2$ layer is converted to CuOOH by the entry of OH species according to **Eq. 4** (Pawar et al., 2017; Halim et al., 2021). Thereafter, ethanol is oxidized on the active CuOOH layer and forms Cu(OH)$_2$ and CO$_2$ (**Eq. 5**), which causes a high increase in the current density.

Based on the results obtained in our previous study (El Attar et al., 2021), the following mechanism could therefore be suggested for EOR at Cu(OH)$_2$–Cu$_2$O/PPy/F-MWCNT/CPE:

$$\mathrm{Cu(OH)_2 + OH^- \rightarrow CuOOH + H2O + e^-} \quad (4)$$

$$\mathrm{CuOOH + C_2H_5OH + 11OH^- \rightarrow Cu(OH)_2 + 2CO_2 + 8H_2O + 11e^-} \quad (5)$$

In order to understand the electrochemical process at the interface electrode solution during the electrooxidation of ethanol, the prepared electrodes (bare CPE, Cu$_2$O/PPy/CPE, and Cu$_2$O/PPy/MWCNT/CPE) were examined by electrochemical impedance spectroscopy in 0.1 M NaOH in the presence of 0.2 M ethanol at a potential of 0.6 V vs Ag/AgCl in the frequency range between 100 kHz and 0.01 Hz. **Figure 5B** shows the impedance spectra recorded at different electrodes.

The equivalent circuit compatible with the results is presented in the inset of **Figure 5B**. In this circuit, R1, Q1, and R2 represent the solution resistance (Rs), a constant phase element (CPE) corresponding to the double layer capacitance, and the charge transfer resistance (R_{ct}) associated with the oxidation of ethanol (Ehsani et al., 2014; Ehsani et al., 2015).

Ehsani et al. reported that the replacement of capacitor C with a constant phase element (CPE) in the equivalent circuit can lead to obtaining a satisfactory impedance simulation of ethanol electrooxidation (Ehsani et al., 2012). The most widely accepted explanation for the presence of CPE behavior is microscopic roughness of the electrocatalyst surface, causing an inhomogeneous distribution in the solution resistance as well as in the double layer capacitance. The parallel combination of charge transfer resistance R_{ct} and constant phase element CPE accounts for the injection of electrons from the conductive polymer to the back metallic contact.

The EIS results are summarized in **Table 3**.

It can be seen that Cu(OH)$_2$–Cu$_2$O/PPy/F-MWCNTs/CPE shows the smaller semicircular diameter R_{ct} (728.2 Ω) and a higher capacitance C_f (96.873 μF) compared to Cu(OH)$_2$–Cu$_2$O/PPy/CPE (R_{ct} = 948.4 Ω, C_f = 44.34 μF). The decrease of R_{ct} value and the increase of C_f after the introduction of F-MWCNTs clearly demonstrate the ease of charge transfer and the electron flux across the electrode/electrolyte interface of Cu(OH)$_2$–Cu$_2$O/PPy/F-MWCNTs/CPE. The same behavior was reported by Datta et al. during the oxidation of ethanol in alkaline medium using the Pt/PANI/CNT electrocatalyst (Ding et al., 2018; Maya-Cornejo et al., 2021).

In order to evaluate the stability of the electrocatalysts, the chronoamperometric experiments of modified electrocatalysts toward EOR were investigated in 0.1 M NaOH with 0.2 M ethanol solution at 0.7 V vs Ag/AgCl for 1800 s. **Figure 5C** shows the obtained results.

We can notice that the three electrodes present a decline in current density trend from their maximum values of current density in the first few seconds. This decrease is due to the adsorption of incomplete oxidation products on the surface of the electrocatalyst (Chemchoub et al., 2020; El

Attar et al., 2020). Cu(OH)$_2$–Cu$_2$O/PPy/CPE and Cu(OH)$_2$–Cu$_2$O/PPy/F-MWCNTs/CPE showed a very small initial drop in current before reaching stability compared to CPE. This result indicates few or no significant adsorbed intermediates species on the electrocatalyst surface (Sulaiman et al., 2017; Mozafari and Parsa, 2020b). It should be noted that the current density curve obtained at the Cu(OH)$_2$–Cu$_2$O/PPy/F-MWCNT/CPE catalyst reached a value of 3.57 mA cm^{-2} at 1800 s, which is much higher than the value obtained by Cu(OH)$_2$–Cu$_2$O/PPy/CPE (1.93 mA cm^{-2}). The availability of a higher number of active sites on the surface of Cu(OH)$_2$–Cu$_2$O/PPy/F-MWCNTs/CPE due to the presence of F-MWCNT is probably the main reason behind this behavior (Farsadrooh et al., 2019).

The comparison of the electrocatalytic performance of our electrocatalyst with that of previously reported materials based on expensive metals is shown in **Table 4**. It was found that Cu(OH)$_2$–Cu$_2$O/PPy/F-MWCNTs/CPE shows a higher value of current density compared with that in similar works.

CONCLUSION

In summary, we report a new, inexpensive, and highly efficient electrocatalyst based on Cu(OH)$_2$–Cu$_2$O supported on PPy/F-MWCNTs for ethanol oxidation, prepared by a simple and rapid strategy. Owing to the excellent properties of F-MWCNTs, including high surface area and high conductivity, and the enrichment of the surface by amine groups of polypyrrole, a good dispersion of copper oxide on the surface is ensured. A systematic characterization of the developed electrocatalyst was conducted using FTIR spectroscopy, SEM, XRD, elemental analysis, cyclic voltammetry, and electrochemical impedance spectroscopy (EIS). The EIS of electrocatalysts in ethanol solution revealed that Cu(OH)$_2$–Cu$_2$O/PPy/F-MWCNTs/CPE presents a smallest R_{ct} and the highest C, which indicate a higher electronic transfer during the ethanol oxidation reaction. The Cu(OH)$_2$–Cu$_2$O/PPy/F-MWCNT/CPE electrocatalyst exhibited a higher electrocatalytic activity (7 mA cm^{-2}) toward EOR in alkaline medium compared to Cu(OH)$_2$–Cu$_2$O/PPy/CPE (4.27 mA cm^{-2}). It has been proved that the introduction of F-MWCNTs facilitates ethanol oxidation on the electrocatalyst surface and enhances the performance of the catalyst in terms of stability and durability confirming the collective contribution and synergistic interaction between all the material components. The good stability of electrocatalyst as well as its low cost makes this catalyst a promising candidate for direct alcohol fuel cell and other applications.

DATA AVAILABILITY STATEMENT

The original contributions presented in the study are included in the article/**Supplementary Materials**, and further inquiries can be directed to the corresponding author.

AUTHOR CONTRIBUTIONS

All authors listed have made a substantial, direct, and intellectual contribution to the work and approved it for publication.

FUNDING

This work was supported by MESRSFC (Ministère de l'Enseignement Supérieur et de la Recherche Scientifique et de la Formation des cadres–Morocco) and CNRST (Centre National pour la Recherche Scientifique et Technique–Morocco) (project number PPR/2015/72).

SUPPLEMENTARY MATERIAL

The Supplementary Material for this article can be found online at: https://www.frontiersin.org/articles/10.3389/fchem.2021.805654/full#supplementary-material

REFERENCES

Abbas, S., Lee, H., Hwang, J., Mehmood, A., Shin, H.-J., Mehboob, S., et al. (2018). A Novel Approach for Forming Carbon Nanorods on the Surface of Carbon Felt Electrode by Catalytic Etching for High-Performance Vanadium Redox Flow Battery. *Carbon* 128, 31–37. doi:10.1016/j.carbon.2017.11.066

Adewoye, T. L., Ogunleye, O. O., Abdulkareem, A. S., Salawudeen, T. O., and Tijani, J. O. (2021). Optimization of the Adsorption of Total Organic Carbon from Produced Water Using Functionalized Multi-Walled Carbon Nanotubes. *Heliyon* 7, e05866. doi:10.1016/j.heliyon.2020.e05866

Aguilar, M. S., and Rosas, G. (2019). Facile Synthesis of Cu2O Particles with Different Morphologies. *J. Solid State. Chem.* 270, 192–199. doi:10.1016/j.jssc.2018.11.019

Boulaghi, M., Ghafouri Taleghani, H., Soleimani Lashkenari, M., and Ghorbani, M. (2018). Platinum-palladium Nanoparticles-Loaded on N-Doped Graphene Oxide/polypyrrole Framework as a High Performance Electrode in Ethanol Oxidation Reaction. *Int. J. Hydrogen Energ.* 43, 15164–15175. doi:10.1016/j.ijhydene.2018.06.092

Brachetti-Sibaja, S. B., Palma-Ramírez, D., Torres-Huerta, A. M., Domínguez-Crespo, M. A., Dorantes-Rosales, H. J., Rodríguez-Salazar, A. E., et al. (2021). CVD Conditions for MWCNTs Production and Their Effects on the Optical and Electrical Properties of PPy/MWCNTs, PANI/MWCNTs Nanocomposites by *In Situ* Electropolymerization. *Polymers* 13, 351. doi:10.3390/polym13030351

Cermenek, B., Ranninger, J., Feketeföldi, B., Letofsky-Papst, I., Kienzl, N., Bitschnau, B., et al. (2019). Novel Highly Active Carbon Supported Ternary PdNiBi Nanoparticles as Anode Catalyst for the Alkaline Direct Ethanol Fuel Cell. *Nano Res.* 12, 683–693. doi:10.1007/s12274-019-2277-z

Chemchoub, S., Oularbi, L., El Attar, A., Younssi, S. A., Bentiss, F., Jama, C., et al. (2020). Cost-effective Non-noble Metal Supported on Conducting Polymer Composite Such as Nickel Nanoparticles/polypyrrole as Efficient Anode Electrocatalyst for Ethanol Oxidation. *Mater. Chem. Phys.* 250, 123009. doi:10.1016/j.matchemphys.2020.123009

Choudhary, A. K., and Pramanik, H. (2020a). Addition of Rhenium (Re) to Pt-Ru/f-MWCNT Anode Electrocatalysts for Enhancement of Ethanol Electrooxidation in Half Cell and Single Direct Ethanol Fuel Cell. *Int. J. Hydrogen Energ.* 45, 13300–13321. doi:10.1016/j.ijhydene.2020.03.044

Choudhary, A. K., and Pramanik, H. (2020b). Enhancement of Ethanol Electrooxidation in Half Cell and Single Direct Ethanol Fuel Cell (DEFC) Using post-treated Polyol Synthesized Pt-Ru Nano Electrocatalysts Supported on HNO3-Functionalized Acetylene Black Carbon. *Int. J. Hydrogen Energ.* 45, 574–594. doi:10.1016/j.ijhydene.2019.10.243

De, A., Adhikary, R., and Datta, J. (2017). Proactive Role of Carbon Nanotube-Polyaniline Conjugate Support for Pt Nano-Particles toward Electro-Catalysis of Ethanol in Fuel Cell. *Int. J. Hydrogen Energ.* 42, 25316–25325. doi:10.1016/j.ijhydene.2017.08.073

Ding, K., Li, C., Zhang, Y., Wang, L., Wei, B., Shi, X., et al. (2018). Using PdO and PbO as the Starting Materials to Prepare a Multi-Walled Carbon Nanotubes Supported Composite Catalyst (PdxPby/MWCNTs) for Ethanol Oxidation Reaction (EOR). *Int. J. Hydrogen Energ.* 43, 1523–1528. doi:10.1016/j.ijhydene.2017.11.142

Ehsani, A., Mahjani, M. G., Jafarian, M., and Naeemy, A. (2012). Electrosynthesis of Polypyrrole Composite Film and Electrocatalytic Oxidation of Ethanol. *Electrochim. Acta* 71, 128–133. doi:10.1016/j.electacta.2012.03.107

Ehsani, A., Mahjani, M. G., Adeli, S., and Moradkhani, S. (2014). Electrosynthesis and Physioelectrochemical Properties of Poly Tyramine Electroactive Film in the Presence of the Surfactant: Comparable Study. *Prog. Org. Coat.* 77, 1674–1681. doi:10.1016/j.porgcoat.2014.05.027

Ehsani, A., Vaziri-Rad, A., Babaei, F., and Shiri, H. M. (2015). Electrosynthesis, Optical Modeling and Electrocatalytic Activity of Ni-MWCNT-PT Nanocomposite Film. *Electrochim. Acta* 159, 140–148. doi:10.1016/j.electacta.2015.01.204

Eisa, T., Mohamed, H. O., Choi, Y.-J., Park, S.-G., Ali, R., Abdelkareem, M. A., et al. (2020). Nickel Nanorods over Nickel Foam as Standalone Anode for Direct Alkaline Methanol and Ethanol Fuel Cell. *Int. J. Hydrogen Energ.* 45, 5948–5959. doi:10.1016/j.ijhydene.2019.08.071

El Attar, A., Oularbi, L., Chemchoub, S., and El Rhazi, M. (2020). Preparation and Characterization of Copper Oxide Particles/polypyrrole (Cu2O/PPy) via Electrochemical Method: Application in Direct Ethanol Fuel Cell. *Int. J. Hydrogen Energ.* 45, 8887–8898. doi:10.1016/j.ijhydene.2020.01.008

El Attar, A., Oularbi, L., Chemchoub, S., and El Rhazi, M. (2021). Effect of Electrochemical Activation on the Performance and Stability of Hybrid (PPy/Cu2O Nanodendrites) for Efficient Ethanol Oxidation in Alkaline Medium. *J. Electroanal. Chem.* 885, 115042. doi:10.1016/j.jelechem.2021.115042

El Rhazi, M., Majid, S., Elbasri, M., Salih, F. E., Oularbi, L., and Lafdi, K. (2018). Recent Progress in Nanocomposites Based on Conducting Polymer: Application as Electrochemical Sensors. *Int. Nano Lett.* 8, 79–99. doi:10.1007/s40089-018-0238-2

El-Houari, H., Allouhi, A., Rehman, S., Buker, M. S., Kousksou, T., Jamil, A., et al. (2020). Feasibility Evaluation of a Hybrid Renewable Power Generation System for Sustainable Electricity Supply in a Moroccan Remote Site. *J. Clean. Prod.* 277, 123534. doi:10.1016/j.jclepro.2020.123534

Fard, L. A., Ojani, R., Raoof, J. B., Zare, E. N., and Lakouraj, M. M. (2017). PdCo Porous Nanostructures Decorated on Polypyrrole @ MWCNTs Conductive Nanocomposite-Modified Glassy Carbon Electrode as a Powerful Catalyst for Ethanol Electrooxidation. *Appl. Surf. Sci.* 401, 40–48. doi:10.1016/j.apsusc.2016.12.240

Farsadrooh, M., Noroozifar, M., Modarresi-Alam, A. R., and Saravani, H. (2019). Sonochemical Synthesis of High-Performance Pd@CuNWs/MWCNTs-CH Electrocatalyst by Galvanic Replacement toward Ethanol Oxidation in Alkaline media. *Ultrason. Sonochem.* 51, 478–486. doi:10.1016/j.ultsonch.2018.06.011

Fontes, E. H., Ramos, C. E. D., Nandenha, J., Piasentin, R. M., Neto, A. O., and Landers, R. (2019). Structural Analysis of PdRh/C and PdSn/C and its Use as Electrocatalysts for Ethanol Oxidation in Alkaline Medium. *Int. J. Hydrogen Energ.* 44, 937–951. doi:10.1016/j.ijhydene.2018.11.049

Ghosh, S., Bhandary, N., Basu, S., and Basu, R. N. (2017). Synergistic Effects of Polypyrrole Nanofibers and Pd Nanoparticles for Improved Electrocatalytic Performance of Pd/PPy Nanocomposites for Ethanol Oxidation. *Electrocatalysis* 8, 329–339. doi:10.1007/s12678-017-0374-x

Guo, J., Chen, R., Zhu, F.-C., Sun, S.-G., and Villullas, H. M. (2018). New Understandings of Ethanol Oxidation Reaction Mechanism on Pd/C and Pd2Ru/C Catalysts in Alkaline Direct Ethanol Fuel Cells. *Appl. Catal. B Environ.* 224, 602–611. doi:10.1016/j.apcatb.2017.10.037

Halim, E. M., Perrot, H., Sel, O., Debiemme-Chouvy, C., Lafdi, K., and El Rhazi, M. (2021). Electrosynthesis of Hierarchical Cu2O-Cu(OH)2 Nanodendrites Supported on Carbon Nanofibers/poly(para-Phenylenediamine) Nanocomposite as High-Efficiency Catalysts for Methanol Electrooxidation. *Int. J. Hydrogen Energ.* 46, 19926–19938. doi:10.1016/j.ijhydene.2021.03.119

Ivanovski, K., Hailemariam, A., and Smyth, R. (2021). The Effect of Renewable and Non-renewable Energy Consumption on Economic Growth: Non-parametric Evidence. *J. Clean. Prod.* 286, 124956. doi:10.1016/j.jclepro.2020.124956

Kathiresan, V., Thirumalai, D., Rajarathinam, T., Yeom, M., Lee, J., Kim, S., et al. (2021). A Simple One-step Electrochemical Deposition of Bioinspired Nanocomposite for the Non-enzymatic Detection of Dopamine. *J. Anal. Sci. Technol.* 12, 5. doi:10.1186/s40543-021-00260-y

Liang, Y.-Y., Wu, Q., and Liang, F. (2021). Analysis of Catalytic Activity of Au@Pd Core-Shell Nanodendrites for Highly Efficient Ethanol Electrooxidation. *Chin. J. Anal. Chem.* 49, e21087–e21095. doi:10.1016/S1872-2040(21)60103-2

Marathey, P., Khanna, S., Pati, R., Mukhopadhyay, I., and Ray, A. (2019). Low Temperature-Controlled Synthesis of Hierarchical Cu2O/Cu(OH)2/CuO Nanostructures for Energy Applications. *J. Mater. Res.* 34, 3173–3185. doi:10.1557/jmr.2019.231

Maya-Cornejo, J., Diaz-Real, J. A., Lopez-Miranda, J. L., Álvarez-Contreras, L., Esparza, R., Arjona, N., et al. (2021). Formation of Cu@Pd Core@shell Nanocatalysts with High Activity for Ethanol Electro-Oxidation in Alkaline Medium. *Appl. Surf. Sci.* 538, 148119. doi:10.1016/j.apsusc.2020.148119

Moharam, M. M., Elsayed, E. M., Nino, J. C., Abou-Shahba, R. M., and Rashad, M. M. (2016). Potentiostatic Deposition of Cu2O Films as P-type Transparent Conductors at Room Temperature. *Thin Solid Films* 616, 760–766. doi:10.1016/j.tsf.2016.10.005

Mondal, A., De, A., and Datta, J. (2019). Selective Methodology for Developing PtCo NPs and Performance Screening for Energy Efficient Electro-Catalysis in Direct Ethanol Fuel Cell. *Int. J. Hydrogen Energ.* 44, 10996–11011. doi:10.1016/j.ijhydene.2019.02.146

Mozafari, V., and Parsa, J. B. (2020a). Electrochemical Synthesis of Pd Supported on PANI-MWCNTs-SnO2 Nanocomposite as a Novel Catalyst towards Ethanol Oxidation in Alkaline media. *Synth. Met.* 259, 116214. doi:10.1016/j.synthmet.2019.116214

Mozafari, V., and Parsa, J. B. (2020b). Promoted Electrocatalytic Performance of Palladium Nanoparticles Using Doped-NiO Supporting Materials toward Ethanol Electro-Oxidation in Alkaline media. *Int. J. Hydrogen Energ.* 45, 28847–28859. doi:10.1016/j.ijhydene.2020.07.276

Oularbi, L., Turmine, M., and El Rhazi, M. (2017). Electrochemical Determination of Traces lead Ions Using a New Nanocomposite of Polypyrrole/carbon Nanofibers. *J. Solid State. Electrochem.* 21, 3289–3300. doi:10.1007/s10008-017-3676-2

Oularbi, L., Turmine, M., and El Rhazi, M. (2019). Preparation of Novel Nanocomposite Consisting of Bismuth Particles, Polypyrrole and Multi-Walled Carbon Nanotubes for Simultaneous Voltammetric Determination of Cadmium(II) and Lead(II). *Synth. Met.* 253, 1–8. doi:10.1016/j.synthmet.2019.04.011

Oularbi, L., Turmine, M., Salih, F. E., and El Rhazi, M. (2020). Ionic Liquid/carbon Nanofibers/bismuth Particles Novel Hybrid Nanocomposite for Voltammetric Sensing of Heavy Metals. *J. Environ. Chem. Eng.* 8, 103774. doi:10.1016/j.jece.2020.103774

Oularbi, L. (2018). *Étude de nanocomposites polypyrrole/nanoparticule de carbone par impédance électrochimique et ac-électrogravimétrie: application aux capteurs électrochimiques*. Ph.D. Thesis. Casablanca, Morocco: Sorbonne and Hassan II Casablanca Universities.

Parreira, L. S., Silva, J. C. M., Simões, F. R., Cordeiro, M. A. L., Sato, R. H., Leite, E. R., et al. (2017). PtSn Electrocatalyst Supported on MWCNT-COOH: Investigating the Ethanol Oxidation Reaction. *ChemElectroChem* 4, 1950–1958. doi:10.1002/celc.201700326

Pawar, S. M., Pawar, B. S., Inamdar, A. I., Kim, J., Jo, Y., Cho, S., et al. (2017). *In-situ* Synthesis of Cu(OH)2 and CuO Nanowire Electrocatalysts for Methanol Electro-Oxidation. *Mater. Lett.* 187, 60–63. doi:10.1016/j.matlet.2016.10.079

Pérez-Fernández, B., Martín-Yerga, D., and Costa-García, A., (2017). Galvanostatic Electrodeposition of Copper Nanoparticles on Screen-Printed Carbon Electrodes and Their Application for Reducing Sugars Determination. *Talanta* 175, 108–113.

Peshoria, S., and Narula, A. K. (2018). One-pot Synthesis of Porphyrin@ polypyrrole Hybrid and its Application as an Electrochemical Sensor. *Mater. Sci. Eng. B* 229, 53–58. doi:10.1016/j.mseb.2017.12.023

Qazi, R. A., Khattak, R., Ali Shah, L., Ullah, R., Khan, M. S., Sadiq, M., et al. (2021). Effect of MWCNTs Functionalization on Thermal, Electrical, and Ammonia-Sensing Properties of MWCNTs/PMMA and PHB/MWCNTs/PMMA Thin Films Nanocomposites. *Nanomaterials* 11, 2625. doi:10.3390/nano11102625

Qiao, F., and West, A. C. (2014). The Impact of Cations on Nucleus Density during Copper Electrodeposition. *Electrochim. Acta* 150, 8–14. doi:10.1016/j.electacta.2014.10.135

Rahman, M. M., and Velayutham, E. (2020). Renewable and Non-renewable Energy Consumption-Economic Growth Nexus: New Evidence from South Asia. *Renew. Energ.* 147, 399–408. doi:10.1016/j.renene.2019.09.007

Rizi, K. S., Hatamluyi, B., Rezayi, M., Meshkat, Z., Sankian, M., Ghazvini, K., et al. (2021). Response Surface Methodology Optimized Electrochemical DNA Biosensor Based on HAPNPTs/PPY/MWCNTs Nanocomposite for Detecting *Mycobacterium tuberculosis*. *Talanta* 226, 122099. doi:10.1016/j.talanta.2021.122099

Salih, F. E., Achiou, B., Ouammou, M., Bennazha, J., Ouarzane, A., Younssi, S. A., et al. (2017a). Electrochemical Sensor Based on Low Silica X Zeolite Modified Carbon Paste for Carbaryl Determination. *J. Adv. Res.* 8, 669–676. doi:10.1016/j.jare.2017.08.002

Salih, F. E., Ouarzane, A., and El Rhazi, M. (2017b). Electrochemical Detection of lead (II) at bismuth/Poly(1,8-Diaminonaphthalene) Modified Carbon Paste Electrode. *Arabian J. Chem.* 10, 596–603. doi:10.1016/j.arabjc.2015.08.021

Salih, F. E., Oularbi, L., Halim, E., Elbasri, M., Ouarzane, A., and El Rhazi, M. (2018). Conducting Polymer/Ionic Liquid Composite Modified Carbon Paste Electrode for the Determination of Carbaryl in Real Samples. *Electroanalysis* 30, 1855–1864. doi:10.1002/elan.201800152

Sarkar, C., Nath, J., Bhuyan, S., and Dolui, S. K. (2019). Multifunctional Ternary Nanocomposites of Ni/Polypyrrole/Reduced Graphene Oxide as Supercapacitor and Electrocatalyst in Methanol Oxidation. *ChemistrySelect* 4, 2529–2537. doi:10.1002/slct.201803386

Shahrokhian, S., Khaki Sanati, E., and Hosseini, H. (2019). Advanced On-Site Glucose Sensing Platform Based on a New Architecture of Free-Standing Hollow Cu(OH)2 Nanotubes Decorated with CoNi-LDH Nanosheets on Graphite Screen-Printed Electrode. *Nanoscale* 11, 12655–12671. doi:10.1039/C9NR02720C

Silva, J. C. M., Ntais, S., Rajaraman, V., Teixeira-Neto, É., Teixeira-Neto, Â. A., Neto, A. O., et al. (2019). The Catalytic Activity of Pt:Ru Nanoparticles for Ethylene Glycol and Ethanol Electrooxidation in a Direct Alcohol Fuel Cell. *Electrocatalysis* 10, 203–213. doi:10.1007/s12678-019-00515-8

Souza, F. M., Böhnstedt, P., Pinheiro, V. S., Oliveira, L. A., Batista, B. L., Parreira, L. S., et al. (2020). Niobium Increasing the Electrocatalytic Activity of Palladium for Alkaline Direct Ethanol Fuel Cell. *J. Electroanal. Chem.* 858, 113824. doi:10.1016/j.jelechem.2020.113824

Stępniowski, W. J., Yoo, H., Choi, J., Norek, M., Jóźwik, P., and Misiolek, W. Z. (2019). Fabrication and Characterization of Oxide Nano-needles Formed by Copper Passivation in Sodium Hydroxide Solution. *Thin Solid Films* 671, 111–119. doi:10.1016/j.tsf.2018.12.023

Sulaiman, J. E., Zhu, S., Xing, Z., Chang, Q., and Shao, M. (2017). Pt-Ni Octahedra as Electrocatalysts for the Ethanol Electro-Oxidation Reaction. *ACS Catal.* 7, 5134–5141. doi:10.1021/acscatal.7b01435

Xaba, N., Modibedi, R. M., Mathe, M. K., and Khotseng, L. E. (2019). Pd, PdSn, PdBi, and PdBiSn Nanostructured Thin Films for the Electro-Oxidation of Ethanol in Alkaline Media. *Electrocatalysis* 10, 332–341. doi:10.1007/s12678-019-0511-9

Yang, T., Ding, Y., Li, C., Yin, N., Liu, X., and Li, P. (2017). Potentiostatic and Galvanostatic Two-step Electrodeposition of Semiconductor Cu2O Films and its Photovoltaic Application. *J. Alloys Comp.* 727, 14–19. doi:10.1016/j.jallcom.2017.08.123

Zeng, Q., Chen, J., Gao, F., Tu, X., Qian, Y., Yu, Y., et al. (2021). Development of a New Electrochemical Sensing Platform Based on MoO3-Polypyrrole nanowires/MWCNTs Composite and its Application to Luteolin Detection. *Synth. Met.* 271, 116620. doi:10.1016/j.synthmet.2020.116620

Zhang, Y., Yi, Q., Deng, Z., Zhou, X., and Nie, H. (2018). Excellent Electroactivity of Ternary Pd-Ag-Sn Nanocatalysts for Ethanol Oxidation. *Catal. Lett.* 148, 1190–1201. doi:10.1007/s10562-018-2335-2

Zhuo, K., An, C. Y., Kannan, P. K., Seo, N., Park, Y.-S., and Chung, C.-H. (2017). Effect of Electrolyte Composition on the Morphological Structures of Dendritic Copper Powders Prepared by a Spontaneous Galvanic Displacement Reaction. *Korean J. Chem. Eng.* 34, 1483–1489. doi:10.1007/s11814-017-0023-3

Conflict of Interest: The authors declare that the research was conducted in the absence of any commercial or financial relationships that could be construed as a potential conflict of interest.

Publisher's Note: All claims expressed in this article are solely those of the authors and do not necessarily represent those of their affiliated organizations, or those of the publisher, the editors, and the reviewers. Any product that may be evaluated in this article, or claim that may be made by its manufacturer, is not guaranteed or endorsed by the publisher.

frontiers in Chemistry

ORIGINAL RESEARCH
published: 17 February 2022
doi: 10.3389/fchem.2022.793759

A DFT Mechanistic Study on Base-Catalyzed Cleavage of the β-O-4 Ether Linkage in Lignin: Implications for Selective Lignin Depolymerization

Mary Mensah[1], *Richard Tia*[1]*, *Evans Adei*[1] *and Nora H. de Leeuw*[2,3,4]

[1]Department of Chemistry, Kwame Nkrumah University of Science and Technology, Kumasi, Ghana, [2]School of Chemistry, Cardiff University, Cardiff, United Kingdom, [3]Department of Earth Sciences, Utrecht University, Utrecht, Netherlands, [4]School of Chemistry, University of Leeds, Leeds, United Kingdom

The detailed mechanism of the base-catalyzed C-C and C-O bond cleavage of a model compound representing the β-O-4 linkage in lignin is elucidated using DFT calculations at the M06/6-31G* level of theory. Two types of this linkage have been studied, a C2 type which contains no γ-carbinol group and a C3 type which contains a γ-carbinol. Cleavage of the C2 substrate is seen to proceed *via* a 6-membered transition structure involving the cation of the base, the hydroxide ion and the α-carbon adjacent to the ether bond. The reaction with KOH has the lowest activation barrier of 6.1 kcal mol^{-1} with a calculated rate constant of 2.1 × 10^{8} s^{-1}. Cleavage of the C3 substrate is found to proceed *via* two pathways: an enol-formation pathway and an epoxide-formation pathway. The first path is the thermodynamically favored pathway which is similar to the pathway for the C2 substrate and is the preferred pathway for the isolation of an enol-containing monomer. The second path is the kinetically favored pathway, which proceeds *via* an 8-membered transition state involving a hydrogen hopping event, and is the preferred pathway for the isolation of an epoxide-containing monomer. The KOH-catalyzed reaction also has the lowest activation barrier of 10.1 kcal mol^{-1} along the first path and 3.9 kcal mol^{-1} along the second path, with calculated rate constants of 2.4 × $10^{5}s^{-1}$ and 8.6 × $10^{9}s^{-1}$ respectively. Overall, the results provide clarity on the mechanism for the base-catalyzed depolymerization of lignin to phenolic monomers. The results also suggest both NaOH and KOH to be the preferred catalysts for the cleavage of the β-O-4 linkage in lignin.

Keywords: lignin, depolymerization, aryl ether, β-O-4, lignin valorization

OPEN ACCESS

Edited by:
James Darkwa, Botswana Institute for Technology Research and Innovation (BITRI), Botswana

Reviewed by:
Ramakrishnan Parthasarathi, Indian Institute of Toxicology Research (CSIR), India
Francisco Martin-Martinez, Swansea University, United Kingdom
Ponnadurai Ramasami, University of Mauritius, Mauritius

***Correspondence:**
Richard Tia
richtiagh@yahoo.com

Specialty section:
This article was submitted to Supramolecular Chemistry, a section of the journal Frontiers in Chemistry

Received: *12 October 2021*
Accepted: *04 January 2022*
Published: *17 February 2022*

Citation:
Mensah M, Tia R, Adei E and de Leeuw NH (2022) A DFT Mechanistic Study on Base-Catalyzed Cleavage of the β-O-4 Ether Linkage in Lignin: Implications for Selective Lignin Depolymerization. Front. Chem. 10:793759. doi: 10.3389/fchem.2022.793759

INTRODUCTION

The feasibility of lignocellulosic biorefineries replacing petroleum and petrochemical refineries depends on conversion of both the cellulose fraction and lignin fraction of biomass to value-added products (Azadi et al., 2013). Over the years, valorization of the cellulose fraction for the production of biofuels and chemicals has been thoroughly studied and developed techniques have been employed industrially (Dutta et al., 2012; Ruppert et al., 2012; Akhtari et al., 2014). Lignin which accounts for 40% by energy in lignocellulose is still mostly a waste stream in the pulping and biorefinery processes and only 5% of lignin is used in low-value commercial applications (Hu et al., 2011). Due to the complex nature of lignin, having strong carbon-carbon bonds and ether

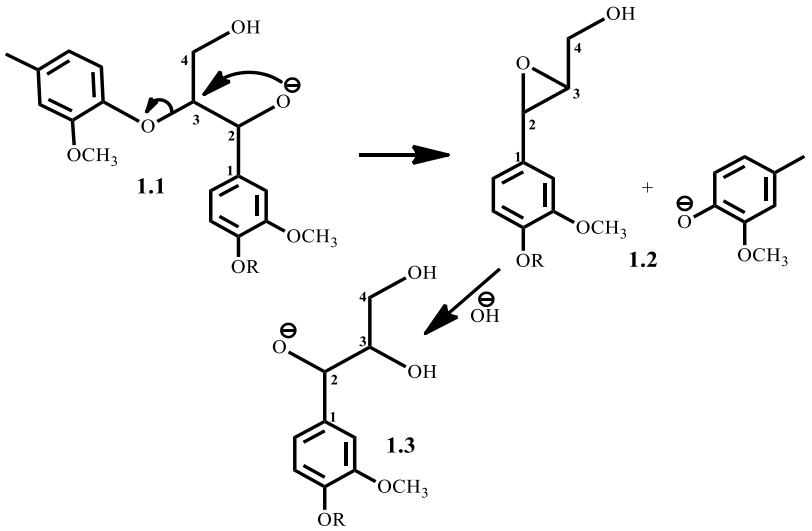

SCHEME 1 | Mcdonough's (Lavoie et al., 2011) proposed mechanism for base catalyzed depolymerization of lignin.

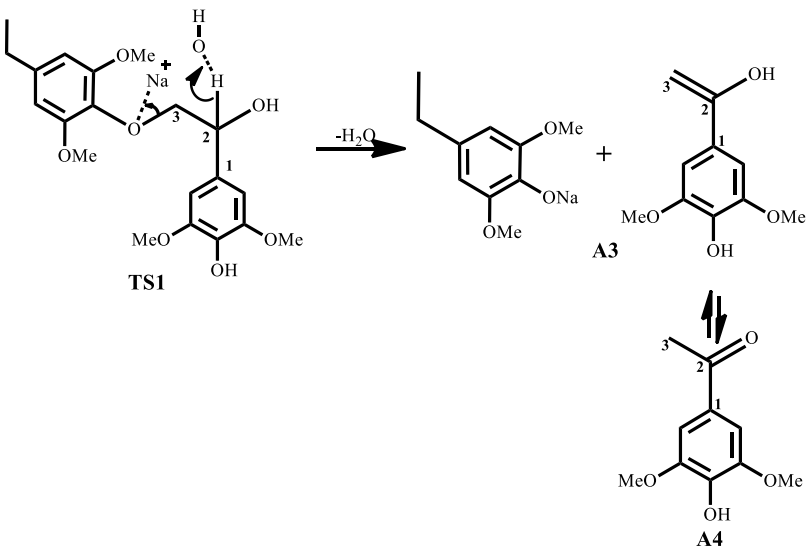

SCHEME 2 | Roberts et al. (Roberts et al., 2010) proposed mechanism for base catalyzed depolymerization of lignin.

bonds holding its three major monomeric units together, there is still a general lack of efficient processes for the utilization of lignin (Parthasarathi et al., 2011; Elder, 2014). One major benefit that lignin valorization holds is the production of 100% biomass-derived jet fuel because lignin is the only abundant renewable source of aromatic hydrocarbons in nature (Chakar and Ragauskas, 2004; Hileman and Stratton, 2014) and aromatics play a vital role in jet fuel quality and safety, specifically the fuel's elastomeric swelling, material compatibility and lubricity characteristics (Huber et al., 2006).

With significant research still ongoing to convert lignin into value-added products, three general routes exist for lignin conversion. The first is the production of oil through pyrolysis, the second is the conversion to syngas (Huber et al., 2006; Pandey and Kim, 2011; Lavoie et al., 2011), while the third is chemical treatment to produce target molecules. Current research focuses on the third route as the first two typically demand severe conditions, while the third is relatively mild and is advantageous for both reaction control and high selectivity. One such mild treatment is the use of sodium hydroxide for the treatment of lignin in aqueous solution at temperatures of about 300°C from which phenols and phenol derivatives are obtained (Huber et al., 2006). This process was formerly used to delignify paper making in the pulping industry, as lignin is an impediment

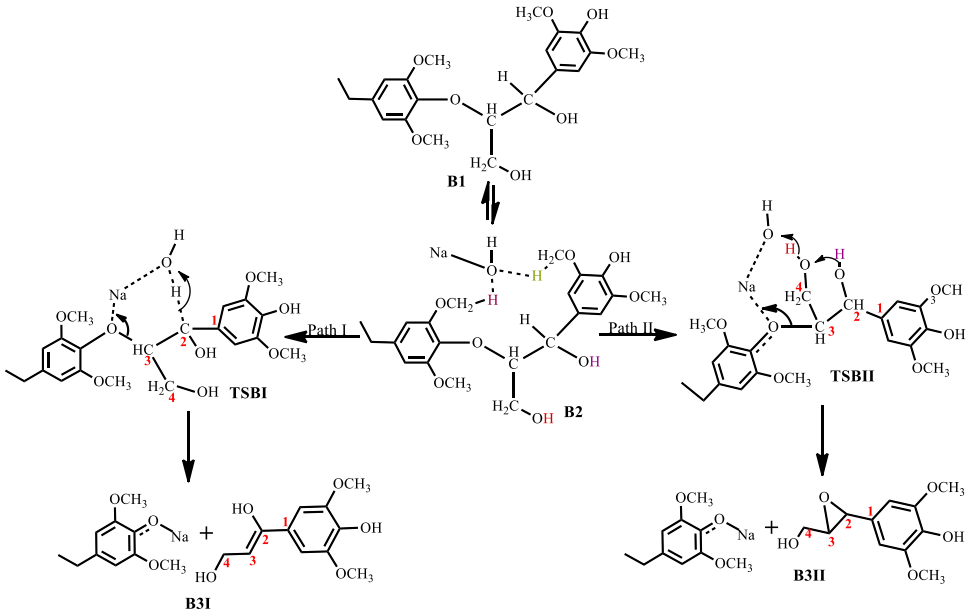

SCHEME 3 | Mechanism for the base catalyzed cleavage of a lignin β-O-4 ether bond containing a γ-glycol.

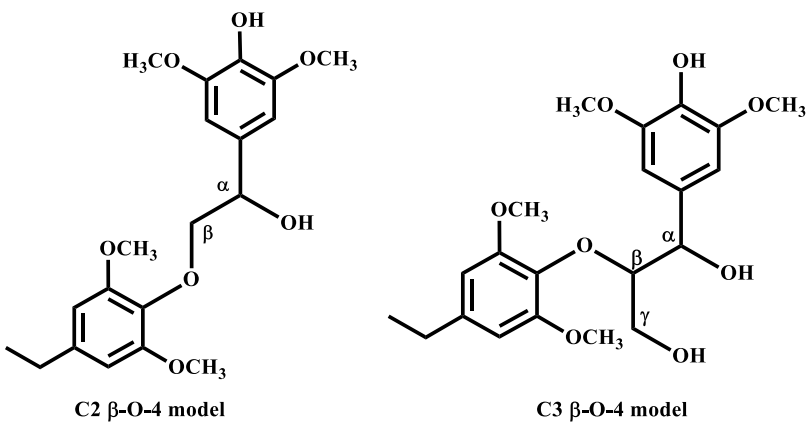

FIGURE 1 | The two types of β-O-4 linkage.

to the paper making process (Mcdonough, 1993). In 2011, Roberts et al. (Roberts et al., 2011a) carried out NaOH-catalyzed treatment of lignin in water to give syringol and its derivatives as major products. Toledano et al. (Toledano et al., 2012) screened various base catalysts, including KOH and LiOH, for the depolymerization of lignin from olive tree pruning in aqueous solution where they reported that the nature of the base governs monomer yield. Hartwig et al. (Sergeev and Hartwig, 2011) also reported the cleavage of the β-O-4 lignin model compound in the presence of NaO^{t}Bu alone when used as a co-catalyst, yielding guaiacol at 89% yield. One major disadvantage of base-catalyzed depolymerization of lignin is the repolymerization reactions which occur during the process, thereby limiting monomer yields. Lercher et al.(Roberts et al., 2011a) reported the success of boric acid as an excellent capping agent in hindering secondary reactions and improving monomer yields. Phenol was reported to be a better capping agent by Toledano et al. (Toledano et al., 2014) since boric acid allowed for more char formation in the final product, while phenol yielded low char content and decreased residual lignin down to 25% (Toledano et al., 2014). It is said that during the alkaline delignification process, cleavage of β-O-4 ether bond is the dominant reaction and according to Mcdonough et al. (Lavoie et al., 2011) the reaction takes place as a result of deprotonated hydroxyl groups on the α-carbon that act as nucleophiles in displacing the neighboring aroxy substituent with the formation

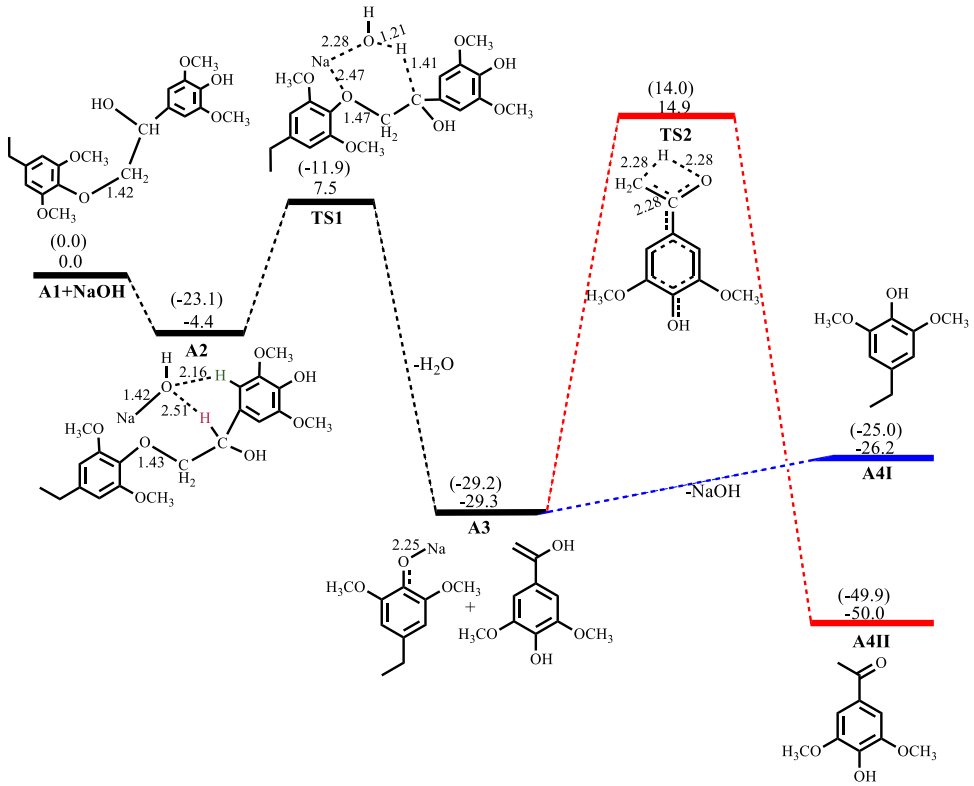

FIGURE 2 | Free energy profile for NaOH catalyzed cleavage of C2 β-O-4 substrate computed at M06/6-31G* level of theory. Relative energies in kcal mol^{-1}. Gas-phase energies in parenthesis and selected bond distances in Å. (XYZ coordinates, **Supplementary Table S2**, Supporting Information).

of an oxirane ring which is subsequently opened by addition of a hydroxide ion to form a glycol (**Scheme 1**). A more recent mechanism proposed by Roberts et al. (Roberts et al., 2010) postulates that the cleavage of the β-O-4 ether bond takes place heterolytically *via* a six-membered transition state in which the sodium ion and hydroxide ion participate (**Scheme 2**). The sodium cation forms a cation adduct with the lignin, thereby polarizing the ether bond which eventually cleaves to form a sodium phenolate intermediate and 4-hydroxylvinyl syringol. A third mechanism results from this study (**Scheme 3**), wherein cleavage of the β-O-4 ether bond which contains the γ-carbinol could proceed *via* two pathways; this mechanism is discussed in detail in *Results and Discussions Section*.

Despite the progress that has been made in the area, there is the need for better understanding of the molecular-level processes of this base-catalyzed depolymerization reactions to delineate what happens at the molecular level. This will help fine-tune reaction selectivity towards higher monomer yields as well as improve energy efficiency for industrial application (Kleine et al., 2013; Toledano et al., 2014).

Here, we have employed calculations based on the density functional theory (DFT) to carry out an exploratory/predictive molecular modelling study to provide molecular-level insight into the details of the base-catalyzed cleavage of the C-O bond in a β-O-4 linkage, which is the predominant linkage found in lignin (Kleine et al., 2013). The β-O-4 substrate chosen for this study would show the formation of syringol derivatives which is reported to constitute the largest fraction of monomer products obtained from the base catalyzed depolymerization of lignin (Mcdonough, 1993; Roberts et al., 2011a). The energetics (thermodynamics and kinetics) of the elementary steps for the catalyzed cleavage of a C2 β-O-4 linkage as well as a C3 β-O-4 linkage using NaOH, KOH, LiOH and NaO^{t}Bu were studied in both the gas phase and the solvated phase following the two mechanisms proposed in **Schemes 1**, **2**. The C2 β-O-4 linkage is a simpler model substrate typically used in both experimental and computational studies, while the C3 β-O-4 linkage better represents the linkage in the actual lignin framework (**Figure 1**).

COMPUTATIONAL DETAILS

All calculations were carried out using the Spartan '14 Molecular Modelling program (Spartan, 2011) and Gaussian 09' package (Frisch et al., 2016). The structures and energies of all the stationary points involved along the reaction pathway were computed at the M06/6-31G* level of theory. The M06 functional is a hybrid meta-gradient-corrected functional (*meta*-GGA) with 27% of Hartree-Fock exchange. Zhao et al. have carried out a comprehensive benchmarking study to evaluate the accuracy of this method against a number of properties, including barrier heights, bond dissociation energies, and non-covalent interactions

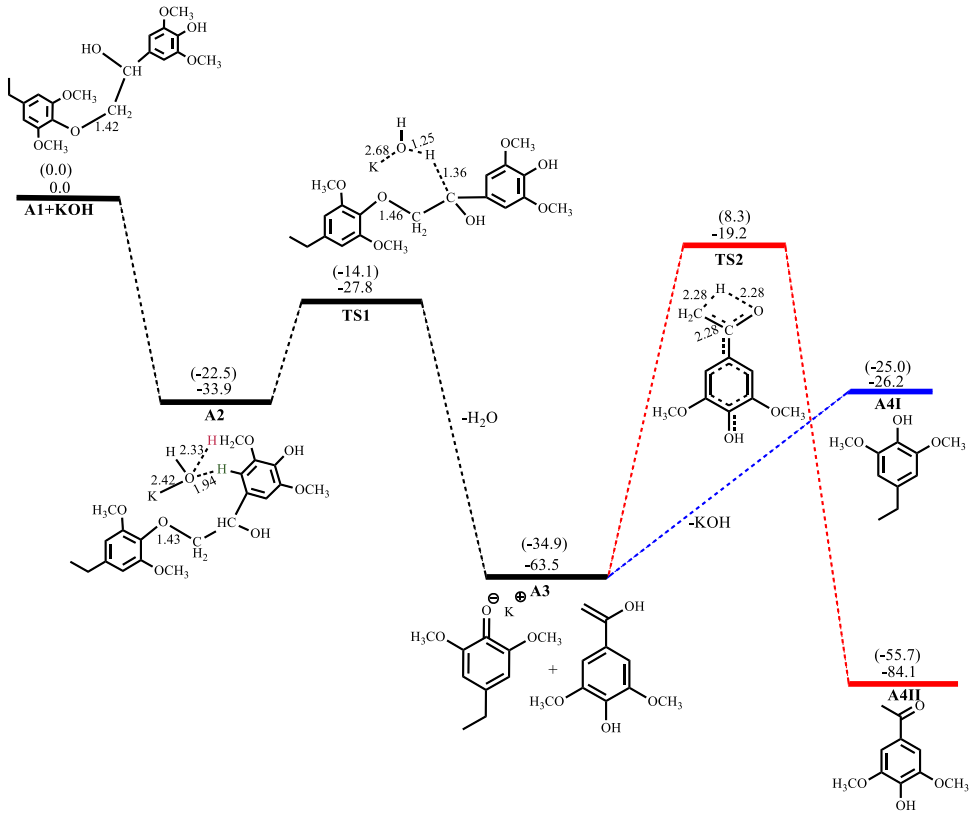

FIGURE 3 | Free energy profile for KOH catalyzed cleavage of C2 β-O-4 substrate. Relative energies in kcal mol^{-1} computed at M06/6-31G* level of theory. Gas-phase energies in parenthesis and selected bond distances in Å. (XYZ coordinates, **Supplementary Table S3**, Supporting Information).

(Zhao and Truhlar, 2008). The parameters considered in their study are the focus of the present work and we have therefore chosen the same method as recommended for the study of organometallic thermochemistry, as well as non-covalent interactions (Zhao and Truhlar, 2008). The 6-31G* basis set is a double-zeta basis set, known to give reliable results for charge-localized anions such as the hydroxide (Rassolov et al., 1998). All stationary points were characterized by full frequency calculations. Minima (reactants, intermediates and products) were shown to have a Hessian matrix whose eigenvalues are all positive, leading to vibrational frequencies which are real, while transition states were shown to have a Hessian matrix having all positive eigenvalues except a single negative eigenvalue characterized by a vibration along the reaction coordinate. In **Supplementary Table S1** of the Supplementary Information, we have provided a comparison of the absolute electronic energies and relative energies computed using both 6-31G* and 6-311G* basis sets and a comparison of optimized geometrical parameters at the double and triple zeta basis sets. The 6-311G* optimized geometries reproduce the 6-31G* structures and the calculated relative energies using the two methods are within 3 kcal mol^{-1}, thus providing confidence that the use of the 6-31G* basis set is suitable for this work.

Input structures for transition state optimizations were obtained after a potential energy surface (PES) scan was performed for each reaction step. This calculation was also useful in showing that the minima obtained do in fact correspond to the reactant and product for that step. The PES scan gives an approximate transition state structure which is then submitted for a transition state calculation using the synchronous Transit-Guided Quasi-Newton (STQN) Method developed by Schlegel and coworkers (Peng and Bernhard Schlegel, 1993). General effects of a surrounding solvent on the computed geometries and energies of the stationary points along the reaction pathway were evaluated using a polarizable continuum model derived with an integral equation formalism (IEF-PCM) (Mennucci et al., 1997) of water solvation, which is the solvent used in experiments. The PCM approach is widely used for this type of computational study and our choice of solvent model was guided by detailed benchmarking studies (Miguel et al., 2016), which indicate that the model should provide reliable energetic trends in reaction pathways. All reported energies are Gibbs free energies.

RESULTS AND DISCUSSIONS

Base Catalyzed Cleavage of C2 β-O-4 Substrate

Figures 2–5 show the optimized geometries and relative energies of the stationary points for the cleavage of the C2 substrate using

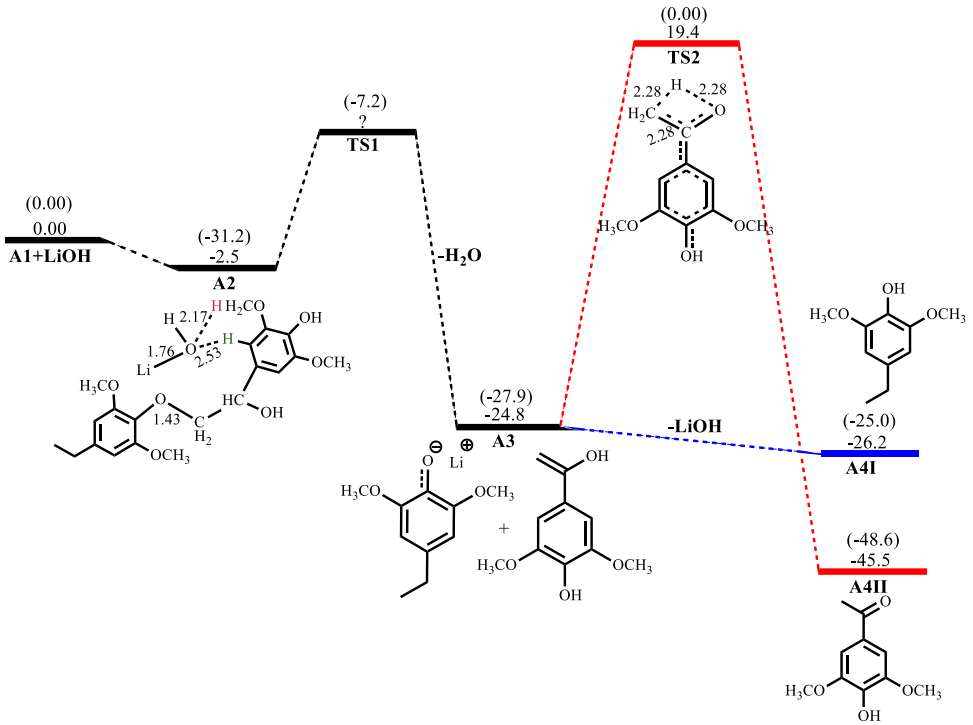

FIGURE 4 | Free energy profile for LiOH catalyzed cleavage of C2 β-O-4 substrate. Relative energies in kcal mol^{-1} computed at M06/6-31G* level of theory. Gas-phase energies in parenthesis and selected bond distances in Å. (XYZ coordinates, **Supplementary Table S4**, Supporting Information).

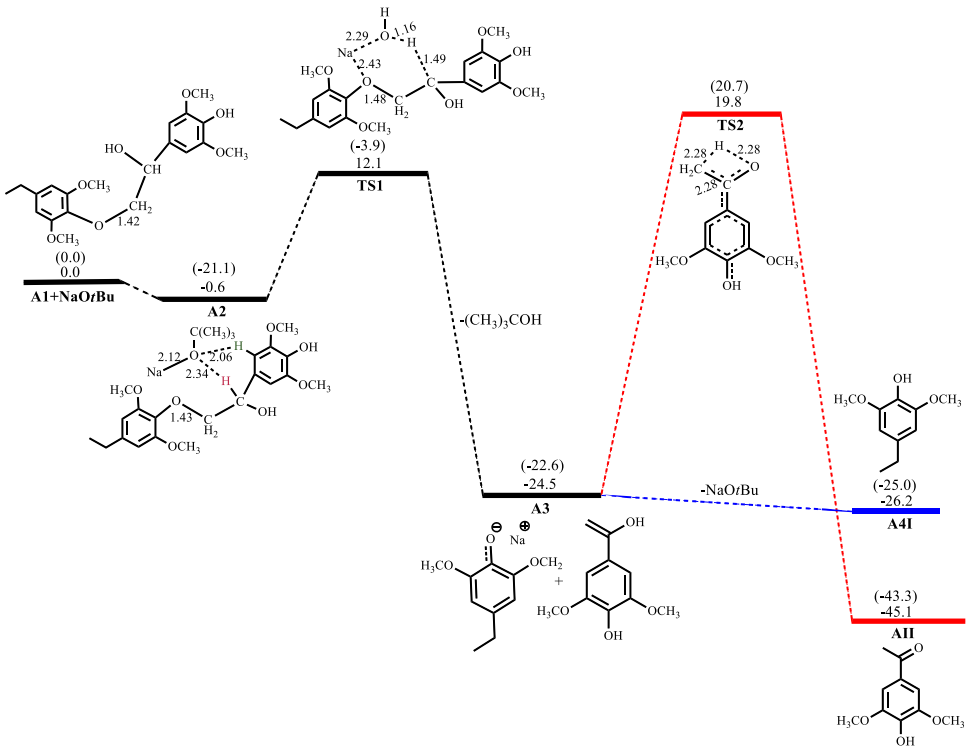

FIGURE 5 | Free energy profile for NaO^{t}Bu catalyzed cleavage of C2 β-O-4 substrate. Relative energies in kcal mol^{-1} computed at M06/6-31G* level of theory. Gas-phase energies in parenthesis and selected bond distances in Å. (XYZ coordinates, **Supplementary Table S5**, Supporting Information).

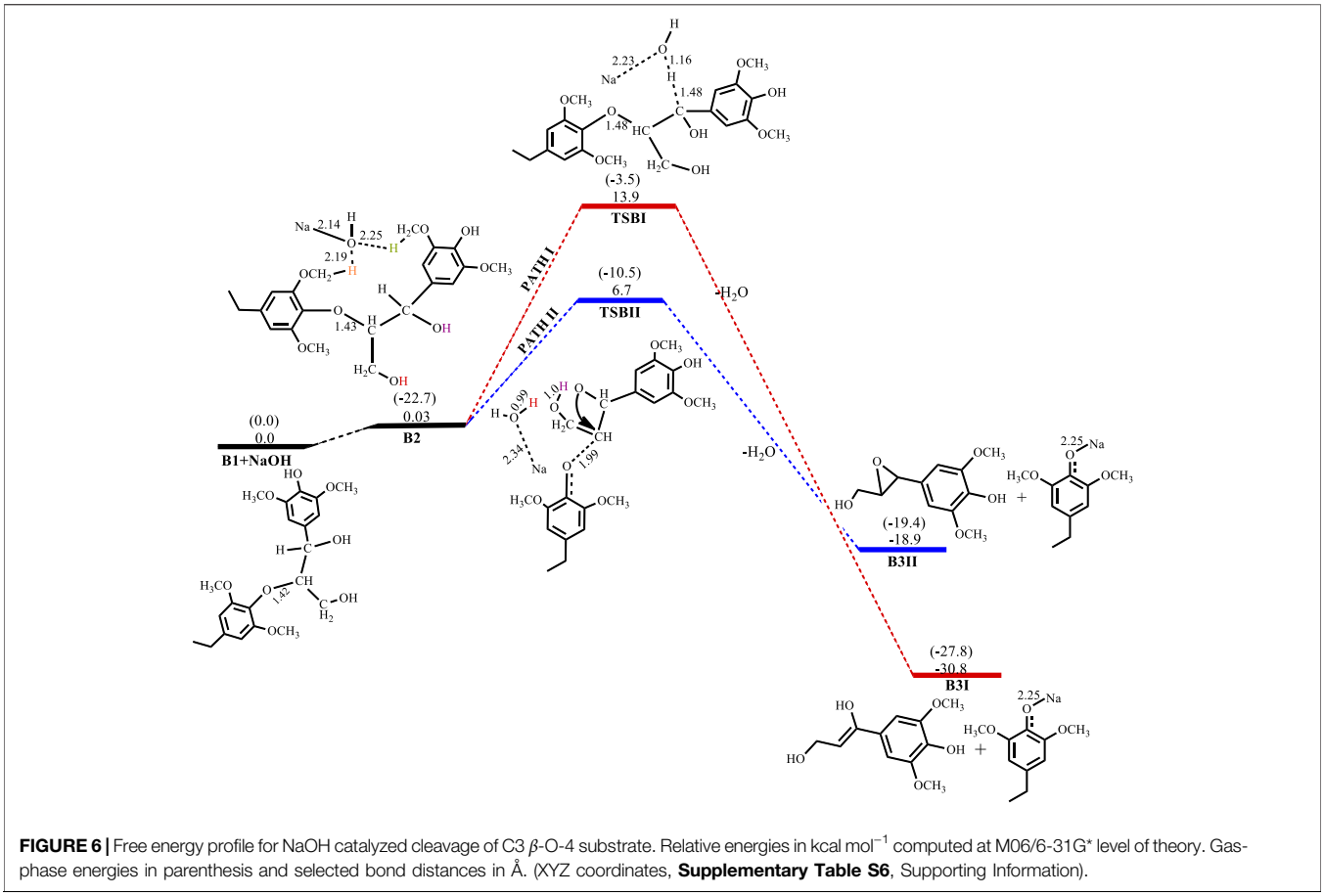

FIGURE 6 | Free energy profile for NaOH catalyzed cleavage of C3 β-O-4 substrate. Relative energies in kcal mol^{-1} computed at M06/6-31G* level of theory. Gas-phase energies in parenthesis and selected bond distances in Å. (XYZ coordinates, **Supplementary Table S6**, Supporting Information).

TABLE 1 | Relative energies computed at M06/6-31G* level of theory for the catalyzed cleavage of the C3 β-O-4 substrate using KOH, LiOH and NaO^{t}Bu. All energies are measured in kcal mol^{-1}.

Base	E_a(TSBI)	E_a(TSBII)	E_f(B3I)	E_f(B3II)
KOH	10.1	3.9	−33.0	−21.1
LiOH	20.7	11.4	−27.6	−15.7
NaO^{t}Bu	16.4	11.3	−27.8	−15.9

NaOH, KOH, LiOH and NaO^{t}Bu, as well as the transformation of the cleaved products to the final products 4-ethylsyringol and methoxy-4-hydroxyacetophenone. The catalytic cleavage is exergonic for all bases used (ΔG^{NaOH} = −24.9 kcal mol^{-1}, ΔG^{KOH} = −29.6 kcal mol^{-1}, ΔG^{LiOH} = −22.3 kcal mol^{-1}, ΔG^{NaOtBu} = −23.9 kcal mol^{-1}) although it was determined that an intermediate (**A2**) is formed before the cleavage occurs. The intermediate shows electrostatic interactions between the hydroxide ion and two of the hydrogens on the β-O-4 substrate which is assumed to stabilize the intermediate. These electrostatic interactions are found to be stronger in the gas phase than in the solvated phase ($A2^{NaOH}$; O---H_{gas} = 1.96Å and 2.08Å, O---H_{solv} = 2.51Å and 2.16Å) which could explain why **A2** is more stable in the gas phase for all the bases except for KOH, where $\mathbf{A2}^{KOH}$ is found to be more stable in the solvated phase than in the gas phase. The catalytic C-O bond cleavage is shown to proceed *via* the 6-membered transition state **TS1** where the hydroxide ion deprotonates the α-carbon to form water and the C-O bond is cleaved (**Scheme 2**). The KOH-catalyzed reaction has the lowest activation barrier of 6.1 kcal mol^{-1}, compared to NaOH and NaO^{t}Bu which have activation barriers of 11.9 and 12.8 kcal mol^{-1}, respectively. The transition state for the LiOH process could only be located in the gas phase. These findings show that, if the reactions are kinetically controlled, the KOH catalyst is the most efficacious for the catalytic cleavage of the C2 β-O-4 ether bond which in turn means that stronger bases facilitate faster cleavage. The NaOH is said to be recovered from the reaction by dissolving the organic fraction in acetone (Roberts et al., 2011a) and although the mechanism for this step is not explored, it is assumed that the hydrogen source for the conversion of the phenolate monomer to its phenol motif **A4I** observed in experiment comes from this step. The phenol monomer **A4I** was found to be much less stable than the acetophenone monomer **A4II**, which suggests that the phenolate monomer could be the most likely precursor for any repolymerization reaction taking place and the KOH-catalyzed system would undergo the highest amount of repolymerization (Toledano et al., 2012) as it forms the least stable phenol motif at $\Delta G(A4I)^{KOH}$ = 37.3 kcal mol^{-1}. The acetophenone monomer **A4II** was formed *via* rearrangement

of the hydroxyvinyl-syringol in **A3** and was found to be the thermodynamically preferred product. This is expected since the equilibrium between an enol and a ketone lies far toward the keto form. It is, however, unlikely that the rearrangement would go *via* **TS2** since the activation barrier is very high (*E*a = 44.2 kcal mol^{-1}). The activation barrier and formation energy obtained for all base-catalyzed reactions is the same for the formation of **A4II**.

In the reaction of NaOH with the C2 β-O-4 substrate, the intermediate $\mathbf{A2}^{\mathbf{NaOH}}$ is exergonic by −4.4 kcal mol^{-1}. Catalytic C-O bond cleavage proceeds with an activation barrier of 11.9 kcal mol^{-1} and formation of the sodium phenolate and hydroxyvinyl-syringol intermediates $\mathbf{A3}^{\mathbf{NaOH}}$ is exergonic by −24.9 kcal mol^{-1}.

Conversion of the phenolate in $\mathbf{A3}^{\mathbf{NaOH}}$ to the phenol $\mathbf{A4I}^{\mathbf{NaOH}}$ is endergonic by 3.1 kcal mol^{-1}, while the rearrangement of the hydroxyvinyl-syringol into the more stable 3,5-dimethoxy-4-hydroxyacetophenone $\mathbf{A4II}^{\mathbf{NaOH}}$ has an activation barrier of 44.2 kcal mol^{-1} and is exergonic by 20.7 kcal mol^{-1}, as shown in **Figure 2**. For the reaction involving KOH, $\mathbf{A2}^{\mathbf{KOH}}$ is exergonic by 33.9 kcal mol^{-1} while C-O bond cleavage is exergonic by 29.6 kcal mol^{-1} and needs to overcome an activation barrier of 6.1 kcal mol^{-1}. Formation of $\mathbf{A4I}^{\mathbf{KOH}}$ is endergonic by 37.3 kcal mol^{-1} while the formation of $\mathbf{A4II}^{\mathbf{KOH}}$ has an activation barrier of 44.3 kcal mol^{-1} and is exergonic by 20.6 kcal mol^{-1}, as shown in **Figure 3**.

The LiOH-catalyzed reaction shows the formation of $\mathbf{A2}^{\mathbf{LiOH}}$ to be exergonic by 2.5 kcal mol^{-1}. the TS for the C-O bond cleavage has not been obtained in the solvated phase, but the C-O cleavage is exergonic by 22.3 kcal mol^{-1}. Formation of $\mathbf{A4I}^{\mathbf{LiOH}}$ is slightly exergonic by 1.4 kcal mol^{-1}, while the formation of $\mathbf{A4II}^{\mathbf{LiOH}}$ has an activation barrier of 44.2 kcal mol^{-1} and is exergonic by 20.7 kcal mol^{-1}, as shown in **Figure 4**. In the reaction with NaO^{t}Bu, the formation of $\mathbf{A2}^{\mathbf{NaO}t\mathbf{Bu}}$ is almost thermos-neutral having a reaction energy of −0.6 kcal mol^{-1}, whilst C-O bond cleavage proceeds with an activation barrier of 12.7 kcal mol^{-1} and is exergonic 23.9 kcal mol^{-1}. Formation of $\mathbf{A4I}^{\mathbf{NaO}t\mathbf{Bu}}$ is slightly exergonic by 1.7 kcal mol^{-1}, while $\mathbf{A4II}^{\mathbf{NaO}t\mathbf{Bu}}$ has an activation barrier of 44.3 kcal mol^{-1} and is found to be exergonic by 20.6 kcal mol^{-1}, as shown in **Figure 5**.

Base-Catalyzed Cleavage of C3 β-O-4 Substrate

The base-catalyzed cleavage of the C3 β-O-4 substrate also shows the presence of an intermediate, as was observed in the C2 cleavage reaction, although the solvated phase calculations show the intermediate **B2** to be quite unstable $\Delta G(B2)^{NaOH}$ = 0.03 kcal mol^{-1}, $\Delta G(B2)^{KOH}$ = −1.8 kcal mol^{-1}, $\Delta G(B2)^{LiOH}$ = 1.3 kcal mol^{-1}, $\Delta G(B2)^{NaOtBu}$ = 1.9 kcal mol^{-1}, where for the NaOH-catalyzed reaction the formation of the intermediate is almost thermos-neutral, while the NaO^{t}Bu-catalyzed reaction gives the least stable intermediate and KOH gives the most stable intermediate. The catalytic cleavage is found to be an exergonic process that proceeds *via* two pathways (**Scheme 3**). The first pathway (Path I) involves a 6-membered transition state **TSBI** similar to that seen for the C2 substrate cleavage, wherein the hydroxide ion deprotonates the α-carbon which promotes C-O bond cleavage. The second pathway (Path II) shows an 8-membered transition state which involves the C-O bond cleavage accompanied by a hydrogen hop from the oxygen on the γ-carbon to the base hydroxide, followed by another hydrogen hop from the oxygen on the α-carbon to the deprotonated oxygen on the γ-carbon, resulting in the formation of an oxirane ring. This mechanism could be said to be akin to the Grotthuss mechanism, (Agmon, 1995) albeit, that the subject has been discussed in respect of hydroxonium ions or a network of water molecules (Roberts et al., 2011b; Chen et al., 2013). The observed mechanism for the proton transfer is similar to that discussed by Tuckerman et al. (Tuckerman et al., 2002) and it involves an initial reorientation of the coordinated complex **B2** (**Scheme 3**), whereas the movement of the hydroxyl ion of the base is accompanied by a hyper-coordination of the hydroxide ion on the γ-carbon, while the hydroxide ion on the α-carbon provides the incoming proton which replaces the proton transferred to the hydroxyl ion. **Figure 6** shows the optimized geometries and relative energies of the stationary points for the cleavage of the C3 substrate using NaOH. Path I is found to be the thermodynamically favored pathway, having an activation barrier of 13.9 kcal mol^{-1} and a reaction energy of −30.8 kcal mol^{-1}, while path II is the kinetically favored pathway having an activation barrier 6.7 kcal mol^{-1} and a reaction energy of −18.9 kcal mol^{-1}.

Table 1 shows the relative energies obtained for the use of KOH, LiOH and NaO^{t}Bu as catalysts for the cleavage of the C3 β-O-4 substrate. Reaction with KOH has the lowest activation barrier along both pathways (Path I and Path II) at E_a^{KOH} = 10.1 and 3.9 kcal mol^{-1}, respectively while C-O bond cleavage is exergonic by 33.0 and 21.1 kcal mol^{-1}. Along Path I, the LiOH-catalyzed reaction has an activation barrier of 20.7 kcal mol^{-1} and a reaction energy of −27.6 kcal mol^{-1}, while the NaO^{t}Bu-catalyzed reaction has an activation barrier of 16.4 and a reaction energy of −27.8 kcal mol^{-1}. Along Path II, the LiOH-catalyzed reaction has an activation barrier of 11.4 kcal mol^{-1} and a reaction energy of −15.7 kcal mol^{-1} while the NaO^{t}Bu-catalyzed reaction has an activation barrier of 11.3 kcal mol^{-1} and a reaction energy of −15.9 kcal mol^{-1}. This shows that along

TABLE 2 | Rate constants (in s^{-1}) for the catalyzed cleavage of the C-O bond in a C2 and C3 β- O-4 linkage using NaOH, KOH, LiOH and NaO^{t}Bu.

Base catalyst	C2 cleavage/S^{-1}	C3 cleavage(path I)/S^{-1}	C3 cleavage(path II)/S^{-1}
NaOH	1.2×10^{4}	4.0×10^{2}	7.6×10^{7}
KOH	2.1×10^{8}	2.4×10^{5}	8.6×10^{9}
LiOH	1.6×10^{-5a}	4.2×10^{-3}	2.7×10^{4}
NaO^{t}Bu	3.0×10^{3}	$5.9 \times 10^{^\circ}$	3.2×10^{4}

[a]*Gas phase activation energy used since TS1 for LiOH, catalyzed cleavage of the C2-substrate could only be obtained in the gas phase.*

path I, the reaction involving NaOH is kinetically favored over the NaO^{t}Bu-catalyzed reaction by 2.5 kcal mol^{-1} and over the LiOH-catalyzed reaction by 6.8 kcal mol^{-1}. However, along path II the NaOH-catalyzed reaction is kinetically favored over both the LiOH-catalyzed and the NaO^{t}Bu-catalyzed reaction by 4.7 and 4.6 kcal mol^{-1}, respectively. This shows LiOH and NaO^{t}Bu to have comparable catalytic activity for the cleavage of the C3 β-O-4 ether linkage found in lignin.

Rate Constants for the Cleavage Reactions

The rate constants for all base-catalyzed cleavage reactions were calculated using the equation derived from the transition state theory (McQuarrie and Simon, 1997):

$$k(T) = \frac{K_B T}{hc^{\circ}} e^{-\Delta^{\ddagger}G^{\circ}/RT} \quad (1)$$

Where c° is the standard concentration taken as 1, T = 298.15 K and $\Delta^{\ddagger}G^{\circ}$ is the free energy of activation obtained for the reactions. The computed rate constants for all three base-catalyzed reactions studied are shown in **Table 2**.

As expected, the KOH-catalyzed reaction proceeds much faster along all pathways and for both types of β-O-4 linkage studied.

CONCLUSION

This study has shown that the base-catalyzed cleavage of the β-O-4 ether linkage in lignin begins with the formation of an intermediate, which is stabilized owing to electrostatic interactions between the hydroxide ion of the base and hydrogens on the phenyl ring adjacent to the ether bond. The transition state for the C-O bond cleavage in the β-O-4 linkage which does not contain a γ-carbinol (C2-substrate) involves a 6-membered transition state in which the hydroxide ion deprotonates the α-carbon adjacent to the ether bond and C-O bond cleavage occurs. In contrast, the cleavage of the β-O-4 linkage containing a γ-carbinol (C3-substrate) can proceed *via* two pathways: a thermodynamically favored pathway involving a TS similar to that of the C2-substrate and a kinetically favored pathway involving a unique 8-membered TS in which the C-O cleavage is accompanied by a hydrogen hopping event which could be akin to the Grotthuss mechanism. The thermodynamically favored pathway is also the preferred pathway for the isolation of the enol-containing monomer, while the kinetically favored pathway is the preferred pathway for the isolation of the epoxide-containing monomer. For the cleavage of the C2 substrate, the order of activation barriers with respect to the bases studied is LiOH > NaO^{t}Bu > NaOH > KOH. The same order is observed along path I for the cleavage of the C3 substrate, while along path II the order of the activation energy barrier is LiOH = NaO^{t}Bu > NaOH > KOH. The rate constants have also been calculated using the activation energies obtained, which show that the stronger base KOH rapidly promotes the C-O bond cleavage, in agreement with reports from experiment. These conclusions provide clarity on the mechanism of the base-catalyzed depolymerization of lignin to form phenolic monomers and suggest KOH and NaOH to be the preferred catalysts for the C-O bond cleavage in the β-O-4 linkage found in lignin.

DATA AVAILABILITY STATEMENT

The original contributions presented in the study are included in the article/**Supplementary Material**, further inquiries can be directed to the corresponding author.

AUTHOR CONTRIBUTIONS

RT, EA, and NHdL conceived study. MM run calculations. MM, RT, and EA analyzed results. MM, RT, EA, and NHdL wrote paper.

ACKNOWLEDGMENTS

The authors are grateful to the Royal Society and the UK Department for International Development for a research grant under the Africa Capacity Building Initiative (ACBI) which funded this research, and to the Centre for High Performance Computing, South Africa, for access to additional computing facilities. MM, RT, and EA are also grateful to the National Council for TertiaryEducation, Ghana, for a Teaching and Learning Innovation Fund (TALIF) grant.

SUPPLEMENTARY MATERIAL

The Supplementary Material for this article can be found online at: https://www.frontiersin.org/articles/10.3389/fchem.2022.793759/full#supplementary-material

REFERENCES

Agmon, N. (1995). The Grotthuss Mechanism. *Chem. Phys. Lett.* 244, 456–462. doi:10.1016/0009-2614(95)00905-j

Akhtari, S., Sowlati, T., and Day, K. (2014). Economic Feasibility of Utilizing forest Biomass in District Energy Systems - A Review. *Renew. Sustain. Energ. Rev.* 33, 117–127. doi:10.1016/j.rser.2014.01.058

Azadi, P., Inderwildi, O. R., Farnood, R., and King, D. A. (2013). Liquid Fuels, Hydrogen and Chemicals from Lignin: A Critical Review. *Renew. Sustain. Energ. Rev.* 21, 506–523. doi:10.1016/j.rser.2012.12.022

Chakar, F. S., and Ragauskas, A. J. (2004). Review of Current and Future Softwood Kraft Lignin Process Chemistry. *Ind. Crops Prod.* 20, 131–141. doi:10.1016/j.indcrop.2004.04.016

Chen, C., Huang, C., Waluyo, I., Nordlund, D., Weng, T.-C., Sokaras, D., et al. (2013). Solvation Structures of Protons and Hydroxide Ions in Water. *J. Chem. Phys.* 138, 154506. doi:10.1063/1.4801512

Dutta, S., De, S., Saha, B., and Alam, M. I. (2012). Advances in Conversion of Hemicellulosic Biomass to Furfural and Upgrading to Biofuels. *Catal. Sci. Technol.* 2, 2025–2036. doi:10.1039/c2cy20235b

Elder, T. (2014). Bond Dissociation Enthalpies of a Pinoresinol Lignin Model Compound. *Energy Fuels* 28 (2), 1175–1182. doi:10.1021/ef402310h

Frisch, M. J., Trucks, G. W., Schlegel, H. B., Scuseria, G. E., Robb, M. A., Cheeseman, J. R., et al. (2016). *Gaussian 09 (Revision A. 02)*. Wallingford CT: Computer Software, Gaussian, Inc.

Hileman, J. I., and Stratton, R. W. (2014). Alternative Jet Fuel Feasibility. *Transport Policy* 34, 52–62. doi:10.1016/j.tranpol.2014.02.018

Hu, L., Pan, H., Zhou, Y., and Zhang, M. (2011). Methods to Improve Lignin's Reactivity as a Phenol Substitute and as Replacement for Other Phenolic Compounds: A Brief Review. *BioRes* 6, 3515–3525. doi:10.15376/biores.6.3.3515-3525

Huber, G. W., Iborra, S., and Corma, A. (2006). Synthesis of Transportation Fuels from Biomass: Chemistry, Catalysts, and Engineering. *Chem. Rev.* 106, 4044–4098. doi:10.1021/cr068360d

Kleine, T., Buendia, J., and Bolm, C. (2013). Mechanochemical Degradation of Lignin and wood by Solvent-free Grinding in a Reactive Medium. *Green. Chem.* 15, 160–166. doi:10.1039/c2gc36456e

Lavoie, J.-M., Baré, W., and Bilodeau, M. (2011). Depolymerization of Steam-Treated Lignin for the Production of green Chemicals. *Bioresour. Techn.* 102, 4917–4920. doi:10.1016/j.biortech.2011.01.010

Mcdonough, T. J. (1993). The Chemistry of Organosolv Delignification. *Tappi.*, 76, 186–193.

McQuarrie, D. A., and Simon, J. D. (1997). "Chemical Kinetics I: Rate Laws," in *Physical Chemistry:A Molecular Approach* (Suasalito: University Science Books), 1165–1169.

Mennucci, B., Cancès, E., and Tomasi, J. (1997). Evaluation of Solvent Effects in Isotropic and Anisotropic Dielectrics and in Ionic Solutions with a Unified Integral Equation Method: Theoretical Bases, Computational Implementation, and Numerical Applications. *J. Phys. Chem. B* 101, 10506–10517. doi:10.1021/jp971959k

Miguel, E. L. M., Calik, I. L., Santos, C. M. S., and Jr Josefredo, R. P. (2016). How Accurate Is the SMD Model for Predicting Free Energy Barriers for Nucleophilic Substitution Reactions in Polar Protic and Dipolar Aprotic Solvents. *J. Chem. Soc. Brazil Sociedade Brasileira de Quimica* 27 (11), 2055–2061. doi:10.5935/0103-5053.20160095

Pandey, M. P., and Kim, C. S. (2011). Lignin Depolymerization and Conversion: A Review of Thermochemical Methods. *Chem. Eng. Technol.* 34, 29–41. doi:10.1002/ceat.201000270

Parthasarathi, R., Romero, R. A., Redondo, A., and Gnanakaran, S. (2011). Theoretical Study of the Remarkably Diverse Linkages in Lignin. *J. Phys. Chem. Lett.* 2 (20), 2660–2666. doi:10.1021/jz201201q

Peng, C., and Bernhard Schlegel, H. (1993). Combining Synchronous Transit and Quasi-Newton Methods to Find Transition States. *Isr. J. Chem.* 33, 449–454. doi:10.1002/ijch.199300051

Rassolov, V. A., Pople, J. A., Ratner, M. A., and Windus, T. L. (1998). 6-31G* Basis Set for Atoms K through Zn. *J. Chem. Phys.* 109, 1223–1229. doi:10.1063/1.476673

Roberts, S. T., Ramasesha, K., Petersen, P. B., Mandal, A., and Tokmakoff, A. (2011). Proton Transfer in Concentrated Aqueous Hydroxide Visualized Using Ultrafast Infrared Spectroscopy. *J. Phys. Chem. A.* 115, 3957–3972. doi:10.1021/jp108474p

Roberts, V., Fendt, S., Lemonidou, A. A., Li, X., and Lercher, J. A. (2010). Influence of Alkali Carbonates on Benzyl Phenyl Ether Cleavage Pathways in Superheated Water. *Appl. Catal. B: Environ.* 95, 71–77. doi:10.1016/j.apcatb.2009.12.010

Roberts, V. M., Stein, V., Reiner, T., Lemonidou, A., Li, X., and Lercher, J. A. (2011). Towards Quantitative Catalytic Lignin Depolymerization. *Chem. Eur. J.* 17, 5939–5948. doi:10.1002/chem.201002438

Ruppert, A. M., Weinberg, K., and PalKovits, R. (2012). Hydrogenolysis Goes Bio: from Carbohydrates and Sugar Alcohols to Platform Chemicals. *Angew. Chem. Int. Ed.* 51, 2564–2601. doi:10.1002/anie.201105125

Sergeev, A. G., and Hartwig, J. F. (2011). Selective, Nickel-Catalyzed Hydrogenolysis of Aryl Ethers. *Science* 332, 439–443. doi:10.1126/science.1200437

Spartan (2011). *Spartan Student Overview*. Irvine, CA: Wavefunction, Inc. 18401 Von Karman Ave., #37092715.

Toledano, A., Serrano, L., and Labidi, J. (2014). Improving Base Catalyzed Lignin Depolymerization by Avoiding Lignin Repolymerization. *Fuel* 116, 617–624. doi:10.1016/j.fuel.2013.08.071

Toledano, A., Serrano, L., and Labidi, J. (2012). Organosolv Lignin Depolymerization with Different Base Catalysts. *J. Chem. Technol. Biotechnol.* 87, 1593–1599. doi:10.1002/jctb.3799

Tuckerman, M. E., Marx, D., and Parrinello, M. (2002). The Nature and Transport Mechanism of Hydrated Hydroxide Ions in Aqueous Solution. *Nature* 417, 925–929. doi:10.1038/nature00797

Zhao, Y., and Truhlar, D. G. (2008). The M06 Suite of Density Functionals for Main Group Thermochemistry, Thermochemical Kinetics, Noncovalent Interactions, Excited States, and Transition Elements: Two New Functionals and Systematic Testing of Four M06-Class Functionals and 12 Other Functionals. *Theor. Chem. Account.* 120, 215–241. doi:10.1007/s00214-007-0310-x

Conflict of Interest: The authors declare that the research was conducted in the absence of any commercial or financial relationships that could be construed as a potential conflict of interest.

Publisher's Note: All claims expressed in this article are solely those of the authors and do not necessarily represent those of their affiliated organizations, or those of the publisher, the editors and the reviewers. Any product that may be evaluated in this article, or claim that may be made by its manufacturer, is not guaranteed or endorsed by the publisher.

frontiers in Chemistry

ORIGINAL RESEARCH
published: 21 February 2022
doi: 10.3389/fchem.2022.839867

Platinum Nanocatalysts Supported on Defective Hollow Carbon Spheres: Oxygen Reduction Reaction Durability Studies

*Victor Mashindi[1], Pumza Mente[1], Tumelo N. Phaahlamohlaka[1], Nobuhle Mpofu[2], Ofentse A. Makgae[3], Beatriz D. Moreno[4], Dean H. Barrett[1], Roy P. Forbes[1], Pieter B. Levecque[2], Kenneth I. Ozoemena[1] and Neil J. Coville[1]**

[1]*Molecular Sciences Institute, School of Chemistry, University of the Witwatersrand, Johannesburg, South Africa,* [2]*HySA Catalysis Centre of Competence, Department of Chemical Engineering, Catalysis Institute, University of Cape Town, Cape Town, South Africa,* [3]*National Centre for High-resolution Electron-microscopy (nCHREM), Centre for Analysis and Synthesis NanoLund, Lund University, Lund, Sweden,* [4]*Canadian Light Source Inc., Saskatoon, SK, Canada*

OPEN ACCESS

Edited by:
Guohua Jia,
Curtin University, Australia

Reviewed by:
Dunfeng Gao,
Dalian Institute of Chemical Physics (CAS), China
Ligang Feng,
Yangzhou University, China

***Correspondence:**
Neil J. Coville
neil.coville@wits.ac.za

Specialty section:
This article was submitted to Nanoscience, a section of the journal Frontiers in Chemistry

Received: *20 December 2021*
Accepted: *24 January 2022*
Published: *21 February 2022*

Citation:
Mashindi V, Mente P, Phaahlamohlaka TN, Mpofu N, Makgae OA, Moreno BD, Barrett DH, Forbes RP, Levecque PB, Ozoemena KI and Coville NJ (2022) Platinum Nanocatalysts Supported on Defective Hollow Carbon Spheres: Oxygen Reduction Reaction Durability Studies. Front. Chem. 10:839867. doi: 10.3389/fchem.2022.839867

The durability and long-term applicability of catalysts are critical parameters for the commercialization and adoption of fuel cells. Even though a few studies have been conducted on hollow carbon spheres (HCSs) as supports for Pt in oxygen reduction reactions (ORR) catalysis, in-depth durability studies have not been conducted thus far. In this study, Pt/HCSs and Pt/nitrogen-doped HCSs (Pt/NHCSs) were prepared using a reflux deposition technique. Small Pt particles were formed with deposition on the outside of the shell and inside the pores of the shell. The new catalysts demonstrated high activity (>380 μA cm^{-2} and 240 mA g^{-1}) surpassing the commercial Pt/C by more than 10%. The catalysts demonstrated excellent durability compared to a commercial Pt/C in load cycling, experiencing less than 50% changes in the mass-specific activity (MA) and surface area-specific activity (SA). In stop-start durability cycling, the new materials demonstrated high stability with more than 50% retention of electrochemical active surface areas (ECSAs). The results can be rationalised by the high BET surface areas coupled with an array of meso and micropores that led to Pt confinement. Further, pair distribution function (PDF) analysis of the catalysts confirmed that the nitrogen and oxygen functional groups, as well as the shell curvature/roughness provided defects and nucleation sites for the deposition of the small Pt nanoparticles. The balance between graphitic and diamond-like carbon was critical for the electronic conductivity and to provide strong Pt-support anchoring.

Keywords: platinum, hollow carbon spheres, oxygen reduction (ORR), nanocarbon, pair distribution function, catalysis

INTRODUCTION

The global dependence on fossil fuels for everyday energy needs is detrimental to the long-term sustainability of the earth. Over the years, scientists have shown that the combustion of fossil fuels for energy is the driver of rising global temperatures, recurring droughts and other adverse weather and climatic conditions (Rashedi et al., 2020). Therefore, research efforts to find new sustainable energy sources and systems that have a neutral carbon footprint with good efficiencies are needed.

The use of hydrogen fuel cells, commonly referred to as proton exchange membrane fuel cells (PEMFCs), could provide one solution to environmental and energy problems. These PEMFCs use platinum or its composites as the cathodes and anodes for the generation of electric currents usable in power machinery and equipment. The critical hydrogen oxidation reaction (HOR, anode) or the oxygen reduction reaction (ORR, cathode) takes place on the Pt (Genorio et al., 2010). Currently, the state-of-the-art PEMFC catalyst is a Pt or a Pt/transition metal bimetallic catalyst placed on a variety of supports. Supports that have been used vary from structured carbons like nanotubes (CNTs), nanofibers (CNFs), carbon black (CB), broken hemispherical hollow carbons (BHCSs) as well as doped metal oxides and carbides (Mao et al., 2019; Jiménez-Morales et al., 2020; Mohideen et al., 2020; Wang et al., 2020; Mashindi et al., 2021). Carbon supports are favoured due to their different structured forms, their lightweight that is important for mobile applications, thermal stability for high-temperature applications, high surface area for nanoparticle deposition and gas diffusion, as well as their earth abundance. In these catalysts, the metal nanoparticles exist in high loadings to mitigate the slow kinetics and high overpotential, especially for ORR at the cathode (Park et al., 2020). These high loadings are one of the drivers of the high cost of fuel cells and their low durability due to agglomeration and dissolution of metal nanoparticles during the stressful events within a fuel cell operation cycle.

The other challenge associated with fuel cells is the modest durability of the carbon supports or the poor conductivity (and low surface area) of other supports like metal oxides. In fuel cells, degradation occurs during load cycling or during the stop-start events where cell potentials can surpass 1.5 V vs. RHE. Above these potentials, carbon is electrochemically oxidized to CO_2 and Pt is known to dissolve and redeposit on larger clusters facilitating the debilitating processes of dissolution and agglomeration (Sandbeck et al., 2020). These degradation processes lower the surface area of the catalyst materials resulting in lowered activities and efficiency of the fuel cells, especially over time. The long-term goal is thus to develop a highly durable catalyst that is cheap and can sustain operation over 5,000 h as proposed by the United States Department of Energy in its fuel cell blueprint (Ren et al., 2020). Though newer non-carbon supports for Pt have been discovered in the previous decade, the other favorable properties of structured carbons have made it difficult to completely dispose of carbon as the support of choice, hence the continuous study on how a structured carbon can enhance the durability of the fuel cell catalysts (Jackson et al., 2017; Mohamed et al., 2018; Jiménez-Morales et al., 2020). Even though a few studies have been conducted on Pt supported on hollow carbon spheres (HCSs) and nitrogen doped HCSs (NHCSs), detailed studies on durability protocols have not been comprehensively elucidated for these catalyst systems. In one study, Qian and colleagues studied platinum nanoparticles placed on the inner walls of hollow carbon spheres using a dual-templating method. In this method, the Pt was first deposited on silica spherical templates followed by covering with polydopamine and di-block copolymer micelles as soft templates. Subsequently, carbonization, annealing and etching of the silica template resulted in the formation of a Pt@HCS-mesoporous catalyst with outstanding stability in the methanol oxidation reaction. The electrochemical stability was attributed to the porous carbon shells providing pathways and channels for diffusion of reactants but also protecting the inner Pt particles from agglomeration (Qian et al., 2017). Separately, Zhang and co-workers studied Pt nanoparticles with high dispersion supported on hierarchical N-doped porous HCSs for methanol oxidation. The prepared Pt catalysts demonstrated higher methanol oxidation activity and tolerance for CO intermediates compared to commercial Pt/C benchmarks. They ascribed the favorable catalytic properties to the high dispersion of Pt particles due to the presence of the nitrogen species, the porous-thin mesoporous shell and the hollow macroporous core structure of the support (Zhang et al., 2015). Yan and co-workers deposited highly stable small-sized Pt particles on mesoporous hollow carbon spheres for the oxygen reduction reaction. They observed that the supports had a high BET surface area (1,163 $m^2 g^{-1}$), large pore volume (2.8 $cm^3 g^{-1}$) and mesoporous structure and they attributed the distribution and dispersion of small-sized Pt particles to these textual properties. In electrocatalytic reactions, they observed that the mass current density on Pt/HCS electrocatalyst was 1.7 times as high as that of commercial Pt/C in ORR. The stability of the electrocatalysts was attributed to the mesopores that provided a physical interaction force between the Pt and the HCSs. The researchers acknowledged both the superiority of Pt nanoparticles in electrocatalysis and the role of the mesoporous hollow carbon spheres. Also in other studies (Yan et al., 2013), the mesoporosity was shown to contribute to pore confinement of metal nanoparticles that enhanced the stability by reducing migration of the metals. However, in all these Pt/HCSs studies, very few comprehensive durability protocols for both the Pt and the carbon support have been reported on the materials (Wang et al., 2006; Wang et al., 2007; Sebastián et al., 2012; Hu et al., 2021).

Therefore, herein we report on the electrochemical activity and load cycling and stop-start durability of Pt nanoparticles supported on HCSs and NHCSs (ca. 40 wt.% loading) and compare the data to a commercial benchmark Pt/C catalyst (Yano et al., 2010; Lu et al., 2013; Lee et al., 2014). The work continues from an earlier paper that investigated placing Pt on broken HCSs (Mashindi et al., 2021). The load cycling and start-stop durability of these materials were investigated and the changes in activity and electrochemical surface area were measured and correlated with the durability data. The new Pt/HCSs and Pt/NHCSs were tested for ORR activity and durability.

Pair distribution functional analysis (combined with other techniques) provided key information on the Pt-C and Pt-NC interactions and allowed for explanation of the data in terms of surface interactions.

EXPERIMENTAL

Hydrofluoric acid (48%), cetyltrimethylammonium bromide (CTAB), ethylene glycol, absolute ethanol, melamine, methanol (99%), sulfuric acid (98%), platinum acetylacetonate

[Pt $(acac)_2$, 97%], tetraethyl orthosilicate (TEOS, 98%), resorcinol, formaldehyde (37%), Nafion perfluorinated resin solution (5 wt.% in aliphatic hydrocarbons and water) and ethylene glycol were all purchased from Sigma-Aldrich and used without further purification. Nochromix crystals (Gordax laboratories), ammonia solution (25%, Associated Chemical Enterprises), absolute ethanol (99.6%, MK chemicals), perchloric acid (70%, Suprapur, Merck), ultrapure water (18.2 MΩ cm, Merck-Millipore), alumina polish (0.05 and 0.1 μm and polishing cloths, Buehler), argon gas (99.99%, Afrox), oxygen gas (99.99%, Afrox), nitrogen gas (99.99%, Afrox), were obtained and used without further purification.

Synthesis of the Silica Templates, HCSs, NHCSs, Pt/HCSs and Pt/NHCSs Materials

The method described by Stober and colleagues was used, with minor changes, to prepare spherical silica templates (Stöber et al., 1968). In the synthesis method, absolute ethanol (490 ml) was stirred together with tetraethyl orthosilicate (TEOS, 50 ml), deionized water (50 ml) and ammonia solution (30 ml, 25%) at room temperature for 6 h. The silica particles were separated from the solution by centrifugation at 18,000 rpm and washed with 300 ml of a 50:50 vol.% absolute ethanol:deionized water solution. The silica particles were dried in an oven at 100°C overnight followed by calcination at 500°C. The formed silica particles (4.8 g) amounted to a yield of 92% based on the TEOS used.

To form the HCSs, a resin of resorcinol-formaldehyde (RF) was deposited on the silica (SiO_2) template. In the procedure, the silica powder (1.5 g) was dispersed by sonication in a solution of absolute ethanol (105 ml) and deionized water (25 ml). The surfactant and porogen, CTAB (2 g), was added to a premixed solution of 37% formaldehyde solution (0.3 ml) and resorcinol (0.3 g) and 25% NH_4OH solution (3 ml). The procedure proceeded with magnetic stirring for 24 h leading to the formation of SiO_2@RF as the solution turned deep brown with vigorous stirring. After 24 h the products were filtered and washed with 500 ml of deionized water, followed by drying in an oven overnight at 100°C (Mente et al., 2021).

The dried brown product (SiO_2@RF) was transformed into a carbonaceous material using a tubular horizontal furnace saturated with argon at 900°C. Typically, the SiO_2@RF (50 mg) was loaded into a quartz boat and placed in the centre of the furnace, under Ar flowing at 50 ml min^{-1}. The furnace was ramped up to 900°C at a heating rate of 10°C min^{-1} and kept isothermal for 2 h. The quartz boat was cooled using a fast flow of compressed air for 30 min. The black soot (SiO_2@C) was etched using a 10% HF solution in water (100 ml) for 24 h to remove the SiO_2 template. To prevent the room temperature evaporation of the HF solution, the etching was conducted in a sealed Teflon container placed in a fume hood. The solution was vacuum filtered, washed with copious amounts of DI water and dried in an oven at 100°C overnight. The formed HCSs were annealed in a tubular horizontal furnace at 900°C for 2 h at a heating rate of 10°C min^{-1} under an argon flow rate of 50 ml min^{-1}. The formed HCSs (600 mg) gave a yield of 88% based on the starting resorcinol and formaldehyde used.

The NHCSs were prepared from SiO_2@RF and melamine using the same tubular horizontal furnace. Typically, 0.2 g of SiO_2@RF was mixed with 0.2 g of melamine in a glass vial containing methanol (5 ml) followed by sonication for 30 min. The products were dried in an oven at 70°C for 2 h. The SiO_2@RF-melamine was transformed to SiO_2@NHCSs using the same procedure used for the SiO_2@HCSs, after etching with HF to give NHCSs (Dlamini et al., 2020).

The nominal 40 wt.% Pt/HCSs or Pt/NHCSs catalysts were prepared by dispersing HCSs or NHCSs (20 mg) and Pt $(acac)_2$ (27 mg) in a solution of absolute ethanol (100 ml), deionized water (10 ml) and ethylene glycol (10 ml) and the mixture sonicated for 30 min to allow for thorough mixing. The composite, placed in a round bottom flask (attached to a reflux condenser), was then placed in an oil bath heater. The bath was heated to 200°C at a slow heating rate of 2.5°C min^{-1} and kept isothermal for 2 h while the reaction continued under reflux. The reactor was allowed to cool naturally to room temperature, and the products were filtered under vacuum and washed twice with 300 ml deionized water followed by drying at 100°C (Teranishi et al., 1999).

Catalyst Characterization

TEM analysis was performed using a Tecnai T12 transmission electron microscope operating at 120 kV. Sample preparation was done by dispersing (under sonication) ca. 10 mg of each catalyst in 1 ml ethanol for 5 min. About 3 drops of the material rich ink were deposited onto a lacey carbon copper grid, and analysis by TEM was done after drying the samples in air. Particle size distributions of the Pt particles, HCSs and NHCSs, were obtained by measuring at least 100 particles using ImageJ. The powder X-ray diffraction measurements were carried out on a Bruker D2 phaser diffractometer with a Cu Kα radiation source operating at 40 kV to determine the crystalline phases present in the catalyst with 2Θ between 10° and 90°. Indexing the compounds detected by the PXRD technique was achieved using the EVA software. Particle sizes of platinum particles were calculated using the EVA software embedded Scherrer equation Thermal stability and metal loading of the catalysts was performed with a Perkin-Elmer STA6000 (TGA) analyser using N_2 as the purge gas (20 ml min^{-1}) and air for combustion (10 ml min^{-1}) and a heating rate of 10°C min^{-1}. Nitrogen adsorption/desorption was measured using a Micromeritics Tristar 3000 surface area and porosity analyser set at −195°C, with sample degassing conducted at 150°C overnight. Raman spectroscopy measurements were performed on a Horiba Jobin-Yvon Raman spectrometer with a laser wavelength of (λ = 514 nm). The XPS measurements were carried out using a Thermo Scientific ESCALAB 250Xi spectrometer with a monochromatic Al Kα (1,486.7 eV) source operating with an X-ray power of 300 W. Total scattering data were collected on the Brockhouse high-energy wiggler beamline at the Canadian Light Source using a wavelength of λ = 0.2081 Å and a PerkinElmer XRD1621 area detector placed 160 mm after the sample. The data were processed using GSAS-II (Toby and Von Dreele, 2013). The Qmax used to produce the PDF of the measured samples was 23.4 $Å^{-1}$. The instrumental resolution parameters Qdamp and

Qbroad, as defined in PDFgui software, were determined by fitting a Ni powder standard measurement. Further data analysis was done using the xPDFsuite.

Electrochemical Characterization

The electrochemical experiments were performed in a three-electrode cell at room temperature (approx. 25°C) in a solution of 0.1 M $HClO_4$ purged with nitrogen for cyclic voltammetry (CV) or oxygen for the oxygen reduction reaction (ORR) experiments. The counter electrode was a high surface area Pt wire and the reference electrode was Ag/AgCl (3.0 M KCl). All Ag/AgCl potentials were converted to RHE by calibrating the potential between the reference electrode and an *in-situ* RHE prepared by saturating a clean Pt wire immersed 0.1 M $HClO_4$ with hydrogen gas. Arbitrarily, no *i*R drop correction was conducted. For Pt and support durability studies, the high surface area Pt wire was replaced with a high surface area gold counter electrode. A catalyst thin film coated glassy carbon (GCE) electrode with a working area of 0.196 cm^2 was used as the working electrode (WE). The catalyst inks were prepared by dispersing about 5 mg of the catalyst in a solution of ultrapure water (1.5 ml, 18.2 MΩcm), isopropyl alcohol (3.5 ml, HPLC grade) and Nafion perfluorinated resin solution (20 µL, 5 wt. % in a mixture of lower aliphatic alcohols and water) followed by a low-temperature 30 min sonication. The electrochemical cell, electrolyte volumetric flasks, purge tubes and reference electrode bridge tubes were all thoroughly cleaned with a solution of Nochromix and concentrated sulfuric acid followed by multiple rinses in Merck-millipore ultra pure water. A Biologic SP300/VMP300 potentiostat coupled to a Gamry RDE (rotating disk electrode) 710 Rotator was used for CV and RDE measurements.

The potential of the WE was cycled between 0.0 and 1.2 V vs. RHE for 100 cycles at 100 mVs^{-1} until a reproducible CV was obtained. The scan rate was then reduced to 50 mVs^{-1} and the third cycle was used for the calculation of the electrochemical active surface area (ECSA) assuming a monolayer charge associated with hydrogen adsorption of 210 µCcm^{-2}. The area under the CV curve, representing the charge associated with the underpotential deposition of hydrogen (Q_{DES}), was integrated and used for the calculation of ECSA according to the equation:

$$ECSA = (Q_{DES}) / (210\mu C\,cm^{-2} \times L_{Pt}) \quad (1)$$

The L_{Pt} is the loaded amount of Pt particles on the 0.196 cm^2 surface area of the working electrode. Oxygen reduction reaction (ORR) I (current)-V (voltage) polarization curves were obtained at 1,600 rpm on the electro-catalyst coated working electrode. The WE was cycled at 10 mV s^{-1} between 0.0–1.2 V vs. RHE in the cathodic direction. To correct for non-ORR background current, the LSV obtained in the nitrogen saturated electrolyte without rotation was subtracted from that obtained from the oxygen saturated electrolyte. The kinetic ORR currents (I_k) were extracted from the measured ORR currents (I) and the limiting currents (I_{lim}) determined at 0.4 V vs. RHE using the Koutecky-Levich equation.

Finally, kinetic currents were normalised with the ECSA and the initial Pt mass loading to obtain the surface area-specific activity (SA), **Eq. 2**, and the mass-specific activity (MA), **Eq. 3**, respectively (Garsany et al., 2010).

$$SA = I_k / (Q_{DES}/210\mu C\,cm^{-2}) \quad (2)$$

$$MA = I_k\,(\mu A\,cm^{-2}) / L_{Pt}\,(\mu g\,cm^{-2}) \quad (3)$$

Durability load cycling was carried out after the measurement of the beginning of life (BOL) CV and ORR activity. Initially, the WE was cycled between 0.0–1.2 V vs. RHE at 100 mV s^{-1} to clean the catalysts of any impurities and contaminants and to produce a reproducible CV. Load cycling for catalyst durability measurements was carried out in a 0.1 M $HClO_4$ solution at 25°C, in a nitrogen saturated electrolyte. The WE was cycled at 50 mV s^{-1} between 0.6–1.0 V vs. RHE. Load cycling was carried out in units of 10, 100, and 1,000 cycles until when the 6,000th cycle was reached after 27 h of continuous cycling. As Pt durability was under investigation, in all durability experiments, the Pt counter electrode was replaced with a gold counter electrode of high surface area (Inaba, 2009).

Start-stop durability cycling was carried out after obtaining the beginning of life (BOL) ECSAs of the three catalysts. The WE electrode was cycled between 1.0–1.6 V vs. RHE at a scan rate of 50 mV s^{-1} in an N_2 saturated 0.1 M $HClO_4$ electrolyte at 25°C. Cycling was carried out for a total of 6,000 cycles with ECSA CVs sampled after 10, 100 and 1,000 cycles until the 6,000th cycle was reached after 27 h of continuous cycling and argon saturation (Ohma et al., 2011).

RESULTS AND DISCUSSION

Physicochemical Properties

The Raman spectra of the HCSs and NHCSs were recorded to determine the extent of carbon graphitization and the presence of defects in the material. The Raman spectra (**Supplementary Figures SI1A,B**) were deconvoluted into their respective D, D1, D2 and G bands (Ferrari and Robertson, 2004). The G band is attributed to the Raman vibration of sp^2 hybridized carbons while the D band is attributed to the Raman vibration of sp^3 hybridized carbons. The extent of graphitization was measured by the ratio of the D and the G band areas (I_D/I_G ratio). As expected, the HCSs with an I_D/I_G ratio of 0.98 were more graphitic when compared to the NHCSs, with an I_D/I_G ratio of 1.22. The nitrogen groups in the NHCSs introduced carbon vacancies in the structure of the NHCSs resulting in defects from displacement of carbon atoms by the nitrogen (Ewels and Glerup, 2005).

TEM images indicated the formation of Pt nanoparticles with a spherical morphology (**Figure 1**, **Supplementary Figure SI1**), with measured particle sizes of 3.9 ± 0.5 nm and 3.8 ± 0.6 nm for the Pt/HCSs and Pt/NHCSs respectively.

A high degree of Pt dispersion and lack of agglomeration is suggested by the small inter-particle distances of the Pt nanoparticles deposited on both supports (6.5 ± 1.9 nm for Pt/HCSs and 6.1 ± 1.1 nm for Pt/NHCSs (**Figure 1**, **Supplementary Figure SI1**). The presence of defects and electron-rich nitrogen

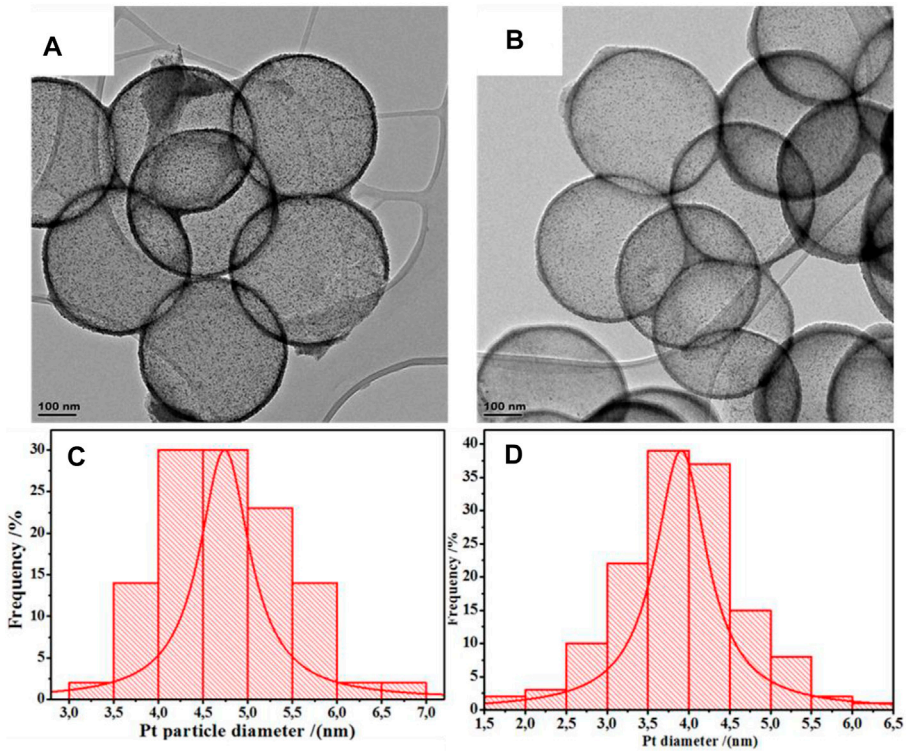

FIGURE 1 | TEM image of **(A)** Pt/HCSs, **(B)** Pt/NHCSs, and particle size distribution of Pt on Pt/HCSs **(C)**, and particle size distribution of Pt on Pt/NHCSs **(D)**.

functionalities on the supports provides numerous nucleation sites for Pt clusters during deposition, resulting in small Pt-Pt cluster distances (Galeano et al., 2014). It is suggested that during Pt deposition, the charge is transferred from the Pt metal particles to the π –conjugated system of the aromatic rings in the carbon structure as well as to the nitrogen groups supported on these carbon structures due to differences in electronegativity. This increase in electron density and uniformity on the support surface then promotes the deposition of particles of smaller size with small Pt –Pt cluster distances (Palaniselvam et al., 2014). Also, the N doped carbon distorts the surface of the supports causing distorted atomic layers on the surface and some dangling bonds which acts as the capture sites for fixing the Pt nanoparticles on the walls of the HCS/NHCSs (Du et al., 2008).

The HCSs and NHCSs were analysed using TGA (**Supplementary Figures SI1C,D**) to investigate the thermal stability of the materials under oxidizing conditions. Both the HCSs showed the expected thermal stability (HCSs at 660°C; NHCSs at 658°C). The TGA and DTGA profiles of Pt/HCSs and Pt/NHCSs recorded the residual PtO/PtO_2 species with Pt content >35 wt.% similar to the nominal 40 wt.% of both the Pt/HCSs and Pt/NHCSs catalysts. The deposition of Pt nanoparticles enhanced the combustion of the carbon, through the expected catalytic reaction of carbon with Pt (Mashindi et al., 2021) and consequently lowered the thermal stability of the materials as shown by the lower decomposition temperatures of the Pt/HCSs The decomposition of Pt/NHCSs also occurred at a lower temperature compared to the NHCSs, in agreement with the presence of defects on the NHCSs, as shown by Raman spectroscopy.

The surface area and porosity of the materials were measured using the BET technique. The materials demonstrated a type IV BET isotherm and microporosity (**Supplementary Figure SI3**). The pristine HCSs and the NHCSs had high BET surface areas of 832 and 604 m^2g^{-1}, respectively. The observed reduction in BET surface area and porosity after deposition in the Pt/HCSs and Pt/NHCSs respectively (**Supplementary Table SI1**) was attributed to pore blockage by the metal nanoparticles. The pore blockage is caused by both the "top of pore" and the "in pore" deposition of Pt, with the latter resulting in the confinement of the Pt particles (Galeano et al., 2012). The pore confinement in these supports was confirmed by the dark-field STEM images and elemental maps of Pt particles, which appear to be highly concentrated in the shell of the supports (**Supplementary Figure SI4**). Also, in these shell regions of the supports, the Pt maps indicate more than a single layer of Pt particles, indicating penetration into the HCSs/NHCSs shells by the Pt particles as it occupies the pores of the support. This is in agreement with studies on broken hemispherical carbon that were similarly prepared (Mashindi et al., 2021).

The XPS survey spectra for both Pt/HCSs and Pt/NHCSs are given in **Supplementary Figure SI5** and the deconvoluted spectra for Pt/NHCSs in **Figure 2**. The C1s spectra we deconvoluted (**Figure 2A**) into the respective sp^2 hybridized carbon, C=C (284.0 eV), amorphous diamond like carbon with sp^3 hybridization, C–C (284.6 eV), C=N/C-O (285.8 eV), C–N/

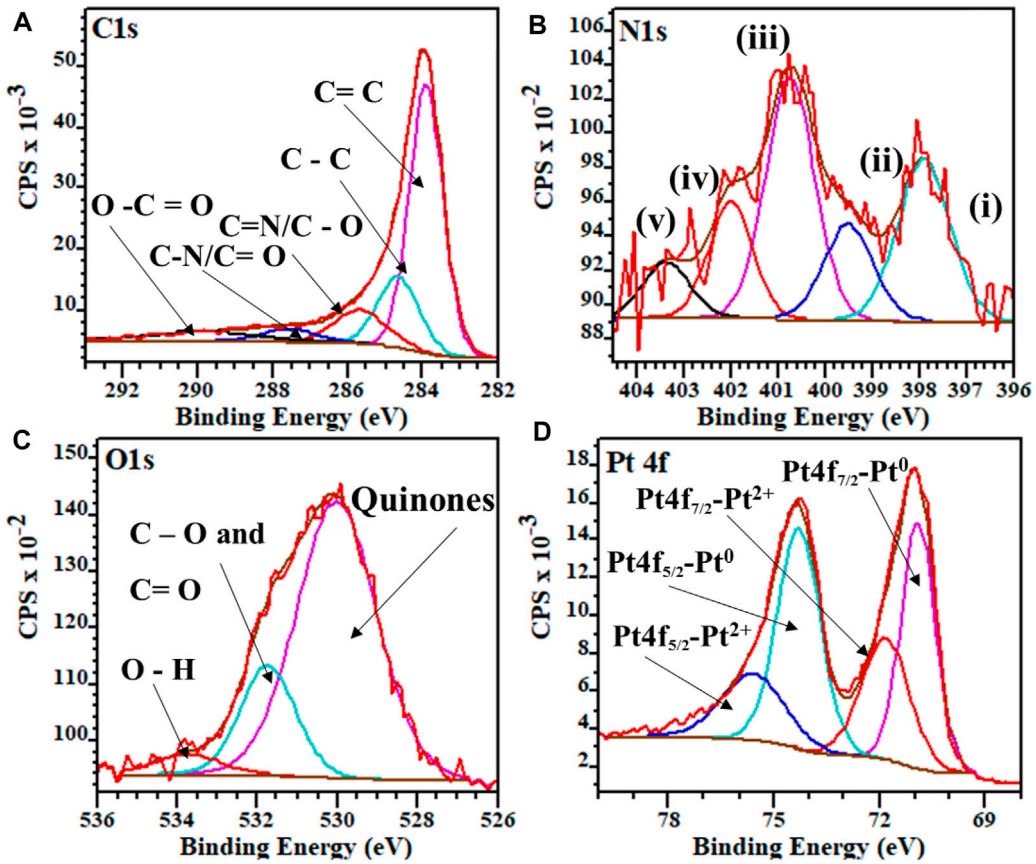

FIGURE 2 | Deconvoluted high-resolution XPS spectra for Pt/NHCSs **(A)** C1s, **(B)** N1s **(C)** O1s and **(D)** Pt 4f.

C=O (287.6 eV) and finally O–C=O (289.9 eV). The C=N and C-N bonds indicate the successful incorporation of the nitrogen functionalities into the carbon matrix of the NHCSs (Matsoso et al., 2016). The N1s spectra of the Pt/NHCSs was deconvoluted (**Figure 2B**) and revealed peaks for pyridinic N (i, 398.3 eV), pyrollic N (iii, 400.7 eV), graphitic N (iv, 401.9 eV), oxidized N (v, 403.1 eV) and metal bonded N (metal-N-pyridyl) nitrogen (ii, 399.7 eV) groups (Chen et al., 2017). The total contribution of the various N species was pyridinic (i, 30%), pyrollic N (iii, 40%), graphitic N (iv, 12%), oxidized N (v, 8%) and the metal bonded N (ii, 10%). The N content of Pt/NHCSs was found to be 7.4%. Deconvolution of the O1s spectra of the Pt/NHCSs (**Figure 2C** and **Supplementary Figure SI5**) showed the presence of quinones (530.1 eV), C=O and C–O bonds (531.8 eV), and terminal O–H bonds (533.9 eV) (Melke et al., 2016). The deconvoluted Pt 4f spectra (**Figure 2D**), indicate the presence of mostly metallic Pt and smaller amounts of oxidised Pt particles. The Pt 4f spectra were deconvoluted into the zero oxidation state metallic Pt, $Pt4f_{7/2}$ (71.1 eV) and $Pt4f_{5/2}$ (74.9 eV) and the +2 oxidation state of the Pt, $Pt4f_{7/2}$ (72.1 eV) and $Pt4f_{5/2}$ (76.2 eV), respectively, (Lu et al., 2016).

The crystallinity of the materials was investigated using PXRD. Both the HCSs and NHCSs showed a structure typical of a mix of

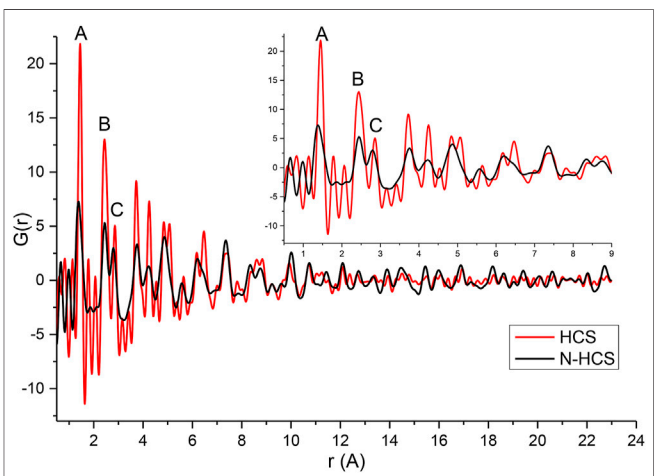

FIGURE 3 | Experimental G(r) of HCSs and NHCSs.

both graphitic and amorphous carbons, characterized by the broad 2ϴ PXRD peaks (25 and 45°) (Mente et al., 2021). The Pt on the HCSs and NHCSs showed reflections characteristic of the fcc unit cell of Pt (Sravani et al., 2020) (**Supplementary Figure SI6**). Using the Scherrer equation, the Pt crystallite sizes

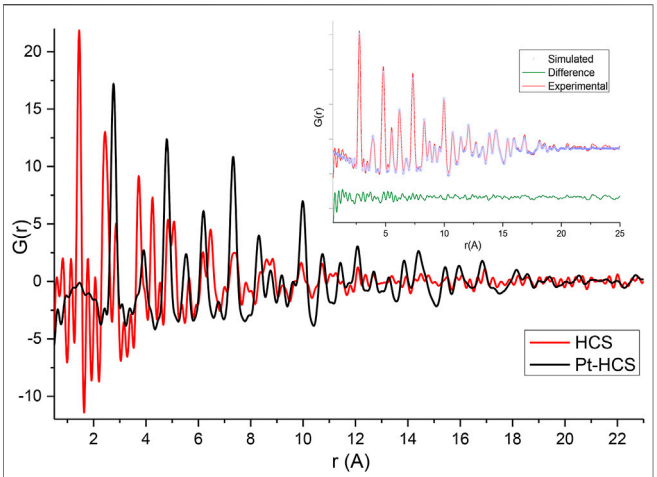

FIGURE 4 | Experimental G(r) of HCSs and Pt/HCSs. Insert—shows the PDF fitting of Pt/HCSs.

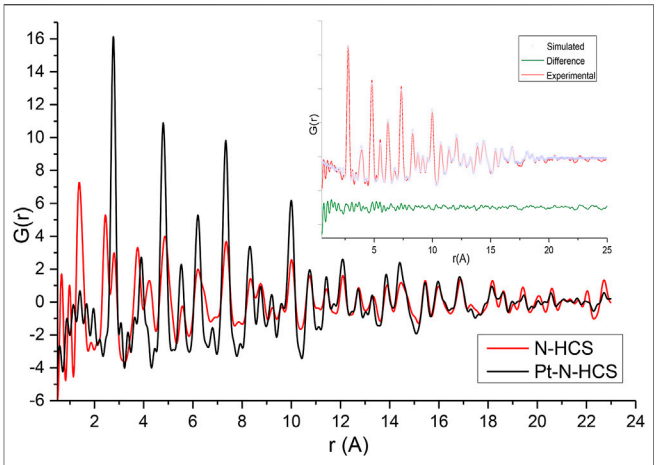

FIGURE 5 | Experimental G(r) of NHCSs and Pt/NHCSs. Insert—PDF fitting of Pt/NHCSs.

were determined to be 4.5 ± 0.8 and 4.3 ± 0.8 nm for Pt/HCSs and Pt/NHCSs, respectively.

To further explore the effect of nitrogen on the HCSs structure, total scattering data were obtained and are plotted in **Figure 3**, showing the experimental G(r) of the HCSs in red, and the NHCSs in black. Considering the pristine HCSs first, the peak position values denoted by A, B, and C closely match the expected real space values for in-plane carbon-carbon bond distances in the aromatic-type ring of graphite/graphene for the first three coordination spheres (Mildner and Carpenter, 1982; Krzton and Niewiara, 1995). The first peak (A) in G(r), at 1.45 Å, corresponds to the C-C bonds with three nearest neighbours to carbons with sp^2 bonding. The second peak (B) at 2.44 Å represents the distance between the three atoms coordinating a central carbon or the shortest diagonal in the hexagon. The third peak (C) at 2.86 Å, which is twice the first C-C distance, is the second, long diagonal in the hexagon. As can be seen from the simulation of graphite C-C bond distances in **Supplementary Figure SI7**. PDF data can easily distinguish between different carbon coordination environments.

The first peak, A, in the HCS is slightly shifted to a higher r with an integrated peak area of 3.24 implying the support also contains sp^3 bonds originating from a R-3m rhombohedral diamond-like structures, albeit in lesser amounts relative to the graphite/ene phase (Dmowski et al., 2012). Peak A in the nitrogen doped HCSs deviates from the expected *r* values due to the presence of pyridinic, pyrrolic, and graphitic nitrogen within the structure characterised by a peak position at 1.36 Å, in addition to peak broadening. Pyridinic type N defects are characterised by a peak at 1.33 Å due to the shortening of the C-N bond in comparison to the C-C bonds at 1.45 Å. As the NHCSs consist of a convolution of these bonds, a shortening and broadening of the bond peak position occurs. Further, a reduction in the diagonal length across the hexagon is observed from the 2.86 Å to 2.77 Å due to nitrogen substitution in the structure.

The carbon plane for both samples shows buckling as the position of the third coordination sphere (C) is not exactly half that of the second coordination sphere (B) (Dmowski et al., 2012). The NHCSs show increased buckling of the carbon plane compared to the pristine sample due to nitrogen doping. Furthermore, broadening of the NHCSs third coordination sphere (C) shows greater variations in the bond distances resulting from the strain induced by the buckling of the carbon plane. The broadening is seen in peaks A, B, and C and is a feature arising from highly defective structures in the NHCS. Broadening is also noted at real space distances coinciding with the peaks at 4.23, 4.86, 5.57, and 6.20 Å.

A gradual reduction in structural coherence with increasing distance (increasing r) from the scatterer is noted along the graphene sheet. This is likely due to the curvature of the sheets to form spheres, and the distribution of varying degrees of curvature in the sample, rather than from termination of sheet fragments. The effective atomic density of the scattering volume can be estimated from the slope of the measured G(r). For the HCSs and NHCSs samples the atomic density is 0.095 and 0.105 atoms/A^3 respectively which is just below the atomic density of graphite at 0.11 atoms/A^3 (Dmowski et al., 2012). No interlayer graphitic peaks are present in the PDFs (**Supplementary Figure SI8**). All peaks can be accounted for with the graphene, however, there is significant turbostratic and positional disorder from one graphene sheet to the next and the sheets are not stacked in perfect unison. This is probably a natural consequence of the curvature of the sheets when forming spheres and creating general disorder (Kane et al., 1996).

Atomic correlations are more significantly damped beyond 13 Å for HCS than NHCS. This is the range corresponding to the lateral coherence of the structures and also where stacking differences are important. This behaviour of G(r) indicates that short-range two-dimensional atomic order is similar to graphite but stacking along the c-axis is strongly disordered (Petkov et al., 1999). However, this is expected due to the relaxation of the edge atoms or strain induced by curvature. With increased deformation, tilting or folding of the layers to form spheres combined with weak van der Waals bonds between

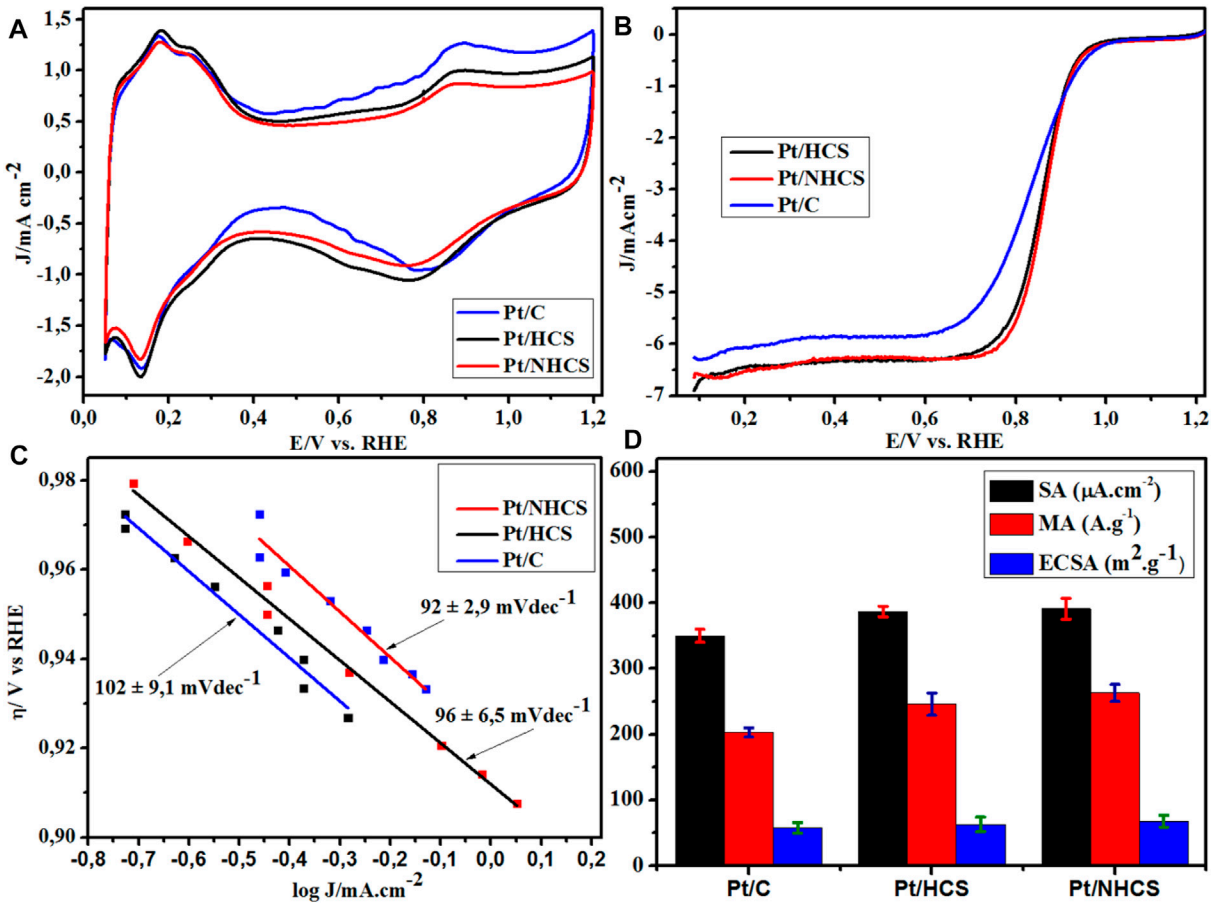

FIGURE 6 | The **(A)** cyclic voltammograms, **(B)** ORR polarization I-V curves, **(C)** Tafel plots and **(D)** ORR activity and ECSA data for the Pt/HCSs, Pt/NHCSs and the commercial benchmark Pt/C.

the layers result in structures that are prone to turbostratic disorder (Ramos-Sanchez and Balbuena, 2013).

The effect of the addition of Pt to the HCSs and N/HCSs was also evaluated from total scattering data. The PDFs of HCSs and Pt/HCSs are shown in **Figure 4**, and the PDFs of NHCSs and Pt/NHCSs are shown in **Figure 5**. The high Pt loading of 40 wt.% coupled with the large scattering cross section of Pt results in a Pt dominated PDF signal.

Fitting of the PDFs revealed mean Pt particle sizes of 2.6 and 2.4 nm for the Pt/HCSs and Pt/NHCSs, respectively. It is important to contrast the Pt particle sizes determined from XRD, TEM and PDF measurements. Considering XRD, Bragg diffraction has limitations in accurately determining particle sizes below 5 nm while the resolution and magnification of the TEM images likely result in an underrepresentation of very small particles smaller than 2.5 nm. PDF is highly sensitive to small particles as both Bragg and diffuse scattering are detected resulting in a more accurate particle size determination. The interaction of the Pt particles with the carbon surface has been shown to result in a local rearrangement of carbon atoms, with the stronger the adsorption energy, the larger the C–C bond elongation (Ramos-Sanchez and Balbuena, 2013). As seen in the TEM results, a distribution of Pt particle sizes is present on the surface of the spheres with high dispersion resulting in unequal Pt-carbon interactions that in turn result in variations in the bond lengths which further increases the disorder and defects in the HCS and NHCS structures.

The interaction energy between Pt and graphitic carbon has contributions from orbital hybridisation and van der Waals interactions. The van der Waals interactions are as large as the covalent bond contribution and cannot be neglected (Ramos-Sanchez and Balbuena, 2013). The van der Waals forces are needed to describe the system and contribute to maintaining the Pt linked to the carbon surface. Even though the adsorption energy of Pt has been shown to be weak *via* DFT calculations, this adsorption energy is proportional to the Pt particle sizes and has been shown to have profound effects on the Pt cluster properties (Ramos-Sanchez and Balbuena, 2013).

The lack of well-defined first, second, and third neighbour C-C distances clearly indicates that the aromatic-type rings are heavily distorted when Pt is present pointing to a significant rearrangement of the support structure caused by Pt addition. It must be noted that the carbon signal is also significantly dampened due to the presence of Pt at high wt% loadings (Li

TABLE 1 | Calculated ECSA and ORR activity for the Pt/HCSs, Pt/NHCSs and the commercial benchmark Pt/C catalysts. MA, SA, I_k measurements obtained at 0.90 V vs. RHE.

Catalyst	ECSA/(m^2g^{-1})	MA (0.90 V)/(Ag^{-1})	SA (0.90 V)/(μA cm^{-2})	I_k (0.90 V)/(mA cm^{-2})	$E_{1/2}$ V vs. RHE	E_{onset} V vs. RHE
Pt/C	58 ± 8	203 ± 7	350 ± 10	2.7 ± 0.6	0.831	1.022
Pt/HCSs	63 ± 11	246 ± 17	387 ± 8	2.9 ± 0.8	0.854	1.027
Pt/NHCSs	68 ± 9	263 ± 13	391 ± 16	3.1 ± 0.2	0.862	1.028

TABLE 2 | Comparison of the activity of the Pt/HCSs, Pt/NHCSs and commercial Pt/C before and after 6,000 durability cycles.

Catalyst	MA/(0.9 V) (m^2g^{-1}) Cycle 1	MA (0.9 V)/(Ag^{-1}) Cycle 6,000	SA (0.9 V)/(μA cm^{-2}) Cycle 1	SA (0.9 V)/(μA cm^{-2}) Cycle 6,000	Δ MA/%	Δ SA/%
Pt/C	203 ± 7	98 ± 13	350 ± 10	210 ± 13	51.7	40.1
Pt/HCSs	246 ± 17	138 ± 21	387 ± 8	300 ± 11	43.9	22.5
Pt/NHCSs	263 ± 13	139 ± 16	391 ± 16	310 ± 21	47.1	20.7

and Lannin, 1990). It is not surprising that no well-defined sheet-like patterns are observed in the corresponding TEM images of these samples.

Catalyst Activity

The Pt materials were studied using cyclic and linear sweep voltammetry for electrochemical surface area (ECSA) and ORR activity. The materials demonstrated a standard Pt/C cyclic voltammogram (**Figure 6A**), with typical peak features for hydrogen desorption, oxidation of the Pt, reduction of the Pt and adsorption/desorption of hydrogen (Garsany et al., 2010). The activity trends of the materials were obtained from the measured linear sweep voltammograms (LSVs), (**Figure 6B**). The Pt/NHCSs showed an earlier onset, higher half-wave potential ($E_{1/2}$) and kinetic current than the Pt/HCSs. The least active was the commercial benchmark Pt/C catalyst. The ORR onset, ECSAs, kinetic current and $E_{1/2}$ data are summarized in **Table 1**. The LSV ORR data was modelled to the Tafel equation,

$$\eta = a + b\log(j) \tag{4}$$

where η is the ORR overpotential, a is the Tafel constant or the over potential intercept of the Tafel plot, b is the Tafel slope and (j) is the ORR current density at a specific overpotential. The Tafel plots for the Pt/HCS, Pt/NHCS and Pt/C are shown in **Figure 6C**. The Pt/NHCSs has the lowest Tafel slope of 92 ± 2.9 $mVdec^{-1}$ compared to 96 ± 6.5 $mVdec^{-1}$ (Pt/HCSs) and 102 ± $mVdec^{-1}$ (commercial Pt/C), thereby confirming that ORR kinetics are more favourable on the nitrogen-doped catalyst, showing superiority to the commercial benchmark Pt/C (Chen et al., 2020).

The area-specific activities (SA) of the catalysts were obtained from the normalization of the kinetic current with the ECSAs of the catalysts. The Pt/NHCSs had a SA of 391 ± 16 A g^{-1}, the Pt/HCSs a value of 387 ± 8 A g^{-1}, both of which are ca. 10% larger than the commercial Pt/C (350 ± 10 A g^{-1}) catalyst (**Table 1**). The kinetic current of the catalysts was then normalized against the Pt loading on the WE to yield the mass-specific activities (MA) (**Figure 6D**). The observed trend shows that the Pt/NHCSs (263 ± 13 μA cm^{-2}) > Pt/HCSs (246 ± 17 μA cm^{-2}) >Pt/C (203 ± 7 μA cm^{-2}).

The variation of catalysts activity was attributed to the physicochemical properties of the supports and N doping which affected the electronic properties of the catalysts. The interaction of the Pt and the N groups altered the electronic properties of the Pt-support resulting in better activity and a better Pt-support interaction. From the Pt surface, electron density is transferred to the π-conjugated system on the surface of the nitrogen groups due to differences in electronegativity creating a sea of electron density between the Pt particles and the N-functionalized surface. The same is less true on a pristine carbon surface. Here charge transfer occurs but the higher electronegativity of oxygen terminal functional groups means more of the electron density from the Pt is transferred to the oxygen functional groups. Thus, less of the charge is transferred to the carbon surface. As a result, the sea of charge on the pristine support is smaller than that on the N doped surface. Thus, electron flow is much easier on the N-doped surface than on the pristine surface, resulting in better activity in the former (Panchenko et al., 2004; Ju et al., 2015; Lu et al., 2020).

The high BET surface area of the Pt/HCSs (555 m^2g^{-1}) and Pt/NHCSs (309 m^2g^{-1}) and an array of micro and mesopores promotes better mass transport of oxygen to the Pt active sites compared to the less porous Pt/C benchmark catalyst with a surface area <200 m^2g^{-1}. The larger pores in the Pt/HCSs (5.1 nm, 0.70 cm^3g^{-1}) and Pt/NHCSs (4.1 nm, 0.62 cm^3g^{-1}) facilitates better "in-pore" confinement of the Pt inside the pores and thereby promotes a better Pt-support contact (**Supplementary Figure SI4**). This is advantageous as it can result in a better support-Pt electronic conductivity and tethering.

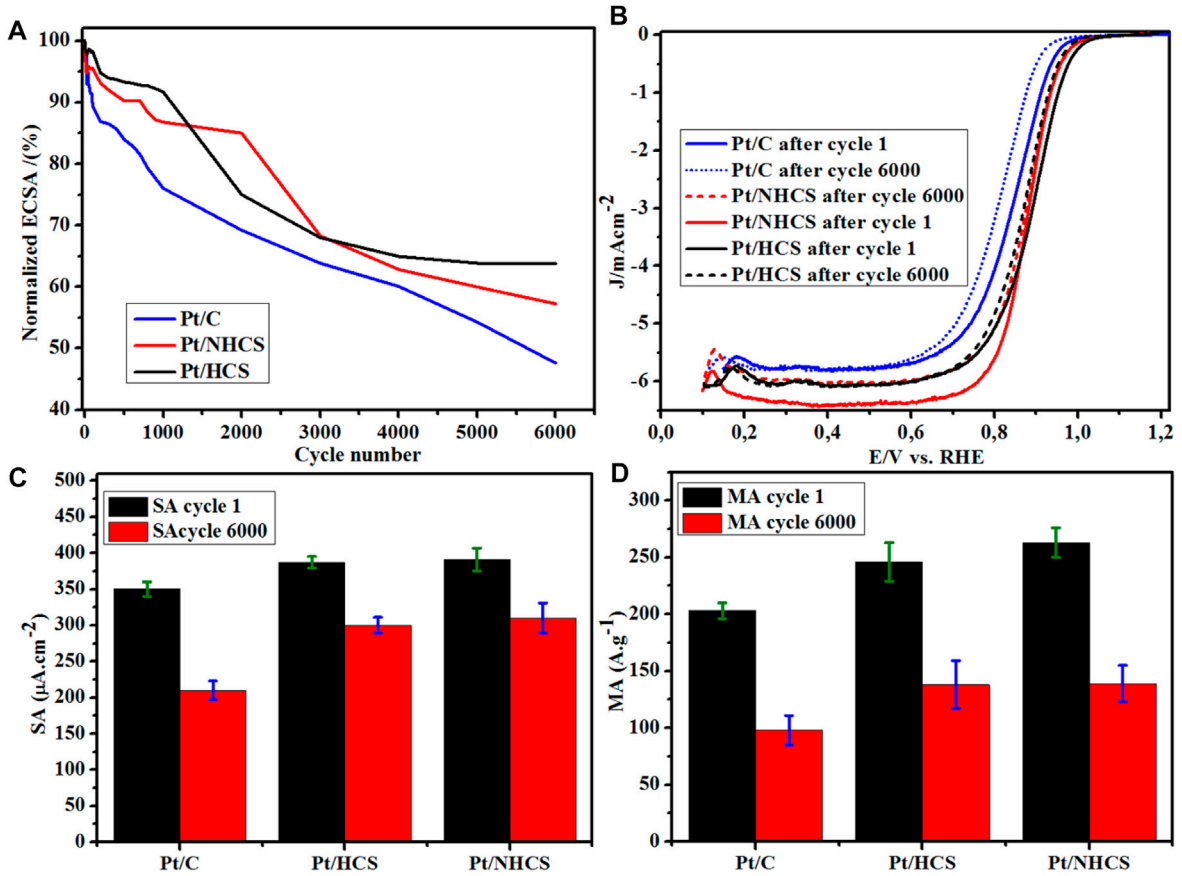

FIGURE 7 | (A) Normalized ECSA% degradation of the catalysts, **(B)** catalyst LSVs before and after durability studies for the Pt/HCSs, Pt/NHCSs and the commercial benchmark Pt/C catalysts, **(C)** SA data before and after durability studies, **(D)** MA data before and after durability studies.

Catalyst Durability

The catalysts were subjected to accelerated stress tests (AST) for 6,000 cycles at 50 mV s^{-1} from 0.6–1.0 V vs. RHE (**Supplementary Figure SI9**). The degradation of the Pt catalysts was observed as a decline in the normalized ECSA % as load cycling was proceeding (**Figure 7A**). Also observed was the reduction in the size of the regions of the CVs associated with hydrogen adsorption/desorption (**Supplementary Figure SI9**). The initial 1,000 cycles, saw the benchmark Pt/C maintaining 76.1% of the initial ECSA compared to 94.5% (Pt/HCSs) and 99.8% (Pt/NHCSs). After 5,000 cycles, the benchmark catalysts maintain 54.3% of initial ECSA compared to Pt/HCS (66.2%) and Pt/NHCS (62.1%). After 6,000 cycles, the lowest ECSA retention was observed for Pt/C (47.6%) compared to Pt/HCSs (65.4%) and Pt/NHCSs (62.1%). The decline in ECSA of the catalysts is evident from the comparison of the CVs of the catalyst before and after durability cycling (**Supplementary Figure SI10**).

The start-stop durability LSVs of the catalysts before and after the tests are shown in **Figure 7B**. Evident is the shift in the overpotential for the ORR reaction as shown in the catalyst LSVs. The bold lines are cycles before, and the dashed lines are data collected after 6,000 cycles of durability testing (**Figure 7B**). For the Pt/C catalyst, a measured 30 mV shift in the LSV is observed whereas for the Pt/HCSs (18 mV) and Pt/NHCSs (22 mV), the shifts are smaller. This shift in LSVs is attributed to the loss of activity due to the degradation of the Pt catalysts. The Pt catalysts degrade by dissolution according to the equations

$$Pt \rightarrow Pt^{2+} + 2e^{-} \qquad E^{\theta} = 1.18\ \text{V vs SHE} \quad (5)$$

Or

$$Pt + H_2O \rightarrow PtO + 2H^{+} + 2e^{-} \qquad E^{\theta} = 0.98\ \text{V vs SHE} \quad (6)$$

$$PtO + 2H^{+} \rightarrow Pt^{2+} + H_2O \quad (7)$$

The presence of a facial layer of oxide on the surface due to the presence of terminal oxygen functional groups as shown in the O1s spectra of the HCSs is responsible for part of the degradation of the Pt. The formation of the Pt –O bonds weakens the pre-existing Pt–Pt bonds. As the PtO can be further oxidised, higher-order Pt oxidation states such as Pt^{4+} in PtO_2, undergo dissolution faster than lower-order Pt species according to the equation.

$$PtO_2 + 4H^{+} + 2e^{-} \rightarrow Pt^{2+} + 2H_2O \quad (8)$$

$$E^{\theta} = 0.837 + 0.0295\log\left[Pt^{2+}\right] \quad (9)$$

(Cherevko et al., 2016).

The oxidation state of the Pt particles is closely related to Pt dissolution and Ostwald ripening processes. The cathodic dissolution of the Pt particles is a thermodynamically feasible process that occurs below 0.837 V according to **Eq. 9**. The low dissolution of the Pt and the retention of higher ECSA % on the HCSs and NHCSs based catalysts compared to the commercial catalysts could be attributed to the low oxygen functionalization and subsequently, the existence of lower percentages of higher-order Pt oxidation states. As shown by XPS data, the Pt in the Pt/HCSs and Pt/NHCSs exists mostly as metallic Pt with intact Pt –Pt bonds difficult to dissolve. The observed degradation could be initiated from Pt–O where dissolution led to the formation of $Pt^{2+}$and subsequently Pt^{4+} as further Pt oxidation occurred. Notwithstanding the quantifiable oxygen functionalities on the HCSs and NHCSs supports, significant confinement of the Pt particles inside the pores reduced the rate of migration of dissolved and undissolved Pt particles to form larger Pt clusters.

The shift in the LSVs is also observed in the changes in the MA and SA of the catalysts after durability tests (**Figures 7C,D**). There is an observed 51.7% change in MA for the benchmark Pt/C catalyst compared to 43.9% (Pt/HCSs) and 20.7% (Pt/NHCSs).

The decline in MA was also coupled with a decline in SA. For the benchmark Pt/C, a 40% decline was observed compared to a 22.4% (Pt/HCSs) and 20.7% (Pt/NHCSs) decline for the two new catalysts. Degradation in fuel cells is known to occur *via* processes that include Pt dissolution, Ostwald ripening, agglomeration, particle detachment as well as support corrosion (Simonsen et al., 2011). These processes result in the formation of bigger particle sizes with less ECSA compared to the initial smaller particles. The smaller ECSA of the newly formed bigger Pt crystallites produces a smaller under potential desorption charge of the hydrogen (Q_{DES}), and as shown by **Eqs 2**, **3** before, there affects the magnitude of the resultant MA and SA values.

The losses in ECSA, MA and SA were attributed to the agglomeration of Pt resulting in the formation of particles that are bigger and with less surface area. The growth in Pt particles can be seen from the comparison of the TEM images before and after stress testing (**Supplementary Figure SI11**). As shown in these figures, the Pt particle size increased for Pt/HCSs (3.9 ± 0.5 to 4.8 ± 1.2 nm), Pt/NHCSs (3.8 ± 0.6 to 4.9 ± 1.7 nm) and Pt/C (3.9 ± 1.1 to 6.3 ± 1.8 nm).

Support Durability

The support durability under load cycling conditions was evaluated by subjecting the WE modified by the materials to an accelerated stress test (AST) for 6,000 cycles at 50 mV s^{-1} from 1.0–1.6 V vs. RHE (**Supplementary Figure SI12**). Under load conditions, the carbon support is known to electrochemically corrode at potentials in the region of 1.5 V vs. RHE according to the equations

$$C + 2H_2O \rightarrow CO_2 + 4H + 4e^{-}tt \quad E^{\theta} = 0.2\ \text{V vs SHE} \quad (10)$$

Even though the thermodynamic potential for this process is lower (**Eq. 10**), at higher cell potentials of about 1.5 V vs. RHE, experimental data has shown that this oxidation process is significant (Labata et al., 2021).

The load cycling durability CVs shows a comparison between the before and after AST tests (**Figures 8A–C**). The CVs show the formation of the quinone/hydroquinone (Q-HQ) couple at about 0.60 V vs. RHE for the catalysts. This redox couple appears as a result of the reversible oxidation of the carbon support according to the equation

$$C{=}O\,(s) + H^{+} + e^{-} \rightarrow C - OH \quad (11)$$

The Q-HQ is a reversible process that does not represent the mass loss of carbon leading to the formation of CO_2 (Park et al., 2014). However, it demonstrates the susceptibility to oxidation of the carbon and its propensity for final corrosion.

There is a significant formation of the quinone/hydroquinone couple in the Pt/HCSs and the Pt/NHCSs compared to the commercial Pt/C. This could be due to the high surface area and a high degree of functionalization with O (and N groups) as confirmed in the XPS C1s and O1s spectra. This presence results in the ease of interfacial oxidation of the thin layers of carbon. The low formation of the Q-HQ couple on the commercial benchmark could be attributed to the low BET surface area as a result of the carbon degradation to CO_2 as well as the presence of fewer graphite-like edge sites at which the hydroxyl functional groups could form during the corrosion process according to **Eq. 11**. The reduction is attributed to the loss of the catalysts ECSA due to the degradation of the carbon supports resulting in migration of the Pt particles and subsequent agglomeration. The other observable feature is the growth of the double-layer capacitance of the Pt/HCSs and Pt/NHCSs catalysts in the 0.3–0.5 V vs. RHE potential window corresponding to the reduced surface area of the catalysts.

Even though the double-layer capacitance and the features associated with the ECSA of the catalysts are reduced, due to degradation of the Pt/HCSs and the Pt/NHCSs catalysts, more degradation is observed for the commercial Pt/C catalyst (**Figure 8**). The AST study resulted in a 59%, 57% and about 61% reduction of the initial ECSA for the Pt/NHCSs, Pt/HCSs and Pt/C catalysts respectively after 6,000 cycles (27 h). The change in ECSA from the 1,000 durability cycles to the 6,000 durability cycles shows a minimal reduction occurring for the Pt/HCSs accounting for a 6% loss. Significant losses are observed for the Pt/C (18%) and the Pt/NHCSs (15%).

The slightly better durability of the HCSs-based supports is attributed to the structure of these materials. The HCSs (832 m^2/g) and NHCSs (604 m^2/g) supports both have a higher BET surface area and an array of mesopores and micropores which promotes the confinement of Pt particles, resulting in better support to metal contact. Also, confined Pt particles are more resistant to migration and agglomeration. The higher loss in activity of the benchmark Pt/C is ascribed to low pore confinement compared to the new materials. Pore confinement of the Pt in the structure of the HCSs based supports was confirmed in a similar study involving broken hemispherical hollow carbon spheres (Mashindi et al., 2021).

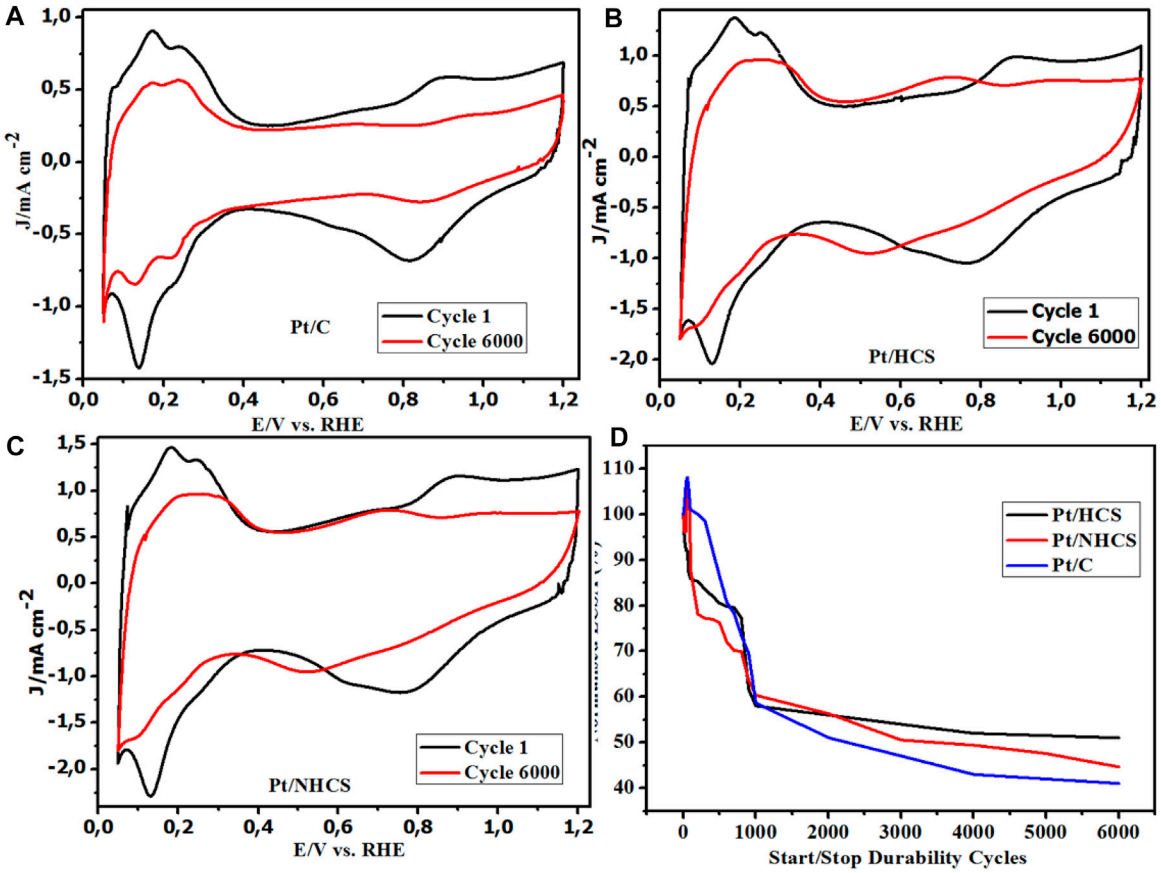

FIGURE 8 | (A–D) Catalyst CVs before and after durability studies for the Pt/HCSs, Pt/NHCSs and the commercial benchmark Pt/C catalysts, **(D)** Normalized ECSA% degradation of the catalysts.

Overall, the confinement of the Pt inside the pores as shown by ABF-DF-STEM (**Supplementary Figure SI4**) and related work with similar materials (Mashindi et al., 2021), as well as the good Pt-support contact due to surface functionalization is critical for better durability under aggressive fuel cell cycles. Equally important is the elongation of bonds and the presence of higher-order rings in the structure of the carbon that results in a poor carbon-carbon bond strength, which produces a reduced stability in the nitrogen-doped support relative to the pristine hollow carbon spheres as elucidated by the PDF analysis of the samples.

CONCLUSION

In this study, the various properties of the HCSs and NHCSs catalysts were studied, and correlated to the observed durability and activity in ORR. Characterization studies on the HCSs, NHCSs and Pt/HCSs and Pt/NHCSs catalysts revealed that the porosity of the supports and their high surface areas promoted good dispersion of the Pt nanoparticles as revealed by BET analysis. Raman spectra indicated that the nitrogen and oxygen functional groups generated numerous defects on the surface of the support where nucleation and growth of small Pt particles was initiated.

The effect of nitrogen on the HCSs structure from total scattering data using pair distribution function (PDF) analysis of the catalysts was studied. Analysis of the data revealed that the NHCSs showed increased buckling of the carbon plane compared to the pristine sample due to the nitrogen doping. Addition of Pt to the spheres also gave rise to a Pt-C interaction that could be detected by PDF analysis and the strength of the interaction of the Pt particles with the carbon surface is such that the larger the interaction the larger the C–C bond elongation. The stronger Pt-C interaction was responsible for part of the observed long-term durability of the Pt/HCSs and Pt/NHCSs catalysts.

The PDF method is highly sensitive to small particles resulting in an accurate particle size determination. The higher proportion of smaller average Pt sizes as determined by the PDF technique compared to PXRD, could partly explain the higher activity in ORR observed for the Pt/HCSs and Pt/NHCSs.

The Pt catalysts prepared by the ethanol reflux method demonstrated higher activity and durability than the commercial benchmark Pt. The durability the Pt catalysts were subjected to accelerated stress tests (AST) for 6,000 cycles at 50 mV s^{-1} from 0.6 to 1.0 V vs. RHE. The data showed that after

6,000 cycles, the ECSA retentions were Pt/C (47.6%) < Pt/NHCSs (62.1%) < Pt/HCSs (65.4%). In other experiments the start-stop durability LSVs of the catalysts, before and after the tests, was studied and the data revealed LSV shifts in the order Pt/HCSs (18 mV) < Pt/NHCSs (22 mV) < Pt/C (30 mV). A shift in LSVs is attributed to the loss of activity due to the degradation of the Pt catalysts. The losses in ECSA, MA (and SA) were attributed to the agglomeration of Pt and this agglomeration was detected by post analysis of the samples from TEM images.

The two effects of pore confinement and the presence of defects/nucleation sites is proposed to be responsible for the enhanced durability of the catalysts. Based on these findings, the Pt/HCSs and Pt/NHCSs are good candidates for PEMFC catalysts and strategies to further enhance the durability of the catalysts and reduce Pt use can be further initiated from the above studies.

DATA AVAILABILITY STATEMENT

The original contributions presented in the study are included in the article/Supplementary Material, and further inquiries can be directed to the corresponding author.

AUTHOR CONTRIBUTIONS

VM: PhD student, did experimental work, wrote paper; PM: PhD student, assisted with synthesis/characterization and paper corrections; TP: post doc, assisted with synthesis/characterization and paper corrections, NM: PhD student, assisted with electrochem experiments; OM: PhD student, assisted with TEM characterization and paper corrections; BM: PDF data collection/interpretation, wrote PDF part of paper; DB: PDF data collection/interpretation, wrote PDF part of paper; RF: XRD data collection/interpretation, assisted with paper writing; PL: electrochemistry experiments and assisted with paper writing; KO: electrochemistry experiments; NC: idea for project with VM, paper writing, data analysis.

ACKNOWLEDGMENTS

We thank the South Africa Department of Science and Innovation for funding the project through a HySA Catalysis student bursary. Financial support from the University of the Witwatersrand postgraduate merit award is also acknowledged. The authors greatly acknowledge the staff from the microscopy and microanalysis unit at the University of the Witwatersrand and the staff at the Aaron Klug Centre for Imaging and Analysis at the University of Cape Town. The National Institute of Meteorology South Africa (NMISA), for XPS measurements is also acknowledged. We acknowledge the the David Cockayne Centre for Electron Microscopy, University of Oxford for the annular dark field (ADF) - bright-field (BF)-STEM measurements. The Chemical Engineering Department at the University of Cape Town is acknowledged for providing electrochemical equipment and laboratory space. We also thank Rirhandzu Rikhotso at the Council for Scientific and Industrial Research (CSIR) for assisting with TEM/STEM for this study. We also thank Dr. Graham King for the PDF measurements performed at the Canadian Light Source, a national research facility of the University of Saskatchewan, which is supported by the Canada Foundation for Innovation (CFI), the Natural Sciences and Engineering Research Council (NSERC), the National Research Council (NRC), the Canadian Institutes of Health Research (CIHR).

SUPPLEMENTARY MATERIAL

The Supplementary Material for this article can be found online at: https://www.frontiersin.org/articles/10.3389/fchem.2022.839867/full#supplementary-material

REFERENCES

Chen, W., Xiang, Q., Peng, T., Song, C., Shang, W., Deng, T., et al. (2020). Reconsidering the Benchmarking Evaluation of Catalytic Activity in Oxygen Reduction Reaction. *iScience* 23 (10), 101532. doi:10.1016/j.isci.2020.101532

Chen, Y., Zhang, Z., Huang, Z., and Zhang, H. (2017). Effects of Oxygen-Containing Functional Groups on the Supercapacitor Performance of Incompletely Reduced Graphene Oxides. *Int. J. Hydrogen Energ.* 42 (10), 7186–7194. doi:10.1016/j.ijhydene.2016.08.054

Cherevko, S., Kulyk, N., and Mayrhofer, K. J. J. (2016). Durability of Platinum-Based Fuel Cell Electrocatalysts: Dissolution of Bulk and Nanoscale Platinum. *Nano Energy* 29, 275–298. doi:10.1016/j.nanoen.2016.03.005

Dlamini, M. W., Phaahlamohlaka, T. N., Kumi, D. O., Forbes, R., Jewell, L. L., and Coville, N. J. (2020). Post Doped Nitrogen-Decorated Hollow Carbon Spheres as a Support for Co Fischer-Tropsch Catalysts. *Catal. Today* 342, 99–110. doi:10.1016/j.cattod.2019.01.070

Dmowski, W., Contescu, C. I., Llobet, A., Gallego, N. C., and Egami, T. (2012). Local Atomic Density of Microporous Carbons. *J. Phys. Chem. C* 116 (4), 2946–2951. doi:10.1021/jp209824f

Du, H.-Y., Wang, C.-H., Hsu, H.-C., Chang, S.-T., Chen, U.-S., Yen, S. C., et al. (2008). Controlled Platinum Nanoparticles Uniformly Dispersed on Nitrogen-Doped Carbon Nanotubes for Methanol Oxidation. *Diamond Relat. Mater.* 17, 535–541. doi:10.1016/j.diamond.2008.01.116

Ewels, C. P., and Glerup, M. (2005). Nitrogen Doping in Carbon Nanotubes. *J. Nanosci. Nanotech.* 5 (9), 1345–1363. doi:10.1166/jnn.2005.304

Ferrari, A. C., and Robertson, J. (2004). Raman Spectroscopy of Amorphous, Nanostructured, diamond-like Carbon, and Nanodiamond. *Phil. Trans. R. Soc. Lond. Ser. A: Math. Phys. Eng. Sci.* 362 (1824), 2477–2512. doi:10.1098/rsta.2004.1452

Galeano, C., Meier, J. C., Peinecke, V., Bongard, H., Katsounaros, I., Topalov, A. A., et al. (2012). Toward Highly Stable Electrocatalysts via Nanoparticle Pore Confinement. *J. Am. Chem. Soc.* 134 (1), 20457–20465. doi:10.1021/ja308570c

Galeano, C., Meier, J. C., Soorholtz, M., Bongard, H., Baldizzone, C., Mayrhofer, K. J. J., et al. (2014). Nitrogen-Doped Hollow Carbon Spheres as a Support for Platinum-Based Electrocatalysts. *ACS Catal.* 4 (11), 3856–3868. doi:10.1021/cs5003492

Garsany, Y., Baturina, O. A., Swider-Lyons, K. E., and Kocha, S. S. (2010). Experimental Methods for Quantifying the Activity of Platinum Electrocatalysts for the Oxygen Reduction Reaction. *Anal. Chem.* 82 (15), 6321–6328. doi:10.1021/ac100306c

Genorio, B., Strmcnik, D., Subbaraman, R., Tripkovic, D., Karapetrov, G., Stamenkovic, V. R., et al. (2010). Selective Catalysts for the Hydrogen

Oxidation and Oxygen Reduction Reactions by Patterning of Platinum with Calix[4]Arene Molecules. *Nat. Mater* 9 (12), 998–1003. doi:10.1038/nmat2883

Hu, Y., Jensen, J. O., Bretzler, P., Cleemann, L. N., Yu, J., and Li, Q. (2021). Revealing the Genuine Stability of the Reference Pt/C Electrocatalyst toward the ORR. *Electrochimica Acta* 391, 138963. doi:10.1016/j.electacta.2021.138963

Inaba, M. (2009). Durability of Electrocatalysts in Polymer Electrolyte Fuel Cells. *ECS Trans.* 25 (1), 573. doi:10.1149/ma2009-02/10/857

Jackson, C., Smith, G. T., Inwood, D. W., Leach, A. S., Whalley, P. S., Callisti, M., et al. (2017). Electronic Metal-Support Interaction Enhanced Oxygen Reduction Activity and Stability of Boron Carbide Supported Platinum. *Nat. Commun.* 8 (1), 15802. doi:10.1038/ncomms15802

Jiménez-Morales, I., Haidar, F., Cavaliere, S., Jones, D., and Rozière, J. (2020). Strong Interaction between Platinum Nanoparticles and Tantalum-Doped Tin Oxide Nanofibers and its Activation and Stabilization Effects for Oxygen Reduction Reaction. *ACS Catal.* 10 (18), 10399–10411.

Ju, M. J., Choi, I. T., Zhong, M., Lim, K., Ko, J., Mohin, J., et al. (2015). Copolymer-Templated Nitrogen-Enriched Nanocarbons as a Low Charge-Transfer Resistance and Highly Stable Alternative to Platinum Cathodes in Dye-Sensitized Solar Cells. *J. Mater. Chem. A.* 3 (8), 4413–4419. doi:10.1039/c4ta07012g

Kane, M. S., Goellner, J. F., Foley, H. C., DiFrancesco, R., Billinge, S. J. L., and Allard, L. F. (1996). Symmetry Breaking in Nanostructure Development of Carbogenic Molecular Sieves: Effects of Morphological Pattern Formation on Oxygen and Nitrogen Transport. *Chem. Mater.* 8 (8), 2159–2171. doi:10.1021/cm960085w

Krzton, H., and Niewiara, M. (1995). Studies on Commercial Carbon Black by Radial Distribution Function and Rietveld Refinement. *Phys. Scr.* T57 (T57), 98–101. doi:10.1088/0031-8949/1995/t57/016

Labata, M. F., Li, G., Ocon, J., and Chuang, P.-Y. A. (2021). Insights on Platinum-Carbon Catalyst Degradation Mechanism for Oxygen Reduction Reaction in Acidic and Alkaline Media. *J. Power Sourc.* 487, 229356. doi:10.1016/j.jpowsour.2020.229356

Lee, K.-Y., Liu, C.-Y., Sung, C.-C., and Hu, L.-H. (2014). Influence of Ink Preparation with the Untreated and the Burned Pt/C Catalysts for Proton Exchange Membrane Fuel Cells. *Int. J. Hydrogen Energ.* 39 (22), 11454–11461. doi:10.1016/j.ijhydene.2014.05.051

Li, F., and Lannin, J. S. (1990). Radial Distribution Function of Amorphous Carbon. *Phys. Rev. Lett.* 65 (15), 1905–1908. doi:10.1103/physrevlett.65.1905

Lu, F., Yi, D., Liu, S., Zhan, F., Zhou, B., Gu, L., et al. (2020). Engineering Platinum-Oxygen Dual Catalytic Sites via Charge Transfer towards Highly Efficient Hydrogen Evolution. *Angew. Chem.* 132 (40), 17865–17871. doi:10.1002/ange.202008117

Lu, J., Li, Y., Li, S., and Jiang, S. P. (2016). Self-assembled Platinum Nanoparticles on Sulfonic Acid-Grafted Graphene as Effective Electrocatalysts for Methanol Oxidation in Direct Methanol Fuel Cells. *Sci. Rep.* 6, 21530. doi:10.1038/srep21530

Lu, Y., Jiang, Y., and Chen, W. (2013). PtPd Porous Nanorods with Enhanced Electrocatalytic Activity and Durability for Oxygen Reduction Reaction. *Nano Energy* 2 (5), 836–844. doi:10.1016/j.nanoen.2013.02.006

Mao, L., Fu, K., Jin, J., Yang, S., and Li, G. (2019). PtFe Alloy Catalyst Supported on Porous Carbon Nanofiber with High Activity and Durability for Oxygen Reduction Reaction. *Int. J. Hydrogen Energ.* 44 (33), 18083–18092. doi:10.1016/j.ijhydene.2019.05.058

Mashindi, V., Mente, P., Mpofu, N., Phaahlamohlaka, T. N., Makgae, O., Kirkland, A. I., et al. (2021). Platinum Supported on Pristine and Nitrogen-Doped Bowl-like Broken Hollow Carbon Spheres as Oxygen Reduction Reaction Catalysts. *J. Appl. Electrochem.* 51751 (7), 991–1008. doi:10.1007/s10800-021-01554-0

Matsoso, B. J., Ranganathan, K., Mutuma, B. K., Lerotholi, T., Jones, G., and Coville, N. J. (2016). J Time-dependent Evolution of the Nitrogen Configurations in N-Doped Graphene filmsTime-dependent Evolution of the Nitrogen Configurations in N-Doped Graphene Films. *RSC Adv.* 6, 106914–106920. doi:10.1039/c6ra24094a

Melke, J., Peter, B., Habereder, A., Ziegler, J., Fasel, C., Nefedov, A., et al. (2016). Metal-Support Interactions of Platinum Nanoparticles Decorated N-Doped Carbon Nanofibers for the Oxygen Reduction Reaction. *ACS Appl. Mater. Inter.* 8 (1), 82–90. doi:10.1021/acsami.5b06225

Mente, P., Phaahlamohlaka, T. N., Mashindi, V., and Coville, N. J. (2021). Polystyrene-b-Poly(Acrylic Acid) Nanospheres for the Synthesis of Size-Controlled Cobalt Nanoparticles Encapsulated inside Hollow Carbon Spheres. *J. Mater. Sci.* 56 (3), 2113–2128. doi:10.1007/s10853-020-05323-w

Mildner, D. F. R., and Carpenter, J. M. (1982). On the Short Range Atomic Structure of Non-crystalline Carbon. *J. Non-Crystalline Sol.* 47 (3), 391–402. doi:10.1016/0022-3093(82)90215-0

Mohamed, R., Binninger, T., Kooyman, P. J., Hoell, A., Fabbri, E., Patru, A., et al. (2018). Facile Deposition of Pt Nanoparticles on Sb-Doped SnO2 Support with Outstanding Active Surface Area for the Oxygen Reduction Reaction. *Catal. Sci. Technol.* 8 (10), 2672–2685. doi:10.1039/c7cy02591b

Mohideen, M. M., Liu, Y., and Ramakrishna, S. (2020). Recent Progress of Carbon Dots and Carbon Nanotubes Applied in Oxygen Reduction Reaction of Fuel Cell for Transportation. *Appl. Energ.* 257, 114027. doi:10.1016/j.apenergy.2019.114027

Ohma, A., Shinohara, K., Iiyama, A., Yoshida, T., and Daimaru, A. (2011). Membrane and Catalyst Performance Targets for Automotive Fuel Cells by FCCJ Membrane, Catalyst, MEA WG. *ECS Trans.* 41, 775–784.

Palaniselvam, T., Valappil, M. O., Illathvalappil, R., and Kurungot, S. (2014). Nanoporous Graphene by Quantum Dots Removal from Graphene and its Conversion to a Potential Oxygen Reduction Electrocatalyst via Nitrogen Doping. *Energy Environ. Sci.* 7 (3), 1059–1067. doi:10.1039/c3ee43648a

Panchenko, A., Koper, M. T. M., Shubina, T. E., Mitchell, S. J., and Roduner, E. (2004). Ab Initio Calculations of Intermediates of Oxygen Reduction on Low-Index Platinum Surfaces. *J. Electrochem. Soc.* 151 (12), A2016. doi:10.1149/1.1809586

Park, C., Lee, E., Lee, G., and Tak, Y. (2020). Superior Durability and Stability of Pt Electrocatalyst on N-Doped Graphene-TiO2 Hybrid Material for Oxygen Reduction Reaction and Polymer Electrolyte Membrane Fuel Cells. *Appl. Catal. B: Environ.* 268, 118414. doi:10.1016/j.apcatb.2019.118414

Park, Y.-C., Kakinuma, K., Uchida, M., Uchida, H., and Watanabe, M. (2014). Deleterious Effects of Interim Cyclic Voltammetry on Pt/Carbon Black Catalyst Degradation during Start-up/Shutdown Cycling Evaluation. *Electrochimica Acta* 123, 84–92. doi:10.1016/j.electacta.2013.12.120

Petkov, V., Difrancesco, R. G., Billinge, S. J. L., Acharya, M., and Foley, H. C. (1999). Local Structure of Nanoporous Carbons. *Philosophical Mag. B* 79 (10), 1519–1530. doi:10.1080/13642819908218319

Qian, H., Tang, J., Hossain, M. S. A., Bando, Y., Wang, X., and Yamauchi, Y. (2017). Localization of Platinum Nanoparticles on Inner Walls of Mesoporous Hollow Carbon Spheres for Improvement of Electrochemical Stability. *Nanoscale* 9 (42), 16264–16272. doi:10.1039/c7nr07267h

Ramos-Sanchez, G., and Balbuena, P. B. (2013). Interactions of Platinum Clusters with a Graphite Substrate. *Phys. Chem. Chem. Phys.* 15 (28), 11950–11959. doi:10.1039/c3cp51791h

Rashedi, A., Khanam, T., and Jonkman, M. (2020). On Reduced Consumption of Fossil Fuels in 2020 and its Consequences in Global Environment and Exergy Demand. *Energies* 13 (22), 6048. doi:10.3390/en13226048

Ren, P., Pei, P., Li, Y., Wu, Z., Chen, D., and Huang, S. (2020). Degradation Mechanisms of Proton Exchange Membrane Fuel Cell under Typical Automotive Operating Conditions. *Prog. Energ. Combustion Sci.* 80, 100859. doi:10.1016/j.pecs.2020.100859

Sandbeck, D. J. S., Secher, N. M., Speck, F. D., Sørensen, J. E., Kibsgaard, J., Chorkendorff, I., et al. (2020). Particle Size Effect on Platinum Dissolution: Considerations for Accelerated Stability Testing of Fuel Cell Catalysts. *ACS Catal.* 10 (11), 6281–6290. doi:10.1021/acscatal.0c00779

Sebastián, D., Ruíz, A. G., Suelves, I., Moliner, R., Lázaro, M. J., Baglio, V., et al. (2012). Enhanced Oxygen Reduction Activity and Durability of Pt Catalysts Supported on Carbon Nanofibers. *Appl. Catal. B: Environ.* 115-116, 269–275. doi:10.1016/j.apcatb.2011.12.041

Simonsen, S. B., Chorkendorff, I., Dahl, S., Skoglundh, M., Sehested, J., and Helveg, S. (2011). Ostwald Ripening in a Pt/SiO2 Model Catalyst Studied by *In Situ* TEM. *J. Catal.* 281 (1), 147–155. doi:10.1016/j.jcat.2011.04.011

Sravani, B., Raghavendra, P., Chandrasekhar, Y., Veera Manohara Reddy, Y., Sivasubramanian, R., Venkateswarlu, K., et al. (2020). Immobilization of Platinum-Cobalt and Platinum-Nickel Bimetallic Nanoparticles on Pomegranate Peel Extract-Treated Reduced Graphene Oxide as Electrocatalysts for Oxygen Reduction Reaction. *Int. J. Hydrogen Energ.* 45 (13), 7680–7690. doi:10.1016/j.ijhydene.2019.02.204

Stöber, W., Fink, A., and Bohn, E. (1968). Controlled Growth of Monodisperse Silica Spheres in the Micron Size Range. *J. Colloid Interf. Sci.* 26 (1), 62–69.

Teranishi, T., Hosoe, M., Tanaka, T., and Miyake, M. (1999). Size Control of Monodispersed Pt Nanoparticles and Their 2D Organization by Electrophoretic Deposition. *J. Phys. Chem. B* 103 (19), 3818–3827. doi:10.1021/jp983478m

Toby, B. H., and Von Dreele, R. B. (2013). GSAS-II: The Genesis of a Modern Open-Source All Purpose Crystallography Software Package. *J. Appl. Cryst.* 46 (2), 544–549. doi:10.1107/s0021889813003531

Wang, J., Yin, G., Shao, Y., Zhang, S., Wang, Z., and Gao, Y. (2007). Effect of Carbon Black Support Corrosion on the Durability of Pt/C Catalyst. *J. Power Sourc.* 171, 331–339. doi:10.1016/j.jpowsour.2007.06.084

Wang, X., Li, W., Chen, Z., Waje, M., and Yan, Y. (2006). Durability Investigation of Carbon Nanotube as Catalyst Support for Proton Exchange Membrane Fuel Cell. *J. Power Sourc.* 158, 154–159. doi:10.1016/j.jpowsour.2005.09.039

Wang, X., Zhao, Z., Sun, P., and Li, F. (2020). One-Step Synthesis of Supported High-Index Faceted Platinum-Cobalt Nanocatalysts for an Enhanced Oxygen Reduction Reaction. *ACS Appl. Energ. Mater.* 3 (5), 5077–5082. doi:10.1021/acsaem.0c00801

Yan, Z., Xie, J., Zong, S., Zhang, M., Sun, Q., and Chen, M. (2013). Small-Sized Pt Particles on Mesoporous Hollow Carbon Spheres for Highly Stable Oxygen Reduction Reaction. *Electrochimica Acta* 109, 256–261. doi:10.1016/j.electacta.2013.07.085

Yano, H., Akiyama, T., Bele, P., Uchida, H., and Watanabe, M. (2010). Durability of Pt/graphitized Carbon Catalysts for the Oxygen Reduction Reaction Prepared by the Nanocapsule Method. *Phys. Chem. Chem. Phys.* 12, 3806–3814. doi:10.1039/b923460h

Zhang, J., Ma, L., Gan, M., Yang, F., Fu, S., and Li, X. (2015). Well-Dispersed Platinum Nanoparticles Supported on Hierarchical Nitrogen-Doped Porous Hollow Carbon Spheres with Enhanced Activity and Stability for Methanol Electrooxidation. *J. Power Sourc.* 288, 42–52. doi:10.1016/j.jpowsour.2015.04.109

Conflict of Interest: The authors declare that the research was conducted in the absence of any commercial or financial relationships that could be construed as a potential conflict of interest.

Publisher's Note: All claims expressed in this article are solely those of the authors and do not necessarily represent those of their affiliated organizations, or those of the publisher, the editors and the reviewers. Any product that may be evaluated in this article, or claim that may be made by its manufacturer, is not guaranteed or endorsed by the publisher.

frontiers in Chemistry

ORIGINAL RESEARCH
published: 16 March 2022
doi: 10.3389/fchem.2022.870393

Electrochemical Sensing of Nitrite Ions Using Modified Electrode by Poly 1,8-Diaminonaphthalene/ Functionalized Multi-Walled Carbon Nanotubes

*Ouissal Salhi, Tarik Ez-zine, Larbi Oularbi and Mama El Rhazi**

Laboratory of Materials Membranes and Environment, Faculty of Sciences and Technologies, University Hassan II Casablanca, Mohammedia, Morocco

A novel electrochemical sensor based on conducting polymer and multi-walled carbon nanotubes was reported for the detection of nitrite ions (NO_2^-). The hybrid material poly 1,8-Diaminonaphthalene (poly 1,8-DAN)/functionalized multi-walled carbon nanotubes (f-MWCNT) was prepared by using a simple electrochemical approach which is based on the deposition of functionalized multi-walled carbon nanotubes (f-MWCNT) on the surface of the electrode followed by the electropolymerization of 1,8-DAN using cyclic voltammetry. The morphology and the electro-catalytic properties of the obtained electrodes were investigated with Fourier Transform Infrared Spectroscopy (FTIR), Transmission Electron Microscopy (TEM), Cyclic Voltammetry (CV), and Electrochemical Impedance Spectroscopy (EIS) showing an improvement of the electronic transfer due to the synergic effect between the proprieties of poly 1,8-DAN and f-MWCNT. Under the optimum experimental conditions, the poly 1,8-DAN/f-MWCNT/CPE exhibited excellent electro-catalytic activity towards nitrite detection. The nitrite anodic peak potential decreased by 210 mV compared to the bare carbon paste electrode. The calibration plot of nitrite detection was linear in the range of concentration from 300 to 6500 nM with a low detection limit of 75 nM.

Keywords: nitrite detection, conducting polymer, 1,8-Diaminonaphthalene, electrochemical sensor, multi-walled carbon nanotubes

OPEN ACCESS

Edited by:
Cosimino Malitesta, University of Salento, Italy

Reviewed by:
Mehdi Baghayeri, Hakim Sabzevari University, Iran
Mani Govindasamy, National Taipei University of Technology, Taiwan

****Correspondence:***
Mama El Rhazi
elrhazim@hotmail.com

Specialty section:
This article was submitted to Analytical Chemistry, a section of the journal Frontiers in Chemistry

Received: *06 February 2022*
Accepted: *02 March 2022*
Published: *16 March 2022*

Citation:
Salhi O, Ez-zine T, Oularbi L and El Rhazi M (2022) Electrochemical Sensing of Nitrite Ions Using Modified Electrode by Poly 1,8-Diaminonaphthalene/Functionalized Multi-Walled Carbon Nanotubes. Front. Chem. 10:870393. doi: 10.3389/fchem.2022.870393

INTRODUCTION

Nitrite ions; one of the inorganic forms of natural nitrogen; take part of the cycle in which nitrogen takes different forms following several processes such as fixation, assimilation, nitrification, and denitrification (Zhu et al., 2015). It is important to highlight that the industrialization, overpopulation, and the progress of the agri-food sector have led to the accumulation of nitrite in our environment in a very significant way (Berardo et al., 2016). Indeed, it is generated during the decomposition of fertilizers and human waste leading to the contamination of the soil and the groundwater. Nitrite is also used as food preservatives and food coloring under the form of sodium nitrite noted (E250) and constitutes a real threat to the human health. In fact, it has been reported that an excess of this element in the body leads to the conversion of the hemoglobin to methemoglobin, which reduce the amount of oxygen distributed by the blood to the tissues called hypoxia (Katabami et al., 2016). Nitrite ions can also react with amines to

form N-nitroamines causing serious health problems such as gastric cancer (Song et al., 2015; Zhang et al., 2019), thyroid cancer (Aschebrook-Kilfoy et al., 2013), and non-Hodgkin's lymphoma (Yu et al., 2020). Moreover, research studies have confirmed a possible relationship between nitrite consumption and neurological damages (Ribeiro et al., 2017). Therefore, there is an urgent need to monitor the presence of nitrite in water and food. For this purpose, the World Health Organization (WHO) has determined a maximum admissible concentration in drinking water of 3 mg/L equivalent to 65.217 µM (Ren et al., 2018). Numerous methods have been developed to detect and quantify nitrite (Wang et al., 2017), such as spectrofluorimetry (Zhan et al., 2019), spectrophotometry (Lo et al., 2017), chemiluminescence (Han and Chen, 2019), chromatography (Lin et al., 2019), capillary electrophoresis (Kalaycıoğlu and Erim, 2016), and electrochemistry (Zhao et al., 2017). The electrochemical techniques possess several advantages such as low cost, rapid response and high sensitivity (Bansod et al., 2017; Oularbi et al., 2019). The electro-oxidation of nitrite leads to the formation of nitrate, unlike its electro-reduction, which can produce several products, and it is limited by the interference of dioxygen (O_2) and nitrate reduction (NO_3^-) (Kesavan et al., 2018). However, the oxidation of nitrite still faces many challenges to overcome, such as the oxidation overpotential, and the slow kinetic of the electronic transfer (Mao et al., 2018). To address this issues, electrochemical sensors and biosensors seem to be a very good alternative. It is, in fact, absolutely necessary to modify the conventional electrodes such as carbon paste (Bijad et al., 2017), screen-printed electrodes (Jaiswal et al., 2017), and glassy carbon electrodes with a suitable agent (Muthumariappan et al., 2017; Velmurugan et al., 2020; Karimi-Maleh et al., 2021). Electrochemical Multi-walled carbon nanotubes (MWCNT), largely used to modify the surface of electrodes for many applications (Mani et al., 2017; Beitollahi et al., 2018; Roy et al., 2018; Rui et al., 2020; Shaikshavali et al., 2020; Baghayeri et al., 2021a); are considered as an ideal choice thanks to their interesting properties. Moreover, they can be combined with metallic nanoparticles, metal organic framework or conducting polymers in order to enhance the sensitivity towards nitrite determination in different matrices (Thirumalraj et al., 2016; Wan et al., 2017; Yu et al., 2019; Baghayeri et al., 2020a; Salagare et al., 2020). Conducting polymers (CPs) constitute a new class of emerging materials and have shown considerable potential for several applications (Gracia and Mecerreyes, 2013; Elbasri and Rhazi, 2015; Salih et al., 2017b; El Rhazi et al., 2018; Salih et al., 2018; Chemchoub et al., 2019; Chemchoub et al., 2020; El Attar et al., 2020; Vagin et al., 2021). They have also shown excellent electrocatalytic activity towards nitrite detection. Recently, several hybrid materials based on CPs have been developed for nitrite sensing (Salhi et al., 2021). Rajalakshmi and John (2015), developed a composite based on 5-amino-1,3,4-thiadiazole-2-thiol and MWCNT for nitrite detection and obtained a very low detection limit of about 0.2 nM. A novel electrochemical approach was also reported in the literature which consists on the combination of poly (3,4-ethylenedioxythiophene) with gold nanoparticles leading to a very good activity toward nitrite oxidation with high stability and selectivity (Lin et al., 2016). Moreover, Shi et al., co-deposited palladium nanoparticles and poly (1.5-Diaminonaphthalene) on MWCNT. The prepared hybrid showed a good electrocatalytic activity towards nitrite oxidation due to its high active surface area and the synergistic effect of Pd nanoparticles, poly 1.5-DAN and MWCNT (Shi et al., 2019). Nevertheless, the main disadvantage of the sensors based on gold and palladium nanoparticles lies in the fact that they are quite expensive.

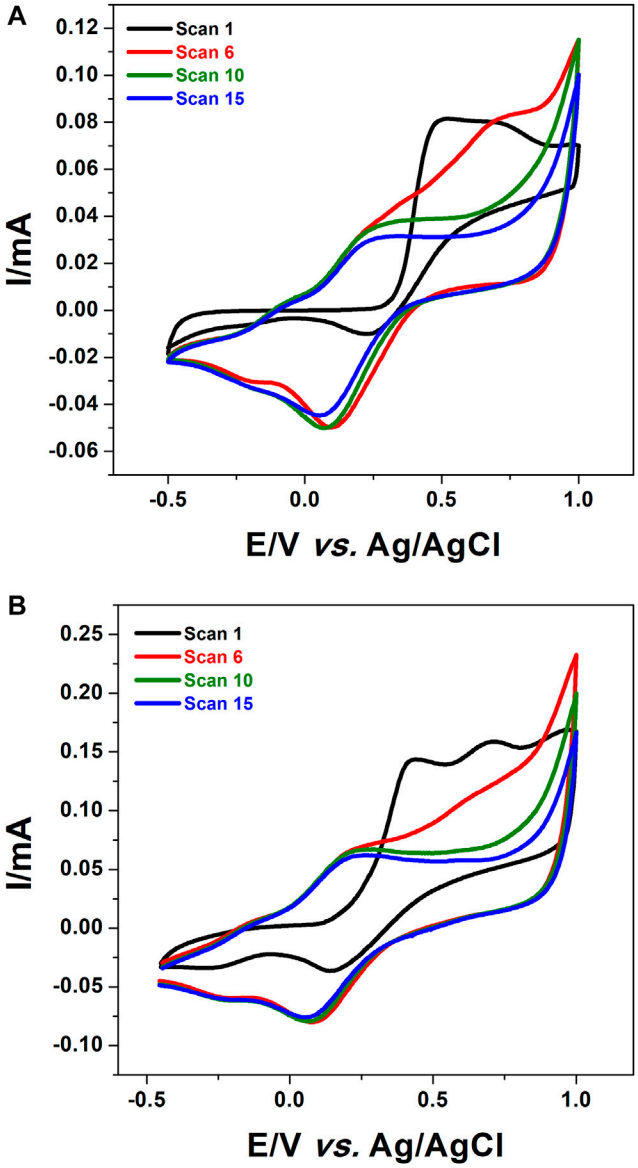

FIGURE 1 | CV of **(A)** CPE and **(B)** f-MWCNT/CPE in 0.1 M HCl containing 5 mM 1,8-DAN for 15 cycles at a scan rate of 50 mV/s.

In this context, we propose a very simple approach which consists on the combination of the two materials (CP and MWCNT) in order to develop an electrochemical sensor; efficient and less expensive; for nitrite determination in water samples. The electropolymerization of 1,8-DAN on carbon nanotubes was carried out using cyclic voltammetry in acidic

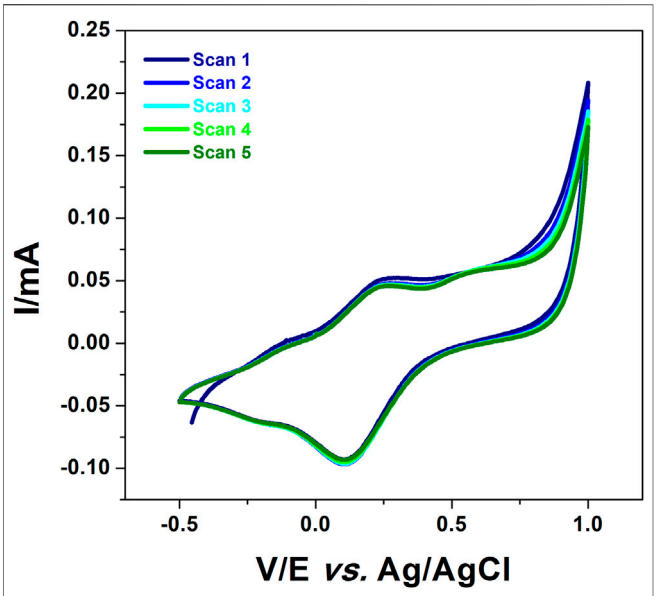

FIGURE 2 | CV of poly 1,8-DAN/f-MWCNT/CPE in 0.1 M HCl at a scan rate of 50 mV/s.

medium, which allowed us to prepare our working electrodes in less than 1 hour. The morphology and the electrochemical behavior of the modified electrodes were investigated using various techniques such as Fourier transform infrared spectroscopy (FTIR), transmission electron microscopy (TEM), cyclic voltammetry (CV), and electrochemical impedance spectroscopy (EIS). The electrocatalytic activity of poly 1,8-DAN/f-MWCNT/CPE towards nitrite oxidation was examined using both cyclic voltammetry and amperometry.

EXPERIMENTAL

Chemical and Reagents

Graphite powder, paraffin oil, 1,8-Diaminonaphthalene (1,8-DAN), potassium Ferri/Ferrocyanide ($K3Fe(CN)_6$/$K_4Fe(CN)_6.3H_2O$; ACS reagent >99%), disodium hydrogen phosphate heptahydrate (Na2HPO4.7H2O) and sodium dihydrogen phosphate dihydrate ($NaH_2PO_4.2H_2O$) were obtained from Sigma Aldrich. Potassium chloride (KCl), hydrochloric acid (HCl, 37%), nitric acid (HNO_3, 69%), and sulfuric acid (H_2SO_4, 98%) were procured from Labo Chimie. Sodium nitrite ($NaNO_2$, ACS reagent >98%) was acquired from Panreac Quimica. Bi-distillated water was used to prepare all the solutions including 0.1 M of phosphate buffer solution (PBS, pH 7.2), which was used as the electrolyte.

Functionalization of Multi Walled Carbon Nanotubes

In order to functionalize multi-walled carbon nanotubes, an appropriate amount of MWCNT was dispersed in a solution of concentred H_2SO_4 and HNO_3, with a volume ratio of 1:3. The suspension was ultrasonicated for a few minutes, then left under magnetic stirring over-night. Afterwards, the functionalized multi walled carbon nanotubes (f-MWCNT) were filtered using a Millipore polycarbonate membrane with a diameter of 0.22 µm, and washed with bi-distillated water until a neutral pH of the filtrate was obtained. Eventually, the f-MWCNT were dried at the oven at 50°C for 5 h.

Preparation of the Modified Electrodes

Firstly, the carbon paste electrode (CPE) was prepared by mixing 1 g of graphite powder with 30% paraffin oil w/w in a mortar until the formation of a homogeneous paste (Salih et al., 2017a; Oularbi et al., 2020; El Attar et al., 2021). Subsequently, the paste was placed in a 3 mm diameter Teflon tube. Then, it was polished until the obtention of a smooth surface. The aqueous suspension of f-MWCNT was prepared by dispersing 1 mg of f-MWCNT in 1 ml of distillated water. Afterward, 20 µL of the suspension was dropped onto the surface of CPE, then dried at the oven at 50°C.

The electrochemical deposition of poly (1,8-DAN) was carried out in a 0.1 M HCl solution containing 5 mM of the monomer (1,8-DAN) using cyclic voltammetry (CV) by sweeping the potential from −0.5 to 1 V vs. Ag/AgCl for 15 cycles at a scan rate of 50 mV/s.

Electrochemical Measurements and Physicochemical Characterization

All the electrochemical measurements including cyclic voltammetry (CV), electrochemical impedance spectroscopy (EIS), and amperometry were performed using a PalmSens4 connected to a PSTrace 5.3 software. A traditional three electrodes system was used, which consists of a modified carbon paste electrode (CPE) as the working electrode, a platinum disk as the counter electrode, and a silver/silver chloride (Ag/AgCl) as the reference electrode.

The CV measurements were carried out in a 0.5 M KCl solution containing 10 mM $[Fe(CN)_6]^{3-/4-}$ at an applied potential ranging from −0.4 to 0.8 V vs. Ag/AgCl, and in 0.1 M phosphate buffer (PBS, pH 7.2) containing 0.1 M KCl and 1 mM NO_2^-, sweeping the potential from −0.2 to 1.1 V vs. Ag/AgCl at different scan rates. Electrochemical impedance spectroscopy (EIS) measurements were performed in 0.1 M PBS (pH 7.2) containing 0.1 M KCl and 1 mM NO_2^- at a fixed potential of 0.85 V vs. Ag/AgCl, a frequency range from 10 mHz to 63 kHz and an amplitude of 10 mV. The amperometry measurements were conducted in 0.1 M PBS containing 0.1 M KCl at a fixed potential of 0.9 V vs. Ag/AgCl under stirring. It should be noted that all the experiments were performed at room temperature.

Fourier Transform Infrared spectroscopy (FTIR) using an Affinity-1S SHIMADZU spectrometer equipped with a golden gate single reflection attenuated total reflectance (ATR) accessory. FTIR spectra were recorded in the range of 500–4000 cm^{-1} at a resolution of 16 cm^{-1} and were used to determine the structural properties of f-MWCNT and poly 1,8-DAN/f-MWCNT. The morphological properties of the electrocatalysts were characterized using Transmission Electron Microscopy-EDX (TALOS F200S).

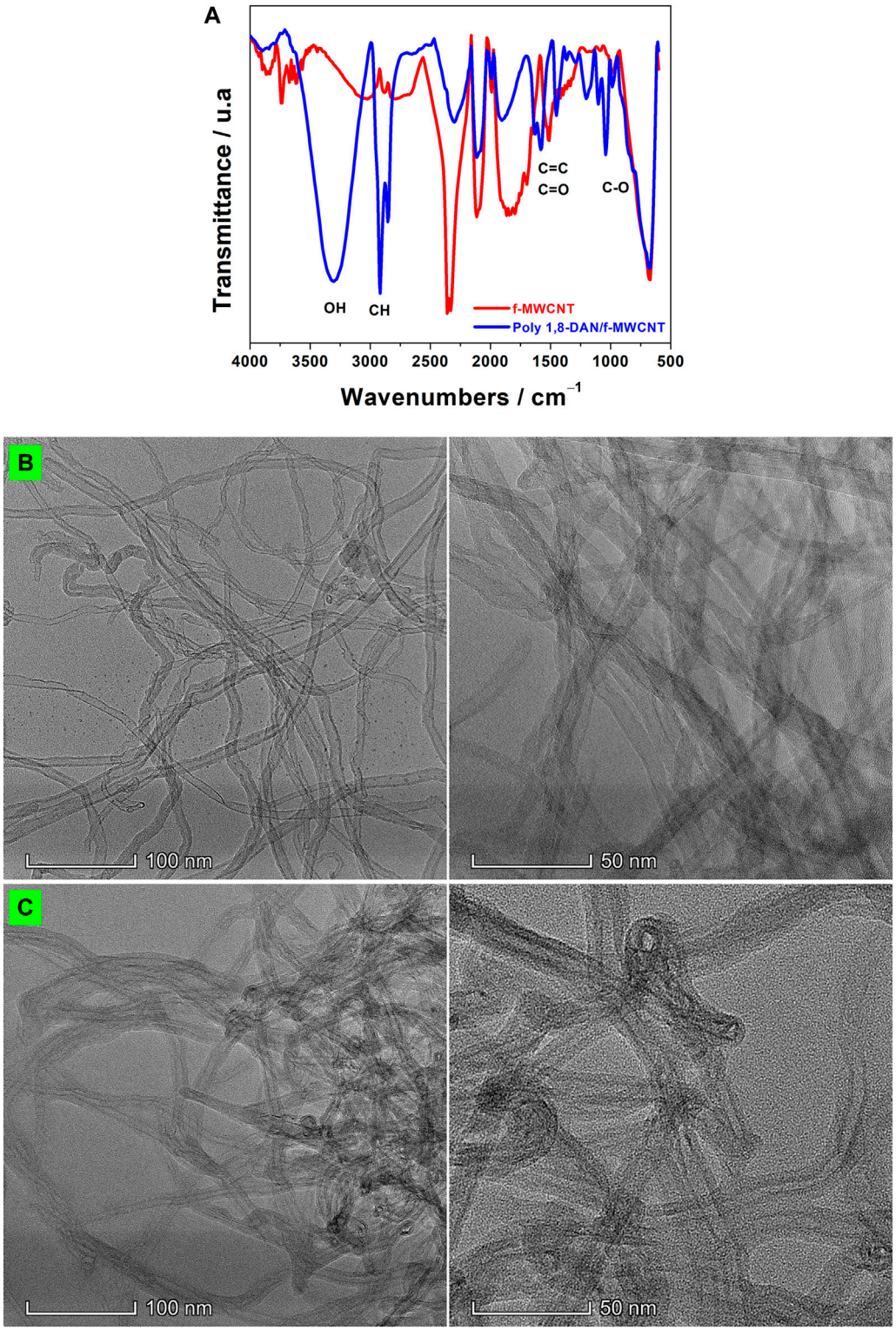

FIGURE 3 | (A) FTIR spectra of f-MWCNT (red line), and poly 1,8-DAN/f-MWCNT (blue line). TEM images of **(B)** f-MWCNT, and **(C)** poly 1,8-DAN/f-MWCNT.

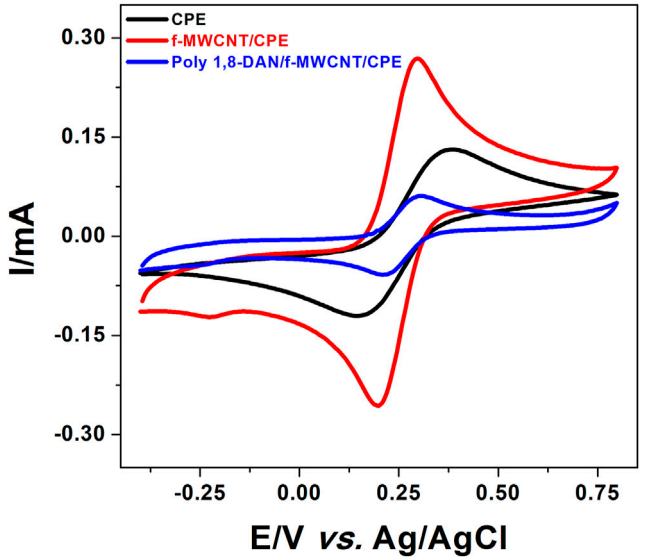

FIGURE 4 | CV of CPE (black line), f-MWCNT/CPE (red line), and poly 1,8-DAN/f-MWCNT/CPE (blue line) in 0.5 M of KCl containing 10 mM of $[Fe(CN)_6]^{3-/4-}$ at a scan rate of 50 mV/s.

RESULTS AND DISCUSSIONS

Polymerization of 1,8-DAN

In order to polymerize 1,8-Diaminonaphthalene onto the surface of CPE and f-MWCNT/CPE, cyclic voltammetry technique was performed in a 0.1 M HCl solution containing 5 mM of the monomer (1,8-DAN) by sweeping the potential from −0.5 to 1 V vs. Ag/AgCl at a scan rate of 50 mV/s for 15 scans. The formation of a brown film on each electrode was observed indicating the formation of poly 1,8-DAN (Oyama et al., 1989). The cyclic voltammograms obtained at CPE and f-MWCNT/CPE were illustrated in **Figure 1**. The bare electrode (**Figure 1A**) shows a peak current at +0.5 V vs. Ag/AgCl corresponding to the irreversible electrooxidation of 1,8-DAN which disappears completely after the sixth scan giving rise to new oxidation-reduction peaks which appear at about +0.05 and +0.2 V vs. Ag/AgCl. This is consistent with the previous results found by Majid et al. (2003). However, at the f-MWCNT/CPE as it is shown in **Figure 1B**, during the first scan, a peak current was observed at + 0.4 V vs. Ag/AgCl which corresponds to the irreversible oxidation of the monomer. The shift of about 100 mV observed on CPE modified by f-MWCNT can be attributed to the 3-dimensional network of f-MWCNT which increases the electrode surface area. It should be noted that a second peak was observed at 0.7 which may correspond to the second oxidation of the amine group. These results are in agreement with the work of Lee et al. (1992), when using platinum electrode for the polymerization of 1,8-DAN. It is important to highlight that after the modification of the electrode with f-MWCNT, the current intensities increased by about 76%. This may be attributed to the higher and good electrical conductivity of f-MWCNT and/or to the 3-dimensional network and large surface area of the f-MWCNT (Guo et al., 2020).

TABLE 1 | Comparison between I_{pa}, I_{pc} and the peak-to-peak separation (Δ_{Ep}) for CPE, f-MWCNT/CPE and 1,8-DAN/f-MWCNT/CPE.

Electrode	I_{pa}/μA	I_{pc}/μA	Δ_{Ep}/V
Bare CPE	235	196	0.332
f-MWCNT/CPE	393	387	0.098
Poly 1,8-DAN/f-MWCNT/CPE	40	47	0.091

In order to check the formation of a stable polymer, the prepared electrode was then placed in a 0.1 M HCl solution free monomer and CV was performed under the potential range of −0.5–1 V at a scan rate of 50 mV/s for 5 cycles. **Figure 2** shows the results obtained on poly 1,8-DAN/f-MWCNT/CPE. It can be seen that the voltammograms kept the same shape after consecutive scans revealing the oxidation/reduction peaks of poly 1,8-DAN in acidic medium, which indicates that a stable film of poly 1,8-Diaminonapththalene was synthesized on f-MWCNT/CPE (Salih et al., 2017b).

FTIR and TEM Characterization of Poly 1,8-DAN/f-MWCNT

FTIR spectroscopy was used to confirm the functionalization of MWCNT with carboxylic groups, and also to confirm the deposition of poly 1,8-DAN film (**Figure 3A**). The FTIR of f-MWCNT (red line) showed two absorption bands at 2334 and 2361 cm^{-1}, which correspond to the hydrogen of the carboxylic group (-COOH). In addition to this, two other bands were noticed at 976 and 1741 cm^{-1}, which are attributed respectively to the C=O and C-O of the -COOH. Another band was observed at 3600 cm^{-1} indicating the presence of the hydroxylic group -OH of -COOH (Oularbi et al., 2017; Oularbi, 2018; El Attar et al., 2022). These results demonstrated that the MWCNT were successively functionalized. The structural properties of poly 1,8-DAN/f-MWCNT have also been investigated using FTIR spectroscopy (blue line). It can be seen that new peaks appeared after the electrodeposition of the polymer. In fact, the absorption band located in 3309 cm^{-1} corresponds to the N-H stretching. Whereas, the peaks that appeared at 1490 and 1581 cm^{-1} are attributed to the C-C of the polymer. Furthermore, the band of 1203 indicates the C-N stretching (Pałys et al., 1997). These results confirm the formation of poly 1,8-DAN on the surface of f-MWCNT/CPE. The morphologies of f-MWCNT/CPE and poly 1,8-DAN/f-MWCNT/CPE were examined using TEM (**Figures 3B,C**). The corresponding images (**Figure 3B**) reveal a slight increase of the carbon nanotubes diameter after the electrochemical deposition of poly 1,8-DAN.

The thickness of the polymeric film (d) was also determined using **Eq. 1** described as follow (Halim et al., 2019):

$$d = (Q \times M_w) / (n \times F \times A \times \varphi) \quad (1)$$

Where M_w is the molar mass of the monomer (158.2 g/mol), Q is the electrical charge associated to the polymer formation, n is the number of the involved electrons (2) (Lee et al., 1992), F is the Faraday (96485 Q/mol), A is the surface area of the working electrode, and φ is

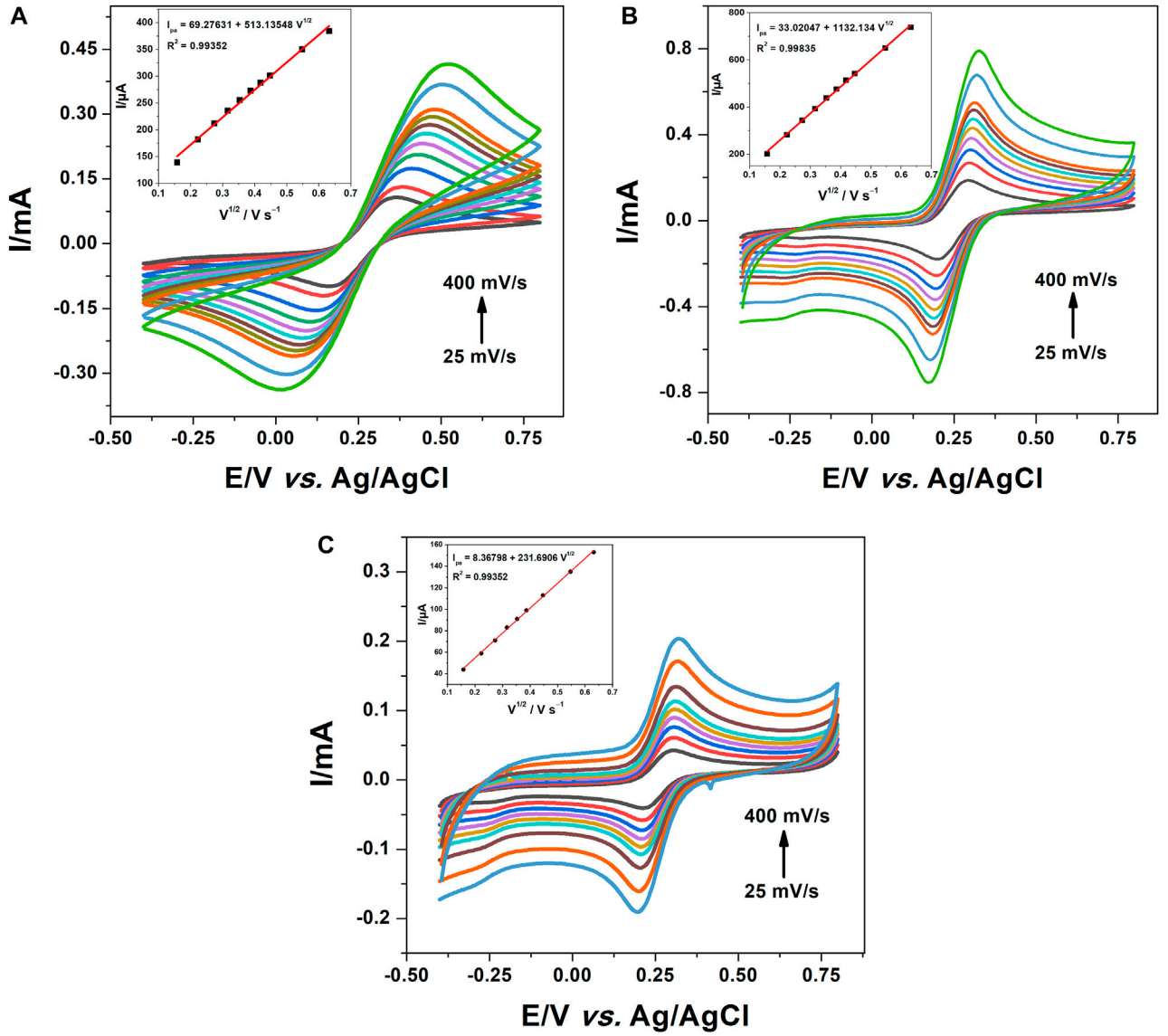

FIGURE 5 | CV of **(A)** CPE, **(B)** f-MWCNT/CPE, and **(C)** poly 1,8-DAN/f-MWCNT/CPE in 0.5 M of KCl containing 10 mM of $[Fe(CN)_6]^{3-/4-}$ at different scan rates.

the monomer density (1.12 g/cm^3). The thickness of poly 1,8-DAN film deposited on the surface of f-MWCNT/CPE was found to be 22 nm, which indicates the formation of a thin film on the surface. This thickness is in agreement with the results found using the transmission electron microscopy.

Electrochemical Characterization of Poly 1,8-DAN/f-MWCNT

Cyclic Voltammetry Characterization in $[Fe(CN)_6]^{3-/4-}$

The preliminary investigations were aimed towards comparing the electrochemical responses of ferri-ferrocyanide system on different electrodes. In this perspective, CV measurements were performed in 0.5 M KCl containing 10 mM $[Fe(CN)_6]^{3-/4-}$ at CPE, f-MWCNT/CPE, poly 1,8-DAN/f-MWCNT/CPE in the potential range from −0.4–0.8 V vs. Ag/AgCl. As can be seen in **Figure 4** and **Table 1**, the peak-to-peak separation on CPE (black line) is equal to 223 mV, which indicate a slow electronic transfer. On the f-MWCNT/CPE, the peak-to-peak separation was reduced to reach the value of 98 mV (red line) and the current intensities increased by about 40%. This behavior could be explained by the large specific surface area and high electrical conductivity offered by f-MWCNT. The same behavior was observed by Oularbi et al. (2017), when using Polypyrrole and Carbon nanofibers. A surprising fact was observed after the electrodeposition of poly 1,8-DAN on f-MWCNT/CPE (blue line). A dramatic decrease of the value of ΔE_p was found, around 91 mV, which is about more than 3 times smaller than the bare CPE. The only possible explanation is that the decrease in ΔE_p is probably due to the improvement of the electronic transfer

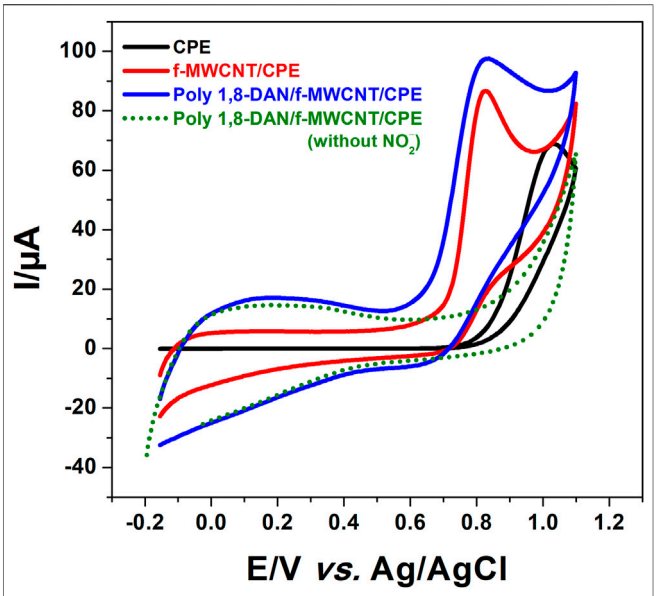

FIGURE 6 | CV of CPE (balck line), f-MWCNT/CPE (red line), and poly 1,8-DAN/f-MWCNT/CPE in 0.1 M PBS containing 0.1 M KCl (green dots) and 1 mM NO_2^- (blue line) at pH 7, 2 and a scanning speed of 50 mV/s.

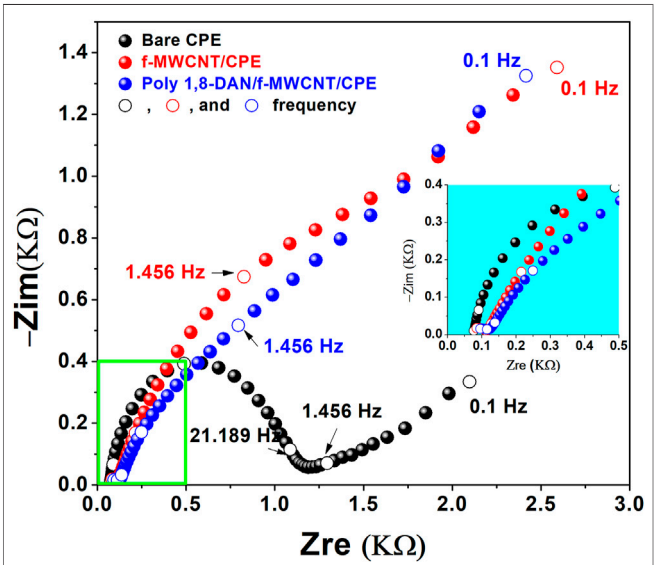

FIGURE 7 | Nyquist plots of CPE (black line), f-MWCNT/CPE (red line), and poly 1,8-DAN/f-MWCNT/CPE (blue line) in 0.1 M PBS containing 0.1 M KCl and 1 mM NO_2^- at pH 7.2 and a fixed Potential of 0.85 V vs. Ag/AgCl.

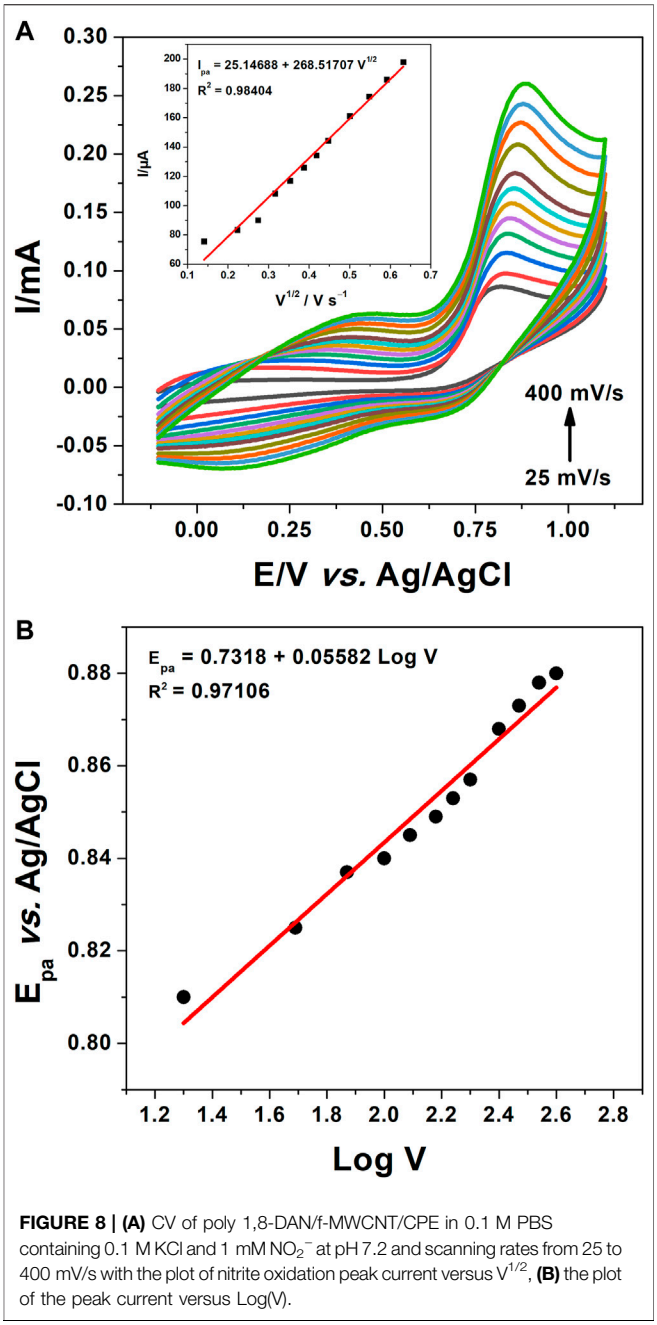

FIGURE 8 | (A) CV of poly 1,8-DAN/f-MWCNT/CPE in 0.1 M PBS containing 0.1 M KCl and 1 mM NO_2^- at pH 7.2 and scanning rates from 25 to 400 mV/s with the plot of nitrite oxidation peak current versus $V^{1/2}$, **(B)** the plot of the peak current versus Log(V).

at the interface electrode-solution due to the presence of a large amount of amine groups all along the polymer backbone (Wang et al., 2016). Indeed, It has been proved that an amine-rich surface enhances the electronic transfer (Li et al., 2017; Ning et al., 2019). Contrary to what one might expect to find, a low current compared to CPE and f-MWCNT/CPE was obtained due to the low conductivity of poly 1,8-DAN at neutral pH (Majid et al., 2003).

The specific surface area of all the electrodes was calculated using the Randles and Sevcik **Eq. 2** (Analytical Electrochemistry, Wang, 2006) as shown in **Figure 5**:

$$I_p = 2.69 \times 10^5 \times n^{3/2} \times A \times C \times D^{1/2} \times V^{1/2} \quad (2)$$

Where, the number of electrons transferred (n) is equal to 1, the concentration (C) is equal to 10 mM and the diffusion coefficient (D) is equal to 6.7 10^{-6} cm^2/s (Halim et al., 2019). The specific surface areas were found to be 0.073, 0.16^2, and 0.033 cm^2, respectively for CPE, f-MWCNT/CPE, and poly 1,8-DAN/

f-MWCNT/CPE. Indeed, the specific surface of f-MWCNT/CPE was about two times higher than the bare CPE. This was due to the large specific surface of multi-walled carbon nanotubes (Shi et al., 2019). It is important to mention that the electrode modified with poly 1,8-DAN and f-MWCNT has the smallest surface area. This phenomena can be explained by the low electrical conductivity of polymer, and the lack of active sites of the poly (1,8-DAN) at neutral pH (Majid et al., 2003).

Electrooxidation Behavior of Nitrite on the Poly 1,8-DAN/f-MWCNT

After the characterization of our electrodes, the behavior of the different electrodes in presence of nitrite was investigated using CV in a pH 7.2, 0.1 M phosphate buffer solution containing 0.1 M KCl and 1 mM nitrite. **Figure 6** presents the corresponding voltammograms at the bare CPE, f-MWCNT/CPE, and poly 1,8-DAN/f-MWCNT/CPE. An irreversible peak at 1.04 V vs. Ag/AgCl (black line) was obtained at bare carbon paste electrode which corresponds to the irreversible oxidation of nitrite. As expected, the peak potential was shifted to more negative value (210 mV) after the modification of CPE with f-MWCNT (red line) with an important increase in the current intensity. After the electrodeposition of poly 1,8-DAN on the surface of f-MWCNT/CPE (blue line). The same results were observed concerning the peak potential with a further increase of the current intensity, indicating that nitrite is much easier to oxidase on the hybrid material. Similar results were obtained by Huang et al., using gold nanoparticles combined with poly (3-methylthiophene), which was explained by the synergistic effect of combining both gold nanoparticles and conducting polymers. It seems that the carbon nanomaterials combined with conducting polymers enhance the electronic transfer as observed by many authors (Zheng et al., 2009; Rajalakshmi and John, 2015, 2; Arulraj et al., 2018). To better understand this phenomenon, electrochemical impedance spectroscopy (EIS) was conducted in the same solution at an applied potential of 0.85 V vs. Ag/AgCl with a small amplitude of 10 mV. **Figure 7** presents the corresponding Nyquist plots. Indeed, it can be seen that the charge transfer resistances (R_{ct}) decreased from 3277 Ω to 11 Ω after the modification of CPE with poly 1,8-DAN/f-MWCNT, which is 300 times smaller. These results are in good agreement with the CV measurements and suggests that the prepared hybrid material promotes the electronic transfer between the supporting electrolyte and the electrode.

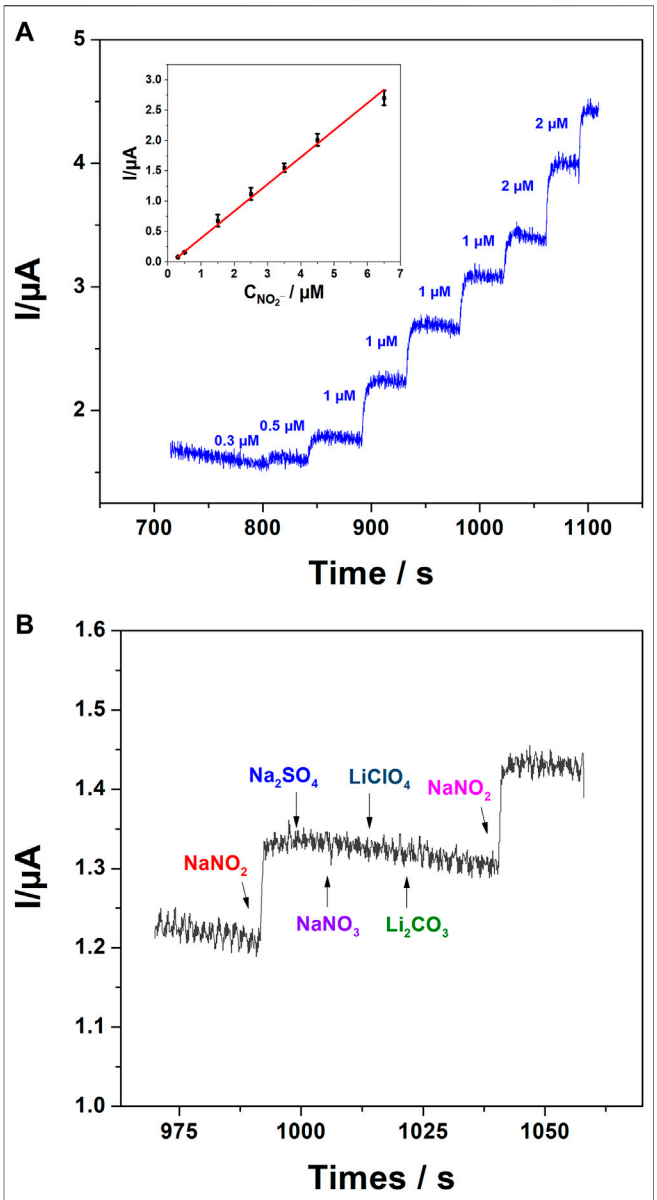

FIGURE 9 | (A) Amperometry of poly 1,8-DAN/f-MWCNT/CPE in 0.1 M PBS containing 0.1 M KCl at pH 7.2 with a fixed potential of 0.9 V vs. Ag/AgCl at consecutive additions of nitrite, insert the calibration plot of the current versus nitrite concentrations. **(B)** Effect of some interference components on nitrite response.

Electrooxidation Mechanism of Nitrite on the Poly 1,8-DAN/f-MWCNT

In order to establish the reaction mechanism of nitrite oxidation, cyclic voltammetry experiments were recorded on poly 1,8-DAN/f-MWCNT/CPE. The corresponding graphs shown in **Figure 8A** present the variation of the oxidation current with the square root of the scan rate.

It can be seen that the nitrite oxidation peak increased linearly with the square root of the scan rate according to the equation I_{pa} = 25.14688 + 268.51707 $V^{1/2}$ with a correlation coefficient of 0.98404 which suggests that the electrochemical reaction is controlled by a diffusion process (Baghayeri et al., 2020b; Baghayeri et al., 2021b). It should be noted that a shift in the oxidation peak potential (E_{pa}) to more positive values with the scan rates confirms the irreversibility of the nitrite oxidation reaction as mentioned by others authors (Zhao et al., 2017; Shi et al., 2019). The number of the transferred electrons can be calculated by plotting the E_{pa} *vs.* Log V. E_{pa} varied linearly with the logarithm of the scan rate as described by the equation E_{pa} = 0.7318 + 0.05582 Log V with a correlation coefficient of 0.97106 (**Figure 8B**). The number of the transferred electrons during the oxidation reaction of nitrite

TABLE 2 | Comparison of the electrocatalytic performance of different hybrid materials.

Catalyst	Technique	Linear range/μM	Detection limit/μM	Refs.
p-ATT/f-MWCNT	Amperometry	0.001–1.0	0.0002	Rajalakshmi and John (2015)
AuNPs/PEDOT	Amperometry	0.2–1400.0	0.06	Lin et al. (2016)
PdNPs-poly (1.5-DAN)/MWCNT	Amperometry	0.25–100	0.08	Shi et al. (2019)
rGO/AuNPs	Chronoamperometry	1.0–6000.0	0.13	Jian et al. (2018)
Pd/Fe3O4/Poly DOPA/rGO	Amperometry	2.5–6470.0	0.5	Zhao et al. (2017)
AuNPs/MWCPE	Amperometry	0.05–250	0.01	Afkhami et al. (2014)
Au-rGO/PDDA	DPV	0.05–8.5	0.04	Jiao et al. (2015)
Poly (1,8-DAN)/f-MWCNT	Amperometry	0.3–6.5	0.075	This Work

was then calculated according to Laviron's **Eq. 3** (Analytical Electrochemistry, Wang, 2006):

$$E_{pa} = E^{\circ} + (RT/anF)\ln(RTK^{\circ}/\alpha nF) + 2.3(RT/\alpha nF)\log(v) \quad (3)$$

Where n is the number of the transferred electrons, α is the electron transfer coefficient which is taken as 0.5 in a totally irreversible reaction (Shi et al., 2019), *v* is the scan rate, and E°' is the formal potential. Whereas R, T and F have their conventional meaning. The number of electron n involved in the oxidation reaction of nitrite was calculated to be about 2 (2.08), which demonstrates that the electrooxidation of nitrite requires the transfer of two electrons according to the following reactions noted (4) and (5). These results are in agreement with the literature (Arulraj et al., 2018):

$$2NO_2^- \leftrightarrow 2NO_2 + 2e^- \quad (4)$$

$$2NO_2 + H_2O \rightarrow NO_3^- + NO_2^- + 2H^+ \quad (5)$$

Calibration Curve and Real Sample Analysis

After the characterization of our sensor, and in order to evaluate the advantages offered by f-MWCNT and poly 1,8-DAN, amperometry was chosen as a sensitive technique to detect nitrite in aqueous solution (Liu et al., 2011; Rajalakshmi and John, 2015; Zhang et al., 2015; Fan et al., 2017). Indeed, amperometry was performed in 0.1 M PBS pH 7.2 containing 0.1 M KCl at a fixed potential of 0.9 V vs. Ag/AgCl under continuous stirring. The corresponding graph shown in **Figure 9A** illustrates the variation of the current intensities versus time after successive additions of nitrite. The oxidation current increased linearly with nitrite concentration in a range between 300 and 6500 nM according to equation I = −0.0537 + 0.44453 [NO_2^-] with a correlation coefficient of 0.99722, a relative standard deviation (RSD) of 2.36% (*n* = 3 tests), and a sensitivity of 0.44453 μA/μM. The detection limit was calculated by the equation LOD = 3 × SD/P. where SD is the standard deviation, and P the slope of the calibration curve, and it was found to be 75 nM.

Prior to the application in real samples, the selectivity of the developed sensor was investigated in the presence of some components such as $NaNO_3$, Na_2SO_4, $LiClO_4$, and Li_2CO_3. From the obtained results (**Figure 9B**), we can assume that these components did not interfere with the nitrite response. Subsequently, the effectiveness application of the developed hybrid sensor for detection of nitrite in real samples was tested in tap water. The determination of nitrite was based on the method of dosed additions, and the concentration of nitrite was found to be 0.28667 ± 0.01528 μM with an RSD of about 5.3% (3 tests) which suggests that our sensor can be used directly in real samples, and without any pretreatment of water. The detection limit, linearity range, and the detection technique of different hybrids reported in the literature are summarized in **Table 2**. Our material seems to be a good choice for nitrite determination in water samples.

CONCLUSION

In summary, a low-cost sensor based on 1,8-Diaminonaphthalene electrodeposited on f-MWCNT/CPE was developed for a rapid and effective determination of nitrite in aqueous solutions. The characterization of the electrode was performed using different techniques such as FTIR, TEM, CV and EIS. The FTIR and TEM characterizations confirm the presence of the polymer on the surface of our sensor, while the electrochemical measurements revealed that the combination of f-MWCNT and poly 1,8-DAN improves the electronic transfer, and has very good electro-catalytic activity towards nitrite oxidation. The sensor was then applied for detection of nitrite showing a good linearity, selectivity and sensitivity with a very low detection limit of 75 nM. It should be highlighted that the sensor can be used directly and without any pretreatment of water samples. More studies are undergoing to enhance the linearity range and to extend the applicability of this sensor.

DATA AVAILABILITY STATEMENT

The original contributions presented in the study are included in the article/Supplementary Material, further inquiries can be directed to the corresponding author.

AUTHOR CONTRIBUTIONS

All authors listed have made a substantial, direct, and intellectual contribution to the work and approved it for publication.

ACKNOWLEDGMENTS

This work was supported by MESRSFC (Ministère de l'Enseignement Supérieur et de la Recherche Scientifique et de la Formation des cadres–Morocco) and CNRST (Centre National pour la Recherche Scientifique et Technique-Morocco) (Project number PPR/2015/72).

REFERENCES

Afkhami, A., Soltani-Felehgari, F., Madrakian, T., and Ghaedi, H. (2014). Surface Decoration of Multi-Walled Carbon Nanotubes Modified Carbon Paste Electrode with Gold Nanoparticles for Electro-Oxidation and Sensitive Determination of Nitrite. *Biosens. Bioelectron.* 51, 379–385. doi:10.1016/j.bios.2013.07.056

Arulraj, A. D., Sundaram, E., Vasantha, V. S., and Neppolian, B. (2018). Polypyrrole with a Functionalized Multi-Walled Carbon Nanotube Hybrid Nanocomposite: A New and Efficient Nitrite Sensor. *New J. Chem.* 42, 3748–3757. doi:10.1039/C7NJ04130F

Aschebrook-Kilfoy, B., Shu, X.-O., Gao, Y.-T., Ji, B.-T., Yang, G., Li, H. L., et al. (2013). Thyroid Cancer Risk and Dietary Nitrate and Nitrite Intake in the Shanghai Women's Health Study. *Int. J. Cancer* 132, 897–904. doi:10.1002/ijc.27659

Baghayeri, M., Amiri, A., Karimabadi, F., Di Masi, S., Maleki, B., Adibian, F., et al. (2021a). Magnetic MWCNT-Dendrimer: A Potential Modifier for Electrochemical Evaluation of as (III) Ions in Real Water Samples. *J. Electroanalytical Chem.* 888, 115059. doi:10.1016/j.jelechem.2021.115059

Baghayeri, M., Ghanei-Motlagh, M., Tayebee, R., Fayazi, M., and Narenji, F. (2020a). Application of Graphene/zinc-Based Metal-Organic Framework Nanocomposite for Electrochemical Sensing of As(III) in Water Resources. *Analytica Chim. Acta* 1099, 60–67. doi:10.1016/j.aca.2019.11.045

Baghayeri, M., Nabavi, S., Hasheminejad, E., and Ebrahimi, V. (2021b). Introducing an Electrochemical Sensor Based on Two Layers of Ag Nanoparticles Decorated Graphene for Rapid Determination of Methadone in Human Blood Serum. *Top. Catal.* 1099, 1–10. doi:10.1007/s11244-021-01483-4

Baghayeri, M., Nodehi, M., Amiri, A., Amirzadeh, N., Behazin, R., and Iqbal, M. Z. (2020b). Electrode Designed with a Nanocomposite Film of CuO Honeycombs/Ag Nanoparticles Electrogenerated on a Magnetic Platform as an Amperometric Glucose Sensor. *Analytica Chim. Acta* 1111, 49–59. doi:10.1016/j.aca.2020.03.039

Bansod, B., Kumar, T., Thakur, R., Rana, S., and Singh, I. (2017). A Review on Various Electrochemical Techniques for Heavy Metal Ions Detection with Different Sensing Platforms. *Biosens. Bioelectron.* 94, 443–455. doi:10.1016/j.bios.2017.03.031

Beitollahi, H., Movahedifar, F., Tajik, S., and Jahani, S. (2018). A Review on the Effects of Introducing CNTs in the Modification Process of Electrochemical Sensors. *Electroanalysis* 31, 1195–1203. doi:10.1002/elan.201800370

Berardo, A., De Maere, H., Stavropoulou, D. A., Rysman, T., Leroy, F., and De Smet, S. (2016). Effect of Sodium Ascorbate and Sodium Nitrite on Protein and Lipid Oxidation in Dry Fermented Sausages. *Meat Sci.* 121, 359–364. doi:10.1016/j.meatsci.2016.07.003

Bijad, M., Karimi-Maleh, H., Farsi, M., and Shahidi, S.-A. (2017). Simultaneous Determination of Amaranth and Nitrite in Foodstuffs via Electrochemical Sensor Based on Carbon Paste Electrode Modified with CuO/SWCNTs and Room Temperature Ionic Liquid. *Food Anal. Methods* 10, 3773–3780. doi:10.1007/s12161-017-0933-z

Chemchoub, S., Elbasri, M., Halim, E. M., and El Rhazi, M. (2019). The Electrocatalytic Oxidation of Methanol on a Carbon Paste Electrode Modified by Poly(para-Phenylenediamine) and Nickel Particles. *Mater. Today Proc.* 13, 720–729. doi:10.1016/j.matpr.2019.04.033

Chemchoub, S., Oularbi, L., El Attar, A., Younssi, S. A., Bentiss, F., Jama, C., et al. (2020). Cost-Effective Non-Noble Metal Supported on Conducting Polymer Composite Such as Nickel Nanoparticles/Polypyrrole as Efficient Anode Electrocatalyst for Ethanol Oxidation. *Mater. Chem. Phys.* 250, 123009. doi:10.1016/j.matchemphys.2020.123009

El Attar, A., Chemchoub, S., Diallo Kalan, M., Oularbi, L., and El Rhazi, M. (2022). Designing New Material Based on Functionalized Multi-Walled Carbon Nanotubes and Cu(OH)2–Cu2O/Polypyrrole Catalyst for Ethanol Oxidation in Alkaline Medium. *Front. Chem.* 9, 805654. Available at: https://www.frontiersin.org/article/10.3389/fchem.2021.805654 (Accessed February 6, 2022). doi:10.3389/fchem.2021.805654

El Attar, A., Oularbi, L., Chemchoub, S., and El Rhazi, M. (2021). Effect of Electrochemical Activation on the Performance and Stability of Hybrid (PPy/Cu2O Nanodendrites) for Efficient Ethanol Oxidation in Alkaline Medium. *J. Electroanalytical Chem.* 885, 115042. doi:10.1016/j.jelechem.2021.115042

El Attar, A., Oularbi, L., Chemchoub, S., and El Rhazi, M. (2020). Preparation and Characterization of Copper Oxide Particles/Polypyrrole (Cu2O/PPy) via Electrochemical Method: Application in Direct Ethanol Fuel Cell. *Int. J. Hydrogen Energ.* 45, 8887–8898. doi:10.1016/j.ijhydene.2020.01.008

El Rhazi, M., Majid, S., Elbasri, M., Salih, F. E., Oularbi, L., and Lafdi, K. (2018). Recent Progress in Nanocomposites Based on Conducting Polymer: Application as Electrochemical Sensors. *Int. Nano Lett.* 8, 79–99. doi:10.1007/s40089-018-0238-2

Elbasri, M., and Rhazi, M. E. (2015). Preparation and Characterization of Carbon Paste Electrode Modified by Poly(1,8-Diaminonaphthalene) and Nickel Ions Particles: Application to Electrocatalytic Oxidation of Methanol. *Mater. Today Proc.* 2, 4676–4683. doi:10.1016/j.matpr.2015.09.022

Fan, X., Lin, P., Liang, S., Hui, N., Zhang, R., Feng, J., et al. (2017). Gold Nanoclusters Doped Poly(3,4-Ethylenedioxythiophene) for Highly Sensitive Electrochemical Sensing of Nitrite. *Ionics* 23, 997–1003. doi:10.1007/s11581-016-1865-0

Gracia, R., and Mecerreyes, D. (2013). Polymers with Redox Properties: Materials for Batteries, Biosensors and More. *Polym. Chem.* 4, 2206–2214. doi:10.1039/C3PY21118E

Guo, H., Fan, T., Yao, W., Yang, W., Wu, N., Liu, H., et al. (2020). Simultaneous Determination of 4-Aminophenol and Acetaminophen Based on High Electrochemical Performance of ZIF-67/MWCNT-COOH/Nafion Composite. *Microchemical J.* 158, 105262. doi:10.1016/j.microc.2020.105262

Halim, E. M., Elbasri, M., Perrot, H., Sel, O., Lafdi, K., and El Rhazi, M. (2019). Synthesis of Carbon Nanofibers/Poly(Para-Phenylenediamine)/Nickel Particles Nanocomposite for Enhanced Methanol Electrooxidation. *Int. J. Hydrogen Energ.* 44, 24534–24545. doi:10.1016/j.ijhydene.2019.07.141

Han, S., and Chen, X. (2019). Copper Nanoclusters-Enhanced Chemiluminescence for Folic Acid and Nitrite Detection. *Spectrochimica Acta A: Mol. Biomol. Spectrosc.* 210, 315–320. doi:10.1016/j.saa.2018.11.051

Jaiswal, N., Tiwari, I., Foster, C. W., and Banks, C. E. (2017). Highly Sensitive Amperometric Sensing of Nitrite Utilizing Bulk-Modified MnO 2 Decorated Graphene Oxide Nanocomposite Screen-Printed Electrodes. *Electrochimica Acta* 227, 255–266. doi:10.1016/j.electacta.2017.01.007

Jian, J.-M., Fu, L., Ji, J., Lin, L., Guo, X., and Ren, T.-L. (2018). Electrochemically Reduced Graphene Oxide/Gold Nanoparticles Composite Modified Screen-Printed Carbon Electrode for Effective Electrocatalytic Analysis of Nitrite in Foods. *Sensors Actuators B: Chem.* 262, 125–136. doi:10.1016/j.snb.2018.01.164

Jiao, S., Jin, J., and Wang, L. (2015). One-Pot Preparation of Au-RGO/PDDA Nanocomposites and Their Application for Nitrite Sensing. *Sensors Actuators B: Chem.* 208, 36–42. doi:10.1016/j.snb.2014.11.020

Kalaycıoğlu, Z., and Erim, F. B. (2016). Simultaneous Determination of Nitrate and Nitrite in Fish Products with Improved Sensitivity by Sample Stacking-Capillary Electrophoresis. *Food Anal. Methods* 9, 706–711. doi:10.1007/s12161-015-0241-4

Karimi-Maleh, H., Orooji, Y., Karimi, F., Alizadeh, M., Baghayeri, M., Rouhi, J., et al. (2021). A Critical Review on the Use of Potentiometric Based Biosensors for Biomarkers Detection. *Biosens. Bioelectron.* 184, 113252. doi:10.1016/j.bios.2021.113252

Katabami, K., Hayakawa, M., and Gando, S. (2016). Severe Methemoglobinemia Due to Sodium Nitrite Poisoning. *Case Rep. Emerg. Med.* 2016, 9013816. doi:10.1155/2016/9013816

Kesavan, S., Kumar, D. R., Baynosa, M. L., and Shim, J.-J. (2018). Potentiodynamic Formation of Diaminobenzene Films on an Electrochemically Reduced Graphene Oxide Surface: Determination of Nitrite in Water Samples. *Mater. Sci. Eng. C* 85, 97–106. doi:10.1016/j.msec.2017.12.004

Lee, J. W., Park, D. S., Shim, Y. B., and Park, S. M. (1992). Electrochemical Characterization of Poly(1,8-Diaminonaphthalene): A Functionalized Polymer. *J. Electrochem. Soc.* 139, 3507–3514. doi:10.1149/1.2069107

Li, L., Liu, D., Wang, K., Mao, H., and You, T. (2017). Quantitative Detection of Nitrite with N-Doped Graphene Quantum Dots Decorated N-Doped Carbon Nanofibers Composite-Based Electrochemical Sensor. *Sensors Actuators B: Chem.* 252, 17–23. doi:10.1016/j.snb.2017.05.155

Lin, P., Chai, F., Zhang, R., Xu, G., Fan, X., and Luo, X. (2016). Electrochemical Synthesis of Poly(3,4-Ethylenedioxythiophene) Doped with Gold

Nanoparticles, and its Application to Nitrite Sensing. *Microchim. Acta* 183, 1235–1241. doi:10.1007/s00604-016-1751-5

Lin, S.-L., Hsu, J.-W., and Fuh, M.-R. (2019). Simultaneous Determination of Nitrate and Nitrite in Vegetables by Poly(Vinylimidazole-Co-Ethylene Dimethacrylate) Monolithic Capillary Liquid Chromatography with UV Detection. *Talanta* 205, 120082. doi:10.1016/j.talanta.2019.06.082

Liu, S., Tian, J., Wang, L., Luo, Y., and Sun, X. (2011). Production of Stable Aqueous Dispersion of Poly(3,4-Ethylenedioxythiophene) Nanorods Using Graphene Oxide as a Stabilizing Agent and Their Application for Nitrite Detection. *Analyst* 136, 4898. doi:10.1039/c1an15799j

Lo, H.-S., Lo, K.-W., Yeung, C.-F., and Wong, C.-Y. (2017). Rapid Visual and Spectrophotometric Nitrite Detection by Cyclometalated Ruthenium Complex. *Analytica Chim. Acta* 990, 135–140. doi:10.1016/j.aca.2017.07.018

Majid, S., Rhazi, M. E., Amine, A., Curulli, A., and Palleschi, G. (2003). Carbon Paste Electrode Bulk-Modified with the Conducting Polymer Poly(1,8-Diaminonaphthalene): Application to Lead Determination. *Microchimica Acta* 143, 195–204. doi:10.1007/s00604-003-0058-5

Mani, V., Govindasamy, M., Chen, S.-M., Chen, T.-W., Kumar, A. S., and Huang, S.-T. (2017). Core-Shell Heterostructured Multiwalled Carbon Nanotubes@ reduced Graphene Oxide Nanoribbons/Chitosan, a Robust Nanobiocomposite for Enzymatic Biosensing of Hydrogen Peroxide and Nitrite. *Sci. Rep.* 7, 11910. doi:10.1038/s41598-017-12050-x

Mao, Y., Bao, Y., Han, D.-X., and Zhao, B. (2018). Research Progress on Nitrite Electrochemical Sensor. *Chin. J. Anal. Chem.* 46, 147–155. doi:10.1016/S1872-2040(17)61066-1

Muthumariappan, A., Govindasamy, M., Chen, S.-M., Sakthivel, K., and Mani, V. (2017). Screen-printed Electrode Modified with a Composite Prepared from Graphene Oxide Nanosheets and Mn3O4 Microcubes for Ultrasensitive Determination of Nitrite. *Microchim. Acta* 184, 3625–3634. doi:10.1007/s00604-017-2379-9

Ning, X., Li, Y., Ming, J., Wang, Q., Wang, H., Cao, Y., et al. (2019). Electronic Synergism of Pyridinic- and Graphitic-Nitrogen on N-Doped Carbons for the Oxygen Reduction Reaction. *Chem. Sci.* 10, 1589–1596. doi:10.1039/C8SC04596H

Oularbi, L. (2018). Étude de nanocomposites polypyrrole/nanoparticule de carbone par impédance électrochimique et ac-électrogravimétrie: application aux capteurs électrochimiques. Aux Capteurs àlectrochimiques, Ph.D. Thesis, Sorbonne and Hassan II Casablanca Universities, Casablanca, Morocco, June 29, 2018. Thesis `NNT : 2018SORUS110b. `tel-02922320b.

Oularbi, L., Turmine, M., and El Rhazi, M. (2017). Electrochemical Determination of Traces lead Ions Using a New Nanocomposite of Polypyrrole/Carbon Nanofibers. *J. Solid State. Electrochem.* 21, 3289–3300. doi:10.1007/s10008-017-3676-2

Oularbi, L., Turmine, M., and El Rhazi, M. (2019). Preparation of Novel Nanocomposite Consisting of Bismuth Particles, Polypyrrole and Multi-Walled Carbon Nanotubes for Simultaneous Voltammetric Determination of Cadmium(II) and Lead(II). *Synth. Met.* 253, 1–8. doi:10.1016/j.synthmet.2019.04.011

Oularbi, L., Turmine, M., Salih, F. E., and El Rhazi, M. (2020). Ionic Liquid/carbon Nanofibers/bismuth Particles Novel Hybrid Nanocomposite for Voltammetric Sensing of Heavy Metals. *J. Environ. Chem. Eng.* 8, 103774. doi:10.1016/j.jece.2020.103774

Oyama, N., Sato, M., and Ohsaka, T. (1989). Preparation of Thin Polymeric Films on Electrode Surfaces by Electro-Polymerization of Aromatic Compounds with Amino Groups. *Synth. Met.* 29, 501–506. doi:10.1016/0379-6779(89)90340-8

Pałys, B. J., Skompska, M., and Jackowska, K. (1997). Sensitivity of Poly 1,8-Diaminonaphthalene to Heavy Metal Ions — Electrochemical and Vibrational Spectra Studies. *J. Electroanal. Chem.* 433, 41–48. doi:10.1016/S0022-0728(97)00144-7

Rajalakshmi, K., and John, S. A. (2015). Highly Sensitive Determination of Nitrite Using FMWCNT-Conducting Polymer Composite Modified Electrode. *Sensors Actuators B: Chem.* 215, 119–124. doi:10.1016/j.snb.2015.03.050

Ren, H.-H., Fan, Y., Wang, B., and Yu, L.-P. (2018). Polyethylenimine-Capped CdS Quantum Dots for Sensitive and Selective Detection of Nitrite in Vegetables and Water. *J. Agric. Food Chem.* 66, 8851–8858. doi:10.1021/acs.jafc.8b01951

Ribeiro, M. C., Bezerra, T. D. S., Soares, A. C., Boechat-Ramos, R., Carneiro, F. P., Vianna, L. M. D. S., et al. (2017). Hippocampal and Cerebellar Histological Changes and Their Behavioural Repercussions Caused by Brain Ischaemic Hypoxia Experimentally Induced by Sodium Nitrite. *Behav. Brain Res.* 332, 223–232. doi:10.1016/j.bbr.2017.06.008

Roy, A., Ray, A., Saha, S., and Das, S. (2018). Investigation on Energy Storage and Conversion Properties of Multifunctional PANI-MWCNT Composite. *Int. J. Hydrogen Energ.* 43, 7128–7139. doi:10.1016/j.ijhydene.2018.02.153

Rui, M., Jiang, Y., and Zhu, A. (2020). Sub-Micron Calcium Carbonate as a Template for the Preparation of Dendrite-Like PANI/CNT Nanocomposites and its Corrosion protection Properties. *Chem. Eng. J.* 385, 123396. doi:10.1016/j.cej.2019.123396

Salagare, S., Shivappa Adarakatti, P., and Venkataramanappa, Y. (2020). Designing and Construction of Carboxyl Functionalised MWCNTs/Co-MOFs-Based Electrochemical Sensor for the Sensitive Detection of Nitrite. *Int. J. Environ. Anal. Chem.* 100, 1–20. doi:10.1080/03067319.2020.1796989

Salhi, O., Ez-zine, T., and El Rhazi, M. (2021). Hybrid Materials Based on Conducting Polymers for Nitrite Sensing: A Mini Review. *Electroanalysis* 33, 1681–1690. doi:10.1002/elan.202100033

Salih, F. E., Achiou, B., Ouammou, M., Bennazha, J., Ouarzane, A., Younssi, S. A., et al. (2017a). Electrochemical Sensor Based on Low Silica X Zeolite Modified Carbon Paste for Carbaryl Determination. *J. Adv. Res.* 8, 669–676. doi:10.1016/j.jare.2017.08.002

Salih, F. E., Ouarzane, A., and El Rhazi, M. (2017b). Electrochemical Detection of lead (II) at Bismuth/Poly(1,8-Diaminonaphthalene) Modified Carbon Paste Electrode. *Arabian J. Chem.* 10, 596–603. doi:10.1016/j.arabjc.2015.08.021

Salih, F. E., Oularbi, L., Halim, E., Elbasri, M., Ouarzane, A., and El Rhazi, M. (2018). Conducting Polymer/Ionic Liquid Composite Modified Carbon Paste Electrode for the Determination of Carbaryl in Real Samples. *Electroanalysis* 30, 1855–1864. doi:10.1002/elan.201800152

Shaikshavali, P., Madhusudana Reddy, T., Venu Gopal, T., Venkataprasad, G., Kotakadi, V. S., Palakollu, V. N., et al. (2020). A Simple Sonochemical Assisted Synthesis of Nanocomposite (ZnO/MWCNTs) for Electrochemical Sensing of Epinephrine in Human Serum and Pharmaceutical Formulation. *Colloids Surf. Physicochem. Eng. Asp.* 584, 124038. doi:10.1016/j.colsurfa.2019.124038

Shi, S., Li, Z., Chen, Y., Yang, J., Xu, H., and Huang, J. (2019). Electrochemically Co-Deposition of Palladium Nanoparticles and Poly(1, 5-Diaminonaphthalene) onto Multiwalled Carbon Nanotubes (MWCNTs) Modified Electrode and its Application for Amperometric Determination of Nitrite. *Int. J. Electrochem. Sci.* 14, 7983–7994. doi:10.20964/2019.08.22

Song, P., Wu, L., and Guan, W. (2015). Dietary Nitrates, Nitrites, and Nitrosamines Intake and the Risk of Gastric Cancer: A Meta-Analysis. *Nutrients* 7, 9872–9895. doi:10.3390/nu7125505

Thirumalraj, B., Palanisamy, S., Chen, S.-M., and Zhao, D.-H. (2016). Amperometric Detection of Nitrite in Water Samples by Use of Electrodes Consisting of Palladium-Nanoparticle-Functionalized Multi-Walled Carbon Nanotubes. *J. Colloid Interf. Sci.* 478, 413–420. doi:10.1016/j.jcis.2016.06.014

Vagin, M., Gueskine, V., Mitraka, E., Wang, S., Singh, A., Zozoulenko, I., et al. (2021). Negatively-Doped Conducting Polymers for Oxygen Reduction Reaction. *Adv. Energ. Mater.* 11, 2002664. doi:10.1002/aenm.202002664

Velmurugan, S., Palanisamy, S., and Yang, T. C.-K. (2020). Single-Crystalline SnS2 Nano-Hexagons Based Non-Enzymatic Electrochemical Sensor for Detection of Carcinogenic Nitrite in Food Samples. *Sensors Actuators B: Chem.* 316, 128106. doi:10.1016/j.snb.2020.128106

Wan, Y., Zheng, Y. F., Wan, H. T., Yin, H. Y., and Song, X. C. (2017). A Novel Electrochemical Sensor Based on Ag Nanoparticles Decorated Multi-Walled Carbon Nanotubes for Applied Determination of Nitrite. *Food Control* 73, 1507–1513. doi:10.1016/j.foodcont.2016.11.014

Wang, J. (2006). *Analytical Electrochemistry*. New York, USA: Wiley, 10, 0471790303.

Wang, Q.-H., Yu, L.-J., Liu, Y., Lin, L., Lu, R.-G., Zhu, J.-P., et al. (2017). Methods for the Detection and Determination of Nitrite and Nitrate: A Review. *Talanta* 165, 709–720. doi:10.1016/j.talanta.2016.12.044

Wang, X., Cao, T., Zuo, Q., Wu, S., Uchiyama, S., and Matsuura, H. (2016). Sensitive Nitrite Detection Using a Simple Electrochemically Aminated Glassy Carbon Electrode. *Anal. Methods* 8, 3445–3449. doi:10.1039/C6AY00015K

Yu, H., Li, R., and Song, K.-l. (2019). Amperometric Determination of Nitrite by Using a Nanocomposite Prepared from Gold Nanoparticles, Reduced Graphene Oxide and Multi-Walled Carbon Nanotubes. *Microchim. Acta* 186, 624. doi:10.1007/s00604-019-3735-8

Yu, M., Li, C., Hu, C., Jin, J., Qian, S., and Jin, J. (2020). The Relationship between Consumption of Nitrite or Nitrate and Risk of Non-Hodgkin Lymphoma. *Sci. Rep.* 10, 551. doi:10.1038/s41598-020-57453-5

Zhan, Y., Zeng, Y., Li, L., Luo, F., Qiu, B., Lin, Z., et al. (2019). Ratiometric Fluorescent Hydrogel Test Kit for On-Spot Visual Detection of Nitrite. *ACS Sens.* 4, 1252–1260. doi:10.1021/acssensors.9b00125

Zhang, F.-X., Miao, Y., Ruan, J.-G., Meng, S.-P., Dong, J.-D., Yin, H., et al. (2019). Association between Nitrite and Nitrate Intake and Risk of Gastric Cancer: A Systematic Review and Meta-Analysis. *Med. Sci. Monit.* 25, 1788–1799. doi:10.12659/MSM.914621

Zhang, S., Li, B.-Q., and Zheng, J.-B. (2015). An Electrochemical Sensor for the Sensitive Determination of Nitrites Based on Pt-PANI-Graphene Nanocomposites. *Anal. Methods* 7, 8366–8372. doi:10.1039/C5AY01710F

Zhao, Z., Xia, Z., Liu, C., Huang, H., and Ye, W. (2017). Green Synthesis of Pd/Fe3O4 Composite Based on polyDOPA Functionalized Reduced Graphene Oxide for Electrochemical Detection of Nitrite in Cured Food. *Electrochimica Acta* 256, 146–154. doi:10.1016/j.electacta.2017.09.185

Zheng, D., Hu, C., Peng, Y., and Hu, S. (2009). A Carbon Nanotube/Polyvanillin Composite Film as an Electrocatalyst for the Electrochemical Oxidation of Nitrite and its Application as a Nitrite Sensor. *Electrochimica Acta* 54, 4910–4915. doi:10.1016/j.electacta.2009.04.004

Zhu, X., Zhang, W., Chen, H., and Mo, J. (2015). Impacts of Nitrogen Deposition on Soil Nitrogen Cycle in forest Ecosystems: A Review. *Acta Ecologica Sinica* 35, 35–43. doi:10.1016/j.chnaes.2015.04.004

Conflict of Interest: The authors declare that the research was conducted in the absence of any commercial or financial relationships that could be construed as a potential conflict of interest.

Publisher's Note: All claims expressed in this article are solely those of the authors and do not necessarily represent those of their affiliated organizations, or those of the publisher, the editors and the reviewers. Any product that may be evaluated in this article, or claim that may be made by its manufacturer, is not guaranteed or endorsed by the publisher.

frontiers in Chemistry

ORIGINAL RESEARCH
published: 23 March 2022
doi: 10.3389/fchem.2022.813533

Evaluation of Scales of Tilapia Sp. and *Sciaenops ocellatus* as Low Cost and Green Adsorbent for fluoride Removal From Water

Marian Asantewah Nkansah[1]*, *Asare Boateng Dua*[1], *Gabriel Adjei Aryee*[1] and *Junias Adusei-Gyamfi*[2]

[1]Department of Chemistry, Kwame Nkrumah University of Science and Technology, Kumasi, Ghana, [2]Department of Environmental Science, Kwame Nkrumah University of Science and Technology, Kumasi, Ghana

Water containing more than 1.5 mg/L of fluoride is considered toxic as it causes dental, kidney, and other health problems. With the purpose of helping alleviate these problems by exploring a treatment method for fluoride contamination, this study was to assess the suitability of scales of Tilapia Sp. and *Sciaenops ocellatus* as a cheaper source of adsorbent for the removal of fluoride from drinking water. The samples which were obtained from the Lapaz Market in Accra, Ghana, underwent treatment to eliminate any impurities. They were then ground into powder and treated with aluminum hydroxide [$Al(OH)_3$]. The treated samples were used for the removal of fluoride from spiked solutions prepared in the laboratory. Batch adsorption was performed by varying parameters such as adsorbent dose (1–8 g/L), initial concentration (2 mg/L to 10 mg/L), and contact time (30–300 min) at pH of 7. A one-way ANOVA was used to validate the significance of the defluoridation process with respect to the different experimental conditions. The optimum adsorbent dose, initial concentration, and contact time were found to be 4 g/L, 10 mg/L, and 300 min, respectively. The results revealed that the maximum percentage removal of fluoride was 76% by Tilapia Sp. and 70% by *Sciaenops ocellatus* at the optimum conditions. This is an indication that both Tilapia Sp. And *Sciaenops ocellatus* scales are suitable adsorbents for the removal of fluoride from water. The fluoride adsorption kinetics followed the pseudo-second-order model, and the adsorption isotherm fitted the Freundlich Isotherm model better than the Langmuir Isotherm model. The adsorption intensity and adsorption capacity for Tilapia Sp. were 3.484 L/mg and 0.065 mg/g, and that of *Sciaenops ocellatus* 3.195 L/mg and 0.045 mg/g respectively.

Keywords: adsorption, green adsorbent, fish scales, drinking water treatment, isotherms, defluoridation

OPEN ACCESS

Edited by:
Francesca D'Anna, University of Palermo, Italy

Reviewed by:
Subbaiah Muthu Prabhu, Hanyang University, South Korea
Nichola J. Coleman, University of Greenwich, United Kingdom

***Correspondence:**
Marian Asantewah Nkansah
maan4gr@yahoo.co.uk

Specialty section:
This article was submitted to Green and Sustainable Chemistry, a section of the journal Frontiers in Chemistry

Received: *11 November 2021*
Accepted: *21 February 2022*
Published: *23 March 2022*

Citation:
Nkansah MA, Dua AB, Aryee GA and Adusei-Gyamfi J (2022) Evaluation of Scales of Tilapia Sp. and Sciaenops ocellatus as Low Cost and Green Adsorbent for fluoride Removal From Water. Front. Chem. 10:813533. doi: 10.3389/fchem.2022.813533

1 INTRODUCTION

As of 2017, about 785 million of the global population was estimated to lack basic drinking-water sources, while about 144 million people depended on surface water for survival. These surface waters are often susceptible to contamination, causing various waterborne diseases (WHO, 2019). One natural element which is found in water and has both beneficial and detrimental effects on human health is fluoride. At low levels in drinking water, the presence of fluoride reduces the prevalence of

dental caries, while the presence of fluoride in drinking water at high concentrations, causes skeletal and dental fluorosis and bone fractures. This is because whereas only about 50–80% of fluoride ingested from food is absorbed, 100% of fluoride ingested from water is absorbed (Yang et al., 2019). As a result, based on World Health Organization (WHO) guidelines, fluoride present in food or water must not exceed 1.5 mg/L (Valdez-Jiménez et al., 2011; Yang et al., 2019; Srivastava and Flora, 2020).

Children are most affected by fluoride toxicity since their skeletal tissue retains up to 50% of ingested fluoride when compared with that of adults, which is approximately 10%. Fluoride is also known to cross the blood-brain-barrier to accumulate in the brain tissue of a developing fetus to cause learning disorders (Qing-Feng et al., 2019). People experiencing these effects are often found in underdeveloped areas of Asia and Africa. Craig et al. (2015) discovered that in the Bongo District of Ghana's Upper East Region, the main source of water is underground, and the average amount of water consumed is twice that of the other regions in the country, but had up to 4 mg/L of fluoride in their water. Through speciation analysis, it has been established that fluoride complexes in groundwater are dominated by free fluoride ions (Li et al., 2017). Therefore, it is a necessity to develop methods to reduce the fluoride content of water to alleviate the detrimental effects of fluorosis and avert half of the world's population from living in water-stressed areas by 2025 (WHO, 2019).

Adsorption has been found to be a convenient method for removing contaminants in water with the use of a wide range of materials as adsorbents. Lavecchia et al. (2012) found alumina rich bauxite (81% Al_2O_3) to adsorb 38.5% fluoride as compared to hematite (Fe_2O_3.X) which adsorbed only 7.3% fluoride. This was improved (Rafique et al., 2013) by immobilizing the adsorbent, pure alumina on sol-gel to attain an adsorption of 95%. Calcium based adsorbents such as calcite have also proven to be good fluoride adsorbents, with fluoride removal reaching up to 80.6%. Aluminum and calcium-based adsorbents are therefore more promising when compared to iron and some other metals (Rafique et al., 2013; Tomar and Kumar, 2013). Natural sources of these adsorbents are usually minerals such as bauxite, limestone etc., and these are mined, thereby increasing costs. Calcium hydroxyapatite ($Ca_5(PO_4)_3OH$) is a potential calcium-based adsorbent that can be derived from fish waste such as scales. It proved useful in the removal of Pb from water and was cost effective (Omar et al., 2019). The 2016 Food and Agriculture Organisation (FAO) outlook projected an annual 2–3% increase in fish production thus fish scales serving as adsorbents is an innovative and sustainable solution in managing fish waste since scales, in particular, have low biodegradability (FAO, 2016; Harikrishna et al., 2017). To add to their economic, and environmental benefits as adsorbents, the composition of fish scales which is mainly collagen type I and calcium hydroxyapatite is thermally stable, with freshwater fish scales having the upper hand (Pati et al., 2010). The mechanical support, and immobilization of calcium hydroxyapatite by collagen type I is also a key feature of fish scales (Pati et al., 2010; Gil-Duran et al., 2016).

The adsorption capabilities of several species of fishes' scales in the removal of a variety of pollutants have been reported in literature (Zhu et al., 2013; Uzunoğlu and Özer, 2016; Bhaumik et al., 2017; Nasiebanda et al., 2020) with fishes like L. rohita, tilapia spp. and oreochromis spp. gaining more research interest probably because of their widespread availability and consumption (Ighalo and Eletta, 2020).

The hydroxyapatite in fish scales is a key component for the adsorption process. The hydroxyl groups are the active sites responsible for pollutant removal *via* adsorption. Fluoride removal is therefore enhanced by increasing the amount of surface hydroxyl groups on the hydroxyapatite by co-precipitation with aluminum hydroxide solution (Nie et al., 2012).

In view of the chemical structure, composition and benefits of using fish scales as adsorbents, this experiment focuses on the removal of fluoride from water using fish scales from two of the most abundant marine and freshwater fish species in Ghana namely *Sciaenops oscellatus* (red drum) and Tilapia sp. The study of the adsorption capacity of *Sciaenops oscellatus,* which is less studied and has limited references in literature makes this study novel, since it provides the opportunity to compare its efficiency with the well-studied *Tilapia sp*.

1.1 Characteristics of the Fish Scales From Other Studies

The use of scanning electron microscopy (SEM) to observe the surface morphology of the tilapia scales samples by Zayadi and Othman (2013), revealed that the SEM images, had two distinct regions: a bright portion which is rich in inorganic material containing a high proportion of calcium and phosphorus, and a dark region that is rich in protein (**Figure 1A**). An energy dispersive X-ray analysis (EDX) (**Figure 1B**), used to identify the elemental composition of the adsorbent showed that carbon is the most dominant element with a mass of about 53% followed by oxygen (31%). Even though the percentage mass of calcium was only about 5%, the X-ray fluorescence (XRF) analysis showed the highest chemical compound was CaO (63.8%) followed by P_2O_5 (32.0%). The presence of CaO confirms that high potential of fish scale to adsorb fluoride ions. After defluoridation however, observed SEM images showed structural defects, irregular shape, and coarse surfaces which were attributed to fluoride adsorption by the adsorbents (Nasiebanda et al., 2020). Proximate analysis of scales of red drum fish (*Sciaenops ocellatus*) also revealed that the adsorbent contained about 41% wet wt of crude protein and about 42% wet wt of Ash (Chen et al., 2016).

2 MATERIALS AND METHODS

2.1 Materials

Tilapia *Sp*. scales and *Sciaenops ocellatus* scales (from Lapaz market, Accra) were the adsorbents used in this study. Anhydrous sodium fluoride (NaF) served as the source of

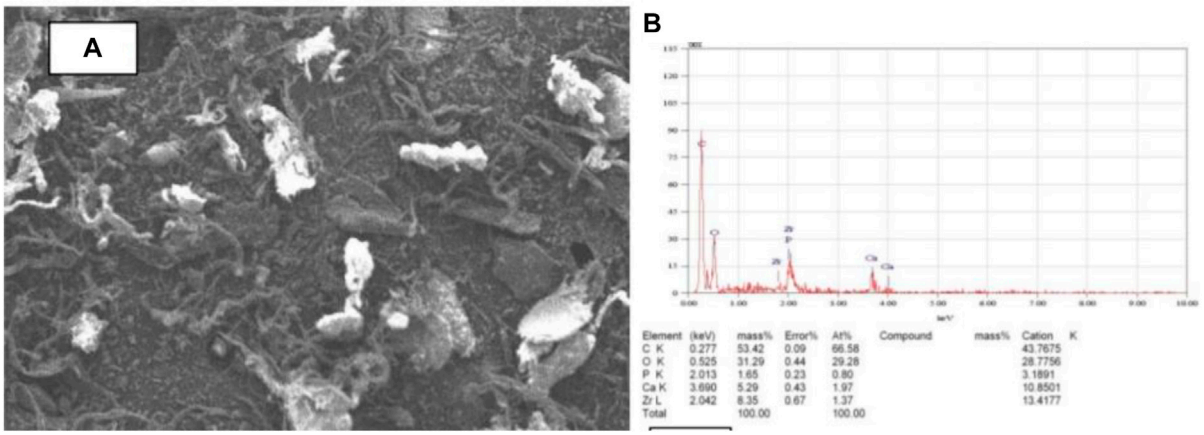

FIGURE 1 | Characterisation of adsorbent **(A)** SEM image for tilapia scales **(B)** EDX analysis of tilapia scales. This figure has been adapted from (Zayadi and Othman, 2013).

fluoride, while concentrated hydrochloric acid (HCl) and sodium hydroxide (NaOH) were used for altering pHs. Distilled water was the solvent used in preparing all solutions in this experiment. Aluminium hydroxide was used in the treatment of the scales before use.

2.2 Experimental Procedures

Factors such as contact time, adsorbent dosage, adsorbate concentration as well as the Freundlich isotherm and Langmuir adsorption isotherm were used in assessing the rate and mechanism of the adsorption processes. Each experimental condition was repeated thrice.

2.2.1 Treatment of Adsorbent

The adsorbent was prepared by washing with distilled water and drying the sample fish scales. Drying first employed a 3 days solar thermal heating, after which an electric oven (Cole-Parmer instrument company, model: 05015-50) was used at 80°C for 24 h to complete the process. Dried fish scales were then ground with clean porcelain mortar and pestle and sieved to 100 µm with mesh, and was later soaked in 150 ml of 0.1 M of Al $(OH)_3$ for 1 h in a shaker (IKA-VIBRAX-VXR) at 220 rpm at room temperature. The adsorbent was then retrieved via filtration and dried in an electric oven at 30 C for 5 h.

2.2.2 Characterization of Fish Scales

FTIR analysis was done to determine the functional groups of the two species of fish scale before and after treatment with aluminium hydroxide solution.

2.2.3 Preparation of Fluoride Solution

A fluoride stock solution of 100 mg/L was prepared from anhydrous NaF for five standard fluoride solutions with concentrations between 2 mg/L and 10 mg/L to be later obtained by dilution using distilled water.

2.2.4 Effect of Adsorbent Dosage

The effect of adsorbent dosage was done using 100 ml of 5 mg/L fluoride solution at pH of 7 in 5,200 ml polyethylene bottles of different batches by varying adsorbent mass. Aliquots of 0.1, 0.2, 0.4, 0.6 and 0.8 g of adsorbent were put into the polyethene bottles, respectively. Bottles were then shaken in a shaker at 220 rpm for 2 hrs and fluoride concentrations were later measured using an ion chromatography (MetrohmHerisau, Switzerland).

2.2.5 Effect of Contact Time Versus Fluoride Concentration

In order to determine the effect of contact time on adsoprtion, residual fluoride concentration was measured at 30, 60, 120, 180, 240, and 300 min respectively. The effect of initial concentration on the adsorption capacity of the adsorbent was studied for optimized conditions of all other parameters by keeping contact time (120 min), adsorbent dose (0.4 g), and pH of 7, and by varying the initial concentration of fluoride solution between 2 and 10 mg/L.

2.2.6 Adsorption Isotherms

Several sorption isotherm models have been extensively used for the modeling of biosorption systems to understand the quantitative relationship between sorbate and sorbent in aqueous phase (Khambhaty et al., 2009).

The Langmuir and Freundlich isotherms were used in this study to explain the adsorption phenomenon. The Langmuir **Eq. 1** is commonly written as:

$$\frac{C_e}{q_e} = \frac{C_e}{b} + \frac{1}{q_m b} \tag{1}$$

Where, q_e is the amount of fluoride adsorbed (mg/g) and C_e is equilibrium concentration of adsorbate (mg/L), q_m and b are Langmuir constants related to monolayer adsorption capacity and energy of adsorption respectively. The Freundlich **Eq. 2** is

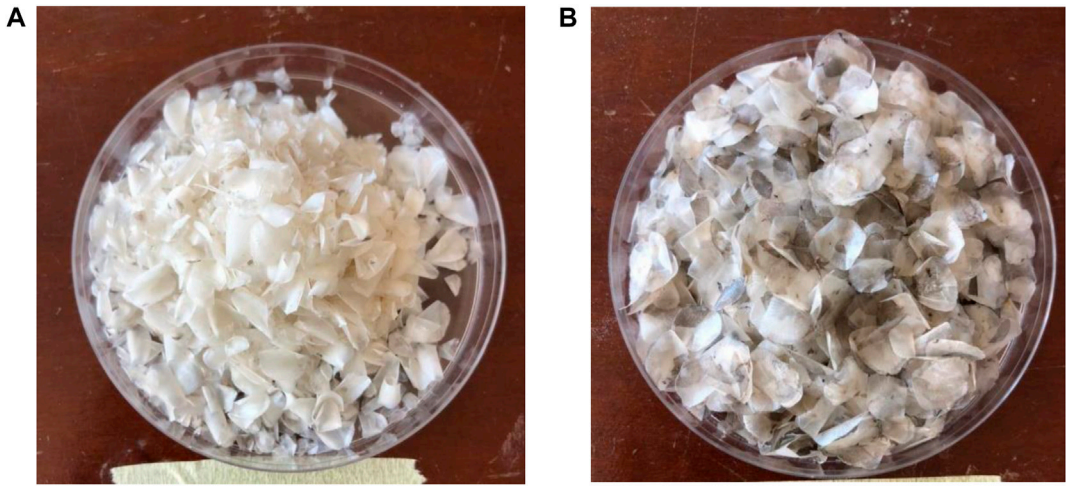

FIGURE 2 | (A) Scales of *Sciaenops ocellatus*. **(B)**: Scales of Tilapia Sp.

basically empirical but it is often useful as a means for data description. The general form of Freundlich isotherm is given in the following equation:

$$q_e = K_f Ce^{1/n} \quad (2)$$

The linearized form of Freundlich isotherm is given by the following **Eq. 3**.

$$\log(q_e) = \log K_f + 1/n \log C_e \quad (3)$$

The intercept K_f is an indicator of sorption capacity, and the slope 1/n is an indicator of sorption strength/intensity and a measure of the deviation from linearity of the adsorption.

2.2.7 Adsorption Kinetics

One of the important factors that controls the rate of adsorbate (fluoride ions) uptake at the solid-liquid interface and the adsorption equilibrium time is the adsorption kinetics (Bhaumik et al., 2017). Different adsorption kinetic models, pseudo-first-order (**Eq. 4**) and pseudo-second-order (**Eq. 5**) were applied to the experimental data to obtain the values of the kinetic constants and predicted the equilibrium adsorption capacities.

$$\log(q_e - q_t) = \log q_e - K_1 \frac{t}{2.303} \quad (4)$$

where q_e and q_t are the amounts of F^- adsorbed (mg/g) at equilibrium and at time *t*, respectively, and k_1 is the adsorption rate constant, which can be determined from the slope of linear plot of $\log(q_e - q_t)$ versus *t*.

$$\frac{t}{q_t} = \frac{1}{K_2 q_e 2} + \frac{t}{q_e} \quad (5)$$

$$h_o = k_2 q_e^2 \quad (6)$$

where k_2 is the adsorption rate constant, which can be determined by plotting t/q_t versus t, h_o represents the initial adsorption rate (**Eq. 6**), (mg/g/min), and k_2 is the pseudo-second-order rate constant (g adsorbent/mg adsorbate/min). The slope and intercept of $t/(q_t)$ vs. t plot gives h_o and k_2 (Adane et al., 2015). The kinetics study at the different contact times was obtained by calculating the instantaneous adsorption capacity, q_e, following **Eq. 7** (Lo et al., 2012):

$$q_e = \frac{(C_i - C_t)v}{m} \quad (7)$$

where C_i, is the initial concentration of the pollutant, C_t (mg/L) is the residual concentration of pollutant in the liquid phase for each contact time t, *m* is the mass (g) of the adsorbent and *V* representing the volume (L).

3 RESULTS AND DISCUSSION

The scales of *Tilapia Sp*. and *Sciaenops ocellatus* (**Figure 2**) before and after $\mathbf{Al(OH)_3}$ treatment have been treated with and characterized for their suitability as adsorbent for fluoride removal and are presented in this section. Data from batch adsorption studies are also illustrated here.

3.1 FTIR Spectra of Fish Scales Before and After Treatment With Aluminium Hydroxide

The natural composition of fish scales includes a surface layer which contains hydroxyapatite ($Ca_5(PO_4)_3OH$), calcium carbonate and a deeper layer which contains collagen type I. minute quantities of elemental Ca, Mg, O, Na and S are sometimes present (Basu and Ajit, 2005; Pati et al., 2010).

From the FTIR data, a characteristic (OH) band around 3,331 cm^{-1} from the hydroxyapatite was expected but this is rather detected at 3,189.90 cm^{-1} and 3,266.21 cm^{-1} for untreated scales of *Sciaenops* and Tilapia Sps. respectively (**Figures 3A,B**). A similar trend was observed for the spectra of the same scales after

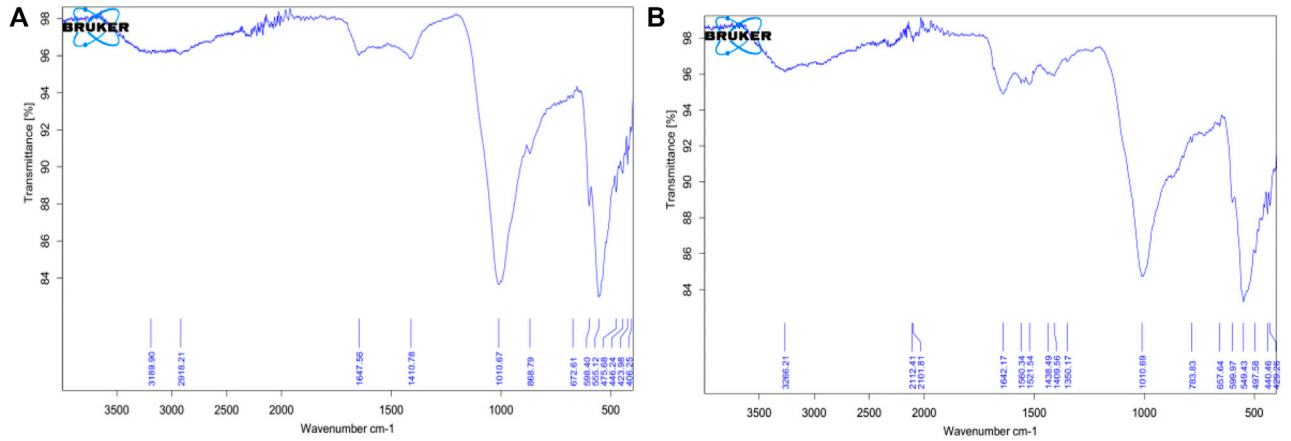

FIGURE 3 | FTIR Spectra of Powdered Scales before chemical treatment (**A**, on the left) Scales of *Sciaenops ocellatus* (**B**, on the right) Scales of *Tilapia* Sp.

treatment with $Al(OH)_3$, with increased wavenumbers of 3,269.20 cm^{-1} and 3,274.32 cm^{-1} respectively (Pati et al., 2010).

Wavenumbers of 1,647.56 cm^{-1} and 1,642.17 cm^{-1} respectively for *Sciaenops* and Tilapia Sps correspond to amide groups of collagen and are associated with stretching vibrations of the –C=O (carbonyl) groups along the polypeptide backbone, which is a sensitive marker of the peptide secondary structure (**Figure 3**). Similar wavenumbers of 1,654.83 cm^{-1} and 1,638.04 cm^{-1} for *Sciaenops* and Tilapia Sps. Respectively (**Figure 4**) (Surewicz and Mantsch, 1988).

Fish scale residue has shown a strong absorption peak at about 1,000–1,100 cm^{-1} which was assigned to phosphate group (PO_4^{3-}) stretching, which comes from the C-C stretching of phospholipids in the fish scales and 500–593 cm^{-1} for phosphate group (PO_4^{3-}) bending (Frost et al., 2013; Pourfarzad et al., 2015; Prekajski et al., 2015; Zhang et al., 2019). This trend corresponds to what was observed for the FTIR data for *Sciaenops* and Tilapia Sps. in **Figures 3**, **4**.

The striking differences in the 1,400 to 1,650 cm^{-1} region of the FTIR spectra of *Sciaenops ocellatus* prior to (**Figure 3A**) and following (**Figure 4A**) treatment with aluminium hydroxide can be attributed to the removal of non-collagenous proteins from the fish scales. The similarity in the FTIR spectra of both fish scales (**Figures 4A,B**) after treatment with $Al(OH)_3$ indicates untreated *Sciaenops ocellatus* fish scales had more non-collagenous proteins, mainly ichthylepidin (Masood et al., 2014; Sockalingam and Abdullah, 2015).

3.2 Effect of Adsorbent Dosage

At a varying adsorbent dose of 0.1–0.8 g/100 ml and constant fluoride concentration of 5 mg/L the effect of adsorbent dosage was studied using a contact time of 2 h at 220 rpm. The statistical significance of the defluoridation efficiency of the different adsorbent doses was confirmed using a one-way ANOVA, which showed that the computed *p*-value (0.014) was lower than the alpha value (0.05). A possible saturation level of fluoride on Tilapia Sp. and *Sciaenops ocellatus* scales was

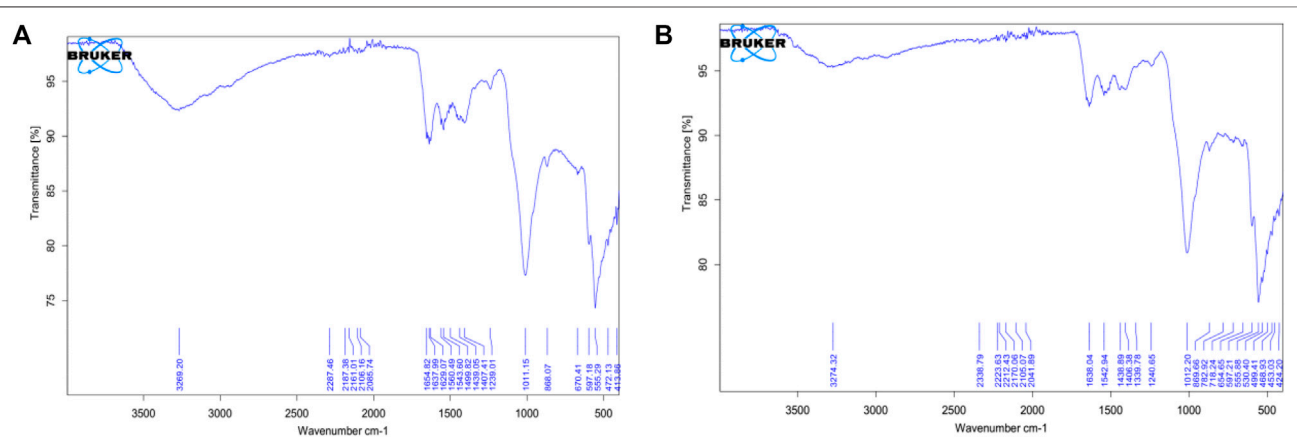

FIGURE 4 | FTIR Spectra of Powdered Scales after chemical treatment (**A**, on the left) Scales of *Sciaenops ocellatus* (**B**, on the right) Scales of *Tilapia* Sp.

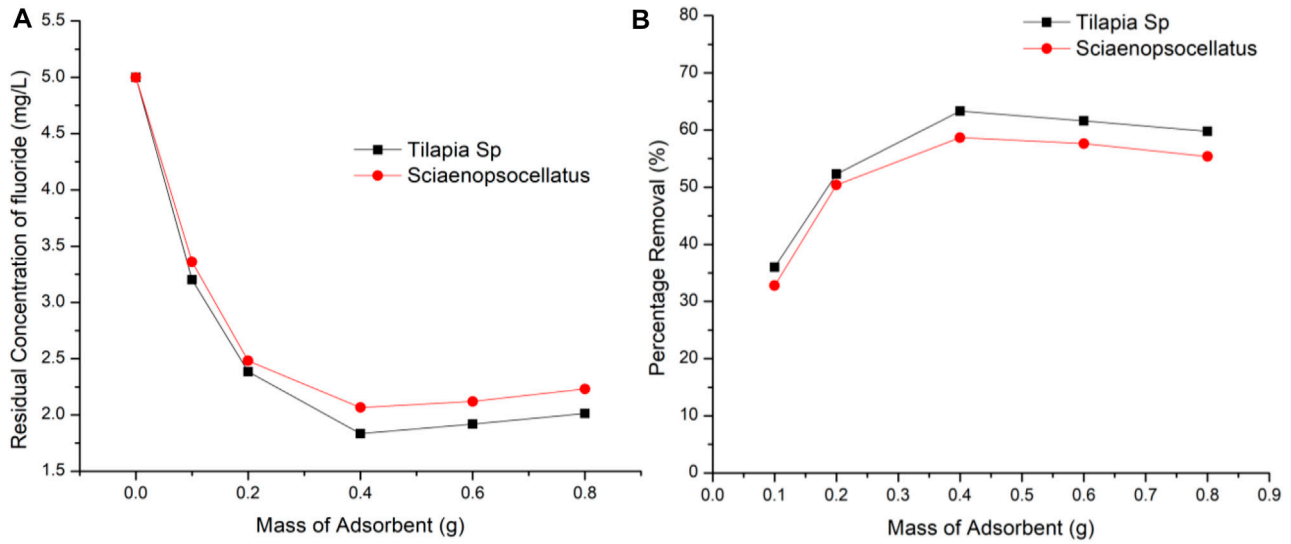

FIGURE 5 | Effect of adsorbent dosage on fluoride removal **(A)** Residual concentration of fluoride **(B)** Percentage removal of fluoride.

found to occur at 0.4 g dose of adsorbent with scales from Tilapia Sp. adsorbing 4.64% more fluoride indicating 0.4 g of Tilapia Sp. scales provides more active sites when compared to *Sciaenops ocellatus scales* (**Figure 5**). FTIR analysis used to study the adsorption behavior of fluoride have established that fluoride prefers to bind more with the hydroxyl functional group (Mohapatra et al., 2011). **Figure 1** shows that there are similar changes in adsorption with respect to adsorbent dose, indicating some similarities between the two adsorbents. As adsorbent dosage exceeds 0.4 g/100 ml it is possible that aggregation occurs thus, inter-particle interaction becomes more prominent, leading to a steady decline in the amount of fluoride removed. The reduction in percentage removal with increasing adsorbent dose which has been reported in previous studies was attributed to the development of aggregates among the adsorbent and the convergence of binding sites, which minimizes the effective active site area (Chowdhury et al., 2011). A similar observation has been reported for the adsorption of fluoride onto Ca-pretreated macrophyte biomass (Miretzky et al., 2008). The possible agglomeration of the adsorbent particles is evidenced by the images of a scanning electron microscope (SEM) which shows morphological defects, irregular shape, and coarse surfaces after fluoride adsorption (Nasiebanda et al., 2020).

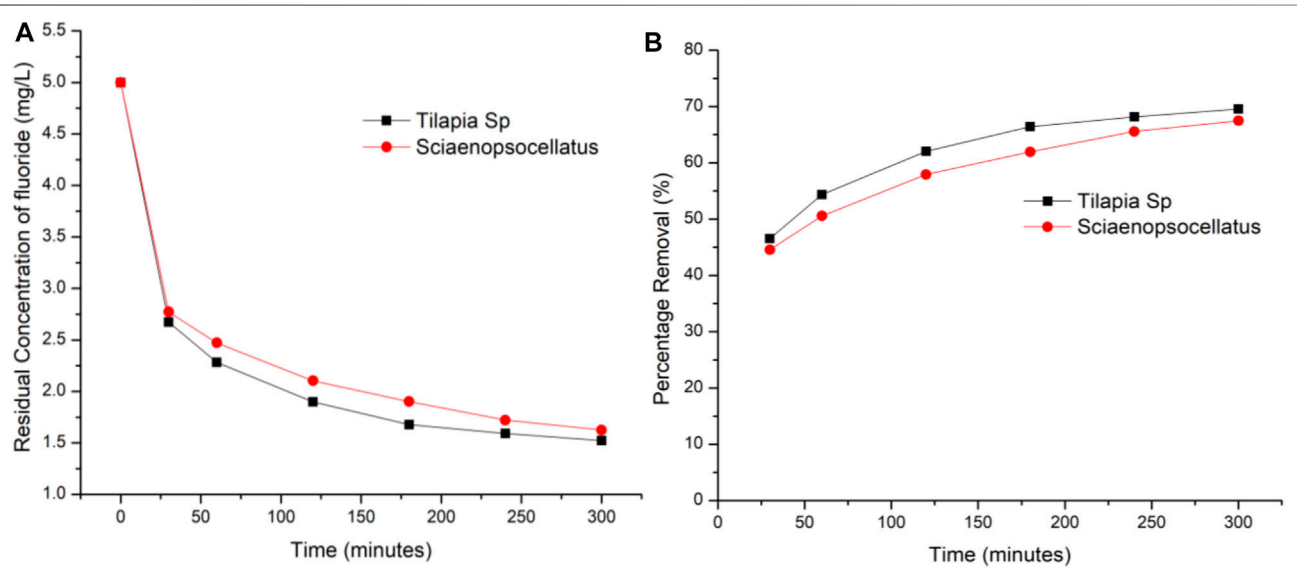

FIGURE 6 | Effect of contact time on fluoride r emoval **(A)** Residual concentration of fluoride **(B)** Percentage removal of fluoride.

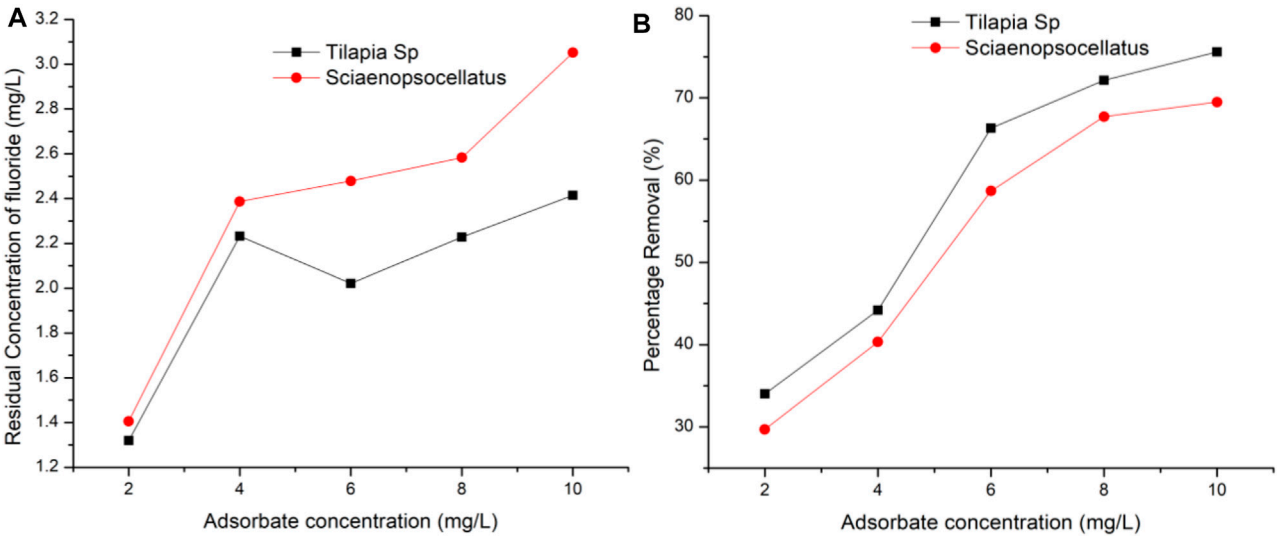

FIGURE 7 | Effect of adsorbate concentration on fluoride removal **(A)** Residual concentration of fluoride **(B)** Percentage removal of fluoride.

3.3 Effect of Contact Time

Using the optimum adsorbent dosage i.e., 0.4 g/100 ml, the effect of contact time was determined by varying adsorption time from 30 to 300 min with a fixed fluoride concentration of 5 mg/L. Results indicated that there was a constant rise in the amount of fluoride adsorbed on both adsorbents with *Tilapia Sp.* scales always adsorbing 2.48% more fluoride as compared to *Sciaenops ocellatus*. The rate of adsorption of Tilapia Sp. within the first 30 min was found to be twice as fast as the proceeding 60 min while that of *Sciaenops ocellatus* was 1.64 times faster (**Figure 6**). This, when combined with the average percentage difference in adsorption capacity, suggests that Tilapia Sp. scales may have more active sites available. The fast adsorption rate at the initial stage has been reported by other studies and attributed to an increased availability in the number of active binding sites on the adsorbent surface (Saha et al., 2010). **Figure 2** clearly shows that, the increase in fluoride removal was progressive with time and adsorption equilibrium was seemingly proximate after 300 min since the curve was of logarithmic growth. Adsorption rates and capacities of both adsorbents were also found to remain constant after 300 min of contact time, indicating maximum adsorption capacity was imminent. At 300 min Tilapia Sp. scales had a capacity of 69.56% of the initial fluoride while *Sciaenops ocellatus* scales had 67.48%. A similar trend has been observed and reported for the biosorption of fluoride by agronomic product and the defluoridation from synthetic fluoride solution using scales of Indian major carp Catla (Catla catla) (Murugan and Subramanian, 2006; Bhaumik et al., 2017).

3.4 Effect of Adsorbate Concentration

At the optimum adsorbent dosage of 0.4 g/100 ml, and fixed contact time of 120 min the effect of increasing adsorbate concentration was found to increase the adsorption on the surface of the adsorbent. From the results, it is clear that the adsorbate was in the least contact with active sites when at 2 and 4 mg/L (**Figure 7**). Most adsorbates were adsorbed at a concentration of 10 mg/L.

The maximum fluoride removal (89.21%) and uptake capacity (17.84 mg/g) have been reported in other studies to also occur at 10.0 mg/L initial fluoride concentration albeit with different fish species (Catla catla) (Bhaumik et al., 2017). **Figure 3**, however, indicates more fluoride would have been adsorbed if its concentration was increased beyond 10 mg/L. It is also evident that at all fluoride concentrations, *Tilapia Sp.* scales adsorbed fairly more fluoride as compared to that of *Sciaenops ocellatus.* However, after the adsorption of fluoride has reached in equilibrium, it is expected that the percentage removal of fluoride would decrease with increase in initial fluoride concentration. This is because at higher concentrations, the available attachment sites for a definite amount of adsorbent get saturated (Saha et al., 2010).

3.5 Study of Adsorption Isotherms

The adsorption isotherm is useful in investigating the feasibility of an adsorbent for an adsorbate. Calculations on the Langmuir and Freundlich isotherm were both conducted. The Langmuir constants, b and monolayer sorption capacity, q_m were calculated from the slope and intercept of the plot between C_e/q_e and C_e as seen in **Figures 8B**, **9B**. The value of the Langmuir constant, q_m, for *Tilapia Sp.* was found to be -0.185 while that of *Sciaenops ocellatus* was -0.197.

The Langmuir constant, b, which denotes adsorption energy for Tilapia *Sp.* and *Sciaenops ocellatus* were found to be -0.371 and -0.308 respectively. Negative q_m values indicate the Langmuir isotherm is invalid for studying the adsorption of fluoride on these adsorbents. Therefore, the Freundlich isotherm was employed, and calculations showed the constants 1/n (adsorption intensity) and K_f (adsorption capacity) for Tilapia Sp. were 3.484 L/mg and 0.065 mg/g respectively and that of *Sciaenops ocellatus* was 3.195 L/mg and 0.045 mg/g. All the sorbents had an exponent (n) lower

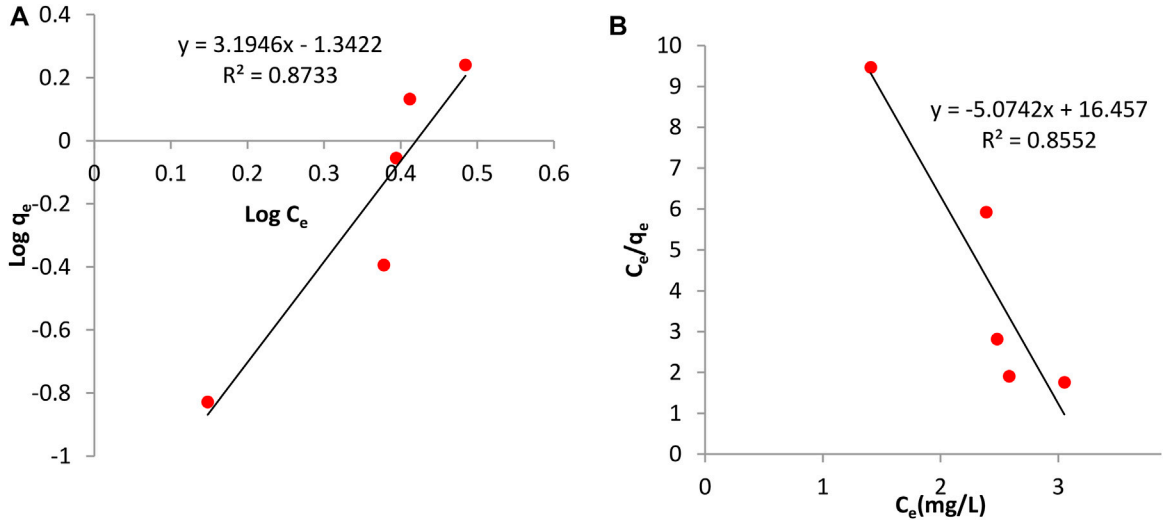

FIGURE 8 | Adsorption isotherms for Sciaenops ocellatus **(A)** Freundlich isotherm **(B)** Langmuir isotherm.

than one, indicating that these materials (Tilapia Sp. and *Sciaenops ocellatus* scales) could be good fluoride adsorbents. One of the assumptions of the Freundlich multilayer sorption isotherm is that, the amount of adsorbate adsorbed increases infinitely with an increase in concentration (Adeniyi and Ighalo, 2019) which confirms why it was observed in this study that increasing the adsorbate concentration increased the adsorption on the surface of the adsorbent. Additionally, the better fitness of the Freundlich model (see **Figures 8A**, **9A**) as compared to the Langmuir model could be attributed to the heterogeneous surface energies and an exponential distribution of active sites, which are characteristics of the adsorbents. Thus, the stronger binding sites are occupied first, which causes the binding strength to decrease with an increasing degree of site occupation (Adeniyi and Ighalo, 2019).

3.6 Adsorption Kinetics

Comparing the plot and Pearson's correlation for both models, it was found that the pseudo-second order model for both adsorbents was more linear with a higher correlation coefficients R^2 = 0.9965 and 0.994 (**Figures 10A,B**), indicating that this order is more applicable to this study. While the pseudo-second order rate constant for Tilapia sp was 1.119 $gmol^{-1}$ s^{-1}, that of Sciaenops ocellatus was 1.172 $gmol^{-1}$ s^{-1}. A similar trend of fluoride adsorption on various adsorbents has been reported in other studies (Singh and Cb, 2016; Nasiebanda et al., 2020). If the kinetic model best fits pseudo-first order, it indicates that the reaction is more inclined towards physisorption, and the sorption process only depends on the number of fluoride ions present at a specific time in the solution, whereas if a reaction fits well to the pseudo-second order model, it is assumed that the reaction is

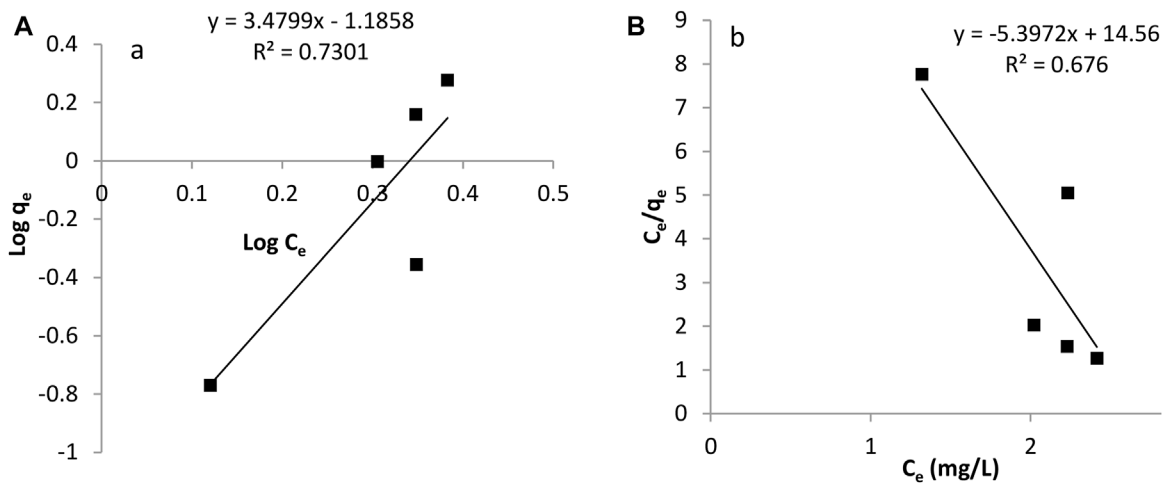

FIGURE 9 | Adsorption isotherms of Tilapia sp. **(A)** Freundlich isotherm **(B)** Langmuir isotherm.

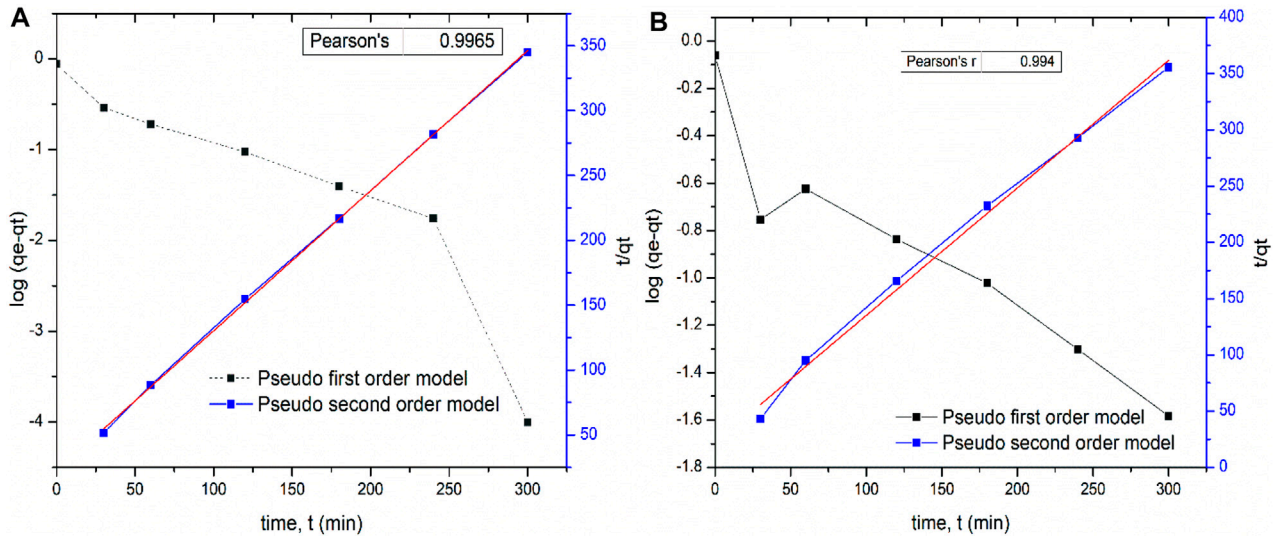

FIGURE 10 | Pseudo-first-order and Pseudo-second-order kinetic plots for the removal of fluoride from solution using scales of (**A**, on the left) Tilapia Sp. (**B**, on the right) *Sciaenops ocellatus*.

more inclined towards chemisorption and the fluoride adsorption process depends on both the number of fluoride ions present in the solution and the free adsorption sites on the biosorbent surface (Bhaumik et al., 2017; Ferreiro et al., 2019). Thus, in this study, it can be concluded that the rate of fluoride adsorption onto the adsorbent was more influenced by surface reactions between the adsorbent sites and fluoride particles than by external transfer processes. Other studies have equally reported fluoride adsorption kinetics following the pseudo-second-order model and the adsorption isotherm fitting Freundlich model better (Bhaumik et al., 2017; Rajkumar et al., 2019).

4 CONCLUSION

The adsorbents produced from treatment of scales Tilapia Sp. and *Sciaenops ocellatus* with aluminium hydroxide were found to be efficient for the removal of fluoride ions from water. The optimal adsorbent dosage was 0.4 g/100 ml of fluoride solution, and adsorption was found to be progressive with contact time. With 0.4 g/100 ml of fluoride, it was found that Tilapia Sp. scales adsorbed 4.64% more than that of *Sciaenops ocellatus* and the maximum fluoride removed was 63.32%. The difference in the removal efficiencies of both adsorbents was found to be statistically significant based on the ANOVA results. The Langmuir isotherm failed to fit the experimental data indicating the nature of the adsorbent might not satisfy the assumptions of Langmuir but fitted well with the Freundlich isotherm, thus, the surface energies of the adsorbent may be heterogeneous whereas the kinetic model best fitted the second order model. The efficiency of fish scales as fluoride adsorbents was much higher than others such as hematite in other studies. Hence considering the abundance of fish scale as waste, it can serve as a sustainable source of fluoride adsorbent. More research is needed to understand the surface morphology of the adsorbents, especially that of *Sciaenops ocellatus*. The spent adsorbent needs to be generated and properly disposed of. Previous studies have shown that the adsorbed fluoride can be regenerated using NaOH solution. Further studies are therefore required to confirm the feasibility of this regeneration process for the adsorbents used for this study.

DATA AVAILABILITY STATEMENT

The original contributions presented in the study are included in the article/Supplementary Material, further inquiries can be directed to the corresponding author.

AUTHOR CONTRIBUTIONS

MN: The originator of the research idea, experimental design, supervision and contributed to drafting the manuscripts—AD: Contributed to experimental work and drafting of the manuscript -GA: Contributed to experimental work and drafting of the manuscript—JG: Contributed to experimental design and drafting of the manuscripts.

ACKNOWLEDGMENTS

The authors are grateful to the Department of Chemistry of the Kwame Nkrumah university of Science and Technology (KNUST), Kumasi-Ghana, for the use of the facilities for this study.

REFERENCES

Adane, B., Siraj, K., and Meka, N. (2015). Kinetic, Equilibrium and Thermodynamic Study of 2-chlorophenol Adsorption onto Ricinus communis Pericarp Activated Carbon from Aqueous Solutions. *Green. Chem. Lett. Rev.* 8 (3–4), 1–12. doi:10.1080/17518253.2015.1065348

Adeniyi, A. G., and Ighalo, J. O. (2019). Biosorption of Pollutants by Plant Leaves: An Empirical Review. *J. Environ. Chem. Eng.* 7 (3), 103100. doi:10.1016/j.jece.2019.103100

Basu, B., and Ajit, K. B. (2005). Production of Protein Rich Organic Fertilizer from Fish Scale by *Aspergillus* Mutant AB100-A media Optimization Study. *J. Sci. Ind. Res.* 64, 293–298. Available at http://nopr.niscair.res.in/handle/123456789/5112.

Bhaumik, R., Mondal, N. K., and Chattoraj, S. (2017). An Optimization Study for Defluoridation from Synthetic Fluoride Solution Using Scale of Indian Major Carp Catla (Catla Catla): An Unconventional Biosorbent. *J. Fluorine Chem.* 195, 57–69. doi:10.1016/j.jfluchem.2017.01.015

Chen, S., Chen, H., Xie, Q., Hong, B., Chen, J., Hua, F., et al. (2016). Rapid Isolation of High Purity Pepsin-Soluble Type I Collagen from Scales of Red Drum Fish (Sciaenops Ocellatus). *Food Hydrocolloids* 52, 468–477. doi:10.1016/j.foodhyd.2015.07.027

Chowdhury, S., Mishra, R., Saha, P., and Kushwaha, P. (2011). Adsorption Thermodynamics, Kinetics and Isosteric Heat of Adsorption of Malachite green onto Chemically Modified rice Husk. *Desalination* 265 (1), 159–168. doi:10.1016/j.desal.2010.07.047

Craig, L., Lutz, A., Berry, K. A., and Yang, W. (2015). Recommendations for Fluoride Limits in Drinking Water Based on Estimated Daily Fluoride Intake in the Upper East Region, Ghana. *Sci. Total Environ.* 532, 127–137. doi:10.1016/j.scitotenv.2015.05.126

FAO (2016). Food Outlook—BIANNUAL REPORT on GLOBAL FOOD MARKETS. Trade and Markets Division of FAO. Available at: https://www.fao.org/3/i6198e/I6198E.pdf (Accessed on: June 26, 2021).

Ferreiro, C., Villota, N., Lombraña, J., Rivero, M., Zúñiga, V., and Rituerto, J. (2019). Analysis of a Hybrid Suspended-Supported Photocatalytic Reactor for the Treatment of Wastewater Containing Benzothiazole and Aniline. *Water* 11 (2), 337. doi:10.3390/w11020337

Frost, R. L., Xi, Y., Beganovic, M., Belotti, F. M., and Scholz, R. (2013). Vibrational Spectroscopy of the Phosphate mineral Lazulite - (Mg, Fe)Al2(PO4)2·(OH)2 Found in the Minas Gerais, Brazil. *Spectrochimica Acta A: Mol. Biomol. Spectrosc.* 107, 241–247. doi:10.1016/j.saa.2013.01.056

Gil-Duran, S., Arola, D., and Ossa, E. A. (2016). Effect of Chemical Composition and Microstructure on the Mechanical Behavior of Fish Scales from Megalops Atlanticus. *J. Mech. Behav. Biomed. Mater.* 56, 134–145. doi:10.1016/j.jmbbm.2015.11.028

Harikrishna, N., Mahalakshmi, S., Kiran Kumar, K., and Reddy, G. (2017). Fish Scales as Potential Substrate for Production of Alkaline Protease and Amino Acid Rich Aqua Hydrolyzate by Bacillus Altitudinis GVC11. *Indian J. Microbiol.* 57 (3), 339–343. doi:10.1007/s12088-017-0664-2

Ighalo, J. O., and Eletta, O. A. (2020). Recent Advances in the Biosorption of Pollutants by Fish Scales: A Mini-Review. *Chem. Eng. Commun.* 208, 1301–1312. doi:10.1080/00986445.2020.1771322

Khambhaty, Y., Mody, K., Basha, S., and Jha, B. (2009). Kinetics, Equilibrium and Thermodynamic Studies on Biosorption of Hexavalent Chromium by Dead Fungal Biomass of marine Aspergillus niger. *Chem. Eng. J.* 145 (3), 489–495. doi:10.1016/j.cej.2008.05.002

Lavecchia, R., Medici, F., Piga, L., Rinaldi, G., and Zuorro, A. (2012). Fluoride Removal from Water by Adsorption on a High Alumina Content bauxite. *Chem. Eng.* 26, 225–230. doi:10.3303/CET1226038

Li, J., Zhou, H., Qian, K., Xie, X., Xue, X., Yang, Y., et al. (2017). Fluoride and Iodine Enrichment in Groundwater of North China Plain: Evidences from Speciation Analysis and Geochemical Modeling. *Sci. Total Environ.* 598, 239–248. doi:10.1016/j.scitotenv.2017.04.158

Lo, S.-F., Wang, S.-Y., Tsai, M.-J., and Lin, L.-D. (2012). Adsorption Capacity and Removal Efficiency of Heavy Metal Ions by Moso and Ma Bamboo Activated Carbons. *Chem. Eng. Res. Des.* 90 (9), 1397–1406. doi:10.1016/j.cherd.2011.11.020

Masood, Z., Yasmeen, R., Haider, M. S., Tarar, O. M., Lakht-e-Zehraand Hossain, M. Y. (2015). Evaluations of Crude Protein and Amino Acid Contents from the Scales of Four Mullet Species (Mugilidae) Collected from Karachi Fish Harbour, Pakistan. *Indian J. Geo-Marine Sci.* 44 (5), 724–731. doi:10.5829/idosi.gv.2015.15.03.9698

Miretzky, P., Muñoz, C., and Carrillo-Chávez, A. (2008). Fluoride Removal from Aqueous Solution by Ca-Pretreated Macrophyte Biomass. *Environ. Chem.* 5 (1), 68–72. doi:10.1071/en07078

Mohapatra, M., Rout, K., Singh, P., Anand, S., Layek, S., Verma, H. C., et al. (2011). Fluoride Adsorption Studies on Mixed-phase Nano Iron Oxides Prepared by Surfactant Mediation-Precipitation Technique. *J. Hazard. Mater.* 186 (2), 1751–1757. doi:10.1016/j.jhazmat.2010.12.076

Murugan, M., and Subramanian, E. (2006). Studies on Defluoridation of Water by Tamarind Seed, an Unconventional Biosorbent. *J. Water Health* 4 (4), 453–461. doi:10.2166/wh.2006.0029

Nasiebanda, R., Wamalwa, E., and Lusweti, K. (2020). *Adsorption of Fluoride from Water by Use of Powdered Tilapia Fish Scales*. Eldoret, Kenya: School of Environmental Studies, University of Eldoret, 145.

Nie, Y., Hu, C., and Kong, C. (2012). Enhanced Fluoride Adsorption Using Al (III) Modified Calcium Hydroxyapatite. *J. Hazard. Mater.* 30 (233-234), 194–199. doi:10.1016/j.jhazmat.2012.07.020

Omar, S., Muhamad, M. S., Te Chuan, L., Hadibarata, T., and Teh, Z. C. (2019). A Review on Lead Sources, Occurrences, Health Effects, and Treatment Using Hydroxyapatite (HAp) Adsorbent Made from Fish Waste. *Water Air Soil Pollut.* 230 (12), 275. doi:10.1007/s11270-019-4312-9

Pati, F., Adhikari, B., and Dhara, S. (2010). Isolation and Characterization of Fish Scale Collagen of Higher thermal Stability. *Bioresour. Techn.* 101 (10), 3737–3742. doi:10.1016/j.biortech.2009.12.133

Pourfarzad, A., Habibi Najafi, M. B., Haddad Khodaparast, M. H., and Khayyat, M. H. (2015). Serish Inulin and Wheat Biopolymers Interactions in Model Systems as a Basis for Understanding the Impact of Inulin on Bread Properties: a FTIR Investigation. *J. Food Sci. Technol.* 52 (12), 7964–7973. doi:10.1007/s13197-015-1939-4

Prekajski, M., Mirkovic, M., Todorovic, B., Matkovic, A., Marinovic-Cincovic, M., Lukovic, J., et al. (2015). Ouzo Effect-New Simple Nanoemulsion Method for Syntheis of Strontium Hydroxyapatite Nanospheres. *J. Eur. Ceram. Soc.* 36 (5), 1293–1298. doi:10.1016/j.jeurceramsoc.2015.11.045

Qing-Feng, S., Ying-Peng, X., and Tian-Tong, X. (2019). Matrix Metalloproteinase-9 and P53 Involved in Chronic Fluorosis Induced Blood-Brain Barrier Damage and Neurocyte Changes. *Arch. Med. Sci.* 15 (2), 457–466. doi:10.5114/aoms.2019.83294

Rafique, A., Awan, M. A., Wasti, A., Qazi, I. A., and Arshad, M. (2013). Removal of Fluoride from Drinking Water Using Modified Immobilized Activated Alumina. *J. Chem.* 2013, 1–7. doi:10.1155/2013/386476

Rajkumar, S., Murugesh, S., Sivasankar, V., Darchen, A., Msagati, T. A. M., and Chaabane, T. (2019). Low-cost Fluoride Adsorbents Prepared from a Renewable Biowaste: Syntheses, Characterization and Modeling Studies. *Arabian J. Chem.* 12 (8), 3004–3017. doi:10.1016/j.arabjc.2015.06.028

Saha, P., Chowdhury, S., Gupta, S., and Kumar, I. (2010). Insight into Adsorption Equilibrium, Kinetics and Thermodynamics of Malachite Green onto Clayey Soil of Indian Origin. *Chem. Eng. J.* 165 (3), 874–882. doi:10.1016/j.cej.2010.10.048

Singh, T. P., and Cb, M. (2016). Comparing Fluoride Removal Kinetics of Adsorption Process from Aqueous Solution by Biosorbents. *Asian J. Pharm. Clin. Res.* 9, 108–112. Available at https://innovareacademics.in/journals/index.php/ajpcr/article/view/11733.

Sockalingam, K., and Abdullah, H. Z. (2015). Extraction and Characterization of Gelatin Biopolymer from Black tilapia (Oreochromis mossambicus) Scales. *AIP Conf. Proc.* 1669, 020053. doi:10.1063/1.4919191

Srivastava, S., and Flora, S. J. S. (2020). Fluoride in Drinking Water and Skeletal Fluorosis: A Review of the Global Impact. *Curr. Envir Health Rpt* 7 (2), 140–146. doi:10.1007/s40572-020-00270-9

Surewicz, W. K., and Mantsch, H. H. (1988). New Insight into Protein Secondary Structure from Resolution-Enhanced Infrared Spectra. *Biochim. Biophys. Acta (Bba) - Protein Struct. Mol. Enzymol.* 952 (2), 115–130. doi:10.1016/0167-4838(88)90107-0

Tomar, V., and Kumar, D. (2013). A Critical Study on Efficiency of Different Materials for Fluoride Removal from Aqueous media. *Chem. Cent. J.* 7 (1), 51. doi:10.1186/1752-153X-7-51

Uzunoğlu, D., and Özer, A. (2016). Adsorption of Hazardous Heavy Metal Copper(II) from Aqueous Effluents onto Waste Material Fish (Dicentrarchus labrax) Scales:

Optimization, Equilibrium, Kinetics, Thermodynamic, and Characterization Studies. *Desalination Water Treat.* 57 (48–49), 22794–22798. doi:10.1080/19443994.2015.1111594

Valdez-Jiménez, L., Soria Fregozo, C., Miranda Beltrán, M. L., Gutiérrez Coronado, O., and Pérez Vega, M. I. (2011). Effects of the Fluoride on the central Nervous System. *Neurología (English Edition)* 26 (5), 297–300. doi:10.1016/S2173-5808(11)70062-1

WHO (2019). Drinking-water, Key Facts. Available at: https://www.who.int/news-room/fact-sheets/detail/drinking-water (Accessed on: June 26, 2021).

Yang, K., Liang, X., and Quan, C. (2019). "Fluoride in Drinking Water: Effect on Liver and Kidney Function☆," in *Encyclopedia of Environmental Health*. Editor J. Nriagu. Second Edition (Wuhan, China: Elsevier), 34–40. doi:10.1016/B978-0-12-409548-9.11083-8

Zayadi, N., and Othman, N. (2013). Removal of Zinc and Ferum Ions Using tilapia Mossambica Fish Scale. *Int. J. Integr. Eng.* 5, 23–29. doi:10.4028/www.scientific.net/AMR.795.260

Zhang, Y-Q., Tu, D., Shen, Q., and Dai, Z. (2019). Fish Scale Valorization by Hydrothermal Pretreatment Followed by Enzymatic Hydrolysis for Gelatin Hydrolysate Production. *Molecules* 24, 2998. doi:10.3390/molecules24162998

Zhu, K., Gong, X., He, D., Li, B., Ji, D., Li, P., et al. (2013). Adsorption of Ponceau 4R from Aqueous Solutions Using Alkali Boiled Tilapia Fish Scales. *RSC Adv.* 3 (47), 25221–25230. doi:10.1039/C3RA43817A

Conflict of Interest: The authors declare that the research was conducted in the absence of any commercial or financial relationships that could be construed as a potential conflict of interest.

Publisher's Note: All claims expressed in this article are solely those of the authors and do not necessarily represent those of their affiliated organizations, or those of the publisher, the editors and the reviewers. Any product that may be evaluated in this article, or claim that may be made by its manufacturer, is not guaranteed or endorsed by the publisher.

frontiers | Frontiers in Chemistry

REVIEW
published: 01 April 2022
doi: 10.3389/fchem.2022.826440

Perspectives on the Development of Filter Media for Point of Use Water Filters: Case Study of Arsenate Removal

Samuel Chigome[1]*, *Dickson Andala*[2], *Moses Kabomo*[3] and *Erick Mobegi*[4]

[1]Nanomaterials Division, Botswana Institute for Technology Research and Innovation, Gaborone, Botswana, [2]Department of Chemistry, Multimedia University of Kenya, Nairobi, Kenya, [3]Department of Chemistry, University of Botswana, Gaborone, Botswana, [4]Department of Chemistry, Kisii University, Kisii, Kenya

The demand for access to clean water will continue to increase as the world population increases. For sustainable development and embracement of technological advancement, it is plausible to consider a filter material development approach that uses locally abundant natural resources as the raw material and nanotechnology techniques for material fabrication. The review and research paper will present a perspective of the authors on how to embrace nanotechnology for filter media development with key focus on the remediation of arsenate. Drinking water contaminated with arsenic is an emerging global challenge. Continuous exposure to drinking water with high levels arsenic could result in several types of cancer. With this in mind, the US EPA in 2001 set 10 ppb as the maximum contaminant level of arsenic from the initial 50 ppb. Therefore, arsenic remediation is key in mitigating these health risks in people residing near water bodies with elevated arsenic levels. Adsorption is considered to be the cheapest. However, from literature, majority of the adsorbents cannot be used in field applications due to challenges associated with low adsorption capacity and a high level of particle leaching into purified water thus posing health dangers. Therefore, it means that many of these adsorbents are economically non-viable. A new chitosan, aluminium, titanium, iron and zirconium (CTS-Al-Ti-Fe-Zr) hybrid was fabricated through the sol-gel process. The material was characterized by scanning electron microscopy, Brunauer–Emmett–Teller and Fourier Transform Infrared spectroscopy before and after adsorption. Batch adsorption properties towards As(V) were separately studied as a function of the effect of adsorbent dose, pH, initial concentration, contact time and competing ions. Characterization results show that the material is a polycrystalline with a specific surface area of 56.4 m^2g^{-1}. Further, FTIR and SEM-EDAX showed adsorption of arsenate on the surface of the nanocomposite. Research findings suggest that with only 100 mg of the adsorbent arsenate can be reduced to less than 10 ppb from an initial concentration of 300 ppb respectively. The maximum adsorption capacity for arsenate removal was recorded as 123 mg/g. The presence of SiO_3^{2-}, CO_3^{2-}, and HCO_3^- ions resulted in a slight decline in the adsorption efficiency of arsenate. The equilibrium data fitted well with the Langmuir isotherm 0.99518. Data from the fabricated prototype Point-of-use filter showed that with 60.0 g of the

OPEN ACCESS

Edited by:
Adebola Omowunmi Oyedeji,
Walter Sisulu University, South Africa

Reviewed by:
Andreina García,
University of Chile, Chile
Aminul Islam,
Jashore University of Science and Technology, Bangladesh

***Correspondence:**
Samuel Chigome
schigome@bitri.co.bw

Specialty section:
This article was submitted to Nanoscience, a section of the journal Frontiers in Chemistry

Received: *30 November 2021*
Accepted: *18 February 2022*
Published: *01 April 2022*

Citation:
Chigome S, Andala D, Kabomo M and Mobegi E (2022) Perspectives on the Development of Filter Media for Point of Use Water Filters: Case Study of Arsenate Removal. Front. Chem. 10:826440. doi: 10.3389/fchem.2022.826440

nanocomposite, it is possible to reduce 650 L of drinking water with an arsenate initial concentration of 300 ppb to less 10 ppb. In conclusion, the research findings suggest that the nanocomposite material is capable of removal of arsenate from contaminated drinking water to WHO acceptable levels with a potential to be up scaled for commercial applications.

Keywords: nanocomposite, water filter, point of use, local materials, nanotechnology

1 INTRODUCTION

It should be noted that about 50% of the global population relies on groundwater as their source of drinking water. However, surface water is continually getting exposed to pollution leaving groundwater as the only viable source However, at present it is not considered as the most secure source since it is increasingly being polluted either by anthropogenic activities or dissolution from natural mineral in the earth's crust (Bootharaju and Pradeep 2010). Studies have established that underground water sources contain pollutants such as heavy metals like arsenic (Shaji et al., 2021) and anions like fluoride (Adak et al., 2016) among other water contaminants.

Drinking water contaminated with arsenic is an emerging global challenge. It is estimated that about 200 million people across the globe are exposed to drinking water with levels of arsenic exceeding 10 ppb (George et al., 2014). Cases of elevated arsenic levels have been identified in several parts of the world such as Bangladesh, India, Vietnam, Mexico and Argentina. Exposure to arsenic affects renal, heart, dermatologic and nervous system (Tchounwou et al., 2012). A number of studies have reported high mortality rates from various cancers (liver, skin, kidney and bladder) in areas characterized by arsenic pollution (Naujokas et al., 2013).

Typical Arsenic levels in groundwater are estimated to range between 0.5–10 ppb. However, these concentrations rise due to oxidation of arsenic pyrite mineral that consequently leaches arsenic into the water. In natural water the predominant oxidation states are trivalent Arsenite (As (III) and pentavalent arsenate (As (V) (Alispahić et al., 2021).

Arsenic does not exist in Free State in the environment. It is found in combination with Iron and Oxygen. Arsenic has four major oxidation states, +3, +5, −0 and −3 and two different forms: inorganic and organic (Tuutijärvi et al., 2013). Organic forms are rarely present in ground water. However, in natural water the predominant oxidation states are trivalent Arsenite (As (III) and pentavalent arsenate (As (V)) (Alispahić et al., 2021). Usually As (III) is mostly found in anaerobic ground water, whereas As (V), is found in aerobic surface water. In terms of toxicity, As (III) is considered to be about 60 times toxic than As (V) (Herath et al., 2016). WHO has set a maximum of 10 ppb as the threshold of Arsenic in drinking water (Giles et al., 2011).

Sources of Arsenic in groundwater can be categorized as either natural or anthropogenic. Natural source is mainly due to the weathering reactions of arsenic bearing minerals, volcanic activity and biological activity. Anthropogenic sources include smelting of metal ores, percolation of water during mining and use of pesticides and herbicides containing arsenic compounds. Anthropogenic sources contribute to higher levels of Arsenic in water compared to natural sources (Jiang et al., 2013). Typical Arsenic levels in groundwater are estimated to range between 0.5–10 ppb. However, these concentrations rise due to oxidation of arsenic pyrite mineral that consequently leaches arsenic into the water (Shaji et al., 2021).

A number of research activities, particularly in the discipline of nanotechnology, have pointed to the fact that application of nano engineered materials can help in resolving water quality issues by using nanoparticles (Ma et al., 2011). These classes of materials have been found to exhibit improved performance vis-à-vis existing compositions, thereby enhancing their effectiveness in point-of-use water purifiers (Savage and Diallo 2005).

Nanoscale engineered adsorbents have gained great attention in the application in water purification compared to existing bulk adsorbents. However, this class of nanomaterials cannot be used in field applications due to challenges in low adsorption capacity, poor particle separation hence a potential danger in view of their leaching into the purified water. Additionally, most of these nanoadsorbents do not have satisfactory wet strength to stay intact as a granular composition. This characterizes them with poor hydraulic conductivity which leads to excessive pressure drop in the water purification cartridge making their application in filtration devices impossible. Lastly majority of adsorbents used in water purification are in powder form which renders filtration difficult (Kumar et al., 2017). Combining all these limitations, it therefore means that many of these adsorbents are economically non-viable making them ineffective in commercial applications.

Adsorption technique is considered to be the cheapest in terms of cost, maintenance and ease of operation with nanoadsorbents gaining attention in the water purification compared to existing bulk adsorbents. However, some adsorbents cannot be used in field applications due to challenges in low adsorption capacity and high level of particle leaching into purified water thus posing health dangers. Further, this characterizes them with poor hydraulic conductivity which leads to excessive pressure drop in the water purification cartridge making their application in filtration devices impossible. (Kumar et al., 2017). Combining all these limitations, it therefore means that many of these adsorbents are economically non-viable making them ineffective in commercial applications. Therefore, there is need to synthesize nanoadsorbents that can overcome the above limitation and that can be easily up-scaled from the laboratory to commercial scale.

The novelty of this work is underpinned on the overcoming the aforementioned limitations of other adsorbents that have been

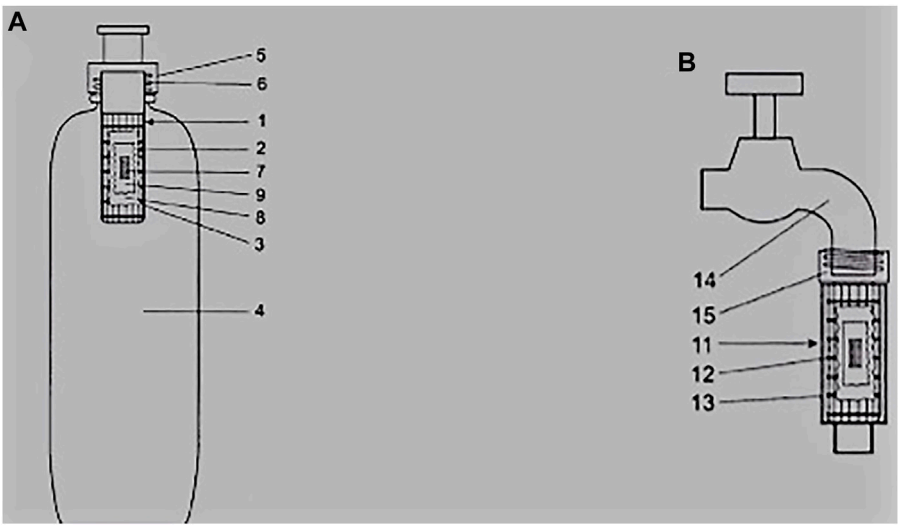

FIGURE 1 | (A) water bottle and **(B)** tap outlet point of use water filters that rely on a teabag containing nanocomposite filter media 1 = cartridge housing, 2 = perforated housing, 3 = biocide/electrospun nanofiber layer, 4 = bottle, 5 = screw thread holder, 6 = threaded fitting, 7 = activated carbon, 8 = teabag, 9 = ion exchange resin,, 11 = rough surface housing, 12 and 13 = filter media housing, 14 = tap, 15 = threaded adaptor to fit to water supply (Dicks et al., 2012).

reported in literature. Whereas other studies have reported higher adsorption capacities many go beyond batch adsorption studies. For instance, the powdered adsorbents cannot be packed into water purification cartridge because filtration will be hampered. Based on this observation chitosan, aluminium, titanium, iron, and zirconium (CTS-Al-Ti-Fe-Zr) is characterized by improved mechanical strength since it exists as a granular nanocomposite which makes filtration easier and that the material is strong mechanically both in dry and wet conditions. An added advantage of this material is its synthesis protocol that is considered cheap and environmental friendly. The only disadvantage of this nanocomposite is that its quaternary hence slightly expensive in terms of the oxides needed for its synthesis.

In the simplest of terms, a point of use water filter is a filter that is employed in the purification of water at the point where it is being used. POU water filters are different from centralized water treatment systems in that they are used at small scale level and purify less amounts of water. POU water filters can be vital in water purification practices, particularly in Africa, where the need for decentralized water purification systems are solutions to key water challenges.

Materials can be classified into five categories according to their chemical composition: metals, semiconductors, polymers, ceramics and composites (Smith 2003). The ability to fabricate large surface area materials with controlled functionality has opened up new possibilities in the development of filter media, particularly enhanced adsorption capacity and miniaturization of filtration devices (Reisner and Pradeep 2015). Therefore, the use of nanotechnology-based techniques to fabricate water filter media can be considered as holding the future for POU water filters to address the current and emerging challenges. A better understanding of techniques that have the ability to fabricate either powdery nanoparticles or nanofibers from the five categories of materials is necessary to have control of advanced water filter media development. It should also be noted that such techniques allow the conversion of conventional bulk filtration materials into superior performing filter media at the nanoscale without changing the chemical composition. This presents a significant benefit to Africa that has got a significant number of natural resources that can possibly be manipulated into nanoscale-based water filtration media (Mulwa and Mariara 2016; Roksana 2016). Although our experimental work on electrospun fibers is not presented in the current contribution, it is plausible to highlight the most practically useful technique for fabricating nanofibrous water filter media which is referred to as electrospinning. This will help the readers to have a broader view of the avenues to explore in their pursuits to develop point of use water filters that rely on locally abundant materials in Africa.

The use of electrospinning, a technique that relies on repulsive electrostatic forces to draw a polymer solution into nanofibers, as a membrane fabrication technique allows the incorporation of filter media either as composites or as multiple layers in a variety of POU water filter formats. In principle; 1) electrospinning allows the fabrication of filter media from all classes of materials into nanofibrous form as long as there is a way of getting the precursor polymer or composite into a solution or a melt, 2) it carries the main benefit of nanoparticles being surface area, it addresses the challenge of powdered filter media as the fibrous network allows ease of tortuous flow of water which reduces the back pressure and making the POU gravity driven, 3) there is also a wide range or pre and post electrospinning modification approaches that broaden the range of functionalities that are possible hence making it possible to remove a broad range of contaminants, 4) there are several formats in which the nanofiber membranes can be arranged primary due to the flexibility of the supporting

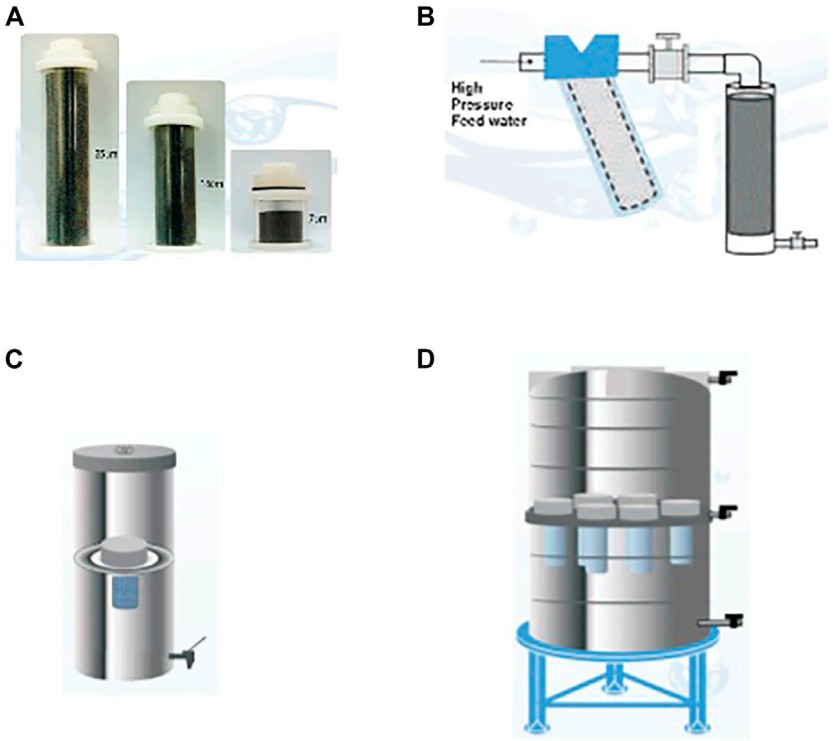

FIGURE 2 | (A) granular filter media cartridges of different sizes for ease of integration into different filtration systems **(B)** cartridge connected to a high pressure online system like a borehole **(C)** granular cartridge incorporate into a kitchen top filter **(D)** multiple granular filter cartridges incorporated into a large tank for a community water filtration system (Pradeep 2012).

FIGURE 3 | Illustration of the correlations between pore size and electrospun fiber diameter at a constant porosity of 80% in a fixed volume (Ma et al., 2011).

electrospinnable polymer backbone, 5) the electrospinning set up is relatively simple and it allows rapid prototyping as scaling up is simple (Chigome et al., 2011; Chigome and Torto 2011; Cheng et al., 2019; Shirazi et al., 2020). In our labs we have laboratory scale and pilot scale facilities of which our biggest pilot scale electrospinning unit allows the fabrication of a nanofiber membrane of 1 km length and 0.5 m width.

Figure 1 shows two types of electrospun fiber based point of use water filters, the first being a water bottle which brings an advantage of being portable while the second one is tap outlet water filter. The driving force for the water bottle is the pressure exerted by a hand during the process of squeezing while for the tap it is the typical municipal water pressure of about 1.5 bar. Both POU water filters in this example rely on the same filter media which is a teabag coated with a biocidal electrospun fiber membrane that contains granular activated carbon and an ion exchange resin (Dicks et al., 2012).

In order to vary the scale of POU water filters from household to community level with mainly an interest in gravity-based filtration systems, coarse granular filter media is packed into a cartridge format of varying sizes as shown in **Figure 2**. The shows the practicality of the concept of granular

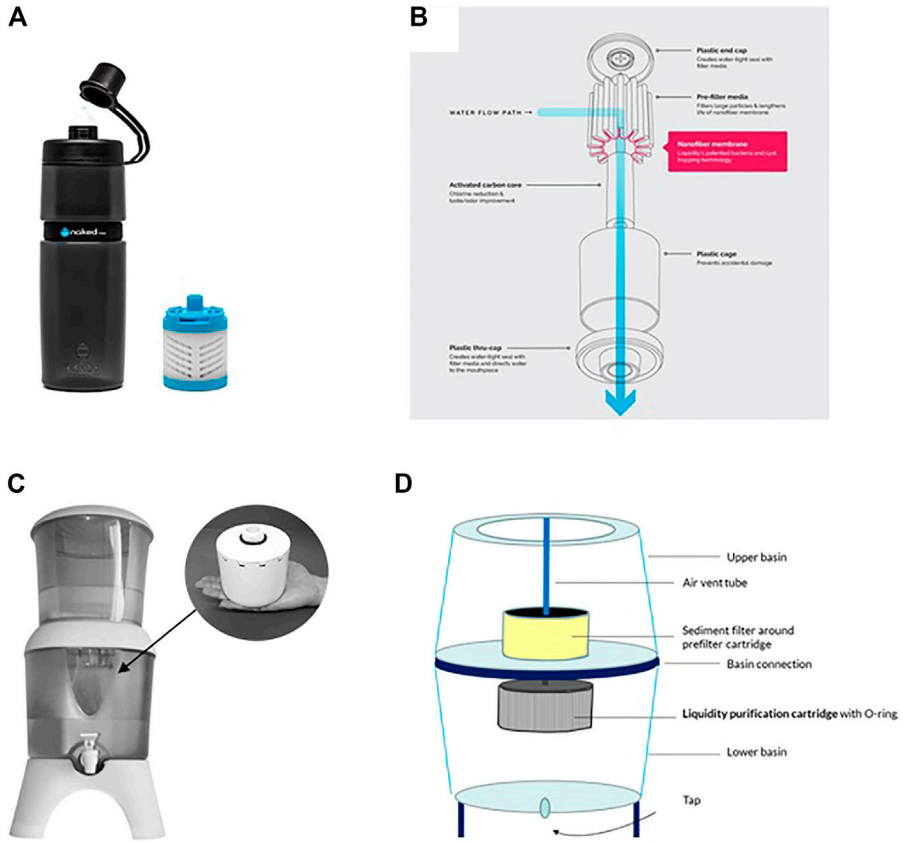

FIGURE 4 | (A) bottle type nanofiber water filter (insert replacement cartridge) that has a filtration capacity of 75 L **(B)** components of the filter **(C)** Counter top nanofiber water filter (insert replacement cartridge) that has a filtration capacity of 1500 L **(D)** components of the filter (Liquidity Corpopration 2014).

filter media of different compositions as scaling up and down is simplified.

To help with the understanding of the electrospun nanofiber membrane properties, **Figure 3** shows 3D simulated non-woven membrane models, having different fiber diameters, which were created to illustrate the relationship between the fiber diameter and the pore size. All the three membrane models are at a constant porosity in a fixed volume with a relative fiber diameter ratio of 1 :3:10.3D non-woven structure can be fully defined by only two parameters, the fiber diameter and the bulk porosity, and has no other adjustable parameters. Thus, the pore sizes can be adjusted by controlling the fiber diameter of the electrospun membrane, allowing them to satisfy the requirements for various microfiltration and ultrafiltration applications. This makes it possible to have high flux gravity driven filtration with the removal of bacteria of average size 200 nm by two mechanisms, size exclusion or bacterial conformational change (Abrigo et al., 2015). The multiple pathways that exist as a result of fiber diameter reduction illustrate the increased filtration efficiency due to increased available fiber surface and tortuous flow. The model therefore illustrates the benefits of having filter media in the electrospun nanofiber format where continuous intertwining fibers provide a effect membrane network for water filtration.

Figure 4 shows two types of POU water filtration formats derived from electrospun nanofibers demonstrating the practical usefulness of the filter media as a small gravity driven cartridge can filter 1,500 L of water.

2 MATERIALS FOR POINT OF USE WATER FILTRATION MEDIA

Chitosan has received greater attention in water purification due to presence of large number of $^{-}NH_2$ and OH^{-}groups. The free amine function of chitosan gives it a better ability to chelate ions (Sudheesh et al., 2013). These chelating properties are of great interest for water treatment and particularly to recover metals present in contaminated water (Koshijima et al., 1973; Kyzas et al., 2009; Rajiv Gandhi et al., 2010).

The use of the metal oxides was to specifically harness their adsorption affinity towards arsenate and more importantly to achieve higher mechanical strength to produce granules of specific sizes instead of powder. Metal oxides that have been used for arsenic remediation include activated alumina, iron oxides, titanium oxides, zirconium oxides, cerium oxides and manganese oxides among other (Chen et al., 2014). The synergistic adsorption parameters of these oxides were

harnessed in the form of a composite in order to increase the surface area of the metal oxides consequently increasing the number of adsorption sites and surface hydroxyl groups on the oxides.

Membrane technologies such as nanofiltration and reverse osmosis have found immense application in water purification. This is because membrane processes are capable of removing high concentrations of inorganic ions, dissolved solids and organic contaminants (Lakherwal 2014). However, membrane technologies are characterized by fouling and require high pressures for operations. This increases the cost of operation. The worst disadvantage of these technologies is that they can decrease mineral content in water, thus rendering the output water unsuitable for drinking (Pangarkar et al., 2011).

Nano-engineered materials can help in resolving water quality issues by using nanoparticles and nano-adsorbents. These materials have been proven to be efficient, strong and more affordable than other water decontamination technologies (Qu et al., 2013). Some of these products include nonporous filters such as ceramics, clays adsorbents, zeolites, dendrimers, metal-containing nanoparticles, carbonaceous and catalysts nanomaterials (Thakre et al., 2010; Ghauri et al., 2013).

Four major functional categories of nano-engineered materials are employed in water purification. To begin with, there are nanoparticles that have been tested and found to have antimicrobial properties such as silver nanoparticles. Next, there are nano-catalysts whose primary application is to reduce pesticides and other organic toxins. Thirdly, there are nanoadsorbents which are commonly applied in removal of inorganic contaminants such as heavy metals. Lastly, there are classes that are used as filtering agents for instance in membranes (Guo and Tian 2013).

3 NANOCOMPOSITE FILTER MEDIA

Fabrication of water purification media has been carried out in our lab using metal oxide biopolymer nanocomposite. The material was synthesized using green approach. In this study we have focused on the removal of arsenate and fluoride at laboratory scale and fabrication of a point of use water filter. At the laboratory level we focused on batch and continuous mode. Factors that affect adsorbent performance (pH, adsorbent dose, kinetics and co-existing ions) were investigated.

3.1 Nanocomposite Synthesis

The granular composite was synthesized using a combination of aluminium sulphate decahydrate, titanium (IV) oxysulfate, Zirconium oxychloride octahydrate and iron oxyhydroxide and chitosan. About 1.3 g of chitosan was dissolved in 100 ml of 1% HCl and mixed using a magnetic stirrer at 400 revolutions per minute (RPM). The mixture was left to incubate for 12 h. Exactly, 25 ml of chitosan solution was measured and incubated for 5 min and to it 10 ml of 0.5 M $Al_2(SO_4)_3.18H_2O$ was added and stirring continued for 30 min. Next, 4 ml of 0.25 M titanium (IV) oxysulfate was added. Thereafter, 4 ml of 0.25 M $ZrOCl_2{\cdot}8H_2O$ was added. After 1 h of continuous stirring, 7 ml of 1 M $FeCl_3.6H_2O$ was added and mixing continued for 30 min. About 3.6 g Na_2SO_4 was then added in one step to the incubating mixture. The mixture was precipitated and the pH brought to 6.5 by slow addition of 2 M NaOH. The final mixture was further left to incubate for 12 h at ambient temperature. The next step was to carry out vacuum filtration to obtain the gel. The subsequent gel was washed with copious amount of water in order to remove excess soluble salts. The gel was dried at room temperature for 12 h. Finally, the material was crushed into specific sizes (52 × 72 μm) and was ready for various adsorption studies.

3.2 Adsorption Experiments

As (V) stock solution (1,000 ppm) was prepared by dissolving sodium arsenate in 1 L distilled water and was preserved with 0.5% trace metal grade HNO_3. All other arsenic solutions were prepared by dilution from the stock solution. The incubation time was chosen to be 2 h for all the experiments. Amount of the adsorbent required was added into the water samples and agitated at 210 RPM. Afterwards, water samples were decanted and centrifuged at 4000 RPM for 5 min and then filtered using 0.22 μm 6,6 Nylon membranes. The sample were then prepared by taking 950 μL of the water sample and digested by adding 50 μL HNO_3. The effect of adsorbent dose on the sorption of As (V) on the adsorbent was carried out using 1,000 ppb as the initial arsenic ion concentration. The dosage was varied from 5 to 200 mg. To examine the effect of contact time, the adsorbent was exposed to As (V) in the range of 1–180 min. The effect of pH, adsorption experiments were conducted in the pH range of 4, 5, 6, 7, 8, 9 and 10. The initial arsenic concentration was taken to be 1,000 ppb. The pH adjustments were achieved using 0.1 M HCl and 0.1 M NaOH. The interference of competing ions such as Cl^-, NO_3^-, SO_4^{2-}, Na^+ SiO_3^{2-}, K^+, Ca^{2+}, Mg^{2+}, HCO_3^-, CO_3^{2-} and HCO_3^- and CO_3^{2-} were investigated to evaluate their effect on adsorption efficiency. The effect of the initial As (V) concentration on the adsorption capacity of the nanocomposite material was tested in the range of 1–200 ppm with an adsorbent dosage of 50.0 mg. Maximum adsorption capacity of the nanocomposite was evaluated at concentrations ranging from 1 to 200 ppm were used.

3.3 Prototype Filter Fabrication

A prototype filter was designed and fabricated after the performance of the batch adsorption experiments was established. Approximately 60.0 g of the nanocomposite material of particle size 72 um was packed in water purification cartridge measuring 35 mm in diameter and 10 mm in height. The filter was assembled in antigravity manner.

3.4 Material Characterization

SEM-EDAX analysis was done on the nanocomposite material's interaction with arsenic in form of As (V). The EDAX spectrum indicates that all the principal elements are present. **Figure 5** presents an EDAX spectrum before (a) and after (b) adsorption.

The elemental composition maps confirm that the distribution of arsenic is homogeneous. It is clear that the level of arsenic before adsorption was 0.00% by percent atomic. However, after adsorption, the adsorbed content of Arsenic is recorded to be 4.71

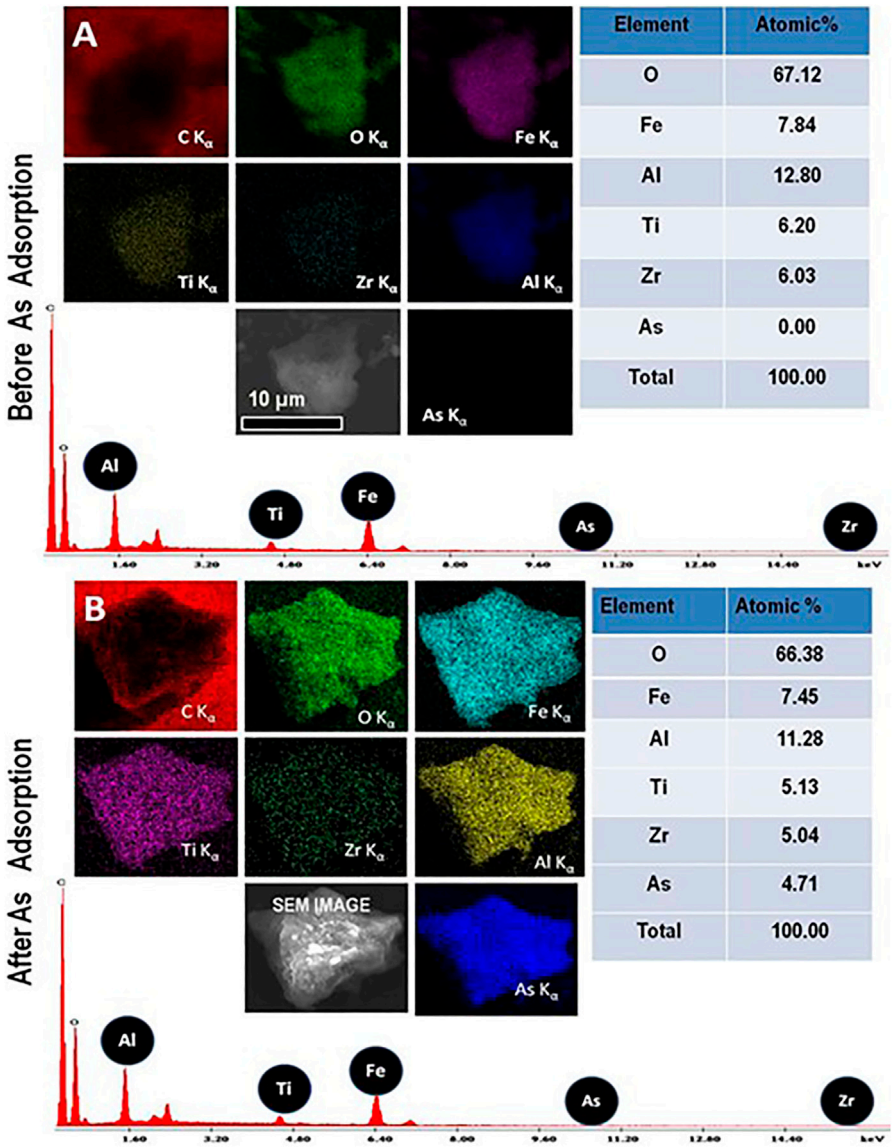

FIGURE 5 | Elemental X-ray images (SEM-EDAX) of **(A)** the nanocomposite before exposing to As solution. **(B)** nanocomposite after exposing to As solution.

atomic percent. This confirms the interaction of the adsorbent and arsenic.

SEM-EDAX analysis was done on the nanocomposite material's interaction with arsenic in form of As (V). The EDAX spectrum indicates that all the principal elements are present. **Figure 5** presents an EDAX spectrum before (a) and after (b) adsorption.

To establish the functional groups that account for the adsorption of arsenic, FTIR spectra of the nanocomposite before and after adsorption was measured. **Figure 6** shows the FTIR spectrum of aluminium-titanium-zirconium-iron oxyhydroxide-chitosan composite before exposure to arsenic solution (a) and after adsorbing arsenic (b).

The frequency band at wavenumber 1107 cm^{-1} is indicative of bending vibration of hydroxyl groups on the metal oxides. The peak intensity at 1,107 cm^{-1} after adsorption, decreased indicating arsenic adsorption. Generally, after exposing the nanocomposite to arsenic ion solution, it is notable that the intensity of the peaks reduced significantly. This phenomenon has been observed in other various studies, where the peak intensity reduces after adsorption (Qiusheng et al., 2014). However, two new broad peaks appear in the region of 600–1,000 cm^{-1} when compared to the spectra before arsenic adsorption. This might correspond to the adsorbent - arsenic interactions.

In addition, the following peaks showed shifts: 3,742 cm^{-1} to 3,749 cm^{-1}, 2,935 cm^{-1} to 2,932 cm^{-1} and 2,854 cm^{-1} to 2,840 cm^{-1}. However, there is a significant shift of peak 896 $cm^{-1}$to 817 cm^{-1}, with the intensity of the peaks increasing. From the FTIR studies, the results suggest that the

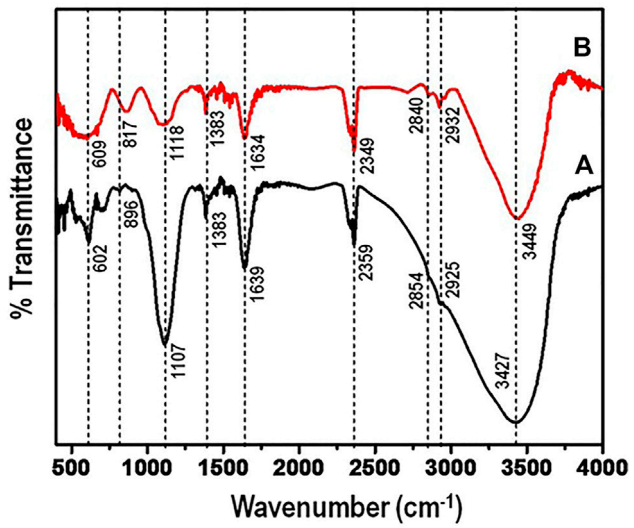

FIGURE 6 | (FTIR) spectrum of aluminium-titanium-zirconium-iron oxyhydroxide-chitosan composite **(A)** along with the composite after adsorbing arsenic **(B)**.

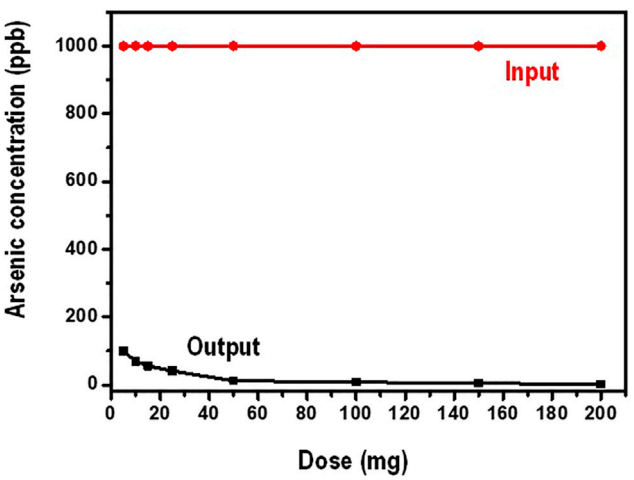

FIGURE 7 | Residual arsenate concentration as a function of adsorbent dose.

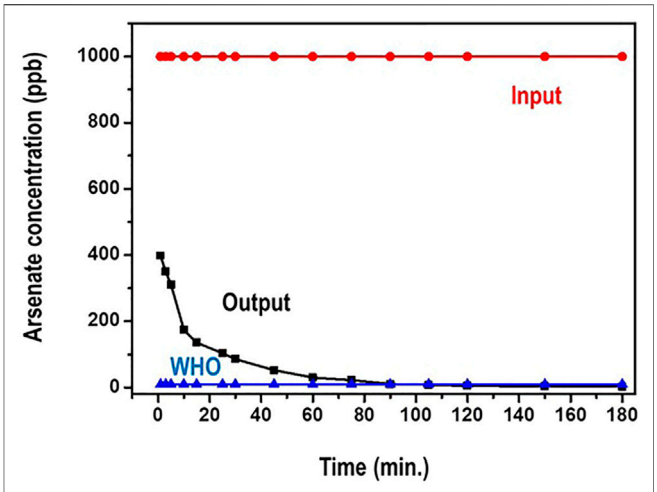

FIGURE 8 | Residual arsenate concentration as a function of time.

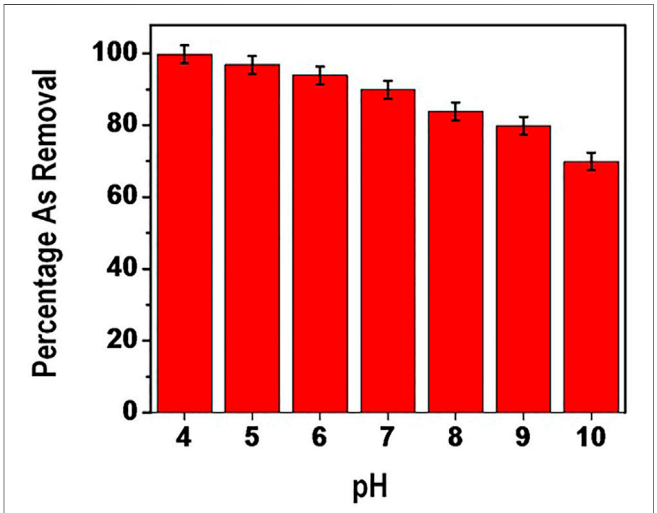

FIGURE 9 | percentage removal of Arsenate as a function of pH.

replacement of the metal-hydroxyl groups by arsenic plays a significant role in the adsorption of arsenic contaminant.

The surface area of the aluminium-titanium-zirconium-iron oxyhydroxide-chitosan composite was investigated using BET. The specific surface area of the nanomaterial was recorded using Micromeritics ASAP 2020. Samples were degassed at 200°C for 4 h under vacuum and analyzed at 77 K with ultra-high pure nitrogen gas. It was found that the nanocomposite recorded a specific surface area of 153 m^2g^{-1}. The increased surface is most likely, among other factors, responsible for the enhanced adsorption capacity for both fluoride and Arsenic contaminants compared to other adsorbents but slightly lower than the one reported by Thakre and co-investigators who did similar study on chitosan based mesoporous Ti-Al binary metal oxide and posted a surface area of 323.8 m^2g^{-1} (Thakre et al., 2010).

3.5 Batch Adsorption Studies

3.5.1 Effect of Adsorbent Dosage

In this investigation, the working volume of water was kept at 100 ml while the amount of the nanocomposite (dosage) was varied between 5 and 200 mg. The initial concentration arsenate was maintained at 1,000 ppb. **Figure 7** shows data on the influence of the amount of the adsorbent dosage on the sorption of arsenate.

It is observed from **Figure 7** that, increasing the amount of the adsorbent, the equilibrium concentration of arsenate

TABLE 1 | pH stability for different species of Arsenate.

Arsenate Species	pH Stability
H_3AsO_4	<2
$H_2AsO_4^-$	2–7
$HAsO_4^{2-}$	7–11
AsO_4^{3-}	>12

decreases gradually. Generally, adsorption is greatly influenced by the number of the active binding sites present for the contaminant (adsorbate) to occupy. In lower adsorbent doses the available binding sites are minimal hence lower adsorption capacity. In higher adsorbent amounts, the presence of binding sites is high for the adsorbate to bind thus high adsorption capacity. This kind of observation is responsible for increased arsenate adsorption at higher a mounts of the adsorbent. In addition, increase in the amount of the adsorbent leads to increase in the number of active sites of adsorption. Moreover, increasing the dosage translates to increasing the surface area of the adsorbent (Sokker et al., 2011).

3.5.2 Effect of Contact Time

The impact of contact time on the adsorption of arsenic species on the adsorbent was studied in the interval of 1–180 min. This was particularly to evaluate the equilibrium time for maximum adsorption. 1,000 ppb concentration of arsenate solutions was used. The amount of the adsorbent was maintained at 100 mg. **Figure 8** presents results on the time dependence of arsenate adsorption on the nanocomposite.

From **Figure 8**, the arsenate uptake on the adsorbent was very rapid and over 95% adsorption was achieved within the first 20 min. Further, the sorption reached equilibrium at about 90 min. During the period after the 90 min, there was no significant increase in arsenate adsorption that was registered as the amount of time increased. Actually, it is noted that the concentration of arsenate reduces from 1,000 ppb to less than 10 ppb (WHO recommended limit) in about 75 min.

Initially, the fast adsorption could be ascribed to the higher concentration gradient and the availability of more adsorption sites (Qiusheng et al., 2015). After equilibrium was attained, it is possible that the available binding sites were strenuous to binding due to the repulsive forces between the solute molecules and the bulk phase of the adsorbent. Such similar phenomenon has been observed by Sokker and co researcher (Sokker et al., 2011).

3.5.3 Effect of pH

The influence of pH was investigated in the range of 4–10 visa Vis the performance of the adsorbent. **Figure 9** shows results the influence of initial solution pH on arsenate adsorption.

Percentage removal of arsenate was reduced from about 99% to about 69% when the pH was increased from 4 to 10. This is explained by the fact that there is minimal repulsion in the wide range pH. Specifically, percentage removal was above 90% in the pH range of between 4 and 7. This can be attributed to the stability of $H_2AsO_4^-$ at pH between 2 and 7 (**Table 1**) hence existence of high amounts ions. However, a gradual decline trend on arsenate adsorption is observed after pH 7.

The above observation can be explained by the influence of pH on the speciation of arsenic in solution whereby beyond neutral pH arsenate particularly $HAsO_4^{2-}$ ions are prevalent compared to $H_2AsO_4^-$. It should be noted that $HAsO_4^{2-}$ ions have got less affinity for the adsorbent compared to $H_2AsO_4^-$ thus the decline adsorption capacity. The table below presents stability of various species of arsenate at different pH levels.

It is evident from **Table 1** above that when equilibrium pH increases the concentration of multivalent species increases in the solution and consequently is not easily adsorbed onto the nanocomposite. Usually As (V) mainly exists as $H_2AsO_4^-$ in the pH range of 3 and 6. In the pH range of 8 and 11 As (V) occurs as $HAsO_4^{2-}$ (Rajiv Gandhi et al., 2010). In the pH range of 4–8 it could be possible that the nanomaterial surface gains negative charge hence high specific adsorption of As (V) onto the nanomaterial. The relatively high percentage (above 90%) of arsenic removal up to about pH 7 can be linked to the high degree of electrostatic attraction between the As (V) and the positively charged surface of the nanocomposite.

From the amphoteric theory on dissociation it is opined that as pH increases there is a decrease in adsorption of As (V) due to the decline in electrostatic interaction between the nanocomposite and As (V). Similar observation has been reported by (Nabi et al., 2009). In their findings they found out that the adsorption efficiency of As (V) using Titanium nanoparticles decreased above pH of 7. Further, there is increased competition for the active site from OH–ions hence decrease in arsenic adsorption. This is in agreement with what has been documented by Yu et al. (2015).

3.5.4 Effect of Competing Ions

The presence of various dissolved ions in water presents a challenge of these ions competing for the active sites with the targeted adsorbate. Their presence in water affects the overall performance of the adsorbent. The effect of the various ions

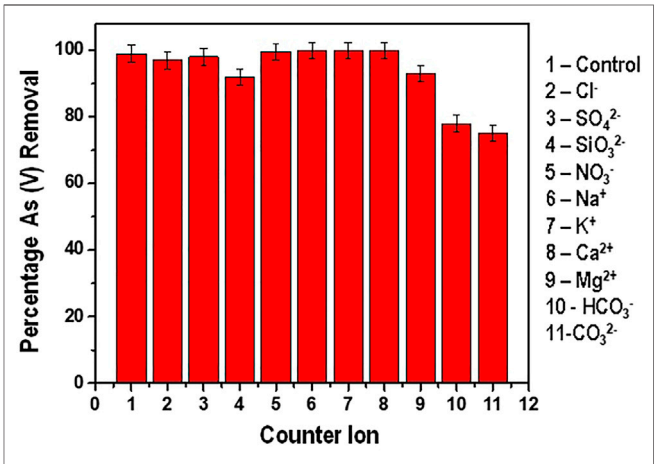

FIGURE 10 | Percentage Arsenic (V) removal in presence of various counter ions.

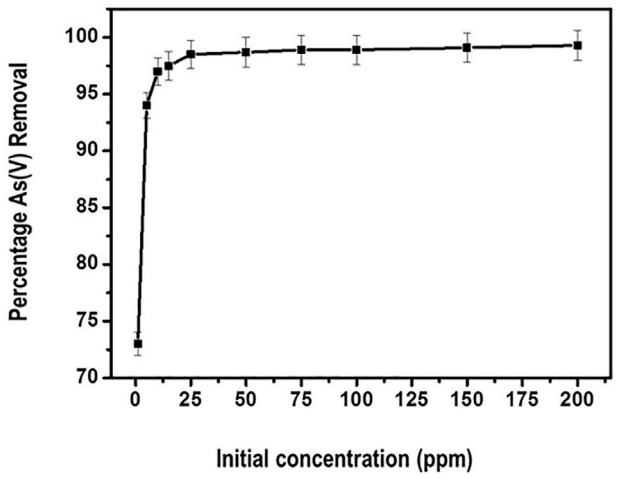

FIGURE 11 | Adsorption as a function of initial arsenate concentration.

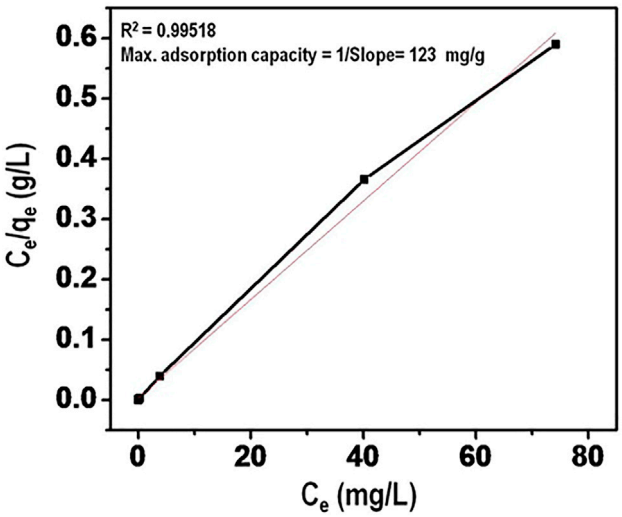

FIGURE 12 | Langmuir adsorption isotherm for Arsenate ion adsorbed (mg/g).

present in water and their effect on As(V) adsorption was studied and the results are presented in **Figure 10**.

From **Figure 10** it is depicted that the presence of Cl^{-}, SO_4^{2-}, NO_3^{-}, Na^{+}, K^{+}, Ca^{2+} and Mg^{2+} did not present significant interference with the adsorption of As (V). In the presence of these competing ions, the reduction efficiency recorded was above 95%. Similar results have been reported by Ghosh and co-investigators in their work on Arsenate removal using iron and magnesium salts. In their findings, they observed that Cl^{-} and NO_3^{-} ions had inconsequential impact on the adsorption efficiency. Contrary to this study, the presence of SO_4^{2-} ions had pronounced effect on the adsorption process (Ghosh et al., 2003).

The presence of SiO_3^{2-}, CO_3^{2-} and HCO_3^{-} had a significant negative effect in the adsorption efficiency. The effect of SiO_3^{2-} on the adsorption efficiency can be attributed to the competition for the binding site with the arsenate species as described by Tresintsi and co-researchers (Tresintsi et al., 2012). Genc-Fuhrman and his co-author have equally documented that silicates can reduce the adsorption efficiency of arsenic from 100% to about 60% in the pH ranges of drinking water (6.5–8.5) (Genç and Tjell 2003).

The $CO_3^{2-}$and HCO_3^{-} ions had the most pronounced negative effect with the adsorption efficiency reducing to less than 80% (reduction from an initial concentration of 300 ppb to an average of about 60 ppb). This observation can be well explained by the fact that when carbonate and hydrogen carbonate ions are present in water, the pH increases significantly. As earlier discussed on the effect of pH on As (V) adsorption, it therefore means that the drop in adsorption efficiency is due to the increase in pH which further leads to the increase in the electrostatic repulsion between the predominant $HAsO_4^{2-}$ species and the negatively charged surface of the adsorbent at pH between 7 and (Saha and Sarkar 2016).

3.5.5 Effect of Arsenic Concentration

The influence of the initial As (V) concentration on the reduction efficiency was tested in the range of 1–200 ppm. The results are presented in **Figure 11**.

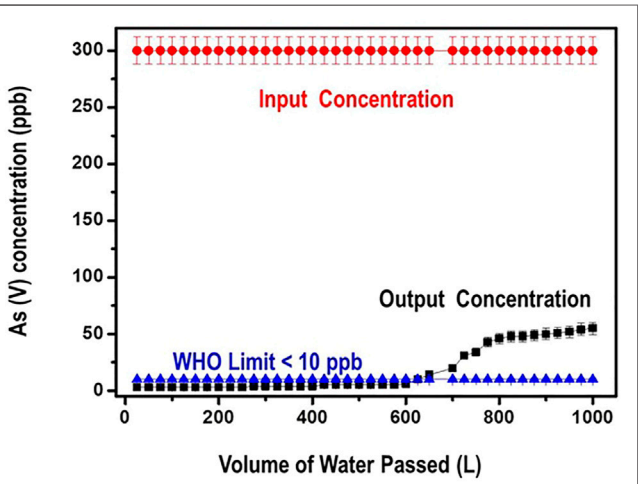

FIGURE 13 | Performance data for Arsenate reduction in tap Water.

From **Figure 11**, generally the removal percentage of arsenate by the adsorbent initially increases with the increasing initial concentration of arsenate. Further, the optimum percentage removal level of about 98% is attained at 50 ppm arsenate concentration. Thereafter a plateau curve is noticed indicating attainment of equilibrium. This kind of observation could be explained by the fact that the availability of binding sites for adsorption remained fairly constant for the fixed amount of the nanocomposite.

The increase in adsorption efficiency as concentration of the adsorbate increased can be attributed to the decline in resistance of arsenate from the solution. This observation is in consistent with a similar study carried out by Roy and co-researchers. In

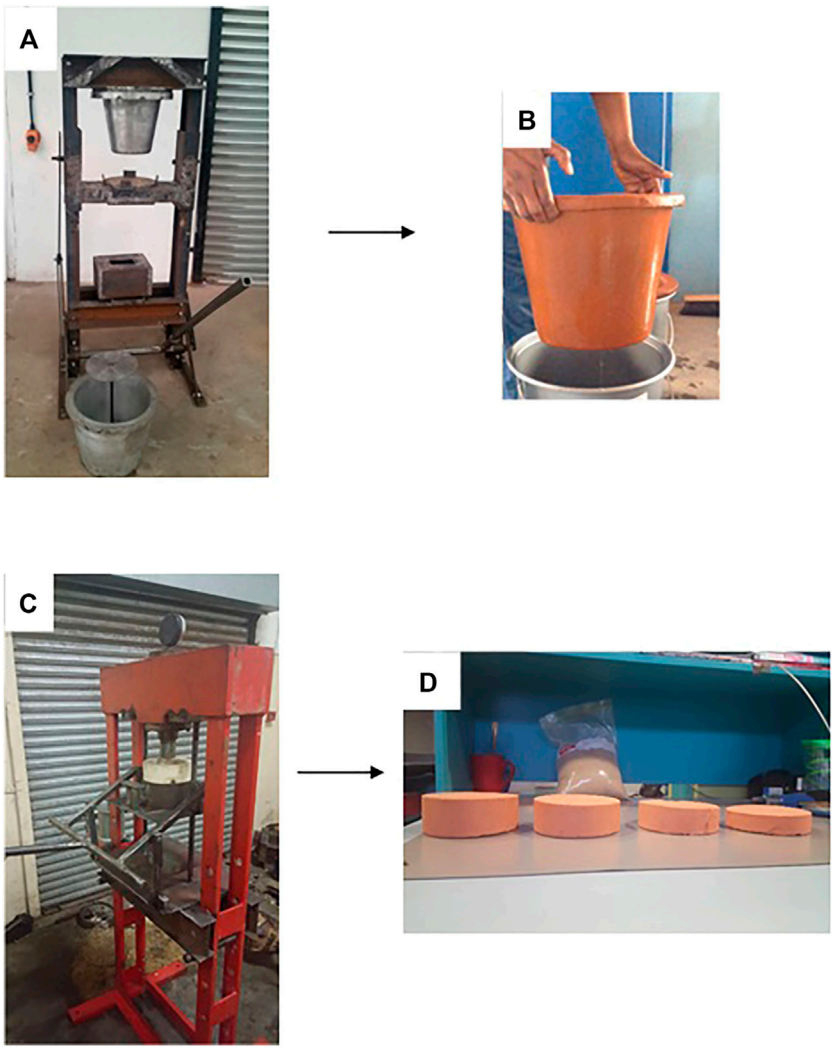

FIGURE 14 | (A) Mechanical clay pot filter mould **(B)** Ceramic pot filter after heat treatment **(C)** Mechanical clay disk filter mould **(D)** Ceramic disk filters of different sizes after heat treatment.

their study, they posted an increase in arsenate adsorption when the concentration was increased to about 85.6%. Thereafter the percentage of arsenate reduction showed little increase (Roy et al., 2013).

3.5.6 Adsorption Isotherm Studies

Maximum arsenate adsorption capacity was evaluated using Langmuir adsorption isotherm. The data is presented in **Figure 12**. The linear plot of Ce/q_e versus C_e in addition to high value of correlation coefficient provides that Langmuir isotherm provides a better fit for the equilibrium data. The Langmuir capacity (mg/g) of the nanomaterial for arsenate adsorption was calculated to be 123 mg/g. This can be linked to the inherent structure of the nanomaterial which provides for generation of effective sites of adsorption. This value is higher than those reported in previous literature.

3.5.7 Prototype Filter Performance Using Tap Water Laden With Arsenate

The filter's performance against As (V) reduction efficiency was investigated with more than 1000 L of water at a flow rate of 10–15 ml/min. The input water had a concentration of 300 ppb of the As (V) contaminant. Output water samples were collected and analyzed for residual Arsenate after digestion with 5% HNO_3. Data obtained from this study is presented in **Figure 13**.

Data from **Figure 13** illustrates that arsenate contaminant was removed to below the WHO limit of 10 ppb for 650 L of tap water with only 60.0 g of the nanocomposite. It is equally noted from the graph that even after running 1,000 L of the arsenate contaminated tap water through the filter, still the performance of the nanocomposite was excellent such that the level of arsenate was reduced from 300 ppb to about 50 ppb. These results can translate to an adsorption capacity of close to

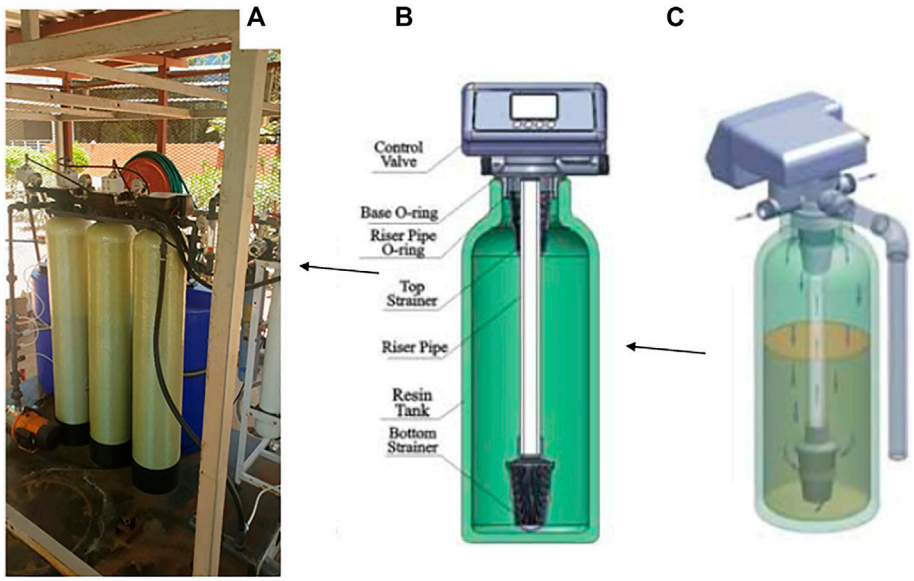

FIGURE 15 | (A) A section of a 500 L/h pilot plant filtration system showing three stages of granular based filtration media **(B)** Components of each filter media vessel **(C)** Flow pathway of water during filtration.

120 mg/g that is 3–8 times greater than the ones reported in literature.

3.6 Configurations for Powdered Filter Media

In our labs, we explored the possibility of fabricating ceramic filter media derived from iron oxide rich clay, saw dust as a pore generator upon heat treatment and silver nanoparticles as the antimicrobial agent. We fabricated mechanical filter moulding devices for ceramic pot and ceramic disk filters (**Figure 14**). Such fabrication approaches could be taken advantage off for application to the fabrication of a variety of nanocomposite filter media particularly the disk configuration as it is less bulky as compared to the ceramic pot filter.

Given the fact that in some instances there is a need for high flow rate multistage point of use water filtration systems to handle the complexities associated with different water sources, it is plausible to consider a configuration for housing a range of nanocomposite filter media. Such systems would benefit a community, or a company set up with more than 300 employees. **Figure 15** shows a pilot scale water filtration experiment station that we have at our labs. The system is currently configured to house three types of nanocomposite filter media within the holding vessels. On the basis of the power rating of the feed pump, it can produce more than 300 L/h of water. In order to allow the use of the pilot scale water purification system in areas that do not have access to electricity, it is also possible to configure it so that the pumps can be solar driven.

4 CONCLUSION AND FUTURE DIRECTION

The development of filter media for POU water filters is an area of importance as it helps to solve the challenge of accessing cleaning drinking water in areas that are far away from municipal water purification systems. Affordability of the resultant water filtration systems is mainly determined by the cost of the filter media. The cost is viewed from the material fabrication which is lowered firstly by using low-cost raw materials of which exploring the use of locally abundant natural resources is plausible. Secondly, the cost of the filter media is lowered by fabricating large capacity filter media which prolongs the filtration lifespan before regeneration of filter media replacement. Nanomaterials based filter media are seen as contributing to an increase filtration capacity mainly because of their large surface area. This implies that research efforts should be directed towards a better understanding of the application of nanotechnology-based fabrication techniques to produce efficient filter media derived from locally available raw materials.

AUTHOR CONTRIBUTIONS

EM, DA contributed work done in Kenya SC and MK contributed work done in Botswana.

REFERENCES

Abrigo, M., Kingshott, P., and McArthur, S. L. (2015). Electrospun Polystyrene Fiber Diameter Influencing Bacterial Attachment, Proliferation, and Growth. *ACS Appl. Mater. Inter.* 7 (14), 7644–7652. doi:10.1021/acsami.5b00453

Adak, M.K., Mondal , B., Dhak, P., Sen, S., and Dhak, D. (2016). A comparative study on fluoride removal capacity from drinking water by adsorption using nano-sized alumina and zirconia modified alumina prepared by chemical route. *Adv. Water Sci. Technol.* 4, 1–10.

Alispahić, A., Krivohlavek, A., and Galić, N. (2021). Novel Preservation Methods for Inorganic Arsenic Speciation in Model and Natural Water Samples by Stripping Voltammetric Method. *Appl. Sci.* 11, 8811. doi:10.3390/app11198811

Bootharaju, M. S., and Pradeep, T. (2010). Uptake of Toxic Metal Ions from Water by Naked and Monolayer Protected Silver Nanoparticles: An X-ray Photoelectron Spectroscopic Investigation. *J. Phys. Chem. C* 114, 8328–8336. doi:10.1021/jp101988h

Chen, L., Xin, H., Fang, Y., Zhang, C., Zhang, F., Cao, X., et al. (2014). Application of Metal Oxide Heterostructures in Arsenic Removal from Contaminated Water. *J. Nanomater.* 2–7. doi:10.1155/2014/793610

Cheng, C., Li, X., Yu, X., Wang, M., and Wang, X. (2019). "Electrospun Nanofibers for Water Treatment," in *Electrospinning: Nanofabrication and Applications*. Editors B. Ding, X. Wang, and J. Yu (New York: William Andrew Publishing), 419–453. Micro and Nano Technologies. doi:10.1016/b978-0-323-51270-1.00014-5

Chigome, S., and Torto, N. (2011). A Review of Opportunities for Electrospun Nanofibers in Analytical Chemistry. *Analyt. Chim. Acta* 706, 25–36. doi:10.1016/j.aca.2011.08.021

Chigome, S., Darko, G., and Torto, N. (2011). Electrospun Nanofibers as Sorbent Material for Solid Phase Extraction. *Analyst* 136, 2879–2889. doi:10.1039/c1an15228a

Dicks, L. M. T., Botes, M., Du Plessis, D. M., Cloete, T. E., De Kwaadsteniet, M., and Diamini, N. (2012). Water Filter Assembly and Filter Element. United States Patent Apllication Publication US 2012/0325735 A1.

Genç, H., and Tjell, J. C. (2003). Effects of Phosphate, Silicate, Sulphate, and Bicarbonate on Arsenate Removal Using Activated Seawater Neutralise Red Mud (Bauxsol). *J. Phys. IV France* 107, 537–540. doi:10.1051/jp4:20030359

George, C. M., Sima, L., Arias, M. H. J., Mihalic, J., Cabrera, L. Z., Danz, D., et al. (2014). Arsenic Exposure in Drinking Water: an Unrecognized Health Threat in Peru. *Bull. World Health Organ.* 92, 565–572. doi:10.2471/blt.13.128496

Ghauri, M., Ilyas, S., and Ahmad, I. (2013). Application of Nanoparticles in the Removal of Micro-organisms from Water. *Sci. Int.* 24, 147–151.

Ghosh, B., Das, M. C., Gangopadhyay, A. K., Das, T. B., Singh, K., Lal, S., et al. (2003). Removal of Arsenic from Water by Coagulation Treatment Using Iron and Magnesium Salt. *Indian J. Chem. Techn.* 10, 87–95.

Giles, D. E., Mohapatra, M., Issa, T. B., Anand, S., and Singh, P. (2011). Iron and Aluminium Based Adsorption Strategies for Removing Arsenic from Water. *J. Environ. Manage.* 92 (12), 3011–3022. doi:10.1016/j.jenvman.2011.07.018

Guo, Q., and Tian, J. (2013). Removal of Fluoride and Arsenate from Aqueous Solution by Hydrocalumite via Precipitation and Anion Exchange. *Chem. Eng. J.* 231, 121–131. doi:10.1016/j.cej.2013.07.025

Herath, I., Vithanage, M., Bundschuh, J., Maity, J. P., and Bhattacharya, P. (2016). Natural Arsenic in Global Groundwaters: Distribution and Geochemical Triggers for Mobilization. *Curr. Pollut. Rep.* 2, 68–89. doi:10.1007/s40726-016-0028-2

Jiang, J. Q., Ashekuzzaman, S. M., Jiang, A., Sharifuzzaman, S. M., and Chowdhury, S. R. (2013). Arsenic Contaminated Groundwater and its Treatment Options in bangladesh. *Int. J. Environ. Res. Public Health* 10, 18–46. doi:10.3390/ijerph10010018

Koshijima, T., Tanaka, R., Muraki, E., Yamada, A., and Yaku, F. (1973). Chelating Polymers Derived from Cellulose and Chitin. *Cellulose Chem. Techn.* 7, 197–208.

Kumar, A. A., Som, A., Longo, P., Sudhakar, C., Bhuin, R. G., Gupta, S. S., et al. (2017). Confined Metastable 2-Line Ferrihydrite for Affordable Point-of-Use Arsenic-free Drinking Water. *Adv. Mater.* 29, 7. doi:10.1002/adma.201604260

Kyzas, G. Z., Kostoglou, M., and Lazaridis, N. K. (2009). Copper and Chromium(VI) Removal by Chitosan Derivatives-Equilibrium and Kinetic Studies. *Chem. Eng. J.* 152, 440–448. doi:10.1016/j.cej.2009.05.005

Lakherwal, D. (2014). Adsorption of Heavy Metals: a Review. *Int. J. Environ. Res. Develop.* 4, 41–48. doi:10.4236/vp.2020.64020

Liquidity Corpopration (2014). Available at: http://liquico.com/products/.

Ma, H., Burger, C., Hsiao, B. S., and Chu, B. (2011). Ultra-fine Cellulose Nanofibers: New Nano-Scale Materials for Water Purification. *J. Mater. Chem.* 21, 7507–7510. doi:10.1039/c0jm04308g

Mulwa, R., and Mariara, J. (2016). *Natural Resource Curse in Africa: Dutch Disease and Institutional Explanations*. AGRODEP Working Paper 0029. Washington, DC: International Food Policy Research Institute-IFPRI.

Nabi, D., Aslam, I., and Qazi, I. A. (2009). Evaluation of the Adsorption Potential of Titanium Dioxide Nanoparticles for Arsenic Removal. *J. Environ. Sci.* 21, 402–408. doi:10.1016/s1001-0742(08)62283-4

Naujokas, M. F., Anderson, B., Ahsan, H., Aposhian, H. V., Graziano, J. H., Thompson, C., et al. (2013). The Broad Scope of Health Effects from Chronic Arsenic Exposure: Update on a Worldwide Public Health Problem. *Environ. Health Perspect.* 121, 295–302. doi:10.1289/ehp.1205875

Pangarkar, B. L., Sane, M. G., and Guddad, M. (2011). Reverse Osmosis and Membrane Distillation for Desalination of Groundwater: A Review. *ISRN Mater. Sci.* 2011, 1–9. doi:10.5402/2011/523124

Pradeep, T. (2012). Arsenic and Metal Removal by Indian Technology (AMRIT). Available at: https://www.dstuns.iitm.ac.in/filesdec2015/1.%20Amrit%20Brochure.pdf. Accessed: 2021.

Qiusheng, Z., Xiaoyan, L., Jin, Q., Jing, W., and Xuegang, L. (2014). Porous Zirconium Alginate Beads Adsorbent for Fluoride Adsorption from Aqueous Solutions. *RSC Adv.* 5, 2100–2112. doi:10.1039/C4RA12036A

Qiusheng, Z., Xiaoyan, L., Jin, Q., Jing, W., and Xuegang, L. (2015). Porous Zirconium Alginate Beads Adsorbent for Fluoride Adsorption from Aqueous Solutions. *RSC Adv.* 5, 2100–2112. doi:10.1039/c4ra12036a

Qu, X., Alvarez, P. J. J., and Li, Q. (2013). Applications of Nanotechnology in Water and Wastewater Treatment. *Water Res.* 47, 3931–3946. doi:10.1016/j.watres.2012.09.058

Rajiv Gandhi, M., Viswanathan, N., and Meenakshi, S. (2010). Preparation and Application of Alumina/chitosan Biocomposite. *Int. J. Biol. Macromol.* 47, 146–154. doi:10.1016/j.ijbiomac.2010.05.008

Reisner, D. E., and Pradeep, T. (2015). *Aquananotechnology: Global Prospects*. Florida: CRC Press, Taylor and Francis Group.

Roksana, M. (2016). Eco-Friendly Alternative for Water Treatment from Nanotechnology. *J. Nano Sc. Tech.* 4, 28–34.

Roy, P., Mondal, N. K., Bhattacharya, S., Das, B., and Das, K. (2013). Removal of Arsenic(III) and Arsenic(V) on Chemically Modified Low-Cost Adsorbent: Batch and Column Operations. *Appl. Water Sci.* 3, 293–309. doi:10.1007/s13201-013-0082-5

Saha, S., and Sarkar, P. (2016). Arsenic Mitigation by Chitosan-Based Porous Magnesia-Impregnated Alumina: Performance Evaluation in Continuous Packed Bed Column. *Int. J. Environ. Sci. Technol.* 13, 243–256. doi:10.1007/s13762-015-0806-1

Savage, N., and Diallo, M. S. (2005). Nanomaterials and Water Purification: Opportunities and Challenges. *J. Nanopart Res.* 7, 331–342. doi:10.1007/s11051-005-7523-5

Shaji, E., Santosh, M., Sarath, K. V., Prakash, P., Deepchand, V., and Divya, B. V. (2021). Arsenic Contamination of Groundwater: a Global Synopsis with Focus on the Indian Peninsula. *Geosci. Front.* 12, 101079. doi:10.1016/j.gsf.2020.08.015

Shirazi, M. M. A., Bazgir, S., and Meshkani, F. (2020). "Electrospun Nanofiber Membranes for Water Treatment," in *Advances in Membrane Technologies*. Editor A. Amira (London: Intech Open). doi:10.5772/intechopen.87948

Smith, W. F. (2003). *Foundation of Materials Science Engineering*. 3rd ed. McGraw-Hill, 864.

Sokker, H. H., El-Sawy, N. M., Hassan, M. A., and El-Anadouli, B. E. (2011). Adsorption of Crude Oil from Aqueous Solution by Hydrogel of Chitosan Based Polyacrylamide Prepared by Radiation Induced Graft Polymerization. *J. Hazard. Mater.* 190 (1–3), 359–365. doi:10.1016/j.jhazmat.2011.03.055

Sudheesh, K., Ajay, K., Omotayo, A., and Bhekie, B. (2013). Chitosan-base Nanomaterials: A State-Of-The-Art Review. *Int. J. Biol. Macromol.* 59, 46–58. doi:10.1016/j.ijbiomac.2013.04.043

Tchounwou, P. B., Yedjou, C. G., Patlolla, A. K., and Sutton, D. J. (2012). Heavy Metal Toxicity and the Environment. *Mol. Clin. Environ. Toxicol.* 101, 133–164. doi:10.1007/978-3-7643-8340-4_6

Thakre, D., Jagtap, S., Sakhare, N., Labhsetwar, N., Meshram, S., and Rayalu, S. (2010). Chitosan Based Mesoporous Ti-Al Binary Metal Oxide Supported Beads for Defluoridation of Water. *Chem. Eng. J.* 158 (2), 315–324. doi:10.1016/j.cej.2010.01.008

Tresintsi, S., Simeonidis, K., Vourlias, G., Stavropoulos, G., and Mitrakas, M. (2012). Kilogram-scale Synthesis of Iron Oxy-Hydroxides with Improved Arsenic Removal Capacity: Study of Fe(II) Oxidation-Precipitation Parameters. *Water Res.* 46, 5255–5267. doi:10.1016/j.watres.2012.06.049

Tuutijärvi, T., Vahalaa, R., Sillanpitää, M., and Chen, G. (2013). Maghemite Nanoparticles for As(V) Removal: Desorption Characteristics and Adsorbent Recovery. *Environ. Technol.* 33, 1927–1936. doi:10.1080/09593330.2011.651162

Yu, L., Ma, Y., Ong, C. N., Xie, J., and Liu, Y. (2015). Rapid Adsorption Removal of Arsenate by Hydrous Cerium Oxide-Graphene Composite. *RSC Adv.* 5, 64983–64990. doi:10.1039/c5ra08922k

Conflict of Interest: The authors declare that the research was conducted in the absence of any commercial or financial relationships that could be construed as a potential conflict of interest.

frontiers | Frontiers in Chemistry

ORIGINAL RESEARCH
published: 14 April 2022
doi: 10.3389/fchem.2022.835832

Photocatalytic Degradation of Rhodamine B Dye and Hydrogen Evolution by Hydrothermally Synthesized $NaBH_4$—Spiked ZnS Nanostructures

Theopolina Amakali[1], Aleksandar Živković[2,3], Michael E. A. Warwick[4], Daniel R. Jones[4], Charles W. Dunnill[4], Likius S. Daniel[1,5], Veikko Uahengo[1], Claire E. Mitchell[2], Nelson Y. Dzade[2] and Nora H. de Leeuw[2,3,6]*

[1]Department of Physics, Chemistry and Material Science, University of Namibia, Windhoek, Namibia, [2]School of Chemistry, Cardiff University, Cardiff, United Kingdom, [3]Department of Earth Sciences, Utrecht University, Utrecht, Netherlands, [4]Energy Safety Research Institute, Swansea University, Swansea, United Kingdom, [5]Multidisciplinary Research, Centre for Research Service, University of Namibia, Windhoek, Namibia, [6]School of Chemistry, University of Leeds, Leeds, United Kingdom

OPEN ACCESS

Edited by:
James Darkwa, Botswana Institute for Technology Research and Innovation (BITRI), Botswana

Reviewed by:
Kezhen Qi, Dali University, China
Chi-Jung Chang, Feng Chia University, Taiwan

***Correspondence:**
Aleksandar Živković
a.zivkovic@uu.nl

Specialty section:
This article was submitted to Catalysis and Photocatalysis, a section of the journal Frontiers in Chemistry

Received: *14 December 2021*
Accepted: *28 March 2022*
Published: *14 April 2022*

Citation:
Amakali T, Živković A, Warwick MEA, Jones DR, Dunnill CW, Daniel LS, Uahengo V, Mitchell CE, Dzade NY and de Leeuw NH (2022) Photocatalytic Degradation of Rhodamine B Dye and Hydrogen Evolution by Hydrothermally Synthesized $NaBH_4$—Spiked ZnS Nanostructures. Front. Chem. 10:835832. doi: 10.3389/fchem.2022.835832

Metal sulphides, including zinc sulphide (ZnS), are semiconductor photocatalysts that have been investigated for the photocatalytic degradation of organic pollutants as well as their activity during the hydrogen evolution reaction and water splitting. However, devising ZnS photocatalysts with a high overall quantum efficiency has been a challenge due to the rapid recombination rates of charge carriers. Various strategies, including the control of size and morphology of ZnS nanoparticles, have been proposed to overcome these drawbacks. In this work, ZnS samples with different morphologies were prepared from zinc and sulphur powders via a facile hydrothermal method by varying the amount of sodium borohydride used as a reducing agent. The structural properties of the ZnS nanoparticles were analysed by X-ray diffraction (XRD), scanning electron microscopy (SEM), and X-ray photoelectron spectroscopy (XPS) techniques. All-electron hybrid density functional theory calculations were employed to elucidate the effect of sulphur and zinc vacancies occurring in the bulk as well as (220) surface on the overall electronic properties and absorption of ZnS. Considerable differences in the defect level positions were observed between the bulk and surface of ZnS while the adsorption of $NaBH_4$ was found to be highly favourable but without any significant effect on the band gap of ZnS. The photocatalytic activity of ZnS was evaluated for the degradation of rhodamine B dye under UV irradiation and hydrogen generation from water. The ZnS nanoparticles photo-catalytically degraded Rhodamine B dye effectively, with the sample containing 0.01 mol $NaBH_4$ being the most efficient. The samples also showed activity for hydrogen evolution, but with less H_2 produced compared to when untreated samples of ZnS were used. These findings suggest that ZnS nanoparticles are effective photocatalysts for the degradation of rhodamine B dyes as well as the hydrogen evolution, but rapid recombination of charge carriers remains a factor that needs future optimization.

Keywords: ZnS, photocatalysis, rhodamine B degradation, NaBH4 adsorption, density functional theory, HSE06, defect states, sulphur vacancies

1 INTRODUCTION

Research on photocatalysis has increased exponentially in recent years and a multitude of materials have been synthesized and explored as photocatalysts for the degradation of organic pollutants in wastewater as well as the photocatalytic degradation of water to generate hydrogen for use as a clean fuel (Lee and Wu, 2017; Cao et al., 2020). Transition metal oxides and chalcogenides including titanium (IV) oxide (TiO_2), cadmium selenide (CdSe), cadmium sulphide (CdS), zinc oxide (ZnO), and zinc sulphide (ZnS) are some of the semiconductor materials that have been widely investigated for photocatalytic applications (Haque et al., 2018; Zhuang et al., 2021). Semiconductor-mediated photocatalysis owes its popularity to a number of advantages including low cost, simplicity, and ease of preparation. Titanium (IV) oxide (TiO_2) has received the most attention, but despite its popularity, its application is hindered by low quantum efficiency and photo-corrosion (Gopinath et al., 2020).

ZnS has attracted much attention as a potential and effective photocatalyst for applications in organic pollutant degradation (Dong et al., 2013; Ma et al., 2016; Ye et al., 2018) and in the hydrogen evolution reaction (HER) via water splitting (Puentes-Prado et al., 2020; Samaniego-Benitez et al., 2021; Xiong et al., 2021). Zinc sulphide is polymorphous with a cubic zinc blende (sphalerite) structure that is more stable at low temperature and a hexagonal wurtzite structure which commonly forms at high temperatures. It has one of the richest and most diverse morphologies, exhibiting different properties that allow its use in various applications, including nanowires (Cao et al., 2014), nanorods (Palanisamy et al., 2020), nanoflowers (Bai et al., 2014), nanospheres (Feng et al., 2020), nanotubes (Wang et al., 2017), nanobelts (Ham and Jang, 2018), and nanosheets (Fang et al., 2011). For example, nanorods, nanoarrays, and nanoflowers exhibit light-trapping effects that enhance light absorption which in turn results in increased photocatalytic activity (Bhushan and Jha, 2020; Ren et al., 2021; Aulakh et al., 2022). A review by Fang et al. (2011) have provided a detailed survey of research activities related to ZnS nanostructures with various morphologies. In this review, the interaction between synthesis conditions and the diverse nanoscale morphologies of ZnS was elucidated as well as their application in various functional devices. In another review, Lee et al. (2017) have presented a comprehensive discussion on band gap engineering studies, synthetic methods and photocatalytic applications of ZnS nanocrystalline semiconductors. The authors also gave a detailed explanation of possible reaction mechanisms for organic pollutant degradation and the photocatalytic hydrogen evolution.

Zinc sulphides show good photocatalytic activity under UV irradiation, high theoretical efficiency, and they rapidly generate charge carriers upon photoexcitation. In addition, ZnS has excellent chemical stability against oxidation and hydrolysis and these properties are maintained when the particle size is reduced to nano levels. However, its main shortcoming is the large negative potential value and limited visible light absorption due to its wide band gap, which is 3.54 and 3.91 eV for the cubic and hexagonal structures, respectively.

One strategy used to improve the light-harvesting properties of ZnS nanostructures is by introducing surface defects, which will serve as adsorption sites where charge transfer to an adsorbed species prevents charge recombination of photogenerated charge carriers (Zhang et al., 2014; Wang et al., 2015a; Dong et al., 2017; Yuan et al., 2019; Liu et al., 2020; Ghosh et al., 2021). These defects however should be controlled, because excessive defects will act as a trap for charge carriers, thereby decreasing the photocatalytic activity.

The preparation method, process parameters, and the synthesis conditions employed during the preparation of ZnS nanostructures play a crucial role in the modification of their surface characteristics, particle size, morphology, and structure, hence affecting the resultant photocatalytic activity (Zhang et al., 2014; Ebrahimi and Yarmand, 2019). Yin et al. (2016) prepared cubic ZnS particles of controlled size and morphologies with enhanced photocatalytic activities by simply manipulating the molar ratio of Zn/S. A degradation efficiency of more than 96% was achieved in just 24 min when the Zn/S molar ratio equalled 1: 2. Sabaghi et al. (2018), using a simple hydrothermal and reflux methods and varying the ratio of precursor materials (zinc acetate dihydrate/thioacetamide) as well as changing the reaction time managed to synthesize cubic sphalerite ZnS nanoparticles of various morphologies and size, e.g., sheetlike, flowerlike, and sphere. All parameters investigated, such as the method of synthesis, mole ratio, and reaction time influenced the photocatalytic degradation of Reactive blue 21 pigment. The hydrothermal method using precursor materials with a molar ratio equal to 1:1 and carried out for 12 h showed the greatest efficiency, completely (100% degradation) removing the pigment after 240 min. Various other works have investigated the effect of synthesis conditions on the photocatalytic performance of ZnS nanoparticles, without the addition of a co-catalyst, but summarising the details of these is beyond the scope of this article (Dong et al., 2013; Zhang et al., 2014; Ma et al., 2016; La Porta et al., 2017; Lee and Wu, 2017; Liu et al., 2020).

The reduction ability of borohydrides has attracted attention, owing to their ability to generate a large number of nucleating cores, thereby causing a disordered growth process with greater diversity in nanoparticle size (Saravanakumar et al., 2017). Wang et al. (2015b) prepared a ZnS photocatalyst with controlled sulphur vacancies by adding small amounts of sodium borohydride ($NaBH_4$) and they observed an increase in the photocatalytic activity of the ZnS photocatalyst (0.5 g) towards hydrogen evolution with increasing amount of $NaBH_4$, which first reached a maximum before decreasing again with a further increase in $NaBH_4$ concentration.

In the present work, ZnS nanoparticles were synthesized using $NaBH_4$ as a reducing agent and the sample was evaluated for the photocatalytic degradation of rhodamine B dye as well as hydrogen evolution from a water splitting reaction. Moreover, theoretical investigations at a hybrid-DFT approximation level were undertaken to study the effect of vacancies on the structural and electronic properties of ZnS. In addition, the adsorption of

$NaBH_4$ atop a ZnS surface was studied and the energetics as well as influence on the electronic properties elucidated.

2 EXPERIMENTAL AND COMPUTATIONAL DETAILS

2.1 Materials

All chemical reagents (Zn powder, sublimed sulphur, NaOH, $NaBH_4$, Na_2S_9 H_2O, Na_2SO_3) used in this study were analytical reagents (AR) procured from Sigma- Aldrich and used as received without any further purification.

2.2 Synthesis of ZnS Samples

Zinc sulphide nanoparticles of different morphologies were synthesized via a hydrothermal route. The precursor solution was prepared by mixing equal amounts (0.0205 mol) of zinc and sulphur powders in 70 ml of concentrated NaOH (21 M) solution. After the suspension was cooled to room temperature, different amounts of $NaBH_4$ (0 mol, 0.003 mol, 0.005 mol, 0.01 mol, 0.02 mol) were added and the mixture was stirred at room temperature for 2 h. The suspension was transferred to a 125 ml Teflon-lined autoclave, sealed, and placed in a furnace at 230°C for 12 h. The product was collected after centrifuging and washing several times with deionized water. Finally, the product was dried in an oven at 40°C for 72 h.

2.3 Characterization

For structural characterization of the samples, X-ray diffraction (XRD) patterns were recorded using a Bruker D8 Advance X-ray diffractometer with Cu-Kα radiation (λ = 1.5406 Å) with the scanning angle ranging from 10° to 80° to determine the phase composition. The morphology of the product was analysed by Field Emission scanning electron microscopy (FE-SEM) using a Hitachi S4800 FE-SEM operating at an accelerating voltage of 10 kV and an emission current of 10 μA.

Surface chemical analysis was achieved through X-ray photoelectron spectroscopy (XPS) performed on a Thermo Scientific K-Alpha$^+$ spectrometer with a monochromated Al K-alpha source (1,486.68 eV) operating at 72 W; spectra were obtained from an elliptical 800 μm × 400 μm analysis area and charge neutralisation was applied throughout. Core spectra were acquired using a dwell time of 500 m and a pass energy of 20 eV, and all binding energies were carbon-corrected by referencing the C 1s peak to a standard value of 284.8 eV. CasaXPS software was employed to carry out spectral deconvolution, for which Gaussian-Lorentzian components with 30% Lorentzian character were fitted to the measured data above a Shirley-type background function. Physically realistic fits were obtained by imposing a 2:1 area ratio and equal full-widths-at-half-maximum for each pair of $2p_{3/2}$ and $2p_{1/2}$ components, whilst the spin orbit separation between them was constrained to characteristic values of 23.00 eV (Wang et al., 2015b; Kwoka et al., 2020) and 1.16 eV (Sarkar et al., 2018) for Zn 2p and S 2p spectra, respectively. After calibrating for the transmission function of the spectrometer and applying mean free path correction, the total measured area of each deconvolved spectrum was divided by the relevant relative sensitivity factor to determine the surface atomic composition of a given sample.

For optical properties, the UV-Vis diffuse reflectance spectra were recorded on a CARY 100 UV-Vis spectrophotometer of Agilent technology in the region between 200 and 700 nm. The band gaps of the samples were calculated from diffuse reflectance using the Kubelka-Munk function by plotting $[h\upsilon F(r)]^2$ vs. hυ, where hυ is the photon energy, f(r) is the Kubelka-Munk function and extending the tangent of the curve to the hυ axis. Room temperature photoluminescence (PL) spectra of the samples were measured using a 7.8 Mw Melles-Griot He-Cd laser (325 nm) with an incident power density of 2.3 × 10^6 mW m^2) over a wavelength region of 350–750 nm.

2.4 Photocatalytic Performance

The photocatalytic performance was evaluated through the degradation of rhodamine B dye (4 mg/ml) under UV irradiation at room temperature in the presence of a ZnS photocatalyst (20 mg). The mixture was first stirred in the dark for 30 min to achieve the absorption-desorption equilibrium. It was then exposed to the UV light over various durations of time. The change in concentration after each duration was recorded on the UV-vis spectrophotometer in the region of 400–650 nm.

The photocatalytic activity of the prepared ZnS samples was evaluated for hydrogen generation via the water splitting reaction under visible light irradiation. Typically, 20 mg of the sample was added to 20 ml aqueous solution containing 0.35 M Na_2S and 0.25 M Na_2SO_3 as a sacrificial reagent. This was placed in a glass vial connected to a closed gas circulation and evacuation system. The reaction solution was kept under continuous magnetic stirring and the irradiation of the system was achieved by using a 100 W LED lamp. An online gas chromatograph (782 A GC system of Agilent Technology) equipped with thermal conductive detector (TCD) was used to determine the generated gas products using argon as a carrier gas.

2.5 Computational Details

Spin-polarized density functional theory (DFT) calculations were performed using the all-electron (AE) code CRYSTAL (2017 release) (Pascale et al., 2004; Zicovich-Wilson et al., 2004; Dovesi et al., 2017; Dovesi et al., 2018). The short-range corrected range separated hybrid Heyd–Scuseria–Ernzerhof (HSE06, unmodified) (Heyd et al., 2003; Heyd and Scuseria, 2004; Heyd et al., 2006) functional was employed together with basis sets based on Gaussian-type orbitals (GTOs). The following GTO basis sets were employed: for Zn constructed and optimized by Jaffe et al. (1994), (Jaffe and Hess, 1993), for S from Lichanot et al. (1993), (Zagorac et al., 2018), for Na from Dovesi et al. (1991), for B the 6–21G* by John Pople (Orlando et al., 1990), and for H by Dovesi et al. (1984). One additional *d*-function (with an exponent of 0.206368) was added to the Zn basis set, while the remaining basis sets were taken without further modification. In the structural optimizations, both the atomic positions and the lattice constants were fully optimized within the constraints imposed by the space group symmetry. The reciprocal space was sampled using 11 × 11 × 11 and 3 × 3 ×

1 Monkhorst-Pack type k-point grids for ZnS bulk and a 3 × 2 × 1 supercell of the (220) surface of ZnS, respectively (Monkhorst and Pack, 1976). For the evaluation of the Coulomb and exchange integrals, the default tolerance factor values of 6, 6, 6, 6, and 12 were used (TOLINTEG). Long range dispersion corrections were included using the semiempirical D3 approach of Grimme et al. (2010) with Becke-Johnson damping (Grimme et al., 2011; Grimme et al., 2016). Band structure calculations were performed on optimized geometries along high-symmetry directions obtained using the SeeK-path interface (Hinuma et al., 2017; Togo and Tanaka, 2018). Graphical drawings were produced using VESTA (Momma and Izumi, 2011). Excitonic and spin-orbit coupling effects were not considered.

The formation energy (E^f) of defects present in the system was defined as:

$$E^f(D) = E_{tot}(D) - E_{tot}(H) - \sum_i n_i \mu_i,$$

where $E_{tot}(D)$ and $E_{tot}(H)$ denote the respective total energies of the system with and without the induced defect. The value n_i represents the number of atoms of element i that are added ($n_i > 0$) or removed ($n_i < 0$) from the supercell to form the defect, and μ_i (which can be written as $\mu_i = \mu_i^{elem} + \triangle\mu_i$) is the chemical potential of element i in its standard phase, referenced to the total energy of the elementary phases at 0 K [i.e., μ_i^{elem} of Zn(s) and S_8(g)]. In the region of phase space where ZnS is stable, the chemical potentials are further constrained by the equilibrium condition:

$$\triangle\mu_{Zn} + \triangle\mu_S = \triangle H_f(ZnS).$$

The formation enthalpy of ZnS is calculated at −2.307 eV, which is in good agreement with the experimental value of −2.136 eV (Richards, 1959). Together with the limit that the chemical potential of the atoms in the reservoir must be lower than the elemental reference energies ($\triangle\mu_{Zn} \leq 0$ and $\triangle\mu_S \geq 0$), the upper bound for the chemical potentials can be obtained: ($\triangle\mu_{Zn} = 0$ eV, $\triangle\mu_S = -2.307eV$) in the Zn-rich environment and ($\triangle\mu_{Zn} = -2.307$ eV, $\triangle\mu_S = 0$ eV) in the S-rich environment.

The surface was modelled as a two-dimensional slab, and no three-dimensional periodicity was imposed. This means that there is no parameter for the vacuum thickness needed. To characterise the surface, the surface energy (γ) as a measure of the thermodynamic stability has been calculated through the following expression:

$$\gamma = \frac{E(n) - n \cdot E_{bulk}}{2 \cdot A},$$

where $E(n)$ is the energy of the slab containing n-layers, E_{bulk} the energy of the bulk, and A the area of one side of the slab.

The binding energy of $NaBH_4$ (E_b) was calculated from the fully relaxed geometries, through the following expression:

$$E_b = E_{slab+ads} - (E_{slab} + E_{ads}),$$

where $E_{slab+ads}$ is the total energy of the slab interacting with the absorbate, while E_{slab} and E_{ads} denote the total energies of the pristine surface and isolated adsorbate, respectively. Within this definition of the binding energy, a negative value indicates a favourable exothermic process, while a positive energy corresponds to an endothermic process. When using atomic-centred localised basis sets, the binding energy is affected by the basis set superposition error (BSSE), which corresponds to an artificial increase (spurious extra-binding that mimics the dispersion energy) in the computed binding energy because the basis set of the final system is larger than that of the component subsystems. One way to estimate the BSSE is using the counterpoise (CP) method, where one recalculates E_{slab} and E_{ads} by supplementing the basis set of each subsystem with all the basis functions of the other without their electrons and nuclei (referred to as "ghost functions"). The BSSE is a positive quantity and equals to:

$$BSSE = \left(E_{ads|system} - E^G_{ads|system}\right) + \left(E_{slab|system} + E^G_{slab|system}\right),$$

where $E^G_{ads|system}$ and $E^G_{slab|system}$ denote the energies of the adsorbate and surface calculated respectively in the presence of the "ghosted atoms" of the surface and of the adsorbate (i.e., including the extra basis set of the surface or the adsorbate). Taking into account the BSSE, the CP-corrected binding energy (E_b^{CP}) reads (Boys and Bernardi, 1970; Scaranto et al., 2011):

$$E_b^{CP} = E_b + BSSE.$$

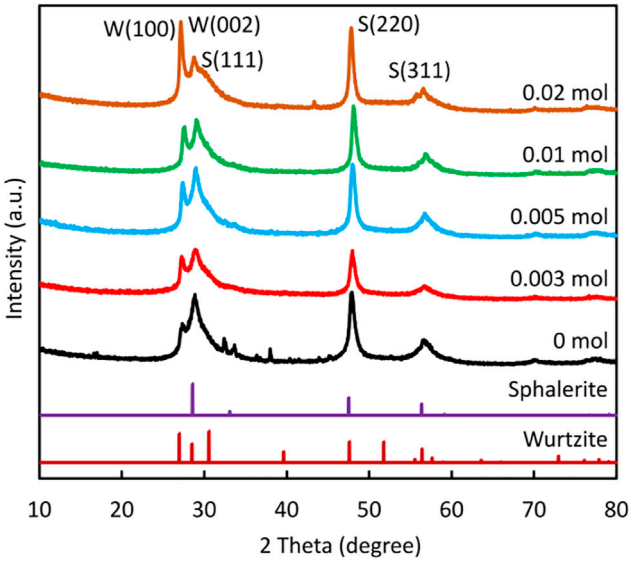

FIGURE 1 | XRD patterns of ZnS prepared using different amounts of $NaBH_4$.

3 RESULTS AND DISCUSSION

3.1 Characterization

Figure 1 shows the XRD pattern of the ZnS nanostructures prepared using different amounts of $NaBH_4$ in NaOH. The

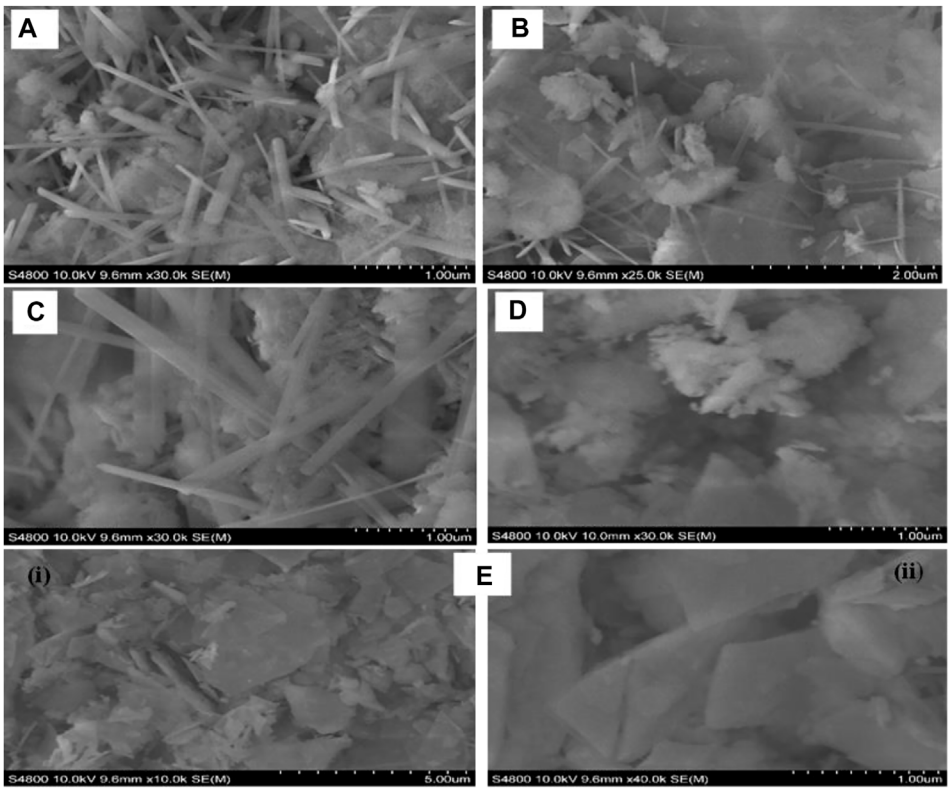

FIGURE 2 | SEM images of ZnS prepared with different amounts of $NaBH_4$ **(A)** 0 mol **(B)** 0.003 mol **(C)** 0.005 mol **(D)** 0.01 mol **(E)** 0.02 mol.

pattern matched that of the low temperature cubic sphalerite ZnS nanostructure (data file card: COD 5000088). The position of the two main diffraction peaks obtained for all samples is the same and were recorded at 2θ values (48.11°) and (57.11°), corresponding to the (220) and (311) crystal plane respectively. In addition, there is a strong -sharp peak and an overlapping peak between 26.94° and 30.4°. Strong and sharp peak patterns at 2θ value (27.2°) can be indexed as the (100) reflection of wurtzite ZnS, and the broader peaks next to it are the overlapping peaks of wurtzite (002) and sphalerite (111). Although the (111), (220), and 311) peaks of the sphalerite ZnS occupy the same position as the (002), (110), and (112) of the ZnS wurtzite structure in the XRD pattern, the missing peaks in the wurtzite standard pattern suggest that a sphalerite ZnS structure, rather than the wurtzite structure, dominates in the nanoparticles.

The crystallite size was calculated from the sharp and intense peak of 48.11° using the Scherrer equation:

$$D = \frac{K\lambda}{\beta \cos \theta},$$

where K is a constant (k = 0.89), λ is the wavelength, β is the full width value at half maximum of the intensity (FWHM) and θ is the Bragg angle corresponding to the (220) peak. The values of the crystallite size were 12.1 nm, 12.5 nm, 12.4 nm, 13.9 nm, and 8.04 nm corresponding to ZnS samples prepared with 0 mol, 0.003 mol, 0.005 mol, 0.01 mol, and 0.02 mol of $NaBH_4$ respectively. The crystallite size grew slightly with an increase in added $NaBH_4$, reaching a maximum (13.9 nm) for 0.01 mol of $NaBH_4$ and then decreasing to 8.04 nm for 0.02 mol of $NaBH_4$.

The SEM morphologies obtained for the ZnS nanostructures differ with the amount of added $NaBH_4$ (**Figures 2A–E**). At lower $NaBH_4$ concentrations (0–0.005 mol $NaBH_4$), the nanoparticles are composed of a mixture of nanorods and agglomerates without defined shape. As the concentration of $NaBH_4$ increases (0.01 mol $NaBH_4$), the nanorods disappeared and the nanoparticles became featureless agglomerates with no particular shape at 0.01 mol $NaBH_4$. However, when the ZnS were synthesized with the addition of 0.02 mol $NaBH_4$, rectangular slabs-like nanostructures were obtained as shown in **Figure 2E** (i) at low magnification and **Figure 2E** (ii) at high magnification. The different morphologies can be attributed to the effect of $NaBH_4$ that was added.

$NaBH_4$ has been shown to induce the formation of long size nanorods in, e.g., metal-doped ferrites (Ni-ferrites) due to the clustering of $NaBH_4$ around the metal ion (Saravanakumar et al., 2017). This effect was not observed in this study and the shape of the nanostructure was rather distorted by the increased concentration of $NaBH_4$. It is reported that borohydrides have the ability to generate a high concentration of nanocrystals with small nuclei in a short time, forming a large number of cores and disfavouring the growth process of nanostructures (Oliveira et al., 2020). This results in a disordered growth process which explains

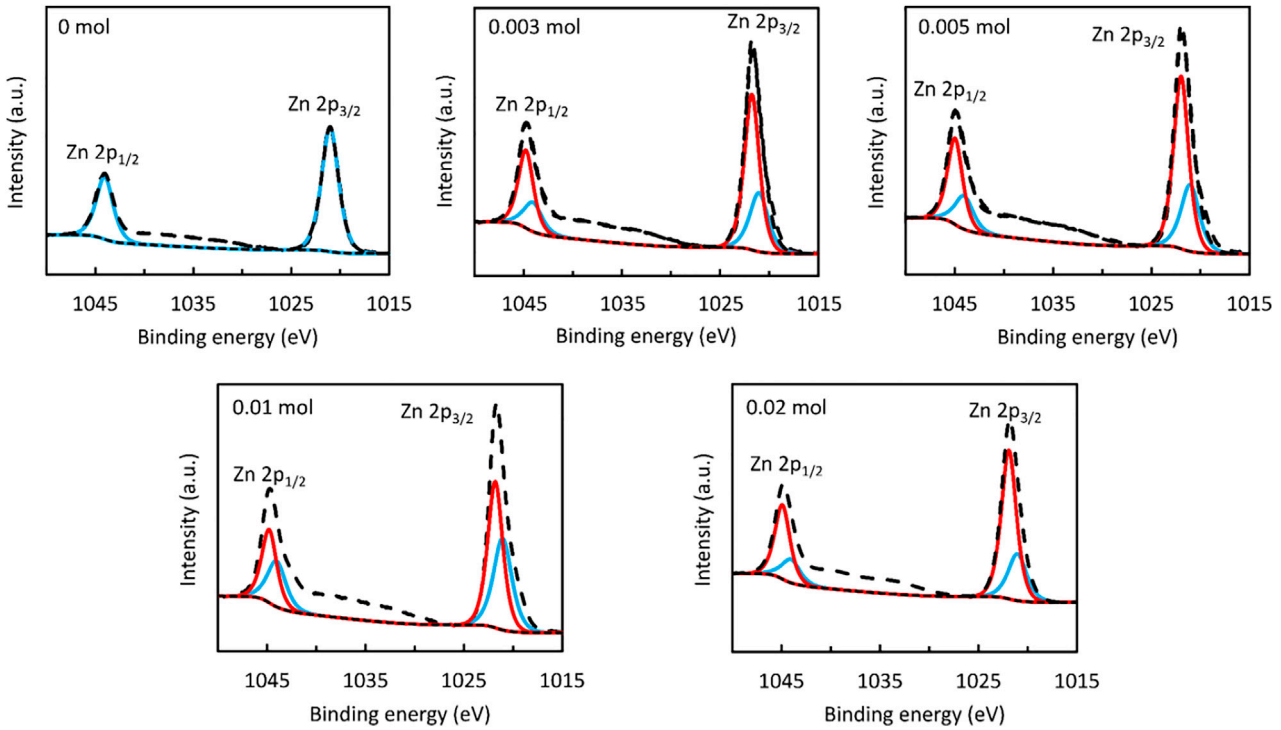

FIGURE 3 | Zn ($2p^3$) XPS spectrum of ZnS nanostructures prepared using different amounts of $NaBH_4$.

the featureless agglomerates formed with increasing concentration of $NaBH_4$. Other factors however, such as such as pH (not investigated in this study) could have an influence on the shape of the nanostructures and as such should be ruled out without further investigation.

For the sample that was synthesized without the addition of $NaBH_4$, the Zn 2p XPS spectrum is well-represented by a single doublet with $2p_{1/2}$ and $2p_{3/2}$ peaks centred at binding energies of 1,044.1 eV and 1,021.1 eV, respectively, as shown in **Figure 3**. Whilst a similar doublet provides the predominant contribution to the corresponding spectra of the $NaBH_4$-treated samples, the asymmetric form of each peak is consistent with a second doublet offset from the first by 0.7–0.9 eV. Since the chemical shifts between Zn 2p spectra associated with different Zn electronic environments are characteristically on the order of 100 meV, even when considering disparate oxidation states of Zn (Biesinger et al., 2010), the comparatively large separation of the Zn 2p doublets suggests that differential charging occurred within the $NaBH_4$-synthesized samples, in turn indicating that they contained a mixture of materials with differing electrical conductivities. It is possible, for instance, that the inclusion of $NaBH_4$ during ZnS synthesis yielded discrete particles of ZnO, which is considerably more conductive than ZnS (Zafar et al., 2021). One should note that as a highly surface-sensitive technique, XPS cannot detect species at a distance greater than ~ 10 nm from the sample surface, in contrast to bulk characterisation procedures such as XRD. For this reason, the high bulk purity of ZnS evident from the XRD data shown in **Figure 1** does not preclude the possibility that ZnO nanoparticles existed at the ZnS surface, thereby influencing the Zn 2p spectra but nevertheless having negligible impact on the diffraction properties of the bulk material.

To address the chemical environments of S within the ZnS samples, deconvolved S 2p spectra are presented in **Figure 4**. As it is possible in all cases to use a single doublet to reproduce the form of the S 2p peak, one may infer that each sample surface comprised only one S-containing compound in significant quantities. Furthermore, the $2p_{1/2}$ and $2p_{3/2}$ components are centred at binding energies of 162.1–162.2 eV and 160.9–161.0 eV, respectively, which are consistent with the S 2p peak positions typically reported for ZnS (Tran et al., 2022).

Finally, estimates of the S/Zn surface atomic ratio were obtained from the measured areas of the Zn 2p and S 2p spectra to provide insight into the relative proportions of S-containing and S-free compounds within each sample. As shown in **Table 1**, the S/Zn ratio was found in all cases to have a value in the range 0.84–0.88, which is significantly lower than the value of unity expected for pristine ZnS. In accordance with discussions regarding the Zn 2p spectra, this discrepancy may be attributed to the presence of S-free species such as ZnO and $Zn(OH)_2$ at the ZnS surface, with the samples containing similar quantities of these compounds.

The optical properties of the ZnS samples were analysed by UV-vis reflectance spectroscopy to evaluate their light absorption ability. As shown in **Figure 5**, the addition of $NaBH_4$ slightly increased the diffuse reflectance until 0.01 mol but then decreased again when the highest concentration of 0.02 mol $NaBH_4$ was reached. However, the samples of ZnS nanoparticles showed very

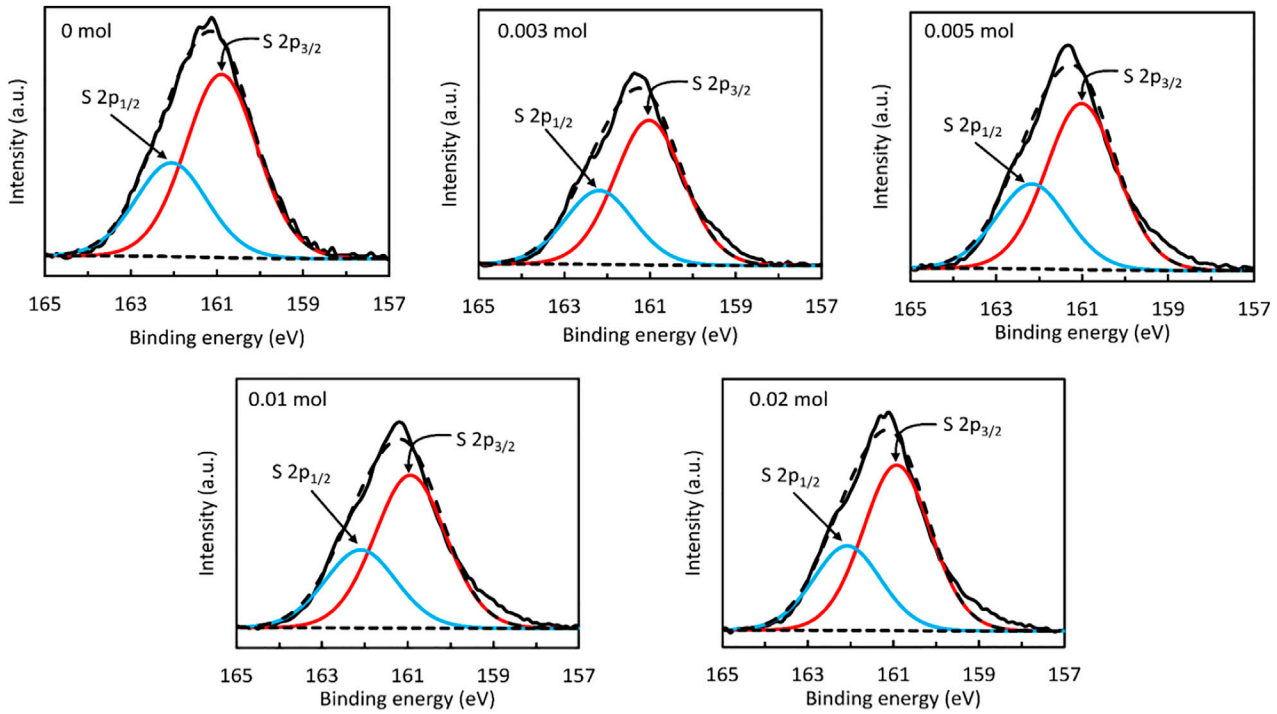

FIGURE 4 | S (2p) XPS spectrum of ZnS nanostructure prepared using different amounts of $NaBH_4$.

TABLE 1 | Chemical composition of ZnS samples measured via XPS.

Sample	S (at%)	Zn (at%)	S/Zn
0 mmol $NaBH_4$	32.34	36.94	0.875
3 mmol $NaBH_4$	36.33	42.28	0.859
5 mmol $NaBH_4$	35.58	42.45	0.838
10 mmol $NaBH_4$	36.36	42.61	0.866
20 mmol $NaBH_4$	35.50	10.83	0.869

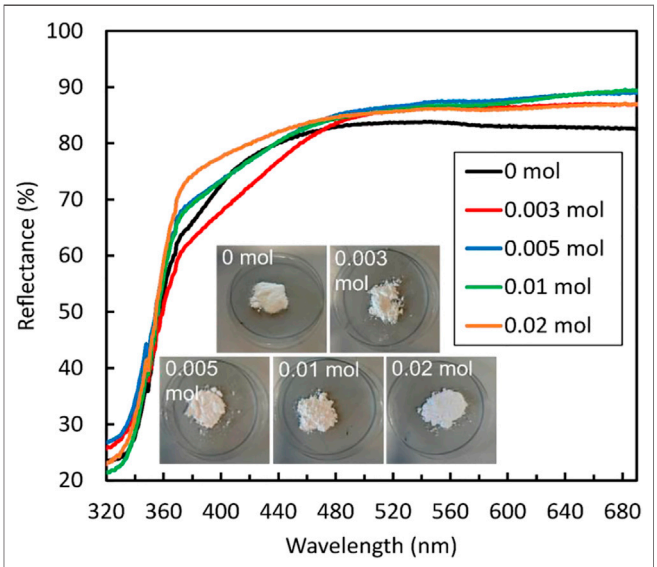

FIGURE 5 | UV-Vis diffuse reflectance spectra of ZnS prepared using different amounts of $NaBH_4$, together with the images of the samples.

little variation in band gap energy value 3.54 eV, 3.54 eV, 3.55 eV, 3.55 eV, and 3.57 eV, for the nanoparticles prepared with 0 mol, 0.003 mol, 0.005 mol, 0.01 mol, and 0.02 mol $NaBH_4$, respectively. The decreasing crystallite size of the sample prepared with 0.02 mol of $NaBH_4$ could be the reason for the slight blue shift in optical band gap observed for this sample. These results are in conflict with what is reported by Wang et al. (2015b) who reported a decreasing optical band gaps with increasing amount of $NaBH_4$, although other factors such as residual internal stress could be the cause of such discrepancies or trend (Ma et al., 2016).

Photoluminescence (PL) emission provides indication of charge separation where high intensities indicate quick recombination of photogenerated carriers. From **Figure 6**, it can be seen that $NaBH_4$-free ZnS has the lowest intensity of photoluminescence emission, indicating that the photogenerated carriers are not quickly recombined. The PL intensities increased gradually with the addition of $NaBH_4$ until the concentration of 0.005 mol of $NaBH_4$ was reached, after which they drop significantly when 0.01 mol of $NaBH_4$ was added. However, when 0.02 mol of $NaBH_4$ was added the intensity increased significantly again. The drop in the PL intensity for the sample prepared with 0.01 mol $NaBH_4$ indicates reduced recombination of charge carrier suggesting better photocatalytic activity. This implies that

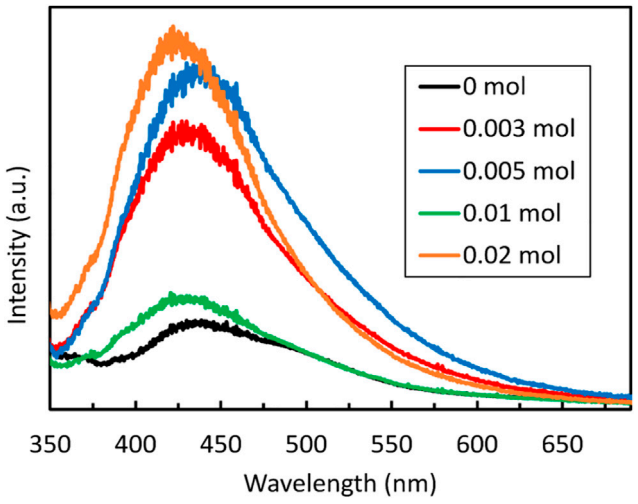

FIGURE 6 | The Photoluminescence (PL) spectra of ZnS synthesized with different amounts of $NaBH_4$.

the aforementioned S vacancies could become centres for the recombination of photogenerated electrons and holes when present in excessive amount as 0.01 mol is a percolation threshold found for the PL intensity of the ZnS samples indicated in earlier works (Wang et al., 2015b). High PL intensities on the other hand suggest few defects and fast recombination of photogenerated charge carriers, resulting in decreased photocatalytic activity. This finding is consistent with the results of the photocatalytic degradation and hydrogen production of these ZnS samples as is further outlined below.

3.2 Computational Modelling

3.2.1 Bulk ZnS

To further elucidate the structural properties of ZnS, DFT calculations were employed. The relaxed crystal structure of ZnS in the sphalerite phase is shown in **Figure 7**. The fully relaxed geometry yields a lattice parameter of 5.407 Å, which is in excellent agreement with the experimental value of 5.409 Å measured by Skinner (Skinner, 1961). ZnS sphalerite crystallizes in a high-symmetry cubic structure with the space group ($F\bar{4}3m$, number 216) where each Zn atom is found in a tetrahedral environment of surrounding S atoms. The same applies for the S atoms, where each S is surrounded by four Zn atoms.

The calculated electronic band structure and density of state (DOS) for ZnS sphalerite are shown on the right of **Figure 7**. The calculated band gap reads 3.76 eV located at the Γ point, which is in reasonable agreement with the experimentally observed value of 3.55 eV outlined earlier. The top of the valence band (VB), up to −2 eV on an energetic scale, is primarily comprised of Zn *d* states weakly mixed with S *p* states. The conduction band (CB) originates from empty Zn and S states mixed almost equally. For comparison, the band gap calculated with the B3LYP global hybrid functional reads 3.91 eV and shows no significant improvement when describing the electronic properties of ZnS.

3.2.2 Bulk Vacancies

Single sulphur and zinc vacancies were introduced into bulk ZnS to probe the potential effect on the electronic structure and subsequently the absorption in the UV visible part of the electromagnetic spectrum. A 3 × 3 × 3 supercell was created from the relaxed bulk ZnS structure, to ensure that there is minimal interaction between the periodically repeated defect images, located at least 16 Å apart in each crystallographic

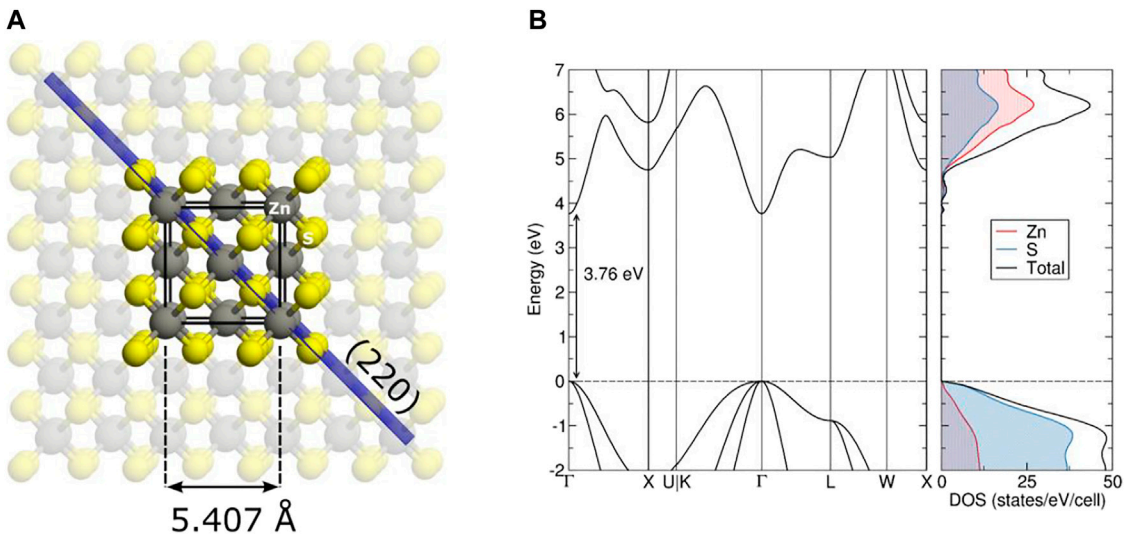

FIGURE 7 | Crystal structure of bulk ZnS sphalerite shown on the **(A)**. The unit cell is indicated with black lines, the (220) crystallographic plane with the blue coloured plane, while zinc and sulphur atoms are coloured grey and yellow, respectively. On the **(B)**, the electronic band structure together with the atom-projected densities of state are shown. The dashed line indicates the highest occupied state.

TABLE 2 | Calculated defect formation energies (E^f) together with the electronic band gap values (E_g, estimated from singe particle Kohn-Sham eigenvalues) of sulphur and zinc vacancies present in the bulk as well as (220) surface of ZnS. The up (down) arrows represent spin up (down) states. All formation energies correspond to neutral defects and were obtained using HSE06.

Defect	E^f (eV)		E_g (eV)
	Zn-rich/S-poor	Zn-poor/S-rich	
V_S^{bulk}	2.06	4.37	3.79
V_{Zn}^{bulk}	5.84	3.53	3.55
$V_S^{surf}\,(top)$	1.19	3.50	3.22
$V_{Zn}^{surf}\,(top)$	4.17	1.87	2.33 (↑)/3.92 (↓)
$V_S^{surf}\,(sub)$	1.64	3.95	3.56
$V_S^{surf}\,(mid)$	1.70	4.01	3.45
$V_{S-double}^{surf}\,(top)$	2.13	6.74	3.19

direction. Single individual sulphur and zinc vacancies were then introduced separately in the supercell (labelled V_S^{bulk} and V_{Zn}^{bulk}).

Removing a zinc atom from the lattice leaves four dangling bonds behind from the nearest neighbouring phosphorus atoms with mainly *p* orbital character. Upon relaxation, the sulphur ions are symmetrically repelled off the vacant site, with their bond length being contracted by roughly 2% ($d_{Zn-S|Zn-vac|}^{bulk}$ = 2.294 Å). The projected DOS of the fully relaxed geometry (not reported for brevity) reveal doubly occupied states present at approximately 0.3 eV above the VB maximum of the pristine bulk material. These states originate predominantly from states localized on sulphur atoms in the immediate proximity of the vacancy and to a lesser extent from states of zinc atoms surrounding the site. However, even under S-rich conditions, the formation energy V_{Zn}^{bulk} is more than 3.5 eV, making this defect difficult to materialize.

In contrast, V_S^{bulk} is energetically more favourable, costing little more than 2 eV to form (under Zn-rich conditions). Sulphur is nominally found in the -2 charge state, leaving two electrons behind when removed from the lattice. These electrons have only the surrounding high energy Zn *p* and *d* states to move into, thus forming a doubly occupied localized state merging the top of the VB as well as acceptor states at the bottom of the CB. The electronic band gap remains mostly unaltered (**Table 2**).

3.2.3 Surfaces

The (220) surface was chosen to model adsorption effects as it results in a non-polar termination and is observed as one of the dominant planes in the outlined XRD analysis. A 1.7 nm thick slab was cleaved from the relaxed bulk of ZnS along the (220) direction and expanded into a 3 × 2 supercell in the a-b plane for subsequent adsorption as well as analysis of occurring surface defects. This results in a simulation cell where periodic images are located at least 10.8 Å apart.

The initially cut slab terminates with a layer of Zn and S atoms residing in the same plane. Upon relaxation, the topmost Zn atoms move towards the slab as a consequence of the missing tetrahedron corner S atom, resulting in an increased Coulomb attractive force towards the remaining three S atoms. In the final relaxed geometry, the top Zn atom has transformed from a tetrahedral to an asymmetric trigonal planar coordination. The undercoordinated surface S atoms are pushed further out and define the surface termination. The surface Zn atom forms two bonds with the most prominent surfaces S atoms ($d_{Zn-S|top}^{surf}$ = 2.274 Å) and one with the first subsurface layer S atom ($d_{Zn-S|sub}^{surf}$ = 2.296 Å), all three being shorter compared to the starting bulk value (d_{Zn-S}^{bulk} = 2.342 Å). The top S atom binds the aforementioned two surface Zn atoms and one subsurface Zn atom at a distance that almost recovers the bulk value ($d_{S-Zn|sub}^{surf}$ = 2.332 Å). The calculated surface energy of ZnS(220) is just 0.571 J/m^2, explaining from an energetic perspective its prominent presence in the observed morphologies. As a result of the structural rearrangement, the electronic band gap of the (220) surface is calculated at 3.88 eV, being around 0.1 eV larger than the initial bulk band gap.

3.2.4 Defects on Surfaces

To gain further insight into the properties of the (220) surface, single vacancies were introduced into the slab and their energetics evaluated. The relaxed geometries of a single sulphur as well as zinc vacancy present in the topmost surface layer are depicted on the right of **Figure 8**. As a results of the induced zinc vacancy, the sulphur moves away from the top zinc by 0.02 Å at the same time shortening the distance to the subsurface zinc by 0.02 Å. The spin density difference (from a calculated Mulliken population analysis) reveals two localized electrons spread between the two top sulphur and one subsurface sulphur atom, with values of $\triangle S_{top} = 0.86\,e^-$ and $\triangle S_{subsurf} = 0.21\,e^-$. These states are clearly visible in the partial DOS (**Figure 9**) as well as two defect hole states localized on the aforementioned sulphur atoms, centred at around 1.5 eV above the VB maximum. As a result of the modified coordination environment in which the top Zn atom is found, the $V_{Zn}^{surf}\,(top)$ formation energy has decreased by almost 2 eV, calculated at 1.87 eV which is much easier to achieve compared to the bulk vacancy.

The single sulphur vacancy present at the surface behaves similarly to its bulk analogue. The electrons remaining at the site when sulphur is removed are localized at the nearest neighbouring zinc atoms, forming occupied states at the top of the VB as well as empty acceptor states at the bottom of the CB. In the relaxed geometry, the zinc atoms surrounding the vacancy move towards the empty site (**Figure 8A**), elongating the zinc-(top)-sulphur bond by 0.11 Å and the zinc-(subsurface)-sulphur bond by 0.06 Å. This rather large geometry change induces a lowering of the band gap by almost 0.6 eV compared to the bulk vacancy. As a consequence of the incomplete tetrahedral coordination, the formation energy of $V_S^{surf}\,(top)$ is only 1.19 eV under Zn-rich condition, which is almost half of the value required to extract a sulphur from the bulk of the material. However, the formation energy increases significantly when trying to remove any sulphur below the top layer (values listed in **Table 2**) and the band gap increases towards a value found in the bulk of ZnS.

A double sulphur vacancy has been tested at the top of the ZnS (220) surface as well. Due to the increased computational cost and for easier comparison, the two vacancies were introduced in the same supercell where the single vacancy was modelled earlier. This way, the vacancies are set apart by only 6.5 Å, yet the relaxed geometry as well as electronic structure reveal little to no overlap between the defect wavefunctions. The calculated band gap of the surface containing $V_{S-double}^{surf}\,(top)$ is 3.19 eV, which is almost

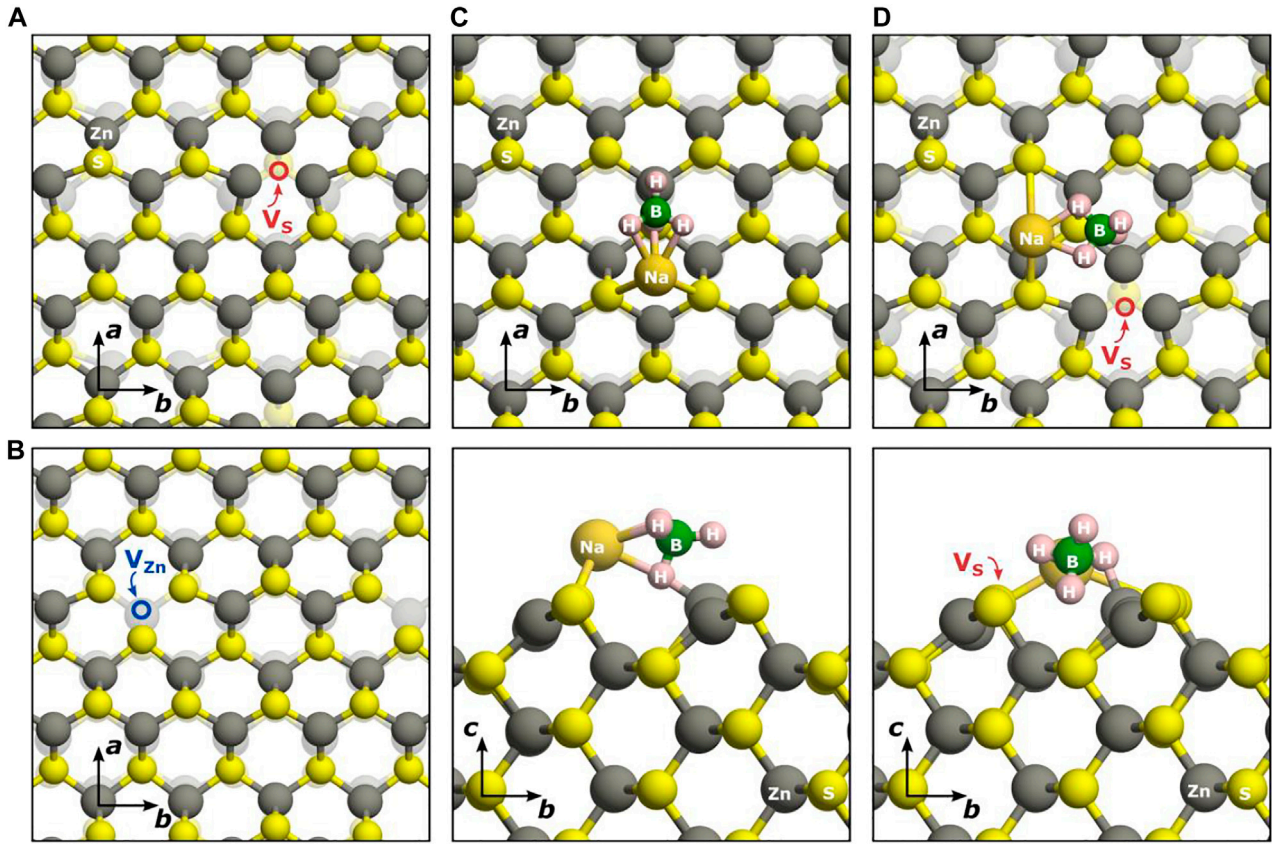

FIGURE 8 | Crystal structure of defects and adsorbates at the ZnS (220) surface: single sulphur vacancy **(A)**, single zinc vacancy **(B)**, adsorption of $NaBH_4$ on the pristine (220) surface **(C)**, adsorption of $NaBH_4$ on a (220) surface where a single sulphur vacancy is present **(D)**.

identical to the band gap of 3.22 eV for the surface containing V_S^{surf} (top). The projected DOS reveal doubling of the states identified in the case of the single sulphur vacancy, with neither new donor nor acceptor states found in the electronic structure of the surface. The formation energy of the two vacancies is calculated at 2.13 eV, indicating that the (220) surface of ZnS can readily accommodate multiple vacancies in its topmost layer.

3.2.5 Adsorption on Pure and Defective Surfaces

The adsorption of sodium borohydride on top of a pristine ZnS(220) surface results in one binding mode, regardless of the initial position of the $NaBH_4$ molecule. The molecule attaches itself such that Na bridges two S atoms and one of the H atoms from the BH_4^- ion binds to the most prominent Zn atom. The electronic structure of the surface with the adsorbed $NaBH_4$ is shown in **Figure 9C**. $NaBH_4$ is an insulating molecule with a band gap of 9.74 eV (calculated at HSE06 level) and does not induce any defect states in the band gap of the pristine ZnS(220) surface, further confirming what was observed in the XPS analysis earlier. The molecule binds strongly to the surface, releasing 1.34 eV in energy upon adsorption. The changes in bond lengths are reported in **Table 3**, with the strongest increase in spatial separation noted between the Na^+ and BH_4^- ions.

Upon addition of a sulphur vacancy on one of the sites where $NaBH_4$ binds to the surface and subsequent geometrical relaxation, the molecule rotates away from the vacant site in order for sodium to find a suitable sulphur to bind to. In this way, $NaBH_4$ binds more strongly to the nearest sulphur site, elongating the bond to the nearest Zn and weakly binding the second sulphur atom at only 3.211 Å. As a consequence, the adsorption energy is reduced by almost 0.3 eV compared to the surface without any defects present. The electronic band gap is again not altered compared to the case with only a single vacancy present at the surface, confirming the inability of sodium borohydride to alter the electronic properties of the ZnS(220) surface, regardless of its pristine or defective form.

3.3 Photocatalytic Performance

The photocatalytic performance of the synthesized ZnS nanoparticles was evaluated for the degradation of RhB under UV light (λ_{max} = 553 nm). After exposure to UV light for 210 min, the intensity of the spectrum decreased sharply, showing no characteristic absorption. This suggests complete decolourisation/degradation of RhB (**Figure 10**). The degradation efficiency of the ZnS nanoparticles prepared under different reaction conditions (**Figure 11A**) was calculated according to the equation below, where C_0 is the initial concentration of RhB solution and C is the concentration of the dye at irradiation time (t).

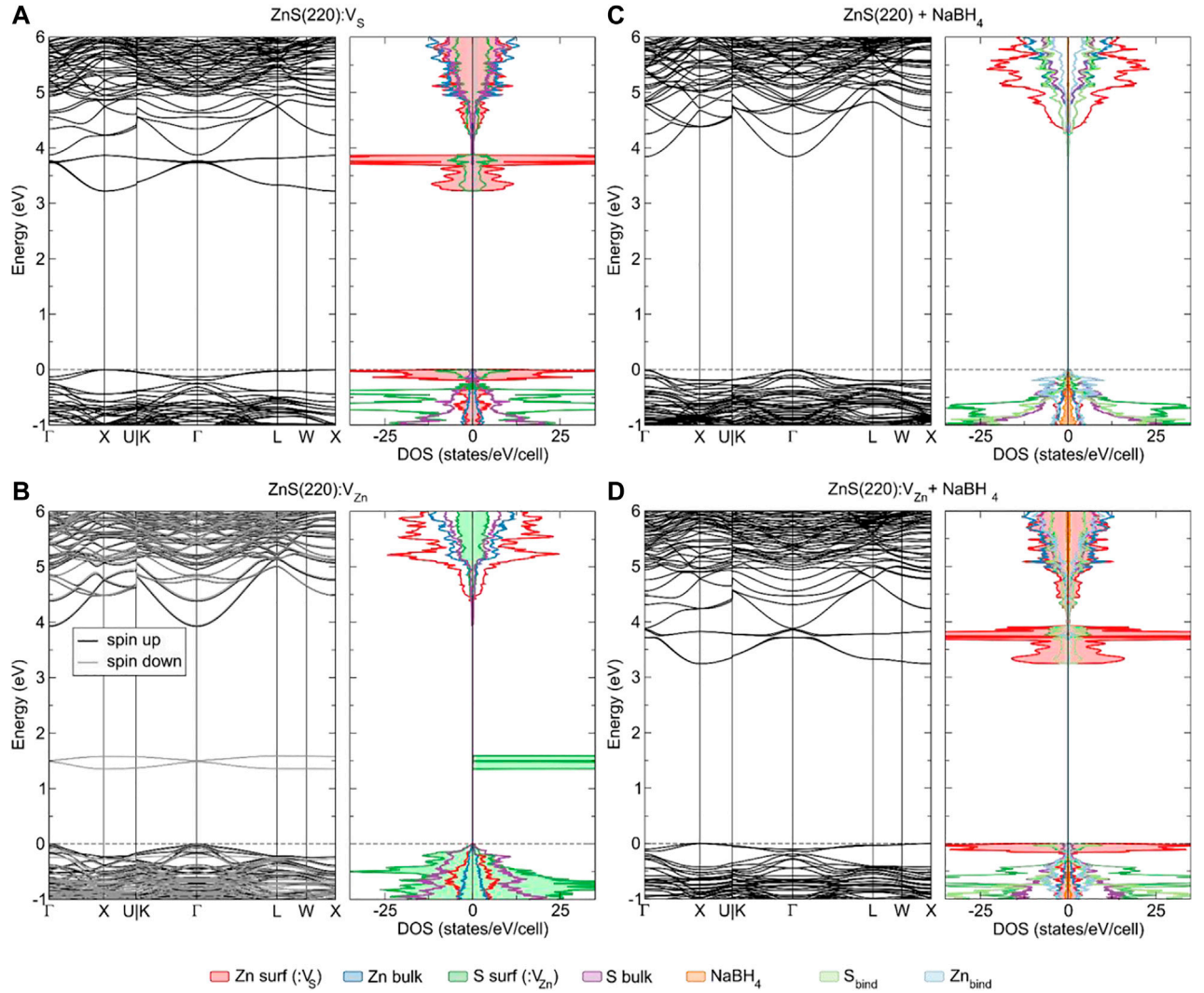

FIGURE 9 | Electronic band structure and densities of states of: ZnS(220):V_S **(A)**, ZnS (220):V_{Zn} **(B)**, ZnS (220) + $NaBH_4$ **(C)**, ZnS (220):V_S + $NaBH_4$ **(D)**. The dashed lines indicate the highest occupied state.

TABLE 3 | Calculated adsorption energy of $NaBH_4$ bound onto ZnS(220) in its pristine and sulphur deficient form and electronic band gap together with the accompanying bond lengths (values reported in Å).

System	E_b^{CP} (eV)	E_g (eV)	*d* (Na-H)	*d* (Na-B)	*d* (B-H)	*d* (Na-S)	*d* (H-Zn)
$NaBH_4$	N/A	9.74	2.179 2.182 2.185	2.293	1.250 1.250 1.250 1.207	N/A	N/A
ZnS(220)+ $NaBH_4$	− 1.34	3.84	2.247 2.309 2.317	2.443	1.224 1.224 1.269 1.212	2.799 2.803	1.780
ZnS (220):V_S + $NaBH_4$	− 1.05	3.25	2.207 2.266 3.351	2.703	1.225 1.228 1.273 1.207	2.677 3.211	1.859

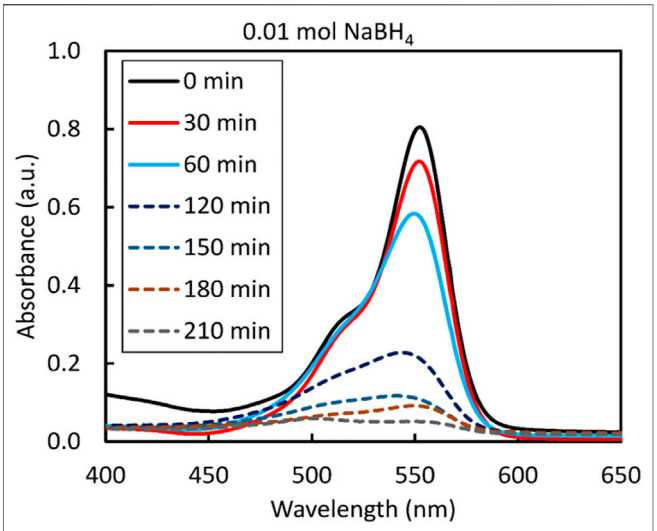

FIGURE 10 | Optical absorption spectra of RhB catalysed by ZnS prepared using 0.01 mol $NaBH_4$.

$$\text{Degradation efficiency } (\%) = \frac{C_0 - C}{C_0} \times 100\%.$$

All samples showed activity greater than 50% for the degradation of RhB, which increased with the amount of added $NaBH_4$. The ZnS nanoparticles prepared with 0.01 mol $NaBH_4$ showed the highest efficiency of 93.60% after 210 min of exposure followed by 0.005 mol (86.39%) and 0.03 mol (80.30%). The degradation of the sample prepared with 0.02 mol $NaBH_4$ fell sharply (52.57%) even below that of ZnS not treated with $NaBH_4$. The behaviour of these two samples, i.e., the ZnS nanoparticles prepared with 0.01 and 0.02 mol of $NaBH_4$, is consistent with the trend observed with PL data.

TABLE 4 | The kinetic curves for the degradation of RhB dye by ZnS prepared using different amounts of $NaBH_4$.

$NaBH_4$ (mol)	D (nm)	E_g (eV)	Rate Constant (min^{-1})
0.000	12.1	3.54	0.0051
0.003	12.5	3.54	0.0065
0.005	12.4	3.55	0.0084
0.010	13.8	3.55	0.0123
0.020	8.04	3.57	0.0029

The reaction kinetics of RhB (**Figure 11B**) can be explained by the pseudo-first order equation:

$$\ln\left(\frac{C_0}{C}\right) = kt,$$

where C_0 is the initial RhB concentration at $t = 0$, C is the concentration at reaction time t, and k the reaction rate constant. The values of the kinetic rate constant of ZnS samples prepared with a varying amount of sodium borohydride are listed in **Table 4**. The ZnS sample prepared with 0.01 mol $NaBH_4$ showed the highest kinetic rate constant, whereas the ZnS sample prepared with 0.02 mol $NaBH_4$ exhibited the lowest kinetic rate constant. The results indicate that 0.01 mol of $NaBH_4$ was the threshold amount at which maximum photocatalytic degradation of RhB can be attained. The photocatalytic activities of these samples for RhB degradation, evaluated under UV light irradiation, show that the photocatalytic activity increases as the concentration of S vacancies increased, until it reaches its percolation threshold of 0.01 M fraction. It then decreases sharply beyond the percolation threshold value because, when present in excessive amounts, S vacancies destroy the morphologies (visible from the SEM images) of the samples and also act as recombination sites of photogenerated electrons and holes (noted from the PL results).

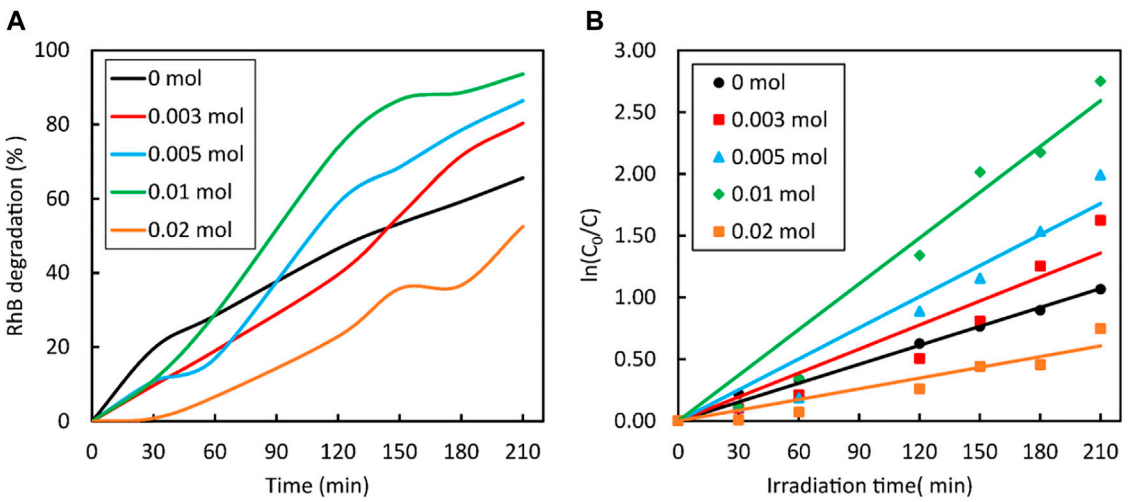

FIGURE 11 | Degradation rate of RhB dye by on the **(A)** and the kinetic curves for the degradation of Rh B dye by ZnS on the **(B)**, both prepared using different amounts of $NaBH_4$.

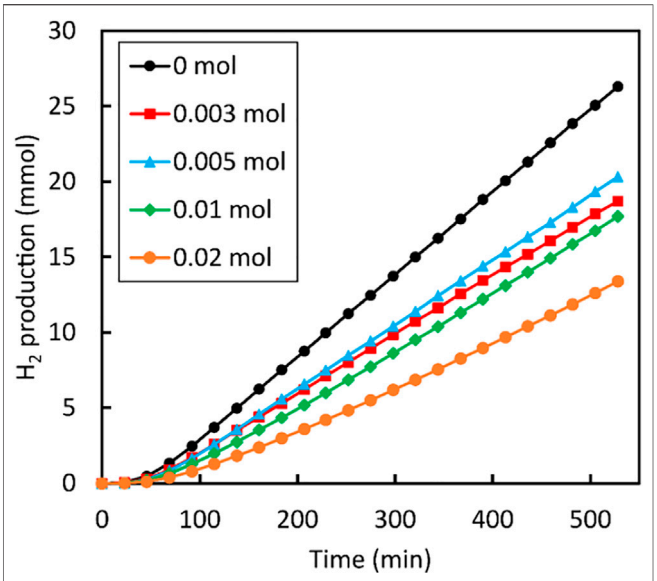

FIGURE 12 | H_2 production by ZnS nanoparticles prepared using different amounts of $NaBH_4$.

When the same ZnS samples were tested for the photocatalytic H_2 generation, the results did not reflect the trend that was obtained for the dye degradation of RhB. All samples showed activity, but the amount of H_2 generated from ZnS samples prepared with the addition of $NaBH_4$ were all below the value of the sample that was not treated with $NaBH_4$ (**Figure 12**). This suggests that the addition of $NaBH_4$ to ZnS nanoparticles prepared in this study did not improve the generation of H_2, which is in conflict with the results reported by Wang et al. (2015b). The rate of reaction is affected by various factors including concentration of reactants, catalyst dose and light intensity. The starting concentration of Zn and S in NaOH used in this study is 0.292 M. This is potentially different when compared to the work of (Wang et al., 2015b), as their procedure did not specify the amount of Zn and S powders added to NaOH. In addition to this, the current study used a low dosage of the catalyst (0.001 g/ml) compared to 0.005 g/ml used in the already mentioned study. Finally, the lamp that was used in our study is a 100 W LED which is less efficient compared to the 300 W arc Xe lamp used by Wang et al. (2015b).

Furthermore, our band gap analysis reveals that these ZnS samples are not photo-responsive to light with wavelength greater than 350 nm. Moreover, the S vacancies which are claimed to generate mid-gap defect states in ZnS from earlier studies are not found in the present work and indicate a possible overestimation of defect levels as a result of using a semi-local functional compared to the hybrid one and not explicitly considering surface defects while rather extrapolating values obtained from the bulk.

4 CONCLUSION

ZnS with various molar fractions of $NaBH_4$ in a ZnS matrix were successfully fabricated using a facile one pot-hydrothermal method, and their structural and photocatalytic properties were clarified. Increasing the $NaBH_4$ molar fractions from 0.005 to 0.01 mol, which increases the number of S vacancies, enhances the photocatalytic degradation of the RhB dye due to the photogenerated carriers which do not quickly recombine. Based on the relationship between the molar fraction of $NaBH_4$ and the photocatalytic activities of the ZnS samples, the percolation threshold of the ZnS/$NaBH_4$ system was found at a $NaBH_4$ molar fraction of 0.01 mol. It was elucidated from XPS, SEM, and PL observations that the decrease in photocatalysis at larger $NaBH_4$ concentrations was attributed to a surplus of S vacancies formed, a change in the morphology of the ZnS samples, and the separation efficiency of photogenerated charge carries in ZnS samples. DFT studies of sulphur vacancies present in the bulk as well as surface of ZnS show favourable formation energies as well as band gap lowering of ZnS. However, the resulting band gap is still not found responsive to the visible part of the UV spectrum and further reduction to achieve so are necessary. The adsorption of $NaBH_4$ atop the (220) surface of ZnS was found to be energetically stable and no defect levels were found in the otherwise pristine band gap, neither from XPS nor DFT characterizations. Ultimately, it is still a challenge to achieve ZnS photocatalysts with a high value of overall quantum efficiency due to rapid recombination rates of charge carriers and further optimizations are required to exhaust their full potential.

DATA AVAILABILITY STATEMENT

The original contributions presented in the study are included in the article/Supplementary Material, further inquiries can be directed to the corresponding author.

AUTHOR CONTRIBUTIONS

Conceptualization—all authors. Investigation and data curation: TA, AŽ, MW, DJ, CD, CM, LD, and VU. Writing—original draft preparation: TA. Writing—review and editing: TA, AŽ, NL. Supervision: CD, ND, NL.

FUNDING

This work was performed using the computational facilities of the Centre for High Performance Computing in Cape Town (CHPC) and the Dutch national e-infrastructure with the support of SURF Cooperative. Via our membership of the UK's HEC Materials Chemistry Consortium, which is funded by EPSRC (EP/R029431), this work used the ARCHER2 United Kingdom National Supercomputing Service (http://www.archer2.ac.uk). AŽ and NL acknowledge the NWO ECHO grant (712.018.005) for funding.

ACKNOWLEDGMENTS

We acknowledge the Royal Society and UK Department for International Development for funding under the Africa Capacity Building (ACBI) programme. We would also like to thank Glynnis Morgan for a thorough proofreading of the manuscript.

REFERENCES

Aulakh, M. K., Dua, J., and Pal, B. (2022). Influence of Capping Agents on Morphology and Photocatalytic Response of ZnS Nanostructures towards crystal Violet Degradation under UV and Sunlight. *Separat. Purif. Tech.* 281, 119869. doi:10.1016/j.seppur.2021.119869

Bai, W., Cai, L., Wu, C., Xiao, X., Fan, X., Chen, K., et al. (2014). Alcohothermal Synthesis of Flower-like ZnS Nano-Microstructures with High Visible Light Photocatalytic Activity. *Mater. Lett.* 124, 177–180. doi:10.1016/j.matlet.2014.03.073

Bhushan, M., and Jha, R. (2020). Surface Activity Correlations of Mesoporous 3-D Hierarchical ZnS Nanostructures for Enhanced Photo and Electro Catalytic Performance. *Appl. Surf. Sci.* 528, 146988. doi:10.1016/j.apsusc.2020.146988

Biesinger, M. C., Lau, L. W. M., Gerson, A. R., and Smart, R. S. C. (2010). Resolving Surface Chemical States in XPS Analysis of First Row Transition Metals, Oxides and Hydroxides: Sc, Ti, V, Cu and Zn. *Appl. Surf. Sci.* 257, 887–898. doi:10.1016/j.apsusc.2010.07.086

Boys, S. F., and Bernardi, F. (1970). The Calculation of Small Molecular Interactions by the Differences of Separate Total Energies. Some Procedures with Reduced Errors. *Mol. Phys.* 19, 553–566. doi:10.1080/00268977000101561

Cao, J., Liu, Q., Han, D., Yang, S., Yang, J., Wang, T., et al. (2014). Highly Enhanced Photocatalytic Properties of ZnS Nanowires-Graphene Nanocomposites. *RSC Adv.* 4, 30798–30806. doi:10.1039/c4ra04164j

Cao, S., Piao, L., and Chen, X. (2020). Emerging Photocatalysts for Hydrogen Evolution. *Trends Chem.* 2, 57–70. doi:10.1016/j.trechm.2019.06.009

Dong, F., Guo, Y., Zhang, J., Li, Y., Yang, L., Fang, Q., et al. (2013). Size-controllable Hydrothermal Synthesis of ZnS Nanospheres and the Application in Photocatalytic Degradation of Organic Dyes. *Mater. Lett.* 97, 59–63. doi:10.1016/j.matlet.2013.01.029

Dong, M., Zhou, P., Jiang, C., Cheng, B., and Yu, J. (2017). First-principles Investigation of Cu-Doped ZnS with Enhanced Photocatalytic Hydrogen Production Activity. *Chem. Phys. Lett.* 668, 1–6. doi:10.1016/j.cplett.2016.12.008

Dovesi, R., Erba, A., Orlando, R., Zicovich-Wilson, C. M., Civalleri, B., Maschio, L., et al. (2018). Quantum-mechanical Condensed Matter Simulations with CRYSTAL. *Wiley Interdiscip. Rev. Comput. Mol. Sci.* 8, 1–36. doi:10.1002/wcms.1360

Dovesi, R., Saunders, V. R., Roetti, C., Orlando, R., Zicovich-Wilson, C. M., Pascale, F., et al. (2017). *CRYSTAL17 User's Manual*. Torino: University of Torino.

Dovesi, R., Ermondi, C., Ferrero, E., Pisani, C., and Roetti, C. (1984). Hartree-Fock Study of Lithium Hydride with the Use of a Polarizable Basis Set. *Phys. Rev. B* 29, 3591–3600. doi:10.1103/physrevb.29.3591

Dovesi, R., Roetti, C., Freyria-Fava, C., Prencipe, M., and Saunders, V. R. (1991). On the Elastic Properties of Lithium, Sodium and Potassium Oxide. An Ab Initio Study. *Chem. Phys.* 156, 11–19. doi:10.1016/0301-0104(91)87032-q

Ebrahimi, S., and Yarmand, B. (2019). Morphology Engineering and Growth Mechanism of ZnS Nanostructures Synthesized by Solvothermal Process. *J. Nanopart Res.* 21, 264. doi:10.1007/s11051-019-4714-z

Fang, X., Zhai, T., Gautam, U. K., Li, L., Wu, L., Bando, Y., et al. (2011). ZnS Nanostructures: From Synthesis to Applications. *Prog. Mater. Sci.* 56, 175–287. doi:10.1016/j.pmatsci.2010.10.001

Feng, Y., Lu, C., Wang, H., Meng, M., Zhang, Y., Rao, D., et al. (2020). Spinel Copper-Iron-Oxide Magnetic Nanoparticles with Cooperative Cu(i) and Cu(ii) Sites for Enhancing the Catalytic Transformation of 1,2-propanediol to Lactic Acid under Anaerobic Conditions. *Catal. Sci. Technol.* 10, 8094–8107. doi:10.1039/d0cy01733g

Ghosh, S., Samanta, M., Sen, D., Sarkar, S., Sarkar, S., and Chattopadhyay, K. K. (2021). Photocatalytic and Sonocatalytic Dye Degradation by Sulfur Vacancy Rich ZnS Nanopowder. *J. Nanopart Res.* 23, 160. doi:10.1007/s11051-021-05283-5

Gopinath, K. P., Madhav, N. V., Krishnan, A., Malolan, R., and Rangarajan, G. (2020). Present Applications of Titanium Dioxide for the Photocatalytic Removal of Pollutants from Water: A Review. *J. Environ. Manage.* 270, 110906. doi:10.1016/j.jenvman.2020.110906

Grimme, S., Antony, J., Ehrlich, S., and Krieg, H. (2010). A Consistent and Accurate Ab Initio Parametrization of Density Functional Dispersion Correction (DFT-D) for the 94 Elements H-Pu. *J. Chem. Phys.* 132, 154104. doi:10.1063/1.3382344

Grimme, S., Ehrlich, S., and Goerigk, L. (2011). Effect of the Damping Function in Dispersion Corrected Density Functional Theory. *J. Comput. Chem.* 32, 1456–1465. doi:10.1002/jcc.21759

Grimme, S., Hansen, A., Brandenburg, J. G., and Bannwarth, C. (2016). Dispersion-Corrected Mean-Field Electronic Structure Methods. *Chem. Rev.* 116, 5105–5154. doi:10.1021/acs.chemrev.5b00533

Ham, S., and Jang, D.-J. (2018). Facile Photohydroxylation of ZnS Nanobelts for Enhanced Photocatalytic Activity. *J. Environ. Chem. Eng.* 6, 228–235. doi:10.1016/j.jece.2017.12.005

Haque, F., Daeneke, T., Kalantar-zadeh, K., and Ou, J. Z. (2018). Two-Dimensional Transition Metal Oxide and Chalcogenide-Based Photocatalysts. *Nano-micro Lett.* 10, 23. doi:10.1007/s40820-017-0176-y

Heyd, J., Scuseria, G. E., and Ernzerhof, M. (2006). Erratum: "Hybrid Functionals Based on a Screened Coulomb Potential" [J. Chem. Phys. 118, 8207 (2003)]. *J. Chem. Phys.* 124, 219906. doi:10.1063/1.2204597

Heyd, J., and Scuseria, G. E. (2004). Efficient Hybrid Density Functional Calculations in Solids: Assessment of the Heyd-Scuseria-Ernzerhof Screened Coulomb Hybrid Functional. *J. Chem. Phys.* 121, 1187–1192. doi:10.1063/1.1760074

Heyd, J., Scuseria, G. E., and Ernzerhof, M. (2003). Hybrid Functionals Based on a Screened Coulomb Potential. *J. Chem. Phys.* 118, 8207–8215. doi:10.1063/1.1564060

Hinuma, Y., Pizzi, G., Kumagai, Y., Oba, F., and Tanaka, I. (2017). Band Structure Diagram Paths Based on Crystallography. *Comput. Mater. Sci.* 128, 140–184. doi:10.1016/j.commatsci.2016.10.015

Jaffe, J. E., Harrison, N. M., and Hess, A. C. (1994). Ab Initio study of ZnO (10Ī0) Surface Relaxation. *Phys. Rev. B* 49, 11153–11158. doi:10.1103/physrevb.49.11153

Jaffe, J. E., and Hess, A. C. (1993). Hartree-Fock Study of Phase Changes in ZnO at High Pressure. *Phys. Rev. B* 48, 7903–7909. doi:10.1103/physrevb.48.7903

Kwoka, M., Kulis-Kapuscinska, A., Zappa, D., Comini, E., and Szuber, J. (2020). Novel Insight on the Local Surface Properties of ZnO Nanowires. *Nanotechnology* 31, 465705. doi:10.1088/1361-6528/ab8dec

La Porta, F. A., Nogueira, A. E., Gracia, L., Pereira, W. S., Botelho, G., Mulinari, T. A., et al. (2017). An Experimental and Theoretical Investigation on the Optical and Photocatalytic Properties of ZnS Nanoparticles. *J. Phys. Chem. Sol.* 103, 179–189. doi:10.1016/j.jpcs.2016.12.025

Lee, G-J., and Wu, J. J. (2017). Recent Developments in ZnS Photocatalysts from Synthesis to Photocatalytic Applications — A Review. *Powder Technol.* 318, 8–22. doi:10.1016/j.powtec.2017.05.022

Lichanot, A., Aprà, E., and Dovesi, R. (1993). Quantum Mechnical Hartree-Fock Study of the Elastic Properties of Li2S and Na2S. *Phys. Stat. Sol. (B)* 177, 157–163. doi:10.1002/pssb.2221770111

Liu, M., Wang, S., Wang, C., Zhang, G., Wang, Y., Li, X., et al. (2020). Understanding of Electronic and Optical Properties of ZnS with High Concentration of point Defects Induced by Hot Pressing Process: The First-Principles Calculations. *Comput. Mater. Sci.* 174, 109492. doi:10.1016/j.commatsci.2019.109492

Ma, Q., Wang, Y., Kong, J., and Jia, H. (2016). Tunable Synthesis, Characterization and Photocatalytic Properties of Various ZnS Nanostructures. *Ceramics Int.* 42, 2854–2860. doi:10.1016/j.ceramint.2015.11.021

Momma, K., and Izumi, F. (2011). VESTA 3for Three-Dimensional Visualization of crystal, Volumetric and Morphology Data. *J. Appl. Cryst.* 44, 1272–1276. doi:10.1107/s0021889811038970

Monkhorst, H. J., and Pack, J. D. (1976). Special Points for Brillouin-Zone Integrations. *Phys. Rev. B* 13, 5188–5192. doi:10.1103/physrevb.13.5188

Oliveira, J. P., Prado, A. R., Keijok, W. J., Ribeiro, M. R. N., Pontes, M. J., Nogueira, B. V., et al. (2020). A Helpful Method for Controlled Synthesis of Monodisperse Gold Nanoparticles through Response Surface Modeling. *Arabian J. Chem.* 13, 216–226. doi:10.1016/j.arabjc.2017.04.003

Orlando, R., Dovesi, R., Roetti, C., and Saunders, V. R. (1990). Ab Initio Hartree-Fock Calculations for Periodic Compounds: Application to Semiconductors. *J. Phys. Condens. Matter* 2, 7769–7789. doi:10.1088/0953-8984/2/38/005

Palanisamy, V. K., Manoharan, K., Raman, K., and Sundaram, R. (2020). Efficient Sunlight-Driven Photocatalytic Behavior of Zinc Sulfide Nanorods towards

Rose Bengal Degradation. *J. Mater. Sci. Mater. Electron.* 31, 14795–14809. doi:10.1007/s10854-020-04043-w

Pascale, F., Zicovich-Wilson, C. M., López Gejo, F., Civalleri, B., Orlando, R., and Dovesi, R. (2004). The Calculation of the Vibrational Frequencies of Crystalline Compounds and its Implementation in the CRYSTAL Code. *J. Comput. Chem.* 25, 888–897. doi:10.1002/jcc.20019

Puentes-Prado, E., Garcia, C. R., Oliva, J., Galindo, R., Bernal-Alvarado, J. J., Diaz-Torres, L. A., et al. (2020). Enhancing the Solar Photocatalytic Hydrogen Generation of ZnS Films by UV Radiation Treatment. *Int. J. Hydrogen Energ.* 45, 12308–12317. doi:10.1016/j.ijhydene.2020.02.180

Ren, Z., Li, X., Guo, L., Wu, J., Li, Y., Liu, W., et al. (2021). Facile Synthesis of ZnO/ZnS Heterojunction Nanoarrays for Enhanced Piezo-Photocatalytic Performance. *Mater. Lett.* 292, 129635. doi:10.1016/j.matlet.2021.129635

Richards, A. W. (1959). The Heats of Formation and Dissociation of Zinc Sulphide. *J. Appl. Chem.* 9, 142–145.

Sabaghi, V., Davar, F., and Fereshteh, Z. (2018). ZnS Nanoparticles Prepared via Simple Reflux and Hydrothermal Method: Optical and Photocatalytic Properties. *Ceramics Int.* 44, 7545–7556. doi:10.1016/j.ceramint.2018.01.159

Samaniego-Benitez, J. E., Lartundo-Rojas, L., García-García, A., Calderón, H. A., and Mantilla, A. (2021). One-step Synthesis and Photocatalytic Behavior for H2 Production from Water of ZnS/MoS2 Composite Material. *Catal. Today* 360, 99–105. doi:10.1016/j.cattod.2019.08.011

Saravanakumar, B., Rani, B. J., Ravi, G., Thambidurai, M., and Yuvakkumar, R. (2017). Reducing Agent (NaBH4) Dependent Structure, Morphology and Magnetic Properties of Nickel Ferrite (NiFe2O4) Nanorods. *J. Magnetism Magn. Mater.* 428, 78–85. doi:10.1016/j.jmmm.2016.12.017

Sarkar, S., Das Mahapatra, A., and Basak, D. (2018). Self-powered Highly Enhanced Broad Wavelength (UV to Visible) Photoresponse of ZnO@ZnO1−xSx@ZnS Core-Shell Heterostructures. *J. Colloid Interf. Sci.* 523, 245–253. doi:10.1016/j.jcis.2018.03.110

Scaranto, J., Mallia, G., and Harrison, N. M. (2011). An Efficient Method for Computing the Binding Energy of an Adsorbed Molecule within a Periodic Approach. The Application to Vinyl Fluoride at Rutile TiO2(110) Surface. *Comput. Mater. Sci.* 50, 2080–2086. doi:10.1016/j.commatsci.2011.02.011

Skinner, B. J. (1961). Unit-cell Edges of Natural and Synthetic Sphalerites. *Am. Mineral.* 46, 1399–1411.

Togo, A., and Tanaka, I. (2018). *$\\texttt{Spglib}$: A Software Library for crystal Symmetry Search*. ARXIV Print.

Tran, M. T., Du, N. V., Tu, N., Huyen, N. T., Hung, N. D., Viet, D. X., et al. (2022). High-quality Optically Defect-free 1D ZnS Nanostructures by a Modified thermal Evaporation Method. *Opt. Mater.* 124, 111963. doi:10.1016/j.optmat.2021.111963

Wang, C., Wu, D., Wang, P., Ao, Y., Hou, J., and Qian, J. (2015). Effect of Oxygen Vacancy on Enhanced Photocatalytic Activity of Reduced ZnO Nanorod Arrays. *Appl. Surf. Sci.* 325, 112–116. doi:10.1016/j.apsusc.2014.11.003

Wang, G., Huang, B., Li, Z., Lou, Z., Wang, Z., Dai, Y., et al. (2015). Synthesis and Characterization of ZnS with Controlled Amount of S Vacancies for Photocatalytic H2 Production under Visible Light. *Sci. Rep.* 5, 8544. doi:10.1038/srep08544

Wang, Z., Zhang, H., Cao, H., Wang, L., Wan, Z., Hao, Y., et al. (2017). Facile Preparation of ZnS/CdS Core/shell Nanotubes and Their Enhanced Photocatalytic Performance. *Int. J. Hydrogen Energ.* 42, 17394–17402. doi:10.1016/j.ijhydene.2017.04.091

Xiong, J., Li, Y., Lu, S., Guo, W., Zou, J., and Fang, Z. (2021). Controllable sulphur Vacancies Confined in Nanoporous ZnS Nanoplates for Visible-Light Photocatalytic Hydrogen Evolution. *Chem. Commun.* 57, 8186–8189. doi:10.1039/d1cc02593g

Ye, Z., Kong, L., Chen, F., Chen, Z., Lin, Y., and Liu, C. (2018). A Comparative Study of Photocatalytic Activity of ZnS Photocatalyst for Degradation of Various Dyes. *Optik* 164, 345–354. doi:10.1016/j.ijleo.2018.03.030

Yin, L., Zhang, D., Ma, J., Kong, X., Huang, J., Zhang, H., et al. (2016). Facile Synthesis and Characterization of ZnS Nano/microcrystallites with Enhanced Photocatalytic Activity. *Powder Technol.* 301, 1085–1091. doi:10.1016/j.powtec.2016.07.058

Yuan, H., Xu, M., Luo, K., and Hu, W. (2019). Relationships between Defect-Related Photoluminescence and Photocatalytic Activity of (F, Na)-Codoped ZnO Nanocrystals. *Ceramics Int.* 45, 16694–16697. doi:10.1016/j.ceramint.2019.05.136

Zafar, A., Younas, M., Fatima, S. A., Qian, L., Liu, Y., Sun, H., et al. (2021). Frequency Stable Dielectric Constant with Reduced Dielectric Loss of One-Dimensional ZnO-ZnS Heterostructures. *Nanoscale* 13, 15711–15720. doi:10.1039/d1nr03136h

Zagorac, D., Zagorac, J., Schön, J. C., Stojanović, N., and Matović, B. (2018). ZnO/ZnS (Hetero)structures: Ab Initio Investigations of Polytypic Behavior of Mixed ZnO and ZnS Compounds. *Acta Crystallogr. Sect. B* 74, 628–642. doi:10.1107/s2052520618014099

Zhang, Y.-P., Liu, W., Liu, B.-D., and Wang, R.-M. (2014). Morphology-structure Diversity of ZnS Nanostructures and Their Optical Properties. *Rare Met.* 33, 1–15. doi:10.1007/s12598-013-0217-8

Zhuang, G., Yan, J., Wen, Y., Zhuang, Z., and Yu, Y. (2021). Two-Dimensional Transition Metal Oxides and Chalcogenides for Advanced Photocatalysis: Progress, Challenges, and Opportunities. *Sol. RRL* 5, 2000403. doi:10.1002/solr.202000403

Zicovich-Wilson, C. M., Pascale, F., Roetti, C., Saunders, V. R., Orlando, R., and Dovesi, R. (2004). Calculation of the Vibration Frequencies of α-quartz: The Effect of Hamiltonian and Basis Set. *J. Comput. Chem.* 25, 1873–1881. doi:10.1002/jcc.20120

Conflict of Interest: The authors declare that the research was conducted in the absence of any commercial or financial relationships that could be construed as a potential conflict of interest.

Publisher's Note: All claims expressed in this article are solely those of the authors and do not necessarily represent those of their affiliated organizations, or those of the publisher, the editors and the reviewers. Any product that may be evaluated in this article, or claim that may be made by its manufacturer, is not guaranteed or endorsed by the publisher.

frontiers | Frontiers in Chemistry

TYPE Review
PUBLISHED 22 July 2022
DOI 10.3389/fchem.2022.807225

OPEN ACCESS

EDITED BY
Neil Coville,
University of the Witwatersrand, South Africa

REVIEWED BY
Rafael Huirache Acuña,
Michoacana University of San Nicolás de Hidalgo, Mexico
Xinying Liu,
University of South Africa, South Africa

*CORRESPONDENCE
Tendai O. Dembaremba,
s212385674@mandela.ac.za
Siphumelele Majodina,
s217553532@mandela.ac.za
Zenixole R. Tshentu,
zenixole.tshentu@mandela.ac.za

SPECIALTY SECTION
This article was submitted to Green and Sustainable Chemistry, a section of the journal Frontiers in Chemistry

RECEIVED 01 November 2021
ACCEPTED 29 June 2022
PUBLISHED 22 July 2022

CITATION
Dembaremba TO, Majodina S, Walmsley RS, Ogunlaja AS and Tshentu ZR (2022), Perspectives on strategies for improving ultra-deep desulfurization of liquid fuels through hydrotreatment: Catalyst improvement and feedstock pre-treatment. *Front. Chem.* 10:807225. doi: 10.3389/fchem.2022.807225

Perspectives on strategies for improving ultra-deep desulfurization of liquid fuels through hydrotreatment: Catalyst improvement and feedstock pre-treatment

Tendai O. Dembaremba[1]*, Siphumelele Majodina[1]*, Ryan S. Walmsley[2], Adeniyi S. Ogunlaja[1] and Zenixole R. Tshentu[1]*

[1]Department of Chemistry, Nelson Mandela University, Gqeberha (Port Elizabeth), South Africa, Nelson Mandela University, Gqeberha, South Africa, [2]Research and Development Division, Sasol Technology (Pty) Ltd, Sasolburg, South Africa

Reliance on crude oil remains high while the transition to green and renewable sources of fuel is still slow. Developing and strengthening strategies for reducing sulfur emissions from crude oil is therefore imperative and makes it possible to sustainably meet stringent regulatory sulfur level legislations in end-user liquid fuels (mostly less than 10 ppm). The burden of achieving these ultra-low sulfur levels has been passed to fuel refiners who are battling to achieve ultra-deep desulfurization through conventional hydroprocessing technologies. Removal of refractory sulfur-containing compounds has been cited as the main challenge due to several limitations with the current hydroprocessing catalysts. The inhibitory effects of nitrogen-containing compounds (especially the basic ones) is one of the major concerns. Several advances have been made to develop better strategies for achieving ultra-deep desulfurization and these include: improving hydroprocessing infrastructure, improving hydroprocessing catalysts, having additional steps for removing refractory sulfur-containing compounds and improving the quality of feedstocks. Herein, we provide perspectives that emphasize the importance of further developing hydroprocessing catalysts and pre-treating feedstocks to remove nitrogen-containing compounds prior to hydroprocessing as promising strategies for sustainably achieving ultra-deep hydroprocessing.

KEYWORDS

desulfurization, denitrogenation, crude oil, fuel refinery, hydroprocessing, hydroprocessing catalysts, adsorptive denitrogenation, metal-organic frameworks

Introduction

Crude oil, and fossil fuels in general, were formed when large amounts of dead organisms buried under sedimentary rock were subjected to intense heat and pressure (Höök et al., 2010). It is predominantly composed of hydrocarbons that are desirable for energy needs (Sami and Hatch, 2001). Demand for petroleum is especially high in motorized transport, particularly long haul air and sea transport, due to its high volumetric density (Saleh, 2015). Consumption of crude oil rose from around 70 million barrels per day (Mb/d) in 1995 to 80 and 95 Mb/d in 2005 and 2015, and to over 100 Mb/d in 2019 (Statistical Review of World Energy, 2022). The overall share of renewable energy sources remains relatively low at 5.7% (Statistical Review of World Energy, 2022). To bridge the gap in adoption of renewables, legislation is being implemented to minimize fossil fuel based emissions, reduce their carbon footprint, and to develop strategies for CO_2 capture, storage and utilization.

The hydrocarbon composition of crude oil is accompanied by several other elements such as oxygen, sulfur, nitrogen, and metals which give rise to most of the challenges associated with its handling, storage and use (Théodet, 2010). Sulfur and nitrogen pose the biggest challenges (Hansmeier et al., 2011). As a result, sweet crude oils (crude oils with lower contamintants, especially sulfur and nitrogen), are generally preferred compared to sour crude oils (crude oils with higher concentrations of contaminants). At the projected demands, the preferred sweet crude sources will soon be depleted forcing the switch to more sour crude sources (Campbell and Laherrère, 1998; Dincer and Zamfirescu, 2018; Bardi, 2019). More than 70% of the world's oil reserves are classified to be of heavier and sourer composition (World Energy Review, 2020).

Due to the rising demand for "clean" energy, pressure is mounting for the world to adopt cleaner energy technologies and improve the use of fossil fuels. Crude oil refining will be with us for a while to come so it is crucial that we continue to develop the technology. Conventionally, hydroprocessing is used to remove sulfur-containing compounds. Several other methods such as oxidative desulfurization, biodesulfurization, extractive desulfurization, and adsorptive desulfurization are also being pursued. It has been difficult to replace hydroprocessing as the industrially preferred method. As such, this work provides perspectives on the advances that are being made in improving the hydroprocessing technology to achieve ultra-deep desulfurization. Emphasis is placed on hydroprocessing catalyst development and improvement of feedstock through pre-treatment to remove nitrogen-containing compounds.

Sulfur- and nitrogen-containing compounds in crude oil

Sulfur and nitrogen content of crude oil is known to vary significantly depending on the source and there is no relationship between the concentrations of the two (Prado et al., 2017). The sulfur- and nitrogen-containing compounds are predominantly in aromatic form and generally increase with the heaviness of the crude source (Wiwel et al., 2000; Zeuthen et al., 2001). In addition to other factors, the sulfur and nitrogen content of crude oils determine their acceptability as feedstock in the refinery industry (Choudhary et al., 2008).

After carbon and hydrogen, sulfur is the next most abundant element in most crude oils (Javadli and de Klerk, 2012). Sulfur levels in crude oils are usually in the range 0.1–5.0 wt% and most have more than 1.0 wt% sulfur and are classified as sour; 0.5–1.0 wt%S is considered medium sour while <0.5 wt%S is considered sweet (World Energy Review, 2020). Sulfur-containing compounds are present in two forms; inorganic (*e.g.* suspended or dissolved elemental sulfur, hydrogen sulfide and pyrite) and organic (thiols and thiophenic compounds), the latter being the more abundant form (Javadli and de Klerk, 2012). Benzothiophenes and dibenzothiophenes are the most dominant sulfur-containing compounds in heavier fuels. Sulfur can also be found in combination with other heteroatoms and some sulfur-containing compounds may have more than one sulfur atoms. Sulfones and sulfoxides can also be found due to naturally occurring oxidation (Javadli and de Klerk, 2012).

Nitrogen levels in crude oil are generally lower compared to sulfur levels. About 90% of crude oils are classified as nitrogen poor, having less than 0.25 wt% nitrogen content while most are below 0.1 wt% (Prado et al., 2017). Four chemical classes of nitrogen-containing compounds are found in fuel oils: aliphatic amines, anilines, and two heterocyclic aromatic compound groups (five-membered pyrrolic and six-membered pyridinic compounds). Aliphatic amines and anilines are not present in significant amounts in most fuel oils (Wiwel et al., 2000). Aliphatic amines, anilines and six-membered pyridinic compounds are classified as basic nitrogen-containing compounds ($pK_a \geq 2$) while the five-membered compounds are classified as neutral, non-basic or acidic ($pK_a < 2$) (Richter et al., 1952; Wiwel et al., 2000; Prado et al., 2017). The ratio of basic nitrogen to non-basic nitrogen remains within the range 0.25–0.35 irrespective of the origin of the crude oil (Prado et al., 2017). The most common basic nitrogen-containing compounds in fuel oils are pyridine, acridine, quinoline and their derivatives, and the most common neutral nitrogen-containing compounds are pyrrole, indole, carbazole and their derivatives (Asumana et al., 2011). In most cases, 75% of the total nitrogen content in the straight run gas oil and light cycle oil used as feed stocks for diesel fuel production consist of indole and carbazole type compounds while the 25% is constituted mainly of quinoline derivatives (Laredo et al., 2002; Prado et al., 2017). Heavier crudes (*e.g.* bitumen and tar sands) are associated with very high nitrogen content, mostly basic nitrogen-containing compounds, particularly quinoline derivatives (Wiwel et al., 2000; Javadli and de Klerk, 2012).

Challenges associated with sulfur and nitrogen containing-compounds in liquid fuels

The primary concern of having sulfur-containing compounds in fuel oil is that upon combustion they produce sulfur oxides (especially sulfur dioxide) that have devastating effects on the environment, biodiversity and human health (Schlesinger and McQueen, 2010; Hansmeier et al., 2011; Thurston, 2017). Diesel engines operate at higher temperatures and pressures producing more sulfur oxide emissions than gasoline engines (Zolotareva et al., 2019). The gases aggravate the contribution of motorized transport to global warming as they poison catalysts required in vehicle emission control systems to minimize the escape of carbon monoxide (Hansmeier et al., 2011).

Sulfur- and nitrogen-containing compounds affect fuel storage and handling (Abro et al., 2016). Nitrogen-containing compounds cause storage problems due to instability and degradation which leads to formation of gums. Five-membered nitrogen-containing heterocycles such as pyrroles can easily undergo oxidative or thermal free-radical addition reactions to form heavy polymeric products commonly observed as gums or red tars (Abro et al., 2016). Sulfur-containing compounds are mostly responsible for promoting gum formation, stabilizing gum and may also react with some components of fuel oil to form materials of high molecular weight (Thompson et al., 1949). The gums formed are undesirable in storage tanks and tanks of vehicles, and negatively impact refinery processes and engine performance.

To make matters worse, sulfur and nitrogen-containing compounds interfere with the processes that are used to remove them from fuel oil. The compounds cause fouling of process equipment (Prado et al., 2017). They also inhibit the catalysts used during fuel refining processes such as hydrocracking and hydrotreatment, of which nitrogen-containing compounds are the main culprits (Sau et al., 2005). That makes sourer crudes difficult to process using conventional methods. High concentrations of refractory sulfur-containing compounds in sour crudes also persistently remain in the final product after most treatment procedures (Hansmeier et al., 2011; Forte et al., 2014).

It is evident that nitrogen-containing compounds are the ones that are mostly associated with the numerous challenges around the processing, handling, and storage of fuel. However, they are often "ignored" in favour of sulfur-containing compounds as they are usually much lower that sulfur-containing compounds and are removed simultaneously during hydrotreatment (Wiwel et al., 2000; Hansmeier et al., 2011; Prado et al., 2017). Considering the drive to achieve ultra-low sulfur levels of sulfur and also pave way for the utilization of sourer crudes, it is now imperative to find ways of removing even the small amounts of nitrogen-containing compounds from crude oil to prevent the inhibition of catalysts used in downstream processes such as hydrocracking and hydrotreatment.

Regulation of sulfur and nitrogen levels in liquid fuels

Most governments have come up with strict legislations to curb the release of sulfur oxides into the environment, by primarily monitoring the amounts of sulfur in carburant fuels. The monitoring started as early as 1990 with specifications for different types of vehicles and designated areas (*e.g.* urban, highway, off-road) and the policies now apply across all vehicle types and areas (US: Fuels: Diesel and Gasoline, 2021; Fuel Regulation, 2022a; Fuel Regulation, 2022b). The most recent Clean Air Act (2021) from the United States Environmental Protection Agency requires liquid fuels to have less that 15 ppm sulfur content (Environmental Protection Agency, 2021). Euoropean Union sulfur limits are set under Euro VI at 10 ppm (ICCT, 2020). Brazil has standards equivalent to the Euro V but additionally banning the sale of diesel cars in the country while promoting ethanol and biofuel blending (Zolotareva et al., 2019; ICCT, 2022). From 2013, major metropolitan areas and selected stations around the country were able to supply 10 ppm diesel to trucks (ICCT, 2022). China's vehicle emissions standards are also equivalent to the Euro V, being China V for light-duty vehicles and China V for heavy-duty vehicles (Zolotareva et al., 2019).

Ships have been lagging behind although some marine areas have been declared to be designated emission-controlled areas (along the shorelines) where ships are required to use light distillate fuels such as marine gas oil to reduce pollution levels. USA and Canada applied to the International Maritime Organization to establish emission control areas along their shorelines where the sulfur limit was 10,000 ppm from 2010 to 1000 ppm from 2015, marking the beginning of international regulation of sulfur limits in marine fuels (IMO, 2022). In 2020 the MARPOL convention introduced the so-called "IMO-2020" regulation which cut the sulfur content in the marine fuel from 3.5% m/m down to 0.5% m/m outside designated emission control areas. The sulfur specification is even lower at 0.1% m/m for designated emission-control areas.

African countries have also been lagging behind. Morocco was the pioneering country in Africa starting with 50 ppm diesel in 2009 and then 10 ppm diesel becoming available from 2011 (UNO, 2022). Other leading countries in adopting legislation for low sulfur levels in fuel Africa are Mauritius, Kenya, Uganda, Tanzania, Rwanda, Burundi, Ghana, Mozambique, Malawi and Zimbabwe (UNO, 2022). In Mauritius 50 ppm diesel had become a standard across all fuel stations from 2012. Mozambique implemented 50 ppm limit for gasoline in 2017. Zimbabwe implemented the 50 ppm limit for diesel in 2018 with a goal

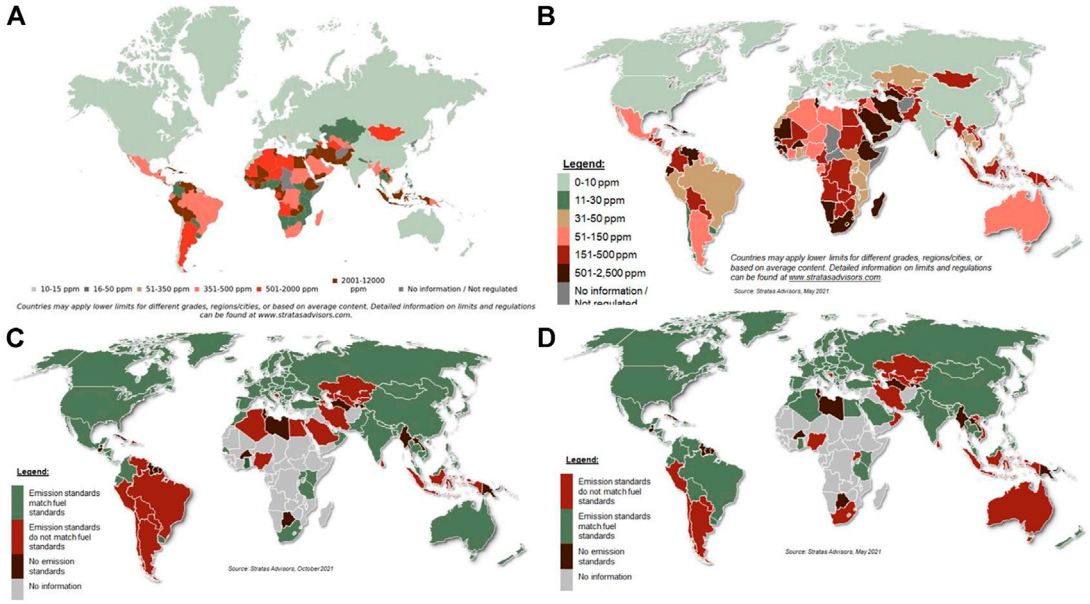

FIGURE 1
Maximum sulfur limits in **(A)** gasoline 2021 and **(B)** on-road diesel 2021, and gap between current vehicle emission standards and **(C)** gasoline quality and **(D)** on-road diesel quality (Global Fuel Specification, 2022).

to progressively phase out 500 ppm diesel. However, despite African countries adopt the legislation for low sulfur diesel implementation remains a challenge as can be seen from Figure 1 (Global Fuel Specification, 2022).

Most of the discussed legislations such as the Clean Air Act of USA and the Euro 5/6 do not directly minitor the amounts of nitrogen-containing compounds in the curbarent fuel but rather control the emission levels of nitrogen oxides, particularly NO_2. Nevertheless, it is important to have nitrogen levels below 10 ppm (Abro et al., 2016).

Overview of crude oil processing

The crude oil refinery process is primarily meant to separate the hydrocarbons according to their boiling points (*viz.* molecular weight) through fractional distillation into fractions suitable for specific applications such as fuels, lubricants, and feedstock for other downstream petrochemical industries. Product improvement is also important during refinery and encompasses processes applied to adjust the boiling range of the products to target more valuable cuts or to introduce special properties that improve the product performance and to ensure adherence to given specifications (Speight, 2018). Common refinery boiling point adjustment technologies include alkylation (increase in boiling point) as well as fluid catalytic cracking and hydrocracking (boiling point reduction). Naphtha reforming and isomerization is used primarily to improve gasoline octane numbers, while hydrotreatment is typically used to remove heteroatoms and improve product stability (Speight, 2018). The main categories of fuel oils from the distillation of crude oil are heavy gas oil, diesel/light gas oil, kerosene and they serve as different carburants in different forms of motorized transport.

Removal of sulfur- and nitrogen-containing compounds is complicated by the complexity of the fuel oil matrix. (Hansmeier et al., 2011) Reductive or oxidative techniques are primarily used in industry to remove sulfur and nitrogen-containing compounds (Forte et al., 2014). The techniques can be applied before the use of the fuel oil or on exhaust fumes (Zolotareva et al., 2019). However, removal of sulfur- and nitrogen-containing compounds from exhaust fumes is more applicable to industrial plants. Practically, the techniques cannot be applied to motorized transport as a primary method for removing the noxious gases that come from the sulfur and nitrogen compounds. Catalytic converters can only sufficiently manage small quantities of sulfur oxides that come from low sulfur fuel oils. That still leaves the removal of sulfur- and nitrogen-containing compounds from oil fuel before use as the most preferred technique. In that regard, hydroprocessing has proven to be the more practical route due to how easily it can be applied on an industrial scale and has been the conventional technique (Huh et al., 2009). However, the technique has limitations and challenges that keep on motivating researchers to find alternative techniques or techniques to aid hydrotreatment.

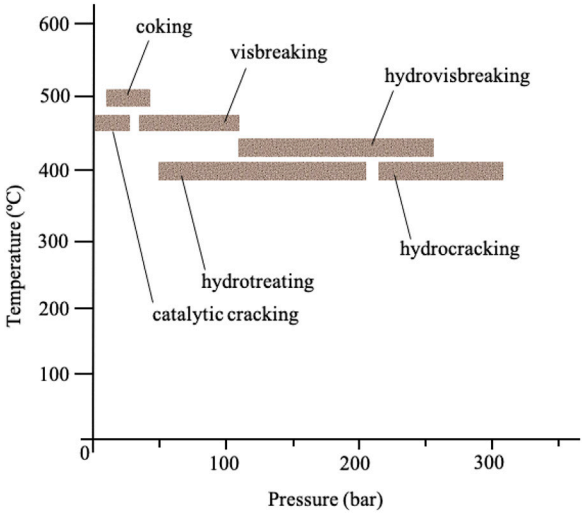

FIGURE 2
Hydroprocessing examples based on the process conditions (temperature and pressure) (Bose, 2015).

Conventional hydroprocessing

Hydroprocessing covers a range of catalytic processes such as hydrotreating, hydropyrrolysis and hydrocracking processes (Figure 2). This process is carried out prior to most processes (*e.g.* catalytic reforming) to alleviate the challenges associated with the heteroatoms found in fuel oil such as sulfur, oxygen, metals and nitrogen (Saleh, 2015). The removal of these unwanted heteroatoms is referred to as hydrodesulfurization (HDS) for removal of sulfur, hydrodenitrogenation (HDN) for removal of nitrogen, hydrodeoxygenation (HDO) for removal of oxygen, and hydrodemetalation (HDM) for removal of metals. The processes occur simultaneously (Hansmeier et al., 2011). During hydroprocessing, the sulfur and nitrogen in sulfur- and nitrogen-containing compounds react with hydrogen under high pressure (typically 15–90 bar) and high heat (typically 300–350°C) in the presence of catalysts to produce H_2S and NH_3, respectively, leaving behind the corresponding hydrocarbons (Huh et al., 2009; Hansmeier et al., 2011; Javadli and de Klerk, 2012; Zolotareva et al., 2019). Additional steps, such as the Claus process, are required to remove and convert H_2S into elemental sulfur (Hansmeier et al., 2011; Saleh, 2015; Zolotareva et al., 2019).

Hydrotreating catalysts consist of two or more metals, at least one being the active metal and the other one a promoter (Brunet et al., 2005). The most common hydrotreating catalysts contain the active metal as Molybdenum (Mo) or Tungsten (W), and Nickel (Ni) or Cobalt (Co) as the promoter metal. The most common hydrotreating catalysts are alumina supported Cobalt-Molybdenum (CoMo) and Nickel-Molybdenum (NiMo), being mainly used for HDS and HDN respectively. This is due to NiMo catalysts having higher hydrogenation activity than CoMo catalysts. The Nickel-Tungsten (NiW) catalyst has a higher denitrogenation activity than NiMo but is more expensive (Prado et al., 2017; Kaiser et al., 2020). The catalysts are commonly supplied in their air-stable oxide form and require sulfidation for activation (Figure 3). Sulfidation forms a metal-sulfide bond between the active metal sites in the catalysts and the sulfur compound used for sulfidation, usually carbon disulfide (CS_2) or dimethyldisulfide. (Chowdari et al., 2020; Tanimu et al., 2021). The role of sulfidation is to form coordinatively unsaturated sites (CUS) or sulfur vacancies on the active metal where sulfur- and nitrogen-containing compounds are preferentially adsorbed by binding *via* the sulfur and nitrogen providing a driving force for their removal (Harris and Chianelli, 1986; Chianelli et al., 2020). In other words, the active forms of the hydroprocessing catalysts are actually transition metal sulfides.

Conventional hydroprocessing challenges

Hydrotreatment does not completely remove sulfur- and nitrogen-containing compounds from fuel (Gray et al., 1995; Ma et al., 1996; Whitehurst et al., 1998). Reactivity is dependent on the molecular structure; paraffinic components, *i.e.* aliphatic acyclic sulfides (thioethers), cyclic sulfides (thiolanes), aliphatic amines and anilines can be easily removed while sulfurs and nitrogens in heterocycles are more resistant. The performance of hydroprocessing catalysts is negatively affected by steric and electronic factors of the heterocyclic compounds. Sulfur-containing compounds remaining in hydrotreated diesel fuels at sulfur levels lower than 500 ppm are predominantly dibenzothiophenes with alkyl substituents at the 4- and/or 6-position. Carbazole and its alkyl-substituted analogues are the most refractory nitrogen-containing compounds (van Looij et al., 1998; Wiwel et al., 2000; Zeuthen et al., 2001). The more the substituents in pyrrole benzologues the less their reactivity (Zeuthen et al., 2001). Carbazoles with methyl substituents at positions 1- and 8- were found to have extraordinarily low reactivity similar to 4,6-substituted dibenzothiophene. Interestingly, alkyl substitution at positions 4- and 5- also reduces reactivity significantly, inconsistent with the normally used steric restriction reasoning (Wiwel et al., 2000). Indoles and quinolines are very reactive compared to carbazoles (Zeuthen et al., 2001). For equivalent sulfur- and nitrogen-containing compounds (*e.g.* carbazole and dibenzothiophene), nitrogen-containing compounds have much lower reactivity (Zeuthen et al., 2001).

Small amounts of aromatic nitrogen-containing compounds in the fuel can easily inhibit the catalysts due to preferential adsorption (Zeuthen et al., 1991; Whitehurst et al., 2000; Koltai et al., 2002; Turaga et al., 2003; Wiwel et al.,

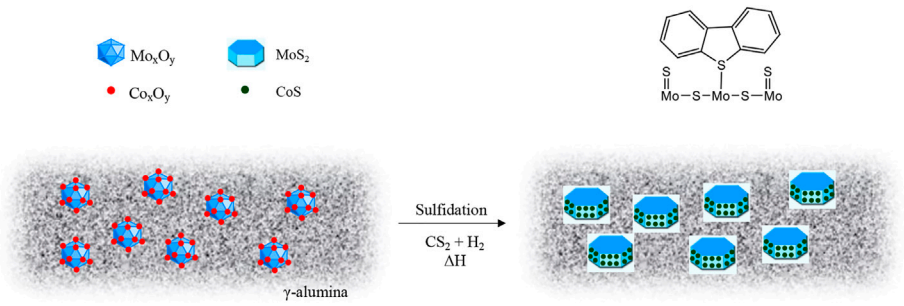

FIGURE 3
Schematic of the sulfidation process for CoMo catalyst showing DBT binding on a coordinatively unsaturated Mo site (Moqadam and Mahmoudi, 2013).

2010; Hidalgo-Vivas et al., 2022). This has a serious negative effect on the kinetics of hydroprocessing, particularly removal of refractory sulfur-containing compounds. Basic nitrogen-containing compounds are considered the biggest problem in that regard as they severely inhibit hydrogenolysis and hydrogenation, steps that are crucial for hydroprocessing of refractory sulfur-containing compounds (Zeuthen et al., 1991; Whitehurst et al., 2000; Zeuthen et al., 2001; Koltai et al., 2002; Turaga et al., 2003; Wiwel et al., 2010; Prado et al., 2017; Hidalgo-Vivas et al., 2022). It has always been feared that even neutral nitrogen-containing compounds have a similar inhibitory effect since strongly basic intermediates (amines) are formed during hydrotreatment of neutral nitrogen-containing compounds (Forte et al., 2014; Prado et al., 2017; Wen et al., 2017). The final product of hydrodenitrogenation (NH_3) is also strongly basic (Nakamura et al., 2005). An investigation by van Looij *et al.* (van Looij et al., 1998) shows that trace amounts of nitrogen compounds (0–30 ppm) have a significant inhibition effect to the reaction rate in deep hydrodesulfurization and are a key factor in achieving deep hydrodesulfurization of fuel oil while the influence of compositional changes *e.g.* content polycyclic aromatics is negligible. Sulfur-containing compounds and their hydrotreatment product H_2S are also capable of the same, albeit to much a lesser extent (Nakamura et al., 2005; Kent, 2010). Neutralization depends on the equilibrium of the acid-base reaction which is determined by the strength of the acidic sites, the basicity of the compounds and temperature. Inhibitory effects are also higher at low temperatures (>350°C) (Prado et al., 2017). The more basic the compounds, the greater the inhibition.

Additionally, hydrodenitrogenation is an unfavourable process, it is a kinetically slow process, consumption of hydrogen is not stoichiometric (much higher quantities are required), and high amounts of ammonia affect the gas cleaning step and complicate other process aspects (Prado et al., 2017).

Strategies for achieving ultra-deep hydroprocessing

Achieving ultra-low sulfur levels using conventional hydroprocessing is still a work in progress and a cause for concern for refiners when it comes to striking a balance between producing such products at reasonable market prices. There is now an increasing need for drastic improvements to the process to meet the required low sulfur specifications as well as accommodate the increasing heavier poorer feeds. Severe hydrotreatment conditions (higher temperature, residence time, pressure and more hydrogen) have been applied to try and remove the persistent sulfur- and nitrogen-containing compounds and also minimize inhibition of catalysts (Hansmeier et al., 2011; Prado et al., 2017). For example, hydrotreating of creosote distillate to produce a distillate blending material for diesel fuel is industrially performed at 280–380°C and 18.5 MPa (Prado et al., 2017). However, the use of severe operating conditions means: consumption of hydrogen is much higher, hydrodearomatization increases, and there is an adiabatic temperature increase since hydrodenitrogenation and hydrodearomatization are very exothermic reactions (Hansmeier et al., 2011; Prado et al., 2017). Often additives need to be added to manage the fuel specifications. Excessive use of hydrogen is also of concern due to increasing demand for hydrogen over the years, especially in green fuel technologies (Lima et al., 2019). Besides, the current production of hydrogen already has a huge carbon footprint (Javadli and de Klerk, 2012).

Better bets have been on catalyst development, better reactor designs and introducing new processing systems. (Lima et al., 2019). With regards to new processing systems, placement of different catalysts in multibed configurations so that they can work synergistically in what is known as catalyst stacking technology has been showing promise in improving hydroprocessing activity and reducing hydrogen consumption and other operating costs (Leal et al., 2022). The technology also

allows expensive catalysts to be easily incorporated into the systems. However, the technology is still at its infancy, how it works is not yet fully understood and there are many factors to consider. Each optimal configuration is on a case-to-case basis as there is no established predictive method. However, just slight increamental gains are achieved at this stage.

Several complementary methods that can aid hydroprocessing to achieve ultra-low sulfur levels are widely reported in literature. These are mainly meant to target the refractory sulfur compounds and they oxidative desulfurization, biodesulfurization, extractive desulfurization and adsorptive desulfurization are the most popular. However, in this work our perspectives are only centered around further improvements that can be made on hydroprocessing catalysts and improving feedstock through pre-treatment to remove nitrogen-containing compounds.

Improvements in conventional hydroprocessing catalysts

The development of novel hydroprocessing catalysts with excellent hydroprocessing performance is theoretically the most effective strategy as it can be easily adopted into existing fuel processing plants with minimal capital requirements (Zhang et al., 2019a). Hydroprocessing catalysts can be improved through new catalytic systems such as engineering new supports and/or new active phases (Huirache-Acuña et al., 2021). For example, replacement of transition metal sulfide active phases with noble metals has been successfully used. (Zhang et al., 2019a; Majodina et al., 2021). Ru and Pt as additives result in enhanced C-S cleavage activity as was demonstrated when they were added to a Rh-P catalyst and tested on 4,6-DMDBT (Kanda et al., 2022). Superior direct desulfurization selectivity has also been reported for Pt_2Si/CNTs, Rh_xSi/CNTs and RuSi/CNTs catalysts, with Pt_2Si/CNTs having the highest activity, excellent stability and sulfur resistance (Yang et al., 2021). Small amounts of Ru were also shown to cause a significant increase in activity and selectivity for the products of the hydrogenation desulfurization pathways (Topalian et al., 2021). Highly active Re and Pd phases in Re/Pd-TiO_2/SiO_2 aerogel and xerogel catalysts have also been reported to result in higher catalytic activity compared to conventional CoMo catalysts (Prokić-Vidojević et al., 2021). However, the high cost and stability of platinum group metals discourages their industrial applications.

Even with the several hydrotreating catalyst improvements, refractory sulfur containing compounds continue to pose several challenges that make it difficult to achieve ultra-deep hydroprocessing. It is therefore important to take catalyst improvement strategies with an understanding that improved catalytic activity does not necessarily translate to completely treating refractory compounds in an economical way. Therefore, there is need for foundational changes to how the improvement of catalysts and the removal of sulfur- and nitrogen-containing compounds are looked at. Considering the several years of development of hydrotreatment catalysts, it has become more and more difficult to find major breakthroughs in catalyst improvement. Continous changes to the catalysts also means continuous changes to the industrial process conditions and these changes can be expensive, *e.g.* pressure increases/new reactors and increased saturation result in high exotherms and requirement for heat management or more hydrogen (cost). As such, the playing field still remains open for other potential strategies and research in those areas has been gaining traction in the past few decades. Considering that catalyst performance is also impeded by nitrogen-containing compounds, particularly basic nitrogen-containing compounds, there is also a need to develop hydrotreatment catalysts that take into cognizance those aspects. It is also important to explore the option of removing nitrogen containing compounds before hydrotreatment is carried out.

In this section, we explore the potential improvements that can be made on hydroprocessing catalysts to improve their catalytic activity and ability to hydrotreat refractory compounds. Inferrences can be made from groups of catalysts incorporating some of the proposed catalyst activity and selectivity strategies (Table 1).

Catalyst support considerations

The primary use of the support is for dispersing the active phase of the catalyst and to stabilize the catalysts. However, supports also influence the catalytic activity in various ways: by influencing the morphology of the active phase, modifying the electronic properties, and participating in bifunctional reactions with acid sites. A good support material has high surface area, optimum pore diameter (5–15 nm), optimum acidity, and moderate metal-support interaction (Shi et al., 2020). Different support materials have different effects on catalytic activity due to their distinct textural and structural properties, and the extent to which they interact with the active metal. Several studies have been conducted on a variety of supports such as TiO_2, ZrO_2, silica-alumina and mixed oxides (Duchet et al., 1991; Grzechowiak et al., 2001). It was discovered that TiO_2 and ZrO_2 show high activity (Caero et al., 2003). However, their low surface areas and small pore sizes make it difficult to disperse active phases and prevent diffusion of large bulky molecules onto the active sites leading to pore blockage and a decrease in catalytic activity (Michaud et al., 1998). The textural properties (morphology), affordability, and thermal and chemical stability, high tolerance for longevity, and good regeneration capacity of alumina supports (mainly ɣ-Al_2O_3) make them more advantageous and they are the most popular in hydrotreatment catalysts.

The chemical nature of the support material dictates the nature of the active phase. Strong metal-support interaction on

TABLE 1 Typical improvements that are being made to improve the performance of hydroprocessing catalysts.

Catalyst	Chelating agent/ Additives	Feed	Findings	References
PGM-containing catalysts				
$RhMo/Al_2O_3$, RhMo-x/ Al_2O_3; x = EDTA, AA, CA)	EDTA, AA or CA	DBT	$RhMo/Al_2O_3$ (88%) achieved the higher HDS activity compared to chelated catalysts	Majodina et al. (2021)
Rh-M-P/SiO_2; M (Ir, Pt, Ru)	P	4,6-DMDBT	The addition of Ru and Pt to Rh-P catalyst enhanced the C-S cleavage, with Rh-Pt-P catalysts having the highest HDS activity	Kanda et al. (2022)
Pt_2Si/CNTs, Rh_xSi/CNTs, RuSi/CNTs	—	DBT and 4,6-DMDBT	Superior selectivity to DDS pathway for deep HDS of DBT and 4,6-DMDBT was observed, with Pt_2Si/CNTs having the highly HDS activity, excellent stability, and sulfur resistance	Yang et al. (2021)
Ni_2P/SiO_2, $Ni_{2-x}Ru_xP/SiO_2$, Ru_2P/SiO_2	P	4,6-DMDBT	$Ni_{1.85}Ru_{0.15}P/SiO_2$ catalyst was more active than Ni_2P/SiO_2 and Ru_2P/SiO_2 catalysts	Topalian et al. (2021)
Re/Pd-TiO_2/SiO_2	—	4,6-DMDBT	All catalysts achieved higher catalytic of 4,6-DMDBT than conventional CoMo catalysts	Prokić-Vidojević et al. (2021)
Co(Ni)Mo(W) catalysts with chelating ligands				
$CoMo/\gamma\text{-}Al_2O_3$	EDTA	2,6-dimethylanline, thiophene	EDTA led to an increase of promoted CoMoS sites with high HDN and HDS activity	Lélias et al. (2010)
NiW/Al_2O_3	CA	4, 6-DMDBT	More N-W-S phase formed and higher HDS activity was observed	Li et al. (2011)
$NiMo/SiO_2\text{-}Al_2O_3$	EDTA	Straight run gas oil (SRGO)	EDTA reduced metal-support interaction and high HDS activity observed	Al-Dalama and Stanislaus, (2011)
$CoMo/Al_2O_3$	CA, TEG	DBT, SRGO	An increase in catalysts activity in HDS DBT and HT SRGO was observed	Budukva et al. (2019)
$NiMo/ZrO_2\text{-}TiO_2$	EDTA, CA	DBT	EDTA and CA catalysts showed superior to a NiMo/ ZrO_2–TiO_2 formulation prepared with no organic additive	Escobar et al. (2008)
NiMo/SBA-15	EDTA, CA	DBT	Better dispersion was observed, highly active catalysts were obtained	Peña et al. (2014)
Co(Ni)Mo(W) with additives				
$NiMo/\gamma\text{-}Al_2O_3$	B and P	diesel fuel	Addition of B/P showed was more effective on HDS compared to HDN process	Soltanali et al. (2020)
$CoMo/\gamma\text{-}Al_2O_3$	P	Straight run gas oil	Inhibition behaviour of N compounds were observed	García-Gutiérrez et al. (2014)
$CoMo/Al_2O_3$	P	DBT	Lower metal support interaction, and increase in HDS activity was observed	Vatutina et al. (2019)
$NiMo/\gamma\text{-}Al_2O_3$	P	DBT and Quinoline	High dispersion of NiMoS, and high HYD selectivity observed, with 1.2 wt% P catalyst the best	Xiang et al. (2011)
$NiMo/\gamma\text{-}Al_2O_3$	B	DBT, 4,6-DMDBT	Maximum HDS of DBT and 4,6-DMDBT was obtained between 3 and 5 wt% B loading	Saih and Segawa, (2009)
$NiMo/\gamma\text{-}\delta\text{-}Al_2O_3$	P and B	Straight run heavy VGO	Catalyst with B resulted in decrease in activity. The addition of P increased catalytic activity	Nadeina et al. (2019)
NiMo/HMS	P	4,6-DMDBT	P favours the sulfidation degree of Co species, creation of medium strength acid sites, and enhance 4,6-DMDBT HDS.	Nava et al. (2011)
$CoMoW/\gamma\text{-}Al_2O_3$	P	Coker light gas oil	High number of active sites, new Bronsted acid sites and enhanced HDN activity was obtained	Sigurdson et al. (2008)

(Continued on following page)

TABLE 1 (*Continued*) Typical improvements that are being made to improve the performance of hydroprocessing catalysts.

Catalyst	Chelating agent/ Additives	Feed	Findings	References
Ternary catalysts				
CoMoW/Al-SBA-16	—	DBT	All catalysts showed high selectivity towards biphenyl, high Al-loading resulted in highest HDS activity	Huirache-Acuña et al. (2015)
NiMoW/clay hybrid	—	DBT and industrial kerosene	Uniformly dispersed NiMoWS particles were observed with high HDS activity and long-term catalytic stability	Liu et al. (2020a)
CoNiMo/γ-Al_2O_3	—	DBT	5% loading of Ni improved the HDS reaction. Increase in Ni decreased the DBT HDS activity	Cervantes et al. (2020)
NiMoW/SBA-16	—	DBT	The best HYD selectivity was archived by Ti *via* post-synthesis method	Alonso-Pérez et al. (2021)
NiMoW/Ti-HMS	—	DBT	The HDS reaction *via* the HYD pathway was increased by the presence of Ti	Huirache-Acuña et al. (2021)
Heteropolyacids (HPAs) as metal precursors				
$Mo_nW_{12-n}S_2/Al_2O_3$	—	DBT, HYD naphthalene	Mixed $MoWS_2$ phase and about 90% sulfidation of W and Mo was obtained	Kokliukhin et al. (2021a)
NiMoW/γ-Al_2O_3	—	DBT, HYD naphthalene and SRGO	Increased sulfidation of W and Mo, formation of highly active NiMoWS sites, and high activity was observed	Kokliukhin et al. (2021b)
Co-MoP/MCM-41-Al_2O_3	—	DBT, HYD naphthalene	mesoporous silica incorporation into Al_2O_3 improved morphological properties of the CoMoS active phase as well as the overall HDT activity	Glotov et al. (2021)

AA, acetic acid; CA, citric acid; TEG, triethylene glycol; EDTA, ethylenediaminetetraacetic acid; P, phosphorous; B, boron.

the alumina support in Co(Ni)Mo-Al_2O_3 catalysts results in the formation of tetrahedral Mo oxides impeding full sulfidation. Due to this, research has focused on obtaining the optimum metal-support interaction, and this can be achieved by developing new supports for HDS and HDN application, or it can be engineered by introducing chelating ligands (Huirache-Acuna et al., 2013; Zhang et al., 2019b). The support needs not to be too acidic or too basic, since too much of either might lead to poor metal-support interactions resulting in poor Mo dispersion (Valencia and Klimova, 2011). However, it is important to note that high acidity leads to other undesirable side reactions such as coke poisoning and blockage of the active phase by basic nitrogen compounds (Alsolami, 2022). The support also has basic sites that contribute to the activity of the catalyst. Basic sites result in better dispersion of MoO_4 and lead to low coke formation. Therefore, optimum metal-support interaction is desired to obtain proper sulfidation and dispersion of active species and to generate more Type II active phases. Type II active phases are the more active CoMoS phases formed from weak metal-support interactions. Weaker tetrahedral metal-support interactions allow for easier reduction and sulfidation process of molybdenum (tungsten) oxide unlike strong interactions that result in the formation of octahedral metal oxides which are difficult to reduce and sulfide resulting in the formation of the less active Type I phases.

The morphology of the alumina support is crucial in determining the physicochemical properties that influence the catalytic behavior of the catalyst. The acidity of the alumina support is one of the most important features that controls the dispersion of Co(Ni)Mo and also affects the metal-support interaction (Chen et al., 2013). Brönsted acid sites found in the support material impart electronic effects on the active sites making it easier for coordinatively unsaturated sites to be formed when sulfur is released as H_2S. They also act as a source of H_2 to push towards the hydrogenation pathway through the S-H group found on the S-edge sites located on the active site of the catalyst (Figure 4). (Wu et al., 2014; Cao et al., 2020) Brönsted acid sites help to overcome the steric hindrance of alkyl DBTs through isomerization thus enhancing HDS activity (Breysse et al., 2003; Breysse et al., 2008). They also enhance C-N cleavage during denitrogenation since the denitrogenation process is linked to the S-H groups around the active site. Therefore, increased hydrogenation activity also results in an overall increased in HDS and HDN activity.

Bimetallic vs. ternary catalyst considerations

Conventional bimetallic catalysts are susceptible to thermal, chemical, or mechanical degradation and metal coke poisoning, which often leads to inefficient ways to treat feedstock (Cervantes

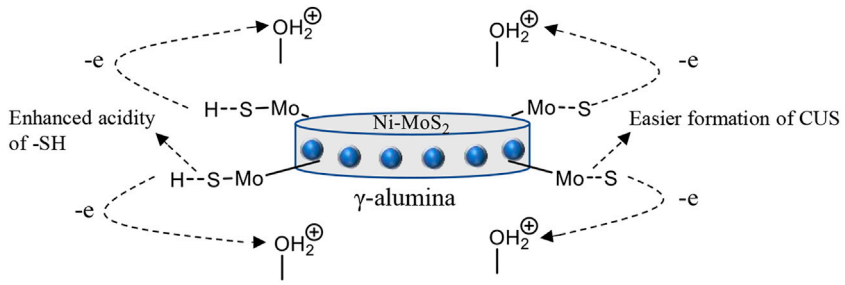

FIGURE 4
A representation of an alumina supported catalyst showing the movement of electrons on the active sites.

et al., 2020). This has motivated the development of trimetallic catalysts such as NiMoW, CoNiW, CoNiMo to increase the versatility of catalysts such as working in various harmful conditions and increased activity due to the additional active phase (Cervantes et al., 2020). These trimetallic catalysts have the advantage of having mixed phases [Ni(Co)MoWS] and their systems can be easily tailored compared to bimetallic and monometallic catalysts (Tanimu and Alhooshani, 2019). However, the catalyst performance results from different literature sources are contradictory. Severino *et al.* (Severino et al., 2000) and Sadeghbeigi (Sadeghbeigi, 2020) concluded that CoNiMo catalysts are less active as compared to bimetallic catalytic systems when they tested the HDS of thiophene and of 4,6-DMDBT, respectively. Mozhaev *et al.* (Mozhaev et al., 2016) and Cervantes *et al.* (Cervantes et al., 2020) obtained higher HDS activity for DBT when using CoNiMo catalysts compared to bimetallic catalysts. Higher catalytic activity for the trimetallic catalysts was also obtained for the desulfurization of heavy gasoline (Badoga, 2015). Monodispersed γ-Al_2O_3 supported NiMoW nanocatalysts also showed higher activity compared to NiMo and NiW bimetallic nanocatalysts when tested by Singh *et al.* (Tanimu and Alhooshani, 2019) With such contradictory results, it is important to note that the rational interpretation of the positive or negative role devoted to the addition of a second promoter has not been proposed yet (Cervantes et al., 2020). Therefore, more research can be focused on this work to improve the performance of the catalyst (Singh et al., 2021).

Unsupported versions of trimettalic catalysts have also been explored in what is known as NEBULA technology (Mendoza-Nieto et al., 2013). NEBULA catalysts predominantly contain metal sulfides in forms that incorporate porosity and avoid the use of catalyst supports to circumvent limitations in catalyst activity that comes from the limit in the amount of active metal that can be deposited on the pore walls of the support material. The catalysts show more superior HDS and HDN activities (about three times higher) than conventional alumina supported catalysts (Stanislaus et al., 2010). This is attributed to the metallic character, *i.e.* the formation of new mixed NiMoWS active phase which has better properties compared to conventional bimetallic NiWS, NiMoS, and CoMoS active phases. They also have better porosity character which is a limiting issue in supported catalyst. They are not limited by base interactions from the support and they contain a greater proportion of the formation of more Type II active phases. They contain more active metal per given volume with greater concentration of highly active Type II phases. The main disadvantage with Nebula catalysts is their high cost due to high metal content (Mendoza-Nieto et al., 2013). A study by Liu *et al.* (Liu et al., 2020b) using unsupported NiMoW catalyst on DBT showed a significant improvement of HDS activity but it was difficult to maintain the overall layered structure of the catalyst at high temperatures.

The success of NEBULA catalysts inspired the Albemarle-ExxonMobil research team to discover a new range of catalysts which they named Celestia catalysts (Leliveld and Slettenhaar, 2022). Celestia catalysts have higher catalytic activity than NEBULA catalysts. They have improved HDS performance and increased diesel yield enabled by turning down the cracking activity while still meeting product sulfur targets. The distillate and gasoline product have improved qualities and overall volume swell due to its exceptional saturation ability because it provides a higher exotherm. Celestia catalysts also provide the option to process more challenging feeds in hydrocracking pre-treatment without sacrificing unit length through increased catalyst deactivation. However, celestia catalysts require longer hold time to sulfide the catalyst fully. Their efficieny is best realized in high pressure applications. They are also typically very expensive. They are heavier (denser) than normal catalysts which is sometimes prohibitive when the equipment design limits are exceeded.

Fine-tuning the active phases of the catalysts

The use of chelating ligands

The catalytic activity mostly depends on the formation of the active phase and its structure. Research has shown that during

TABLE 2 Catalysts with and without chelating agents and their overall DBT conversions.

Catalysts	Chelating agent	MoO_3 (wt%)	CoO_3 (wt%)		DBT conversion (%)	
					4 h	8 h
CoMo6	—	6	1.5	4:1	15.5	37.4
CoMo12	—	12	3	4:1	25.2	53.2
CoMo6E	EDTA	6	1.5	4:1	33.9	61.9
CoMo12E	EDTA	12	3	4:1	38.4	76.5
CoMo18E	EDTA	18	4.5	4:1	47.6	91.6
CoMo6C	CA	6	1.5	4:1	22.2	42.8
CoMo12C	CA	12	3	4:1	30.5	61.5
CoMo18C	CA	18	4.5	4:1	35.2	77.4

EDTA, ethylenediaminetetraacetic acid; CA, citric acid.

the activation of the catalyst the promoter sulfides first, *e.g.*, Co or Ni (50–150°C) and then the Mo sulfides later from 175°C (Kishan et al., 2000; Coulier et al., 2001). The formation of the active phase requires the presence of a promoter (Co or Ni). Considering that the promoter sulfides first to form inactive phases (Co_xS_y or Ni_xS_y), it is important to create a way of preserving promoter ions for the formation of the active MoS_2 phase which only happens after the sulfidation of Mo (Kibsgaard et al., 2010). When there are fewer promoter ions remaining after the sulfidation of Mo there will be less chances of the promoter ions locating the MoS_2 resulting in fewer CoMoS active phases forming and ultimately the formation of a catalyst with poor activity. Addition of chelating ligands during catalyst synthesis decreases the interaction of the promoter and the support by forming a promoter ion-chelating ligand complex which later decomposes to react with MoS_2 to form the CoMoS active phases (Sundaramurthy et al., 2005). Most promoter ion-chelating ligand complexes only start to decompose above 200°C preventing early sulfidation of the promoter ions. Chelating ligands that have been applied for improving the formation of active phases include citric acid (CA), ethylenediaminetetraacetic acid (EDTA), glycol, nitriloacetic acid (NTA) (Sun et al., 2003). The addition of ligands also leads to the formation of polymolybdates in the oxide phase which are easily reducible, and metal dispersion is favorable during sulfidation of both cobalt and molybdenum oxides as they will start sulfiding at similar temperatures, thus resulting in the formation of more active phases (Badoga et al., 2012). The nature of the chelating ligand also imposes changes on the catalyst such as thermal stability, modulate the metal-support interaction, improve the dispersion of metal sulfides, and acidity leading to the formation of more CUS in the catalyst (de León et al., 2010; Rashidi et al., 2013; Zhang et al., 2016). Some of the advances that have been made in the use of chelating ligands to improve catalyst activity were summarized in Table 1.

A comparative study was carried out on HDS with catalysts synthesized on SBA-15 support with and without EDTA as a chelating ligand (Badoga, 2015). The sulfided catalysts were CAT 0 (NiMo/SBA-15), CAT 1 (NiMo/SBA-15, EDTA/Ni molar ratio 1), and CAT 2 (NiMo/SBA-15, EDTA/Ni molar ratio 2). A $NiMo/Al_2O_3$ catalyst (with no EDTA) was used for benchmarking. It was observed that all chelated catalysts had greater HDS catalytic activity compared to the standard $NiMo/Al_2O_3$ catalyst. The sulfur conversion followed the order: CAT2 (82%) > CAT1 (75%) > CAT 0 (70%) > $NiMo/\gamma$-Al_2O_3 (68%). Pena *et al.* (Peña et al., 2014) conducted a study on CoMo-SBA-15 catalysts with different amounts of MoO_3 and CoO_3 (Table 2). Benchmarking with CoMo6 and CoMo12, the chelated catalysts showed higher activity in the hydrotreatment of DBT in the order EDTA chelated catalysts > CA chelated catalysts > non-chelated catalysts.

Majodina *et al.* (Majodina et al., 2021) recently tested a series of catalysts with and without chelating ligands tested for DBT HDS ($RhMo_x/Al_2O_3$, x = EDTA, acetic acid, citric acid) and observed the following: $RhMo/Al_2O_3$ (88%) > $RhMo\text{-}AA/Al_2O_3$ (73%) > $RhMo\text{-}CA/Al_2O_3$ (72%) > $RhMo\text{-}EDTA/Al_2O_3$ (68%). The observed trend is contrary to the previous studies carried out on base metal catalysts where the importance of delaying sulfidation of the promoter (Co or Ni) sulfide, using chelating liagnds, was demonstrated. This opens up more questions around where chelation can be advantageous or how it can be applied for the different metals.

The use of additives

The addition of additives such as boron and phosphsorus also greatly improves the catalytic activity of conventional HDS and HDN catalysts (Table 1) (Rashidi et al., 2013; Vatutina et al., 2019; Soltanali et al., 2020). The addition of boron or phosphorous helps improve the acidity of the catalyst and the dispersion of the active phase. The acidity of the catalyst helps sterrically hindered refractory compounds to access the active sites. When Soltanani *et al.* (Soltanali et al., 2020) used

phosphorus as an additive they additionally found that phosphorous can act as a promoter atom, helping with the distribution of MoS_2 as it reduces Mo(VI) to Mo(IV). They also realized that phosphorous encourages the formation of octahedral Ni and Co structures vs. tetrahedral structures that cause polymerization of Mo-S bonds. Phosphorous also improves the degree of sulfidation of Co or Ni particles by reducing the metal support interaction. Additionally, phosphorous improves the formation of Brönsted acid sites on the catalyst, hydrogenation of aromatic rings, stability of the impregnation solution resulting in better metal distribution on the support, and the thermal stability of alumina. It also prevents the formation of inactive $NiAl_2O_4$ particles during catalyst synthesis and coke formation during hydrotreatment (Poulet et al., 1993; Jian and Prins, 1998; Maity et al., 2008; Rayo et al., 2012; Rashidi et al., 2013; Soltanali et al., 2020). The same properites can also be obtained using boron; increasing dispersion of the active phase, modifying the acidity of the support and reducing metal-support interaction.

Changing synthesis strategies (using different precursor compounds)

Replacement of conventional active metal precursors with precursors having two or more metals in the form of heteropolyacids (HPAs) in the preparation of oxidic precursors of metal-sulfide catalysts enhances catalyst activity (Ramírez et al., 2012; Minaev et al., 2015). Starting with such multimetal precursor compounds results in all metals being in close proximity allowing them to interact better with each other. Keggin-type HPAs such as B-$H_4[SiMo_3W_9O_{40}]$ have been used as precursors for alumina supported catalysts giving the advantage to introduce simultaneously both metals in the same compound allowing to maintain a Mo-W nanoscape proximity (Nikulshina et al., 2018; Nikulshina et al., 2020) obtained $Mo_xW_{1-x}S_2$ active phases using $SiMo_nW_{12-n}$ HPA precursors and observed higher catalytic activity for DBT (Nikulshina et al., 2018). Higher hydrodrogenation activity for naphthalene using the same catalyst was also observed by Nikulshina *et al.* (Nikulshina et al., 2020) Monometallic HPAs have also been investigated and it was found that the use of a mixture of $H_4SiMo_{12}O_{40}$ and $H_4SiW_{12}O_{40}$ leads to preferential formation of corresponding MoS_2 and WS_2 active phases, respectively (Kokliukhin et al., 2021a). Thomazeau *et al.* (Thomazeau et al., 2007) reported that the formation of mixed $MoWS_2$ crystallites is possible only from a precursor which contains both closely related metals in the structure at once. The introduction of HPAs as precursors has also inspired a new method for preparing trimetallic catalysts (Kokliukhin et al., 2021a).

Metal borides, phosphides, carbides, and nitrides have also been investigated as metal precursors (Alexander and Hargreaves, 2010; Prins and Bussell, 2012; Carenco et al., 2013; Topalian et al., 2021). Transition metal phosphides (Ni_2P, Co_2P, MoP) have been found to produce highly active phases that lead to high HDS and HDN activity (Cecilia et al., 2009; Shamanaev et al., 2021). Ni_2P gives the highest activity and performs better when it comes to hydroprocessing refractory compounds (Miles et al., 2020; Jiang et al., 2021). Metal phosphides optimize the acidity of the material support, positively affecting the dispersion of the active phase resulting in improved catalytic performance (Cecilia et al., 2009). Metal phosphides have high thermal and electrical conductivity, high thermal stability, and are resistant to the inhibition of sulfur- and nitrogen-containing compounds under standard hydrotreating conditions (Yun and Lee, 2014; Topalian et al., 2021). However, Jiang *et al.* (Jiang et al., 2021) investigated Ni_2P catalysts and found contradictory results that showed challenges with dispersion, limited total HDS activity and instability. Transition metal carbides and nitrides such as molybdenum carbides and molybdenum nitrides have simple crystal structures that possess similar properties to those of transitions metals normally used for hydroprocessing catalysts, *e.g.* desirable electronic and magnetic properties, extreme hardness, and ionic charactericsts (Chen, 1996). However, they have additional advantages of being resistant to sintering at high temperatures, having strong interactions with nitrogen, sulfur and other heteroatoms in fuel and not causing C-C bond scission which leads to undesirable saturation of aromatics (Lin et al., 2021; Yue et al., 2021). They also have noble metal-like properties that make them effective hydrogenation catalysts (Yue et al., 2021). However, transition metal carbides and nitrides do not sustain long-term stability, they are easily deactivate due to their strong affinity with the adsorbates, especially at high temperatures (Lin et al., 2021).

The catalyst selection for ultra-deep desulfurization would be pre-mature at this stage as there is a lot of research work being undertaken. It is possible that a mix of catalysts, including those containing PMGs, may be a way to go in the application of the catalyst stacking technology.

Removal of nitrogen-containing compounds prior to hydrotreatment

It is clear from the discussion in Section 1.6 that nitrogen-containing compounds make it difficult for hydroprocessing to be efficiently carried out. In summary, the compounds act as temporary poisons and inhibit hydroprocessing catalysts, they are precursors to coke formation and their hydroprocessing is not economical. Overall, they are one of the biggest hurdles to achieving ultra-low sulfur levels using standard hydroprocessing conditions and catalysts. Intensifying hydroprocessing conditions to overcome some of the challenges is expensive, increases coke formation and affects the quality of the product.

García-Gutiérrez *et al.* (García-Gutiérrez et al., 2014) demonstrated how hydroprocessing significantly improves with the ability to easily obtain ultra-low sulfur diesel after nitrogen-containing compounds were removed from straight run gas oil. They investigated the kinetics of hydroprocessing

feedstock of varying nitrogen and sulfur concentrations in straight run gas oil: (0.0020–0.0357 wt%) and (1.3985–1.2130 wt%), respectively, using a commercial CoMoP/γ-Al_2O_3 catalyst at 5.49 MPa, liquid hourly space velocity of 2.5 h^{-1}, and a temperature range of 622–643 K. The rate of desulfurization varied proportionally with sulfur concentration and inversely with the nitrogen concentration. From their experimental work, they developed a model that showed the sulfur levels that can be achieved as nitrogen levels are varied. The model shows that it is possible to reach 0.0010 wt % sulfur levels if nitrogen compounds are removed prior to hydrodesulfurization. Sau *et al.* (Sau et al., 2005) also showed that hydroprocessing catalyst activity increases by at least 60% and hydrogen consumption is significantly reduced when they carried out a similar investigation of removing nitrogen-containing compounds from straight run gas oil and vacuum gas oil prior to hydroprocessing.

Zeuthen *et al.* (Zeuthen et al., 2001) demonstrated that even though carbazoles are not very reactive and are among the predominant nitrogen compounds, it is the basic nitrogen-containing compounds that play a major inhibitory effect during hydrotreatment of fuel oil. The inhibitory effect of basic nitrogen compounds is magnitudes higher than that of neutral nitrogen compounds while carbazoles are not very inhibiting. Similar studies using different sets of neutral and basic nitrogen compounds are reported throughout literature (Zeuthen et al., 1991; van Looij et al., 1998; Whitehurst et al., 2000; Koltai et al., 2002; Turaga et al., 2003; Wiwel et al., 2010; Hidalgo-Vivas et al., 2022). The behaviour of even trace amounts of basic nitrogen compounds strongly resembles the effect of high concentrations of nitrogen compounds (van Looij et al., 1998; Whitehurst et al., 2000; Zeuthen et al., 2001). The more basic the nitrogen compounds the more the inhibitory effect (Wiwel et al., 2010; Hidalgo-Vivas et al., 2022). Zeuthen and Blom (Zeuthen et al., 1991) characterized the nitrogen on aged hydroprocessing catalysts using temperature-programmed oxidation. They concluded that the nitrogen compounds were attached to the catalyst surface and were not necessarily in the bulk of the coke that was on the surface of the catalyst providing further evidence of the inhibitory effect of the nitrogen compounds on the catalysts.

With that in mind, removing nitrogen-containing compounds (especially the basic ones) as a primary step should improve the efficacy of hydroprocessing and all the other upstream and downstream processes that are affected by these compounds. It is possible that pre-treating to remove nitrogen compounds may be more economical compared to applying more intense hydroprocessing conditions (higher hydrogen pressure, temperature and residence time), improved infrastructure and process design, reduced catalyst lifespan requiring constant replenishment, and obtaining quality product which is not compromized by harsh processing conditions. More importantly, high nitrogen and sulfur content feedstocks such as creosote that are usually shunned by industry can also be pre-treated to remove nitrogen-containing compounds and be economically hydroprocessed to achieve ultra-deep desulfurization. Key to the success of this approach is achieving high selectivity for the nitrogen-containing compounds since the fuel matrix is complex. The fuel matrix is composed of other components (*e.g.* moisture, aromatics, metals and oxygenates) that affect the performance of methods that target nitrogen-containing compounds (Khan et al., 2013; Ahmed and Jhung, 2016a). Some of the compounds in fuel that are important for the quality of the fuel (*e.g.* octane and cetane numbers) also have physichochemical properties close to those of the target nitrogen-containing compounds, *e.g.* aromatics and other heteroatomic compounds (Ghosh et al., 2006). Most approaches can be considered as either *1*) modification of the nitrogen-containing compounds so that extractive or adsorptive techniques can be easily applied or *2*) improvements of the solvents or materials used for extractive or adsorptive separation. Oxidative, extractive, and adsorptive techniques have also been widely researched for desulfurization and the process may also contribute to simultaneous removal of the harsher refractory sulfur compounds. Extraction or adsorption using affordable solvents or materials are more practical approaches and the purified compounds obtained as by-products can also become feedstock for other industries, *e.g.* quinoline and carbazole which are obtained exclusively from coal tar (Fetzner, 1998). We consider it much more beneficial to fine-tune extractive and adsorptive techniques for the selective removal of nitrogen-containing compounds as a complementary technique to hydrodesulfurization.

Denitrogenation by chemical modification followed by separation

Nitrogen-containing compounds can be derivatized *via* the nitrogen using addition or substitution reagents to precipitate them out of fuel or to make them more polar so that they can be preferentially separated from the rest of the fuel oil using extractive or adsorptive techniques due to their increased relative polarity. Alkylation and oxidation have been extensively investigated in that regard. Alkylating agents usually lead to precipitation. Shiraishi *et al.* (Shiraishi et al., 2001a; Shiraishi et al., 2001b; Shiraishi et al., 2001c) investigated the denitrogenation of aniline, indole and carbazole from xylene (representing light oil feedstocks) using CH_3I and $AgBF_4$ for alkylation. *N*-methylation and subsequent precipitation of the compounds occurred under moderate conditions. The nitrogen content was reduced to less than 20% of the feed concentrations and application on light oil feedstocks was also demonstrated. Bromoacetic acid has been extensively tested for alkylation of nitrogen compounds (Prado et al., 2017). Metallic salts (*e.g.* $CuCl_2$, $SnCl_2$ and $FeCl_3$) have also been used to precipitate

basic nitrogen compounds through Lewis acid-base complexation (Prado et al., 2017). *N*-alkylation and precipitation is lucrative as it also simultaneously removes sulfur-containing compounds. However, the method struggles with refractory compounds such as carbazole as electron density on the nitrogen decreases with increasing carbon number of the alkyl substituents. Alkylation of other aromatics is also possible and it is especially difficult to selectively apply the method on high oxygenate content oils.

Catalysts based on strong Lewis acid transition metals (titanium, tungsten, platinum group metals, polyoxometalates, molybdenum and vanadium) have proven to be efficient for the oxidation of nitrogen-containing compounds (Dembaremba et al., 2019a). Various support materials have also been used for the catalysts, *e.g.* silica, alumina, zeolites and organic polymers, and these also have an influence in the performance of the catalysts (Dembaremba et al., 2019a; Dembaremba et al., 2019b). Selective oxidants such as nitric acid and/or nitrogen oxides, organic hydroperoxides, peroxyacids, and hydrogen peroxide are usually employed as oxidants (Dembaremba et al., 2019a; Dembaremba et al., 2019b). Some of the by-products generated by the organic oxidants influence the quality of the fuels; for example, *tert*-butyl alcohol is obtained from *tert*-butylhydroperoxide and improves the octane number (Karas et al., 2008). Hydrogen peroxide is much cheaper but is difficult to use since it is aqueous. Research has been carried out around the introduction of surfactants which help to disperse oxidant in the form of small spherical droplets in fuel oil, a process described as an emulsion catalysis system (Jiang et al., 2011).

Other methods such as autooxidation (using atmospheric oxygen), photochemical oxidation and ultrasound oxidation have also been attempted to cut costs (Shiraishi et al., 2000; Whitehurst et al., 2000). Photochemical oxidation is based on free radical formation and although promising results have been obtained in model samples it is difficult to predict the various reactions that can occur in a complex medium such as fuel oil (Forte et al., 2014). Photodecomposition of nitrogen-containing compounds has been reported by Shiraishi *et al.* (Shiraishi et al., 2000) in model fuel oils with hydrogen peroxide being required in an oil/water biphase to enhance photoreactivity of the nitrogen-containing compounds.

The advantage of the oxidative process is that, unlike hydrotreatment, it operates at lower reaction temperatures and pressure, and in the absence of hydrogen which is expensive. However, large amounts of expensive oxidants are required to completely oxidize the compounds. Our previous work was on improving the catalysts for oxidation in order to reduce the amount of oxidant required but even with good catalysts the amounts of oxidant required still remain high. (Dembaremba et al., 2019a). Using this already expensive process prior to hydrotreatment will result in an expensive product. The capital investment for the additional units is also significant. Product selectivity is also a major challenge (Ishihara et al., 2005). A study by Ogunlaja *et al.* (Ogunlaja et al., 2017) shows the complexity around the oxidation of nitrogen-containing compounds, attributing the array of products to reactions that occur following the formation of hydroxy radicals. Formation of this vast array of products further complicates removal of products after oxidation.

Extractive denitrogenation

Choice of solvent for the extraction of nitrogen-containing compounds from fuel oils is critical, it must be thermodynamically compatible with the compounds (Dembaremba et al., 2020). Polar solvents with low boiling points such as ethanol, ethanol and acetonitrile have been tested for denitrogenation of fuel oil but these solvents are too volatile for practical application on an industrial scale (Campos-Martin et al., 2010; Mokhtar et al., 2014). Polyalkyleneglycol, polyalkylene glycol ether, imidazolidinones, pyrrolidones, pyrimidinones, dimethyl sulfoxide and dimethyl formamide which have much higher boiling points have shown higher extraction levels of nitrogen-containing compounds (Mokhtar et al., 2014; Abro et al., 2016). However, the boiling points of these solvents are in the same range as some nitrogen-containing compounds, and thus may not be easily separated from the extracted compounds, discouraging solvent recovery by distillation. Besides boiling points, poor selectivity still stands as the major deterrent in the application of solvent extraction.

Considering the poor selectivity witnessed with the use of organic solvents, researchers redirected their efforts towards the use of ionic liquids (ILs) to try and selectively remove nitrogen-containing compounds from fuel. Ionic liquids are described as liquids composed entirely of ions at or below 100°C - more like an ambient temperature molten salt (Abro et al., 2016; Ibrahim et al., 2017). The cations are normally organic and are a basis upon which much of their physicochemical properties are derived, and the anions can be organic or inorganic. Extraction of nitrogen-containing compounds using ILs is based on their solubility that is determined by the chemical interactions involving the acid proton and steric factors in the IL. The use of ionic liquids gained momentum over the past decade with researchers attempting to use various combinations of cations and anions, dialkylimidazolium salts being the most common due to their desirable physical properties and ease of synthesis (Abro et al., 2016).

The chemical structures of ILs are now being tailor made to target certain physicochemical properties to obtain what are termed task specific or designer solvents which allow for better selectivity. In some cases, ILs have been designed to act as both oxidation catalysts and extractants. The ILs catalyse the oxidation of the sulfur- and nitrogen-containing compounds, improving their solubility in the ILs which also act as the

extractant (Bhutto et al., 2016). The performance of the ILs in the presence of oxidant is remarkably higher, although efforts are needed to reduce the amounts of oxidant (Abro et al., 2016). Normally polyoxometalates such as vanadium and tungsten are used as the catalytic cations and H_2O_2 as oxidant (Lu et al., 2007). Researchers have also explored the use of supported ionic liquid phase (SILP) systems where the ionic liquid is dispersed on a support such as silica to increase surface area, reduce mass transfer limitations and for ease of use (Kuhlmann et al., 2009; Kohler et al., 2010). Leaching is still a challenge, an area that still requires more attention. The development of these SILPs demonstrate the importance of ease of separation in the fuel refinery process which leads use to adsorptive separation (Forte et al., 2014).

Overall, the biggest limit for solvent extraction is poor selectivity. The use of ILs is also mired by the presence of potent complex-forming agents in the fuel matrix. The presence of water, acids, halide ion and other impurities is known to significantly affect their structure and ultimately their physicochemical properties *e.g.*, ILs based on $AlCl_3$ and $AlCl_4$ form precipitates when exposed to moisture (Dembaremba et al., 2020). The fuel matrix is a complex mixture that contains such components that may incapacitate the ILs over a number of cycles.

Adsorptive denitrogenation

The use of adsorbents to selectively adsorb nitrogen-containing compounds from fuel oil is the most lucrative option and a lot of research has been revolving around this technique. This is because of the advantages offered by adsorbents that make upscaling feasible and affordable: ease of separation after use, lower risk of noxious sub-products and easy to set-up and operate with the possibility of having a continuous flow system (Putra et al., 2009). However, the challenge has been on finding suitable adsorbents with high capacities and selectivity, and these are dependent on the mechanisms of adsorption.

Adsorption in primitive materials is mainly based on trapping molecules in their cavities based on their sizes (critical diameters and volumes) while in more advanced materials interactive forces that are important for improved selectivity are involved, *e.g.* acid-base interactions, coordination bond formation, π-complexation, hydrogen-bonding and van der Waals forces (Khan et al., 2013; Hasan and Jhung, 2015; Ahmed and Jhung, 2016a). Van der Waals forces are the most popular with hydrogen bonding being more relevant to adsorption of nitrogen-containing compounds. However, van der Waals forces are very weak in nature. Adsorption *via* π-complexation requires the donation of electrons from the π-orbitals of the adsorbates to vacant s-orbitals of the metal and back donation of d-elections of the metal to the empty π antibonding orbitals of the adsorbates. Transition metals in the d-block such as Cu^+ and Ag^+ and Ni^{2+} are good candidates for π-complexation, Cu^+ being more prominent since it is cheaper and more readily available. Basic nitrogen-containing compounds can also undergo a special type of acid-base interaction that forms coordination bonds. The adsorbent serves as the Lewis acid while the nitrogen-containing compounds are the Lewis bases. Based on the Pearson's hard and soft acid-base theory, basic nitrogen-containing compounds are in the hard to intermediate category and prefer hard Lewis acid sites (*e.g.* Fe^{3+}, Cr^{3+}, and Al^{3+}) (Pearson, 1963). Suitable materials are those with coordinatively unsaturated sites (Kim et al., 2011; Maes et al., 2011; Van de Voorde et al., 2013a).

The drive is now on refining the materials through designing and testing to achieve high selectivity for nitrogen-containing compounds. Research contributions on this subject have been increasing and materials summarized in Table 3 are meant to provide a guide in that regard.

Adsorptive denitrogenation using traditional adsorbents

Several primitive general adsorbents have been tested as potential adsorbents for removing nitrogen-containing compounds from fuel and these include clays (Mambrini et al., 2013; Baia et al., 2017), silicas and aluminosilicates (Kim et al., 2006; Kwon et al., 2008; Zhang et al., 2010; Rashidi et al., 2015; Laredo et al., 2017; Suganuma et al., 2020), zeolites (Hernández-Maldonado and Yang, 2004; Tian et al., 2020; Ofoghi et al., 2021), activated carbon (Sano et al., 2004; Kim et al., 2006; Ahmed and Jhung, 2015a; Anisuzzamana et al., 2018; Suganuma et al., 2020) and ion exchange resins (Marcelin et al., 1986; XiE et al., 2010) (Table 3). Composite materials that include these materials have also been widely tested (Song et al., 2017; Wang et al., 2019). The biggest advantage is that most of these materials are cheap and readily available. Althought most model fuel studies have yielded wonderful results in terms of loading capacities and recoverability of the adsorbents selectivity remains a challenge when they are applied on real fuel samples. Nevertheless, testing of these materials has provided a lot of information that has inspired the development of various tailor made adsorbents for the removal of nitrogen compounds.

Adsorptive denitrogenation using tailored organic polymers

Organic polymers can be effective adsorbents through hydrogen bonding, π-π interactions, van der Waals forces and electrostatic interactions. They can be tactically synthesized to achieve high selectivity for nitrogen-containing compounds through these adsorption mechanisms by creating selective binding sites that recognize and have a higher affinity for template molecules of interest. One approach is to polymerize monomers in the presence of template molecules of interest which are then removed after polymerization through leaching to

TABLE 3 Typical examples of adsorbents that have been tested for adsorptive denitrogenation.

Adsorbent	Feedstock	Performance	References
General adsorbents			
Fe(III) impregnated bentonite clay	Quinoline and methylene blue	Total adsorbed nitrogen (39 mg g^{-1})	Mambrini et al. (2013)
Activated carbon, MAXSORB-II	Straight run gas oil	0.039 g N g adsorbent	Sano et al. (2004)
CuCl/activated carbon	Quinoline and indole in *n*-octane/*p*-xyene (75:25)	AC: quinoline (64 mg/g), indole (63 mg/g); CuCl/AC: quinoline (126 mg/g), indole (168 mg/g)	Ahmed and Jhung, (2015a)
Mesoporous silicas	Light gas oils	Up to 8.05 mg N per g adsorbent	Kwon et al. (2008)
Zeolites containing cuprous cations	Commercial diesel	Alkyl carbazoles completely removed	Hernández-Maldonado and Yang, (2004)
Yttrium ion-exchanged Y zeolite	Indole and quinoline in *n*-octane	Up to 12.37 mg per g adsorbent	Tian et al. (2020)
X-type zeolites	Quinoline in isooctane	Up to 17 mg N per g adsorbent	Ofoghi et al. (2021)
Hexagonal mesoporous silicas (molecular sieves) Ti–HMS	Pyridine, quinoline and indole in *n*-octane (N concentration 200 μg g^{-1}) and diesel	Pyridine > quinoline > indole diesel (90% N removal)	Zhang et al. (2010)
Ion exchange resins	Shale-derived oils	Up to 0.072 g N/g resin	Marcelin et al. (1986)
Aluminosilicate mesostructures (MSU-S) and HPW and NiO-HPW modified MSU-S	Quinoline and carbazole in n-hexadecane/*n*-octane (50:50)	MSU-S (0.4 mmol/g), HPW-MSU-S (0.43 mmol/g) and NiO/HPW-MSU-S (0.44 mmol/g) ~7% increase in nitrogen uptake in modified MSU-S	Rashidi et al. (2015)
Tailored organic polymers			
Styrene-divinylbenzene copolymer	Model fuel and crude oil	pyridine (99.9%), pyrrole (99.7%)	Awokoya et al. (2021)
Vinylpyridine based polymer	Indole in *n*-octane	Indole (31.80 mg g^{-1})	Cao et al. (2014)
Polybenzimidazole fibres	Model fuel and spiked diesel	pyrimidine (11.5 mg g^{-1}), carbazole (11.8 mg g^{-1}), quinoline (11.0 mg g^{-1})	Abdul-quadir et al. (2019)
Poly 4-vinyl aniline-*co*-divinylbenzene	Model fuel and Sasol diesel 500	pyridine (30.2 mg g^{-1})	Mathidala and Ogunlaja, (2019)
Poly-2-(1H-imidazol-2-yl)-4-phenol microspheres	Model fuel and diesel	pyrimidine (10.56 mg g^{-1}), carbazole (11.71 mg g^{-1}), quinoline (10.84 mg g^{-1})	Abdul-Quadir et al. (2018a)
Poly 2-(1H-imidazol-2-yl)-4-phenol nanofibers	Model fuel and diesel	quinoline (11.7 mg g^{-1}), pyrimidine (11.9 mg g^{-1}), carbazole (11.3 mg g^{-1})	Abdul-Quadir et al. (2018b)
Fe_3O_4 nanoparticles equipped magnetic molecularly imprinted polymers	Model fuel	indole (37.58 mg g^{-1})	Niu et al. (2014)
Coordination polymers			
MIL-101 (Cr)	Straight run gas oil (SRGO) and light cycle oil (LCO)	SRGO (9.0 mg N per g), LCO (19.6 mg N per g) Adsorption due to π-π stacking interactions with terephthalate bridges of MOF	Nuzhdin et al. (2010)
MIL-100 (Al^{3+}, Cr^{3+}, Fe^{3+}, V^{3+})	Indole and 1,2-dimethylindole in heptane	Indole (V>Cr>Fe>Al) 1,2-Dimethylindole (V>Cr>Al>Fe) MIL-100(V)vac has best performance due to CUSs Indole>1,2-Dimethylindole	Van de Voorde et al. (2013a)
MIL-101 (Cr)	Pyridine	Pyridine (950 mg/g) pyridine adsorption *via* CUSs	Kim et al. (2011)
MIL-101 (Cr)	SRGO and LCO	MIL-101 (Cr) showed better adsorption than silica gel, Selexsorb® CD, Selexsorb® CDX and activated carbon (2.3 times higher adsorption capacity, two times rate of adsorption) Adsorbent regenerated 280 times using acetone No significant uptake (<1 wt%) in MOFs without open metal sites (MIL-47/MIL53)	Laredo et al. (2016) Maes et al. (2011)

(Continued on following page)

TABLE 3 (*Continued*) Typical examples of adsorbents that have been tested for adsorptive denitrogenation.

Adsorbent	Feedstock	Performance	References
MIL-100(Fe, Cr, Al), MIL-101(Cr), $[Cu_3(BTC)_2]$, CPO-27(Ni), CPO-27(Co), MIL-47/MIL-43	Indole, 2-methylindole, 1,2-dimethylindole in heptane or heptane/toluene (80:20)	Reduced uptake when solvent was changed to heptane/toluene (80:20)	
MIL-96(Al), MIL-53(Al) and MIL-101(Cr)	Pyridine, pyrrole, quinoline and indole in *n*-octane	Highest adsorption in MIL-101(Cr) due to CUSs Adsorption in MIL-96(Al) and MIL-53(Al) demonstrated importance of pore shape and size	Wang et al. (2013)
MIL-53(Fe)	Indole and benzothiazole in heptane/isopropanol	Indole (22 wt%), benzothiazole (59 wt%) Hydrogen bonding	Van de Voorde et al. (2013b)
UiO-66—SO_3H	Indole in *n*-octane	Indole (37% improved uptake compared to pristine UiO-66) Hydrogen bonding with O in (-SO_3H)	Ahmed et al. (2015)
UiO-66 and UiO-66-NH_2	Pyridine	Improved adsorption capacity and kinetics in UiO-66-NH2 compared to pristine UiO-66	Hasan et al. (2014)
UiO-66 and UiO-66-NH_2	Indole	UiO-66 (213 mg/g) > UiO-66-NH2(100) (312 mg/g) due to increased hydrogen bonding from amine group	Ahmed and Jhung, (2015b)
CuCl impregnated MIL-100(Cr)	Quinoline, indole in n-octane/p-xylene (75:25 v/v)	Quinoline (9%) and indole (15%) improved uptake comparedto pristine MIL-100(Cr)	Ahmed and Jhung, (2014)
Phosphotungstic acid impregnated MIL-101	Quinoline, indole	20% increase in quinoline uptake, no change for indole Acidic MOFs good for the adsorption of hard bases	Ahmed et al. (2013a)
$AlCl_3$ loaded MIL-100(Fe)	Quinoline and indole	17% increase in uptake of quinoline, no change for indole $AlCl_3$ is a Lewis acid salt	Ahmed et al. (2014)
MIL-101(Cr) functionalized with -SO_3Ag	Quinoline, indole in *n*-octane/toluene (85:15 v/v)	50% increase in uptake, maintained uptake in presence of toluene	She et al. (2018)
Composite materials			
$Fe_3O4@SiO_2$@PILs (magnetic polymeric ionic liquids) PILs were grafted on silica-coated Fe_3O_4	Pyridine, quinoline, indole, carbazole in toluene/heptane (80:20)	Pyridine (80.28%), quinoline (84.45%), indole (32.48), carbazole (28.47)	Wang et al. (2019)
Mesoporous Ti-HMS/KIL-2 composite	Pyridine and quinoline in *n*-octane	Pyridine(90%), quinoline (90%) Increased surface area compared to precursor compounds	Song et al. (2017)
ZIF-67(x)@H_2N-MIL-125 [Z67(x)@M125]	Indole, 1-metylindole, quinoline, pyrrole and pyridine in *n*-octane	Indole (680 mg/g) Indole>1-methylindole>quinoline>pyrrole>pyridine H-bonding, cation-π, acid-base and π-complexation	Bhadra and Jhung, (2020)
Graphene oxide (GnO)/MIL-101 (Cr) composite	Indole or quinoline in n-octane	GnO/MIL-101 indole (593 mg/g), quinoline (484 mg/g) > MIL-101 indole (416 mg/g), quinoline (446 mg/g)	Ahmed and Jhung, (2016b)
Graphite oxide/MIL-101(Cr)	Quinoline and indole in *n*-octane/*p*-xylene (75:25)	Improved uptake of quinoline (24%) and indole (30%) in GO/MIL-101 compared to pristine MIL-101	Ahmed et al. (2013b)

obtain molecularly imprinted polymers (MIPs) (Awokoya et al., 2021). Several molecularly imprinted polymer materials in different forms (beads, nanofibers *etc.*) have been synthesized and tested for the removal of nitrogen-containing compounds. Typical MIPs and their performances have been summarized in Table 3. (Cao et al., 2014; Niu et al., 2014; Abdul-Quadir et al., 2018a; Abdul-Quadir et al., 2018b; Abdul-quadir et al., 2019; Mathidala and Ogunlaja, 2019; Awokoya et al., 2021). These include Fe_3O_4 nanoparticles equipped MIPs that are magnetic for ease of separation (Niu et al., 2014). A method for removing nitrogen compounds from gasoline or diesel fuel using molecularly imprinted polymers has been patented (Rinne and Risto, 2022). Literature search revealed limited study on the use of molecularly imprinted polymer for the selective adsorption of organonitrogen compounds in real fuel samples.

Adsorptive denitrogenation using coordination polymers

Research around the refinement of materials to achieve high selectivity has been tending towards coordination polymers (CPs), particularly metal organic frameworks (MOFs) due to the several provisions they offer. CPs are classes of crystalline repeating coordination entities between transition-metal clusters or ions and multidentate organic linkers extending in 1, 2 or

3 dimensions (Kitagawa et al., 2004; Batten et al., 2013). Three-dimensional CPs (MOFs) are the most popular for adsorption work as they contain uniformly sized pores, high total pore volume and very high surface areas (Kitagawa et al., 2004; Jiang, 2015). Due to the ability to tap into both the inorganic and organic aspects, MOFs are ideal candidates for tailoring good selectivity. The design strategies used to obtain particular pore sizes and modify pore properties are also simple, and these include control of their composition, structure, scale and the bulk properties (Schneemann et al., 2014; Kenta, 2017). There is a also a vast range of transition metal clusters/ions and organic building blocks to choose from.

Due to the preferential adsorption of nitrogen-containing compounds, especially on coordinatively unsaturated sites, adsorptive denitrogenation using MOFs is prominent (Ahmed and Jhung, 2016a). Nuzhdin *et al.* (Nuzhdin et al., 2010) pioneered the use of MOFs in adsorptive denitrogenation by testing the performance of the common MIL-101 (Cr^{3+}) MOF using indole, carbazole and their alkyl substituted derivatives. They realized an uptake of 9.0 mg nitrogen per gram of MIL-101 from straight run gas oil and 19.6 mg nitrogen per gram of MIL-101 from light cycle oil. They attributed the high sorption capacity to coordination of the nitrogen-containing compounds (*via* nitrogen) to the unsaturated Cr^{3+} centres. Selectivity for nitrogen-containing compounds decreased in the order indole > indole derivatives > carbazole > carbazole derivatives which they explained in terms of indole and derivatives having better steric accessibility of the nitrogen atom to the Cr^{3+} centre while the alkyl substituents cause steric hindrance. Simultaneous adsorption of other aromatic molecules was observed due to π-π stacking interactions with terephthalate bridges of metal-organic framework.

Maes *et al.* (Maes et al., 2011) screened a wide variety of MOFs with and without open metal sites for the selective adsorption of indole (IND), 2-methylindole (2MI), 1,2-dimethylindole (1,2DMI), carbazole (CBZ), and *N*-methyl carbazole (NMC) over TP, BT, and DBT (Table 3). They concluded that the availability and nature of open sites were crucial in the adsorption of nitrogen-containing compounds in the presence of other aromatic compounds. However, uptake was greatly reduced when the solvent system was switched from heptane/toluene (H/T, ratio 80:20 v/v) to toluene/heptane (T/H, 80:20 v/v). The reduction was attributed to the contribution of the aromatic rings in the MOFs and co-adsorption of competing toluene molecules.

Van de Voorde *et al.* (Van de Voorde et al., 2013a) found an Fe terephthlate MOF MIL100(Fe) to be efficient for the selective removal of *N*-heterocyclic compounds (Table 3). They extended their studies to isostructural terephthalate MOFs by varying the metal centre, MIL-100 (Al^{3+}, Cr^{3+}, Fe^{3+}, V^{3+}) and investigated the role of the metal centre in the adsorptive removal of nitrogen-containing compounds from fuel. Their calorimetric observations were coherent with the trend in the initial slopes of the isotherms, decreasing in the order: V > Cr > Fe > Al. They

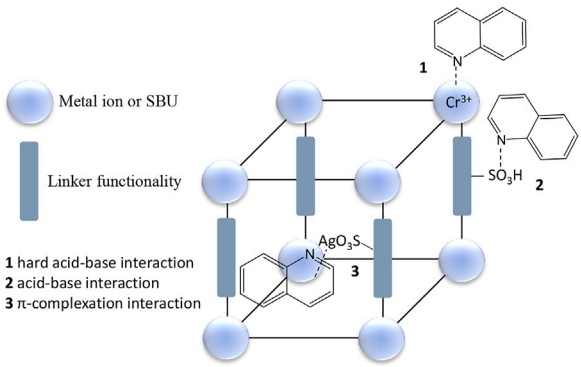

FIGURE 5
Schematic representation of the multiple interaction sites in the highly selective MOF, (Cr)-MIL-101-SO_3Ag, reported by She *et al.* (She et al., 2018).

confirmed the formation of coordinated species for indole and dimethyl indole. The results for the polarizing power of the Lewis acid centres were inconclusive, similar with most other studies in literature, but it was clear that Fe^{3+} possesses the weakest Lewis acidity in perfect agreement with the observed lack of stable indole-Fe^{3+} coordination complexes in MIL-100(Fe). Al^{3+} in MIL-100(Al) had the lowest affinity for indole. Investigations on the adsorption of pyridine on MIL-101(Cr^{3+}) by Kim *et al.* (Kim et al., 2011) also confirmed the formation of a coordination bond between the pyridine N and the coordinatively unsaturated sites in Cr^{3+}. Wang *et al.* (Wang et al., 2013) showed that the stronger the basicity of the nitrogen-containing compounds the better the adsorption on MIL-101 (Cr^{3+}). They also clarified the importance of pore shape and size in adsorption using MIL-53(Al) and MIL-96(Al). MIL-101(Cr^{3+}) which is the best performing MOF in the MIL series was also shown to outperform silica gel, Selexsorb® CD, Selexsorb® CDX and activated carbon by far in the adsorption of nitrogen-containing compounds from straight run gas and light cycle oil with exceptional adsorption capacity and the fastest kinetics (Laredo et al., 2016). Adsorption studies on IL-53(Fe) which contains no coordinatively unsaturated metal sites showed that the material relies on adsorbates being good hydrogen bond acceptors (Van de Voorde et al., 2013b).

Following these revelations on what matters regarding adsorption of nitrogen-containing compounds using MOFs researchers went on a drive to improve the adsorption performance of other MOFs through modifications which include incorporation of functional groups (*e.g.* $–SO_3H$, amino group) (Hasan et al., 2014; Ahmed et al., 2015; Ahmed and Jhung, 2015b) and Lewis acid sites (*e.g.* CuCl, phosphotungstic acid and $AlCl_3$) (Ahmed et al., 2013a; Ahmed et al., 2014; Ahmed and Jhung, 2014) (Table 3). Composites between MOFs, and MOFs with other materials such as graphene oxide have also been tested

(Table 3) (Ahmed et al., 2013b; Ahmed and Jhung, 2016b; Bhadra and Jhung, 2020). Lewis acid sites are also used to add functional moieties inside the pores of the MOFs (Van de Voorde et al., 2013b). She *et al.* (She et al., 2018) reported a highly selective metal organic framework with immobilized Ag(I) sites, (Cr)-MIL-101-SO_3Ag, which nitrogen-containing compounds to interact with adsorption sites through multiple ways simultaneously (Figure 5).

The approach of using MOFs is not impeccable. Firstly, MOFs are generally expensive due to the types of ligands or synthesis protocols used to obtain them. It can be capital intensive in industries such as the fuel industry where bulk quantities are required. In that regard, development of MOFs is being carried out with ease of separation and reusability in mind. Magnetism has been applied in some MOFs for ease of separation from the fuel matrix (Jin et al., 2014). Carrying out adsorption under continuous flow conditions can also be helpful. Secondly, synthesizing the desired MOF in a short period of time when scaling up remains a challenge. Sometimes the bulk powder form does not always match the structure of the target product. Bulk quantities are also usually obtained in a fine powder form with poor mechanical strength which makes re-use difficult. Aggregation during use or recycling may compromise the performance of the MOFs. Thirdly, some MOFs are sensitive to the environment, *e.g.*, temperature and moisture. Lastly, adsorption in MOFs is based on small pore apertures which result in high diffusion resistance due to steric and dynamic hindrance limiting the movement of sulfur- and nitrogen-containing compounds into the inner pores. Nevertheless, if adsorptive denitrogenation is to be achieved it will most likely be through coordination polymer based-materials due to the several advantages they offer.

Perspectives and advances

Hydrotreament remains the main process used for removing sulfur- and nitrogen-containing compounds from crude oil. It is easier for industry to adopt improvements around this process compared to introducing new processes. The limits of the technique (remaining economically viable and the ability to process harsh feedstocks) are now being challenged by the recently imposed legislations that require ultra-low sulfur levels (<10 ppm) in fuel oil products. This has prompted major reconsiderations into process optimizations, catalyst designs, use of additives, blending with cleaner streams, and possible complimentary or alternative desulfurization methods. To date, none of the proposed alternative desulfurization methods such as biodesulfurization, extractive desulfurization, oxidative desulfurization and adsorptive desulfurization has resulted in a commercially viable process. The main inhibiting factor is the additional processing units required to incorporate the alternative technologies, such as the oxidation unit and extraction unit which require a high capital investment. It may be cheaper to add an adsorptive denitrogenation pre-treatment step since pre-treatment steps already exist in industry for example towards demulsifying, desalting, deasphalting and demetallization.

Improvements around the hydroprocessing technique has reached its apex, especially process optimization, and major changes will be difficult to achieve unless fundamental changes are made to the catalysts. There are still gaps that can be addressed in the design and use of catalysts, an area that was extensively covered in this review. Catalyst improvements range from perfecting the support materials, fine-tuning the active phases of standard catalysts by using chelating agents and additives, design of PMs-containing catalysts and trimetallic systems, and other synthesis strategies. From the works cited, catalyst activity improves with these changes. However, the efficiency of the improved catalysts on refractory compounds still remains a challenge. Even with those improvements, the catalysts are still not immune to the inhibitory effects that mostly come of nitrogen containing compounds. The inhibitory effects of nitrogen-containing compounds also have a serious impact on achieving ultra-deep hydrodesulfurization. As a result, there is huge motivation for pre-treatment of feedstocks to remove nitrogen-containing compounds prior to hydroprocessing in order to achieve deep hydrotreatment.

Despite the lack of industrial application of adsorbents currently for removal of nitrogen-containing compounds from crude oil, research in this direction is promising. Several strides have been made in the refinement of liquid-liquid partitioning techniques, with ionic liquids addressing most of the challenges that limit the selectivity of extraction solvents. The use of traditional adsorbents such as zeolites and carbon materials suffer lack of specificity for the nitrogen-containing compounds but nanoarchitectured coordination polymers (CPs) have recently been overcoming most of the challenges. It was identified that lack of synergy among the key features during adsorption, especially the metal centre and linker properties, is the biggest shortfall in most of the CPs from achieving good selectivity. It is assumed that an entity is either adsorbed based on its interaction with the linker or through interaction with the metal centre, but not effectively with both at the same time. That could also explain the lack of coherence in the results reported by authors so far with change in linkers, target molecules and when toluene was added as no resolute trend can be interpreted from the data. It was also noted that when looked at independently, coordination *via* coordinatively unsaturated sites provides a better chance to achieve good selectivity compared to any other mechanism. As considerations for the key features to work together are being made, it is important to have coordinatively unsaturated sites as the primary focus and exclude the other adsorption mechanisms as much as possible if good selectivity is to be achieved. This is particularly more important for crude oil since it

is a very complex mixture with several competing molecules. Recent work from She *et al.* (Ahmed et al., 2015) has clearly demonstrated how focusing on design strategies can lead to highly remarkable selectivity for nitrogen-containing compounds. The governing factors should also be affordability and reusability of the coordination polymers.

Pre-treatment of crude oil to remove nitrogen-containing compounds undoubtedly helps to achieve ultra-deep hydrodesulfurization using conventional hydroprocessing. Coupled with the successes being made with coordination polymers, as well as as other adsorbents and solvents for liquid-liquid partitioning, it warrants research to put more effort in this direction. Removal of nitrogen-containing compounds from feedstock can also result in significant improvements of other downstream processes. High nitrogen content feedstock such as creosote are becoming more readily available syncrude oil sources and this approach will make it possible to process them sustainably. Besides, hydrodenitrogenation in itself is not an economical process hence pre-treatment of feedstock to remove nitrogen-containing compounds should improve the efficiency of hydroprocessing and also reduce operational costs. With concerted efforts on adsorbent and catayst development/catalyst stacking technology, it should be possible to study the application of these techniques in tandem for ultra-deep desulfurization. It will be important to consider the economical aspects for the implementation of this technique, of which there is no literature that clearly provides answers in that regard. It is crucial to provide more literature on the total cost and benefits of adding the pre-treatment step compared to intensifying hydroprocessing conditions and continuously replacing catalyst.

Author contributions

TD and SM: writing—original draft preparation; RW, AO, and ZT: Review and editing; ZT—Conceptualization.

Funding

This work is funded through the Sasol-NRF University Collaborative Research Grants (UID 138605).

Conflict of interest

Ryan Walmsley is employed by Sasol Technology (Pty) Ltd. All authors declare no other competing interests.

The remaining authors declare that the research was conducted in the absence of any commercial or financial relationships that could be construed as a potential conflict of interest.

Publisher's note

References

Abdul-Quadir, M. S., Ferg, E. E., Tshentu, Z. R., and Ogunlaja, A. S. (2018). Remarkable adsorptive removal of nitrogen-containing compounds from hydrotreated fuel by molecularly imprinted poly-2-(1H -imidazol-2-yl)-4-phenol nanofibers. *RSC Adv.* 8 (15), 8039–8050. doi:10.1039/c8ra00543e

Abdul-Quadir, M. S., van Der Westhuizen, R., Welthagen, W., Ferg, E. E., Tshentu, Z. R., Ogunlaja, A. S., et al. (2018). Adsorptive denitrogenation of fuel over molecularly imprinted poly-2-(1H-imidazol-2-yl)-4-phenol microspheres. *New J. Chem.* 42 (15), 13135–13146. doi:10.1039/c8nj02818d

Abdul-quadir, M. S., van der Westhuizen, R., Welthagen, W., Ferg, E. E., Tshentu, Z. R., Ogunlaja, A. S., et al. (2019). Selective removal of organonitrogen compounds in fuel using functional polybenzimidazole nanofibres: A combined experimental and theoretical study. *S. Afr. J. Chem.* 72, 88–100. doi:10.17159/0379-4350/2019/v72a12

Abro, R., Abro, M., Gao, S., Bhutto, A. W., Ali, Z. M., Shah, A., et al. (2016). Extractive denitrogenation of fuel oils using ionic liquids: A review. *RSC Adv.* 6, 93932–93946. doi:10.1039/c6ra09370a

Ahmed, I., and Jhung, S. H. (2014). Adsorptive denitrogenation of model fuel with CuCl-loaded metal–organic frameworks (MOFs). *Chem. Eng. J.* 251, 35–42. doi:10.1016/j.cej.2014.04.044

Ahmed, I., and Jhung, S. H. (2016). Adsorptive desulfurization and denitrogenation using metal-organic frameworks. *J. Hazard. Mat.* 301, 259–276. doi:10.1016/j.jhazmat.2015.08.045

Ahmed, I., and Jhung, S. H. (2015). Effective adsorptive removal of indole from model fuel using a metal-organic framework functionalized with amino groups. *J. Hazard. Mat.* 283, 544–550. doi:10.1016/j.jhazmat.2014.10.002

Ahmed, I., and Jhung, S. H. (2016). Remarkable adsorptive removal of nitrogen-containing compounds from a model fuel by a graphene oxide/MIL-101 composite through a combined effect of improved porosity and hydrogen bonding. *J. Hazard. Mat.* 314, 318–325. doi:10.1016/j.jhazmat.2016.04.041

Ahmed, I., and Jhung, S. H. (2015). Remarkable improvement in adsorptive denitrogenation of model fossil fuels with CuCl/activated carbon, prepared under ambient condition. *Chem. Eng. J.* 279, 327–334. doi:10.1016/j.cej.2015.05.035

Ahmed, I., Jun, J. W., Jung, B. K., and Jhung, S. H. (2014). Adsorptive denitrogenation of model fossil fuels with Lewis acid-loaded metal-organic frameworks (MOFs). *Chem. Eng. J.* 255, 623–629. doi:10.1016/j.cej.2014.06.099

Ahmed, I., Khan, N. A., Hasan, Z., and Jhung, S. H. (2013). Adsorptive denitrogenation of model fuels with porous metal-organic framework (MOF) MIL-101 impregnated with phosphotungstic acid: Effect of acid site inclusion. *J. Hazard. Mat.* 250–251, 37–44. doi:10.1016/j.jhazmat.2013.01.024

Ahmed, I., Khan, N. A., and Jhung, S. H. (2013). Graphite oxide/Metal–Organic framework (MIL-101): Remarkable performance in the adsorptive denitrogenation of model fuels. *Inorg. Chem.* 52, 14155–14161. doi:10.1021/ic402012d

Ahmed, I., Tong, M., Jun, J. W., Zhong, C., and Jhung, S. H. (2015). Adsorption of nitrogen-containing compounds from model fuel over sulfonated metal-organic framework: Contribution of hydrogen-bonding and acid-base interactions in adsorption. *J. Phys. Chem. C* 120 (1), 407–415. doi:10.1021/acs.jpcc.5b10578

Al-Dalama, K., and Stanislaus, A. (2011). Temperature programmed reduction of SiO_2–Al_2O_3 supported Ni, Mo and NiMo catalysts prepared with EDTA. *Thermochim. Acta* 520 (1-2), 67–74. doi:10.1016/j.tca.2011.03.017

Alexander, A. M., and Hargreaves, J. S. (2010). Alternative catalytic materials: Carbides, nitrides, phosphides and amorphous boron alloys. *Chem. Soc. Rev.* 39 (11), 4388. doi:10.1039/b916787k

Alonso-Pérez, M. O., Pawelec, B., Zepeda, T. A., Alonso-Núñez, G., Nava, R., Navarro, R. M., et al. (2021). Effect of the titanium incorporation method on the morphology and HDS activity of supported ternary Ni–Mo–W/SBA-16 catalysts. *Microporous Mesoporous Mat.* 312, 110779. doi:10.1016/j.micromeso.2020.110779

Alsolami, B. H. (2022). HDS for fuel cell applications. AvaliableAt: http://resolver.tudelft.nl/uuid:1d9702c6-5365-49a3-93db-70e350688093 (Accessed on April 07, 2022).

Anisuzzamana, S. M., Krishnaiah, D., and Alfred, D. (2018). Adsorption potential of a modified activated carbon for the removal of nitrogen containing compounds from model fuel. *AIP Conf. Proc.* 1930, 020013. doi:10.1063/1.5022907

Asumana, C., Yu, G., Guan, Y., Yang, S., Zhou, S., Chen, X., et al. (2011). Extractive denitrogenation of fuel oils with dicyanamide-based ionic liquids. *Green Chem.* 13, 3300. doi:10.1039/c1gc15747g

Awokoya, K. N., Okoya, A. A., and Elujulo, O. (2021). Preparation, characterization and evaluation of a styrene-based molecularly imprinted polymer for capturing pyridine and pyrrole from crude oil. *Sci. Afr.* 13, e00947. doi:10.1016/j.sciaf.2021.e00947

Badoga, S., Mouli, K. C., Soni, K. K., Dalai, A. K., and Adjaye, J. (2012). Beneficial influence of EDTA on the structure and catalytic properties of sulfided NiMo/SBA-15 catalysts for hydrotreating of light gas oil. *Appl. Catal. B Environ.* 125, 67–84. doi:10.1016/j.apcatb.2012.05.015

Badoga, S. (2015). *Synthesis and characterization of NiMo supported mesoporous materials with EDTA and phosphorus for hydrotreating of heavy gas oil*. University of Sakatchewan. Available at: https://central.bac-lac.gc.ca/.item?id=TC-SSU-2015042019&op=pdf&app=Library&oclc_number=1033227891 (Accessed July 10, 2022).

Baia, L. V., Souza, W. C., de Souza, R. J. F., Veloso, C. O., Chiaro, S. S. X., Figueiredo, M. A. G., et al. (2017). Removal of sulfur and nitrogen compounds from diesel oil by adsorption using clays as adsorbents. *Energy fuels.* 31 (11), 11731–11742. doi:10.1021/acs.energyfuels.7b01928

Bardi, U. (2019). Peak oil, 20 years later: Failed prediction or useful insight? *Energy Res. Soc. Sci.* 48, 257–261. doi:10.1016/j.erss.2018.09.022

Batten, S. R., Champness, N. R., Chen, X., Garcia-Martinez, J., Kitagawa, S., Öhrström, L., et al. (2013). Terminology of metal–organic frameworks and coordination polymers (IUPAC Recommendations 2013. *Pure Appl. Chem.* 85 (8), 1715–1724. doi:10.1351/pac-rec-12-11-20

Bhadra, B. N., and Jhung, S. H. (2020). Remarkable metal–organic framework composites for adsorptive removal of nitrogenous compounds from fuel. *Chem. Eng. J.* 398 (15), 125590. doi:10.1016/j.cej.2020.125590

Bhutto, A. W., Abro, R., Gao, S., Abbas, T., Chen, X., Yu, G., et al. (2016). Oxidative desulfurization of fuel oils using ionic liquids: A review. *J. Taiwan Inst. Chem. Eng.* 62, 84–97. doi:10.1016/j.jtice.2016.01.014

Bose, D. (2015). Design parameters for a hydro desulfurization (HDS) unit for petroleum naphtha at 3500 barrels per day. *World Sci. News* 3, 99–111.

Breysse, M., Afanasiev, P., Geantet, C., and Vrinat, M. (2003). Overview of support effects in hydrotreating catalysts. *Catal. Today* 86 (1-4), 5–16. doi:10.1016/s0920-5861(03)00400-0

Breysse, M., Geantet, C., Afanasiev, P., Blanchard, J., and Vrinat, M. (2008). Recent studies on the preparation, activation and design of active phases and supports of hydrotreating catalysts. *Catal. Today* 130 (1), 3–13. doi:10.1016/j.cattod.2007.08.018

Brunet, S., Mey, D., Pérot, G., Bouchy, C., and Diehl, F. (2005). On the hydrodesulfurization of FCC gasoline: A review. *Appl. Catal. A General* 278 (2), 143–172. doi:10.1016/j.apcata.2004.10.012

Budukva, S. V., Klimov, O. V., Uvarkina, D. D., Chesalov, Y. A., Prosvirin, I. P., Larina, T. V., et al. (2019). Effect of citric acid and triethylene glycol addition on the reactivation of CoMo/γ-Al_2O_3 hydrotreating catalysts. *Catal. Today* 329, 35–43. doi:10.1016/j.cattod.2018.10.017

Caero, L. C., Romero, A. R., and Ramirez, J. (2003). Niobium sulfide as a dopant for Mo/TiO_2 catalysts. *Catal. Today* 78 (1-4), 513–518. doi:10.1016/s0920-5861(02)00342-5

Campbell, C. J., and Laherrère, J. H. (1998). The end of cheap oil: Global production of conventional oil will begin to decline sooner than most people think, probably within 10 years. *Sci. Am.* 278 (3), 78–83.

Campos-Martin, J. M., Capel-Sanchez, M. C., Perez-Presas, P., and Fierro, J. L. G. (2010). Oxidative processes of desulfurization of liquid fuels. *J. Chem. Technol. Biotechnol.* 85, 879–890. doi:10.1002/jctb.2371

Cao, Y., Liu, L., Xu, W., Wu, X., and Huang, W. (2014). Surface molecularly imprinted polymer prepared by reverse atom transfer radical polymerization for selective adsorption indole. *J. Appl. Polym. Sci.* 131, 40473. doi:10.1002/app.40473

Cao, Z., Zhang, X., Guo, R., Ding, S., Zheng, P., Fan, J., et al. (2020). Synergistic effect of acidity and active phases for NiMo catalysts on dibenzothiophene hydrodesulfurization performance. *Chem. Eng. J.* 400, 125886. doi:10.1016/j.cej.2020.125886

Carenco, S., Portehault, D., Boissiere, C., Mezailles, N., and Sanchez, C. (2013). Nanoscaled metal borides and phosphides: Recent developments and perspectives. *Chem. Rev.* 113 (10), 7981–8065. doi:10.1021/cr400020d

Cecilia, J. A., Infantes-Molina, A., Rodríguez-Castellón, E., and Jiménez-López, A. (2009). A novel method for preparing an active nickel phosphide catalyst for HDS of dibenzothiophene. *J. Catal.* 263 (1), 4–15. doi:10.1016/j.jcat.2009.02.013

Cervantes, J. M., Huirache-Acuna, R., de Leon, J. D., Moyado, S. F., Paraguay-Delgado, F., Berhault, G., et al. (2020). CoNiMo/Al_2O_3 sulfide catalysts for dibenzothiophene hydrodesulfurization: Effect of the addition of small amounts of nickel. *Microporous Mesoporous Mat.* 309, 110574. doi:10.1016/j.micromeso.2020.110574

Chen, J. G. (1996). Carbide and nitride overlayers on early transition metal surfaces: Preparation, characterization, and reactivities. *Chem. Rev.* 96 (4), 1477–1498. doi:10.1021/cr950232u

Chen, W., Mauge, F., van Gestel, J., Nie, H., Li, D., Long, X., et al. (2013). Effect of modification of the alumina acidity on the properties of supported Mo and CoMo sulfide catalysts. *J. Catal.* 304, 47–62. doi:10.1016/j.jcat.2013.03.004

Chianelli, R. R., Berhault, G., Raybaud, P., Kasztelan, S., Hafner, J., Toulhoat, H., et al. (2020). Periodic trends in hydrodesulfurization: In support of the sabatier principle. *Appl. Catal. A General* 227 (1-2), 83–96. doi:10.1016/s0926-860x(01)00924-3

Choudhary, T. V., Parrott, S., and Johnson, B. (2008). Understanding the hydrodenitrogenation chemistry of heavy oils. *Catal. Commun.* 9, 1853–1857. doi:10.1016/j.catcom.2008.03.002

Chowdari, R. K., de León, J. N. D., and Fuentes-Moyado, S. (2020). Single step and template-free synthesis of Dandelion flower-like core-shell architectures of metal oxide microspheres: Influence of sulfidation on particle morphology & hydrodesulfurization performance. *Appl. Catal. B Environ.* 277, 119213. doi:10.1016/j.apcatb.2020.119213

Coulier, L., De Beer, V. H. J., Van Veen, J. A. R., and Niemantsverdriet, J. W. (2001). Correlation between hydrodesulfurization activity and order of Ni and Mo sulfidation in planar silica-supported NiMo catalysts: The influence of chelating agents. *J. Catal.* 197 (1), 26–33. doi:10.1006/jcat.2000.3068

de León, J. D., Picquart, M., Villarroel, M., Vrinat, M., Llambias, F. G., Murrieta, F., et al. (2010). Effect of gallium as an additive in hydrodesulfurization WS_2/γ-Al_2O_3 catalysts. *J. Mol. Catal. A Chem.* 323 (1-2), 1–6. doi:10.1016/j.molcata.2010.03.008

Dembaremba, Tendai O., Ogunlaja, Adeniyi S., and Tshentu, Zenixole R. (2020). "Coordination polymers and polymer nanofibers for effective adsorptive desulfurization," in *Nanocomposites for the desulfurization of fuels* (Hershey, Pennsylvania, United States: IGI Global), 168–234. AvaliableAt: https://www.igi-global.com/book/nanocomposites-desulfurization-fuels/235700. doi:10.4018/978-1-7998-2146-5

Dembaremba, T. O., Correa, I., Hosten, E. C., Kuznetsov, M. L., Gerber, W. J., Pessoa, J. C., et al. (2019). New $V^{IV}O$-complexes for oxidative desulfurization of refractory sulfur compounds in fuel: Synthesis, structure, reactivity trend and mechanistic studies. *Dalton Trans.* 48, 16687–16704. doi:10.1039/c9dt02505g

Dembaremba, T. O., van Der Westhuizen, R., Welthagen, W., Ferg, E., Ogunlaja, A. S., Tshentu, Z. R., et al. (2019). Comparing the catalytic activity of silica-supported vanadium oxides and the polymer nanofiber-supported oxidovanadium(IV) complex toward oxidation of refractory organosulfur compounds in hydrotreated diesel. *Energy fuels.* 33 (8), 7595–7603. doi:10.1021/acs.energyfuels.9b01579

Dincer, I., and Zamfirescu, C. (2018). 1.4 sustainability dimensions of energy. *Compr. Energy Syst.* 1, 101–152. doi:10.1016/b978-0-12-809597-3.00104-8

Duchet, J. C., Tilliette, M. J., Cornet, D., Vivier, L., Perot, G., Bekakra, L., et al. (1991). Catalytic properties of nickel molybdenum sulphide supported on zirconia. *Catal. Today* 10 (4), 579–592. doi:10.1016/0920-5861(91)80040-g

Environmental Protection Agency (2021). Air plan approval; New Hampshire; sulfur content limitations for fuels. AvaliableAt: https://www.govinfo.gov/content/pkg/FR-2021-02-08/pdf/2021-02535.pdf.

Escobar, J., Barrera, M. C., De los Reyes, J. A., Toledo, J. A., Santes, V., Colín, J. A., et al. (2008). Effect of chelating ligands on Ni-Mo impregnation over wide-pore ZrO_2-TiO_2. *J. Mol. Catal. A Chem.* 287 (1-2), 33–40. doi:10.1016/j.molcata.2008.02.022

Fetzner, S. (1998). Bacterial degradation of pyridine, indole, quinoline, and their derivatives under different redox conditions. *Appl. Microbiol. Biotechnol.* 49, 237–250. doi:10.1007/s002530051164

Forte, P., Sachse, A., Maes, M., Galarneau, A., and De Vos, D. (2014). Selective continuous flow extractive denitrogenation of oil containing S- and N-heteroaromatics using metal-containing ionic liquids supported on monolithic silica with hierarchical porosity. *RSC Adv.* 4, 1045–1054. doi:10.1039/c3ra43585g

Fuel Regulation (2022a). Diesel fuel grades. AvaliableAt: https://dieselnet.com/standards/us/fuel.php (Accessed on April 07, 2022).

Fuel Regulation (2022b). EU: Fuels: Automotive diesel fuel. AvaliableAt: https://dieselnet.com/standards/eu/fuel_automotive.php#:~:text=EN%20590%3A2004%E2%80%94Sulfur%20limits (Accessed on April 07, 2022).

García-Gutiérrez, J. L., Laredo, G. C., Fuentes, G. A., García-Gutiérrez, P., and Jiménez-Cruz, F. (2014). Effect of nitrogen compounds in the hydrodesulfurization of straight-run gas oil using a CoMoP/δ-Al_2O_3 catalyst. *Fuel* 138, 98–103. doi:10.1016/j.fuel.2014.08.008

Ghosh, P., Hickey, K. J., and Jaffe, S. B. (2006). Development of a detailed gasoline composition-based octane model. *Ind. Eng. Chem. Res.* 45, 337–345. doi:10.1021/ie050811h

Global Fuel Specification (2022). Diesel sulfur reduction remains critical as prerequisite for cleaner vehicle sales. AvaliableAt: https://stratasadvisors.com/insights/2021/10282021-global-on-road-diesel-quality-outlook (Accessed on April 07, 2022).

Glotov, A. P., Vutolkina, A. V., Vinogradov, N. A., Pimerzin, A. A., Vinokurov, V. A., Pimerzin, A. A., et al. (2021). Enhanced HDS and HYD activity of sulfide Co-PMo catalyst supported on alumina and structured mesoporous silica composite. *Catal. Today* 377, 82–91. doi:10.1016/j.cattod.2020.10.010

Gray, M. R., Ayasse, A. R., Chan, E. W., and Veljkovic, M. (1995). Kinetics of hydrodesulfurization of thiophenic and sulfide sulfur in Athabasca bitumen. *Energy fuels.* 9, 500–506. doi:10.1021/ef00051a015

Grzechowiak, J. R., Rynkowski, J., and Wereszczako-Zielinska, I. (2001). Catalytic hydrotreatment on alumina-titania supported NiMo sulphides. *Catal. Today* 65 (2-4), 225–231. doi:10.1016/s0920-5861(00)00562-9

Han, W., Nie, H., Long, X., Li, M., Yang, Q., Li, D., et al. (2017). Effects of the support Brønsted acidity on the hydrodesulfurization and hydrodenitrogention activity of sulfided NiMo/Al2O3 catalysts. *Catal. Today* 292, 58–66. doi:10.1016/j.cattod.2016.11.049

Hansmeier, A. R., Meindersma, G. W., and de Haan, A. B. (2011). Desulfurization and denitrogenation of gasoline and diesel fuels by means of ionic liquids. *Green Chem.* 13, 1907. doi:10.1039/c1gc15196g

Harris, S., and Chianelli, R. R. (1986). Catalysis by transition metal sulfides: A theoretical and experimental study of the relation between the synergic systems and the binary transition metal sulfides. *J. Catal.* 98 (1), 17–31. doi:10.1016/0021-9517(86)90292-7

Hasan, Z., and Jhung, S. H. (2015). Removal of hazardous organics from water using metal-organic frameworks (MOFs): Plausible mechanisms for selective adsorptions. *J. Hazard. Mat.* 283, 329–339. doi:10.1016/j.jhazmat.2014.09.046

Hasan, Z., Tong, M., Jung, B. K., Ahmed, I., Zhong, C., Jhung, S. H., et al. (2014). Adsorption of pyridine over amino-functionalized Metal–Organic frameworks: Attraction via hydrogen bonding versus Base–Base repulsion. *J. Phys. Chem. C* 118, 21049–21056. doi:10.1021/jp507074x

Hernández-Maldonado, A. J., and Yang, R. T. (2004). Denitrogenation of transportion fuels by zeolites at ambient temperature and pressure. *Angew. Chem.* 116, 1022.

Hidalgo-Vivas, A., Wiwel, P., Hinnemann, B., Zeuthen, P., Petersen, B. O., and Duus, J. Ø. (2022). Refractory nitrogen compounds in hydrocracking pretreatment identification and characterization. AvaliableAt: www.researchgate.net/publication/268362629 (Accessed on April 07, 2022).

Höök, M., Bardi, U., Feng, L., and Pang, X. (2010). Development of oil formation theories and their importance for peak oil. *Mar. Pet. Geol.* 27 (9), 1995–2004. doi:10.1016/j.marpetgeo.2010.06.005

Huh, E. S., Zazybin, A., Palgunadi, J., Ahn, S., Hong, J., Kim, H. S., et al. (2009). Zn-containing ionic liquids for the extractive denitrogenation of a model oil: A mechanistic consideration. *Energy fuels.* 23, 3032–3038. doi:10.1021/ef900073a

Huirache-Acuna, R., Nava, R., Peza-Leddesma, C. L., Lara-Romero, J., Alonso-Nuez, G., Pawelec, B., et al. (2013). SBA-15 mesoporous silica as catalytic support for hydrodesulfurization catalysts—review. *Materials* 6 (9), 4139–4167. doi:10.3390/ma6094139

Huirache-Acuña, R., Pérez-Ayala, E., Cervantes-Gaxiola, M. E., Alonso-Núñez, G., Zepeda, T. A., Rivera-Muñoz, E. M., et al. (2021). Dibenzothiophene hydrodesulfurization over ternary metallic NiMoW/Ti-HMS mesoporous catalysts. *Catal. Commun.* 148, 106162. doi:10.1016/j.catcom.2020.106162

Huirache-Acuña, R., Zepeda, T. A., Rivera-Muñoz, E. M., Nava, R., Loricera, C. V., Pawelec, B., et al. (2015). Characterization and HDS performance of sulfided CoMoW catalysts supported on mesoporous Al-SBA-16 substrates. *Fuel* 149, 149–161. doi:10.1016/j.fuel.2014.08.045

Ibrahim, M. H., Hayyan, M., Hashima, M. A., and Hayyan, A. (2017). The role of ionic liquids in desulfurization of fuels: A review. *Renew. Sustain. Energy Rev.* 76, 1534–1549. doi:10.1016/j.rser.2016.11.194

ICCT (2020). Diesel sulfur content impacts on euro VI soot-free vehicles: Considerations for emerging markets. AvaliableAt: https://theicct.org/publication/diesel-sulfur-content-impacts-on-euro-vi-soot-free-vehicles-considerations-for-emerging-markets/#:~:text=As%20the%20major%20vehicle%20markets,known%20as%20ultralow%2Dsulfur%20diesel.

ICCT (2022). Technical and economic analysis of the transition to ultra-low sulfur fuels in Brazil, China, India and Mexico. AvaliableAt: https://theicct.org/sites/default/files/publications/ICCT_ULSF_refining_Oct2012.pdf (Accessed on April 07, 2022).

IMO (2022). Imo 2020 – cutting sulphur oxide emissions. AvaliableAt: https://www.imo.org/en/MediaCentre/HotTopics/Pages/Sulphur-2020.aspx (Accessed on April 07, 2022).

Ishihara, A., Wang, D., Dumeignil, F., Amano, H., Qian, E. W., Kabe, T., et al. (2005). Oxidative desulfurization and denitrogenation of a light gas oil using an oxidation/adsorption continuous flow process. *Appl. Catal. A General* 279, 279–287. doi:10.1016/j.apcata.2004.10.037

Javadli, R., and de Klerk, A. (2012). Desulfurization of heavy oil. *Appl. Petrochem. Res.* 1, 3–19. doi:10.1007/s13203-012-0006-6

Jian, M., and Prins, R. (1998). Reaction Kinetics of the hydrodenitrogenation of decahydroquinoline over NiMo (P)/Al_2O_3 catalysts. *Ind. Eng. Chem. Res.* 37 (3), 834–840. doi:10.1021/ie9703292

Jiang, J. (2015). *Metal-organic frameworks materials modeling towards engineering applications*. Newton, Singapore: Jenny Stanford Publishing. AvaliableAt: www.crcpress.com/9789814613453.

Jiang, N., Jiang, B., Wang, S., and Song, H. (2021). Efficient Ni_2P/Al_2O_3 hydrodesulfurization catalysts from surface hybridization of Al_2O_3 particles with graphite-like carbon. *J. Taiwan Inst. Chem. Eng.* 121, 139–146. doi:10.1016/j.jtice.2021.03.053

Jiang, Z., Lu, H., Zhang, Y., and Li, C. (2011). Oxidative desulfurization of fuel oils. *Chin. J. Catal.* 32, 707–715. doi:10.1016/s1872-2067(10)60246-x

Jin, T., Yang, Q., Meng, C., Xu, J., Liu, H., Hu, J., et al. (2014). Promoting desulfurization capacity and separation efficiency simultaneously by the novel magnetic Fe3O4@PAA@MOF-199. *RSC Adv.* 4, 41902–41909. doi:10.1039/c4ra06515h

Kaiser, M. J., de Klerk, A., Gary, J. H., and Handwerk, G. E. (2020). *Petroleum refining technology, economics, and markets*. 6th edition. Boca Raton, Florida, United States: CRC Press.

Kanda, Y., Saito, R., Ono, T., Kon, K., Toyao, T., Furukawa, S., et al. (2022). Enhancement of the hydrodesulfurization and C–S bond cleavage activities of rhodium phosphide catalysts by platinum addition. *J. Catal.* 408, 294–302. doi:10.1016/j.jcat.2022.03.001

Karas, L. J., Grey, R. A., and Lynch, M. W. (2008). *Desulfurization process*. US Patent 2008047875.

Kent, J. A. (2010). *Kent and riegel's handbook of industrial Chemistry and biotechnology*. New York: Springer.

Kenta, K. (2017). Network polymers derived from the integration of flexible organic polymers and rigid metal–organic frameworks. *Polym. J.* 49, 345–353. doi:10.1038/pj.2016.122

Khan, N. A., Hasan, Z., and Jhung, S. H. (2013). Adsorptive removal of hazardous materials using metal-organic frameworks (MOFs): A review. *J. Hazard. Mat.* 244–245, 444–456. doi:10.1016/j.jhazmat.2012.11.011

Kibsgaard, J., Tuxen, A., Knudsen, K. G., Brorson, M., Topsoe, H., Laegsgaard, E., et al. (2010). Comparative atomic-scale analysis of promotional effects by late 3d-transition metals in MoS_2 hydrotreating catalysts. *J. Catal.* 272 (2), 195–203. doi:10.1016/j.jcat.2010.03.018

Kim, J. H., Ma, X., Zhou, A., and Song, C. (2006). Ultra-deep desulfurization and denitrogenation of diesel fuel by selective adsorption over three different adsorbents: A study on adsorptive selectivity and mechanism. *Catal. Today* 111, 74–83. doi:10.1016/j.cattod.2005.10.017

Kim, M. J., Park, S. M., Song, S., Won, J., Lee, J. Y., Yoon, M., et al. (2011). Adsorption of pyridine onto the metal organic framework MIL-101. *J. Colloid Interface Sci.* 361, 612–617. doi:10.1016/j.jcis.2011.05.067

Kishan, G., Coulier, L., De Beer, V. H. J., Van Veen, J. A. R., and Niemantsverdriet, J. W. (2000). Sulfidation and thiophene hydrodesulfurization activity of nickel tungsten sulfide model catalysts, prepared without and with chelating agents. *J. Catal.* 196 (1), 180–189. doi:10.1006/jcat.2000.3013

Kitagawa, S., Kitaura, R., and Noro, S. (2004). Functional porous coordination polymers. *Angew. Chem. Int. Ed.* 43, 2334–2375. doi:10.1002/anie.200300610

Kohler, F., Roth, D., Kuhlmann, E., Wasserscheid, P., and Haumann, M. (2010). Continuous gas-phase desulfurisation using supported ionic liquid phase (SILP) materials. *Green Chem.* 12, 979. doi:10.1039/c004883f

Kokliukhin, A., Nikulshina, M., Mozhaev, A., Lancelot, C., Blanchard, P., Briois, V., et al. (2021). Study of hydrotreating performance of trimetallic NiMoW/Al_2O_3 catalysts prepared from mixed MoW Keggin heteropolyanions with various Mo/W ratios. *J. Catal.* 403, 141–159. doi:10.1016/j.jcat.2021.02.019

Kokliukhin, A., Nikulshina, M., Mozhaev, A., Lancelot, C., Lamonier, C., Nuns, N., et al. (2021). Bulk hydrotreating MonW12-nS2 catalysts based on SiMonW12-n heteropolyacids prepared by alumina elimination method. *Catal. Today* 377, 26–37. doi:10.1016/j.cattod.2020.07.018

Koltai, T., Macaud, M., Guevara, A., Schulz, E., Lemaire, M., Bacaud, R., et al. (2002). Comparative inhibiting effect of polycondensed aromatics and nitrogen compounds on the hydrodesulfurization of alkyldibenzothiophenes. *Appl. Catal. A General* 231, 253–261. doi:10.1016/s0926-860x(02)00063-7

Kuhlmann, E., Haumann, M., Jess, A., Seeberger, A., and Wasserscheid, P. (2009). Ionic liquids in refinery desulfurization: Comparison between biphasic and supported ionic liquid phase suspension processes. *ChemSusChem* 2, 969–977. doi:10.1002/cssc.200900142

Kwon, J. M., Moon, J. H., Bae, Y. S., Lee, D. G., Sohn, H. C., Lee, C. H., et al. (2008). Adsorptive desulfurization and denitrogenation of refinery fuels using mesoporous silica adsorbents. *ChemSusChem* 1, 307–309. doi:10.1002/cssc.200700011

Laredo, G. C., Leyva, S., Alvarez, R., Mares, M. T., Castillo, J., and Cano, J. L. (2002). Nitrogen compounds characterization in atmospheric gas oil and light cycle oil from a blend of Mexican crudes. *Fuel* 81, 1341–1350. doi:10.1016/s0016-2361(02)00047-9

Laredo, G. C., Vega-Merino, P. M., Fuente, J. A. M., Mora-Vallejo, R. J., Meneses-Ruiz, E., Castillo, J. J., et al. (2016). Comparison of the metal–organic framework MIL-101 (Cr) versus four commercial adsorbents for nitrogen compounds removal in diesel feedstocks. *Fuel* 180, 284–291. doi:10.1016/j.fuel.2016.04.038

Laredo, G. C., Vega-Merino, P. M., Pérez-Romo, P., Navarrete-Bolaños, J., and Trejo-Zárraga, F. (2017). Adsorption of nitrogen compounds from diesel fuels over alumina-based adsorbent towards ULSD production. *Pet. Sci. Technol.* 35, 392–398. doi:10.1080/10916466.2015.1021012

Leal, E., Torres-Mancera, P., and Ancheyta, J. (2022). Catalyst stacking technology as a viable solution to ultralow sulfur diesel production. *Energy fuels.* 36 (6), 3201–3218. doi:10.1021/acs.energyfuels.1c04038

Lélias, M. A., Le Guludec, E., Mariey, L., Van Gestel, J., Travert, A., Oliviero, L., et al. (2010). Effect of EDTA addition on the structure and activity of the active phase of cobalt–molybdenum sulfide hydrotreatment catalysts. *Catal. Today* 150 (3-4), 179–185. doi:10.1016/j.cattod.2009.07.107

Leliveld, B., and Slettenhaar, B. (2022). CELESTIA™: A revolutionary new hydroprocessing catalyst providing ultra-high activity. AvaliableAt: https://www.albemarle.com/storage/wysiwyg/cat_catalyst_courier_89_celestia_final_article.pdf (Accessed on April 07, 2022).

Li, H., Li, M., Chu, Y., Liu, F., and Nie, H. (2011). Essential role of citric acid in preparation of efficient NiW/Al2O3 HDS catalysts. *Appl. Catal. A General* 403 (1-2), 75–82. doi:10.1016/j.apcata.2011.06.015

Lima, F., Dave, M., Silvestre, A. J. D., Branco, L. C., and Marrucho, I. M. (2019). Concurrent desulfurization and denitrogenation of fuels using deep eutectic solvents. *ACS Sustain. Chem. Eng.* 7, 11341–11349. doi:10.1021/acssuschemeng.9b00877

Lin, Z., Denny, S. R., and Chen, J. G. (2021). Transition metal carbides and nitrides as catalysts for thermochemical reactions. *J. Catal.* 404, 929–942. doi:10.1016/j.jcat.2021.06.022

Liu, X., Zhang, C., Liu, T., Jiang, Z., and Li, C. (2020). Effect of Zr on catalytic performance of unsupported Ni (Zr) Mo and Ni (Zr) W sulfide catalysts for quinoline hydrodenitrogenation. *Appl. Catal. A General* 604, 117744. doi:10.1016/j.apcata.2020.117744

Liu, Y., Xu, B., Qin, B., Tao, C., Cao, L., Shen, Y., et al. (2020). Novel NiMoW-clay hybrid catalyst for highly efficient hydrodesulfurization reaction. *Catal. Commun.* 144, 106086. doi:10.1016/j.catcom.2020.106086

Lu, L., Cheng, S., Gao, J., Gao, G., and He, M. (2007). Deep oxidative desulfurization of fuels catalyzed by ionic liquid in the presence of H_2O_2. *Energy fuels.* 21 (1), 383–384. doi:10.1021/ef060345o

Ma, X., Sakanishi, K., and Mochida, I. (1996). Hydrodesulfurization reactivities of various sulfur compounds in vacuum gas oil. *Ind. Eng. Chem. Res.* 35, 2487–2494. doi:10.1021/ie960137r

Maes, M., Trekels, M., Boulhout, M., Schouteden, S., Vermoortele, F., Alaerts, L., et al. (2011). Selective removal of N-heterocyclic aromatic contaminants from fuels by Lewis acidic metal-organic frameworks. *Angew. Chem. Int. Ed.* 50, 4210–4214. doi:10.1002/anie.201100050

Maity, S. K., Flores, G. A., Ancheyta, J., and Rana, M. S. (2008). Effect of preparation methods and content of phosphorus on hydrotreating activity. *Catal. Today* 130 (2-4), 374–381. doi:10.1016/j.cattod.2007.10.100

Majodina, S., Tshentu, Z. R., and Ogunlaja, A. S. (2021). Effect of adding chelating ligands on the catalytic performance of Rh-promoted MoS_2 in the hydrodesulfurization of dibenzothiophene. *Catalysts* 11 (11), 1398. doi:10.3390/catal11111398

Mambrini, R. V., Saldanha, A. L. M., Ardisson, J. D., Araujo, M. H., and Moura, F. C. C. (2013). Adsorption of sulfur and nitrogen compounds on hydrophobic bentonite. *Appl. Clay Sci.* 83–84, 286–293. doi:10.1016/j.clay.2013.08.030

Marcelin, G., Cronauer, D. C., Vogel, R. F., Prudich, M. E., and Solash, J. (1986). Shale oil denitrogenation with ion exchange. 2. Evaluation of ion-exchange adsorbents and resin treatment procedures. *Ind. Eng. Chem. Proc. Des. Dev.* 25 (3), 747–756. doi:10.1021/i200034a026

Mathidala, S., and Ogunlaja, A. S. (2019). Selective removal of pyridine in fuel by imprinted polymer (poly 4-vinyl aniline-*co*-DVB) as adsorbent. *Pet. Sci. Technol.* 37, 1691–1703. doi:10.1080/10916466.2019.1602641

Mendoza-Nieto, J. A., Vera-Vallejo, O., Escobar-Alarcón, L., Solís-Casados, D., and Klimova, T. (2013). Development of new trimetallic NiMoW catalysts supported on SBA-15 for deep hydrodesulfurization. *Fuel* 110, 268–277. doi:10.1016/j.fuel.2012.07.057

Michaud, P., Lemberton, J. L., and Pérot, G. (1998). Hydrodesulfurization of dibenzothiophene and 4, 6-dimethyldibenzothiophene: Effect of an acid component on the activity of a sulfided NiMo on alumina catalyst. *Appl. Catal. A General* 169 (2), 343–353. doi:10.1016/s0926-860x(98)00021-0

Miles, C. E., Carlson, T. R., Morgan, B. J., Topalian, P. J., Schare, J. R., Bussell, M. E., et al. (2020). Hydrodesulfurization properties of nickel phosphide on boron-treated alumina supports. *ChemCatChem* 12 (19), 4939–4950. doi:10.1002/cctc.202000755

Minaev, P. P., Nikulshin, P. A., Kulikova, M. S., Pimerzin, A. A., and Kogan, V. M. (2015). NiWS/Al_2O_3 hydrotreating catalysts prepared with 12-tungstophosphoric heteropolyacid and nickel citrate: Effect of Ni/W ratio. *Appl. Catal. A General* 505, 456–466. doi:10.1016/j.apcata.2015.05.012

Mokhtar, W. N. A. W., Bakar, W. A. W. A., Ali, R., and Abdul-Kadir, A. A. (2014). Deep desulfurization of model diesel by extraction with *N, N*-dimethylformamide: Optimization by Box–Behnken design. *J. Taiwan Inst. Chem. Eng.* 45, 1542–1548. doi:10.1016/j.jtice.2014.03.017

Moqadam, S. I., and Mahmoudi, M. (2013). Advent of nanocatalysts in hydrotreating process: Benefits and developments. *Am. J. Oil Chem. Technol.* 1 (2), 13–21.

Mozhaev, A. V., Nikulshin, P. A., Pimerzin, A. A., Maslakov, K. I., and Pimerzin, A. A. (2016). Investigation of co-promotion effect in NiCoMoS/Al2O3 catalysts based on Co2Mo10-heteropolyacid and nickel citrate. *Catal. Today* 271, 80–90. doi:10.1016/j.cattod.2015.11.002

Nadeina, K. A., Kazakov, M. O., Danilova, I. G., Kovalskaya, A. A., Stolyarova, E. A., Dik, P. P., et al. (2019). The influence of B and P in the impregnating solution on the properties of NiMo/γ-δ-Al_2O_3 catalysts for VGO hydrotreating. *Catal. Today* 329, 2–12. doi:10.1016/j.cattod.2018.12.035

Nakamura, H., Amemiya, M., and Ishida, K. (2005). Inhibition effect of hydrogen sulfide and ammonia on NiMo/Al_2O_3 CoMo/Al_2O_3, NiCoMo/Al_2O_3 catalysts in hydrodesulfurization of dibenzothiophene and 4, 6-dimethyldibenzothiophene. *J. Jpn. Pet. Inst.* 48 (5), 281–289. doi:10.1627/jpi.48.281

Nava, R., Infantes-Molina, A., Castaño, P., Guil-López, R., and Pawelec, B. (2011). Inhibition of CoMo/HMS catalyst deactivation in the HDS of 4, 6-DMDBT by support modification with phosphate. *Fuel* 90 (8), 2726–2737. doi:10.1016/j.fuel.2011.03.049

Nikulshina, M., Blanchard, P., Lancelot, C., Griboval-Constant, A., Marinova, M., Briois, V., et al. (2020). Genesis of active phase in MoW/Al_2O_3 hydrotreating catalysts monitored by HAADF and in situ QEXAFS combined to MCR-ALS analysis. *Appl. Catal. B Environ.* 269, 118766. doi:10.1016/j.apcatb.2020.118766

Nikulshina, M. S., Blanchard, P., Mozhaev, A., Lancelot, C., Griboval-Constant, A., Fournier, M., et al. (2018). Molecular approach to prepare mixed MoW alumina supported hydrotreatment catalysts using $H_4SiMon\ W_{12-n}O_{40}$ heteropolyacids. *Catal. Sci. Technol.* 8 (21), 5557–5572. doi:10.1039/c8cy00672e

Niu, D., Zhou, Z., Wu, C., and Xu, W. (2014). Preparation and properties of magnetic molecularly imprinted polymers and their use as adsorbents for selective adsorption of indole. *Adsorp. Sci. Technol.* 32 (7), 509–519. doi:10.1260/0263-6174.32.7.509

Nuzhdin, A. L., Kovalenko, K. A., Dybtsev, D. N., and Bukhtiyarova, G. A. (2010). Removal of nitrogen compounds from liquid hydrocarbon streams by selective sorption on metal-organic framework MIL-101. *Mendeleev Commun.* 20, 57–58. doi:10.1016/j.mencom.2010.01.022

Ofoghi, S., Soleimani, M., and Ravanchi, M. T. (2021). Quinoline adsorption from organic phase on X-type zeolites: Experimental and DFT study. *Can. J. Chem. Eng.* 100 (4), 838–848. doi:10.1002/cjce.24201

Ogunlaja, A. S., Abdul-quadir, M. S., Kleyi, P. E., Ferg, E. E., Watts, P., Tshentu, Z. R., et al. (2017). Towards oxidative denitrogenation of fuel oils: Vanadium oxide-catalysed oxidation of quinoline and adsorptive removal of quinoline-*N*-oxide using 2, 6-pyridine-polybenzimidazole nanofibers. *Arab. J. Chem.* 12 (2), 198–214. doi:10.1016/j.arabjc.2017.05.010

Pearson, R. G. (1963). Hard and soft acids and bases. *J. Am. Chem. Soc.* 85 (22), 3533–3539. doi:10.1021/ja00905a001

Peña, L., Valencia, D., and Klimova, T. (2014). CoMo/SBA-15 catalysts prepared with EDTA and citric acid and their performance in hydrodesulfurization of dibenzothiophene. *Appl. Catal. B Environ.* 147, 879–887. doi:10.1016/j.apcatb.2013.10.019

Poulet, O., Hubaut, R., Kasztelan, S., and Grimblot, J. (1993). Modification of the site structure of MoS_2/γ-Al_2O_3 catalysts by addition of P, F and alkaline elements. *Stud. Surf. Sci. Catal.* 75, 2075–2078.

Prado, G. H. C., Rao, Y., and de Klerk, A. (2017). Nitrogen removal from oil: A review. *Energy fuels.* 31, 14–36. doi:10.1021/acs.energyfuels.6b02779

Prins, R., and Bussell, M. E. (2012). Metal phosphides: Preparation, characterization and catalytic reactivity. *Catal. Lett.* 142 (12), 1413–1436. doi:10.1007/s10562-012-0929-7

Prokić-Vidojević, D., Glišić, S. B., Krstić, J. B., and Orlović, A. M. (2021). Aerogel Re/Pd-TiO2/SiO2 and Co/Mo-Al2O3/SiO2 catalysts for hydrodesulphurisation of dibenzothiophene and 4, 6-dimethyldibenzothiophene. *Catal. Today* 378, 10–23. doi:10.1016/j.cattod.2020.11.022

Putra, E., Pranowo, R., Sunarso, J., Indraswati, N., and Ismadji, S. (2009). Performance of activated carbon and bentonite for adsorption of amoxicillin from wastewater: Mechanisms, isotherms and kinetics. *Water Res.* 43, 2419–2430. doi:10.1016/j.watres.2009.02.039

Ramírez, J., Gutiérrez-Alejandre, A., Sánchez-Minero, F., MacÍas-Alcántara, V., Castillo-Villalón, P., Oliviero, L., et al. (2012). HDS of 4, 6-DMDBT over NiMoP/(x) Ti-SBA-15 catalysts prepared with $H_3PMo_{12}O_{40}$. *Energy fuels.* 26 (2), 773–782. doi:10.1021/ef201590g

Rashidi, F., Sasaki, T., Rashidi, A. M., Kharat, A. N., and Jozani, K. J. (2013). Ultradeep hydrodesulfurization of diesel fuels using highly efficient nanoalumina-supported catalysts: Impact of support, phosphorus, and/or boron on the structure and catalytic activity. *J. Catal.* 299, 321–335. doi:10.1016/j.jcat.2012.11.012

Rashidi, S., Nikou, M. R. K., and Anvaripour, B. (2015). Adsorptive desulfurization and denitrogenation of model fuel using HPW and NiO-HPW modified aluminosilicate mesostructures. *Microporous Mesoporous Mat.* 211, 134–141. doi:10.1016/j.micromeso.2015.02.041

Rayo, P., Ramírez, J., Torres-Mancera, P., Marroquín, G., Maity, S. K., Ancheyta, J., et al. (2012). Hydrodesulfurization and hydrocracking of Maya crude with P-modified $NiMo/Al_2O_3$ catalysts. *Fuel* 100, 34–42. doi:10.1016/j.fuel.2011.12.004

Richter, F. P., Caesar, P. D., Meisel, S. L., and Offenhauer, R. D. (1952). Distribution of nitrogen in petroleum according to basicity. *Ind. Eng. Chem.* 44 (11), 2601–2605. doi:10.1021/ie50515a037

Rinne, J., and Risto, A. (2022). Scienceon. AvaliableAt: https://scienceon.kisti.re.kr/srch/selectPORSrchPatent.do?cn=USP2010087771587 (Accessed on April 07, 2022).

Sadeghbeigi, R. (2020). *Fluid catalytic cracking handbook: An expert guide to the practical operation, design, and optimization of FCC units*. Oxford, United Kingdom: Butterworth-Heinemann.

Saih, Y., and Segawa, K. (2009). Catalytic activity of CoMo catalysts supported on boron-modified alumina for the hydrodesulphurization of dibenzothiophene and 4, 6-dimethyldibenzothiophene. *Appl. Catal. A General* 353 (2), 258–265. doi:10.1016/j.apcata.2008.10.037

Saleh, T. A. (2015). *Applying nanotechnology to the desulfurization process in petroleum engineering, for the book series "the advances in chemical and materials engineering (ACME)*. United States of America: IGI Global, 281–336. AvaliableAt: http://www.igi-global.com/book/applying-nanotechnology-desulfurization-process-petroleum/134808.

Sami, M., and Hatch, L. F. (2001). *Chemistry of petrochemical processes*. Houston, Texas, United States: Gulf Professional Publishing. doi:10.1016/B978-0-88415-315-3.X5000-7

Sano, Y., Choi, K. H., Korai, Y., and Mochida, I. (2004). Adsorptive removal of sulfur and nitrogen species from a straight run gas oil over activated carbons for its deep hydrodesulfurization. *Appl. Catal. B Environ.* 49, 219–225. doi:10.1016/j.apcatb.2003.12.007

Sau, M., Basak, K., Manna, U., Santra, M., and Verma, R. P. (2005). Effects of organic nitrogen compounds on hydrotreating and hydrocracking reactions. *Catal. Today* 109, 112–119. doi:10.1016/j.cattod.2005.08.007

Schlesinger, R. B. (2010). "Sulfur oxides,". Editor C. A. McQueen. Second Edition (Amsterdam, Netherlands: Elsevier Science), 8, 277–290. 9780080468846. doi:10.1016/B978-0-08-046884-6.00915-5*Compr. Toxicol.*

Schneemann, A., Bon, V., Schwedler, I., Senkovska, I., Kaskel, S., Fischer, R. A., et al. (2014). Flexible metal–organic frameworks. *Chem. Soc. Rev.* 43, 6062–6096. doi:10.1039/c4cs00101j

Severino, F., Laine, J., and Lopez-Agudo, A. (2000). Compensation effect and dual promotion effect in activated carbon-supported CoNiMo hydrodesulfurization catalysts. *J. Catal.* 189 (1), 244–246. doi:10.1006/jcat.1999.2683

Shamanaev, I. V., Suvorova, A. O., Gerasimov, E. Y., Pakharukova, V. P., Panafidin, M. A., Yakovlev, I. V., et al. (2021). SRGO hydrotreating over Ni-phosphide catalysts on granulated Al_2O_3. *Catal. Today* 378, 24–32. doi:10.1016/j.cattod.2021.04.001

She, H., Ma, X., and Chang, G. (2018). Highly efficient and selective removal of *N*-heterocyclic aromatic contaminants from liquid fuels in a Ag(I) functionalized metal-organic framework: Contribution of multiple interaction sites. *J. Colloid Interface Sci.* 518 (15), 149–155. doi:10.1016/j.jcis.2018.01.114

Shi, Y., Wang, G., Mei, J., Xiao, C., Hu, D., Wang, A., et al. (2020). The Influence of pore structure and acidity on the hydrodesulfurization of dibenzothiophene over nimo-supported catalysts. *ACS omega* 5 (25), 15576–15585. doi:10.1021/acsomega.0c01783

Shiraishi, Y., Hirai, T., and Komasawa, I. (2001). A novel desulfurization process for fuel oils based on The formation and subsequent precipitation of S-alkylsulfonium salts. 4. Desulfurization and simultaneous denitrogenation of vacuum gas oil. *Ind. Eng. Chem. Res.* 40, 3398–3405. doi:10.1021/ie001091b

Shiraishi, Y., Hirai, T., and Komasawa, I. (2000). Photochemical denitrogenation processes for light oils effected by a combination of UV irradiation and liquid-liquid extraction. *Ind. Eng. Chem. Res.* 39, 2826–2836. doi:10.1021/ie990917a

Shiraishi, Y., Tachibana, K., Hirai, T., and Komasawa, I. (2001). A novel desulfurization process for fuel oils based on The formation and subsequent precipitation of S-alkylsulfonium salts. 3. Denitrogenation behavior of light oil feedstocks. *Ind. Eng. Chem. Res.* 40, 3390–3397. doi:10.1021/ie001090j

Shiraishi, Y., Tachibana, K., Hirai, T., and Komasawa, I. (2001). A novel desulfurization process for fuel oils based on The formation and subsequent precipitation of S-alkylsulfonium salts. 5. Denitrogenation reactivity of basic and neutral nitrogen compounds. *Ind. Eng. Chem. Res.* 40, 4919–4924. doi:10.1021/ie0104565

Sigurdson, S., Sundaramurthy, V., Dalai, A. K., and Adjaye, J. (2008). Phosphorus promoted trimetallic $NiMoW/\gamma$-Al_2O_3 sulfide catalysts in gas oil hydrotreating. *J. Mol. Catal. A Chem.* 291 (1-2), 30–37. doi:10.1016/j.molcata.2008.05.011

Singh, R., Kunzru, D., and Sivakumar, S. (2021). Enhanced catalytic activity of ultrasmall NiMoW trimetallic nanocatalyst for hydrodesulfurization of fuels. *Fuel* 288, 119603. doi:10.1016/j.fuel.2020.119603

Soltanali, S., Mashayekhi, M., and Mohaddecy, S. R. S. (2020). Comprehensive investigation of the effect of adding phosphorus and/or boron to $NiMo/\gamma$-Al_2O_3 catalyst in diesel fuel hydrotreating. *Process Saf. Environ. Prot.* 137, 273–281. doi:10.1016/j.psep.2020.02.033

Song, H., You, J., Liab, B., Chen, C., Huang, J., Zhang, J., et al. (2017). Synthesis, characterization and adsorptive denitrogenation performance of bimodal mesoporous Ti-HMS/KIL-2 composite: A comparative study on synthetic methodology. *Chem. Eng. J.* 327 (1), 406–417. doi:10.1016/j.cej.2017.06.055

Speight, J. G. (2018). *Petroleum refinery processes*. Hoboken, New Jersey, United States: John Wiley & Sons Inc., 1–46. doi:10.1002/0471238961.1805060919160509

Stanislaus, A., Marafi, A., and Rana, M. S. (2010). Recent advances in the science and technology of ultra-low sulfur diesel (ULSD) production. *Catal. Today* 153 (1-2), 1–68. doi:10.1016/j.cattod.2010.05.011

Statistical Review of World Energy. (2022). *British petroleum statistical review of world energy 2021*. London, United Kingdom: BP plc, AvaliableAt: https://www.bp.com/en/global/corporate/energy-economics/statistical-review-of-world-energy.html (Accessed on 07 April 2022).

Suganuma, S., Arita, K., Nakano, F., Tsuji, E., and Katada, N. (2020). Adsorption kinetics in removal of basic nitrogen-containing compounds from practical heavy oils by amorphous silica-alumina. *Fuel* 266, 117055. doi:10.1016/j.fuel.2020.117055

Sun, M., Nicosia, D., and Prins, R. (2003). The effects of fluorine, phosphate and chelating agents on hydrotreating catalysts and catalysis. *Catal. Today* 86 (1-4), 173–189. doi:10.1016/s0920-5861(03)00410-3

Sundaramurthy, V., Dalai, A. K., and Adjaye, J. (2005). Effect of EDTA on hydrotreating activity of CoMo/γ-Al_2O_3 catalyst. *Catal. Lett.* 102 (3), 299–306. doi:10.1007/s10562-005-5872-4

Tanimu, A., and Alhooshani, K. (2019). Advanced hydrodesulfurization catalysts: A review of design and synthesis. *Energy fuels.* 33 (4), 2810–2838. doi:10.1021/acs.energyfuels.9b00354

Tanimu, A., Ganiyu, S. A., Kozhevnikov, I., and Alhooshani, K. (2021). *In-situ* activation of NiMo catalyst based on support surface-bound thiols: A green approach to catalyst sulfidation and improved activity. *Arab. J. Chem.* 14 (4), 103030. doi:10.1016/j.arabjc.2021.103030

Théodet, M. (2010). *New generation of "bulk" catalyst precursors for hydrodesulfurization synthesized in supercritical fluids.* Doctoral dissertation.

Thomazeau, C., Geantet, C., Lacroix, M., Danot, M., Harlé, V., Raybaud, P., et al. (2007). Predictive approach for the design of improved HDT catalysts: γ-Alumina supported (Ni, Co) promoted $Mo_{1-x}W_xS_2$ active phases. *Appl. Catal. A General* 322, 92–97. doi:10.1016/j.apcata.2007.01.016

Thompson, R. B., Druge, L. W., and Chenicek, J. A. (1949). Stability of fuel oils in storage: Effect of sulfur compounds. *Ind. Eng. Chem.* 41, 2715–2721. doi:10.1021/ie50480a016

Thurston, G. D. (2017). *Stella R. Quah, international encyclopedia of public health*. Second Edition. Cambridge, Massachusetts, United States: Academic Press, 367–377. 9780128037089. doi:10.1016/B978-0-12-803678-5.00320-9

Tian, F., Sun, X., Liu, X., Zhang, H., Liu, J., Guo, H., et al. (2020). Effective adsorptive denitrogenation from model fuels over yttrium ion-exchanged Y zeolite. *Chin. J. Chem. Eng.* 28 (2), 414–419. doi:10.1016/j.cjche.2019.05.014

Topalian, P. J., Carrillo, B. A., Cochran, P. M., Takemura, M. F., and Bussell, M. E. (2021). Synthesis and hydrodesulfurization properties of silica-supported nickel-ruthenium phosphide catalysts. *J. Catal.* 403, 173–180. doi:10.1016/j.jcat.2021.02.006

Turaga, U. T., Ma, X., and Song, C. (2003). Influence of nitrogen compounds on deep hydrodesulfurization of 4, 6-dimethyldibenzothiophene over Al_2O_3 and MCM-41-supported Co-Mo sulfide catalysts. *Catal. Today* 86, 265–275. doi:10.1016/s0920-5861(03)00464-4

UNO (2022). Four more countries in Africa switch to low sulfur fuels. AvaliableAt: https://www.unep.org/news-and-stories/blogpost/four-more-countries-africa-switch-low-sulfur-fuels#:~:text=Morocco%20is%20actually%20the%20first,low%20sulphur%20fuels%20as%20well (Accessed on April 07, 2022).

US: Fuels: Diesel and Gasoline (2021). Transportpolicy. AvaliableAt: https://www.transportpolicy.net/standard/us-fuels-diesel-and-gasoline/#:~:text=Sulfur%20Content&text=500%20ppm%20%E2%80%93%20Sulfur%20limit%20of,for%20heavy%2Dduty%20highway%20engines (Accessed 02 26, 21).

Valencia, D., and Klimova, T. (2011). Effect of the support composition on the characteristics of NiMo and CoMo/(Zr)SBA-15 catalysts and their performance in deep hydrodesulfurization. *Catal. Today* 166 (1), 91–101. doi:10.1016/j.cattod.2010.08.006

Van de Voorde, B., Boulhout, M., Vermoortele, F., Horcajada, P., Cunha, D., Lee, J. S., et al. (2013). N/S-Heterocyclic contaminant removal from fuels by the mesoporous Metal–Organic framework MIL-100: The role of the metal ion. *J. Am. Chem. Soc.* 135, 9849–9856. doi:10.1021/ja403571z

Van de Voorde, B., Munn, A. S., Guillou, N., Millange, F., De Vos, D. E., Walton, R. I., et al. (2013). Adsorption of N/S heterocycles in the flexible metal–organic framework MIL-53(FeIII) studied by in situ energy dispersive X-ray diffraction. *Phys. Chem. Chem. Phys.* 15, 8606. doi:10.1039/c3cp44349c

van Looij, F., van der Laan, P., Stork, W. H. J., Di Camillo, D. J., and Swain, J. (1998). Key parameters in deep hydrodesulfurization of diesel fuel. *Appl. Catal. A General* 170 (1), 1–12. doi:10.1016/s0926-860x(98)00028-3

Vatutina, Y. V., Klimov, O. V., Stolyarova, E. A., Nadeina, K. A., Danilova, I. G., Chesalov, Y. A., et al. (2019). Influence of the phosphorus addition ways on properties of CoMo-catalysts of hydrotreating. *Catal. Today* 329, 13–23. doi:10.1016/j.cattod.2019.01.005

Wang, F., Li, J., Xu, L., Jiang, F., and Zhang, J. (2019). Magnetic composites Fe_3O_4@SiO_2@PILs as sorbents for efficient denitrogenation of fuel oil. *Micro Nano Lett.* 14 (13), 1287–1292. doi:10.1049/mnl.2019.0245

Wang, Z., Sun, Z., Kong, L., and Li, G. (2013). Adsorptive removal of nitrogen-containing compounds from fuel by metal-organic frameworks. *J. Energy Chem.* 22, 869–875. doi:10.1016/s2095-4956(14)60266-7

Wen, J., Lin, H., Han, X., Zheng, Y., and Chu, W. (2017). Physicochemical studies of adsorptive denitrogenation by oxidized activated carbons. *Ind. Eng. Chem. Res.* 56, 5033–5041. doi:10.1021/acs.iecr.6b05015

Whitehurst, D. D., Isoda, T., and Mochida, I. (1998). Present state of the art and future challenges in the hydrodesulfurization of polyaromatic sulfur compounds. *Adv. Catal.* 42, 345.

Whitehurst, D. D., Knudsen, K. G., Nielsen, I. V., Wiwel, P., and Zeuthen, P. (2000). The influence of trace amounts of nitrogen compounds on the achievement of future sulfur specifications in diesel fuels - Part 1: HDS inhibition studies with model N-compounds. *Am. Chem. Soc. Div. Pet. Chem. Prepr.* 45 (4), 692–696.

Wiwel, P., Hinnemann, B., Hidalgo-Vivas, A., Zeuthen, P., Petersen, B. O., Duus, J. Ø., et al. (2010). Characterization and identification of the most refractory nitrogen compounds in hydroprocessed vacuum gas oil. *Ind. Eng. Chem. Res.* 49 (7), 3184–3193. doi:10.1021/ie901473x

Wiwel, P., Knudsen, K., Zeuthen, P., and Whitehurst, D. (2000). Assessing compositional changes of nitrogen compounds during hydrotreating of typical diesel range gas oils using a novel preconcentration technique coupled with gas chromatography and atomic emission detection. *Ind. Eng. Chem. Res.* 39, 533–540. doi:10.1021/ie990554e

World Energy Review (2020). *Eni World Oil, Gas and Renewables Review, annual statistical report*. Report. AvaliableAt: https://www.eni.com/assets/documents/eng/scenari-energetici/WORLD-OIL-REVIEW-2020-vol1.pdf (Accessed on April 07, 2022).

Wu, H., Duan, A., Zhao, Z., Qi, D., Li, J., Liu, B., et al. (2014). Preparation of NiMo/KIT-6 hydrodesulfurization catalysts with tunable sulfidation and dispersion degrees of active phase by addition of citric acid as chelating agent. *Fuel* 130, 203–210. doi:10.1016/j.fuel.2014.04.038

Xiang, C. E., Chai, Y. M., and Liu, C. G. (2011). Effect of phosphorus on the hydrodesulfurization and hydrodenitrogenation performance of presufided NiMo/Al_2O_3 catalyst. *J. Fuel Chem.Technol.* 39 (5), 355–360. doi:10.1016/S1872-5813(11)60026-1

XiE, L., Favre-Reguillon, A., Wang, X., Fu, X., and Lemaire, M. (2010). Selective adsorption of neutral nitrogen compounds from fuel using ion-exchange resins. *J. Chem. Eng. Data* 55 (11), 4849–4853. doi:10.1021/je100446p

Yang, K., Chen, X., Bai, Z., and Liang, C. (2021). Noble metal silicides catalysts with high stability for hydrodesulfurization of dibenzothiophenes. *Catal. Today* 377, 205–212. doi:10.1016/j.cattod.2020.08.027

Yue, S., Xu, D., Sheng, Y., Yin, Z., Zou, X., Wang, X., et al. (2021). One-step synthesis of mesoporous alumina-supported molybdenum carbide with enhanced activity for thiophene hydrodesulfurization. *J. Environ. Chem. Eng.* 9 (4), 105693. doi:10.1016/j.jece.2021.105693

Yun, G. N., and Lee, Y. K. (2014). Dispersion effects of Ni_2P catalysts on hydrotreating of light cycle oil. *Appl. Catal. B Environ.* 150, 647–655. doi:10.1016/j.apcatb.2014.01.010

Zeuthen, P., Blom, P., and Massoth, F. (1991). Characterization of nitrogen on aged hydroprocessing catalysts by temperature-programmed oxidation. *Appl. Catal.* 78, 265–276. doi:10.1016/0166-9834(91)80111-9

Zeuthen, P., Knudsen, K. G., and Whitehurst, D. D. (2001). Organic nitrogen compounds in gas oil blends, their hydrotreated products and the importance to hydrotreatment. *Catal. Today* 65, 307–314. doi:10.1016/s0920-5861(00)00566-6

Zhang, C., Brorson, M., Li, P., Liu, T., Jiang, Z., and Li, C. (2019). CoMo/Al_2O_3 catalysts prepared by tailoring the surface properties of alumina for highly selective hydrodesulfurization of FCC gasoline. *Appl. Catal. A General* 570, 84–95. doi:10.1016/j.apcata.2018.10.039

Zhang, H., Li, G., Jia, Y., and Liu, H. J. (2010). Adsorptive removal of nitrogen-containing compounds from fuel. *J. Chem. Eng. Data* 55, 173–177. doi:10.1021/je9003004

Zhang, P., Mu, F., Zhou, Y., Long, Y., Wei, Q., Liu, X., et al. (2019). Synthesis of highly ordered TiO_2-Al_2O_3 and catalytic performance of its supported NiMo for HDS of 4, 6-dimethyldibenzothiophene. *Appl. Catal. B Environ.* 268, 118428.

Zhang, Y., Han, W., Long, X., and Nie, H. (2016). Redispersion effects of citric acid on CoMo/γ-Al_2O_3 hydrodesulfurization catalysts. *Catal. Commun.* 82, 20–23. doi:10.1016/j.catcom.2016.04.012

Zolotareva, D., Zazybin, A., Rafikova, K., Dembitsky, V. M., Dauletbakov, A., Yu, V., et al. (2019). Ionic liquids assisted desulfurization and denitrogenation of fuels. *Vietnam J. Chem.* 57 (2), 133–163. doi:10.1002/vjch.201900008

frontiers | Frontiers in Chemistry

ORIGINAL RESEARCH
published: 17 August 2022
doi: 10.3389/fchem.2022.806433

Natural Resources Exploitation in Sulfate-Resisting Portland Cement Manufacturing: Towards Quality Improvement and Reduction of Environmental Impact

Islem Labidi and Adel Megriche**

Laboratoire de Chimie Minérale Appliquée LRCMA (LR19ES02), Faculté des Sciences de Tunis, Université de Tunis El Manar, Campus Universitaire Farhat Hached El Manar, Tunis, Tunisia

OPEN ACCESS

Edited by:
Mama El Rhazi,
Faculty of Sciences and Technologies of Mohammedia, Morocco

Reviewed by:
Marcelo Medeiros,
Federal University of Paraná, Brazil
Nakshatra Singh,
Sharda University, India

***Correspondence:**
Islem Labidi
engislem@gmail.com
Adel Megriche
adel.megriche@fst.utm.tn

Specialty section:
This article was submitted to Green and Sustainable Chemistry, a section of the journal Frontiers in Chemistry

Received: *31 October 2021*
Accepted: *30 May 2022*
Published: *17 August 2022*

Citation:
Labidi I and Megriche A (2022) Natural Resources Exploitation in Sulfate-Resisting Portland Cement Manufacturing: Towards Quality Improvement and Reduction of Environmental Impact. Front. Chem. 10:806433. doi: 10.3389/fchem.2022.806433

Sulfate-resisting (SR) Portland cement is commonly used in building works to improve concrete's durability against external sulfate attack. This attack is considered a very serious chemical aggression that causes damage and cracking of concrete structures. These special cements have a very particular mineralogical composition, $C_3A \leq 3\%$ and $(2C_3A + C_4AF) \leq 20\%$, which makes the cementitious matrix resistant to sulfate attack. This kind of product is very difficult to manufacture since low alumina (C_3A) necessitates the use of a high kiln temperature in order to keep a sufficient liquid phase necessary to maintain the stability of the cement manufacturing process. In this context, this study aims to optimize SR Portland cement raw meals using natural materials collected from different regions in Tunisia, mainly ordinary limestone, siliceous limestone, black marl, grey marl, iron ore, and natural fluorapatite. The collected specimens were characterized by an X-ray fluorescence spectrometer in order to determine its elemental chemical composition. The optimization of the SR Portland cement raw meal combinations was done by means of a calculation tool based on the chemical composition of each used raw material and the variation of burning modules (LSF, SIM, and ALM). It has been found that natural fluorapatite integration (0%–15%) in raw mix preparation leads to the raw meals required for the SR Portland cement standard ($C_3A \leq 3\%$ et $2\ C_3A + C_4AF \leq 20\%$). Moreover, it was shown that the estimated SR raw meals ensure the cement manufacturing process stability (acceptable burning modules "LSF = 100; SIM = 3; ALM = 0.91 and sufficient liquid phase) and decrease the CO_2 emissions in cement production.

Keywords: SR Portland cement-C_3A, manufacturing process-stability, CO_2 emission, burning modules of raw meals, calculation tool

Abbreviations: C, CaO; S, SiO_2; A, Al_2O_3; F, Fe_2O_3; N, Na_2O; K, K_2O; $\bar{S}$, SO_3; P, P_2O_5; C_3S, Ca_3SiO_5; C_2S, Ca_2SiO_4; C_3A, $Ca_3Al_2O_6$; C_4AF, $Ca_4Al_2Fe_2O_{10}$; C_2F, $Ca_2Fe_2O_5$; CH, Ca $(OH)_2$; LSF, Lime saturation factor; SIM, Silica ratio; ALM, Alumina ratio; L.P, Liquid phase; LOI, Loss in ignition; NAF, Natural fluorapatite.

1 INTRODUCTION

Industrial and technological progress provide the basis for unrestrained growth in all fields, and in particular the building sector. Cement, undoubtedly, is considered an essential building block and it is a sign of the economic and social development of countries.

Cement is formed basically from an artificial stone called Portland clinker. The latter is obtained from the burning at a very high temperature, above 1,450°C, of a mixture of natural materials, mainly limestone and clay. The clinker is characterized by a very special composition and four main mineralogical phases: alite (C_3S), belite (C_2S), aluminate (C_3A), and ferrite (C_4AF) (Telschow et al., 2012; Ghosh et al., 2022). The cement generally used in the design of construction work is characterized by mechanical strength, although the interaction between concrete and the environment is often neglected. These environments can induce concrete deterioration either by physical attacks through surface erosion, freezing/thawing, and heat, or by chemical aggressions such as acids, sulfates, alkali-aggregate reactions, and steel corrosion (Association, 2002). All these phenomena have a negative impact on concrete durability (Al-Amoudi, 2002). Sulfate ions' penetration in cement matrix presents a fairly dangerous pathology for concrete due to its expansive consequences. This kind of attack was observed for the first time in 1887 by Candolt during their investigation into mortars in the fortifications of the city of Paris (Ragoug, 2016). Indeed, these mortars were in contact with aggressive waters rich in sulfate ions. The mitigation of external sulfate attack is considered a necessity to maintain the concrete's durability. So, many methods were adopted to minimize external sulfate attack (Kanaan et al., 2022), which are based on the use of mineral additives as partial cement replacement, such as silica fume, blast furnace slag, fly ash, metakaolin, pozzolana natural, and limestone. The European standard "Cement—Part 1: composition, specifications, and conformity criteria for common cements" (CEN, Cement, 2011) introduces a family of sulfate-resisting common cements (SR-cements). Certain types of these cements, such as CEMIII/B-SR, CEMIII/C-SR, CEMIV/A-SR, and CEMIV/B-SR, pose difficulties during their production in certain situations, such as in Tunisian cement plants, since they require blast furnace slag, natural pozzolana, and siliceous fly ash, and the availability of these materials is very delicate. So, in this case, the only way to combat the external sulfate attack is the use of sulfate-resisting (SR) Portland cement. SR Portland cement is a hydraulic binder used in sulfate-rich construction environments (Neville, 1995) to protect the concrete from external sulfate attack. These cements have a very special mineralogical composition: $C_3A \leq 3\%$ and $2C_3A + C_4AF \leq 20\%$ (NT, 47.26, 1999).

SR Portland cement production is very complicated since low aluminate content necessitates the use of high kiln temperature (Consumption of enormous energy) in order to keep a suitable liquid phase (LP) required to maintain clinkering stage stability (Labidi et al., 2019a; Dorn et al., 2022).

In fact, the cement industry used two tricks to limit the alumina content in SR Portland cement during its manufacturing:

- The first method involves using limestone as a partial clinker replacement during the cement milling process to artificially lower the C_3A content. But this behaviour affects the durability of SR Portland cement (Labidi et al., 2019a), since limestone in contact with sulfate ions induces the thaumasite formation. This leads to concrete deterioration (Schmidt, 2007; Schmidt et al., 2009).
- The second method deals with the increase of iron ore raw material at the moment of raw mix preparation, which is considered an apparent industrial solution. But in reality, this practice can cause a serious disequilibrium of the cement process and also affect the cement mineralogy (Chatterjee, 2011; Sorrentino, 2011).

It seems that studies dealing exclusively with the optimization of SR Portland cement raw meal formulas from Tunisian natural raw materials, especially without iron ore increasing, are not being conducted. The aim of the present research is to optimize different raw meals for sulfate-resisting Portland cement from natural resources (ordinary limestone, siliceous limestone, black marl, grey marl, iron ore, and natural fluorapatite) collected from different locations in Tunisia. These optimized combinations are expected to meet SR Portland cement standards, guarantee the stability of the cement production process and, above all, reduce the environmental impact, since cement manufacturing is the third most CO_2-emitting industrial sector in the world (652 kg–894 kg CO_2/t_{cement}) (Altun, 1999a; Kajaste and Hurme, 2016; Mishra et al., 2022). This work is done essentially by means of a raw meal calculation program based on the chemical composition of the raw materials.

The chemical composition analysis of each raw material was determined by X-ray fluorescence (XRF).

This paper is subdivided into three major sections: the first one presents an overview of the SR Portland cement manufacturing process, its mineralogical phases, its standards, and its chemical specifications. Following this, it was necessary to present and discuss the mechanisms of external sulfate attack. In other words, this will explain the usefulness of SR Portland cement in the fight against external sulfate attacks. The second presents the materials and methods used to carry out this research study, followed by the third section involving the results and discussions of different studied cases of SR Portland cement raw meal combinations optimization.

2 BIBLIOGRAPHIC REVIEW

2.1 Sulfate-Resisting Portland Cement

SR Portland cement is a hydraulic binder used for massive structures exposed to aggressive environment construction works (Essawy and Abd El.Aleem, 2014). Its manufacturing is similar to ordinary Portland cement. It is characterized by a low content of aluminate phase (0%–5%) compared to ordinary Portland cement of about 12%.To produce this kind of binder, most cement industries increased the iron oxide (iron ore) content in their raw meals for purposes of obtaining a clinker with a small amount of C_3A (Essawy and Abd El.Aleem, 2014). This behaviour induces the decrease of the clinker liquid phase noted L.P (or clinker melt) viscosity during raw mill burning

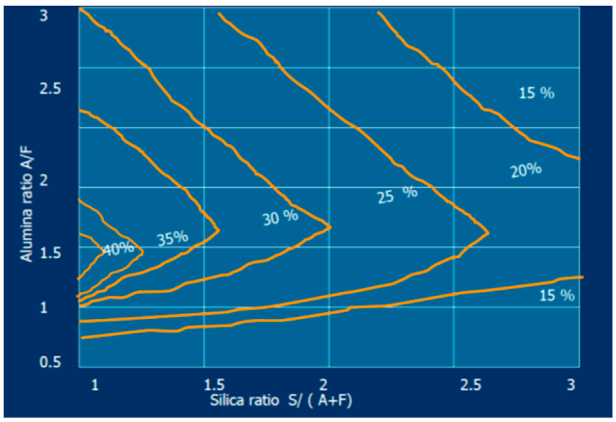

FIGURE 1 | Variation in % liquid phase at 1,338°C with change in silica ratio (SIM = S/[A + F]) and alumina ratio (AR) at LSF = 100, LSF = C/[2.8S + 1.1 A + 0.7F] (Kumar, 2013).

since the liquid phase viscosity increases linearly with the alumina ratio (ALM = Al_2O_3/Fe_2O_3).

The amount of L.P at 1,450°C Eq. (A.1) is computed according to the relation between the Al_2O_3, Fe_2O_3, MgO, K_2O, Na_2O, and SO_3 contents (Mosci, 2000).

$$\%\text{L.P. at } 1450\,^{\circ}\text{C} = 3 \times A + 2.25 \times F + M + K + N + S\,(\text{MgO} \leq 2) \quad \text{(A.1)}$$

Moreover, the quantity of liquid phase depends strongly on the burning modulus (ALM and SIM) variation as presented in **Figure 1** and, at the same time, it controls the coating formation (see **Figure 2**).

The latter protects the refractory bricks of the cement kiln and its continuance is considered a necessity (Belgacem et al., 2016). Indeed, as the viscosity of L.P is increased, the coating will be heavier and the risk of brick removal will be increased. **Figure 2** gives three different intervals:

- %L.P < 20: The formed liquid phase is not sufficiently pasty and is regarded as very low. In this case, alite (the most important clinker mineral and the controller of the mechanical strength development of the concrete at an early stage) formation is extremely slow and difficult since the liquid phase creates the reaction medium for the conversion of C_2S to C_3S. The formed coating is thin, weak, not stable, and has a rough surface.
- 20% < %L.P < 28%: The liquid phase has a pasty form and it is suitable for mineralogical phases' formation. The coating is strong and stable, and the refractory bricks are almost protected.
- %L.P > 28%: The liquid phase is very fluid and there is a high risk of ring formation in the kiln, which causes the blockage of the burning lining.

On the one hand, the liquid phase has a serious role in clinker nodulization and clinker mineralogical phases' formation. In the absence of the liquid phase, the reaction between C_2S and free lime (CaO) to generate an alite phase (C_3S) would be almost impossible

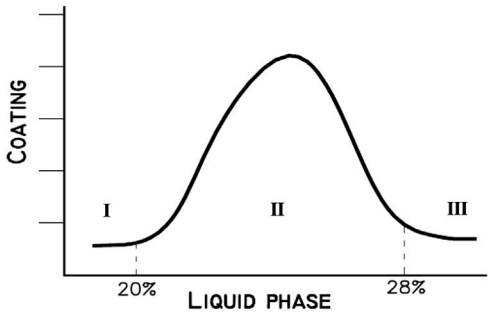

FIGURE 2 | Liquid phase % versus coating formation (I: L.P is not a sufficiently pasty form, II: Pasty form of L.P, and III: L.P is very fluid-liquid) (Sengupta, 2020).

during clinkerization. On the other hand, for a given burning temperature, high C_3A clinkers tend to nodulize better than low C_3A clinkers.

So, it is imperative to optimize a good raw meal (especially one that is not doped with iron ore) to obtain SR Portland cement with a low amount of aluminate and to prevent poor operation of the cement kiln.

Sulfate-resisting Portland cement is a special purpose hydraulic binder used where sulfates are present in high concentrations that would damage concrete formed by ordinary Portland cement. External sulfate attack strength is achieved by setting the mineralogical composition to limit the amount of aluminate compound (C_3A) in the sulfate-resisting Portland cement. Indeed, the degradation rate of concrete exposed to aggressive sulfate environments depends essentially on C_3A content (Adedoud, 2019). The lower the quantity of aluminate, the more sulfate resistance is increased (Nawy, 2008). This parameter is considered the most important characteristic of sulfate-resisting Portland cement.

The quality and performance of all sulfate-resisting Portland cement produced by any cement industry in the world must conform to the characteristics and specifications of SR Portland cement as indicated in the standard. **Table 1** summarizes the main sulfate-resisting Portland cement standards.

Moreover, the Tunisian standards [NT 47.26 (1998) and NT 47.25 (1998)] (NT, 47.26, 1999) introduced the classification of severity of sulfate environments:

- Sulfate-rich environments:
  - Solutions: the concentration of sulfate ions is greater than or equal to 1,500 mg/L;
  - Soils: the sulfate ion amounts are greater than or equal to 1.2%.
- Sulfate environments of moderate severity:
  - Solutions: the concentration of sulfate ions is situated between 600 mg/L and 1,500 mg/L,
  - Soils: the sulfate ion amounts are situated between 0.6% and 1.2%.

The quantification of aluminate (C_3A) and ferrite (C_4AF) phases as indicated in European standard EN 197-1 is based on the Bogue calculation method (Labidi et al., 2019b).

TABLE 1 | Sulfate-resisting Portland cement standards.

Standards		Designations of the sulfate resisting Portland cement		Requirements		
				Mineralogical	Chemical	Medium specifications
European standard (EN)	EN197-1:2011: cement-Part 1: Composition, specifications, and conformity criteria for common cements (CEN, Cement, 2011)	Sulfate resisting Portland cement	CEMI-SR0	$C_3A = 0$	—	—
			CEMI-SR3	$C_3A \leq 3\%$		
			CEMI-SR5	$C_3A \leq 5\%$		
American society for testing and method standard (ASTM)	ASTM C 150/150M-19a: Standard specification for Portland cement (ASTM, 2017)	Sulfate-resisting Portland cement: Type V		$C_3A \leq 5\%$ $2 \times C_3A + C_4AF \leq 25\%$	$SO_3 \leq 2.3\%$ $MgO \leq 6\%$	—
British standard (BS)	BS 4027:1996-Specification for sulfate resisting Portland cement (Hooton and Thomas, 2002)	Sulfate resisting Portland cement: SRPC		$C_3A \leq 3.5\%$ $2 \times C_3A + C_4AF \leq 25\%$	$SO_3 \leq 2.5\%$ $MgO \leq 4\%$ $Cl^- \leq 0.02\%$	—
Tunisian standard (NT)	NT 47.26 (1998) (NT, 47.26, 1999)	High sulfate resisting Portland cement:HRS1		$C_3A \leq 3\%$ $2 \times C_3A + C_4AF \leq 20\%$	$SO_3 \leq 3.5\%$ $MgO \leq 4\%$	$-[SO_4^{2-}] > 600$ mg/L in solutions $-\%SO_3 > 2.4\%$ in dry soils
		High sulfate resisting Portland cement: HRS2		$3\% \leq C_3A \leq 5\%$ $2 \times C_3A + C_4AF \leq 20\%$	$SO_3 \leq 2.5\%$ $MgO \leq 4\%$	$-1{,}500 < [SO_4^{2-}] < 6{,}000$ mg/L in solutions $-1.2\% < \%SO_3 < 2.4\%$ in dry soils

Bogue calculation method remains a primary estimation of the major cement phases. This tool is applied only in the perfect conditions of clinker burning, in the absence of minor's elements: all Fe_2O_3 quantity reacted with a part of Al_2O_3 and lime to form the C_4AF and the residual alumina is combined with CaO to make aluminate phase. However, this assumption does not take account of Fe_2O_3 and Al_2O_3 insertions in the alite and belite phases during the real clinkering process (Labidi et al., 2019b). Thus, the aluminate and ferrite amounts by using Bogue method probably contained an error and should be revised or another more accurate means should be used to quantify C_3A and C_4AF such as X-rays diffraction coupled with Rietveld refinement (Mohamed et al., 2017).

So, the ASTM C150/150M-19a (ASTM, 2017), BS 4027:1996, and NT 47.26 (1998) imposed a second condition "$2 \times C_2A + C_4AF$" to limit the quantity of iron oxide in the raw mill. It seems that this requirement is stricter in Tunisian standards than the other standards.

2.2 Why the Use of SR Sulfate Portland Cement is Necessary?

2.2.1 External Sulfate Attack

The durability of concrete structures can be significantly improved if the effects of the surrounding environment are taken into account ahead of the formulation of the material and the dimensioning of the structure. Despite the various studies and expertise, some degradation mechanisms remain unclear and controversial. This is the case, for example, with external sulfate attack (ESA) or external sulfate reaction. Sulfate ions can originate from groundwater (Lothenbach et al., 2010), soils rich in gypsum or pyrite (Schmidt et al., 2009), sulfates from industrial products, fertilizers or organic substances, river water, or sea water (Aziez, 2017). It is also important to note that dry salts do not react with concrete. The presence of sulfate in solution is essential for the transfer of SO_4^{2-} ions into the concrete matrix (Neville, 2004). The external sulfate attack is associated with the precipitation of secondary sulfate products, expansions, and the deterioration of physicochemical properties of concrete, which induces the loss of strength and cohesion, and even the scaling, cracking, and disintegration of the cement matrix (see **Figure 3**).

2.2.2 External Sulfate Attack Mechanisms

The mechanisms of external sulfate attack have been largely studied and reviewed (Al-Amoudi, 2002; Whittaker and Black, 2015) since 1983 (Mehta, 1983). So, this section explains briefly the different steps of the ESA process.

The external sulfate attack depends on the type of cation associated with sulfate ions. In fact, sulfate ions can be found in the environment as Na_2SO_4, $MgSO_4$, K_2SO_4, $CaSO_4$,, and $(NH_4)_2SO_4$ (Xiong et al., 2014).

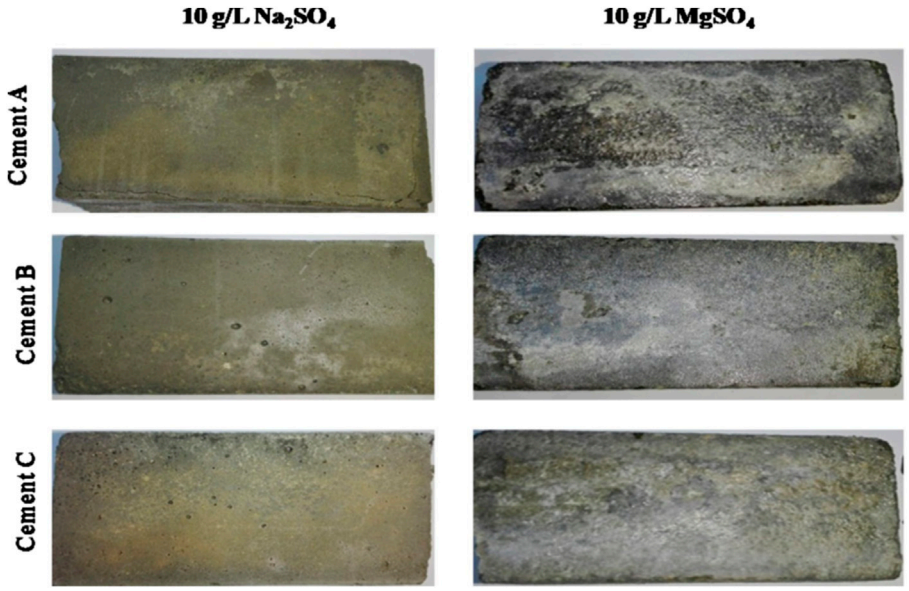

FIGURE 3 | Photograph of mortars of different samples of Tunisian sulfate-resisting Portland cement conserved for 2 years in 10 g/L Na_2SO_4 and 10 g/L $MgSO_4$ (Labidi et al., 2019a).

TABLE 2 | The sodium sulfate and magnesium sulfate attacks mechanisms.

External sulfate attack types	Attack mechanisms	Description and consequences
Sodium sulfate attack (Al-Amoudi, 2002)	$Ca(OH)_2 + NaSO_4 + 2H_2O \rightarrow CaSO_4.2H_2O + 2\ NaOH$ (R°1) $Ca_3Al_2O_6 + 3CaSO_4.2H_2O + 26H_2O \rightarrow Ca_6Al_2(SO_4)_3(OH)_{12}.26H_2O$ (R°2)	• The secondary gypsum ($CaSO_4.2H_2O$) caused an increase in volume and a loss of rigidity and force to the concrete, thereby increasing the degradation (Rondeux et al., 2014) • The secondary ettringite ($Ca_6Al_2(SO_4)_3(OH)_{12}.26H_2O$) has a hazardous effect on the cementitious materials since it grows in the concrete in the form of needles. The latter induces the expansion, deterioration, and even breaking of the concrete structure (Rondeux et al., 2014)
Magnesium sulfate attack (Santhanam et al., 2003)	$Ca(OH)_2 + MgSO_4 + 2H_2O \rightarrow CaSO_4.2H_2O + Mg(OH)_2$ (R°3) $Ca_3Al_2O_6 + 3CaSO_4.2H_2O + 26H_2O \rightarrow Ca_6Al_2(SO_4)_3(OH)_{12}.26H_2O$ (R°5)	• The magnesium sulfate attack induced the disintegration or decalcification of the cement matrix by the conversion of C-S-H to M-S-H (Labidi et al., 2019a).Therefore, the concrete will lose its binding character since the magnesium silicate hydrate (M-S-H) is a non-cementitious materials • This attack is more damaging than sodium sulfate aggression, since it is characterized by softening and deterioration of the superficial layers of the hardened cement paste (Rasheeduzzafar et al., 1994; Al-Amoudi, 2002)

In this part, the attack mechanisms in sodium sulfate and magnesium sulfate environments are described in **Table 2** since they are considered the most common sulfate attack studied (Collepardi, 2001; Neville, 2004; Page and Page, 2007; Rheinheimer, 2008; Irassar, 2009; Whittaker and Black, 2015; Sengupta, 2020) and reviewed around the world.

The cement matrix is characterized by the presence of hydrated phases that results from the hydration of mineralogical phases of cement. Indeed, during cement hydration, calcium silicate hydrate named C-S-H, and portlandite or calcium hydroxide [$Ca(OH)_2$] are formed from the alite and belite dissolution. Aluminate compound reacts with gypsum, which is added to the cement during clinker milling, to form the primary ettringite ($C_3A.3C\bar{S}\,32H$) and the monosulfoaluminate ($C_3A.C\bar{S}\,12H$). For the ferrite phase (C_4AF), it adopts the same mechanism as the aluminate phase hydration. Calcium silicate hydrate is the majority phase in the cement concrete, and it participates in the development of mechanical strength and the maintenance of the particles' adhesion to the cement concrete.

Because the portlandite (CH) content in cement paste plays a significant role in the progression of the sulfate attack mechanism (De Souza et al., 2018; De Souza et al., 2020), it is preferable to use a

FIGURE 4 | Thaumasite formation under external sulfate attack (groundwater [SO_4^{2-}] = 653 mg/L) in the Yongan Dan in Keshi of China (Mingyu et al., 2006).

sulfate-resistant Portland cement that produces a minimum amount of portlandite (a small amount of C_3S) in the system and contains a lower quantity of aluminate phase (Labidi et al., 2019a).

Another consequence of the external sulfate attack is the thaumasite "$C_3\overline{C}S\overline{S}H_{15}$" formation, also called the thaumasite sulfate attack (TSA), considered a serious danger to concrete durability, especially in cold environments, since it causes concrete degradation. This kind of attack has attracted a great deal of attention in the world since 1995 in the United Kingdom (Crammond and Halliwell, 1995); this issue has been observed in many regions around the world, such as Yongan Dam in Keisha, China, in February 2005 (Mingyu et al., 2006) (see **Figure 4**). Thaumasite formation requires the presence of sulfate ions, a carbonate source, and a low temperature (<15°C) (Rahman and Bassuoni, 2014). This kind of attack has been observed in Tunisian SR Portland cements mortars immersed in aggressive sulfate solution for 2 years (Labidi et al., 2019a).

The thaumasite is the result of two possible routes:

- Thaumasite is formed from secondary ettringite [$Ca_6Al_2[(OH)_4SO_4]_3.26H_2O$] by replacing aluminate ions Al^{3+} with silicate ions Si^{4+} and the interstitial substitution of [$(SO_4^{2-})_3(H_2O)_2$] by [$(SO_4^{2-})_3(CO_3^{2-})_2$] (Ramachandran et al., 2002):Ca_6 $[Si(OH)_6]_2(CO_3)_2(SO_4)_2.24H_2O$ = $CaCO_3.CaSO_4.CaSiO_3.15H_2O$ = $C_3\overline{C}S\overline{S}H_{15}$.
- The second mechanism to obtain the thaumasite product, an interaction between sulfate ions, carbonates, and the C-S-H gel, as mentioned in the following reaction (R°5) (Torres et al., 2003):

$$C\bar{S}H_2 + C\bar{C} + C - S - H + 12H \rightarrow C_3\overline{C}S\overline{S}H_{15}\,(R°5)$$

Another important external sulfate attack studied using the ammonium sulfate solution (Girardi and Maggio, 2011; Martins et al., 2021) presents a deterioration of concrete due to the secondary gypsum and secondary ettringite formation (Brown, 2002), similar to Na_2SO_4 and $MgSO_4$ mechanism attacks. Moreover, the C-S-H degradation was detected in this chemical aggression type (Marchand et al., 2001; Martins et al., 2021), which may eventually convert into amorphous hydrated silica (R°6). This external attack caused cracks and decomposition of concrete mainly in the interfacial zone (Girardi and Maggio, 2011).

$$xCa.SiO_2aq + x\,(NH_4)_2SO_4 + xH_2O \rightarrow SiO_2.aq + xCaSO_4.2H_2O + 2xNH_3\,(R°6)$$

3 MATERIALS AND METHODS

3.1 Materials

In this study, seven raw materials were selected for the optimization of the raw meal combinations:

- Ordinary limestone, grey, and black marls: these raw materials are used in the production of CEM I and CEMII cement types at the Bizerte cement plant "SCB." This cement industry is located in BP 53- Sebra bay, Bizerta-Tunisia.
- Siliceous limestone, yellow marl, black limestone, and flint: These natural resources are located in abandoned deposits of the SCB quarry. These materials are not used in cement production within the Bizerte cement factory. The used siliceous limestone is characterized by its pink color, and the flint is a hard sedimentary rock rich in silica oxide.
- Iron ore: It is considered a corrective material essentially used in Portland cement production in the SCB plant, which is extracted from the El Harach Tamara ore in Nefza-Tunisia.
- Natural fluorapatite: This natural material is exploited from the phosphates deposits of the Mdhilla region of the Gafsa phosphate company (CPG) in the southeast of Tunisia. The CPG is a Tunisian phosphate mining company based in Gafsa.

3.1.1 Sampling and Treatment

As mentioned previously, some of the raw materials used in the Sulfate Resisting Portland cement Raw Meals (SRRM) optimization are derived from the SCB plant's own quarries (Bir Massiougha, Jbel Abiodh, and Jebel Baccar deposits). These quarries are located 3.5 km west of Bizerte city and extend over an overall area at about 176 ha.

Limestone is extracted from the rock walls of an open pit quarry. Rock blasting is assured by using explosives. The resulting materials are transported to the crushing unit by dumper trucks.

The marl is extracted by means of wheel loaders directly from the deposit without blasting. The excavated material is transported to the processing site by transport vehicles.

Thus, the sampling of limestone and marl samples was carried out in the quarries of the SCB factory under the guidance of a consulting geologist in order to take a

TABLE 3 | Adopted designations used to explain the raw meal (raw mix) calculation program.

Chemical composition	M1	.....	Mn	Optimized raw meal	Relative clinker
$\%SiO_2$	S_{M1}	.....	S_{Mn}	S	S_{ck}
$\%Al_2O_3$	A_{M1}	.....	A_{Mn}	A	A_{ck}
$\%Fe_2O_3$	F_{M1}	.....	F_{Mn}	F	F_{ck}
%CaO	C_{M1}	.....	C_{Mn}	C	C_{ck}
%MgO	M_{M1}	.....	M_{Mn}	M	M_{ck}
$\%SO_3$	$\bar{S}_{M1}$	.....	$\bar{S}_{Mn}$	$\bar{S}$	$\bar{S}_{ck}$
$\%K_2O$	K_{M1}	.....	K_{Mn}	K	K_{ck}
$\%Na_2O$	N_{M1}	.....	N_{Mn}	N	N_{ck}
$\%P_2O_5$	P_{M1}	.....	P_{Mn}	P	P_{ck}
%F	$\bar{F}_{M1}$	.....	$\bar{F}_{Mn}$	$\bar{F}$	$\bar{F}_{ck}$

minimum quantity of 2.5 kilos of each sample (limestone, marl, and flint).

The choice of these materials is based on their availability in significant quantities in the SCB quarries, according to the various operation surveys conducted by the Bizerte cement plant.

In this study, sample treatment is considered a key operation in order to guarantee accurate and reliable X-ray fluorescence analysis results.

In the first step, each raw material is crushed to a particle size of less than 5 mm by means of a jaw crusher in order to eliminate the size factor. The latter is a guiding vector for the variation of the crushing material fineness.

In the second step, each sample undergoes a drying operation (in the oven for 24 h at 100°C ± 5) to remove the water from moisture, which subsequently facilitates secondary grinding. This grinding was carried out with a grinder-shaker on hold of about 250 g of the powder obtained by crushing followed by drying. The crushed powder usually gives a zero refusal on a sieve of 60 μm after grinding for about 2 min, which gives it an appreciable fineness. Finally, the homogenizing step consists of mixing the samples obtained in the previous phase in order to obtain a homogeneous, simple, and harmonic approximation. It is done by introducing four catches (of about 250 g each) into a one-liter box and shaking it manually for 2–3 min. The samples are then stored in boxes and numbered for analysis by X-ray fluorescence.

3.2 Methods

3.2.1 X-Ray Fluorescence

The X-ray fluorescence technique provides a precise determination of both quantitative and qualitative analysis of chemical oxides (CaO, SiO_2, Al_2O_3, Fe_2O_3, MgO, SO_3, K_2O, Na_2O, P_2O_5, and F) composition (Khelifi et al., 2017). All treated raw materials were analyzed by the X-Ray florescence ARL9900 spectrometer.

3.2.2 Raw Meal Combination Calculation Tool: Calculation Basis

This part described the calculation tool used to optimize the raw meal combinations; it gives information about the chemical compositions in oxides of optimized raw meals and the mineralogical composition of their corresponding clinkers. The numerical application of this calculation basis is carried on the EXCELL software, which is based on the chemical analysis from XRF of each raw material (ordinary limestone, black marl, flint, etc.) and the burning modules variation (LSF, SIM, and ALM) (Chatterjee, 1983; Mezza et al., 2020).

$$\text{Lime saturation factor}: \ \mathbf{LSF} = \frac{100 \times \mathrm{C}}{2,8 \times \mathrm{S} + 1,18 \times \mathrm{A} + 0,65 \times \mathrm{F}}$$

$$\mathbf{96 \le LSF \le 100}$$

$$\text{Silica ratio}: \ \mathrm{SIM} = \frac{S}{A+F} \ \mathbf{2 \le SIM \le 3.5}$$

$$\text{Alumina ratio}: \ \mathrm{ALM} == \frac{A}{F} \ \mathbf{0.64 \le ALM \le 1.8}$$

The LSF, SIM, and ALM ratio are considered the main parameters for raw mix design. So, the steps to be taken to carry out this work are:

- Determination of chemical composition (CaO, SiO_2, Al_2O_3, Fe_2O_3, MgO, SO_3, K_2O, Na_2O, P_2O_5, and F) in weight percentages of each raw material by means X-ray fluorescence. The raw materials (limestone, marl, etc.) are designated M1, . . ., Mn ($1 < n \le 4$)as presented in **Table 3** by means X-ray fluorescence.

S_{M1} is the silica content in M1 (determined from XRF analysis), S is the silica amount in the optimized raw meal combination, and S_{ck} is the SiO_2 weight percentage in its corresponding clinker.

- Then, with the knowledge of necessary proportions ($x1$, $x2$, . . ., xn) from each raw material (M1. . .Mn), the chemical composition $(\mathrm{S}, \mathrm{C}, \ldots, \bar{\mathrm{F}})$ of optimized raw mix is simply obtained by means the following **Eqs 1–10**:

$$\mathrm{S} = \mathrm{x1SM1} + \ldots + \mathrm{xnSMn} \quad (1)$$

$$\mathrm{C} = \mathrm{x1CM1} + \ldots + \mathrm{xnCMn} \quad (2)$$

$$\mathrm{A} = \mathrm{x1AM1} + \ldots + \mathrm{xnAMn} \quad (3)$$

$$\mathrm{F} = \mathrm{x1FM1} + \ldots + \mathrm{xnFMn} \quad (4)$$

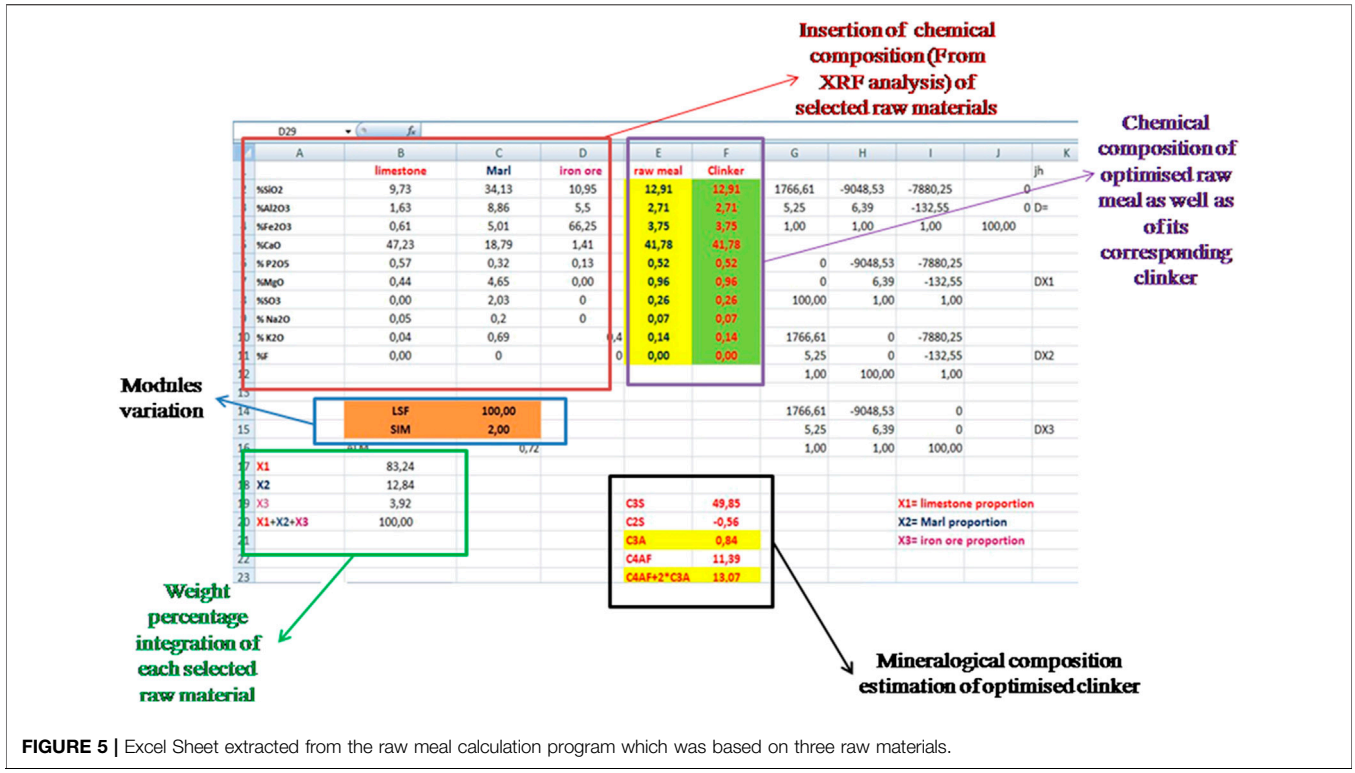

FIGURE 5 | Excel Sheet extracted from the raw meal calculation program which was based on three raw materials.

$$M = x1MM1 + \ldots + xnMMn \quad (5)$$

$$\bar{S} = x1\bar{S}M1 + \ldots + xn\bar{S}Mn \quad (6)$$

$$K = x1KM1 + \ldots + xnKMn \quad (7)$$

$$N = x1NM1 + \ldots + xnNMn \quad (8)$$

$$P = x1PM1 + \ldots + xnPMn \quad (9)$$

$$\bar{F} = x1\bar{F}M1 + \ldots + x\bar{n}\bar{F}Mn \quad (10)$$

- Using Bogue calculation (Le Saoût et al., 2011; Standard, 2011; Labidi et al., 2019b), the mineralogical composition (C_3S, C_2S, C_3A, and C_4AF) is determined in order to study the suitability of used raw materials to produce the desired cement type (in our case, SR Portland cement).

3.2.2.1. The Use of Three Raw Materials (n = 3) in Optimized Raw Meal Calculation Program

As mentioned in the previous section, it is necessary to determine the necessary quantities ($x1$, $x2$, and $x3$) from used raw materials, in order to calculate the chemical composition oxides of the optimized raw mix as explained in **Figure 5**.

So, the calculation of the different percentage integration of raw materials is based on the different stages of the following calculation system:

- Integration of the **Eqs 1–4** already elaborated in the previous section, on (I), (II), and (III) formulas:

$$LSF = \frac{100 \times C}{2.8 \times S + 1.18 \times A + 0.65 \times F} \quad (I)$$

$$SIM = \frac{S}{A + F} \quad (II)$$

$$x1 + x2 + x3 = 100 \quad (III)$$

The (I), (II), and (III) take new forms as following:

$$a_1 \times x1 + a_2 \times x2 + a_3 \times x3 = 0 \quad (I - 1)$$

$$a_4 \times x1 + a_5 \times x2 + a_6 \times x3 = 0 \quad (II - 1)$$

$$x1 + x2 + x3 = 100 \quad (III - 1)$$

Since

$$a_1 = 100 \times C_{M1} - LSF \times (2.8 \times S_{M1} + 1.18 \times A_{M1} + 0.65 \times F_{M1});$$

$$a_2 = 100 \times C_{M2} - LSF \times (2.8 \times S_{M2} + 1.18 \times A_{M2} + 0.65 \times F_{M2});$$

$$\text{et } a_3 = 100 \times C_{M3} - LSF \times (2.8 \times S_{M3} + 1.18 \times A_{M3} + 0.65 \times F_{M3});$$

$$a_4 = S_{M1} - SIM \times (A_{M1} + F_{M1});$$

$$a_5 = S_{M2} - SIM \times (A_{M2} + F_{M2});$$

$$a_6 = S_{M3} - SIM \times (A_{M3} + F_{M3}).$$

- Resolution of the computing system includes (I-1), (II-1), and (III-1) by means of Cramer mathematical method as present:

$$\begin{pmatrix} a1 & a2 & a3 \\ a4 & a5 & a6 \\ 1 & 1 & 1 \end{pmatrix} \times \begin{pmatrix} X1 \\ X2 \\ X3 \end{pmatrix} = \begin{pmatrix} 0 \\ 0 \\ 100 \end{pmatrix}$$

$$A1 = \det\begin{vmatrix} a1 & a2 & a3 \\ a4 & a5 & a6 \\ 1 & 1 & 1 \end{vmatrix}$$

$$= a1 \times (a5 \times 1 - a6 \times 1) - a4 \times (a2 \times 1 - a3 \times 1) + 1 \times (a2 \times a6 - a5 \times a3);$$

$$A2 = \det\begin{vmatrix} 0 & a2 & a3 \\ 0 & a5 & a6 \\ 100 & 1 & 1 \end{vmatrix} = 100\,(a2 \times a6 - a5 \times a3);$$

$$A3 = \det\begin{vmatrix} a1 & 0 & a3 \\ a4 & 0 & a6 \\ 1 & 100 & 1 \end{vmatrix}$$

$$= a1 \times (-a6 \times 100) - a4 \times (-a3 \times 100);$$

$$A4 = \det\begin{vmatrix} a1 & a2 & 0 \\ a4 & a5 & 0 \\ 1 & 1 & 100 \end{vmatrix} = a1 \times (a5 \times 100) - a4 \times (a2 \times 100);$$

And the x1 = A2/A1, x2 = A3/A1and x3 = A4/A1.

- Once the *x*1, *x*2, and *x*3 rates are calculated, the chemical composition of the optimized raw meal is determined **Eq 1–10**, which are used subsequently to estimate the mineralogical composition of its corresponding clinker (see **Figure 5**).

*3.2.2.2 The Use of Four Raw Materials (*n = 4*) in Optimized Raw Meal Calculation Program*

The same methodology is used as in the previous part:

- Integration of the **Eqs 1–4** already elaborated in the previous section, on (I), (II), (III), and (IV) formulas:

$$LSF = \frac{100 \times C}{2.8 \times S + 1.18 \times A + 0.65 \times F} \quad (I)$$

$$SIM = \frac{S}{A + F} \quad (II)$$

$$ALM == \frac{A}{F} \quad (III)$$

$$x1 + x2 + x3 + x4 = 100 \quad (IV)$$

The (I), (II), (III), and (IV) equations take new forms as follows:

$$b1 \times x1 + b2 \times x2 + b3 \times x3 + b4 \times x4 = 0 \quad (I - 2)$$

$$b5 \times x1 + b6 \times x2 + b7 \times x3 + b8 \times x4 = 0 \quad (II - 2);$$

$$c1 \times x1 + c2 \times x2 + c3 \times x3 + c4 \times x4 = 0 \quad (III - 2);$$

$$x1 + x2 + x3 + x4 = 100 \quad (IV - 2);$$

Since

$$b_1 = 100 \times C_{M1} - LSF \times (2.8 \times S_{M1} + 1.18 \times A_{M1} + 0.65 \times F_{M1});$$

$$b_2 = 100 \times C_{M2} - LSF \times (2.8 \times S_{M2} + 1.18 \times A_{M2} + 0.65 \times F_{M2});$$

$$b_3 = 100 \times C_{M3} - LSF \times (2.8 \times S_{M3} + 1.18 \times A_{M3} + 0.65 \times F_{M3});$$

$$b_4 = 100 \times C_{M4} - LSF \times (2.8 \times S_{M4} + 1.18 \times A_{M4} + 0.65 \times F_{M4});$$

$$b_5 = S_{M1} - SIM \times (A_{M1} + F_{M1});$$

$$b_6 = S_{M2} - SIM \times (A_{M2} + F_{M2});$$

$$b_7 = S_{M3} - SIM \times (A_{M3} + F_{M3});$$

$$b_8 = S_{M4} - SIM \times (A_{M4} + F_{M4});$$

$$c_1 = A_{M1} - (ALM \times F_{M1});$$

$$c_2 = A_{M2} - (ALM \times F_{M2});$$

$$c_3 = A_{M3} - (ALM \times F_{M3});$$

$$c_4 = A_{M4} - (ALM \times F_{M4});$$

- Resolution of the computing system includes (I-2), (II-2), (III-2), and (IV-2) equations by means of the Cramer mathematical method as follows:

$$\begin{pmatrix} b1 & b2 & b3 & b4 \\ b5 & b6 & b7 & b8 \\ c1 & c2 & c3 & c4 \\ 1 & 1 & 1 & 1 \end{pmatrix} \times \begin{pmatrix} X1 \\ X2 \\ X3 \\ x4 \end{pmatrix} = \begin{pmatrix} 0 \\ 0 \\ 0 \\ 100 \end{pmatrix}$$

$$B1 = \det\begin{vmatrix} b1 & b2 & b3 & b4 \\ b5 & b6 & b7 & b8 \\ c1 & c2 & c3 & c4 \\ 1 & 1 & 1 & 1 \end{vmatrix} = b1 \times \det\begin{vmatrix} b6 & b7 & b8 \\ c2 & c3 & c4 \\ 1 & 1 & 1 \end{vmatrix} - b5 \times \det\begin{vmatrix} b2 & b3 & b4 \\ c2 & c3 & c4 \\ 1 & 1 & 1 \end{vmatrix} + c1 \times \det\begin{vmatrix} b2 & b3 & b4 \\ b6 & b7 & b8 \\ 1 & 1 & 1 \end{vmatrix} - \det\begin{vmatrix} b2 & b3 & b4 \\ b6 & b7 & b8 \\ c2 & c3 & c4 \end{vmatrix}$$

$$= b1 \times [b6 \times (c3 - c4) - c2 \times (b7 - b8) + (b7 \times c4 - c3 \times b8)]$$

$$-b5 \times [b2 \times (c3 - c4) - c2 \times (b3 - b4) + (b3 \times c4 - c3 \times b4)] + c1 \times [b2 \times (b7 - b8) - b6 \times (b3 - b4) + (b3 \times b80b7 \times b8) \times] - [b2 \times (b7 \times c4 - c3 \times b8) - b6 \times (b3 \times c4 - c3 \times b4) + c2 \times (b3 \times b8 - b7 \times b4)]$$

$$B2 = \det\begin{vmatrix} 0 & b2 & b3 & b4 \\ 0 & b6 & b7 & b8 \\ 0 & c2 & c3 & c4 \\ 100 & 1 & 1 & 1 \end{vmatrix} = -100 \times \det\begin{vmatrix} b2 & b3 & b4 \\ b6 & b7 & b8 \\ c2 & c3 & c4 \end{vmatrix}$$

$$= 100 \times b2 \times (b7 \times c4 = c3 \times b8) - b6 \times (b3 \times c4 - c3 \times b4) + c2 \times (b3 \times b8 - b7 \times b4)$$

$$B3 = \det\begin{vmatrix} b1 & 0 & b3 & b4 \\ b5 & 0 & b7 & b8 \\ c1 & 0 & c3 & c4 \\ 1 & 100 & 1 & 1 \end{vmatrix} = b1 \times \det\begin{vmatrix} 0 & b7 & b8 \\ 0 & c3 & c4 \\ 100 & 1 & 1 \end{vmatrix} - b5 \times \det\begin{vmatrix} 0 & b3 & b4 \\ 0 & c3 & c4 \\ 100 & 1 & 1 \end{vmatrix} + c1 \times \det\begin{vmatrix} 0 & b3 & b4 \\ 0 & b7 & b8 \\ 100 & 1 & 1 \end{vmatrix} - \det\begin{vmatrix} 0 & b3 & b4 \\ 0 & b7 & b8 \\ 0 & c3 & c4 \end{vmatrix}$$

$$= b1 \times 100 \times (b7 \times c4 - b8vc3) - b5 \times 100 \times (b3 \times c4 - c3 \times b4) + c1 \times 100 \times (b3 \times b8 - b7 \times b4)$$

TABLE 4 | Chemical analysis of collected raw materials (in weight percentages).

	% SiO_2	%Al_2O_3	%Fe_2O_3	%CaO	%MgO	%SO_3	%K_2O	%Na_2O	%P_2O_5	%F	%$CaCO_3$
Ordinary limestone	9.73	1.63	0.61	47.23	0.44	0.00	0.04	0.05	0.57	—	83.33
Grey marl	28.46	9.20	4.35	23.79	2.57	0.75	0.47	0.07	0.27	—	42.48
Black marl	34.13	8.86	5.01	18.79	4.65	2.08	0.69	0.20	0.32	—	33.55
Iron ore	10.95	5.50	66.25	1.41	0.00	0.00	0.40	0.00	0.13	—	—
Siliceous limestone	15.17	1.89	0.73	44.57	0.64	0.00	0.06	0.05	0.69	—	79.60
Yellow marl	21.67	6.52	5.42	35.10	1.72	0.88	0.54	0.09	0.42	—	62.69
Black limestone	9.60	2.10	0.6	45.86	0.51	0.64	0.06	0.04	0.37	—	81.36
Flint	72.45	0.78	0.91	15.37	2.13	0.83	0.00	0.09	0.31	—	27.44
NFA	5.60	0.65	0.35	48.50	0.60	3.50	—	—	28.00	3.30	—

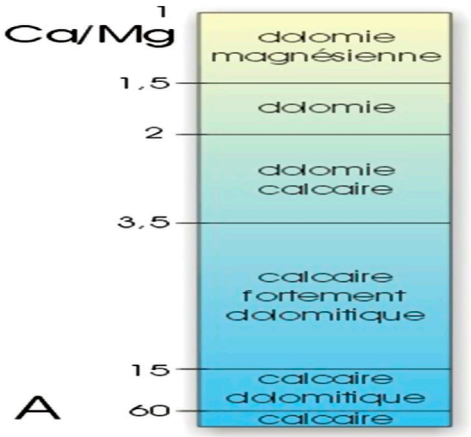

FIGURE 6 | Classification of carbonate rocks according to the Ca/Mg ratio (Boulvain, 2014).

TABLE 5 | Ca/Mg values of collected limestone sample**s.**

	Ordinary limestone	Siliceous limestone	Black limestone
Ca/Mg	107.34	69.64	89.92

$$B4 = \det\begin{vmatrix} b1 & b2 & 1 & b4 \\ b5 & b6 & b7 & b8 \\ c1 & c2 & c3 & c4 \\ 1 & 1 & 100 & 1 \end{vmatrix} = b1 \times \det\begin{vmatrix} b6 & 0 & b8 \\ c2 & 0 & c4 \\ 1 & 100 & 1 \end{vmatrix} - b5 \times \det\begin{vmatrix} b2 & 0 & b4 \\ c2 & 0 & b4 \\ 1 & 100 & 1 \end{vmatrix} + c1 \times \det\begin{vmatrix} b2 & 0 & b4 \\ b6 & 0 & b8 \\ 1 & 100 & 1 \end{vmatrix} - \det\begin{vmatrix} b2 & 0 & b4 \\ b6 & 0 & b8 \\ c2 & 0 & c4 \end{vmatrix}$$

$$= b1 \times [b6 \times (-100 \times c4) - c2 \times (-100 \times b8)] - b5 \times [b2 \times (-100 \times c4) - c2 \times (-100 \times b4)] + c1 \times [b2 \times (-100 \times b8) - b6 \times (-100 \times b4)]$$

$$B5 = \det\begin{vmatrix} b1 & b2 & b3 & 0 \\ b5 & b6 & b7 & 0 \\ c1 & c2 & c3 & 0 \\ 1 & 1 & 1 & 100 \end{vmatrix} = b1 \times \det\begin{vmatrix} b6 & b7 & 0 \\ c2 & c3 & 0 \\ 1 & 1 & 100 \end{vmatrix} - b5 \times \det\begin{vmatrix} b2 & b3 & 0 \\ c2 & c3 & 0 \\ 1 & 1 & 100 \end{vmatrix} + c1 \times \det\begin{vmatrix} b2 & b3 & 0 \\ b6 & b7 & 0 \\ 1 & 1 & 100 \end{vmatrix} - \det\begin{vmatrix} b2 & b3 & 0 \\ b6 & b7 & 0 \\ c2 & c3 & 0 \end{vmatrix}$$

$$= b1 \times [b6 \times (c3 \times 100) - c2 \times (100 \times b7)] - b5 \times [b2 \times (-100 \times c3) - c2 \times (b3 \times 100)] + c1 \times [b2 \times (b7 \times 100) - b6 \times (100 \times b3)]$$

And finally, the rates of each raw material are:

$$x1 = B2/B1, x2 = B3/B1, x3 = B4/B1 \text{et } x4 = B5/B1$$

- Once the x1, x2, x3, and x4 rates are calculated, the chemical composition of the optimized raw meal is determined **Eqs 1–10**, which are used subsequently to estimate the mineralogical composition of its corresponding clinker.

4 RESULTS AND DISCUSSIONS

4.1 XRF Analysis

The chemical composition analysis, determined by XRF, of different raw materials was presented in **Table 4**, as well as the quantities of carbonate calcium.

As shown in **Table 4**, ordinary limestone is characterized by 47.23% of CaO content and close to 10% of silica oxide content. This limestone type is used as the foundation in the SCB factory's raw meal preparation because it produces high-quality Portland clinker that meets the company's technical and commercial requirements. However, the siliceous limestone presents a high SiO_2 amount, about 15.17%. That is why this raw material is known as siliceous limestone. In addition, the black limestone has a similar chemical composition to ordinary limestone.

Comparing the marl samples, the black marl is rich in magnesium oxide (4.65%), while the yellow marl has the lowest MgO content 1.72% and the highest Fe_2O_3 amount at

TABLE 6 | SR Portland raw meal combinations by using three raw materials used in ordinary cement production in the SCB factory.

Combinations	LSF	SIM	%x_1 = integration rate of ordinary limestone	%$x2$ = integration rate of marl	%$x3$ = integration rate of iron ore	% C_3A	2 × %C_3A + % C_4AF	ALM
SR RM1	100	2.5	81.90	16.90	1.71	5.53	22.17	1.21
SR RM 2	99	2.5	81.47	16.85	1.69	5.64	22.41	1.22
SR RM 3	98	2.5	81.03	17.31	1.67	5.75	22.65	1.23
SR RM 4	97	2.5	80.58	17.77	1.65	5.87	22.90	1.24
SR RM 5	96	2.5	80.12	18.25	1.63	5.98	23.14	1.25
SR RM 6	100	2.1	81.88	14.92	3.20	2.94	21.58	0.86
SR RM 7	100	2.2	81.89	15.33	2.78	3.66	21.46	0.94
SR RM 8	100	2.3	81.89	15.71	2.40	4.33	21.72	1.02
SR RM 9	100	2.4	81.90	16.06	2.04	4.95	21.95	1.11
SR RM 10	100	2	81.88	14.47	3.65	2.16	20.88	0.79
SR RM 11	99	2	81.49	14.97	3.64	2.25	21.11	0.79
SR RM 12	98	2	81.07	15.36	3.36	2.34	21.34	0.80
SR RM 13	97	2	80.57	15.80	3.63	2.43	21.57	0.81
SR RM 14	96	2	80.12	16.26	3.62	2.52	21.81	0.81

Marl = 50% grey marl+50% black marl.

about 5.42%. The grey marl is considered an aluminous marl since it contains a high content of alumina (Al_2O_3). Concerning the flint, which is considered a very hard sedimentary rock, it is characterized by a very high content of SiO_2 of 72.45% and low quantities of CaO, Al_2O_3, and Fe_2O_3. These elements are considered impurities in this rock, which belongs to the family of carbonate rocks (Paul and Kouamé, 2022).

According to the limestone classification scale given in **Figure 6**, which is based on the Ca/Mg ratio (Boulvain, 2014; Chilingar, 1956; Zeyen et al., 2017; Taha1 and Abdullah2, 2020), the collected limestone samples, as shown in **Table 5**, are considered pure limestone, poor in dolomite phase [$CaMg(CO_3)_2$]. This means that most of the CaO quantity exists in these samples as $CaCO_3$ phase. This constatation is very important to be sure that the CO_2 emission source is only from $CaCO_3$ burning.

The chemical analysis of natural fluorapatite "$Ca_5(PO_4)_3F$"shows that this raw material presents an important source of CaO (48.50%), which thereafter provides the necessary quantity of lime for the formation of the principal mineralogical phases of Portland cement (C_3S, C_2S, C_3A, and C_4AF). While the NAF contains an important amount of P_2O_5 (28%), phosphorus is considered a detrimental element for both the clinker mineralogy and the physical-mechanical properties of the cement during hydration (Hökfors et al., 2015; Ismail et al., 2015). Moreover, the presence of CaF_2 (Da et al., 2022) in the NAF structure is considered a key strength since the existence of fluorite in cement raw meal improves the burnability process and lowers the clinkering temperature, which favors the C_3S formation and reduces the free lime content (Yamashita and Tanaka, 2012; Boughanmi et al., 2018a; Xie et al., 2021).

The natural fluorapatite sample used in this study is already used in published research work (Boughanmi et al., 2018b) about the synthesis of Portland clinker by means of NAF as a raw material at laboratory scale (by using pure commercially available limestone, silica, alumina, and iron oxide as raw materials to prepare raw meals). This work aims to study the influence of the replacement of the proportion of limestone in the raw meals of laboratory made by NAF (0%–15%). It was found (Boughanmi et al., 2018b) that the detrimental impact of phosphorus on the transformation of C_2S and lime in C_3S, which is generally remarked for lower amounts, becomes efficient but remains suitable for up to 8% natural fluorapatite in the raw meal. This shows that a beneficial impact of fluorine counterbalances the negative effect of phosphorous. Cements obtained from up to 8% natural fluorapatite incorporation still present acceptable properties (Boughanmi et al., 2018b).

4.2 Sulfate-Resisting Portland Cement Raw Meal Optimization

4.2.1 Feasibility Study of SR Portland Cement Raw Meal Preparation

In general, Portland cement manufacturing using only limestone and marl is not usually sufficient to achieve the suitable raw mix in question. Therefore, the use of corrective elements such as iron ore (Fe_2O_3 source), sand (SiO_2 source), or bauxite (Al_2O_3 source) is essential in order to balance and correct the raw meal combinations (Michaux et al., 1990; Kurdowski, 2014).

The SCB plant's raw mix manufacturing uses iron ore as a corrective element in addition to ordinary limestone and gray and black marls. So, based on the raw meal calculation program (the use case three raw materials), the LSF and SIM ratios varied in the range of 96–100 and 2–2.5, respectively, in order to check the suitability of optimized SR raw meal (SR RM) to give a sulfate-resisting Portland clinker ($C_3A \leq 3\%$ and $2C_3A + C_4AF \leq 20\%$).

Table 6 presents the calculation results of different SR raw meal combinations; the SR RM10 is considered the only optimized raw meal. It can provide an approximate SR Portland cement ($C_3A \leq 3$), but the second requirement "$2C_3A + C_4AF \leq 20\%$" seems not to be met.

TABLE 7 | SR Portland raw meal combinations by using three raw materials (substituting the marl mix with black marl).

Combinations	LSF	SIM	%x_1 = integration rate of ordinary limestone	%$x2$ = integration rate of black marl	%$x3$ = integration rate of iron ore	% C_3A	2 × %C_3A + % C_4AF	ALM
SR RM 15	100	2	83.25	12.85	3.89	1.27	19.78	0.72
SR RM 16	99	2	82.87	13.24	3.90	1.34	19.97	0.73
SR RM 17	98	2	82.47	13.63	3.90	1.40	20.17	0.73
SR RM 18	97	2	82.07	14.03	3.90	1.46	20.37	0.73
SR RM 19	96	2	81.66	14.43	3.91	1.56	20.57	0.74

The SR RM10combination contains a high iron ore incorporation percentage (3.65%), which explains the decrease in aluminate content (C_3A) and consequently the increase of $2C_3A + C_4AF$.This behaviour can favor the formation of C_2F phase during the clinkering process. However, the increase of iron oxide in raw meal affects the cement kiln process. In fact, the high amount of Fe_2O_3 induces the decrease of the clinker liquid phase "L.P" viscosity during the burning process. In this case, the liquid phase becomes very fluid and there is a high risk of ring formation in the kiln, which causes the blockage of the burning lining (Kumar, 2013; Belgacem et al., 2016; Sengupta, 2020). So, it is imperative to optimize a good raw meal (especially if it is not doped with iron ore) to obtain SR Portland cement with a low amount of aluminate phase (C_3A) and to prevent poor operation of the cement kiln.

The LSF = 100 and SIM = 2 are considered acceptable values since they are situated in a suitable range of values for Portland cement manufacturing.

The C_2S content of the SR RM 10 combination is negative (−0.44%), indicating that the relative clinker is poor in belite phase. Subsequently, the clinker grinding becomes easier since the alite amount increases and ameliorates the clinker grindability (Unland, 2001).

To improve the quality of optimized SR raw meal without increasing the iron ore incorporation, a replacement of marl by only black marl was necessary, in order to increase the silica content and maintain the $2C_3A + C_4AF$ at less than 20%. This study (**Table 7**) provides the possibility to obtain a SR Portland raw meal (SR RM 16) required to meet the SR Portland cement requirements ($C_3A \leq 3$ and $2C_3A + C_4AF \leq 20\%$) (NT, 47.26, 1999; En, 2001).

So incorporating siliceous marl (black marl) can be a solution to produce an SR Portland clinker. Whereas, the manufacturing of this combination (SR RM 16) on an industrial scale is difficult since the use of ALM value of about 0.73 makes the burning process hard (Spence, 1980).

4.2.2 SR Portland Raw Meal Optimization With Correction

In this part, the calculation of optimized raw meals is based on the variation of all three burning modules (LSF, SIM, and ALM) and the integration of the fourth raw material (flint and siliceous limestone) being extracted. The choice of these materials is related to the important content of silica, as shown in **Table 4**.

Based on Bogue equations ($C_3A = 2.650 \times \%Al_2O_3 - 1.692 \times \%Fe_2O_3$ and $C_4AF = 3.043 \times \%Fe_2O_3$), if C_3A was fixed at 3%, the ALM modulus would be taken to a value of about 0.91. This ALM value will be used in raw meals' optimization since it offers a high probability of manufacturing SR Portland cement and guarantees the stability of the burning lining (kiln) of the cement manufacturing process.

4.2.2.1 SR Portland Raw Meal Correction With Flint and Siliceous Limestone

This study of raw meal optimization (calculation program of four raw materials) is based on the incorporation (%x4) of a fourth raw material (flint or siliceous limestone) in addition to limestone (% x1), marl (%x2), and iron ore (%x3). The choice of these corrective materials is based on the high silica content they contain (see **Table 4**).

- Flint integration

The calculation results of optimized raw meal combinations with flint correction are as listed below:

- SR RM 20: LSF = 100, SIM = 2, ALM = 0.91; %$x1$ = 80.71, %$x2$ = 17.75, %$x3$ = 2.73; %$x4$ = −0.91; %C_3A = 3.59 and 2 × %C_3A + %C_4AF = 22.37.
- SR RM 21: LSF = 100, SIM = 2.3, ALM = 0.91; %$x1$ = 82.91, %$x2$ = 13.87, %$x3$ = 2.42, %$x4$ = 0.78; % C_3A = 3.24 and 2 × %C_3A + %C_4AF = 20.15.
- SR RM 22: LSF = 100, SIM = 2.5, ALM = 0.91; %$x1$ = 84.17, %$x2$ = 11.69, %$x3$ = 2.25, %$x4$ = 1.89; %C_3A = 3.04 and 2 × %C_3A + %C_4AF = 18.90.
- SR RM 23: LSF = 100, SIM = 3, ALM = 0.91; %$x1$ = 86.66, %$x2$ = 7.32, %$x3$ = 1.90, %$x4$ = 4.12; %C_3A = 2.63 and 2 × %C_3A + %C_4AF = 16.36.
- SR RM 24: LSF = 99, SIM = 3, ALM = 0.91; %$x1$ = 86.32, %$x2$ = 7.55, %$x3$ = 1.92, %$x4$ = 4.12; %C_3A = 2.65 and 2 × %C_3A + %C_4AF = 16.48.
- SR RM 25: LSF = 98, SIM = 3, ALM = 0.91; %$x1$ = 85.97, %$x2$ = 7.79, %$x3$ = 1.93, %$x4$ = 4.31; %C_3A = 2.66 and 2 × %C_3A + %C_4AF = 16.59
- SR RM 26: LSF = 97, SIM = 3, ALM = 0.91; %$x1$ = 85.61, %$x2$ = 8.04, %$x3$ = 1.95, %$x4$ = 4.40; %C_3A = 2.68 and 2 × %C_3A + %C_4AF = 16.70.

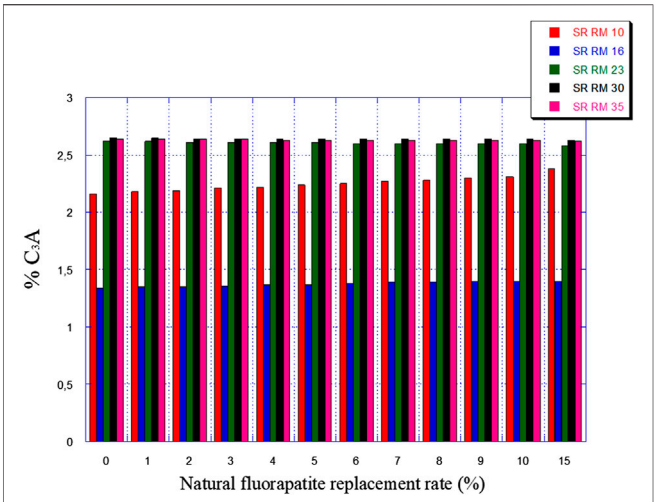

FIGURE 7 | Expected C_3A amounts variation in function of the natural fluorapatite replacement.

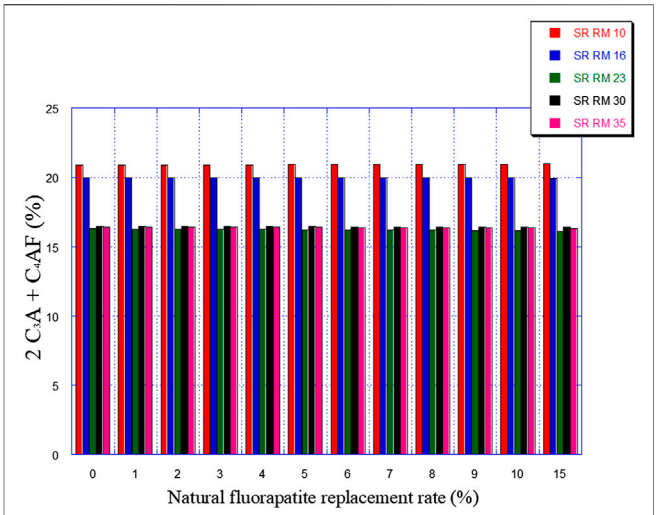

FIGURE 8 | Expected $2C_3A + C_4AF$ amounts variation in function of the natural fluorapatite replacement.

- SR RM 27: LSF = 96, SIM = 3, ALM = 0.91; %$x1$ = 85.25, %$x2$ = 8.28, %$x3$ = 1.97, %$x4$ = 4.50; %C_3A = 3.70 and 2 × %C_3A + %C_4AF = 16.52.

The flint incorporation improved the specific mineralogical composition of the optimized SR Portland clinker. So, in this case, the SR Portland cement manufacturing cement is possible from the flint incorporation, satisfying the appropriate integration level of flint. The raw mix "SR RM 22" is the best optimized combination since it presents the optimum conditions of SR Portland cement.

- Siliceous limestone integration

The siliceous limestone is characterized by a silica content of about 15% and a hardness of three according to the Mohs hardness scale (Gibson et al., 2018). This rock is easy to grind because its humidity is on order of 5%. The calculation results of optimized raw meal combinations with siliceous limestone correction are as listed below:

- SR RM 27: LSF = 100, SIM = 2, ALM = 0.91; %$x1$ = 80.71, %$x2$ = 17.75, %$x3$ = 2.73, %$x4$ = −0.91; %C_3A = 3.59 and 2 × %C_3A + %C_4AF = 22.37.
- SR RM 28: LSF = 100, SIM = 2.5, ALM = 0.91; %$x1$ = 60.05, %$x2$ = 10.54, %$x3$ = 2.40, %$x4$ = 27.01; %C_3A = 3.05 and 2 × %C_3A + %C_4AF = 18.97.
- SR RM 29: LSF = 100, SIM = 2.6, ALM = 0.91; %$x1$ = 54.20, %$x2$ = 6.24, %$x3$ = 2.23, %$x4$ = 34.19; %C_3A = 2.96 and 2 × %C_3A + %C_4AF = 18.42.
- SR RM 30: LSF = 100, SIM = 3, ALM = 0.91; %$x1$ = 33.98, %$x2$ = 4.77, %$x3$ = 2.23, %$x4$ = 59.02; %C_3A = 2.65 and 2 × %C_3A + %C_4AF = 16.50.
- SR RM 31: LSF = 99, SIM = 3, ALM = 0.91; %$x1$ = 35.45, %$x2$ = 4.95, %$x3$ = 2.26, %$x4$ = 60.34; %C_3A = 2.67 and 2 × %C_3A + %C_4AF = 16.61.
- SR RM 32: LSF = 98, SIM = 3, ALM = 0.91; %$x1$ = 30.90, %$x2$ = 5.13, %$x3$ = 2.28, %$x4$ = 61.69; %C_3A = 2.69 and 2 × %C_3A + %C_4AF = 16.73.
- SR RM 33: LSF = 97, SIM = 3, ALM = 0.91; %$x1$ = 29.32, %$x2$ = 5.32, %$x3$ = 2.30, %$x4$ = 63.06; %C_3A = 2.71 and 2 × %C_3A + %C_4AF = 16.85.
- SR RM 34: LSF = 96, SIM = 3, ALM = 0.91; %$x1$ = 27.72, %$x2$ = 5.51, %$x3$ = 2.33, %$x4$ = 64.45; %C_3A = 2.73 and 2 × %C_3A + %C_4AF = 16.97.

The results of the calculation show that SR Portland cement manufacturing with this limestone type is possible and that its integration rates vary from 27% to 64%. Moreover, the burning module values in this studied case are considered suitable in the rage of Portland cement manufacturing without undesirable effects on the operation of the cement factory.

It is possible to prepare a SR raw meal using flint, but this latter can eventually induce a problem in the raw materials grinding operation. Since flint is a very hard rock (rich in quartz), its hardness was estimated to be seven on the mohs hardness scale (Bennett et al., 1989; Beuker, 2012). Therefore, the manufacturing of SR clinker using flint requires enormous energy during the operation of raw mix milling and subsequently high and costly energy consumption.

So the only way to exploit the flint deposit is to mix a low quantity of this material with a high rate of siliceous limestone, since the latter is a brittle material and improves the flint grindability. So the fourth material requires a combination of "95% siliceous limestone + 5% flint."

The calculation results of optimized raw meal combinations with combined siliceous limestone and flint correction are as listed below:

- SR RM 35: LSF = 100, SIM = 3, ALM = 0.91; %$x1$ = 56.63, %$x2$ = 5.86, % $x3$ = 2.09, %$x4$ = 35.42; %C_3A = 2.65 and 2 × %C_3A + %C_4AF = 16.44.

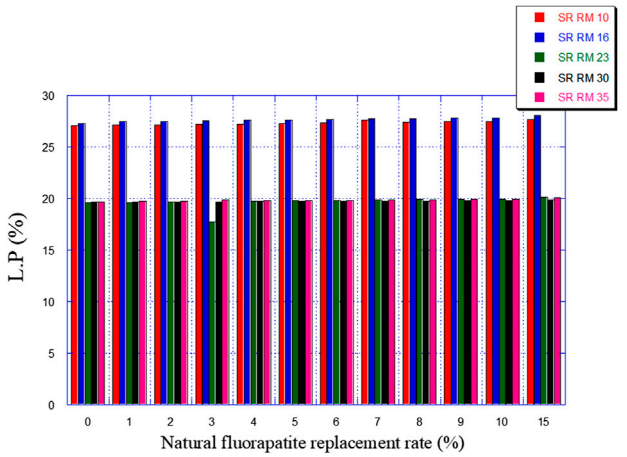

FIGURE 9 | Predicted liquid phase (L.P) amounts in function of the natural fluorapatite replacement.

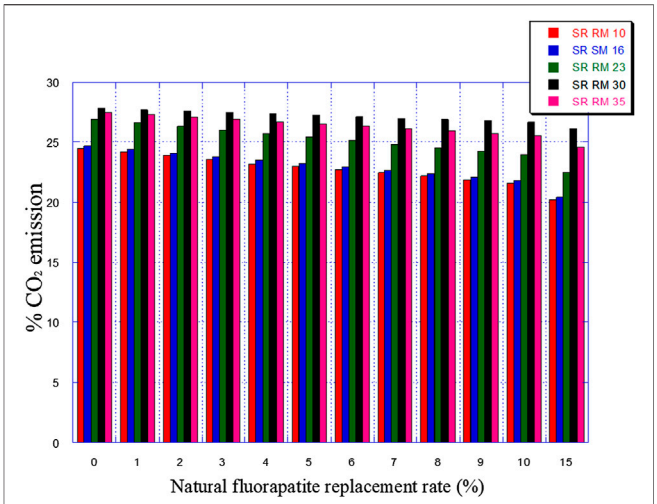

FIGURE 10 | Expected CO_2 emissions in function of the natural fluorapatite replacement.

- SR RM 36: LSF = 99, SIM = 3, ALM = 0.91; %$x1$ = 55.62, %$x2$ = 6.07, %$x3$ = 2.11, %$x4$ = 36.21; %C_3A = 2.66 and 2 × %C_3A + %C_4AF = 16.55.
- SR RM 37: LSF = 98, SIM = 3, ALM = 0.91; %$x1$ = 54.57, %$x2$ = 6.28, %$x3$ = 2.13, %$x4$ = 37.02; %C_3A = 2.68 and 2 × %C_3A + %C_4AF = 16.67.
- SR RM 38: LSF = 97, SIM = 3, ALM = 0.91; %$x1$ = 53.52, %$x2$ = 6.49, %$x3$ = 2.15, %$x4$ = 37.84; %C_3A = 2.70 and 2 × %C_3A + %C_4AF = 16.79
- SR RM 39: LSF = 96, SIM = 3, ALM = 0.91; %$x1$ = 52.46, %$x2$ = 6.49, %$x3$ = 2.17, %$x4$ = 38.67; % C_3A = 2.72 and 2 × %C_3A + %C_4AF = 16.90.

From the calculation results of the different possible formulas of SR raw mix using the mix integration between flint and siliceous limestone, it is clear that this kind of combination presents a good solution to produce the SR Portland cement required to standard specification, since the used values of burning modules are strictly in the ranges of the well performing cement kiln: 96 ≤ LSF ≤ 100, SIM = 3 and ALM = 0.91.

4.2.3. Natural Fluorapatite Integration in SR Raw Meals

According to previous research works, the primary goal of using natural fluorapatite in this study is to:

- Improve the quality of SR Portland cement ($C_3A \leq 3\%$ and $2C_3A + C_4AF \leq 20\%$.)
- Ensure the stability of the cement manufacturing process.
- Reduce the CO_2 emissions in the cement industry.

So, this was studied in the present paper by following the effect of the replacement of a part of the ordinary limestone in the raw materials (SRRM 10, SRRM 16, SRRM 23, SRRM 30, and SRRM 35) with natural fluorapatite (0%–15%)on their mineralogical composition (mainly C_3A) and the liquid phase percentage formation. The latter plays a critical role in the clinkering development and the burning stability process, as explained in **Section 2**.

Figures 7, **8** illustrate the expected variation in C_3A and $2C_3A + C_4AF$ amounts as a function of natural fluorapatite replacement.

The natural fluorapatite replacement on raw meals (SR RM 10, SR RM 16, SR RM 23, and SR RM 35) showed that:

- The natural fluorapatite substitution promotes the liquid phase formation (see **Figure 9**). The calculated LP values seem satisfactory since these estimated melts belong to the range of the coating stability of the cement kiln refractory lining. (Aye and Oguchi, 2011). Liquid phase prediction is considered an important and fundamental task for a cement manufacturer in order to ensure the good functioning of the cement production line (burning phase).
- All the estimated raw mix combinations are in agreement with the SR Portland cement normative requirements ($C_3A \leq 3\%$ et $2C_3A + C_4AF \leq 20\%$), as indicated in **Figures 7**, **8**.
- The natural fluorapatite replacement reduces the iron oxide amount in the SR Portland cement raw meals (**Figure 8**); this behavior decreases the polymorphic conversion probability of the belite phase from β C_2S to γ C_2S during the clinkering process (Odigure, 1996; Odigure, 1999; Labidi et al., 2019b)and the γ C_2S mineral formation has a lower reactivity with water (de Noirfontaine, 2000) and consequently affects the mechanical and physical properties of cement (Odigure, 1999).
- An important reduction of greenhouse gas emissions "% CO_2" (see **Figure 10**)

Moreover, the fluorite (CaF_2) in natural fluorapatite, as known as a melting agent, improves the burning phase by increasing the liquid phase formation and decreasing the clinkering temperature

(Johansen and Christensen, 1979; Klemm et al., 1979; Odler and Schmidt, 1980; Raina and Janakiraman, 1998; Altun, 1999b; Yamashita and Tanaka, 2012).

5 CONCLUSION

In the present work, different cases were studied to estimate the raw meal combinations suitable for sulfate-resisting Portland cement manufacturing.

The raw materials (ordinary limestone, black marl, grey marl, and iron ore) used for the ordinary Portland cement production in the SCB cement plant were not sufficient to produce SR raw meals. Thus, the materials abandoned in the SCB quarries (siliceous limestone and flint) were a solution to preparing a SR raw meal.

The results show that the integration of "5% flint with 95% siliceous limestone" mixture is considered a suitable combination for SR clinker while maintaining the same raw materials, burning modules (LSF = 100, SIM = 3, and ALM = 0. 91), and the same manufacturing process. This integration allows the cement factory (SCB plant) to take care of its own integration of all abandoned fronts in the preparation of the raw mix. Furthermore, the use of these abandoned fronts will alleviate the environmental problems at the SCB quarry, allowing to gain this deposit for a period of up to 30 years, and will facilitate the exploitation of the marl deposits below these rocks, which are currently classified as waste.

The addition of natural fluorapatite seems to be a specific asset to contribute to the solution of current and future problems related to the management of natural resources (limestone), energy saving, and environmental protection. This increases the manufacturing sustainability of SR Portland cement by reducing CO_2 emissions from the decarbonation of $CaCO_3$ (from limestone) and combustion (petroleum coke).

As perspectives, this study can be completed by:

- making an energy study of estimated SR raw meal combinations in order to optimize its energy consumption
- manufacturing optimized SR Portland cement raw meals at laboratory and industrial scales.

DATA AVAILABILITY STATEMENT

The original contributions presented in the study are included in the article/Supplementary Material, further inquiries can be directed to the corresponding authors.

AUTHOR CONTRIBUTIONS

All authors listed have made a substantial, direct, and intellectual contribution to the work and approved it for publication.

REFERENCES

Adedoud, M. M. (2019). *Protocole pour évaluer la durabilité des mélanges de sédiments cimentés face aux attaques sulfatiques*. Canada.

Al-Amoudi, O. S. B. (2002). Attack on Plain and Blended Cements Exposed to Aggressive Sulfate Environments. *Cem. Concr. Compos.* 24 (3-4), 305–316. doi:10.1016/s0958-9465(01)00082-8

Altun, I. A. (1999). Influence of Heating Rate on the Burning of Cement Clinker. *Cem. Concr. Res.* 29 (4), 599–602. doi:10.1016/s0008-8846(98)00196-3

Altun, I. A. (1999). Effect of CaF2 and MgO on Sintering of Cement Clinker. *Cem. Concr. Res.* 29 (11), 1847–1850. doi:10.1016/s0008-8846(99)00151-9

Association, P. C. (2002). *Types and Causes of Concrete Deterioration*. Skokie, IL, USA: Portland Cement Association.

ASTM, A. (2017). *C150/C150M-17, Standard Specification for Portland Cement*. West Conshohocken, PA, USA: American Society for Testing Materials.

Aye, T., and Oguchi, C. T. (2011). Resistance of Plain and Blended Cement Mortars Exposed to Severe Sulfate Attacks. *Constr. Build. Mater.* 25 (6), 2988–2996. doi:10.1016/j.conbuildmat.2010.11.106

Aziez, M. N. (2017). *Attaques sulfatiques externes des matériaux cimentaires: influence de la température*. Algeria.

Belgacem, S., Galai, H., and Tiss, H. (2016). Qualitative and Quantitative Investigation of Post-mortem Cement Refractory: The Case of Magnesia-Spinel Bricks. *Ceram. Int.* 42 (16), 19147–19155. doi:10.1016/j.ceramint.2016.09.077

Bennett, W., Jr, Sollberger, J., and Gettys, A. F. (1989). Flint tools. *Tell el Hesi. The Persian Period (Stratum V)*, 231–256.

Beuker, J. (2012) "Hälleflinta-'Next Best'or Even Beter Than Flint?," in *A Mind Set on Flint. Studies*. Editor M. T. L. Th. Niekus ea.

Boughanmi, S., Labidi, I., Megriche, A., Tiss, H., and Nonat, A. (2018). Does Phosphorus Affect the Industrial Portland Cement Reactivity? *Constr. Build. Mater.* 188, 599–606. doi:10.1016/j.conbuildmat.2018.08.060

Boughanmi, S., Labidi, I., Megriche, A., El Maaoui, M., and Nonat, A. (2018). Natural Fluorapatite as a Raw Material for Portland Clinker. *Cem. Concr. Res.* 105, 72–80. doi:10.1016/j.cemconres.2018.01.006

Boulvain, F. (2014). *Eléments de sédimentologie et de pétrologie sédimentaire*. Spain: Cours de l'université de Liège.

Brown, P. (2002). Thaumasite Formation and Other Forms of Sulfate Attack. *Cem. Concr. Compos.* 3 (24), 301–303. doi:10.1016/s0958-9465(01)00081-6

CEN, Cement (2011). *Part 1: Composition, specifications and conformity criteria for common cements*. European Committee for Standardization Brussels.

Chatterjee, A. K. (2011). Chemistry and Engineering of the Clinkerization Process - Incremental Advances and Lack of Breakthroughs. *Cem. Concr. Res.* 41 (7), 624–641. doi:10.1016/j.cemconres.2011.03.020

Chatterjee, A. K. (1983). "Role of Volatiles in Cement Manufacture and in the Use of Cement," in *Advances in Cement Technology* (Elsevier), 203–263. doi:10.1016/b978-0-08-028670-9.50012-0

Chilingar, G. V. (1956). Relationship between Ca/Mg Ratio and Geologic Age. *AAPG Bull.* 40 (9), 2256–2266. doi:10.1306/5ceae577-16bb-11d7-8645000102c1865d

Collepardi, M. (2001). *Ettringite Formation and Sulfate Attack on Concrete*, 200. United States: ACI SPECIAL PUBLICATIONS, 21–38.

Crammond, N., and Halliwell, M. (1995). *The Thaumasite Form of Sulfate Attack in Concretes Containing a Source of Carbonate Ions-Aa Microstructural Overview*, 154. United States: Special Publication, 357–380.

Da, Y., He, T., Shi, C., Lin, Y., and Feng, Y. (2022). Revealing the Co-doping Effects of Fluorine and Copper on the Formation and Hydration of Cement Clinker. *Constr. Build. Mater.* 335, 127516. doi:10.1016/j.conbuildmat.2022.127516

de Noirfontaine, M.-N. (2000). *Etude structurale et cristallographie des composés du ciment anhydre*. France: Ecole Polytechnique X.

De Souza, D., Medeiros, M., and Hoppe Filho, J. (2018). *Evaluation of the SR Portland cement against sodium and magnesium sulfate attack: a physical and comparative analysis of mortars Avaliação do cimento Portland RS frente ao ataque por sulfato de sódio e magnésio: uma análise física*.

De Souza, D. J., Medeiros, M. H. F., Hoppe, J., and Sanchez, L. F. M. (2020). "The Uses of Finely Ground Materials to Mitigate the External Sulphate Attack (ESA) on Cementitious Materials," in *External Sulphate Attack–Field Aspects and Lab Tests* (Springer), 139–151. doi:10.1007/978-3-030-20331-3_11

Dorn, T., Blask, O., and Stephan, D. (2022). Acceleration of Cement Hydration - A Review of the Working Mechanisms, Effects on Setting Time, and Compressive

Strength Development of Accelerating Admixtures. *Constr. Build. Mater.* 323, 126554. doi:10.1016/j.conbuildmat.2022.126554

En, N. (2001). *197–1-Ciment—Partie 1: composition, spécifications et critères de conformité des ciments courants*. Paris: AFNOR.

Essawy, A. A., and Abd El.Aleem, S. (2014). Physico-mechanical Properties, Potent Adsorptive and Photocatalytic Efficacies of Sulfate Resisting Cement Blends Containing Micro Silica and Nano-TiO2. *Constr. Build. Mater.* 52, 1–8. doi:10.1016/j.conbuildmat.2013.11.026

Ghosh, S. K., Parlikar, U. V., and Karstensen, K. H. (2022). "Cement Manufacturing-Technology, Practice, and Development," in *Sustainable Management of Wastes through Co-processing* (Springer), 73–90. doi:10.1007/978-981-16-6073-3_4

Gibson, M. A., Byerly, D. W., Engel, A. S., and Hatcher, R. D. (2018). "Lessons from Limestone: How to Teach All Sciences with Limestone," in *Geology at Every Scale: Field Excursions for the 2018 GSA Southeastern Section Meeting in Knoxville, Tennessee* (United States: Geological Society of America).

Girardi, F., and Maggio, R. D. (2011). Resistance of Concrete Mixtures to Cyclic Sulfuric Acid Exposure and Mixed Sulfates: Effect of the Type of Aggregate. *Cem. Concr. Compos.* 33 (2), 276–285. doi:10.1016/j.cemconcomp.2010.10.015

Hökfors, B., Boström, D., Viggh, E., and Backman, R. (2015). On the Phase Chemistry of Portland Cement Clinker. *Adv. Cem. Res.* 27 (1), 50–60. doi:10.1680/adcr.13.00071

Hooton, R. D., and Thomas, M. D. (2002). *The use of limestone in Portland cements: effect on thaumasite form of sulfate attack*. United States: Portland Cement Association.

Irassar, E. F. (2009). Sulfate Attack on Cementitious Materials Containing Limestone Filler - A Review. *Cem. Concr. Res.* 39 (3), 241–254. doi:10.1016/j.cemconres.2008.11.007

Ismail, S., Sashidhar, C., and Kumar, D. P. (2015). EFFECT OF SULPHATES IN THE PRESENCE OF WATER ON THE STRENGTH CHARACTERISTICS OF BLENDED CEMENT. *Int. Res. J. Eng. Technol.* 2, 1228.

Johansen, V., and Christensen, N. H. (1979). Rate of Formation of C3S in the System CaOSiO2Al2O3Fe2O3MgO with Addition of CaF2. *Cem. Concr. Res.* 9 (1), 1–5. doi:10.1016/0008-8846(79)90089-9

Kajaste, R., and Hurme, M. (2016). Cement Industry Greenhouse Gas Emissions - Management Options and Abatement Cost. *J. Clean. Prod.* 112, 4041–4052. doi:10.1016/j.jclepro.2015.07.055

Kanaan, D., Soliman, A. M., and Suleiman, A. R. (2022). Zero-Cement Concrete Resistance to External Sulfate Attack: A Critical Review and Future Needs. *Sustainability* 14 (4), 2078. doi:10.3390/su14042078

Khelifi, S., Ayari, F., Tiss, H., and Hassan Chehimi, D. B. (2017). X-Ray Fluorescence Analysis of Portland Cement and Clinker for Major and Trace Elements: Accuracy and Precision. *J. Aust. Ceram. Soc.* 53 (2), 743–749. doi:10.1007/s41779-017-0087-x

Klemm, W. A., Jawed, I., and Holub, K. J. (1979). Effects of Calcium Fluoride Mineralization on Silicates and Melt Formation in Portland Cement Clinker. *Cem. Concr. Res.* 9 (4), 489–496. doi:10.1016/0008-8846(79)90046-2

Kumar, K. P. P. (2013). Raw mix characteristics. *Training kiln operation and optimization*.

Kurdowski, W. (2014). *Cement and concrete chemistry*. Springer Science & Business.

Labidi, I., Boughanmi, S., Khelidj, A., El Maaoui, M., and Megriche, A. (2019). Effect of Low Calcite Addition on Sulfate Resisting (SR) Portland Cements: Hydration Kinetics at Early Age and Durability Performance after 2 Years. *Chem. Afr.* 2, 1–14. doi:10.1007/s42250-019-00047-0

Labidi, I., Boughanmi, S., Tiss, H., and Megriche, A. (2019). Critical Research Study of Quantification Methods of Mineralogical Phases in Cementitious Materials. *J. Aust. Ceram. Soc.* 55 (4), 1127–1137. doi:10.1007/s41779-019-00327-5

Labidi, I., Boughanmi, S., Khelidj, A., El Maaoui, M., and Megriche, A. (2019). Effect of Llow Ccalcite Aaddition on Ssulfate Rresisting (SR) Pportland Ccements: Hhydration Kkinetics at Eearly Aage and Ddurability Pperformance after 2 Yyears. *Chemistry Africa* 2 (3), 401–414. doi:10.1007/s42250-019-00047-0

Le Saoût, G., Kocaba, V., and Scrivener, K. (2011). Application of the Rietveld Method to the Analysis of Anhydrous Cement. *Cem. Concr. Res.* 41 (2), 133–148. doi:10.1016/j.cemconres.2010.10.003

Lothenbach, B., Bary, B., Le Bescop, P., Schmidt, T., and Leterrier, N. (2010). Sulfate Ingress in Portland Cement. *Cem. Concr. Res.* 40 (8), 1211–1225. doi:10.1016/j.cemconres.2010.04.004

Marchand, J., Odler, I., and Skalny, J. P. (2001). *Sulfate attack on concrete*. London: CRC Press.

Martins, M. C., Langaro, E. A., Macioski, G., and Medeiros, M. H. F. (2021). External Ammonium Sulfate Attack in Concrete: Analysis of the Current Methodology. *Constr. Build. Mater.* 277, 122252. doi:10.1016/j.conbuildmat.2021.122252

Mehta, P. K. (1983). Mechanism of Sulfate Attack on Portland Cement Concrete - Another Look. *Cem. Concr. Res.* 13 (3), 401–406. doi:10.1016/0008-8846(83)90040-6

Mezza, S., Ben M'Barek Jemaï, M., Ben Salah, I., and Tiss, H. (2020). Geochemical Suitability of Lower Eocene Extra-siliceous Limestone for Cement Making (Bizerte Deposit-Extreme North of Tunisia). *Environ. Earth Sci.* 79, 1–21. doi:10.1007/s12665-020-08930-7

Michaux, M., Nelson, E. B., and Vidick, B. (1990). "2 Chemistry and Characterization of Portland Cement," in *Developments in Petroleum Science* (Elsevier), 2 1–2 17. doi:10.1016/s0376-7361(09)70300-0

Mingyu, H., Fumei, L., and Mingshu, T. (2006). The Thaumasite Form of Sulfate Attack in Concrete of Yongan Dam. *Cem. Concr. Res.* 36 (10), 2006–2008. doi:10.1016/j.cemconres.2006.04.005

Mishra, U. C., Sarsaiya, S., and Gupta, A. (2022). A Systematic Review on the Impact of Cement Industries on the Natural Environment. *Environ. Sci. Pollut. Res.* 29, 1–12. doi:10.1007/s11356-022-18672-7

Mohamed, B., Haykel, G., Rabah, A., Marouene, B., Abdessalem, B. H. A., and Hafsia, B. R. (2017). Inter-comparative Study of Quantitative Methods of Industrial Clinker. *J. Wuhan. Univ. Technol.-Mat. Sci. Ed.* 32 (6), 1250–1260. doi:10.1007/s11595-017-1738-z

Mosci, R. A. (2000). FEATURES-understanding Clinker Liquid Phase-Although the Amount of Liquid Phase in the Burning and Transition Zones of the Kiln Is Important to Clinker Formation and Brick Performance, the. *Rock Prod.* 8, 26–29.

Nawy, E. G. (2008). *Concrete construction engineering handbook*. Boca Raton, FL: CRC Press.

Neville, A. M. (1995). *Properties of Concrete*, 4. London: Longman London.

Neville, A. (2004). The Confused World of Sulfate Attack on Concrete. *Cem. Concr. Res.* 34 (8), 1275–1296. doi:10.1016/j.cemconres.2004.04.004

NT, 47.26 (1999). *NT, 47.26- Ciment Portland à haute résistance aux sulfates-spécifications*. Tunisie: INNORPI.

Odigure, J. O. (1996). Kinetic Modelling of Cement Raw Mix Containing Iron Particles and Clinker Microstructure. *Cem. Concr. Res.* 26 (9), 1435–1442. doi:10.1016/0008-8846(96)00112-3

Odigure, J. O. (1999). Grindability of Cement Clinker from Raw Mix Containing Metallic Particles. *Cem. Concr. Res.* 29 (3), 303–307. doi:10.1016/s0008-8846(98)00175-6

Odler, I., and Schmidt, O. (1980). Structure and Properties of Portland Cement Clinker Doped with Zinc Oxide. *J. Am. Ceram. Soc.* 63 (1-2), 13–16. doi:10.1111/j.1151-2916.1980.tb10638.x

Page, C. L., and Page, M. M. (2007). *Durability of concrete and cement composites*. Elsevier.

Paul, A. F. Y., and Kouamé, A. (2019). Conception de diagrammes ternaires de classification des sédiments et roches sédimentaires mixtes clastiques terrigénes. *Int. J. Inn. App. Stu.* 26 (4), 1193–1202.

Ragoug, R. (2016). *Attaque sulfatique externe des matériaux cimentaires: Impact de différents facteurs âge, composition du liant, présence de chlorures*.

Rahman, M. M., and Bassuoni, M. T. (2014). Thaumasite Sulfate Attack on Concrete: Mechanisms, Influential Factors and Mitigation. *Constr. Build. Mater.* 73, 652–662. doi:10.1016/j.conbuildmat.2014.09.034

Raina, K., and Janakiraman, L. K. (1998). Use of Mineralizer in Black Meal Process for Improved Clinkerization and Conservation of energy22Communicated by F. Massazza. *Cem. Concr. Res.* 28 (8), 1093–1099. doi:10.1016/s0008-8846(98)00082-9

Ramachandran, V. S., Paroli, R. M., Beaudoin, J. J., and Delgado, A. H. (2002). *Handbook of thermal analysis of construction materials*. United States: William Andrew.

Rasheeduzzafar, A. O. S. B., Abduljauwad, S. N., and Maslehuddin, M. (1994). Magnesium-Sodium Sulfate Attack in Plain and Blended Cements. *J. Mat. Civ. Eng.* 6 (2), 201–222. doi:10.1061/(asce)0899-1561(1994)6:2(201)

Rheinheimer, V. (2008). *Sulphate attack and the role of thaumasite in historical constructions*. Spain: Universitat Politècnica de Catalunya.

Rondeux, M., Courard, L., Michel, F., Vanhamme, G., Pierre, C., Pollet, V., et al. (2014). *Durabilité des ciments ternaires à base de laitier vis-à-vis des attaques sulfatiques*.

Santhanam, M., Cohen, M. D., and Olek, J. (2003). Mechanism of Sulfate Attack: a Fresh Look. *Cem. Concr. Res.* 33 (3), 341–346. doi:10.1016/s0008-8846(02)00958-4

Schmidt, T., Lothenbach, B., Romer, M., Neuenschwander, J., and Scrivener, K. (2009). Physical and Microstructural Aspects of Sulfate Attack on Ordinary and Limestone Blended Portland Cements. *Cem. Concr. Res.* 39 (12), 1111–1121. doi:10.1016/j.cemconres.2009.08.005

Schmidt, T. (2007). *Sulfate attack and the role of internal carbonate on the formation of thaumasite*. Lausanne: EPFL.

Sengupta, P. (2020). "Coating and Burnability of Clinker," in *Refractories for the Cement Industry* (Springer), 185–192. doi:10.1007/978-3-030-21340-4_8

Sorrentino, F. (2011). Chemistry and Engineering of the Production Process: State of the Art. *Cem. Concr. Res.* 41 (7), 616–623. doi:10.1016/j.cemconres.2011.03.013

Spence, R. J. (1980). *Small-scale production of cementitious materials*. United Kingdom: Intermediate Technology.

Standard, A. (2011). *Standard Specification for Portland Cement*. West Conshohocken: ASTM International.

Taha1, T. M., and Abdullah2, E. J. (2020). Mineralogy and Geochemistry of Mishrif Formation from Selected Oilfield, South East of Iraq. *Tikrit J. Pure Sci.* 25 (1), 75–84. doi:10.25130/j.v25i1.939

Telschow, S., Frandsen, F., Theisen, K., and Dam-Johansen, K. (2012). Cement Formation-A Success Story in a Black Box: High Temperature Phase Formation of Portland Cement Clinker. *Ind. Eng. Chem. Res.* 51 (34), 10983–11004. doi:10.1021/ie300674j

Torres, S. M., Sharp, J. H., Swamy, R. N., Lynsdale, C. J., and Huntley, S. A. (2003). Long Term Durability of Portland-limestone Cement Mortars Exposed to Magnesium Sulfate Attack. *Cem. Concr. Compos.* 25 (8), 947–954. doi:10.1016/s0958-9465(03)00160-4

Unland, G. (2001). Assessment of the Grindability of Cement Clinker, Part 1. *ZKG Int.* 54 (2), 61–65.

Whittaker, M., and Black, L. (2015). Current Knowledge of External Sulfate Attack. *Adv. Cem. Res.* 27 (9), 532–545. doi:10.1680/jadcr.14.00089

Xie, L., Deng, M., Tang, J., and Liu, K. (2021). The Effect of Fluorapatite in Limestones on the Mineral Compositions of Portland Cement Clinkers. *Constr. Build. Mater.* 273, 122042. doi:10.1016/j.conbuildmat.2020.122042

Xiong, C., Jiang, L., Song, Z., Liu, R., You, L., and Chu, H. (2014). Influence of Cation Type on Deterioration Process of Cement Paste in Sulfate Environment. *Constr. Build. Mater.* 71, 158–166. doi:10.1016/j.conbuildmat.2014.08.042

Yamashita, M., and Tanaka, H. (2012). Low-temperature Burnt Portland Cement Clinker Using Mineralizer. *Cem. Sci. Concr. Technol.* 65 (1), 82–87. doi:10.14250/cement.65.82

Zeyen, N., Daval, D., Lopez-Garcia, P., Moreira, D., Gaillardet, J., and Benzerara, K. (2017). Geochemical Conditions Allowing the Formation of Modern Lacustrine Microbialites. *Procedia Earth Planet. Sci.* 17, 380–383. doi:10.1016/j.proeps.2016.12.096

Conflict of Interest: The authors declare that the research was conducted in the absence of any commercial or financial relationships that could be construed as a potential conflict of interest.

frontiers | Frontiers in Chemistry

TYPE Original Research
PUBLISHED 07 September 2022
DOI 10.3389/fchem.2022.806772

OPEN ACCESS

EDITED BY
Svetlana Ivanova,
University of Seville, Spain

REVIEWED BY
Vesna Krstic,
Mining and Metallurgy Institute Bor, Serbia
Cristina Megías-Sayago,
Université de Strasbourg, France

*CORRESPONDENCE
Veronica C. Obuseng,
obusengvc@ub.ac.bw

SPECIALTY SECTION
This article was submitted to Green and Sustainable Chemistry, a section of the journal Frontiers in Chemistry

RECEIVED 01 November 2021
ACCEPTED 08 August 2022
PUBLISHED 07 September 2022

CITATION
Obuseng VC, Moshoeshoe MN, Nareetsile FM, Kwaambwa H and Maina I (2022), Plant biomass as potential economic commodities for agricultural purposes.
Front. Chem. 10:806772.
doi: 10.3389/fchem.2022.806772

Plant biomass as potential economic commodities for agricultural purposes

Veronica C. Obuseng[1]*, Mohau N. Moshoeshoe[2], Florence M. Nareetsile[1], Habauka Kwaambwa[3] and Irene Maina[4]

[1]Department of Chemistry, University of Botswana, Gaborone, Botswana, [2]National University of Lesotho, Roma, Lesotho, [3]Department of Natural and Applied Sciences, Namibia University of Science and Technology, Windhoek, Namibia, [4]Department of Chemical and Forensic Sciences, Botswana International University of Science and Technology, Palapye, Botswana

The world's population is growing continually and is projected to reach nine billion by the year 2050. This growth rate requires increased and economically viable food production and an adequate supply of quality water to sustain life. Increased food production and supply of water require adding fertilizers and possible recycling of wastewater, to address the improvement of soils' nutritional status and potable water shortages, respectively. The objectives of this work were to determine the nutrients in sewage-impacted wastewater, borehole water, agricultural waste, and commercial fertilizer (control) materials, and their heavy metal content was also carried out to determine their suitability for use. In addition, Moringa seed pods and Morula nutshells were investigated as a bioremedial approach for the removal of toxic metals from aqueous samples. An attempt to regenerate sorbent was made since the saturated sorbents that contain the metal ions are not safe for disposal as they can pollute the environment. Nutrients were analyzed by HPLC, while metals were analyzed using a Varian 220FS Atomic Absorption Spectrometer operated with air/acetylene. Nonedible agricultural materials were found to contain appreciable amounts of plant nutrients such as nitrates (NO_3^-), nitrites (NO_2^-), and phosphates (PO_4^{3-}) as well as metal ions such as magnesium, copper, and zinc, which are beneficial for plant growth. Results obtained from analysis of sewage water effluent showed that heavy metal and nutrient concentrations decreased in the treatment stage. The utilization of *Moringa oleifera* seed pods for metal removal from wastewater is viable and would reduce costs for waste disposal and can offer alternatives to conventional methods for the removal of unwanted or toxic species from the environment. It showed potential for removing selected metal ions such as Pb, Cd, Cu, Fe, and Zn from polluted water. This organically treated wastewater is environmentally friendly and may be used for applications which do not require potable water, such as irrigating golf courses, lawns, and crops, or for industrial purposes, if proper measures are taken to ensure its quality.

KEYWORDS

heavy metal, nitrates, nitrites, phosphates, wastewater

1 Introduction

Plants serve as the main source of food for humanity. These plants, in turn, need nutrients for their growth and other life processes, which they source mainly from soil. A fertile soil should contain proper, balanced levels of the different nutrients. In many cases, these nutrients often fall short of the optimum levels and must be supplemented by the use of fertilizers. Inorganic fertilizers such as ammonium nitrate, potassium nitrate, and urea as well as green manures such as organic compost (Melaj and Daraio, 2013; Babrauskas, 2016), and wastewater treatment sludge (Zorpas et al., 2000) have been utilized for this purpose. Some of these soil amendment strategies introduce components that may be harmful to the environment, leading to environmental concerns such as nitrate water pollution (Chaudhry and Malik, 2017; Singh and Craswell, 2021), the introduction of potentially toxic trace metals (Chaudhry and Malik, 2017). The presence of NO_3^- in food and drinking water is a health concern because the microbial reduction process in food products and saliva may act as carcinogens (Alonso et al., 2020) and cause other related illnesses.

Biosorption has gained important credibility during recent years as a low-cost, readily available, and efficient treatment technology for the high-capacity removal of heavy metals from wastewaters (Bashir et al., 2019; Redha, 2020). For example, acid-treated soybean hulls were used to effectively remove metal ions (Cd, Ni, Cu, Pb, and Zn) from industrial and municipal wastewater. Orange peels have also been used for the removal and recovery of Ni^{2+} ions from electroplating water. The effectiveness of metal removal was dependent on operational conditions such as temperature, pH, initial concentration, and sorbent dose. Other adsorbents which have been used include *Moringa oleifera* seed pods and *Sclerocarya birrea* (Morula) nutshells.

Moringa oleifera (MO) and *Sclerocarya birrea* (Morula) are essential for food security, health and nutrition, and economic welfare of rural communities in the developing world (Mojeremane and Tshwenyane, 2004). The Morula tree is a multipurpose tree with highly nutritive fruits which can be consumed fresh or commercially processed. Its fruits are used in the preparation of juices, jams, jellies, and alcoholic beverages as they contain high amounts of vitamin C (Mojeremane and Tshwenyane, 2004; Ojewole et al., 2010; Moatshe et al., 2011; Maina et al., 2016). The seed biomass has been used for water treatment for generations in several countries by local communities (Nwagbara et al., 2022).

Nutrients (NO_3^-, NO_2^-, and PO_4^{3-}) as well as heavy metals (Pb, Cd, Cu, Fe, and Zn) are commonly monitored for environmental protection purposes in natural and wastewaters as well as in agricultural and food samples (Lockhart et al., 2013; Yun et al., 2018; Mehri et al., 2021). Although techniques such as electrophoresis, electroanalytical methods, GC, IEC, and HPLC have been successfully applied in the determination of nitrates, nitrites, and phosphates, very few applications carried out simultaneous analysis of the three analytes. HPLC equipped with an ultraviolet (UV) detector in the analysis of NO_3^-, NO_2^-, and PO_4^{3-} has proven to afford high efficiency, precision, accuracy, sensitivity, and specificity and reduced interference (Moshoeshoe and Obuseng, 2018).

When analyzing solid samples using HPLC, several sample preparation procedures exist which are meant to make the sample compatible with the technique of analysis and reduce the effects of matrix components, thus reducing interferences during analysis. The sample preparation procedures used to extract NO_3^-, NO_2^-, and PO_4^{3-} in liquid matrices may include dissolution with hot water (Brkić, et al., 2017; Ferreira and Silva, 2008) and homogenization (Nam et al., 2008). The use of extraction procedures such as the Bremner method (López Pasquali et al., 2010), adsorption on activated, carbon and the alkaline extraction methods (Prasad and Chetty, 2008) may also be necessary. For solid matrices, pretreatment procedures may include drying (Elrashidi et al., 2003, Ferreira and Silva, 2008) or freeze-dry techniques (Prasad and Chetty, 2008), mechanical shaking (Turrión et al., 1999), ultrasonic extraction, and/or blending (Butt et al., 2001). Use of extraction solvents such as hot water (Ferreira and Silva, 2008) or cold water (Burns, 2000) with or without salts or pH adjustment, clean-up techniques such as activated charcoal (Ferreira and Silva, 2008), deproteinization agents, for e.g., Carrez solution (Bashiry et al., 2016; Ferreira and Silva, 2008), or a solid phase extraction column (Jobgen et al., 2007) may also be needed. Although these procedures have been developed to improve the selectivity, specificity, and detection of the analytes of interest, the existing wide range of procedures may have been the source of variations in analytical results in the literature. Based on the comparison of their performances in the literature, five extraction methods were selected and examined. The selection of these extraction methods was based on 1) ability of the method to simultaneously extract nitrate (NO_3^-), nitrite (NO_2^-), and phosphate (PO_4^{3-}), without oxidizing the nitrite to nitrate; 2) specificity of the extraction technique was also considered, with preference given to methods which can extract only the analytes of interest; 3) "soft" extraction methods (i.e., those methods which extract only the readily available analyte) were also favored over those methods which extract analyte; 4) use of chemical reagents that have safety concerns (all methods which use such reagents were disregarded); and 5) sample throughput, whereby procedures which are simple were preferred over those which are complicated. This also reduces the possibility of artefact production, possible sample contamination, and/or analyte loss.

Extraction using boiling water also satisfies all the aforementioned requirements as water is expected to be able to dissolve all ionic compounds. Moreover, water is non-toxic, and fewer steps are used in the extraction. The alkaline extraction

method and the modified alkaline extraction method employ the use of NaOH as an extracting agent. $ZnSO_4$ is later used as a precipitating agent to remove most unrequired ions from solution. Both extraction procedures also satisfy all the aforementioned requirements as they use non-toxic and specific reagents, which are also capable of the simultaneous extraction of the analytes of interest. Boiling water, alkaline extraction and modified alkaline extraction methods, and oxalate extraction and AOAC extraction methods were selected and compared for extraction of NO_3^-, NO_2^-, and PO_4^{3-} in a commercial NPK fertilizer. This article showcases some applications of agricultural waste (non-edible parts) such as *Moringa oleifera* seed pods, maize plant stalks, and Jugo bean husks as potential organic materials for wastewater treatment and soil amendment. The objectives of this work were to determine the nutrients in sewage-impacted wastewater, borehole water, agricultural waste, and commercial fertilizer (control) materials, and their heavy metal content was also carried out to determine their suitability for use. In addition, Moringa seed pods and Morula nutshells were investigated as a bioremedial approach for the removal of toxic metals from aqueous samples. An attempt to regenerate sorbent was made since the saturated sorbents that contain the metal ions are not safe for disposal as they can pollute the environment.

2 Materials and methods

2.1 Materials

Commercially available reagents and solvents were used without further purification. Activated carbon, oxalic acid ($H_2C_2O_4$), calcium chloride ($CaCl_2$), EDTA ($C_{10}H_{14}N_2Na_2O_8{\bullet}2H_2O$), and zinc sulfate ($ZnSO_4.7H_2O$) were obtained from Merck (PTY) Ltd. (Modderfontein, South Africa). Orthophosphate, nitrite, and nitrate stock solutions were prepared using potassium dihydrogen phosphate (KH_2PO_4), sodium nitrite ($NaNO_2$), and sodium nitrate ($NaNO_3$), respectively, all of which were purchased from Saarchem (Krugersdorp, South Africa). Potassium thiocyanate (KSCN) and diethylenetriaminepentaacetic acid (DTPA) were also purchased from Saarchem (Krugersdorp, South Africa). Sodium hydroxide (NaOH), potassium chloride (KCl), ammonium oxalate ($(NH_4)_2C_2O_4{\bullet}H_2O$), ammonium bicarbonate (NH_4HCO_3), and ammonium citrate ($(NH_4)_2HC_6H_5O_7$) were all purchased from Rochelle Chemicals, RSA. All reagents used for optimization of extraction methods were of analytical-reagent grade. Distilled, de-ionized water (DDW, 18 MΩ cm^{-1}; Milli-Q, Millipore) was used for all sample preparation procedures. All glassware used was soaked in 10% HCl for 24 h and rinsed several times with DDW prior to use.

2.2 Extraction of NO_3^-, NO_2^-, and PO_4^{3-}

Different sample extraction procedures were compared for their efficiency in extracting NO_3^-, NO_2^-, and PO_4^{3-} from solid samples using commercial N:P:K fertilizer samples. They were freeze-dried, ground, and sieved through a 2-mm mesh and then processed using the different extraction procedures described in the following paragraphs.

A comparison of the extraction efficiency of the different procedures in extracting NO_3^-, NO_2^-, and PO_4^{3-} from liquid samples was carried out using sewage-impacted wastewater samples obtained from the final effluent at the Glen Valley Wastewater Treatment Plant in Gaborone (GVWTP). Liquid samples were filtered first through a Whatman filter paper (No. 1) to remove insoluble materials.

The alkaline extraction procedure described by Prasad and Chetty, (2008) was used without modification. In brief, 10 g of NPK fertilizer was weighed and shaken for 30 min with 70 ml of water in a Labcon shaking water bath. A volume of 12 ml of 2% NaOH was then added, and the water bath temperature was increased to 50°C while shaking. The resulting precipitate was filtered, and then 10 ml of $ZnSO_4$ was added to the filtrate, while the temperature of the suspension was maintained at 50°C for further 10 min. The contents were then cooled to room temperature by immersing the flask in tap water. The suspension was then filtered through a 0.45-µm Minisart® Plus syringe membrane filter into a 100-ml volumetric flask, to which was added the internal standard (KSCN) to give a final concentration of 20 mg/L and made up to the mark with water. The resulting solution was analyzed following the HPLC method.

The boiling procedure as described by Chou *et al.* (2003) was employed by weighing 10 g of a sample, adding it to 50 ml of water in an Erlenmeyer flask, and shaking the mixture in a boiling water bath (Labcon shaking water bath) for 20 min. The sample was then shaken up and left on the table until cooled down to room temperature, after which it was filtered through a 0.45-µm Minisart® Plus syringe membrane filter into a 100-ml volumetric flask. The internal standard (KSCN) was added to give a final concentration of 20 mg/L, and the solution was made up to the mark with water. The resulting solution was analyzed using the HPLC method.

The modified alkaline extraction was applied as described by Akyüz and Ata, (2009). A measure of 0.5 M aqueous NaOH was added to 10 g of the sample. The mixture was sonicated at 40°C for 20 min and then filtered using a Whatman filter paper (No. 1). The aqueous phase was collected in a beaker. A measure of 0.5 M $ZnSO_4$ was added dropwise to this aqueous phase until the white precipitate of $Zn(OH)_2$ no longer appeared on further addition. The aqueous phase containing nitrite and nitrate ions was filtered through a 0.45-µm Minisart® Plus syringe membrane filter into a 50-ml volumetric flask. The internal standard (KSCN) was added to give a final concentration of 20 mg/L,

TABLE 1 Average concentrations of NO_2^-, NO_3^-, and PO_4^{3-} obtained from NPK fertilizers using different extraction methods.

Analyte concentration (in mg/kg)	Extraction procedure				
	Alkaline extraction	Boiling	Modified alkaline extraction	Oxalate	AOAC
NO_2^- (mg/kg)	41.99 ± 1.84	38.56 ± 1.71	45.65 ± 1.83	41.53 ± 1.82	40.97 ± 1.91
NO_3^- (mg/kg)	685.38 ± 22.99	667.52 ± 26.59	701.29 ± 16.91	670.19 ± 26.46	688.56 ± 26.82
PO_4^{3-} (mg/kg)	864.64 ± 8.15	881.89 ± 15.29	992.25 ± 7.37	1,638.56 ± 28.54	1,414.53 ± 15.43

and the solution was made up to the mark with water, followed by HPLC analysis.

The oxalate extraction procedure was adapted from Kleinman & Sharpley, (2007). A measure of 10 g of the sample was shaken in 80 ml of acid oxalate solution (0.1 M $(NH_4)_2C_2O_4•H_2O$+ 0.1 M $H_2C_2O_4•2H_2O$) for 4 h in the dark. The resulting extracts were centrifuged for 20 min and then filtered through a 0.45-µm Minisart® Plus syringe membrane filter into a 100-ml volumetric flask. KSCN was added as an internal standard to give a final concentration of 20 mg/L, and the solution was made up to the mark with doubly distilled water (DDW), followed by HPLC analysis.

The AOAC official procedure described by Bartos *et al.* (2014) was used without modification. A measure of 10 g of the sample was added to a 250-ml volumetric flask containing 100 ml ammonium citrate–EDTA solution, previously heated to 65°C. The flask was shaken for 60 min in a water bath at 65°C and 200 rpm. It was then removed from the water bath and left to cool to room temperature. The cool solution was filtered through a 0.45-µm Minisart® Plus syringe membrane filter into a 250-ml volumetric flask. KSCN was added as an internal standard to give a final concentration of 20 mg/L, and the solution was made up to the mark with DDW, followed by HPLC analysis. The obtained concentrations are reported in Table 1.

No modifications were made to the described procedures, except for the addition of the internal standard (KSCN). All samples were analyzed within 1 h after sample preparation. All extractions and analyses were carried out in triplicate. The resulting extracts were then analyzed by HPLC. The resultant sample peak area ratios were fitted into the previously calculated calibration equation to yield concentrations, which were then compared to determine the most efficient extraction procedure.

2.3 HPLC analysis

An HPLC method for the simultaneous analysis of nitrates, nitrites, and phosphates in several environmental samples developed by Moshoeshoe and Obuseng, (2018) was utilized for all the analyses. HPLC analyses were carried out using an Agilent Technologies HPLC-UV (Agilent Infinity Series 1,260—DAD) equipped with a diode array detector and manual injection using OpenLAB CDS ChemStation software. Detection was carried out at a wavelength of 210 nm, at which absorbance was found to be adequate for all the analytes. Baseline resolution for all the analytes was achieved on a Phenomenex Synergi Polar-RP column (150 × 4.6 mm, 4 µm, 80 Å), using a mobile phase consisting of acetonitrile:acidified water (pH 2.4; 55:45 v/v) in an isocratic elution mode. Optimum results were obtained at a mobile phase flow rate of 0.80 ml/min and a temperature of 30°C. The eluents were degassed manually before being added into the mobile phase reservoir and online after mixing.

2.4 Liquid and solid sample collection and nutrient analysis

Borehole water samples were obtained from a local farm in Artesia, Botswana, at two different boreholes using the grab sampling technique. Water samples were stored in dark bottles, which were placed in a cooler box. They were then taken to the laboratory and stored at 4°C until further analysis. Five replicates were filtered through a Whatman filter paper (No. 1), and 0.5 M NaOH was added to each sample, sonicated, and then filtered again using a Whatman filter paper (No. 1). A volume of 0.5 M $ZnSO_4$ was added dropwise to the filtrate until precipitation no longer occurred. The mixture was then filtered through a 0.45-µm Minisart® Plus syringe membrane filter into a 50-ml volumetric flask. The internal standard (KSCN) was added to give a final concentration of 20.00 mg/L, and the solution was made up to the mark with water, followed by HPLC analysis.

Wastewater samples were collected from the Glen Valley Wastewater Treatment Plant (GVWTP) in Gaborone, Botswana. Five different samples were collected from the treatment plant at the inlet and final effluent (contact tank). Five replicates were filtered through a Whatman filter paper (No. 1), added to 0.5 M NaOH, sonicated, and then filtered again using a Whatman filter paper (No. 1). A volume of 0.5 M $ZnSO_4$ was added dropwise to the filtrate until precipitation no longer occurred. The mixture was then filtered through a 0.45-µm Minisart® Plus syringe membrane filter into a 50-ml volumetric flask. The internal standard (KSCN) was added to give a final concentration of

TABLE 2 Efficiency of the GVWTP on nutrient removal and amounts to maximum limits set by WUC (n = 5).

Holding tank	NO_2^- (mg/L)		NO_3^- (mg/L)		PO_4^{3-} (mg/L)	
	Obtained amount	WUC limit	Obtained amount	WUC limit	Obtained amount	WUC limit
Inlet	1,409.06 ± 63.41	200	173.75 ± 6.17	100	63.34 ± 1.79	30
Final effluent (contact tank)	33.87 ± 0.76	1.5	20.87 ± 0.71	10	5.77 ± 0.28	1.5
Removal efficiency (9%)	97.59	--	87.99	--	90.89	--

20 mg/L, and the solution was made up to the mark with water, followed by HPLC analysis (Table 3).

Agricultural waste material was obtained from a farm in Artesia, Botswana, from three different plowing fields after harvest, using the random sampling technique in each field. These included maize stalks and Jugo bean husk samples. *Moringa oleifera* seed pods and Morula nutshells were obtained from areas around Gaborone, Botswana. Grab samples, which were collected from each field, were combined into a single composite sample and freeze-dried. The solid samples were ground using a pestle and mortar. Simultaneous quantitative extraction of NO_3^-, NO_2^-, and PO_4^{3-} was obtained when applying the modified alkaline extraction method (Prasad and Chetty, 2008). In brief, ground solid samples were air-dried, after which five replicates were weighed, added to 0.5 M NaOH, sonicated, and then filtered again using a Whatman filter paper (No. 1). A volume of 0.5 M $ZnSO_4$ was added dropwise to the filtrate until precipitation no longer occurred. The mixture was then filtered through a 0.45-µm Minisart® Plus syringe membrane filter into a 50-ml volumetric flask. The internal standard (KSCN) was added to give a final concentration of 20 mg/L, and the solution was made up to the mark with water, followed by HPLC determination under optimized conditions as published by Moshoeshoe and Obuseng, (2018).

2.5 Determination of heavy metals

2.5.1 Determination of initial metal concentration in water samples

Water samples collected from the sampling points (boreholes and wastewater samples) were acid-digested following a method adopted from the EPA 1999 method 200.2 for wastewater samples. A volume of 50 ml of each water sample from the inlet and effluent points of the GWWTP and borehole was put into 250-ml conical flasks. A volume of 1 ml of 69% HNO_3 and 0.5 ml of 37% HCl were added to each flask to digest the samples. The mixture was heated until the initial volume was reduced to approximately 0.5 ml. It was then filtered using a 0.45-µm Minisart® Plus syringe membrane filter into a 50-ml volumetric flask, and deionized water was added to the mixture to make up to the mark. The sample was then analyzed with AAS to determine the concentration of six metals (Pb, Fe, Mn, Zn, Cu, and Cd). This was carried out in triplicate.

2.5.2 Determination of initial metal concentration in sorbent materials

A volume of 2 g of each ground sorbent was weighed and then digested with an aqua regia solution of HCl:HNO_3 in a ratio of 3:1 v/v. Each mixture was put in 100-ml conical flasks and heated at 85 °C until the volume was approximately 1 ml. The resulting volume was filtered using a Whatman No. 1 filter paper into 50-ml volumetric flasks. Deionized water was added to the flasks up to the mark and then analyzed using FAAS, and the initial concentrations are reported in Table 5.

2.5.3 Instrumental analysis

A Varian 220FS Atomic Absorption Spectrometer operated with air/acetylene was used for the determination of six selected metal ions, namely, Pb, Mn, Fe, Zn, Cu, and Cd. Varian hollow cathode lamps for each of the analyzed metals were used as radiation sources. A measure of 1,000 mgL^{-1} stock solutions of metals were used to prepare working standards (in the range of 0.0–5.0 mgL^{-1}) in deionized water. The instrument was calibrated manually by aspirating the prepared working standards of the cations of interest one by one into the flame. The samples were then also aspirated manually into the flame for atomization. The instrumental conditions applied were according to the FAAS manual.

2.6 Sorption studies

MO seed pods and Morula nutshells were washed with double deionized water and dried in an oven at 105°C for 24 h. The dried samples were ground and then sieved using a 100-µm mesh sieve and stored in glass bottles until further analysis.

Acid treatment of MO seed pods (MSP) and Morula nutshells (MNS) was carried out and 15 g of each sorbent was weighed and put in a conical flask, 200 ml of 0.1 M HNO_3 was

TABLE 3 Concentrations of NO_2^-, NO_3^-, and PO_4^{3-} in borehole water on a farm (n = 5).

Analyte	Concentration (mg/L)	
	Borehole 1	Borehole 2
NO_2^-	80.58 ± 6.86	ND
NO_3^-	108.41 ± 12.59	1.22 ± 0.26
PO_4^{3-}	0.23 ± 0.14	1.98 ± 0.87

added, and the mixture was soaked for 24 h as described in Won *et al.* (2014). The mixture was then filtered using a Whatman No. 1 filter paper, and the sorbent was washed several times with deionized water until the pH of the sorbent was neutral (around pH 7). The sorbent was then dried in an oven at 50°C overnight and then put in a glass bottle for further use. Following the optimized parameters (Maina et al., 2016), the sorbent was used on wastewater samples and the results of the acid-treated and untreated sorbents were compared. In brief, 2 g each of the sorbents (both untreated MSP and MNS) was ground and sieved to a 100 µm particle size. This was added to both wastewater and borehole samples, with pH adjusted to 8 for optimum sorption. A measure of 50 ml of water samples was used, and the mixture was shaken for 120 and 60 min, respectively. The mixture was then filtered using a Whatman No. 1 filter paper, and the filtrate was transferred into a 50-ml volumetric flask and filled with deionized water to the mark, followed by metal ion analysis with AAS. The optimized conditions were applied to both water samples. The analysis was carried out in triplicate, and the concentration was determined by FAAS.

3 Results

3.1 Nutrient extraction method

The preliminary results obtained when these extraction procedures for NO_3^-, NO_2^-, and PO_4^{3-} were applied to commercial NPK fertilizers, with emphasis on the extraction efficiency of a method, including recovery, selectivity, and lack of production of artefacts, are shown in Table 1. In addition, other factors such as the number of steps involved in the method, the duration of the preparation, and ease of the method were also considered.

Simultaneous quantitative extraction of nitrate, nitrite, and phosphate was obtained when applying the modified alkaline extraction method. The higher pH of reagents used in this method prevents the oxidation of NO_2^- to NO_3^- (which occurs in other methods) and is known to lead to sub-standard NO_2^- levels in the results. In addition, the modified alkaline extraction method gave results which closely approximate the amount of plant-available P in soils and fertilizers, together with the estimation of P loss in runoff and subsurface waters. Therefore, the modified alkaline extraction procedure appears to be an effective multi-ion extraction procedure with respect to the extraction of NO_2^-, NO_3^-, and PO_4^{3-} and has been used to extract the nutrients in the samples analyzed in this study.

3.2 Nutrient in water samples from GVWTP

The wastewater entering the Glen Valley Wastewater Treatment Plant (GVWTP) contains considerable amounts of nitrates, nitrites, and phosphates due to the chemicals used in both households and industries. The purpose of the treatment plant is to reduce the amount of these analytes as the water goes through the different treatment stages.

The amounts of nutrients at the inlet were found to be very high but reduced as the treatment process continued. This can be attributed to the fact that domestic wastewater consists of gray and black wastewater as shown in Table 2. The water obtained from the final effluent tank was found to have 9.11% of the amount of phosphate initially present at the inlet. This translates to a percentage removal of 90.89%. Similar trends were observed for nitrites and nitrates, with a percentage removal of 97.59% and 87.99%, respectively (Table 2).

Although the percentage removal of these nutrients is high, the amounts of the analytes in the effluent were still above the quality control limits set by the WUC, Botswana, as shown in Table 2. The effluent is, however, environmentally friendly with

TABLE 4 Average concentrations of NO_3^-, NO_2^-, and PO_4^{3-} in different agricultural waste and soil samples. NPK fertilizer was included as quality standard.

Sample	$[NO_2^-]$ (in mg/kg)	$[NO_3^-]$ (in mg/kg)	$[PO_4^{3-}]$ (in mg/kg)
Maize stalks	14.45 ± 0.63	98.59 ± 4.02	18.05 ± 0.46
Jugo bean husks	3.92 ± 0.19	254.61 ± 10.93	19.66 ± 0.50
Moringa seed pods	5.35 ± 0.21	165.56 ± 7.06	27.40 ± 0.41
NPK fertilizer (quality standard)	45.65 ± 1.83	701.29 ± 16.91	864.64 ± 8.15

TABLE 5 Concentration of selected metals in MSP and MNS biomass.

Sorbent	Metal concentration (mg/g)					
	Pb	Cu	Cd	Fe	Zn	Mn
Maximum permissible limit in edible plants	0.3	3	0.2	20	27.4	2
MSP	0.0175 ± 0.002	0.0120 ± 0.009	BDL	0.1114 ± 0.026	0.0358 ± 0.015	0.0470 ± 0.007
MNS	0.015 ± 0.004	0.0118 ± 0.005	BDL	0.0875 ± 0.031	0.0259 ± 0.033	0.0285 ± 0.007

BDL: below detectable limit.

TABLE 6 Percentage removal of selected metals using MNS and MSP.

Sorbent	Water sample holding tank	Percentage removal ± standard deviation of heavy metal				
		Mn	Cu	Fe	Pb	Cd
MNS	Inlet	64.7 ± 1.24	67.3 ± 3.59	84.4 ± 1.94	67.4 ± 3.63	31.2 ± 0.38
	Effluent	56.8 ± 1.68	60.4 ± 2.19	64.6 ± 5.59	56.6 ± 2.70	44.1 ± 5.44
MSP	Inlet	34.9 ± 0.73	76.7 ± 2.27	73.5 ± 2.90	78.9 ± 2.49	53.8 ± 1.4
	Effluent	52.0 ± 1.82	73.5 ± 3.43	68.7 ± 1.644	69.8 ± 1.37	62.7 ± 0.25

regards to the analytes of interest and may be used for applications which do not require potable water (such as irrigational or industrial purposes). Some of the water is used to irrigate golf courses, lawns, and crops grown under the Glen Valley Irrigation Project. The concentration levels of the nutrients from the current study contrast with the results obtained by Nkegbe et al. (2005), who found the effluents to be below the maximum allowable effluent levels of <1 mg/L for PO_4^{3-} and <5 mg/L for NO_3^-. The results could indicate the state of the plant during the sampling period, whereby it may not have been functioning accordingly in the removal of the analytes of interest from wastewater. This water, however, undergoes further natural treatment as the effluent is released to maturation ponds and then discharged into the Notwane River. In this study, the presence/absence of pathogenic organisms has not been tested, so the water cannot be recommended for drinking purposes.

3.3 NO_2^-, NO_3^-, and PO_4^{3-} in borehole water

The results obtained from the analysis of the borehole water samples by HPLC are shown in Table 3.

Groundwater purity depends on various factors, such as the geological conditions of the soil through which the groundwater flows, and some anthropogenic activities (EPA, 2012). The amount of nitrate and nitrite which was found in borehole 1 exceeds 50 mg/L nitrate and 3 mg/L nitrite limits set by the World Health Organization (WHO, 2017). The high concentrations of nitrate and nitrite in this borehole water could be due to the application of inorganic or organic fertilizer and the excretory materials from farm animals as well as wild animals (WHO, 2011). These may contribute to the adulteration of groundwater with various contaminants.

In general, water obtained from borehole 2 contained lower concentration levels of NO_2^-, NO_3^-, and PO_4^{3-} that were below the maximum contaminant limits (WHO, 2011), therefore could be safe for human consumption.

3.4 NO_3^-, NO_2^-, and PO_4^{3-} in fertilizers and agricultural waste products

The obtained amounts of NO_3^-, NO_2^-, and PO_4^{3-} in solid agricultural waste samples are shown in Table 4.

Generally, the nitrite content in the parts was about a tenth of what was in the fertilizer. The lowest amounts of both NO_2^- and NO_3^- were found in Jugo bean husks. In general, the amount of NO_2^- in the samples followed the trend: maize stalks > Moringa seed pods > Jugo bean husks.

The trend observed for NO_3^- in the samples was different from that realized for NO_2^-. The amount of NO_3^- in the samples was according to the following trend: Jugo bean husks > Moringa

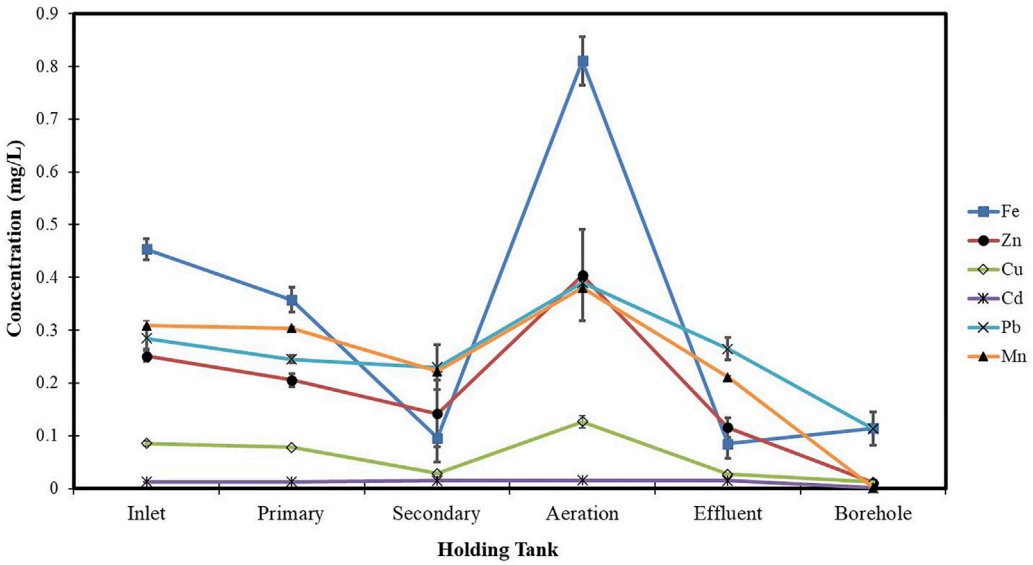

FIGURE 1
Concentration profile of selected heavy metals along the different holding tanks in the GVWTP.

seed pods > maize stalks. Jugo beans have the highest amount of NO_3^- due to being leguminous plants, thus having the highest capacity for nitrogen fixation.

The observed trend for PO_4^{3-} in the samples was as follows: Jugo bean husks > maize stalks > Moringa seed pods. Phosphates, nitrates, and nitrites were found to be present in agricultural waste samples, albeit at very small concentrations as compared to their concentrations in field soil and fertilizers. The replowing into the soils of these degradable materials could be utilized as fertilizers to improve agricultural yields. Although the samples were found to contain lesser amounts of nutrients than the NPK-fertilizer, if these agricultural waste samples were to be used, the fertility of the arable land could be maintained as most of the nutrients would be returned to the soil.

3.5 MSP- and MNS-selected metal ion composition

Table 5 shows the selected metal ion composition in the sorbents, MNS and MSP. Cadmium was not detected in both sorbents, while the other elements were ≤0.12 mg/g. All the analyzed metals had concentrations within the maximum permissible limits for edible plants set by FAO/WHO (2017).

Figure 1 shows the concentration profile of selected heavy metals along the different holding tanks in the Glen Valley Wastewater Treatment Plant (GVWTP). In general, there was a significant decrease in all the heavy metals throughout the treatment process.

Further work was carried out to determine how effective the MNS and MSP can remove metal ions in the wastewater.

The percentage removal when MNS and MSP were used is given in Table 6. When using MSP, Zn desorbed from MSP into the wastewater, and hence removal of Zn by MSP was impossible. This could be attributed to the saturation of binding sites for Zn in the sorbents.

Morula nutshells were found to be a better sorbent than Moringa seed pods as all metals showed a higher percentage of removal. Use of untreated plant biomass is capable of directly removing metal ionic species from aqueous solutions (Singh et al., 2006; Zwain et al., 2014). However, these sorbents can be chemically pre-treated to enhance better performance and/or suitability for process applications. This treatment normally removes organic and inorganic matter from the sorbent surface. Chemical treatments that are commonly employed are alkaline solutions, phosphoric acid, and citric acids. After acid treatment using 0.4 M of HNO_3, the treated MNS and MSP sorbents were used for the extraction of heavy metals from the wastewater samples. To compare their effectiveness, the treated MNS and MSP were used in effluent wastewater samples. There was increased removal efficiency for all the metals, as shown in Figures 2, 3. There was an increase in removal efficiency. Zn ions were desorbing before the sorbents were treated, but it was noticed that the removal increased up to 55.6% for Zn. The increased removal efficiency could be because more binding sites were available after treating the sorbents, and hence more ions could bind to many adsorption sites.

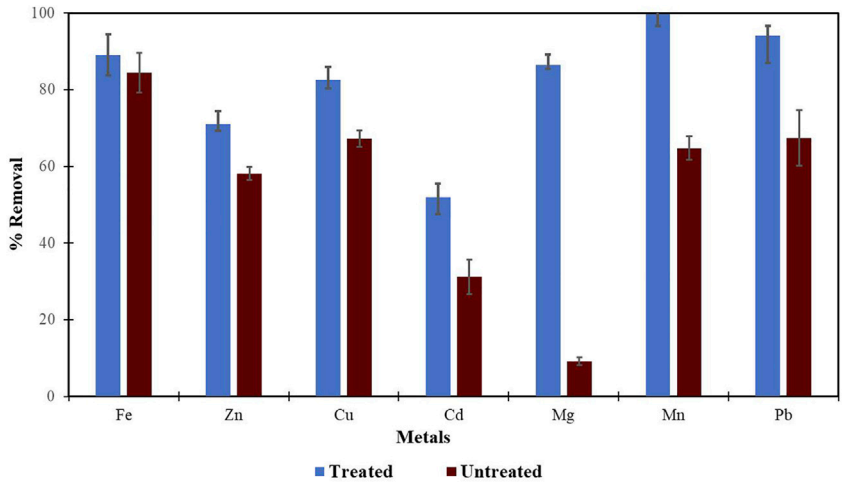

FIGURE 2
Comparison of acid treated and untreated MNS for removal of metals from wastewaters at inlet point.

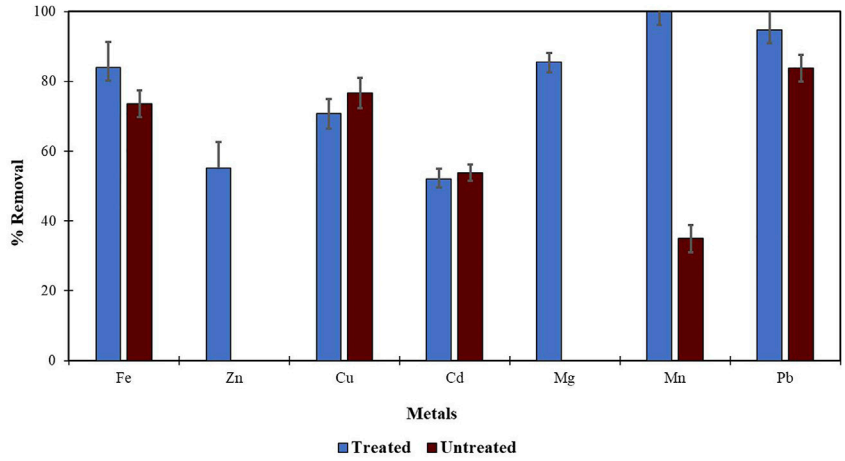

FIGURE 3
Comparison of acid treated and untreated MSP for removal of metal from wastewaters at inlet point.

Treating the sorbents with acid helps to extract any metal cations on the sorbents, thereby creating new sorption sites and increasing the surface area of the sorbent and hence increasing the metal removal efficiency (Chan, et al., 2006; Gupta and Babu 2009). Acid-treated sorbents like maize bran (Singh et al., 2006) and tea waste (Mahvi et al., 2005) have been reported to have a high metal removal efficiency of >90%.

Conditions such as contact time, pH, temperature, particle size, sorbent dose, and initial metal concentration were optimized for MSP and MNS for the removal of selected metal ions (lead, cadmium, copper, manganese, iron, zinc, and magnesium) from wastewater and borehole water samples (Maina et al., 2016). The acid-treated sorbents showed higher removal efficiencies than the non-treated sorbents. These non-edible plant parts of Morula and Moringa plants are proposed as a cheap, simple, and effective alternative for the purification of water contaminated with heavy metals.

Metal ions such as potassium, calcium, and magnesium were found to be in higher concentrations in Moringa seed pods, implying that the pods can be a source of these essential elements. Morula nutshells had relatively high concentrations of sodium, potassium, magnesium, and aluminum. Other metals such as

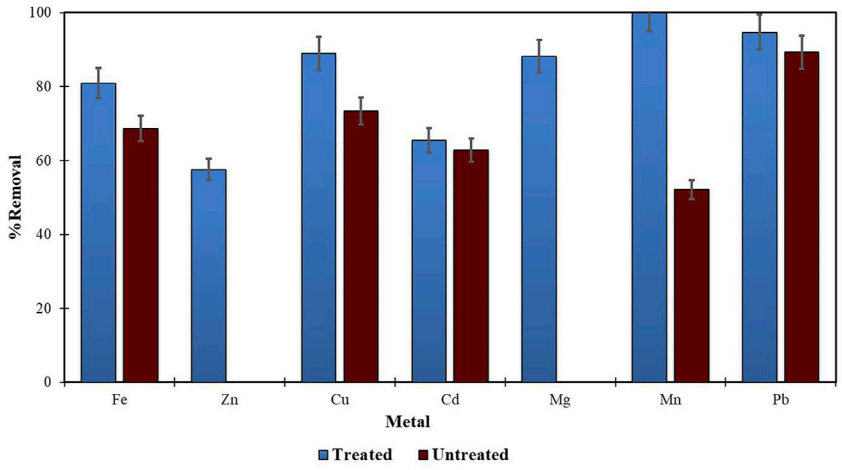

FIGURE 4
Comparison of treated and untreated MSP for removal of metal from wastewaters at final effluent point.

TABLE 7 Heavy metal content of borehole water.

Metal	Concentration (mg/L)	RSD (%)	MAL* (mg/L)
Fe	0.3440 ± 0.0036	1.04	None
Zn	0.0110 ± 0.0021	19.09	None
Cu	0.0123 ± 0.0012	9.75	2.0
Cd	0.0011 ± 0.0001	10.01	0.003
Pb	0.1133 ± 0.0321	28.33	0.01
Mn	0.0012 ± 0.0009	75.02	None

*Maximum allowed limits (WHO, 2017).

zinc, copper, iron, lead, and manganese were found to be at trace levels. All selected metals were within the limits set by FAO/WHO (2017).

The wastewater collected from the GVWTP was found to be conducive for agricultural use. On the other hand, the water from the boreholes was found to be good for human consumption. The concentration of the selected metal ions in both water samples was within the required limits for agricultural uses (wastewater) and drinking water (borehole) set by the US EPA. Method recoveries were obtained in the range of 86.49 ± 1.53% to 99.63 ± 1.99%. The low detection limits were also recorded (lower than 2 ppm) with a good linear correlation ($R^2 > 0.99$). Removal of the selected metals from the water samples by the sorbents could be through adsorption, ion exchange, or through precipitation where the sorbent would act like a filter.

Heavy metals were detected in the borehole water (Table 7) albeit at very low concentrations, which are below the maximum allowed limits (MALs) suggested by WHO (2017). This could be because the farm is very far from the urban environment and is therefore not prone to pollution from the industrialization activities, which are normally carried out in urban places.

Only lead occurred at levels higher than its MAL (0.01 mg/L). This could be because the farm is near the road, where fumes from motor vehicles could have an impact on the soil and subsequently the groundwater below that soil. The presence of iron, manganese, and magnesium in the water is beneficial to both farm animals and humans.

4 Discussion

4.1 Nutrient analysis

Agricultural wastes such as maize stalks, moringa seed pods, and Jugo beans husks were found to contain NO_3^-, NO_2^-, and PO_4^{3-} in considerable amounts. Recycling of these agricultural waste materials is economic and eco-friendly due to their unique chemical composition, availability in abundance, renewability, and low cost. In addition, these substances contain organic matter which improves the soil's structure, water-holding capacity, water infiltration, aeration, pH, and buffering capacity.

The farm from which the borehole water was obtained has no supply of potable water, and its inhabitants (both humans and animals) depend largely on borehole water. This is a common situation in Botswana as farms are very far from municipal areas, which are supplied with treated, potable water and proper sanitation measures. Due to this, the inhabitants of farms normally depend on private borehole water supplies, which are drawn from groundwater of uncertain quality.

The presence of NO_3^- and NO_2^- in drinking water is a concern because the microbial reduction process in food

products and saliva can convert NO_3^- to NO_2^- (Burakham et al., 2004). NO_2^- is harmful to human health primarily because of its ability to react with the ferrous ion (Fe^{2+}) in the blood's hemoglobin to produce methemoglobin (Jobgen et al., 2007; Bellavia et al., 2013). Normal hemoglobin in the blood contains iron (II). Nitrite can oxidize this iron to the iron (III) state, resulting in a molecule that has no oxygen-carrying capacity. This condition limits the blood's ability to carry oxygen from the lungs to the rest of the body, giving rise to a situation called methemoglobinemia, which might be described as chemical suffocation (Jobgen et al., 2007; Makridin et al., 2020). According to Cemek et al. (2007), it has been ascertained that in severe cases of methemoglobinemia, the deprivation of hemoglobin and oxygen delivery to the brain may lead to intellectual disability.

Groundwater phosphate occurs naturally from the weathering processes of rocks and from anthropogenic activities. Investigations of farming practices need to be undertaken to ascertain the trend of phosphorus in water, plants, and soil on this farm.

4.2 Metal analysis

The Glen Valley Wastewater Treatment Plant (GVWTP) in Gaborone, Botswana, uses the activated sludge process (ASP) as the main technique of treating wastewater. This is a biological treatment system in which a specific concentration of biomass is maintained along with a sufficient dissolved oxygen concentration in an aeration tank that serves as a bioreactor—the purpose of which is to enhance the effect of biodegradation of soluble organic impurities (Mittal, 2011). The main products of this process in wastewater are sludge, water, carbon dioxide, and methane. Heavy metals also occur at concentrations that are quite higher than their toxicity limits and strongly affect and reduce microbial activity. This, in turn, has a negative impact on the biological wastewater treatment processes, and it leads to the reduction of the microbial oxidation of organic compounds and inhibition of the nitrification and denitrification processes (Kapoor et al., 2015). It is for this reason that many industries which produce effluents which are heavily contaminated with heavy metals are investing on on-site effluent treatment facilities to reduce the concentration of heavy metals (Ahluwalia and Goyal, 2007; Kurniawan et al., 2006).

The major source of wastewater in sewage treatment plants is municipal wastewater which may contain pathogens and potentially toxic elements and organic compounds. If ingested, these substances may result in health issues such as diarrhea. Diarrhea is responsible for the deaths of 1.8 million people every year, and it mostly affects children in developing countries because of unsafe water supplies and poor sanitation facilities. It is also of critical concern that additional traces of inorganic compounds such as heavy metals could be present in treated water due to treatment failure or inability to remove them (Qureshi et al., 2016). Wastewater resulting from homes and industries is often discharged into rivers after treatment. In studies conducted by Okuda et al. (2001) and Ghebremichael et al. (2005), the presence of bivalent cations such as Ca^{2+} and Mg^{2+} significantly enhanced the coagulating properties of MO seeds, where the cations may have adsorbed to the active components to form an insoluble net-like structure to capture suspended particles of kaolin clay that was present in water samples. The active ingredients extracted from MO seeds are cationic and able to remove dirt in water which is normally negatively charged (Kwaambwa and Rennie, 2012; Moulin et al., 2019). MO seed biomass were used to remove several metal ions including Pb, Cu, Cd, Ni, Mn, and Zn (Sharma et al., 2006; Obuseng et al., 2012). An attempt to add value to waste material by developing an eco-friendly method for removing Pb, Cu, Cd, Zn, and Fe ions from aqueous water was conducted (Maina et al., 2016). These studies demonstrated that pH, particle size, sorbent dose, contact time, temperature, and concentration are significant factors in adsorption. The percentage removal efficiency of Fe, Cu, Cd, Zn, and Pb ions using treated *Moringa oleifera* seed pods (MOSP) was found to be 99.0 ± 4.27, 98.7 ± 3.89, 72.5 ± 2.14, 65.9 ± 1.64, and 99.6 ± 6.69, respectively. This work also demonstrated that the performance of this sorbent could work at a wide range of pH 3.5 to 8 and that it was possible to adsorb a mixture of metal ions without significantly affecting sorption capacity. At a high pH, the surface charge of the sorbent is negatively charged and therefore the sorption of metal ions on the sorbent is high. At a low pH, the metals ions compete with the H^+ ions for the active sites, therefore decreasing the sorption (Guyo et al., 2015). In the study of Bhatti et al. (2007), biomass from MO pods was also used to investigate the removal of Zn(II). It was compared to the biomass treated with NaOH and noted that removal efficiency increased from 36.07% to 45.76% when treated biomass was used. The experimental results showed that the maximum pH (pH max) for efficient sorption of Zn(II) was 7 ± 0.1 at which evaluated biosorbent dosage and biosorbent particle size were 0.5 g/L and <0.255 mm, respectively. An increase in sorbent dose increases the number of particles and hence increasing the removal efficiency due to an increase in number of the binding sites for sorption. Small particle size also increases the sorption capacity as results of larger surface area for the adsorption of the metal ions onto the sorbent (Arunlertaree et al., 2007). The seed pods have also been used to remove organics (benzene, toluene, and cumene) from aqueous solution (Adeleye et al., 2016). It was observed that the removal of the organic contaminants onto the pods was in the order of cumene > toluene > benzene. This was attributed to their solubility, as more soluble substances in alcohol and water prefer to remain in solution rather than the sorbent material. However, some parts of these plants are not edible and are considered waste, for example, MO seed pods and Morula nutshells. MO bark was considered a viable alternative to activated carbon, ion-exchange-resin, and other synthetic adsorbents used for this purpose (Reck et al., 2018; Viotti et al., 2019). The use of this plant waste material demonstrates effective, economic, and available methods that can be used to remove metal ions from water and wastewater and therefore

applicable even in rural areas where resources to acquire the expensive and complicated technologies are limited. Minimal studies have been directed toward sorption behavior for the removal of toxic metals from water samples using the nonedible plant parts of MO and Morula trees.

Recycling and reuse of treated wastewater can be a supplementary source to already existing water sources, especially in arid and semi-arid regions.

Nonedible plant parts of *Moringa oleifera* seed pods and Morula nutshells were used to remove selected heavy metals from water samples. The biosorption capacity of agricultural waste has also been demonstrated, hence revealing the potential of the use of agricultural waste for the purification of water. This introduces possibilities of recycling and reuse of water generated by industries and wastewater treatment plants, etc., to curb the problem of water scarcity. The developed method can be used in rural areas where there are no resources to obtain the conventional expensive techniques. To improve efficiency, both Moringa seed pods and Morula nutshells were acid-treated with nitric acid (HNO_3), and the percentage removal was increased due to an increase in surface area that ultimately increased the binding sites of the sorbents. Although the concentrations of the selected metal ions in the water samples collected from the Glen Valley Wastewater Treatment Plant were found to be within the required limits for agricultural uses set by the US EPA, they were much higher than the required limits for the water to be used for drinking purposes. Optimization of pH, initial metal concentration, sorbent dose, particle size, and temperature helped to achieve desirable extraction efficiencies.

Conclusion

The study demonstrated a simple, cheap, and environmentally friendly method of remediating wastewater without the need for trained personnel. It emphasized on the importance of utilizing all unwanted biomass materials such as agricultural waste for reclamation of wastewater. The method can be used in rural areas where there are no resources to obtain the conventional expensive techniques and chemicals. In addition, this is a demonstration of green chemistry and its applicability in the African continent, which quite often does not afford expensive fertilizers and water purification systems from developed economies. The use of agricultural waste also adds value to the plants from which the waste has been obtained.

Data availability statement

The original contributions presented in the study are included in the article/Supplementary Material; further inquiries can be directed to the corresponding author.

Author contributions

All authors listed have made a substantial, direct, and intellectual contribution to the work and approved it for publication.

Funding

This study was financially assisted by the University of Botswana Office of Research and Development (ORD).

Conflict of interest

The authors declare that the research was conducted in the absence of any commercial or financial relationships that could be construed as a potential conflict of interest.

Publisher's note

All claims expressed in this article are solely those of the authors and do not necessarily represent those of their affiliated organizations, or those of the publisher, the editors, and the reviewers. Any product that may be evaluated in this article, or claim that may be made by its manufacturer, is not guaranteed or endorsed by the publisher.

References

Adeleye, A. S., Conway, J. R., Garner, K., Huang, Y., Su1, Y., and Keller, A. A. (2016). Engineered nanomaterials for water treatment and remediation: Costs, benefits, and applicability. *Chem. Eng. J.* 286, 640–662. doi:10.1016/j.cej.2015.10.105

Ahluwalia, S. S., and Goyal, D. (2007). Microbial and plant derived biomass for removal of heavy metals from wastewater. *Bioresour. Technol.* 98, 2243–2257. doi:10.1016/j.biortech.2005.12.006

Alonso, M., González-Montaña, J., and Lomillos, J. (2020). Consumers' Concerns and Perceptions of Farm Animal Welfare. *Animals.* 10, 385. doi:10.3390/ani10030385

Akyüz, M., and Ata, Ş. (2009). Determination of low level nitrite and nitrate in biological, food and environmental samples by gas chromatography–mass spectrometry and liquid chromatography with fluorescence detection. *Talanta* 79, 900–904. doi:10.1016/j.talanta.2009.05.016

Arunlertaree, C., Kaewsomboon, W., Kumsopa, A., Pokethitiyook, P., and Panyawathanakit, P. (2007). Removal of lead from battery manufacturing wastewater by eggshell. Songklanakarin. *J. Sci. Technol.* 29, 857–868.

Babrauskas, V. (2016). Explosions of ammonium nitrate fertilizer in storage or transportation are preventable accidents. *J. Hazard. Mat.* 304, 134–149. doi:10.1016/j.jhazmat.2015.10.040

Bartos, J. M., Boggs, B. L., Falls, J. H., and Siegel, S. A. (2014). Determination of phosphorus and potassium in commercial inorganic fertilizers by inductively coupled plasma-optical emission spectrometry: Single-laboratory validation. *J. AOAC Int.* 97, 687–699. doi:10.5740/jaoacint.12-399

Bashir, A., Malik, L. A., Ahad, S., Manzoor, T., Pandith, A. H., Dar, G. N., et al. (2019). Removal of heavy metal ions from aqueous system by ion-exchange and biosorption methods. *Environ. Chem. Lett.* 17, 729–754. doi:10.1007/s10311-018-00828-y

Bashiry, M., Mohammadi, A., Hosseini, H., Kamankesh, M., Aeenehv, S., and Mohammadi, Z. (2016). Application and optimization of microwave-assisted extraction and dispersive liquid–liquid microextraction followed by high-performance liquid chromatography for sensitive determination of polyamines in Turkey breast meat samples. *Food Chem.* 190, 1168–1173. doi:10.1016/j.foodchem.2015.06.079

Bellavia, L., DuMond, J. F., Perlegas, A., King, B. S., and Kim-Shapiro, D. B. (2013). Nitroxyl accelerates the oxidation of oxyhemoglobin by nitrite. *Nitric Oxide* 31, 38–47. doi:10.1016/j.niox.2013.03.006

Bhatti, H. N., Mumtaz, B., Hanif, M. A., and Nadeem, R. (2007). Removal of Zn(II) ions from aqueous solution using Moringa oleifera Lam . (horseradish tree) biomass.. *Process Biochem.* 42, 547–553. doi:10.1088/0143-0807/27/4/007

Burakham, R., Oshima, M., Grudpan, K., and Motomizu, S. (2004). Simple flow-injection system for the simultaneous determination of nitrite and nitrate in water samples. *Talanta*. 64, 1259–1265.

Burns, I. (2000). Development of a decision support system for nitrogen fertilizer application in soil grown glasshouse crops. LINK-Technologies for Sustainable Farming Systems LK 0438. *Hortic. Res. Int.* Available at: http://www.hridir.org/hri/search/lk_0438.html (Accessed May 16, 2015).

Butt, S .B., Riaz, M., and Iqbal, M. Z. (2001). Simultaneous determination of nitrite and nitrate by normal phase ion-pair liquid chromatography. *Talanta*. 55, 789–797.

Brkić, D., Bošnir, J., Bevardi, M., Bošković, A. G., Miloš, S., Lasić, D., et al. (2017). Nitrate in leafy green vegetables and estimated intake. *Afr. J. Tradit. Complement. Altern. Med.* 14, 31–41. doi:10.21010/ajtcam.v14i3.4

Cemek, M., Akkaya, L., Birdane, Y. O., Seyrek, K., Bulut, S., and Konuk, M. (2007). Nitrate and nitrite levels in fruity and natural mineral waters marketed in western Turkey. *J. Food Compost. Anal.* 20, 236–240.

Chan, K. M., Ku, L. L., Chan, P. C. Y., and Cheuk, W. K. (2006). Metallothionein gene expression in zebrafish embryo-larvae and ZFL cell-line exposed to heavy metal ions. *Mar. Environ. Res.* 62, S83–S87. doi:10.1016/j.marenvres.2006.04.012

Chaudhry, F. N., and Malik, M. F. (2017). Factors affecting water pollution: A review. *J. Ecosyst. Ecogr.* 7, 1000225. doi:10.4172/2157-7625.1000225

Chou, S. S., Chung, J. C., and Hwang, D. F. (2003). A high-performance liquid chromatography method for determining nitrate and nitrite levels in vegetables. *J. Food Drug Anal.* 11, 233–238. doi:10.38212/2224-6614.2702

Elrashidi, M. A., Mays, M. D., and Lee, C. W. (2003). Assessment of Mehlich3 and ammonium bicarbonate-DTPA extraction for simultaneous measurement of fifteen elements in soils. *Commun. Soil Sci. Plant Anal.* 34, 2817–2838. doi:10.1081/css-120025208

EPA (2012). *Effluent standards and limitations for phosphorus*. Chapter NR 217. Washington, D.C., USA: EPA, 149–150.

FAO/WHO (2017). *Evaluation of certain contaminants in food: Eighty-third report of the joint FAO/WHO expert committee on food additives*. Geneva, Switzerland: World Health Organization.

Ferreira, I. M. P. L. V. O., and Silva, S. (2008). Quantification of residual nitrite and nitrate in ham by reverse-phase high performance liquid chromatography/diode array detector. *Talanta*. 74, 1598–1602.

Ghebremichael, K. A., Gunaratna, K. R., Henriksson, H., Brumer, H., and Dalhammar, G. (2005). A simple purification and activity assay of the coagulant protein from Moringa oleifera seed. *Water Res.* 39, 2338–2344. doi:10.1016/j.watres.2005.04.012

Gupta, S., and Babu, B. V. (2009). Removal of toxic metal Cr(VI) from aqueous solutions using sawdust as adsorbent: equilibrium, kinetics and regeneration studies. *Chem. Eng. J.* 150, 352–365. doi:10.1016/j.cej.2009.01.013

Guyo, U., Mhonyera, J., and Moyo, M. (2015). Pb(II) adsorption from aqueous solutions by raw and treated biomass of maize stover – a comparative study. *Process Saf. Environ. Prot.* 93, 192–200. doi:10.1016/j.psep.2014.06.009

Jobgen, W. S., Jobgen, S. C., Li, H., Meininger, C. J., and Wu, G. (2007). Analysis of nitrite and nitrate in biological samples using high-performance liquid chromatography. *J. Chromatogr. B* 851, 71–82. doi:10.1016/j.jchromb.2006.07.018

Kapoor, V., Li, X., Elk, M., Chandran, K., Impellitteri, C. A., and Santo Domingo, J. W. (2015). Impact of heavy metals on transcriptional and physiological activity of nitrifying bacteria. *Environ. Sci. Technol.* 49, 13454–13462. doi:10.1021/acs.est.5b02748

Kleinman, P. J. A., and Sharpley, A. N. (2007). Estimating soil phosphorus sorption saturation from Mehlich-3 data. *Commun. Soil Sci. Plant Anal.* 33, 1825–1839. doi:10.1081/css-120004825

Kwaambwa, H. M., and Rennie, A. R. (2012). Interactions of surfactants with a water treatment protein from *Moringa oleifera* seeds in solution studied by zeta potential and light scattering measurements. *Biopolymers* 97 (4), 209–218. doi:10.1002/bip.22014

Kurniawan, T. A., Chan, G. Y. S., Lo, W.-H., and Babel, S. (2006). Physico-chemical treatment techniques for wastewater laden with heavy metals. *Chem. Eng. J.* 118, 83–98.

Lockhart, K. M., King, A. M., and Hartera, T. (2013). Identifying sources of groundwater nitrate contamination in a large alluvial groundwater basin with highly diversified intensive agricultural production. *J. Contam. Hydrol.* 151, 140–154. doi:10.1016/j.jconhyd.2013.05.008

López Pasquali, C. E., Gallego-Picó, A., Fernández Hernando, P., Velasco, M., and Durand Alegría, J. S. (2010). Two rapid and sensitive automated methods for the determination of nitrite and nitrate in soil samples. *Microchem. J.* 94, 79–82. doi:10.1016/j.microc.2009.09.005

Mahvi, A. H., Naghipour, D., Vaezi, F., and Nazmara, S. (2005). Teawaste as an adsorbent for heavy metal removal from industrial wastewaters. *Am. J. Appl. Sci.* 2, 372–375. doi:10.3844/ajassp.2005.372.375

Maina, I. W., Obuseng, V., and Nareetsile, F. (2016). Use of moringa oleifera (moringa) seed pods and sclerocarya birrea (morula) nut shells for removal of heavy metals from wastewater and borehole water. *J. Chem.* 2016, 9312952. doi:10.1155/2016/9312952

Makridin, E., Markov, S., Murko, E., Lesin, Y., and Hellmer, M. (2020). Theoretical background of quarry wastewater filtering through filters of coarse-grained blasted overburden rocks. *E3S Web Conf.* 174, 01056. doi:10.1051/e3sconf/202017401056

Mehri, F., Heshmati, A., Moradi, M., and Khaneghah, A. M. (2021). The concentration and health risk assessment of nitrate in vegetables and fruits samples of Iran. *Toxin Rev.* 40, 1215–1222. doi:10.1080/15569543.2019.1673424

Melaj, M. A., and Daraio, M. E. (2013). Preparation and characterization of potassium nitrate controlled-release fertilizers based on chitosan and xanthan layered tablets. *J. Appl. Polym. Sci.* 130, 2422–2428. doi:10.1002/app.39452

Mittal, A. (2011). "Biological wastewater treatment" in water today august – 2011. Available at: https://www.watertoday.org/Article%20Archieve/Aquatech%2012.pdf (Accessed on May 12, 2013).

Moatshe, O. G., Emongor, V. E., and Oagile, O. (2011). Effect of benzyladenine (BA) on fruit set and mineral nutrition of morula (Sclerocarya birrea subspecies caffra). *Afr. J. Plant Sci.* 5, 268–272.

Mojeremane, W., and Tshwenyane, S. O. (2004). The resource role of morula (sclerocarya birrea): A multipurpose indigenous fruit tree of Botswana. *J. Biol. Sci.* 4 (6), 771–775. doi:10.3923/jbs.2004.771.775

Moshoeshoe, M. N., and Obuseng, V. (2018). Simultaneous determination of nitrate, nitrite and phosphate in environmental samples by high performance liquid chromatography with UV detection. *S. Afr. J. Chem.* 71, 79–85. doi:10.17159/0379-4350/2018/v71a10

Moulin, M., Mossou, E., Signor, L., Kieffer-Jaquinod, S., Kwaambwa, H. M., Nermark, F., et al. (2019). Towards a molecular understanding of the water purification properties of *Moringa* seed proteins. *J. Colloid Interface Sci.* 554, 296–304. doi:10.1016/j.jcis.2019.06.071

Nam, P. H., Alejandra, B., Frédéric, H., Didier, B., Olivier, S., and André, P. (2008). A new quantitative and low-cost determination method of nitrate in vegetables, based on deconvolution of UV spectra. *Talanta* 76, 936–940. doi:10.1016/j.talanta.2008.04.048

Nkegbe, E., Emongor, V., and Koorapetsi, I. (2005). Assessment of effluent quality at Glen Valley wastewater treatment plant. *J. Appl. Sci.* 5, 647–650. doi:10.3923/jas.2005.647.650

Nwagbara, V. U., Chigayo, K., Iyama, W. A., and Kwaambwa, H. M. (2022). Removal of lead, cadmium, and copper from water using Moringa oleifera seed biomass. *J. Water Clim. Change* 10, 2747–2760. doi:10.2166/wcc.2022.091

Obuseng, V., Nareetsile, F., and Kwaambwa, H. M. (2012). A study of the removal of heavy metals from aqueous solutions by Moringa oleifera seeds and amine-based ligand 1, 4-bis[N, Nbis(2-picoyl)amino]butane. *Anal. Chim. Acta X.* 730, 87–92. doi:10.1016/j.aca.2012.01.054

Ojewole, J. A., Mawoza, T., Chiwororo, W. D., and Owira, P. M. (2010). Sclerocarya birrea (A. Rich) hochst.['marula'](anacardiaceae): A review of its phytochemistry, pharmacology and toxicology and its ethnomedicinal uses. *Phytother. Res.* 24 (5), 633–639. doi:10.1002/ptr.3080

Okuda, T., Baes, A. U., Nishijima, W., and Okada, M. (2001). Isolation and characterization of coagulant extracted from Moringa oleifera seed by salt solution. *Water Res.* 35 (2), 405–410. doi:10.1016/s0043-1354(00)00290-6

Prasad, S., and Chetty, A. A. (2008). Nitrate-N determination in leafy vegetables: Study of the effects of cooking and freezing. *Food Chem. x.* 106, 772–780. doi:10.1016/j.foodchem.2007.06.005

Qureshi, A. S., Hussain, M. I., Ismail, S., and Khan, Q. M. (2016). Evaluating heavy metal accumulation and potential health risks in vegetables irrigated with treated wastewater. *Chemosphere* 163, 54–61. doi:10.1016/j.chemosphere.2016.07.073

Reck, I. M., Paixão, R. M., Bergamasco, R., Vieira, M. F., and Vieira, A. M. S. (2018). Removal of tartrazine from aqueous solutions using adsorbents based on activated carbon and Moringa oleifera seeds. *J. Clean. Prod.* 171, 85–97. doi:10.1016/j.jclepro.2017.09.237

Redha, A. A. (2020). Removal of heavy metals from aqueous media by biosorption. *Arab. J. Basic Appl. Sci.* 27, 183–193. doi:10.1080/25765299.2020.1756177

Sharma, P., Kumari, P., Srivastava, M. M., and Srivastava, S. (2006). Removal of cadmium from aqueous system by shelled Moringa oleifera Lam. seed powder. *Bioresour. Technol.* 97, 299–305. doi:10.1016/j.biortech.2005.02.034

Singh, B., and Craswell, E. (2021). Fertilizers and nitrate pollution of surface and ground water: An increasingly pervasive global problem. *SN Appl. Sci.* 3, 518. doi:10.1007/s42452-021-04521-8

Singh, K. K., Talat, M., and Hasan, S. H. (2006). Removal of lead from aqueous solutions by agricultural waste maize bran. *Bioresour. Technol.* 97, 2124–2130. doi:10.1016/j.biortech.2005.09.016

Turrión, M. B., Gallardo, J. F., and González, M. I. (1999). Extraction of soil-available phosphate, nitrate, and sulphate ions using ion exchange membranes and determination by ion exchange chromatography. *Commun. Soil Sci. Plant Anal.* 30, 1137–1152. doi:10.1080/00103629909370274

Viotti, P. V., Moreira, W. M., dos Santos, O. A. A., Bergamasco, R., Vieira, A. M. S., and Vieira, M. F. (2019). Diclofenac removal from water by adsorption on Moringa oleifera pods and activated carbon: Mechanism, kinetic and equilibrium study. *J. Clean. Prod.* 219, 809–817. doi:10.1016/j.jclepro.2019.02.129

Won, S. W., Choi, S. B., and Yun, Y-S. (2014). On the reason why acid treatment of biomass enhances the biosorption capacity of cationic pollutants. *Korean J. Chem. Eng.* 31 (1), 68–73. doi:10.1007/s11814-013-0184-7

World Health Organization (2011). Guidelines for drinking-water quality, 4th edition. Available at: http://www.who.int/water_sanitation_health/publications/2011/dwq_guidelines/en/ (Accessed March 03, 2015).

World Health Organization (2017). *Guidelines for drinking - water quality: Fourth edition incorporating the first addendum*. Geneva: World Health Organization. Available at: https://www.who.int/teams/environment-climate-change-and-health/water-sanitation-and-health/water-safety-and-quality/drinking-water-quality-guidelines#:~:text=The%20Guidelines%20for%20drinking-water%20quality%20%28GDWQ%29%20promote%20the,effective%20and%20that%20national%20standards%20are%20being%20met (Accessed July 09, 2022).

Yun, Y., Li, Z., Chen, Y., Saino, M., Cheng, S., and Zheng, L. (2018). Elimination of nitrate in secondary effluent of wastewater treatment plants by Fe0 and Pd-Cu/diatomite. *J. Water Reuse Desalination* 8, 29–37. doi:10.2166/wrd.2016.122

Zorpas, A. A., Kapetanios, E., Zorpas, G. A., Karlis, P., Vlyssides, A., Haralambous, I., et al. (2000). Compost produced from organic fraction of municipal solid waste, primary stabilized sewage sludge and natural zeolite. *J. Hazard. Mat.* 77, 149–159. doi:10.1016/s0304-3894(00)00233-8

Zwain, H. M., Vakili, M., and Dahlan, I. (2014). Waste material adsorbents for zinc removal from wastewater: A comprehensive review. *Int. J. Chem. Eng.* 2014, 347912. doi:10.1155/2014/347912

Advantages of publishing in Frontiers

OPEN ACCESS
Articles are free to read for greatest visibility and readership

FAST PUBLICATION
Around 90 days from submission to decision

HIGH QUALITY PEER-REVIEW
Rigorous, collaborative, and constructive peer-review

TRANSPARENT PEER-REVIEW
Editors and reviewers acknowledged by name on published articles

Frontiers
Avenue du Tribunal-Fédéral 34
1005 Lausanne | Switzerland

Visit us: www.frontiersin.org
Contact us: frontiersin.org/about/contact

REPRODUCIBILITY OF RESEARCH
Support open data and methods to enhance research reproducibility

DIGITAL PUBLISHING
Articles designed for optimal readership across devices

FOLLOW US
@frontiersin

IMPACT METRICS
Advanced article metrics track visibility across digital media

EXTENSIVE PROMOTION
Marketing and promotion of impactful research

LOOP RESEARCH NETWORK
Our network increases your article's readership